

Nanostructure Science and Technology

Series Editor:

David J. Lockwood, FRSC
National Research Council of Canada
Ottawa, Ontario, Canada

For further volumes:

<http://www.springer.com/series/6331>

Marcelo Mario Mariscal • Oscar Alejandro Oviedo
Ezequiel Pedro Marcos Leiva

Metal Clusters and Nanoalloys

From Modeling to Applications

 Springer

Marcelo Mario Mariscal
INFQC-CONICET
Universidad Nacional de Córdoba
Córdoba
Argentina

Oscar Alejandro Oviedo
INFQC-CONICET
Universidad Nacional de Córdoba
Córdoba
Argentina

Ezequiel Pedro Marcos Leiva
INFQC-CONICET
Universidad Nacional de Córdoba
Córdoba
Argentina

ISSN 1571-5744

ISBN 978-1-4614-3267-8

ISBN 978-1-4614-3643-0 (eBook)

DOI 10.1007/978-1-4614-3643-0

Springer New York Heidelberg Dordrecht London

Library of Congress Control Number: 2012938545

© Springer Science+Business Media New York 2013

This work is subject to copyright. All rights are reserved by the Publisher, whether the whole or part of the material is concerned, specifically the rights of translation, reprinting, reuse of illustrations, recitation, broadcasting, reproduction on microfilms or in any other physical way, and transmission or information storage and retrieval, electronic adaptation, computer software, or by similar or dissimilar methodology now known or hereafter developed. Exempted from this legal reservation are brief excerpts in connection with reviews or scholarly analysis or material supplied specifically for the purpose of being entered and executed on a computer system, for exclusive use by the purchaser of the work. Duplication of this publication or parts thereof is permitted only under the provisions of the Copyright Law of the Publisher's location, in its current version, and permission for use must always be obtained from Springer. Permissions for use may be obtained through RightsLink at the Copyright Clearance Center. Violations are liable to prosecution under the respective Copyright Law.

The use of general descriptive names, registered names, trademarks, service marks, etc. in this publication does not imply, even in the absence of a specific statement, that such names are exempt from the relevant protective laws and regulations and therefore free for general use.

While the advice and information in this book are believed to be true and accurate at the date of publication, neither the authors nor the editors nor the publisher can accept any legal responsibility for any errors or omissions that may be made. The publisher makes no warranty, express or implied, with respect to the material contained herein.

Printed on acid-free paper

Springer is part of Springer Science+Business Media (www.springer.com)

Preface

Exceeding the limits of the academic realm where it started, the “nanowave” or current nanotechnology trend, has already reached the industrial and governmental markets and nanotechnology has thus become a key area of public interest, since not only researchers—but also politicians and economists—have realized the social and economic implications of the developments in this field. In fact, *Think nano to earn giga* will probably become one of the favorite expressions in the business world in the future, as it is widely accepted that—after microtechnology—nanotechnology is the technology of the next century. Metallic and semiconducting nanoparticles—subject of the present book—currently represent one of the most tangible applications in nanotechnology.

From the point of view of academic research, nanoparticles show remarkable properties due to the transition from the atomic quantum mechanical behavior to the classical behavior which governs bulk materials, making them ideal candidates for testing and developing new theories.

In particular, metallic nanoparticles seem to be promising materials for potential applications in various technological areas related to different spheres of human life ranging from catalysis of chemical reactions to cancer detection and healing

As it usually happens in cases of hasty technological developments, the urge for generating these new nanomaterials is so strong that in many cases things are put to work—and they work pretty well!—without much wondering about the subtle reasons behind such results. After all, life evolution, a typical nanophenomenon, just happened that way. This lack of modeling of nanophenomena—as compared to the abundant experimental research—is of course not on purpose, but rather the result of the intrinsic complexity of modeling systems and situations where chemical and physical phenomena are strongly entangled. For instance, light absorption by nanoparticles, a typical physical phenomenon, may be found to be strongly modified by the chemical nature of molecules chemically bound to them. Thus, the quantum physical tools usually used to study the collective excitation of electrons in a metal must be coupled with the quantum chemical tools that describe binding in molecules, a challenge addressed in this book.

Awakening the interest of experimental researchers in the newest modeling tools applied to metal nanoparticles is one of the main goals of the present book. Thus, in ten chapters written by experts in the field we present the most advanced techniques employed to model and simulate metallic nanoparticles, with emphasis on their application to experimental results. These tools range from statistical mechanics and molecular dynamic simulations to very specific quantum mechanical calculations.

Since many of the topics represent cutting edge research developments, we hope this work will help fill the existing gap between theory and experiment of nanosystems, promoting fruitful exchanges between both approaches.

Córdoba, Argentina

Marcelo Mario Mariscal
Oscar Alejandro Oviedo
Ezequiel Pedro Marcos Leiva

Contents

Part I Recent Advances in High Resolution Electron Microscopy

- 1 Experimental and Simulated Electron Microscopy in the Study of Metal Nanostructures** 3
Sergio Mejía-Rosales and Miguel José-Yacamán

Part II Electron Structure, Optics, and Magnetism

- 2 Density-Functional Theory of Free and Supported Metal Nanoclusters and Nanoalloys** 29
Alessandro Fortunelli and Giovanni Barcaro
- 3 Closed-Shell Metal Clusters** 81
René Fournier and Satya Bulusu
- 4 Optical Properties of Metal Nanoclusters from an Atomistic Point of View** 105
Christian F.A. Negre and Cristián G. Sánchez
- 5 Spin-Fluctuation Theory of Cluster Magnetism** 159
R. Garibay-Alonso, J. Dorantes-Dávila, and G.M. Pastor

Part III Thermodynamics and Kinetics Using Semiempirical Approaches

- 6 Global Optimization of Free and Supported Clusters** 195
Riccardo Ferrando
- 7 Structure and Chemical Ordering in Nanoalloys: Toward Nanoalloy Phase Diagrams** 215
Christine Mottet

8	Modelling Janus Nanoparticles	243
	Francesca Baletto	
9	Modeling of Protected Nanoparticles	275
	Jimena A. Olmos-Asar and Marcelo M. Mariscal	
10	Thermodynamic Modeling of Metallic Nanoclusters	305
	Oscar A. Oviedo and Ezequiel P.M. Leiva	
	Index	351

Part I
Recent Advances in High Resolution
Electron Microscopy

Chapter 1

Experimental and Simulated Electron Microscopy in the Study of Metal Nanostructures

Sergio Mejía-Rosales and Miguel José-Yacamán

1.1 Introduction

One of the most exciting features of nanostructures relays on the fact that matter organized as objects at the nanoscale may have chemical and physical properties different from those of the same material in its common bulk presentation. This size-dependent properties are related to several physical phenomena, such as quantum behavior, high surface-to-volume ratio, and thermal effects [1, 2]. Far from being an unfortunate fact, the unique properties of nanostructures may in principle be fine-tuned to be used for a specific purpose, but to be able to dominate matter at this range of sizes, high precision tools must be used in order to investigate, measure, and modify the physical and chemical characteristics of the nanostructures. The problem is similar to the one of constructing a phase diagram for the bulk materials, but taking also into consideration size and shape, besides temperature and crystalline structure. Several groups have concentrated some of their efforts to this task (with varying degrees of success), but these attempts are inherently incomplete or, at best, restricted to one specific material and to a narrow range of sizes and temperatures [3, 4]. On the other hand, these studies are generally based either on theoretical results or on indirect experimental measurements, and there is just a relatively small number of papers that concentrate on first-hand measurements of the detailed crystal structure and local chemical composition of the nanostructures. This is, to certain degree, understandable: A detailed analysis of the structure and composition

S. Mejía-Rosales (✉)

Center for Innovation and Research in Engineering and Technology, and CICFIM-Facultad de Ciencias Físico-Matemáticas, Universidad Autónoma de Nuevo León, San Nicolás de los Garza, NL 66450, México
e-mail: sergio.mejiars@uanl.edu.mx

M. José-Yacamán

Department of Physics and Astronomy, University of Texas at San Antonio,
One UTSA Circle, San Antonio, TX 78249, USA
e-mail: miguel.yacaman@utsa.edu

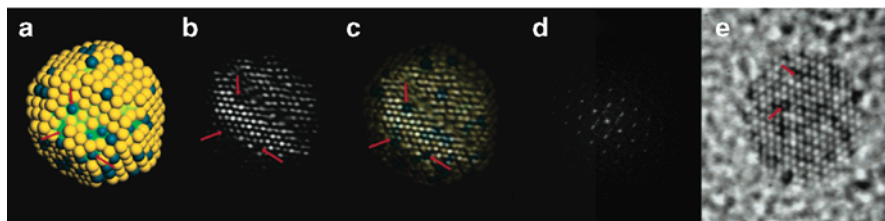


Fig. 1.1 (a) Model of AuPd particle of 923 atoms used to simulate the features of the particle shown in (e); (b) the corresponding simulated TEM image; (c) overlap of parts (a) and (b); (d) calculated FFT pattern for the simulated particle. In the model, blue spheres represent Pd atoms, and yellow spheres correspond to Au atoms. Reprinted with permission from [6]. Copyright 2007 American Chemical Society

requires sub-nanometric resolution, and the electron microscopy facilities capable of reaching this resolution are not always easy to access. Besides, the interpretation of the electron micrographs is not always straightforward, since the intensity signal that correlates with the atomic positions depends not only on the length of the atomic columns parallel to the direction of the electron beam, but also on the chemical species, and on the microscope's parameters at which the micrograph was obtained [5]. Thus, the solution to the problem of extracting a third dimension from the information contained in a strictly two-dimensional image has to be similar to the one that the human mind uses to recognize macroscopic objects sensed by the naked eye: through (a) the comparison of the observed patterns against simple models acquired by previous experience or inherited, and (b) the rough estimation of the probability of a particular model to correspond to the pattern, taking into consideration a small set of rules. An example of this use is shown in Fig. 1.1, taken from [6]. Here, a TEM micrograph of a gold-palladium nanoparticle of 2 nm of diameter shows that some specific spots on the particle have a different intensity from the rest (Fig. 1.1e); a model is proposed in Fig. 1.1a, and a simulated TEM micrograph, shown in Fig. 1.1b, is obtained. The image of the ball-and-stick model is superposed on the simulated TEM image (Fig. 1.1c), and a correlation is found between the position of the spots and some specific sites at the surface of the particle, where a Pd atom is surrounded by Au atoms that are not in the same plane of the Pd atom. It is likely that these specific isolated Pd sites have a relevant effect on the chemical activity of the particle, and at least one theoretical study has investigated these kind of sites [7].

In Fig. 1.1, as in the other figures where we present simulated TEM micrographs, we used the SimulaTEM program developed by Gómez-Rodríguez et al. that, unlike other programs with similar purposes, allows non-periodic structures as input [8]. The principles underlying the creation of this kind of simulated TEM micrographs (and also the real ones) will be discussed in the following sections.

This chapter deals with the specific issues that need to be considered in order to make an adequate interpretation of the micrograph of a nanostructure, with a particular emphasis in the imaging of nanoalloys. We will concentrate in the use of high angular annular dark field scanning transmission electron microscopy

(HAADF-STEM) imaging, since in this technique the electron signal is strongly dependent on Z , the atomic number of the atoms that form the structure [9], which makes it the most appropriate choice for the study of metal nanoparticles.

This review does not intend to be a complete essay on the simulation of electron microscopy but a hands-on guide for researchers interested in the generation of high resolution electron micrographs of metal nanostructures. In accordance with this approach, we will only discuss briefly the working principles of electron microscopy, the role of aberration correctors, and how the theory supporting the imaging of micrographs can be used to simulate the imaging process, to concentrate later on the practical issues to be taken into consideration in the comparison and interpretation of real and simulated electron micrographs of nanostructures. The first sections give a comprehensive (but incomplete) review of the fundamental concepts related to the TEM and HAADF-STEM techniques, and to the multislice method of simulation. The remaining sections will discuss the use of real and simulated HAADF-STEM micrographs for the recognition of nanoalloys, using for this purpose several examples of shapes, sizes, and compositions.

1.2 The Transmission Electron Microscope in a Nutshell

In order to study the structure of matter at Angstrom and even sub-Angstrom resolution, a beam with a wavelength on the same order of magnitude is needed. The electron microscope accelerates electrons with a potential difference of several hundreds of kV in order to produce a beam with this range of energies. In modern electron microscopes, the electrons are usually produced by a cold field-emission gun. The beam is filtered to make it practically monochromatic, and a system of condenser lenses narrows the beam divergence angle. The resulting beam interacts with the specimen, and the transmitted beam is collected by an objective lens and projected to the image plane, normally a ccd array. A simplified schematic diagram is shown in Fig. 1.2.

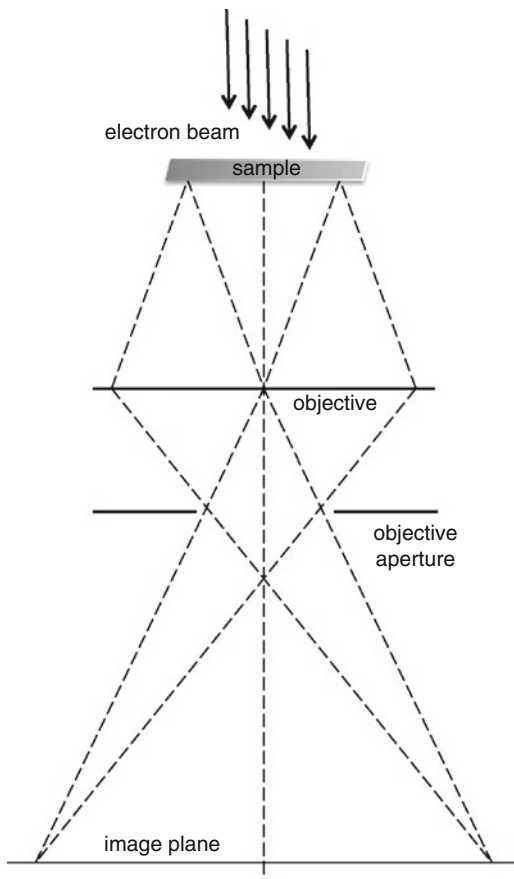
The electron beam interaction with the sample is better understood if one considers the sample electrostatic potential or, more specifically, the projected potential of the sample. Let's assume as a starting point that the sample is a periodic crystal, and that its electrostatic potential is described by $\phi(r)$. The projected potential will of course depend on the structural information of the sample, and also on the temperature. Then, the interaction of an electron of relativistic mass m with the sample is described by

$$\left[-\frac{\hbar^2}{8\pi^2 m} \nabla^2 - e\phi(r) \right] \Psi(r) = E\Psi(r),$$

with the original electron wave described by a simple plane wave:

$$\Psi_0(r) = \exp\{i(\omega t - 2\pi k_0 \cdot r)\}.$$

Fig. 1.2 An overly simplified diagram of the conventional transmission electron microscope



The solution to the Schrodinger equation will describe the electron wave function after interacting with the sample. Even with the periodicity assumption, the solution cannot be found directly without making additional simplifications. We will come back to this point in the section devoted to approximation methods of calculation.

The objective lens, located after the sample in a TEM, focuses the electron beam, which mathematically can be described by the Fourier transform of the wave at the exit of the sample. The objective lens is far from a perfect lens, and it will introduce aberrations in the image-plane wavefunction (the optical elements after the condenser lens, in charge of the amplification, won't produce important aberrations to the image). High resolution microscopes include in their design aberration correctors that make sub-Angstrom resolution possible. In an ideal microscope, without any aberrations, the image observed will be directly related to the squared modulus of the image-plane wavefunction [5].

1.3 Aberrations

Aberrations will occur, though, and this implies that not all the Fourier components of the wave function will transfer equally. The contrast transfer function (CTF) is a broadly used quantity that determines the range of characteristic spatial frequencies that can be directly interpreted in a TEM image. In other words, the CTF imposes the conditions at which “what you see is what you get.” In a concise way, the electron wave function at the image plane will be related to the CTF applied to the wavefunction just at the exit of the sample. Objective apertures will affect the CTF, as well as the spatial coherence of the electron beam and its wavelength:

$$CTF(k) = -\sin \left[\frac{\pi}{2} C_s \lambda^3 k^4 + \pi \Delta z \lambda k^2 \right].$$

Here, C_s is the spherical aberration of the objective lens, and Δz is its defocus. The special case where

$$\Delta z = -\sqrt{4/3 C_s \lambda}$$

is known as the Scherzer condition, and at Scherzer defocus the CTF does not change its sign in a large spatial frequency range, and hence all distances in this range can be interpreted directly as they appear in the image [5, 10]. Figure 1.3 shows the plot of two CTF, calculated for two different values of C_s . Both graphs were calculated at the same voltage (200 kV). The dark blue CTF was generated

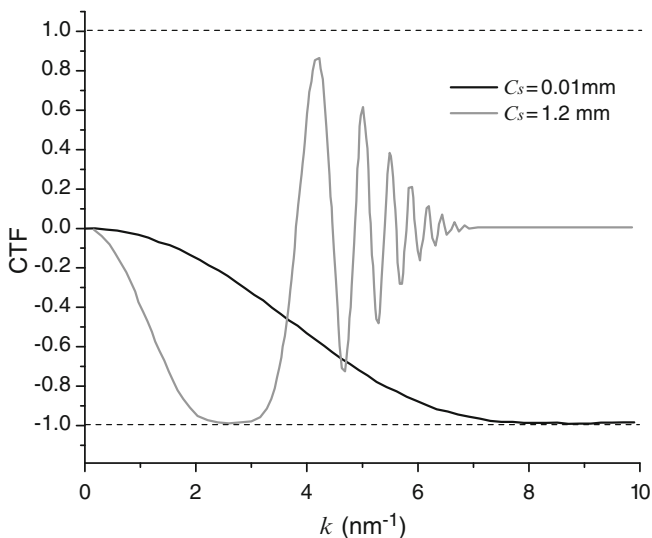


Fig. 1.3 Contrast transfer functions (CTF) for two different values of C_s . The darker line represents a CTF calculated at a C_s of 0.01 mm, and the lighter wavy line was calculated at a C_s of 1.2 mm. Both CTFs were obtained at Scherzer conditions

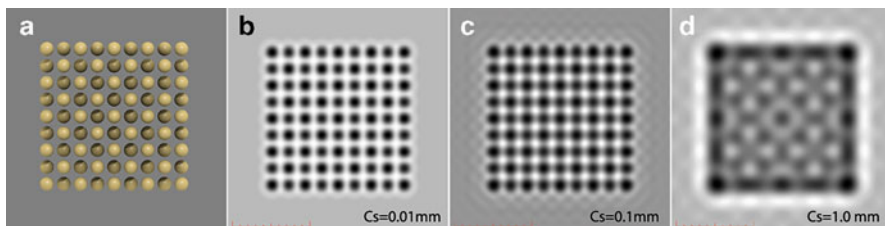


Fig. 1.4 HRTEM simulation of a cubic fcc gold nanostructure obtained at three different values of C_s aberration; (a) Toy representation of the nanostructure, and simulated TEM micrographs with (b) 0.01 mm of C_s aberration; (c) 0.1 mm of C_s aberration; (d) 1.0 mm of C_s aberration. All the micrographs were simulated at the Scherzer condition

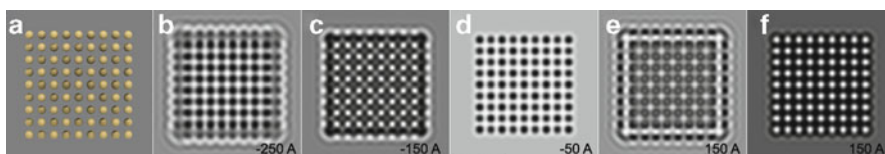


Fig. 1.5 HRTEM simulations of a cubic fcc gold nanostructure calculated at different defocus values. The image labeled as (d) corresponds to the Scherzer defocus

for a C_s of just 0.01 mm, trying to simulate the conditions in a C_s -corrected TEM. In this virtual TEM, the theoretical resolution is of 0.08 nm. The light blue CTF was calculated with a C_s of 1.2 mm, for comparison purposes. In this case, the theoretical resolution is 0.25 nm, not quite good for the measurement of interatomic distances. Both CTFs were obtained at Scherzer conditions. The curves were plotted using the CtfExplorer software created by M. V. Sidorov [11].

The generation of TEM images at the Scherzer condition allows that atomic positions to correspond with dark spots in the micrograph, if the beam is parallel to the axis zone and the aberrations are small. The effect of aberrations in the resolution should be obvious from the CTF, but it is always interesting to see this effect directly on the images, real or simulated. A comparison of three simulated TEM micrographs is made in Fig. 1.4 for the same sample, a small fcc cubic volume of gold atoms. The figure shows that even at Scherzer defocus the images are difficult to interpret if aberrations are not as small as in Fig. 1.4b, and that the effect of spherical aberration may appear particularly remarked at the border of the structure.

Figure 1.5 shows the results of conventional HRTEM simulations of a section of a gold lattice at different values of defocus, Scherzer included (-50 Angstrom). The voltage was 200 kV at all cases, and a small C_s aberration of 0.01 mm was used, with zero astigmatism. At Scherzer defocus, the atomic columns are completely resolved, even at the surface of the structure.

1.4 High Angle Annular Dark Field Scanning Transmission Electron Microscope

From the point of view of the reciprocity theorem, the STEM is optically equivalent to an inverted TEM, in the sense that if the source and the detector exchange positions, the electron ray paths remain the same [10]. In the STEM, the objective lens—and all the relevant optics—is positioned before the specimen (see Fig. 1.6). For the specific case of the Annular Dark Field (ADF) detector, only the electrons scattered between $\theta_1 \leq \theta \leq \theta_2$ contribute to the image, since these are the electrons that reach the annular detector. Working at 200 kV (appropriate for imaging metals), in a typical HAADF-STEM microscope the inner angle θ_1 of the ADF detector is set around 50 mrad, and the outer angle θ_2 is set around 100–200 mrad. At these range of voltages, the electrons momentum is large enough to require a relativistic treatment, and the use of Schrödinger equation to analyze the system is not completely correct without some adjustments at the values of mass and wavelength (strictly speaking, one should use the relativistic Dirac equation instead of Schrödinger's, but this would greatly complicate the already nontrivial set of equations.)

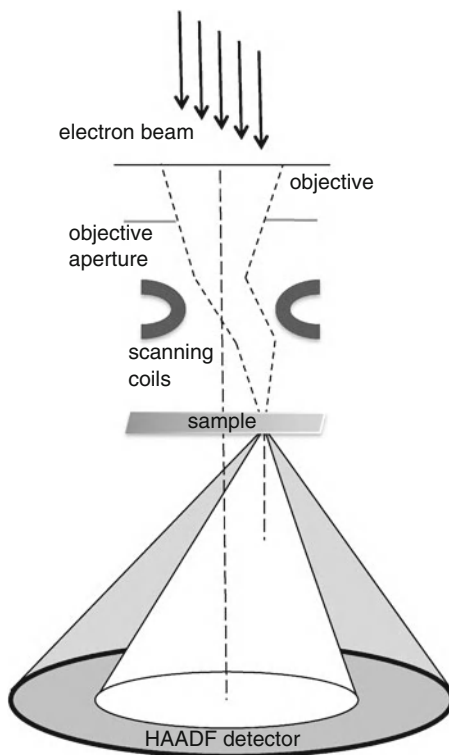


Fig. 1.6 Simplified diagram representing the functioning principle of the HAADF-STEM microscope

STEM differs from conventional TEM in that, unlike conventional TEM, the electron beam interacts only with a small section of the sample at a time, and the scan process is the one in charge of generating the image as a whole.

But even before taking care of the scanning issue, it is appropriate to review the different methods used to simulate the imaging process of a single area section of the sample. Some approximations are needed in each of these methods, and here we will present them in a succinct way. The reader is encouraged to review elsewhere the details of the methods and the justifications behind the approximations [10].

1.5 Approximation Methods

In the Weak Phase Object (WPO) approximation, useful for very thin samples, it is assumed that the electrons are scattered only once by the sample, so the projected potential can be averaged. When the observed sample can be regarded as a WPO, the image is linearly related to the object wavefunction. Even though this is not strictly the case in nanometer-sized structures, we will nevertheless follow this approach, and additional considerations will be taken later.

First, we can assume that the linear image approximation is valid, which means that we take as valid that the intensity $g(r)$ on the image is obtained by a linear convolution of the ideal image of the sample $f(r)$ with the point spread function of the microscope $h(r)$:

$$g(r) = \int f(r') h(r-r') \, dr' = f(r) \otimes h(r-r');$$

or, in reciprocal space,

$$G(u) = H(u)F(u).$$

$F(u)$ is the Fourier transform of the specimen function, and $H(u)$ is the CTF. The reciprocal vector \mathbf{u} is the spatial frequency. The fact that the intensity on the image is the convolution of $f(r)$ and $h(r)$ means that each point in the image is a collective result of the whole of the sample.

In the WPO approximation, the specimen function is approximated by

$$f(x,y) = 1 - i\sigma V_t(x,y),$$

where the projected potential $V_t(x,y)$ is very small since the sample is very thin. But of course, this is not the case in the imaging of metal nanoparticles.

In the Bloch Wave Approximation, the electron wavefunctions are considered as linear combination of Bloch waves, and each reflection is considered explicitly. The BWA is extensively used in periodic systems, but the computing time scales at N^3 , where N is the number of Bloch waves. Several simulation packages, such as JEMS, have implemented BWA in an efficient manner [12].

1.6 The Multislice Method

The basic idea underlying the multislice method is that the potential of the sample can be approximated by defining a number of slices of thickness dz , and projecting the potential due to the atoms of a particular slice to the central plane of this slice (see Fig. 1.7).

Thus, a solution to the electron wavefunction is obtained for one slice, and used as input for the calculation of the next slice [13]. This means that the choice of very thick slices will speed up the calculations, but the potential function will be poorly approximated. On the other hand, the use of very thin slices will improve the calculation of the projected potential, but the errors due to approximations will accumulate and undermine the final result. The appropriate choice of the number of slices is an issue that requires a generous amount of effort and computing time, and the final decision must consider the benefits of a fast calculation (STEM simulations by the very nature of the technique are computationally expensive and the computing time depends on both the number of slices and the scan resolution) against the benefits of a very precise calculation (that may be critical in quantitative

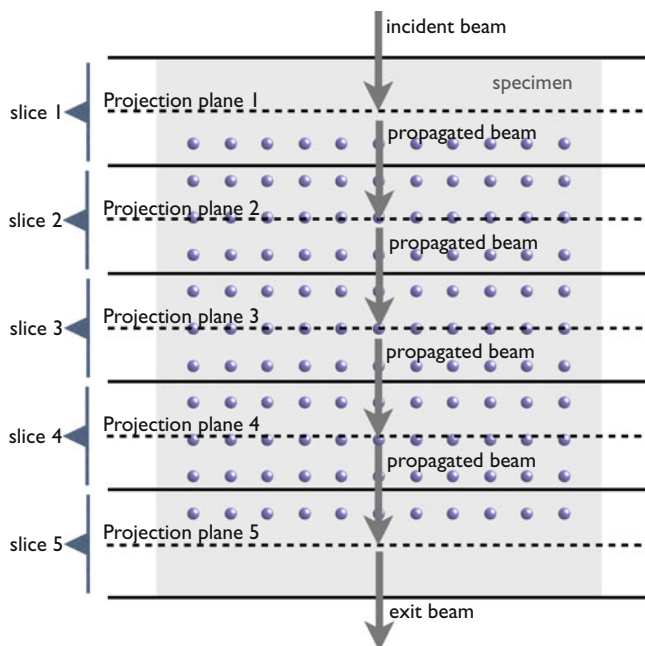


Fig. 1.7 The principle of the multislice method. The sample is sliced, and the potential due to the atoms of a particular slice is projected on a plane; the electron wavefunction corresponding to that slice is then used as input for the interaction with the next slice

STEM). As pointed out by Ishizuka [14], the multislice method requires several approximations that could be critical in the interpretation of results for inclined illumination, so the orientation of the sample may also affect the final result.

1.7 STEM Intensity Dependence on Atomic Number

In a series of papers in the 1970s by Crewe et al., it was found that the annular detector in a HAADF-STEM microscope collects a large amount of the elastic scattered electrons, in such a way that the intensity of the signal collected by the HAADF detector will have a dependence on the scattering cross section, and thus on the atomic number of the atoms present in the sample [15]. Pennycook, one of the pioneers in the technique, gives arguments to this dependence to be close to $Z^{3/2}$ (see [9]). In order to investigate how the intensity signal generated by the HAADF detector depends on the atomic number of a column formed by just one atom of a specific element, we performed a simulation of HAADF for a system of 16 isolated atoms laying on a plane perpendicular to the microscope column. The resulting image is shown in Fig. 1.8, where the positions of the atoms are labeled by the symbols of their respective chemical element.

The HAADF image intensity measured over a line that passes through the center of the atomic positions is shown in Fig. 1.9. Here, it can easily be noted that the contrast between heavy and light atoms is remarkably high.

The maxima in Fig. 1.9 are plotted against the atomic numbers in Fig. 1.10, and a least squares adjustment shows that the HAADF signal follows approximately a $Z^{1.46}$ relation. This dependence is very close to the prediction of Pennycook.

All of the STEM simulations shown and discussed in this chapter, including the simulations presented in the next sections, were made using the commercial version of the xHREM package, a proprietary software designed and coded by Ishizuka [14]. The xHREM suite uses an algorithm based on the Fast Fourier Transform method, and it allows the use of a large number of slices, as many as 1,000 in the latest editions.

1.8 The Interpretation of an Image

How can we infer the shapes, sizes, and composition of the objects studied under the electron microscope? The problem of interpretation of electron micrographs is similar to the problem that the human mind has to solve to make a correct interpretation of the two-dimensional images imprinted on the retina. As the experimental psychologist Steven Pinker puts it: *Optics is easy but inverse optics impossible* [16]. The solution to this factual impossibility lays on the capacity of the human mind to make educated assumptions about the observed objects and their surroundings, or, as Pinker explains,

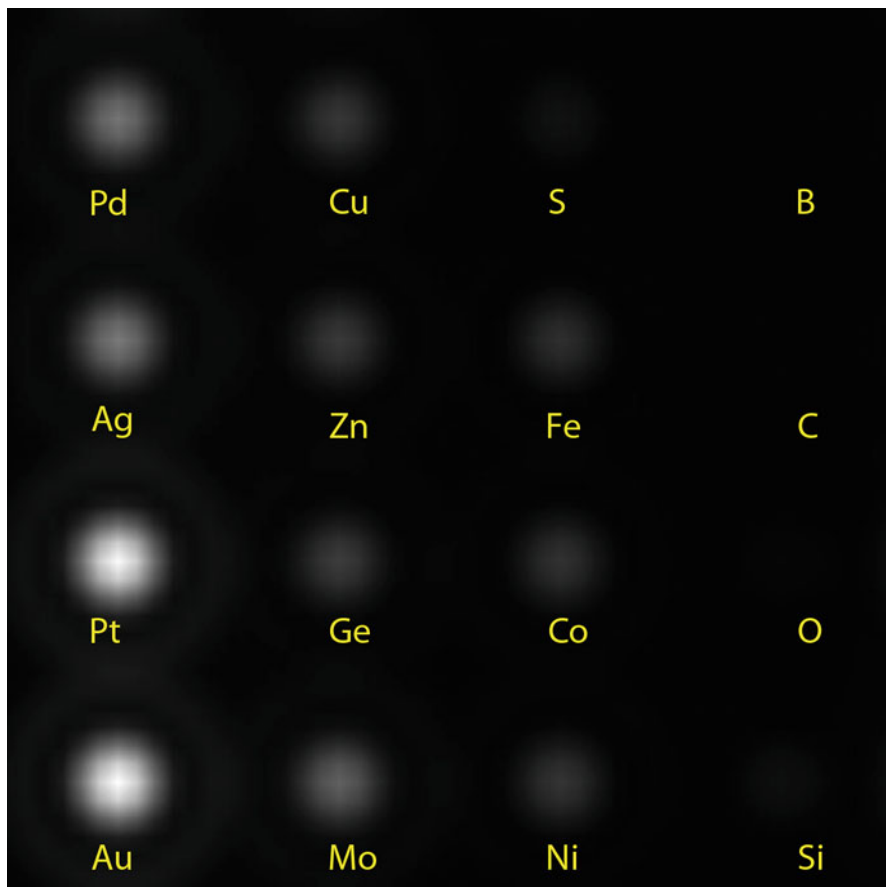


Fig. 1.8 STEM-simulated micrograph showing the intensity signal due to the presence of atoms of different elements

“The answer is that *the brain supplies the missing information*, information about the world we evolved in and how it reflects light. If the visual brain “assumes” that it is living in a certain kind of world—an evenly lit world made mostly of rigid part with smooth, uniformly colored surfaces—it can make good guesses about what is out there.” [16]

The interpretation of the electron microscope images must be made under the same kind of assumptions: As a first approximation, one considers that the nanostructures are laying on an even surface (usually carbon), and that in inner regions of the nanostructure and far from twin boundaries, point-defects and dislocations, the atomic arrangement is close to that of the bulk. Furthermore, it is assumed that the electron beam and the nanoparticle, like the human visual brain, live *in a certain kind of world* where some geometries are more expected than others.

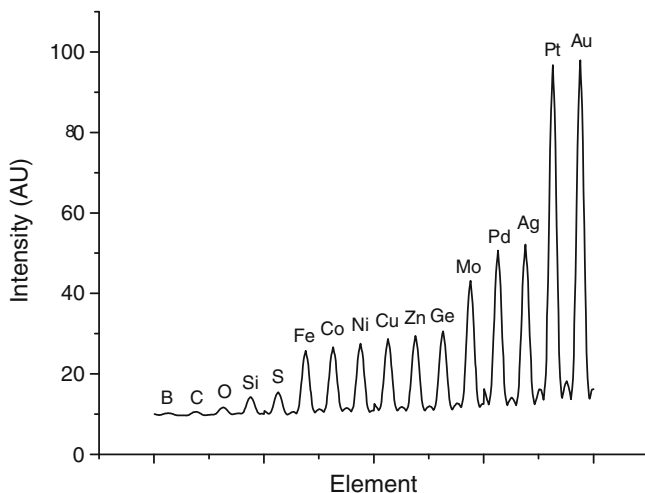


Fig. 1.9 HAADF-STEM intensity signal (arbitrary units) for several chemical elements

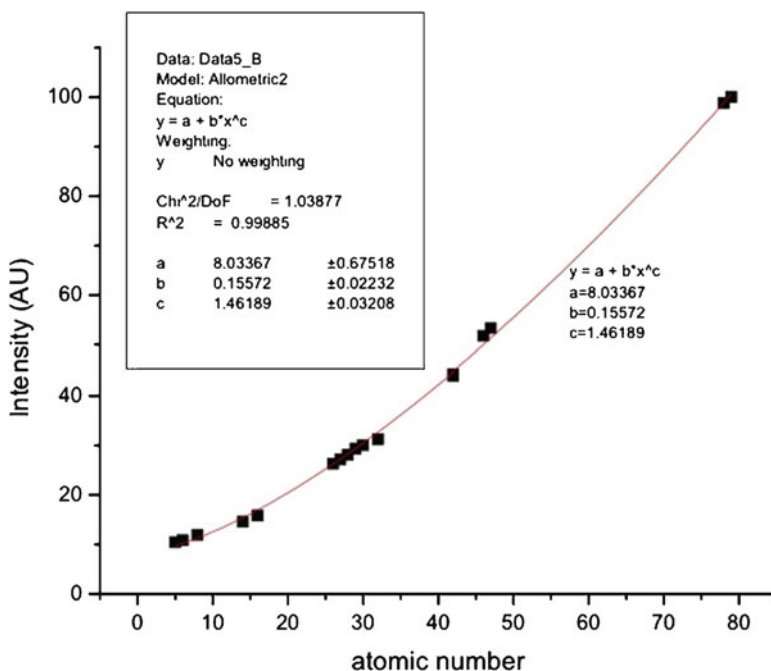


Fig. 1.10 STEM intensity vs. atomic number obtained by STEM simulation. The least-squared regression predicts an intensity dependence as $Z^{1.46}$

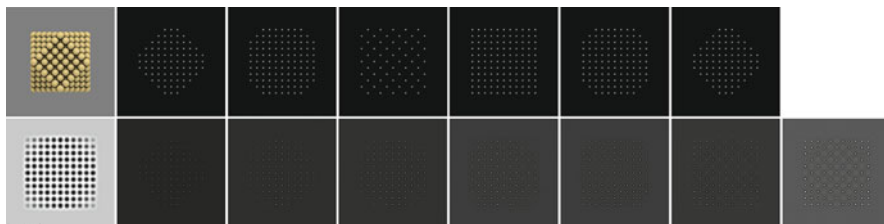


Fig. 1.11 Upper row: Atomistic model of a cuboctahedral gold nanoparticle, and the calculated projected potentials for each slice. Lower row: Output wavefunctions of each slice. The model was divided into ten slices, but only the nontrivial ones are presented

As it was mentioned before, the approximations used in the different simulation techniques are strictly true only when the sample is thin enough for the linear assumption to be correct. One of the most common approaches to implement HRTEM simulation take this assumption as the starting point, and for instruction purposes, the discussion of other difficulties will be avoided. The reader is encouraged to read the excellent text by Kirkland on this matter [10]. On the remaining of this section, we will concentrate on the use of the multislice method for the simulation of HAADF-STEM micrographs, and on the technical issues that may simplify—or make practically impossible—an interpretation of a simulated image.

1.8.1 *The Problem of Slicing a Sample*

As was pointed out before, in the multislice method the sample is dissected into several slices, each treated independently through an averaged projected potential. The selection of the number of slices is a tricky job, and it will depend on the thickness of the sample (the size of the nanostructure in the case of metal nanoparticles), the orientation, and the computational capabilities. The projected potential is calculated for each slice, and the corresponding output wavefunction is obtained. Figure 1.11 shows the result of the calculation of potentials and wavefunctions for a model of a gold cuboctahedral nanoparticle. The model was dissected into ten slices (only the relevant ones are represented in the figure).

If the number of slices is increased, the number of projected potentials will increase as well. This will reflect on the final result of the image, as can be seen in Fig. 1.12, where a model of an icosahedral gold particle—shown in Fig. 1.12a—was used to generate two simulated STEM micrographs, being the only difference between both the number of slices, 10 in (b), 20 in (c). It is not a simple task to find out which of the images follows in a better way the experimental one, since the orientation and lattice parameters must be considered.

For the rest of the chapter, in order to compare the figures related with the Z-contrast in STEM, we will use STEM simulations where the samples have been

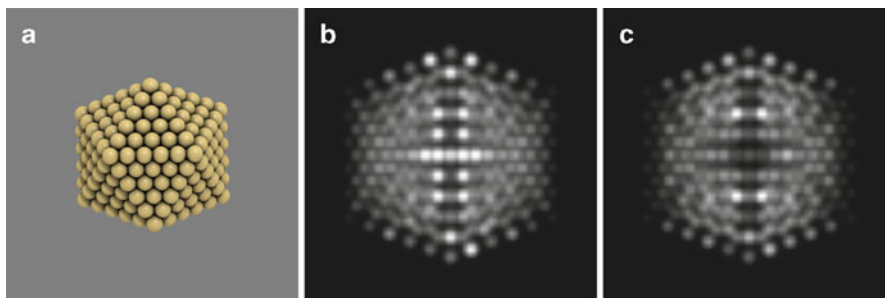


Fig. 1.12 (a) Atomistic model of an icosahedral gold nanoparticle; (b) STEM simulation of the nanoparticle, using ten slices; (c) STEM simulation of the nanoparticle, using 20 slices

divided into ten slices, irrespective of the model being used in the simulations. We encourage the reader interested in the multislice method to dedicate generous amounts of time to try out different slicing possibilities.

1.8.2 Orientations

One of the first pieces of information that appear when analyzing electron micrographs of metal nanostructures is that there is a remarked tendency for the particles to appear with some specific geometries. The reason for this tendency is mostly energetic (apparently these geometries imply the best compromise between surface energy, conservation of crystal structure, energy of twinning boundaries, and surface/volume ratio), but it is well established that the specific geometry depends not only on the chemical constitution of the particle, but also on its size, and on the specific details of the kinetics involved in the synthesis process [2]. Typical geometries in mono and multimetallic particles include decahedra, icosahedra, tetrahedral, and cuboctahedra. How evident the shape of a particle is depends on how close is the particle to the ideal geometry, and also on the orientation of the particle with respect to the electron beam. Figure 1.13 exemplifies this for the case of a small icosahedral gold particle.

1.8.3 Chemical Composition

Returning back to the issue of the Z-contrast dependency on STEM, we take advantage of the previous figure to compare it against the simulated STEM micrographs of particles of the same size and shape, but with different composition. Figure 1.14 shows the STEM-simulated images of an icosahedral $\text{Au}_{\text{core}} - \text{Pd}_{\text{shell}}$ particle, at the same orientations used in Fig. 1.13. The orientation of (b) and (b')

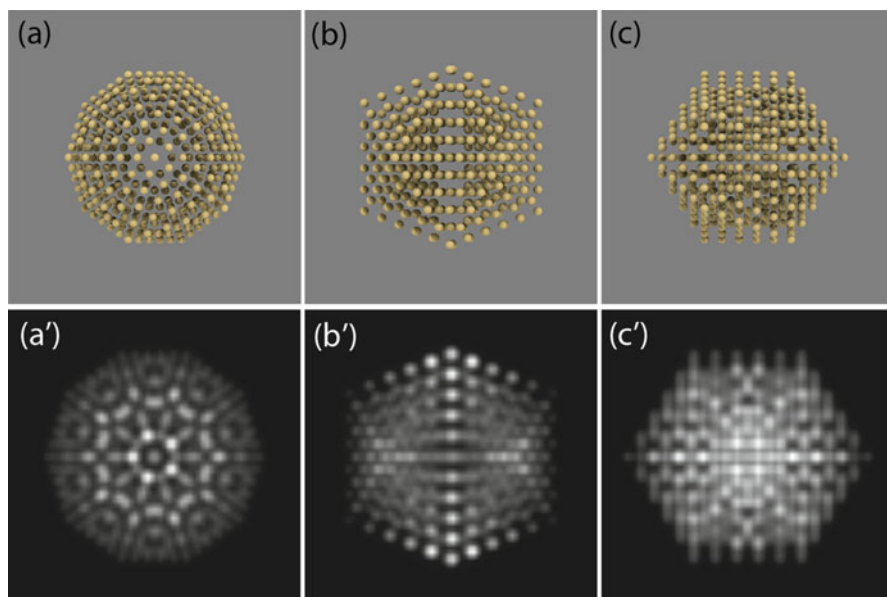


Fig. 1.13 Icosahedral gold nanoparticle at three different orientations, and their corresponding STEM-simulated images

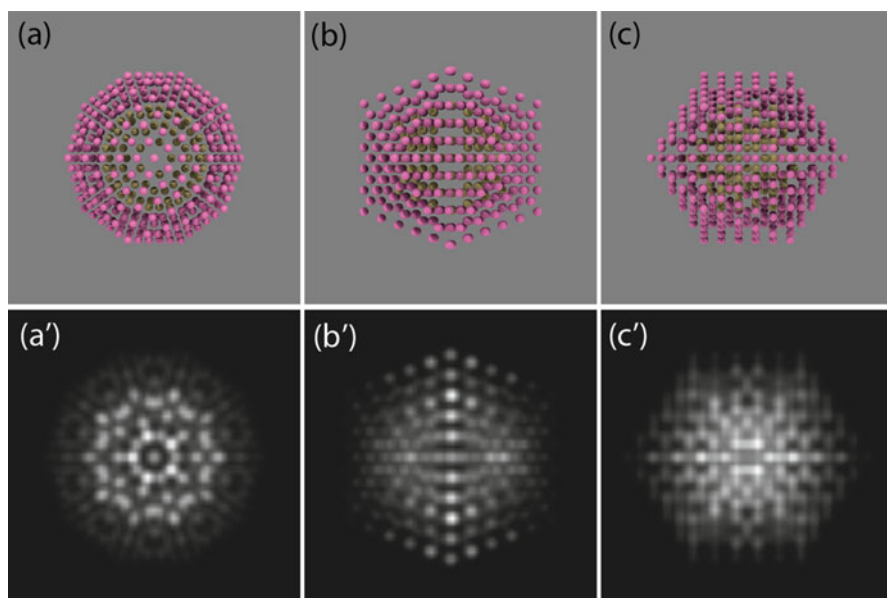


Fig. 1.14 Au_{core} - Pd_{shell} nanoparticle at three different orientations, and their corresponding STEM-simulated images

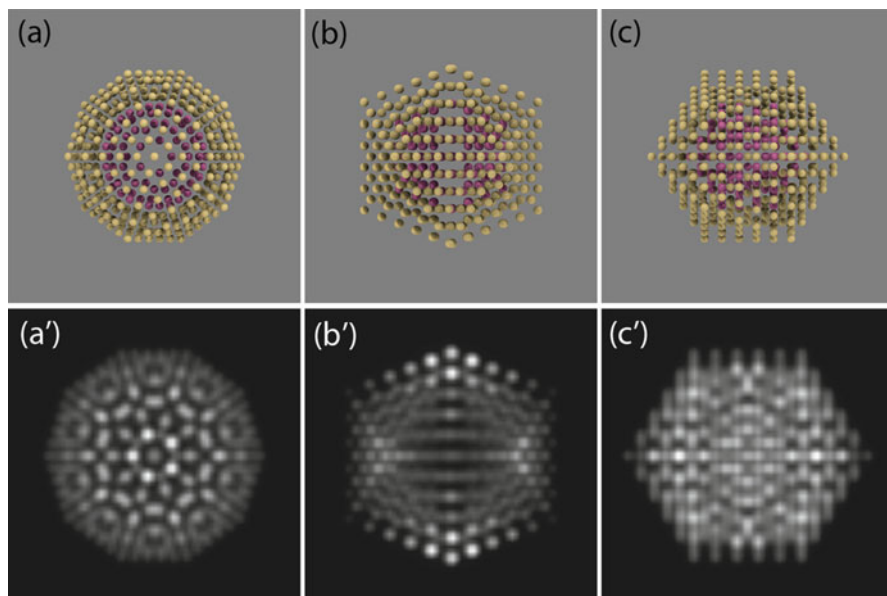


Fig. 1.15 Pd_{core} – Au_{shell} nanoparticle at three different orientations, and their corresponding STEM-simulated images

is 30° with respect to (a), and (c) and (c') are rotated 90° with respect to (a). The difference in intensity between core and shell are evident.

A particle with the opposite relative concentration is used in the STEM simulations shown in Fig. 1.15. Here, the particle's core and shell are not as easily distinguishable as in the previous case, since, unlike the opposite composition, the thickness of the gold regions compensates the difference in the atomic number of the elements (see Fig. 1.16).

The signal generated by a true Au-Pd nanoalloyed particle is different enough from the core-shell cases to be directly identified. Figure 1.17 shows the results of the STEM simulations for this particle. The relative composition of this particle is close to 50%–50%, and both species are distributed randomly along the whole of the particle.

How can the Z-contrast capabilities of HAADF-STEM be used in the investigation of real metal particles? As an example, consider the Au-Co particle presented in Fig. 1.18a. This particle was produced by the coalescence of a gold particle with a cobalt particle, both originally synthesized by inert gas condensation and deposited on a carbon substrate. After deposition, the system was subjected to a heating process [17]. The particle in Fig. 1.18a is shown in false colors to remark the differences in intensity (red is more intense, blue is less intense). Chemical analysis showed that the low intensity regions were rich in cobalt and oxygen—the cobalt oxidized with the thermal treatment—while the high intensity region was rich in gold. A model consisting on a decahedron with a gold core and a CoO external region was prepared

Fig. 1.16 Diagram of a $\text{Pd}_{\text{core}} - \text{Au}_{\text{shell}}$ nanoparticle, showing that gold volume fraction explains the poor contrast between core and shell in a STEM micrograph

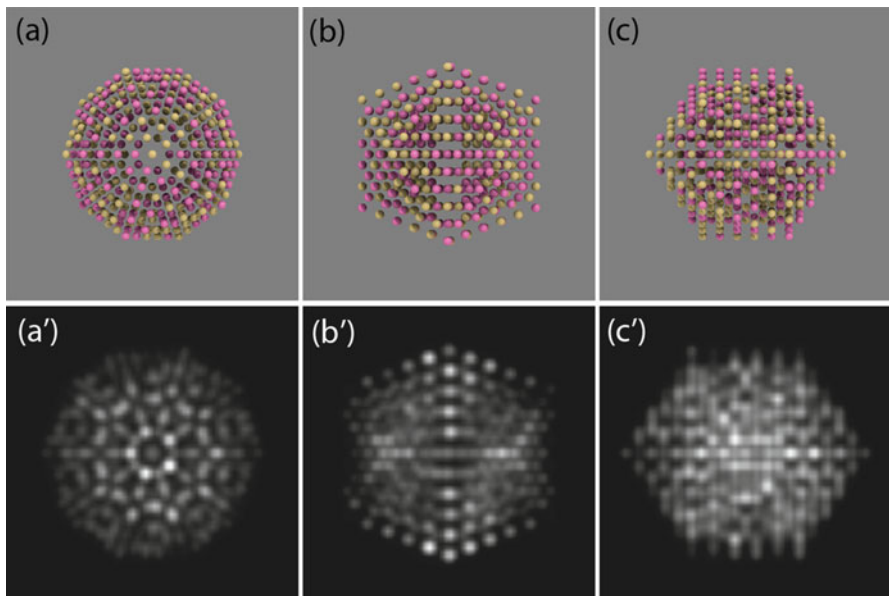
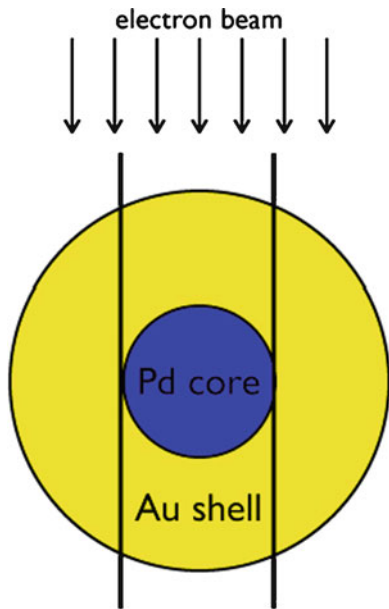


Fig. 1.17 Nanoalloyed Au-Pd icosahedral nanoparticle at three different orientations, and their corresponding STEM-simulated images

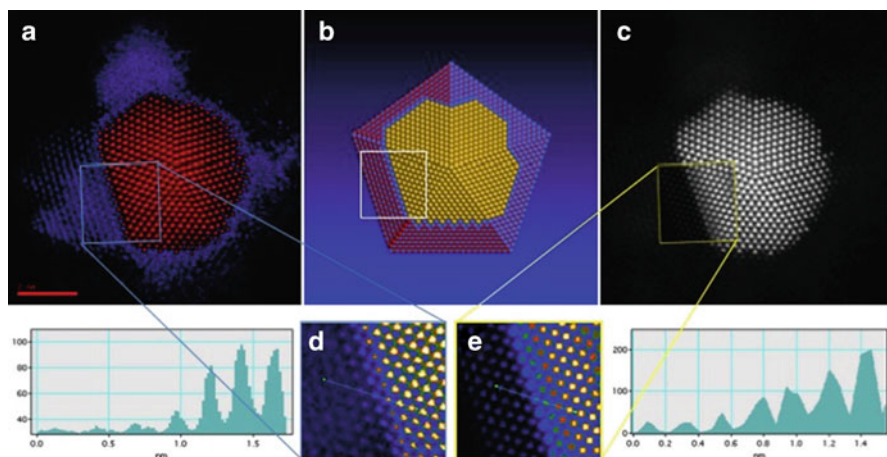


Fig. 1.18 (a) STEM micrograph of a Au-Co nanoparticle, shown in false colors (red: high intensity, blue: low intensity). (b) Atomistic model used to describe the particle on (a); yellow spheres represent gold, blue spheres are cobalt, red spheres are oxygen. (c) The small squared region marked in (a) is substituted for the STEM simulation of the squared region marked in (b), and (d) the real micrograph of this region is compared against (e) the simulated one. The real and simulated line intensity profiles are also shown for comparison. Adapted from [17]. Reproduced with permission from The Royal Society of Chemistry (RSC)

to investigate the Co-Au interface; this model is shown in Fig. 1.18b. The model does not intend to reproduce exactly the shape of the particle, but to give a qualitative description of the particle. Figure 1.18c is a composite of the real image and a small section generated by STEM simulation; the corresponding real section is shown in Fig. 1.18d, and compared against the simulated micrograph (Fig. 1.18e). The two intensity profiles represented by lines in (d) and (e) are also shown for comparison. As can be seen, the simulated STEM micrograph succeeds in reproducing the main features of the real image. This result exemplifies the use of STEM simulations for an approximate description of composition and shape of metal particles.

Quantitative STEM simulation at atomic level is quite more complicated. Fluctuations in intensity on the background of a STEM micrograph can be of the same order of magnitude than the intensity generated by a single metal atom, and in multimetallic systems the problem becomes combinatorial. Nevertheless, the use of single-tilt tomography holders altogether with C_s correctors and 3D image reconstruction algorithms allow a very precise description of shapes and structures in nanoparticles, even at atomistic level [18–20].

1.8.4 Thermal Effects

The scattering strength is controlled by the effective form factor that depends on the value of the Debye–Waller factor, and variations in this factor may strongly affect

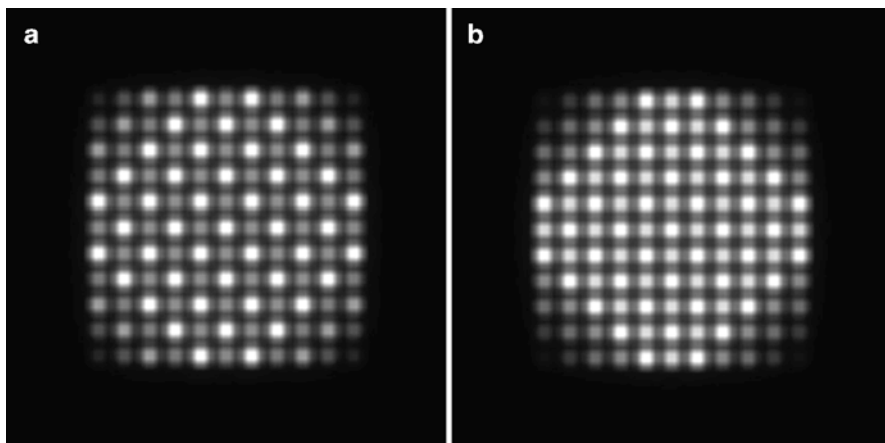


Fig. 1.19 Comparison between two simulated STEM micrographs of a cuboctahedral nanoparticle. (a) Debye–Waller set to zero. (b) Debye–Waller set at 0.69

the STEM signal. It is usual to find that an electron microscopy simulation program calculate the effective form factors through the Mott formula [21]. The Debye–Waller factor is not necessarily the same at the nanoscale than the bulk value. Buffat [22] measured a decrease in the Debye–Waller factor in gold particles ranging from 0.85 in 20 nm particles, to a value of 0.69 in 2 nm particles. We used this value to simulate a gold cuboctahedral particle and compare the result against a simulation where the Debye–Waller factor was set to zero. Both images are shown in Fig. 1.19. As can be noted, the thermal effects may be a determining factor on the contrast in ultra-high resolution STEM micrographs, and should not be underestimated.

1.8.5 *Interatomic Distances*

One of the most straightforward uses of TEM and STEM is the measurement of distances based on the intensity peaks (or valleys in bright field imaging) on the micrographs. For this direct kind of measurements, it is assumed that the spatial frequencies are uniformly transferred, this is, that the transfer function does not change its sign in the range of spatial frequencies that correspond to interatomic distances. Even if this condition is accomplished, this does not warranties the match between the measured and the real distances, since also the orientation of the sample has to be considered. The interpretation, though, is not necessarily straightforward: First, even in the best tuned-up TEMs, the background intensity is not homogeneous, and this can complicate the interpretation of distance measurements at the vicinity of the borders of a particle. Second, usually the interplanar distances are measured as an average over several planes, since the variance in

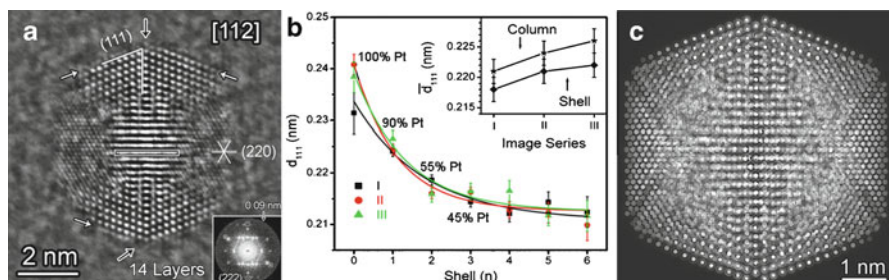


Fig. 1.20 (a) Sub-Angstrom resolution FePt icosahedral nanoparticle. (b) Interplanar (111) distances vs. position of shell (shell 0 is the external shell). (c) TEM simulation of model nanoparticle. In order to reproduce the measurements of the interplanar distances, the distribution of Pt must follow the percentages shown in (b). Reprinted with permission from [23]. Copyright 2009 American Chemical Society

the size of a spot that represents a single atomic column is on the same order of magnitude as the interplanar distance itself. High resolution STEM simulations can be used to verify the experimental measurements, if an appropriate atomistic model is taken for granted. Consider for example the case of FePt icosahedral nanoparticles [23], as the one shown in Fig. 1.20. FePt nanoparticles with sizes on the range of [5, 6] nm were produced by an inert gas condensation, which implies that there is no passivation agent on the surface of the particles. Their structure was analyzed as icosahedral with shell periodicity. The sub-Angstrom resolution was achieved by focal series reconstruction, and it was enough to extract the position of individual atomic columns with a precision of about 0.002 nm, and to measure shell spacing differences of 0.02–0.03 nm. The measurements showed that the external shells of the nanoparticle were more spaced than the inner ones, a trend that could be interpreted as a consequence of the segregation of Pt to the external shells (see Fig. 1.20b). Comparative Molecular Dynamics calculations used jointly with electron microscopy simulations (Fig. 1.20c) confirmed that the structural relaxations could be attributed to Pt segregation at the outer shells generating a specific concentration gradient.

1.9 STEM, Geometrical Phase Analysis, and Its Range of Validity

Sub-Angstrom resolution in TEM and STEM, altogether with the ability of tilting the samples to orientations where a specific zone axis coincides with the direction of the electron beam, opens the possibility of analyzing the structures from a geometric perspective in order to obtain a strain map of the lattice. This possibility is particularly important in metal structures with Platonic and Archimedean polyhedral shapes, where strains may not be evenly distributed. An archetypical example of

this is the decahedron, that in order to exist as a closed structure formed by five tetrahedra, it has to deform its atomic lattice, originating internal strain. A commonly used method to measure strains directly from high resolution micrographs is the one called geometric phase analysis, or GPA in short [24]. The method, which in principle can be applied to any image with two or more sets of periodicities, is based on the local measurement of amplitude and geometric phase in reciprocal space, i.e., by the measurement of the displacement of lattice fringes in the Fourier transform of the image. There exist free and paid versions of the GPA code, both implemented to work as add-ons of the DigitalMicrograph suite [25]. The measurement procedure, in a nutshell, is as follows: (1) The power spectrum of the image (the squared modulus of the Fourier transform of the micrograph) is calculated; each periodicity present in the image will generate a bright spot in the power spectrum, and the dispersion of the spot will be at least partially due to variations in the structure. (2) A region of interest enclosing a particular bright spot is selected; this will be the reciprocal area where the phase variations will be measured. (3) The phase image is calculated following the relation

$$P_g(r) = -2\pi g \cdot u(r),$$

where g is the reciprocal vector that defines the periodicity. (4) A reference area is chosen, and the phase image is recalculated, referenced to this area. The ideal reference area must be a region where the periodicity is not distorted, i.e., where the non-referenced phase image does not change abruptly. (5) The process is repeated for a second region of interest, since two sets of lattice fringes are needed for the calculation of strains. The displacement vector is expressed in terms of the base vectors defining the two periodicities:

$$u(r) = -\frac{1}{2\pi} [P_{g1}(r) a_1 + P_{g2}(r) a_2],$$

where

$$g_i \cdot a_j = \delta_{ij}.$$

(6) The strain tensor is calculated:

$$\varepsilon_{ij} = \frac{1}{2} \left(\frac{\partial u_i}{\partial u_j} + \frac{\partial u_j}{\partial u_i} \right),$$

and (7) rotations of the lattice are calculated:

$$\omega_{ij} = \frac{1}{2} \left(\frac{\partial u_j}{\partial x_i} - \frac{\partial u_i}{\partial x_j} \right).$$

Johnson et al. [26] calculated in this way the strain distribution in a decahedral gold 17-nm-radius nanoparticle, using a high resolution Aberration-corrected TEM

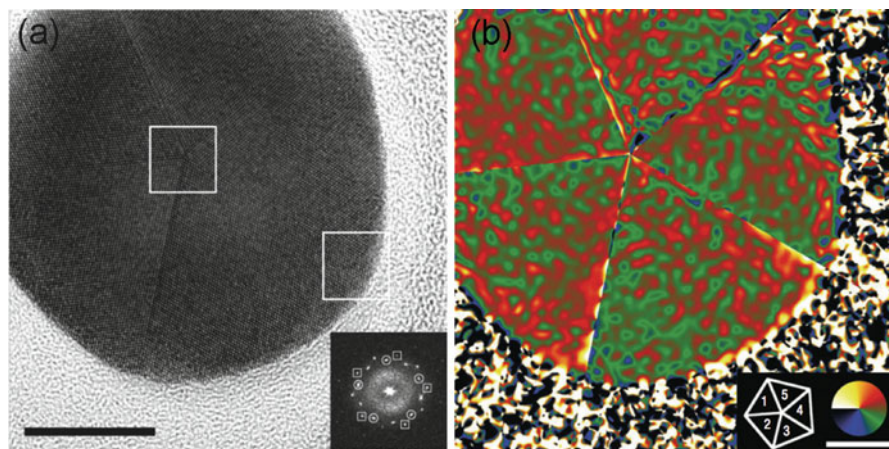


Fig. 1.21 (a) TEM micrograph of a fivefold gold nanoparticle. The scale bar is 10 nm long. (b) Shear strain map obtained by geometric phase analysis. Adapted by permission from Macmillan Publishers Ltd: [26], copyright 2007

image obtained with a Tecnai F20 ST (FEI) microscope. The results are shown in Fig. 1.21.

They found that, in order to close the 7.35 degree gap left by five perfect tetrahedra, each tetrahedron is strained nonhomogeneously (see Fig. 1.21b).

Is it possible to use STEM micrographs to generate strain maps by GPA? It would be interesting to give it a try, since the contrast in STEM may be as good as or even better than that of conventional TEM, and the interpretation of STEM is more direct than the interpretation of TEM, but the scanning process may introduce some artifacts in the geometric analysis. This source of error can be partially overcome by aligning the scan parallel to a principal axis of strain [27], or by rotating the STEM image and then repeating the GPA process.

The use of GPA on STEM micrographs is exemplified in Fig. 1.22. Here, a decahedral gold particle very well orientated along its fivefold axis was imaged by HAADF-STEM, and subjected to GPA analysis using the GPA Phase plugin for DigitalMicrograph by HREM Research, based on the original algorithm by Hytch [24]. Here we can note a qualitatively different strain distribution from the particle of Fig. 1.21; in this case, the strain is distributed nonhomogeneously in each tetrahedron, and some almost horizontal stripes of higher strain than the rest of the particle appear crossing the frontiers between adjacent tetrahedra. Whether these stripes are related to the scanning process is still uncertain, and here we present the results to remark the need of double checking the GPA results by improving the statistics of the measurement, repeating the GPA process to several micrographs of the same particle, rotating the micrographs (or even the sample), and carefully filtering the images.

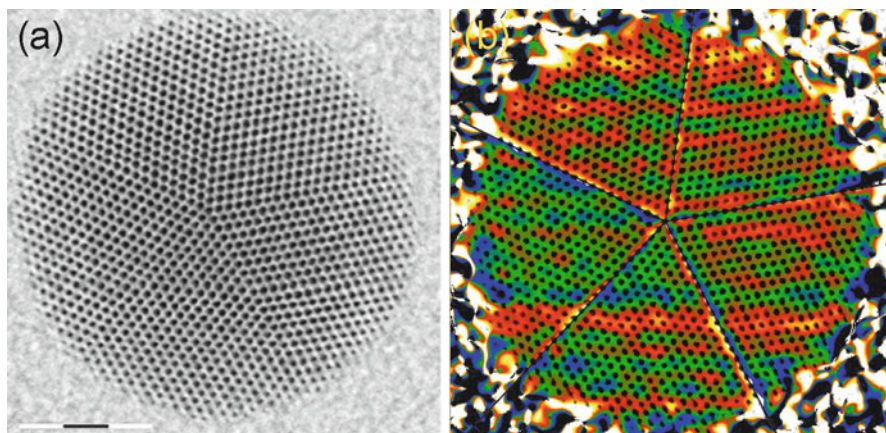


Fig. 1.22 (a) HAADF-STEM micrograph of a fivefold gold nanoparticle. (b) Shear strain map obtained by geometric phase analysis

1.10 Conclusions

Electron microscopy at sub-Angstrom resolution has reached such a high level of precision that we can investigate the composition and structure of metal nanoparticles in an atom-by-atom fashion. This gives an invaluable capacity for the study of the interaction of metal and alloy nanostructures with biological tissue, since now it is possible to look for structure/function correlations in real time, and with a resolution high enough to investigate individual bonds. The simultaneous use of real and simulated microscopy makes the process of interpreting a micrograph more science and less craftsmanship, and gives the conclusions extracted from the measurements a more quantitative and less speculative character. Some conditions must be fulfilled to take full advantage of the top electron microscopy facilities when studying metal nanostructures: The capacity of preparing high quality samples, a fair understanding of the interaction between the sample and the electron beam, a conscious awareness of the capabilities and limitations of the different instruments and techniques, and the familiarity with different analysis approaches. And, above all, the essential element: an experienced and skillful microscopist.

Acknowledgments The authors would like to acknowledge The Welch Foundation Agency Project # AX-1615, “Controlling the Shape and Particles Using Wet Chemistry Methods and Its Application to Synthesis of Hollow Bimetallic Nanostructures.” The authors would also like to acknowledge the NSF PREM Grant # DMR 0934218, Title: Oxide and Metal Nanoparticles—The Interface between life sciences and physical sciences. The authors would also like to acknowledge RCMI Center for Interdisciplinary Health Research CIHR. *The project described was supported by Award Number 2G12RR013646-11 from the National Center for Research Resources. The content is solely the responsibility of the authors and does not necessarily represent the official views of the National Center for Research Resources of the National Institutes of Health.*

References

1. Ercolessi F, Andreoni W, Tosatti E (1991) Melting of small gold particles: mechanism and size effects. *Phys Rev Lett* 66:911–914
2. Ferrando R, Jellinek J, Johnston RL (2008) Nanoalloys: from theory to applications of alloy clusters and nanoparticles. *Chem Rev* 108:845–910
3. Barnard AS, Young NP, Kirkland AI, van Huis MA, Xu H (2009) Nanogold: a quantitative phase map. *ACS Nano* 3:1431–1436
4. Antúñez-García J, Mejía-Rosales S, Perez-Tijerina E, Montejano-Carrizales JM, José-Yacamán M (2011) Coalescence and collisions of gold nanoparticles. *Materials* 4:368–379
5. Carter CB, Williams DB (2009) *Transmission electron microscopy: a textbook for materials science*. Springer, New York
6. Fernández-Navarro C. et al. (2007) On the structure of Au/Pd bimetallic nanoparticles. *J Phys Chem C* 111:1256–1260
7. Yuan D, Gong X, Wu R (2008) Peculiar distribution of Pd on Au nanoclusters: First-principles studies. *Phys Rev B* 78: 035441
8. Gómez-Rodríguez A, Beltrán-del-Río LM, Herrera-Becerra, R (2009) SimulaTEM multislice simulations for general objects. *Ultramicroscopy* 110:95–104
9. Pennycook S (1989) Z-contrast STEM for materials science. *Ultramicroscopy* 30:58–69
10. Kirkland EJ (1998) *Advanced computing in electron microscopy*, vol. 250. Springer, New York
11. CtfExporer. CtfExporer (Sidorov, M. V.): at <http://www.maxsidorov.com>
12. Stadelmann P. JEMS. <http://cimewww.epfl.ch/people/stadelmann/jemsWebSite/jems.html>
13. Ishizuka K (2001) A practical approach for STEM image simulation based on the FFT multislice method. *Ultramicroscopy* 90:71–83
14. Ishizuka K (1998) Multislice implementation for inclined illumination and convergent-beam electron diffraction. *Proc Intl Symp Hybrid Anals*
15. Wall J, Langmore J, Isaacson M, Crewe AV (1974) Scanning transmission electron microscopy at high resolution. *Proc Natl Acad Sci USA* v71: 1–5
16. Pinker S (1997) *How the mind works*. W. Norton & Company, New York
17. Mayoral A, Mejía-Rosales S, Mariscal MM, Perez-Tijerina E, José-Yacamán M (2010) The Co–Au interface in bimetallic nanoparticles: a high resolution STEM study. *Nanoscale* 2:2647
18. Gontard LC, Dunin-Borkowski RE, Gass MH, Bleloch AL, Ozkaya D (2009) Three-dimensional shapes and structures of lamellar-twinned fcc nanoparticles using ADF STEM. *J Electron Microsc* 58:167–174
19. Kimoto K et al. (2007) Element-selective imaging of atomic columns in a crystal using STEM and EELS. *Nature* 450:702–704
20. Muller DA (2009) Structure and bonding at the atomic scale by scanning transmission electron microscopy. *Nat Mater* 8:263–270
21. Ishizuka K (2002) A practical approach for STEM image simulation based on the FFT multislice method. *Ultramicroscopy* 90:71–83
22. Buffat P, Borel JP (1976) Size effect on the melting temperature of gold particles. *Phys Rev A* 13:2287
23. Wang R et al. (2009) FePt Icosahedra with magnetic cores and catalytic shells. *J Phys Chem C* 113:4395–4400
24. Hytch M, Snoeck E (1998) Quantitative measurement of displacement and strain fields from HREM micrographs. *Ultramicroscopy* 74:131–146
25. Mitchell DRG, Schaffer B Scripting-customised microscopy tools for Digital Micrograph (TM). *Ultramicroscopy* 103:319–332
26. Johnson CL et al. (2007) Effects of elastic anisotropy on strain distributions in decahedral gold nanoparticles. *Nat Mater* 7:120–124
27. Diercks D, Lian G, Chung J, Kaufman M (2011) Comparison of convergent beam electron diffraction and geometric phase analysis for strain measurement in a strained silicon device. *J Microsc* 241:195–199

Part II
Electron Structure, Optics, and Magnetism

Chapter 2

Density-Functional Theory of Free and Supported Metal Nanoclusters and Nanoalloys

Alessandro Fortunelli and Giovanni Barcaro

The recent years have witnessed an explosive surge in the development and applications of computational science. The availability of increasingly more powerful, faster, and cheaper computers and of an increasing number of computational packages (many of which freely accessible) that are more and more reliable, efficient, and user-friendly has stimulated this surge, and a large community of computationally oriented people is now active in practically all fields of science, ranging from both experimental and theoretical researchers to undergraduate and graduate students. The field of metal nanoclusters and nanoalloys is no exception to this general trend. Paralleling the impressive recent advances in the experimental characterization techniques [92, 116, 126, 154], in the latest years an increasing number of theoretical and computational studies have appeared on this topic, especially dealing with the prediction of the structural properties of these systems, and also extending to magnetic, optical and catalytic response. This explosive behavior is not without its drawbacks. A risk of indiscriminate use is always present, also considering the fact that a bit of empiricism is required in the choice of the numerical parameters of the simulations. This risk can be avoided if the basic concepts on which first-principles approaches rely are kept in mind. The aim of this chapter is to provide an introductory description of these basic concepts and tools, and at the same time to present examples of recent applications which can give a flavor of what is the current status of the research in this field.

The chapter is organized as follows. We first present a brief basic introduction to first-principles approaches, focusing special attention on advantages and limitations of density-functional theory (DFT). The problem of how to achieve accurate structural predictions in the field of metal nanoparticles and nanoalloys is then dealt with, and a multi-scale computational protocol is discussed. The use of

A. Fortunelli (✉) • G. Barcaro

CNR-IPCF, Istituto per i Processi Chimico-Fisici del Consiglio Nazionale delle Ricerche,
Molecular Modeling Laboratory, via G. Moruzzi 1, Pisa, I-56124, Italy
e-mail: alessandro.fortunelli@cnr.it; barcaro@ipcf.cnr.it

electronically and/or structurally “magic” clusters is successively described together with the associated advantages and assured simplifications. Attention is then focused on supported clusters, highlighting specific concepts and issues related to these systems. Three illustrative examples of the application of the techniques previously described are then presented, to provide the reader with some concrete test cases. A brief section on dynamic processes such as growth and how they can be dealt with at the first-principles level concludes the presentation, followed by a chapter’s summary.

2.1 First-Principles Approaches to the Theoretical Description of Metal Nanoclusters and Nanoalloys

Let us start by defining a general framework for our analysis: the considerations that follow can be found in standard textbooks [42,95] and are here summarized for the convenience of the reader. The phenomena we are interested in involve energies typically in the range from a few cm^{-1} to a few tens of electron-Volts (eV). In this energy range, which includes much of chemistry, molecular, and solid state physics and materials science, the behavior of the system is well described by one variant of Quantum Mechanics (QM). Specifically, for systems constituted of light elements, a full solution of the Schrödinger equation [132] would provide an accurate description of the system, whereas for systems containing heavy elements relativistic corrections, described for a single electron by the Dirac equation [46], come into play. Even though, in fact, the typical energies and thus the physics of the valence electrons (those determining the chemistry of the system) are nonrelativistic, the interaction of the valence electrons with the core ones, i.e., the electrons closer to and strongly affected by the proximity to the nuclei and whose speed can approach that of light, appreciably modifies the field in which valence electrons move and thus ultimately their chemical behavior, with gold being the prototypical example in this context [125]. Metal nanoclusters and nanoalloys, both bare and in various environments, perfectly fit in this framework, in the sense that bonding in these systems can be accurately described by QM. The problem, however, is that it is impossible with the present computational resources to obtain accurate solutions even of the nonrelativistic Schrödinger equation for systems exceeding few particles (nuclei and electrons). One is therefore necessarily led to some sort of approximate theoretical treatments, which are traditionally distinguished into first-principles and (semi-)empirical ones. Theoretical approaches are named “first-principles” when they do not rely on input sources other than basic physical constants, such as the Planck’s constant and the speed of light in vacuum. In these approaches one aims at an explicit (though approximate) description of the electronic wave function of the system. With respect to empirical approaches, in which the bonding interactions are expressed in terms of analytic functions of the system coordinates containing atomic or molecular parameters fitted on experimental or theoretical data, first-principles

methods tend to be more accurate but certainly much more demanding in terms of computational resources, and thus applicable to a more restricted set of material systems. To study more complex systems, a multi-scale approach is usually invoked. This approach, which will be described in the next section, is based on the idea that systems containing a limited number of atoms are best described by rigorous first-principles approaches which are also used to single out the basic interactions and phenomena occurring in these systems, while by increasing the number of atoms the same physics of the system simplifies and some details of the Quantum Mechanical description become progressively less important, whereas those still surviving as essential can be described in terms of a limited set of effective parameters. For definitiveness, we assume to work from the start in the so-called Born–Oppenheimer approximation [32], i.e., we take advantage of the much larger mass of the nuclei with respect to electrons and thus of their lesser mobility to solve the electronic problem at fixed nuclear coordinates, then providing the nuclei with a potential energy surface (PES) for their movement, and considering residual effects such as electron–phonon coupling as perturbations.

The main problem in solving the Schrödinger equation for the electrons in the Born–Oppenheimer approximation is that the electronic wave function has a strong many-body character. In other words, the behavior of an electron in any region of space in principle depends on the relative position of all the other electrons. The first decisive simplification (or approximation) therefore consists in disentangling the behavior of a single particle (electron) from that of the rest of the system, and thus to formulate the many-body problem in terms of uncoupled or independent sets of single-particle equations. In the simplest instance, this is realized in the Hartree–Fock approximation, whose equations are the following:

$$\left(-\frac{\hbar^2}{2m}\nabla^2 + V(\mathbf{r}) + \int \frac{\sum_{j=1}^N [\varphi_j^*(\mathbf{r}')\varphi_j(\mathbf{r}')] }{|\mathbf{r}-\mathbf{r}'|} d\mathbf{r}' \right) \varphi_i(\mathbf{r}) - \sum_{j=1}^N \left(\int \frac{\varphi_j^*(\mathbf{r}')\varphi_i(\mathbf{r}')}{|\mathbf{r}-\mathbf{r}'|} d\mathbf{r}' \right) \times \varphi_j(\mathbf{r}) = \lambda_i \varphi_i(\mathbf{r}) \quad (2.1)$$

In (2.1) the $(-\frac{\hbar^2}{2m}\nabla^2)$ term is the kinetic energy operator, the $V(\mathbf{r})$ term is the external electrostatic potential due to the nuclei, $\int \frac{\sum_{j=1}^N [\varphi_j^*(\mathbf{r}')\varphi_j(\mathbf{r}')]}{|\mathbf{r}-\mathbf{r}'|} d\mathbf{r}' = \int \frac{\rho(\mathbf{r}')}{|\mathbf{r}-\mathbf{r}'|} d\mathbf{r}'$, and $\sum_{j=1}^N (\int \frac{\varphi_j^*(\mathbf{r}')\varphi_j(\mathbf{r}')}{|\mathbf{r}-\mathbf{r}'|} d\mathbf{r}')$ are the Coulomb and exchange operators, respectively, describing the average field generated by all the electrons, and λ_i is the one-electron or orbital energy of the $\varphi_i(\mathbf{r})$ orbital, while $\rho(\mathbf{r})$ is the total electron density. The Hartree–Fock equations are obtained by assuming that the electronic wave function can be written as a (properly anti-symmetrized) product of wave functions for each single electron (i.e., a so-called Slater determinant) and minimizing the total energy as a function of the $\varphi_i(\mathbf{r})$ orbitals (the wave functions for the single electrons). As can be seen from (2.1), according to the Hartree–Fock approximation one has to solve a single-particle (or one-electron) Hamiltonian and to derive

the single-particle (or one-electron) wave functions (or orbitals) and energies, from which the total energy of the system can be obtained. As the Coulomb and exchange operators in turn depend on the one-electron orbitals $\varphi_i(r)$, the Hartree–Fock equations are usually solved in a self-consistent fashion, in which trial orbitals are used to construct the Coulomb and exchange operators and thus the Hartree–Fock Hamiltonian, from whose solution one derives new orbitals that are again used as input to build a new Hartree–Fock Hamiltonian and so on until convergence is achieved. It should be noted that—due to the *nonlinear* character of the Hartree–Fock equations—the total energy does *not* coincide with the sum of the single-particle or orbital energies: this is necessary to avoid double-counting of the Coulomb and exchange contributions and is a typical feature of single-particle approaches, at variance with the original Schrödinger equation which is many-body but linear. The advantages of the Hartree–Fock approximation are apparent: the complexity of the complete solution of the Schrödinger equation reduces to finding an average description of the electron cloud which produces an effective field in which the electrons themselves move. This implies a self-consistent character of the problem: the average or effective field generated by the one-electron orbitals must be consistent with the motion predicted for electrons moving in this same field. The switch from linear to nonlinear mathematics entails well-known issues (e.g., convergence problems, that in some cases can be severe). These issues should always be kept in mind when applying black-box electronic structure codes, but this drawback is more than compensated by the enlargement of the set of systems that can now be treated. Presently, self-consistent calculations can indeed be conducted on systems composed of several thousand electrons, and further progress (both in terms of the size of affordable systems and in terms of speed of computations) are expected to come about in the future following the continuous advances in hardware and software. An important feature in this respect is that, even though the interaction between the single particle (electron) and the effective field in which the particles are moving needs to be described, it is possible to devise techniques which exploit the local character of this particle/field interaction and achieve so-called “linear scaling,” i.e., a simple proportionality between the size of the system (typically the total number of atoms, N) and the cost of the simulation [70]. It should be noted that linear scaling is far from being automatically achieved: a naively implemented Hartree–Fock method scales as N^{3-4} , while an advanced and very accurate post-Hartree–Fock method such as coupled cluster perturbation expansion including single and double excitations and a perturbative treatment of triple excitation (CCSD-T) in principle scales as N^{7-8} if the simplifications due to locality of interactions are not exploited. This means that doubling the size of the system entails a computational cost at least eight times higher for an untamed Hartree–Fock calculation (and up to 256 times higher for an untamed CCSD-T calculation). A proper and efficient numerical solution of the single-particle equations is therefore mandatory to extend the scope of simulations to realistic systems.

Apart from technical issues of efficient implementation, what is lacking in the Hartree–Fock approximation from the first-principles point of view is the treatment of correlation effects, i.e., the phenomena and the energy contributions due to the

fact that electrons in reality do not move in an average or effective field generated by the other electrons, but interact among each other in a many-body fashion, so that their motion is “correlated.” This aspect becomes crucial when electrons get close in real space: the associated effects are grouped under the term of short-range correlation. For example, one speaks of the Coulomb hole, i.e., the depletion in the pair electron density with respect to the Hartree–Fock predictions due to the Coulombic repulsion when two electrons approach each other. Still relying on an explicit description of the electronic wave function, one can improve upon the Hartree–Fock approximation by using so-called post-Hartree–Fock or “ab initio” first-principles approaches. In these approaches variational or perturbative methods are applied to expand the electronic wave function in terms of excitations with respect to the Hartree–Fock wave function (the Slater determinant): by moving one electron from an orbital which is occupied in the ground-state Slater determinant to an unoccupied (or virtual) orbital, one obtains a single excitation, by moving two electrons from occupied to virtual orbitals one obtains a double excitation, etc. Configuration Interaction (CI) or multi-configuration self-consistent-field (MC-SCF) are the most popular among the post-Hartree–Fock variational methods, while Moeller-Plesset (MP) or Coupled Cluster (CC) methods are eminent among the perturbative methods [140]. In principle, these approaches can reach a high accuracy. However, one main difficulty lies in the inefficient description of short-range correlation or the Coulomb hole, associated with the slow convergence of the expansion of the two-body electronic wave function for small values of the relative electron distance in terms of product functions of the coordinates of the two electrons. For metal clusters, other problems also come from so-called long-range correlation effects. Metallic systems in fact as a rule present a very small band or HOMO-LUMO gap, i.e., a very small energy difference between their highest occupied molecular orbital (HOMO) and lowest unoccupied molecular orbital (LUMO). This makes them quite different from insulating systems in terms of localization properties of the electronic wave function [96] and convergence of post-Hartree–Fock methods, as it entails the presence of a wealth of low-energy electronic excitations and the need of a delicate balance in the description of their interaction to achieve an accurate assessment of the system energetics. It can be recalled in this connection that the Hartree–Fock approximation is known to describe very poorly a system which is usually taken as model of the metallic bond, i.e., the electron gas or “jellium” (an idealized system composed of electrons moving in a constant external potential). In detail, it is known that the band width and the density of electronic states at the Fermi level (i.e., the energy threshold between occupied and unoccupied orbitals) are severely exaggerated at the Hartree–Fock level [87]. Remnants of this behavior can be observed also for metal clusters, undermining the use of the Hartree–Fock exchange in hybrid DFT approaches for these systems (see below) [63].

The problems associated with short-range and some long-range correlation effects can be overcome by DFT. DFT in its Kohn–Sham version is a single-particle

(or one-electron) method. Its equations are therefore formally equivalent to the Hartree–Fock ones, and read:

$$\left(-\frac{\hbar^2}{2m}\nabla^2 + V(\mathbf{r}) + \int \frac{(\mathbf{r}')}{|\mathbf{r}-\mathbf{r}'|} d\mathbf{r}' + V_{xc}[\rho(\mathbf{r})](\mathbf{r}) \right) \varphi_i(\mathbf{r}) = \lambda_i \varphi_i(\mathbf{r}) \quad (2.2)$$

where the exchange operator in the Hartree–Fock equations is now replaced by an exchange–correlation (or xc-) operator, $V_{xc}[\rho(\mathbf{r})]$, which is a functional of the electron density, thus an xc-functional. Two theorems from the 1960 [80, 88] assure that the method is in principle exact, i.e., that it exists an exact xc-functional of the electron density such that the total energy constructed on the basis of the one-electron orbitals derived from the solutions of (2.2) provides the exact energy of the system. It should be noted in passing that, as in the Hartree–Fock case, the nonlinear character of the Kohn–Sham equations makes that the total energy is not the sum of one-electron energies. The problem is that the exact xc-functional is unknown. Even worse, in the few exactly soluble model cases in which it has been possible to derive the correct expression for the xc-functional, this has proved to be extremely complicated. It is thus generally thought that knowledge of the exact xc-functional is tantamount to the exact solution of the Schrödinger equation and is thus practically out of question. The goal of the present research is to derive increasingly accurate approximations to the exact xc-functional. This goal is often framed within the so-called Jacob’s ladder [121], which allows one to rank the various approximations to the exact xc-functional according to a well-defined hierarchy. The xc-functionals currently most commonly employed are the first two rungs of the ladder: the local density approximation (LDA), in which the xc-functional is composed of the Slater exchange (simply proportional to the third root of the electron density) [47, 136] plus a correlation functional parametrized on accurate results derived for the homogeneous electron gas, and the generalized gradient approximation (GGA), in which LDA is correct via terms depending on the gradient of the electron density [118–120]. LDA and GGA are called local or semi-local xc-functionals. Other very common xc-functionals consist in a mixture of a GGA exchange and the Hartree–Fock exchange, and are named hybrid xc-functionals [24]. It should be noted that the Hartree–Fock exchange is a functional *not* of the one-electron density but of the one-electron density matrix [100]:

$$\rho(x, x') = N \int \Psi(x, x_2, \dots, x_N) \times \int \Psi^*(x', x_2, \dots, x_N) dx_2 \dots dx_N \quad (2.3)$$

where $\Psi(x, x_2, \dots, x_N)$ is the many-electron wave function and x is a compound coordinate representing space (r) and spin variables. It can be noted that the electron density is the diagonal part of $\rho(x, x')$: $\rho(x) = \rho(x, x)$. The fact that the Hartree–Fock approximation implies the use of the one-electron density matrix rather than the one-electron density has consequences from both in-principle and practical points of view. From an in-principle point of view, this opens the way to xc-functionals explicitly depending on one-electron orbitals. This is advantageous

in some respect. In particular, local or semi-local xc-functionals inherently suffer from the self-interaction correction (SIC) error, i.e., an erroneous attribution of a correlation energy even to single-electron systems [117]. The use of the density matrix instead of the density allows hybrid xc-functionals to correct for this error. From a practical point of view, however, the evaluation of the Hartree–Fock exchange is numerically more complicated than that of a functional of the electron density. To make an example, while hybrid xc-functionals have been implemented in periodic codes using localized basis functions since a long time [48], their implementation in periodic codes using extended or delocalized (plane waves) basis sets is recent and computationally demanding [131]. Moreover, auxiliary basis sets for expanding the electron density can be introduced and utilized to achieve linear scaling [49, 58, 59, 133], but the extension to the density matrix is more complicated [150]. In this connection, recent hybrid xc-functionals take advantage of so-called range-separation [76], i.e., they partition the $1/r_{12}$ term in the Hartree–Fock exchange into a short-range and a long-range component, thus allowing a much more efficient numerical evaluation. The advantage of using hybrid xc-functionals is recognized when treating insulators or in general systems with a substantial HOMO-LUMO gap, such as oxides, but also organic molecules, for whose energetics the introduction of a Hartree–Fock term is often beneficial [24]. Also the description of the magnetic properties of transition metal complexes is often improved by the use of hybrid DFT approaches [22]. As mentioned above, these advantages can be undermined in the case of metal clusters (or in general gap-less systems) by an erroneous treatment of the electron-gas bonding [63]. A promising recent approach in this respect is represented by modulating the Hartree–Fock component by a space-dependent factor [143] in such a way that different parts of the systems are described by a different combination of Hartree–Fock and GGA exchanges [36, 143].

An extension of DFT is the so-called DFT + U method [5]. In this approach, a Hubbard U term [83] is added to the DFT Hamiltonian, consisting of an energy penalty for the double occupation of specific orbitals, see Fig. 2.1. This addition improves upon the description of localized electronic states via DFT and is widely used, e.g., to treat magnetic insulator such as NiO [41]. The U value can in principle be evaluated a priori, but it is a common practice to derive it empirically by comparison with experiment, see, e.g., [19]. One of the advantages of the DFT + U approach is that it is possible to add the U term selectively on certain atoms. In this way, one can describe composite systems such as metal/oxide ones by simultaneously retaining a satisfactory treatment of the metal component (described via a GGA DFT method) together with a fair description of the oxide component (via the DFT + U approach). In this connection, it can be added that the U value for the oxide layer at the interface with a metal support should be reduced with respect to the value appropriate to the bulk because of screening effects [4, 19], as depicted in Fig. 2.1.

Another source of inaccuracy in the standard DFT approach is represented by long-range correlation effects connected with dispersion effects. Their origin lies in the dynamical polarization of the electron cloud induced by the presence of electrons

electronic band structure method: Hubbard Hamiltonian

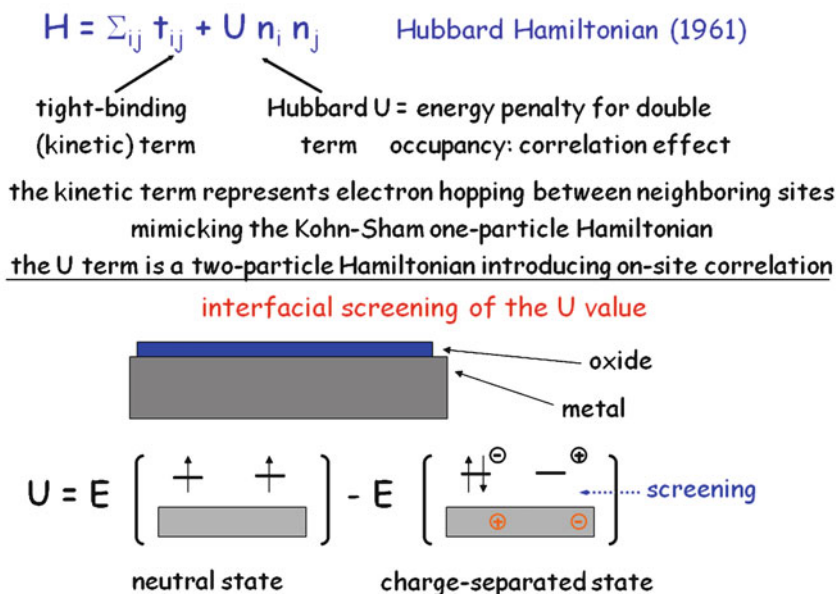


Fig. 2.1 Definition of the Hubbard Hamiltonian

belonging to nearby species. These are as a norm quantitatively smaller than typical bonding contributions, but originate terms in the PES decaying as inverse powers of atom–atom distances, and are thus awkward to describe in standard DFT using a functional of the electron density whose tails decay exponentially outside the atoms [96]. The most common way to include these effects is to add semiempirical corrections to the total energy [61, 72, 142].

Apart from the so-called *ab initio* or post-Hartree–Fock approaches, first-principles methods that go beyond DFT also exist. Among these post-DFT methods we can mention the random phase approximation (RPA) [112] and the so-called GW approach [112]. A different path to the solution of the Schrödinger equation passes through methods of statistical integration such as the Quantum Monte Carlo one [27]. Despite the intrinsically high computational demands of these methods, their use is constantly increasing and it can be foreseen that it will become widespread in a next future, especially for those systems and properties for which DFT has known limitations.

Despite these limitations and the on-going research of improved and more versatile xc-functionals and on post-DFT approaches, DFT is the first-principles method most often employed in calculations on metal nanoclusters and nanoalloys, as it currently represents the best compromise between accuracy and computational effort. Being a single-particle (or one-electron) method, it can scale linearly with the size of the system, i.e., it presents the lowest computational cost among first-principles

approaches. Moreover, it is thought to efficiently describe short-range correlation effects and long-range effects associated with electron-gas bonding, which are both difficult to deal with by using post-Hartree–Fock or *ab initio* first-principles approaches (see the discussion above). Many black-box packages are nowadays available to perform a wide range of electronic structure simulations within DFT, from total energy calculations, to structure optimizations, to the search for saddle points, to response properties, etc. Some of them are open-source codes that can be freely downloaded from the Web, and an increasing number of them has graphical interfaces that allow users to build up the system of their interest with a modest effort (for one example among the many possible ones, see e.g. [69, 89]). A risk of indiscriminate use is of course present, especially considering the fact that a bit of empiricism or at least consolidated experience is strongly required in the crucial choice of numerical parameters able to produce results that are numerically robust and make physical sense. This risk is reduced if the basic principles behind such simulations are kept in mind. In any case the availability of such packages (cumulating decades of experience in applied mathematics and being continuously developed and improved) has significantly widened the scope and enhanced the impact of computational disciplines on both basic and applied research and even on industrial applications.

2.2 Tools for Structure Prediction: A Hierarchical Multi-Scale Approach

Among the peculiar features of the metallic bond, the two ones that are probably the most important in the study of the structural properties of metal nanoclusters and nanoalloys are its “greedy” and nondirectional (or, better, scarcely directional) character [101, 115]. As greedy character, it is meant that the coordination number of a metal atom can reach high values, spanning from 0 to 12 or more (coordination numbers of 13, 14 are also observed [64]) with a relatively slow saturation in terms of bond energies, i.e., the average bond strength is only slowly decreasing with increasing the coordination number. Moreover, the metal–metal interaction is scarcely directional: even though in some transition metals such as Au the hybridization of *s* and *d* orbitals entails some bonding directionality [75, 110, 125], especially for simple metals one encounters a nearly isotropic dependence of the bond energy on the bond angular variables.

These two features makes that metal nanoclusters present a highly “fluxional” character, i.e., they can be found in structurally rather different configurations which however all lie in a narrow energy range. This effect is particularly apparent in small clusters. To make an example, the energy differences between the global minimum and the lowest-energy isomers of small Ag clusters in the gas-phase or adsorbed on defected oxide surface—namely, the F_s -defected MgO(100) surface (see the next sections for more details on this surface)—are reported in Fig. 2.2 [12]. It can be

Ag_N clusters on the F_s-defected MgO(100) terrace

fluxional character

ΔE	Ag ₄	Ag ₆	Ag ₈	Ag ₁₀
gas-phase	-	0.2-0.6	0.1-0.2	0.1-0.3
adsorbed	0.01-0.03	0.03-0.20	0.03-0.30	0.11-0.98

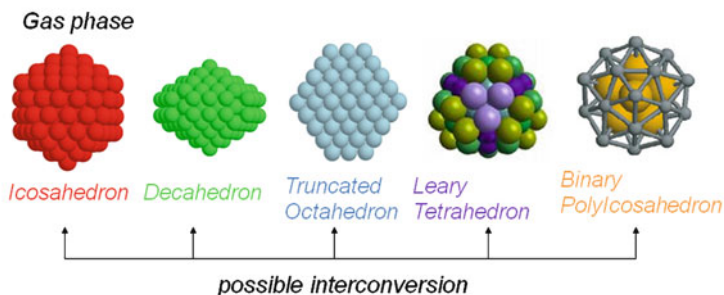
Fig. 2.2 Energy differences between the global minimum and the lowest-energy isomers of small Ag clusters in the gas-phase or adsorbed on the F_s-defected MgO(100) surface

issue in structure prediction: variety of cluster structures

“greedy” and “fluxional” character of metal-metal interaction



a variety of possible structural motifs



⇒ how to predict the cluster structure(s) ?

Fig. 2.3 Some examples of structural motifs which are observed in metal nanoclusters

seen that the lower values for such differences amount to at most 0.1–0.2 eV, and that the effect of the interaction with the surface in this case is to further increase this fluxional character, i.e., to reduce these energy differences.

It is thus an experimental observation with a sound theoretical basis that metal nanoparticles and nanoalloys can exhibit an impressive variety of different structures and morphologies: some representative examples are shown in Fig. 2.3. The fact that the PES of a metal cluster system is characterized by a large number of

theoretical tools for structure determination and growth

- **“small” systems ($N \leq 40$):**
density-functional basin-hopping (DF-BH) algorithm
- **“intermediate” systems ($40 \leq N \leq 200$):**
density-functional empirical-potential (DF-EP) algorithm
- **“large” systems ($200 \leq N \leq 1000$):**
empirical-potential global optimization (EP-GO) algorithm
- **“very large” systems ($1000 \leq N \leq 10000$):**
extrapolation based on structural motifs

Fig. 2.4 Hierarchy of computational methods for structure prediction as a function of the size of the particle

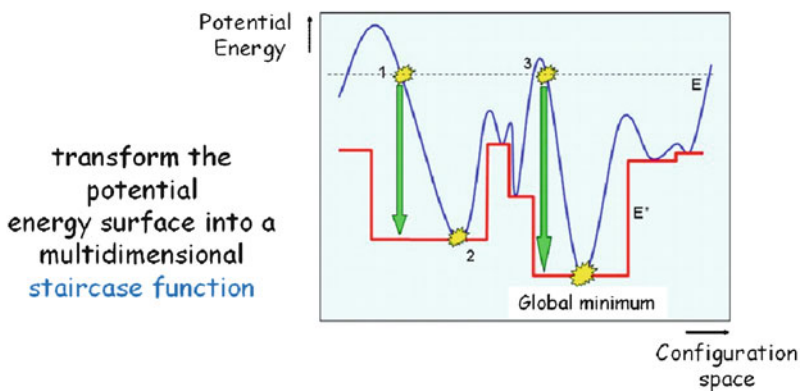
local minima with relatively small energy differences represents a challenge at the theoretical/computational level if accurate quantitative predictions are sought for. A convenient connection can be made here with the general topic and the theory of rough energy landscapes [148]. This feature is in fact shared by many different materials, such as biological molecules and amorphous polymers, so that general tools have been developed to tackle this problem.

In the field of metal nanoclusters, the most successful approaches that have been developed in recent years to perform a systematic sampling of their PES are based on a hierarchy of length scales, i.e., in these approaches the choice of the theoretical modeling to be employed in performing simulations on a specific system is tuned according to its size, as illustrated in Fig. 2.4. The idea behind this hierarchical approach is to use for systems of different size the approach which is most efficient and also makes physical sense for each one of them.

All the methods aimed at a systematic sampling of the PES are based on global optimization techniques [130], i.e., those computational techniques aimed at finding the absolute minimum (or global minimum) of a mathematical function which can be very complex and exhibit very many minima differing by small energy amounts (as in the case of metal clusters due to their fluxional character). This is the problem of sampling in the most efficient and at the same time thorough way a very complex and rough PES. One of the simplest and most efficient techniques among global optimization ones is the so-called Monte Carlo with minimization or Basin-Hopping (BH) algorithm. This approach has been proposed more than 20 years ago [91] and used in pioneering investigations in the field of gas-phase metal nanoclusters (described within empirical potentials) conducted by Doye and Wales [146, 147]. It is pictorially described in Fig. 2.5. In this algorithm, Metropolis Monte Carlo

global optimization: basin-hopping (BH) algorithm

global optimization via a basin-hopping (BH) algorithm



make a **Metropolis Monte Carlo walk** on the staircase PES
(in the field of free clusters BH pioneered by D. Wales and J. Doye)

Fig. 2.5 Schematic (one-dimensional) depiction of the Basin Hopping (BH) or Monte Carlo with minimization approach

walks are performed on a modified PES, which is obtained by associating with each point of the configuration space the energy of its closest local minimum. In practice, the BH algorithm consists of the following steps:

1. An initial random configuration of the metal cluster is chosen, a local geometry optimization is performed, and the final energy (the fitness parameter) is registered as E_1 .
2. Starting from the relaxed configuration, the atoms of the metal cluster are subjected to a random move, a new local geometry optimization is performed, and the final energy is registered as E_2 .
3. A random number (rndm) between 0 and 1 is generated and the movement of step 2 is accepted only if $\exp[(E_1 - E_2)/k_B T] > \text{rndm}$ (Metropolis criterion).
4. Steps 2 and 3—the Monte Carlo steps—are repeated a given number of times.

Depending on the $k_B T$ parameter, which plays the role of a fictitious temperature, some high-energy configurations are accepted and the search is able to explore different structural motifs (belonging to different funnels of the PES) of the metal cluster. A crucial point in the implementation of the BH search is choice of the random move. This can be simply a spatial “kick,” realized by randomly displacing the Cartesian coordinates of all atoms up to a certain amount, or more sophisticated choices, such as short runs of unstable Molecular Dynamics (MD)

especially effective for larger clusters. In the case of multicomponent systems such as alloyed nanoclusters or nanoalloys, an important random move is an exchange of the coordinates of two species, as realized in the BH exchange-only algorithm [28]. The thoroughness of the BH search is much increased when the BH protocol is coupled with *structural recognition* algorithms, i.e., algorithms which classify geometrical configurations as belonging to a given structural motif (or structural family). For example, this can be a fcc motif, or a icosahedral, or decahedral one, or more exotic ones, as depicted in Fig. 2.3. Structural recognition is achieved by defining one or several order parameters, i.e., analytic functions of the systems coordinates such as those derived from a common neighbor analysis [81]. The coupling between the BH algorithm and structural recognition can be realized in many ways. In the simplest case, one can group a posteriori the low-energy configurations obtained by the BH search into structural families, as in the DF-EP approach (see below). In more sophisticated protocols, one can use structural recognition to orient the BH search, i.e., to avoid parts of the PES that have been already explored or belong to a structural funnel which is not of interest. A further enhancement of the thoroughness of the BH search is obtained by performing both unseeded BH searches and (usually shorter) seeded searches starting from properly chosen initial configurations, for example from structures belonging to motifs found at nearby sizes or from structures found at the same size for other metals (system comparison from databases), see [54] and the chapter by Riccardo Ferrando in this book for an overview of the many possibilities. Other popular global optimization tools comprise genetic algorithms (see, e.g., [86]).

The hierarchy described in Fig. 2.4 is implemented in the following way. For small clusters (with a number of atoms, N , less than a few tens, presently $N \leq 40$), it is computationally feasible to conduct a global optimization (in the form of the BH algorithm) using energy and forces derived from DFT in the so-called DF-BH method, see, e.g., [6] for one of the first implementations for gas-phase metal clusters and [12] for the first implementation for supported metal clusters. A scheme of the DF-BH scheme is shown in Fig. 2.6. It makes sense to use a DFT approach for such small clusters since in this size range the metallic bond is not yet (or not fully) developed, the systems have a pronounced molecular character, and the transferability of empirical potentials (EP) is extremely limited. In short, for small clusters the finite character of the system is best described at the first-principles level.

For medium-size clusters (presently $40 \leq N \leq 200$), the DF-BH approach becomes progressively less and less feasible, and more approximate methods such as EP must be employed. An efficient possibility is to replace the DF-BH approach with a combination of DFT and EP simulations, in the DF-EP method. In this approach, proposed in [10, 29] and reviewed in [54], an EP for the given system is first selected (or developed). Second, a thorough global optimization search using, e.g., the BH technique with structural recognition algorithms is conducted using this EP. Third, the low-energy configurations produced by the BH search are grouped into structural families or basins. Fourth, a few of the low-energy configurations belonging to each structural basin are subjected to local geometry relaxation

computational approach for small clusters: DF-BH algorithm

density-functional basin-hopping (DF-BH) algorithm

density-functional: standard GGA functional
NWChem or PWscf software

global-optimization: basin-hopping (also called
Monte-Carlo minimization)

recipe: start with a random configuration, minimize its energy, make a random move, minimize the energy, accept the move if $\exp(-\Delta E/kT) > \text{random.number} \in [0, 1]$
Metropolis criterion

requirements: VERY cpu consuming: $N \leq 20\text{-}40$ (optimistically)
robust DF minimization procedure

first example on metal clusters: Au₂₀ PRB 73, 205414 (2006)
on supported clusters: Ag_N/F_s Chem. Eur. J. 13, 6408 (2007)

Fig. 2.6 Schematic implementation of the DF-BH method

using a DFT method, and the changes in the relative energy ordering of the structural families are analyzed. Finally, if these changes highlight inconsistencies or inaccuracies in the EP, the DFT results are used to refine the EP in a self-consistent process. The idea behind this approach is that in this size range the system progressively tends toward bulk metallic behavior, which is however not yet fully developed: for such systems, the EP can be in error in predicting the relative energy ordering among the various structural families, but it should be more accurate for the lowest-energy configurations belonging to the same structural family, see Figs. 2.7 and 2.9 for a schematic description of the DF-EP approach.

For yet larger clusters (presently $200 \leq N \leq 1,000$), even performing DFT calculations becomes progressively unfeasible, at least to conduct them in large numbers, and one has to rely entirely on global optimization searches based on EP approaches. The size of the system justifies the use of an EP and thus an average description of the metallic bond. At some point (the current limit is around 1,000–2,000 atoms) even the BH algorithm using EP becomes computationally unaffordable. An efficient solution then is to use extrapolations based on structural motifs. The idea is that for these large particles the competing motifs have been singled out and are known, so that large clusters belonging to these motifs can be constructed and locally optimized and their energy can be compared to predict energetic crossover and phase transformations among structural families [7]. As discussed in the next section “magic” structures are very helpful in defining a convex envelope of the energetics of structural families as functions of the size of the cluster. Moreover, in this size range some details of the structural relaxation which

computational approach for larger clusters: DF-EP algorithm

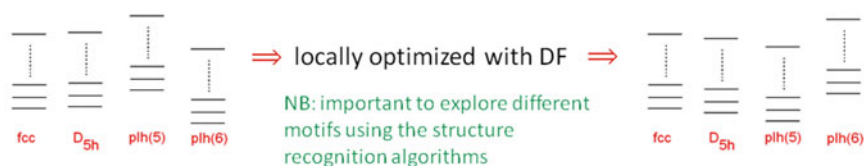
density-functional empirical-potential (DF-EP) algorithm

density-functional: standard GGA functional
 NWChem or PWscf software

empirical-potential: existing atom-atom potential or to be derived

recipe: use an EP global optimization approach with structural recognition to generate a data base of structural motifs
 locally optimize the lowest-energy structures
 for each structural motif

requirements: less cpu consuming: $N \leq 70$ optimistically
 robust DF minimization procedure



review: Ferrando, A.F., Johnston PCCP 10, 640 (2008)

Fig. 2.7 Schematic implementation of the DF-EP method

are thought to be reasonably well described by EP become less and less important. Effective models based on site energetics thus become more and more accurate and have been successfully used [1, 124].

Such a hierarchical approach to structure prediction can thus be rephrased or recast in terms of a multi-scale framework, see Fig. 2.8.

Starting from few-atom systems in which DFT can be routinely applied, the first and from the point of view of the topic of this chapter the most crucial step of such a multi-scale approach is depicted in Figs. 2.8 and 2.9, and connect first-principles or QM calculations, e.g., DFT ones, with EP modeling. From an analysis of QM calculations one singles out the basic physics of the system and which are the basic physical ingredients that an empirical force field must contain. An analytic EP is then built and used in a thorough search combined with structure recognition. The energy ordering among the competing structural families predicted by the EP is then tested and cross-checked at the DFT level. If this test suggests that an improvement of the EP is necessary, a new fit of the EP parameters is conducted, a new EP is generated, and a thorough search is performed again using the newly derived parameters. This search may (and often will) produce a different set of structural motifs, whose low-energy configurations are then tested and cross-checked again at the DFT level. This procedure is repeated as many times as needed until self-consistency is achieved.

multiple length scales: bottom-up rescaling

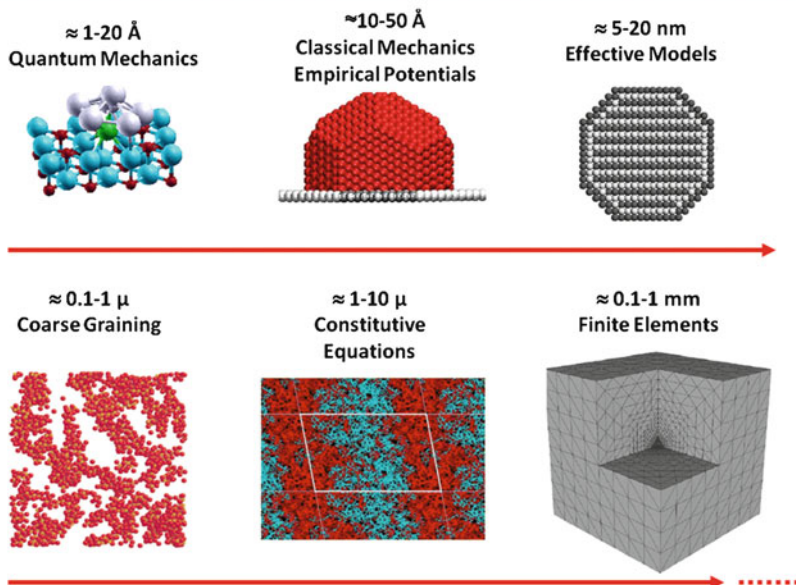


Fig. 2.8 Multi-scale framework for structure prediction

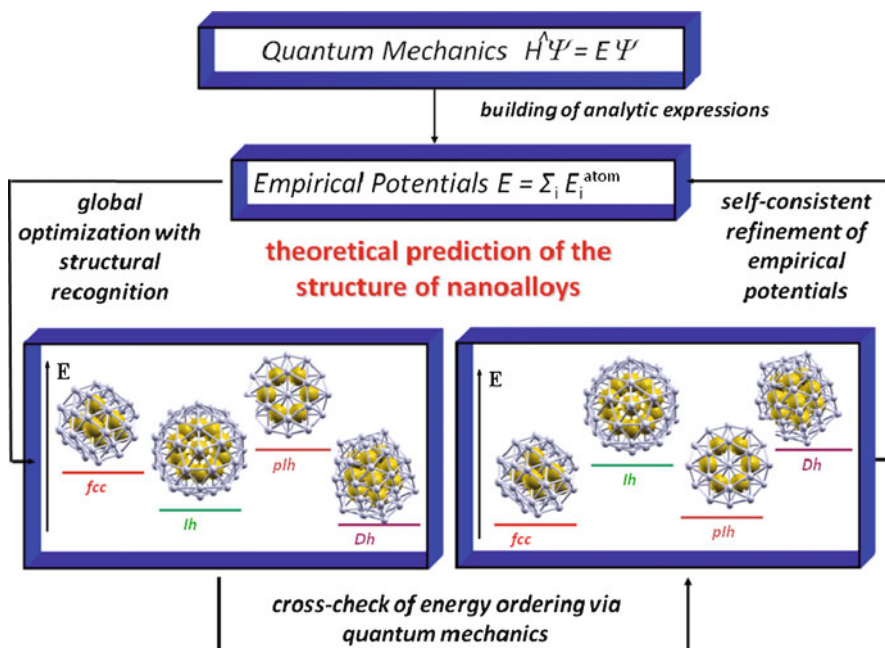


Fig. 2.9 Flow diagram of the DF-EP approach

multiple length scales: self-consistency in overlap regions

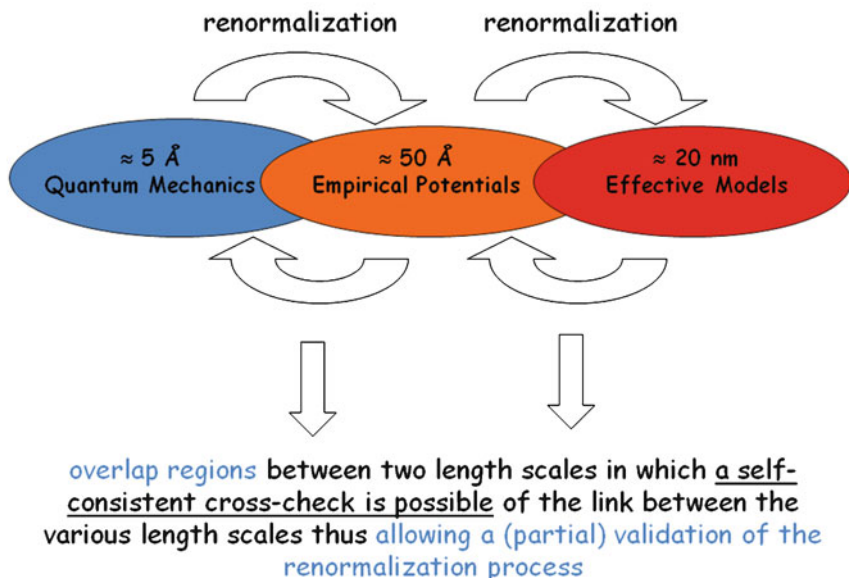


Fig. 2.10 Schematic depiction of the intersection of computational methods for different length scales and their overlap regions

From personal experience, the achievement of self-consistency between DFT and EP is often important, and its lack points to an intrinsic deficiency in the physical principles upon which the EP has been built. Development of an EP, apart from being considered an art in itself [122], is therefore also important in stimulating a deeper analysis of the DFT results from which a sounder knowledge of the physics of the system usually derives. It happens in fact that the first version of the EP predicts an energy landscape which is rather different from the DFT one, and self-consistent refinement is strongly needed. This is realized by an enlargement of the fitting set, i.e., the set of configurations which are included in the fit of the EP parameters, which corresponds to an increase of information on the physics of the system. In this respect, the “overlap” regions of the length scale framework in which both approaches (DFT and EP in the present case) can simultaneously be applied assume a crucial importance, see Fig. 2.10. These are the regions in which it is important to achieve as large a structural diversity as possible [54].

2.3 Magic Clusters

Magic metal clusters are aggregates of metal atoms which present electronic and/or structural shell closure, often associated with a peculiar energetic stability. Structural shell closure is achieved when the number of atoms is such that a

high-symmetry structural motif is completed, such as icosahedral, decahedral, and octahedral, see Fig. 2.3. When the electrons of the cluster complete a valence shell, and a substantial energy gap (of the order of 1–2 eV) exists between the HOMO and LUMO levels, an electronic shell closure is also achieved, usually rationalized in terms of the jellium model [44], i.e., a model in which an electron gas of nearly free valence electrons is assumed to move in a homogeneous ionic background, with the predicted magic numbers of valence electrons for the spherical homogeneous jellium model at $N = 2, 8, 20$, etc. The great interest arisen by magic clusters from an experimental point of view lies in the expectation that their high stability favors the synthesis of fully monodisperse systems, while structural and electronic shell closures may entail peculiar properties, which may lend themselves to use in technological applications. Structure–property relationships are particularly transparent for magic clusters.

Small magic clusters are particularly interesting in terms of electronic shell closure, and thus of electronic properties. To make one example, in Fig. 2.11 the first example of a surface magic (binary) metal cluster is presented, which is also helpful to exemplify what can typically be expected in this field. Small PdAg_N clusters in the gas phase, studied via a DF-BH algorithm in [13], present a transition from planar to 3D global minimum structures between PdAg_4 , which is still planar, and PdAg_5 , which is 3D. PdAg_6 , however, represents an exception to this rule, and is still planar due to an electronic shell-closure effect. Assuming in fact that Pd has a d^{10} configuration as in the single atom (and thus formally no valence electrons) and counting 1 valence electron per Ag atom, one finds for PdAg_6 a total of six valence electrons, thus achieving shell closure in the 2D jellium model. This stabilizes the planar configuration with respect to the compact one despite the fact that compact configurations are more stable than planar ones already for PdAg_5 . The HOMO-LUMO gap of the planar global minimum of PdAg_6 is indeed significant: 1.51 eV, to be compared with the 1.1 eV gap of PdAg_8 . PdAg_6 has also a 3D isomer which is only slightly higher in energy than the planar global minimum (energy difference of 0.15 eV, see Fig. 2.11). This isomer has a HOMO-LUMO gap reduced due to breaking of the planar symmetry: 1.1 eV. When these small Pd-Ag clusters are deposited on an F_s -defected $\text{MgO}(100)$ surface (see the next section for more details on this surface), the interaction with the surface favors a configuration in which the Pd atom is bound directly to the defect (Pd interacts with the surface more strongly than Ag) and the geometry is distorted to 3D to allow a better adhesion of the crown of Ag atoms to the surface. Furthermore, the F_s defect now contributes with two electrons to the valence electron count (see the next section), for a total of eight valence electrons, thus achieving shell closure for the 3D spherical homogeneous jellium model. The HOMO-LUMO gap for the supported cluster is indeed higher than its 3D analogue in the gas phase, being restored to about 1.5 eV.

For larger clusters, electronic shells get closer in energy and electronic shell closure effects become progressively less important (see however a nice example in [3]). Structural shell closure instead can still play a relevant role in assuring an extra stability to magic structures [44]. Apart from the extra stability associated with

PdAg_N clusters on the F_s-defected MgO(100) terrace

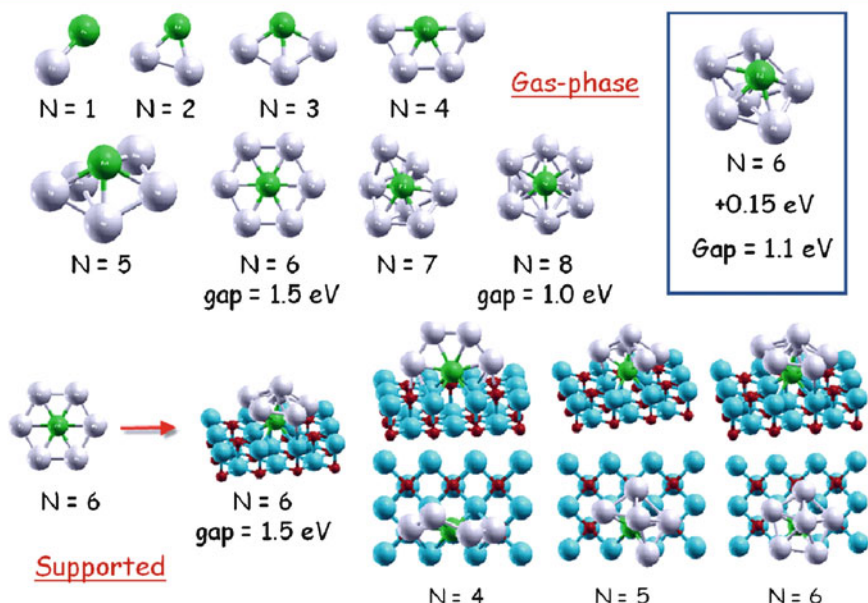


Fig. 2.11 Small PdAg_N clusters studied via a DF-BH algorithm both in the gas-phase and supported on the F_s-defected MgO(100) surface (see text for details). Reproduced with permission from [13]. Copyright 2007 American Chemical Society

shell closure, structurally magic clusters are also very helpful in other respects in the theoretical analysis. Magic clusters in fact as a rule exhibit high symmetry, which can be exploited in several ways.

First, some first-principles codes (especially those utilizing localized basis sets) can efficiently exploit the point group symmetry to reduce the computational effort [2, 74]. This reduction can reach up to the order of the symmetry group in some parts of the code (e.g., the calculation of the Coulomb two-electron integrals in codes using finite basis sets) or even up to a power of the order of the symmetry group higher than one in some other parts (e.g., the dimension of the matrices to be diagonalized can be reduced by a factor roughly equal to the order of the symmetry group, so that the computational effort to diagonalize them is reduced by a power of the symmetry group of at least two).

Second, structurally magic clusters can be useful in structure prediction, as mentioned in the previous section, see Fig. 2.4. It is in fact possible to construct large clusters belonging to a given structural motif, locally optimize their structure, and obtain the behavior of the binding energy as a function of size for the given structural motif [7]. Moreover, as it is known that the energy of metal clusters belonging to a given structural family often present an irregular behavior with cluster size between non-magic structures, due to the different site energies of atoms belonging

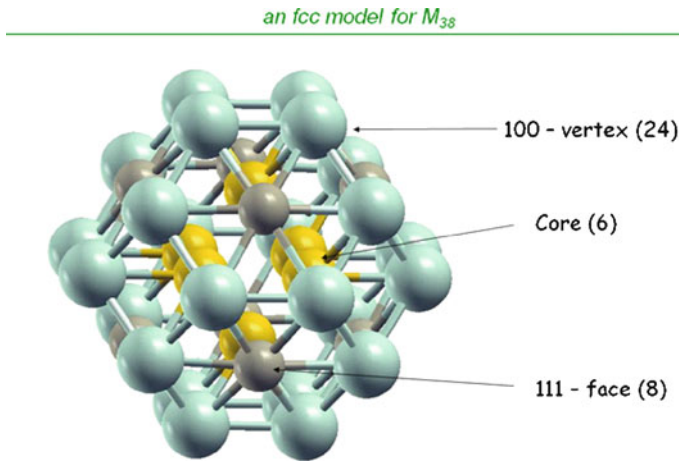


Fig. 2.12 Shell structure in the 38-atom truncated octahedral cluster

to incomplete shells, drawing the envelope of the binding energy as a function of size for the magic or structurally shell closed configurations provides a convenient way of defining the minimum of the excess energy for that particular motif, and thus allows one to study the ideal energetic crossover and phase transformations among different motifs [56].

Moreover, the full point group symmetry can be used to partition the atoms into symmetry “orbits” or symmetry “shells” [62, 148], i.e., groups of symmetry-equivalent species (which are converted into one another by the operations of the symmetry group). Just to make a very simple example, let us consider a 38-atom truncated octahedral cluster, as shown in Fig. 2.12. It is made of an inner (core) shell of six octahedral atoms and an outer shell of 32 atoms. The number of orbits is three: orbit-1 is formed by the six atoms of the inner shell; orbit-2 by the eight atoms at the center of the (111) facets, and orbit-3 by the 24 atoms on the (100) facets. One can thus describe a 38-atom cluster by defining the coordinates of only three atoms. In passing we note that, in general, a given truncated octahedral cluster is characterized by two indexes: the length of the edge of the complete octahedron and the number of layers cut at each vertex. A similar analysis can be done for the other structural motifs that are commonly encountered in the study of metal nanoclusters and nanoalloys, some of them shown in Fig. 2.3. They range from simple pieces of a crystal lattice, such as variously truncated octahedral (from regular octahedra to cubes) for the fcc lattice, to noncrystalline arrangements, such as all those containing fivefold symmetry axes: icosahedra and (possibly Marks-truncated) decahedra [97]. More recently also poly-icosahedra [129] or in general poly-tetrahedra, and mixed or hybrid arrangements combining in various ways crystalline and noncrystalline motifs have been shown to be competitive for medium-sized (especially alloyed) clusters.

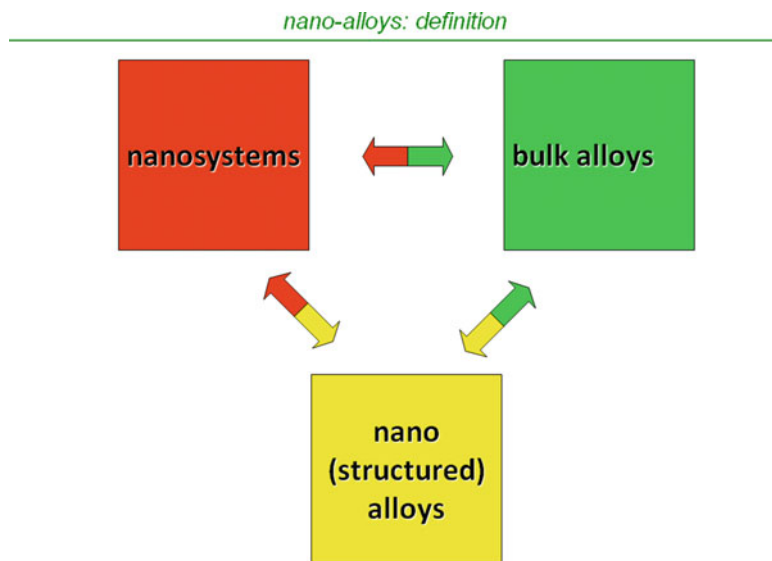


Fig. 2.13 Definition of nanoalloys

Magic structures are also important in the study of nanoalloys. Combining nanostructured metal systems or metal nanodots with alloying results in a class of systems of great interest in terms of both basic and applied science: alloyed metal nanoparticles or nanoalloys [55, 85], see Fig. 2.13.

These systems have several applications ranging from catalysis, to optics and magnetism. The reasons of their importance lie in the fact that additional structural motifs with respect to pure systems can be created, and the chemical and physical properties of the particles can be tuned by varying the composition and the degree of atomic mixing (chemical ordering or compositional structure). Ag–Au particles, for example, exhibit a different optical response depending on whether they are core-shell or random solutions [33]. Mechanical properties are equally known to be strongly affected by surface segregation [25]. The precise arrangement of the species in the particle is also important in catalysis, dominated by processes occurring at surface or subsurface shells, and changes in the segregation pattern under operating conditions have been observed [141]. Several mixing patterns have been described in the literature [55], such as core-shell or in general multishell ordering (in which concentric shells of different elements alternate), random solutions, ordered arrangements (more or less related to the known ordered phases of bulk alloys), and Janus-like segregation typical of immiscible components. To compare the stability of nanoalloys of different chemical composition, a very useful concept is that of mixing energy. Its definition represents the natural generalization of the corresponding concept used for bulk alloys and was proposed for the first time in

[62] in the context of empirical methods and later applied to DFT energetics in [53], and reads:

$$\Delta[N_A, N_B] = E_{\text{alloy}}[N_A, N_B] - N_A E_A[N] / N - N_B E_B[N] / N \quad (2.4)$$

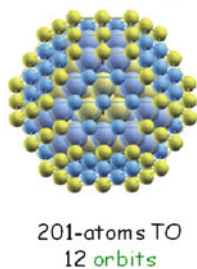
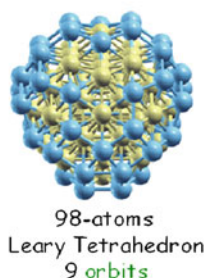
where $E_{\text{alloy}}[N_A, N_B]$ is the global minimum energy of a nanoalloy cluster composed of N_A atoms of the species A and N_B atoms of the species B , $N = N_A + N_B$ is the total number of atoms in the cluster, $E_A[N]$ is the global minimum energy of a pure cluster of N atoms, and $E_B[N]$ is the corresponding quantity for the B species. $\Delta[N_A, N_B]$ is the mixing energy of the given nanoalloy at a specific composition, i.e., the energy released by mixing $N_A A$ -type clusters and $N_B B$ -type clusters all of size N to produce N alloyed clusters of size N with composition (N_A, N_B) , with all clusters in their global minimum configuration, divided by N . The quantity $\Delta[N_A, N_B]$ provides a measure of how thermodynamically favorable is alloying at the given size and composition. In the context of the study of the compositional structure of nanoalloys, theoretical methods can provide relevant information which nicely complements and sometimes prefigures experiment, but the prediction of the correct chemical ordering is not an easy task, especially at the first-principles level, due to the combinatorial increase in the number of possible “homotops” (isomers sharing the same skeletal structure and composition but differing in the mixing pattern) [85]. In general, for a cluster with a given structure and N atoms of which N_A of species A and N_B of species B , one has $(N)! / ((N_A)!(N_B)!)$ possible different homotops. A possible solution to this problem is to consider structurally magic clusters. In this approach, proposed in [62], the point group symmetry is exploited to partition the atoms into symmetry orbits: the degrees of freedom of the system are thus reduced from N to the number of symmetry-inequivalent orbits, N_{orb} , and correspondingly the number of distinct homotops is exponentially decreased, making first-principles simulations feasible even for medium-sized particles. For example, the segregation patterns of face-centered-cubic-like (fcc-like) PdPt nanoparticles in the size range between 38 and 201 atoms and over a broad range of compositions was recently studied [20], finding that the interplay of metal–metal homo- and hetero-interactions produces an unusual Pt surface segregation in Pd-rich particles (in spite of the larger Pt bulk energy) and a novel patchy multishell pattern around equimolar composition in which each shell is decorated by “patches” of like atoms, see Fig. 2.14.

In this connection it can be added that another very efficient tool to drastically reduce the computational effort and to enlarge the scope of systems amenable to first-principles simulations is based on the use of periodic models, see, e.g., [103]. Instead of studying a 0D nanodot, in fact, one can consider a 1D or “wire” model, as depicted in Fig. 2.15. In this figure, the correspondence between a truncated octahedral 0D cluster, supported on a square-symmetry oxide surface to a 1D wire in which the section of the cluster is replicated ad infinitum, is clearly shown. As in the case of magic clusters, in this approach one exploits symmetry (in this case, periodic symmetry) to strongly reduce the number of nonequivalent atoms (in this case, those contained in the unit cell). In Fig. 2.15 the indexes defining the level of truncation of the wire corners are shown. These often correspond to the Wulff (for free particles)

Prediction of Chemical Ordering in Nanoalloys

$$N_{\text{tot}} \begin{cases} N_A \\ N_B \end{cases} \quad \text{How many combinations?} \quad \binom{N_{\text{tot}}}{N_A} = \frac{N_{\text{tot}}!}{N_A! N_B!} \approx 2^{N_{\text{tot}}} \quad \text{Huge number!}$$

At specific chemical compositions one finds **magic clusters** where atoms can be distinguished into **shells or orbits**



patterns of chemical ordering sampled by 2^m calculations (m = number of orbits) much reduced number wrt $2^{N_{\text{tot}}}$ calculations

First proposal: Velasco and Fortunelli, THEOCHEM, 487, 251 (1999)
Also: Paz-Borbon et al., PCCP, 9, 5202 (2007)

Fig. 2.14 Basic ideas behind the symmetry shell or orbit approach and the associated simplifications in the computational sampling of the chemical ordering phase space, with two examples of magic structures and their subdivision into symmetry orbits

or Wulff–Kaishev (for supported particles) construction, i.e., the optimal shape of the wire predicted by proportioning the truncations to the surface and interfacial energies, see [71, 78] for more details. The simplifications assured by the use of wire models in terms of reduction of the number of atoms in the unit cell and also of the degrees of freedom of the system are apparent. Through the use of such models, 1D system with a unit cell of 110–120 atoms can be constructed resembling or mimicking 0D particles with 7–8 times this number of atoms, which would be otherwise extremely expensive or hardly affordable with the present computational facilities.

Structurally magic clusters can finally be very useful in the prediction of the properties of metal nanoclusters and nanoalloys.

For example, an approach based on the study of magic clusters has recently been applied to investigate the optical properties of Au clusters in the size range of 150–170 atoms with various shapes [50]. In this case, the use of symmetry can reduce by orders of magnitude the computational effort, as the electronic excitations which make up the optical response can be catalogued into appropriate irreducible representations of the symmetry group, and the interactions among excitations belonging to different irreducible representations are automatically null by symmetry. The size range around 150–200 atoms is about the maximum that can be confidently treated

wire model for larger clusters

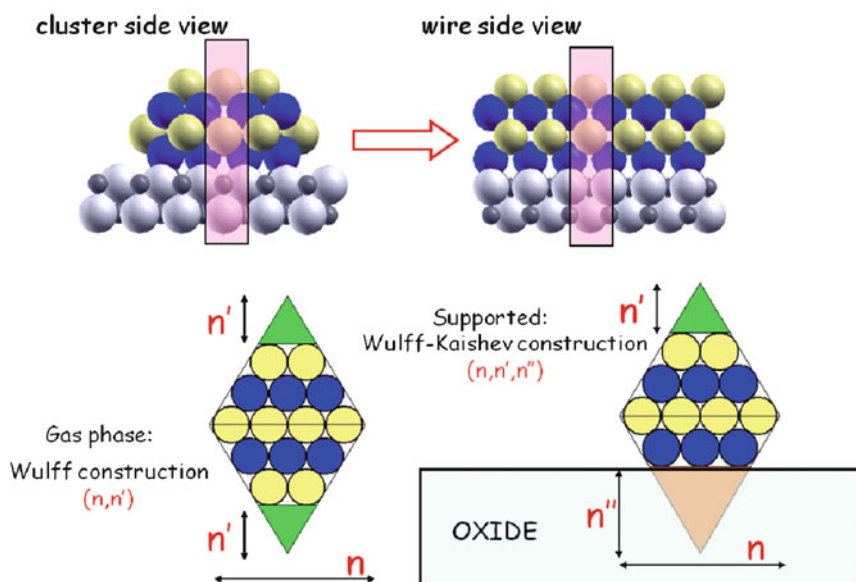
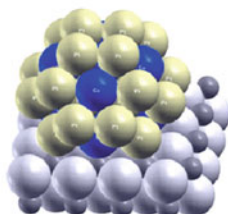


Fig. 2.15 Study of supported binary particles via a 1D wire approach. Reproduced with permission from [21]. Copyright 2011 American Chemical Society

when studying optical response using current computational resources even with a full exploitation of point group symmetry, but future developments can probably double this size limit in the next future. The approach employed in [50] is currently being extended to other pure metal nanoclusters (such as Ag) and from pure metal nanoclusters to the study of the optical properties of nanoalloys, i.e., Ag–Au and other alloyed nanoclusters, and coupled with 1D (wire) models [51].

As another example, magic clusters can be used in the study of magnetic properties of metal nanoclusters and nanoalloys. In Fig. 2.16 a 34-atom Co–Pt cluster with L_{12} chemical ordering is shown supported on the MgO(100) surface. Partitioning the atoms of the cluster into layers and shells allows one to investigate the spin–spin coupling constants in this cluster. The results (also shown in Fig. 2.16) indicate that significant spin–spin coupling constants are found in the cluster. Other magnetic properties such as the magnetic anisotropy energy (MAE), i.e., the energy difference between different orientations of the magnetization axis of a nanoparticle, can in general be also calculated. An approach similar in spirit to this one is presently being developed in which a wire model is applied to investigate interface effects on the magnetism of CoPt particles supported on MgO(100) [21].

magnetic properties of $L1_2$ phases: chemical ordering of $Co_{10}Pt_{24}$



Spin State	Not Spin-Orbit Coupling	Spin-Orbit Coupling
Ferromagnetic	+0.00	+0.00
Ferrimagnetic	+0.44	+0.54
$\uparrow\uparrow\uparrow$	+0.65	+0.51
$\uparrow\downarrow\uparrow$		
$\uparrow\downarrow\uparrow$	not stable	+0.65
$\uparrow\uparrow\uparrow$		

$Co_{10}Pt_{24}$: construction of the chemical ordering of the structure:

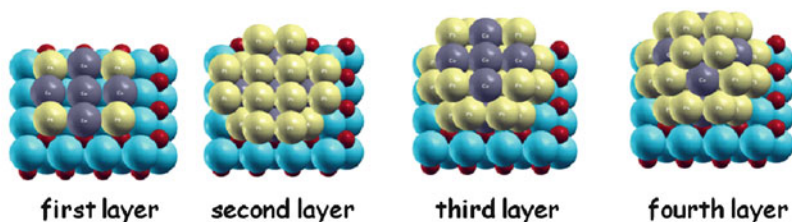


Fig. 2.16 Magnetic ordering in PtCo nanoparticles supported on MgO(100)

2.4 Supported Clusters

One important issue in surface chemistry and catalysis is to clearly identify the effect of dimensionality on the chemical reactivity of heterogeneous systems, and this has produced the new field of nanocatalysis, i.e., catalysis by pure and alloyed metal particles with dimensions in the nanometer range [77]. However, a major general problem that needs to be overcome in the applications of metal nanoparticles and nanoalloys is related to the intrinsic instability of the nanoparticles: due to their high surface/volume ratio, nanoparticles tend to decrease their energy by coalescing into larger particles (Ostwald ripening and sintering processes). This makes their characterization difficult and the exploitation of their innovative properties on a long time scale or under realistic reaction conditions nontrivial. Being intrinsically unstable, nanoparticles can only survive in the presence of kinetic barriers which avoid mass transfer and agglomeration processes, due, e.g., to the presence of surfactants or when stabilized by specific nanoparticle–substrate interactions. In this context, metal oxide substrates are often used as supports for the growth of metal particles, as defects in oxides have been demonstrated to be effective in stabilizing metal nanoparticles [65]. This practice has prompted a wealth of surface science studies [52] in which model metal-on-oxide systems are created by depositing gas-phase atoms or preformed clusters onto a single-crystal oxide surface, and then the processes of adsorption, diffusion, and self-organization are characterized in great

oxide surfaces: substrates for metal cluster self-organization

widespread use of metal oxide surfaces as substrates for metal clusters

surface science studies on well-characterized *model* systems

e.g.: growth of metal clusters by UHV deposition of single atoms:

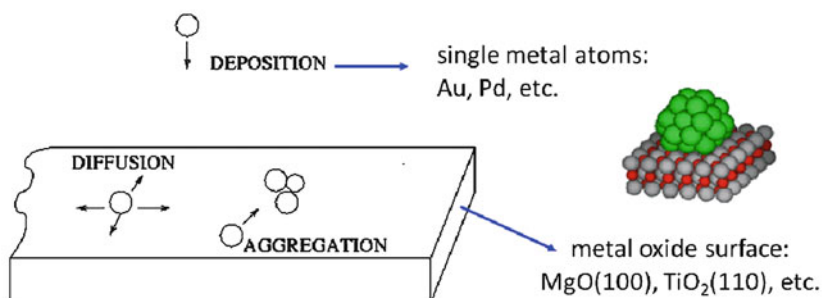


Fig. 2.17 Processes of adsorption, diffusion, and self-organization of metal atoms deposited on an oxide surface

detail, see Fig. 2.17. This section is concerned with the theoretical description of the structure of supported metal nanoparticles and nanoalloys. It can be added in passing that a very important topic but one which has not been much investigated from the theoretical point of view is the thermal stability of the supported particles. This is a central issue especially in heterogeneous catalysis when the reactions to be catalyzed are strongly exothermic (as in the case of CO and NO oxidation catalyzed by gold particles [84]), as the evolved heat can induce particle detachment from the substrate, Ostwald ripening and sintering [114] leading to larger particles and/or to the loss of beneficial particle/substrate interactions [38,98], and thus to deactivation of the catalyst.

The first issue to be faced when studying the structure of supported metal nanoparticles concerns the epitaxial relationships between the substrate and the particles. In the case of oxides made of simple metals, such as MgO, metal atoms prefer to stay on top of O atoms [99,155], see Fig. 2.18, a phenomenon which can be rationalized. The metal/substrate interaction can in fact be partitioned into several contributions. First, the Coulomb potential generated by the ionic surface induces electrostatic effects: the metal system polarizes under the influence of the oxide electrostatic field. The induced polarization can in turn polarize the charge cloud of the oxide atoms: in the case of, e.g., MgO, this effect will of course be much larger for the diffuse and “soft” oxygen anions than for the compact and “hard”

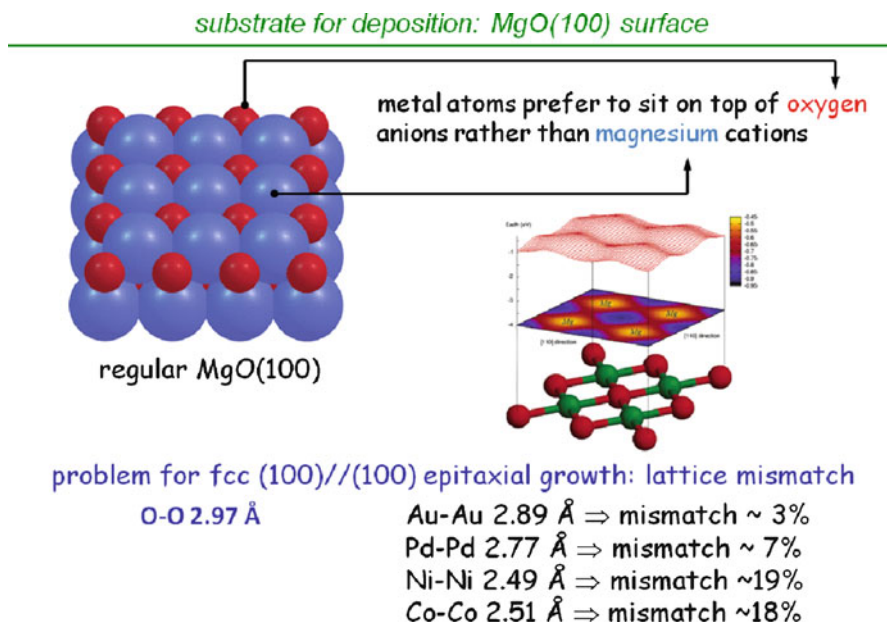


Fig. 2.18 Schematic structure of the regular MgO(100) surface (*left*), potential energy surface of a metal atom deposited on this surface (*right*), and comparison of lattice parameters for MgO and selected metals (*bottom*). Reproduced with permission from [11]. Copyright 2006 American Chemical Society

magnesium cations. Another effect (which however is not taken into account in standard DFT calculations) is due to the dispersion interactions originating in the dynamical polarization of electron clouds by the presence of nearby electrons (see the first section of this chapter). This effect will again be larger for metal positions on-top of oxygen rather than magnesium. Finally, a chemical (covalent) bonding component can also be present even in simple oxides, in which case it will as a rule be larger for the oxygen anions than for the cations. Three effects thus conjure to make oxygen anions more favorable adsorption sites than metal cations in simple oxide supports such as MgO(100). It can be noted in passing that a full analysis of the metal/surface interaction in prototypical cases has not yet been developed due to the computational burden of performing accurate *ab initio* or post-DFT calculations on relatively large systems [94], thus free from SIC errors and including dispersion interactions, but it would be very interesting to ascertain the weight of the various contributions and investigations are being conducted in this direction [31].

A subtle effect which is particularly important in determining the structure of small cluster is the so-called “metal-on-top” effect [8]. This is an increase in the metal–surface interaction energy due to the presence of metal atoms on top of the atom directly in contact with the oxide substrate, and is connected with the fact that the electron density of metal atoms sitting on top of oxygen ions is repelled and

polarized away from the surface: the presence of other metal atoms on top of those directly in contact with the oxide that can receive this excess of electron charge thus decreases the energy.

Other effects are connected with epitaxial relationships, see Fig. 2.18. Since metal atoms prefer to stay on top of oxygen atoms and the O–O first-neighbor distance for example in MgO(100) is 2.97 Å, if the optimal metal–metal distance in the bulk is smaller than this value (as it is usually the case), the lattice mismatch between the substrate and the growing particle will produce frustration and strain that need to be alleviated. For nanoparticles, this mismatch will be even more pronounced than for extended systems as a consequence of the shrinking of metal–metal distances due to the reduced coordination. This strain can be reduced by the creation of interfacial dislocations [66], i.e., defect lines at the interface by which the nanoparticles achieve a better match to the substrate. Another possibility is to develop exotic morphologies which are not favored in the bulk but become favored because of a better adhesion and interfacial energy, a possibility which is particularly likely if the lattice mismatch between metal and oxide is large [56]. Of course, these interface-stabilized phases must eventually produce a crossover to the thermodynamically stable bulk phase, depending on the growth conditions and on the associated kinetic energy barriers [56].

Concerning the metal/surface interaction, an issue which has long been debated in the theoretical literature is that of the charge transfer between the metal and the oxide. For a single Au atom on the regular MgO(100) surface as a model of an ionic and inert oxide surface, it has been proved both experimentally and theoretically that no much charge transfer exists, but rather a significant polarization of the Au electron cloud [155]. However, other systems may be different. Some useful information in this regard can be drawn from an analysis of extended model systems such as oxide ultra-thin films on metal surfaces [67]. These are composite systems formed by a very thin (ultra-thin) film, i.e., few-monolayer-thick, of an oxide grown on a single-crystal metal surface, see Figs. 2.19 and 2.20, and are interesting in a variety of ways, e.g., in this context to study the basics of metal/surface interaction. The availability of extended metal/oxide interfaces is interesting from an experimental point of view as it allows one to use space-averaged characterization techniques rather than local probes. In some cases a charge transfer between the metal and oxide components has then been clearly demonstrated. For example, it has been shown that MgO(100) yields electronic charge to Mo(100) [113]. This charge transfer strongly reduces the surface dipole moment of the Mo(100) surface, and thus its work function, i.e., the amount of energy necessary to take one electron from the interior of the system and bring it to the vacuum. It can thus be expected that sufficiently large Ag nanoparticles deposited on MgO(100) will acquire electronic charge from the substrate. The opposite effect, i.e., a transfer of electronic charge from the metal support to the oxide, can be found in other metal/oxide combinations. For example, it is found for a monolayer of NiO on the same Ag(100) substrate, see Fig. 2.19 for a pictorial view. In this picture, it can also be appreciated that the charge transfer is much reduced in passing from an NiO monolayer to a NiO

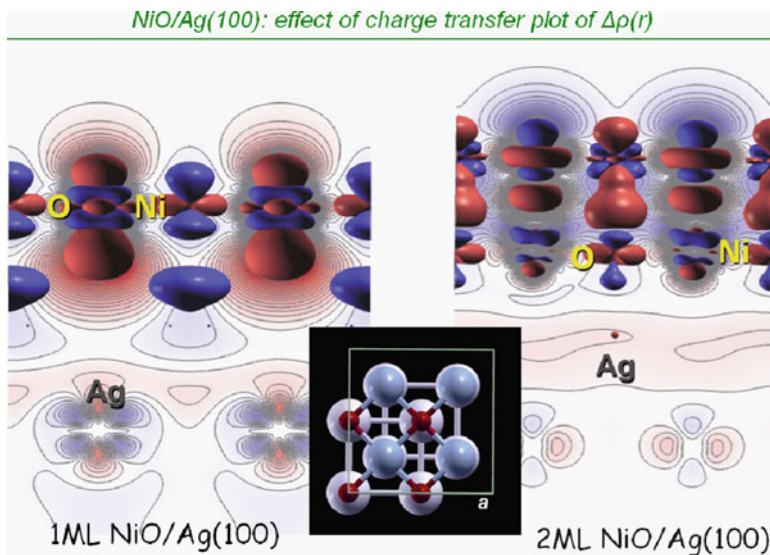


Fig. 2.19 Electron density difference plots are shown between the composite oxide-on-metal systems and the separated fragments. *Red regions* represent an increase in the electronic density, whereas *blue regions* represent a depletion. Reproduced with permission from [134]. Copyright 2011 American Chemical Society

bilayer, a subtle effect proving that charge exchange between interacting systems depend sensitively on dimensionality and geometrical parameters.

The work function of a system is an important quantity, as it determines its redox properties. Charge transfer effects modulating the work function are thus relevant as they can appreciably modify properties such as adsorption or interaction with deposited species. For example, it has been shown that the work function of the system composed of a MgO(100) ultra-thin film grown on Ag(100) is particularly low, due to the transfer of electronic charge from the oxide to the metal. In this case the work function is so low that it becomes smaller than the electron affinity of small Au clusters deposited on top in such a way that the Au clusters can therefore acquire a sizable charge from the metal support, get negatively charged and thus exhibit very unusual morphologies, being planar and parallel (fully adhering) to the surface instead of perpendicular to it or compact [93, 128]. Other so far unexplored possibilities concern the use of external electric fields to modify charge transfer effects at the interface and thus orient the physics and chemistry of adsorption. This in principle can be realized via a simple condenser arrangement, see Fig. 2.20, a possibility which is currently being investigated.

So far we have mainly considered regular, undefected oxide surfaces. It has been shown however that metal cluster can easily diffuse on regular, undefected surface [9, 107, 153] (see also the final section). This implies that a perfect surface can be unable to stabilize metal nanoparticles and avoid the danger of sintering. It is

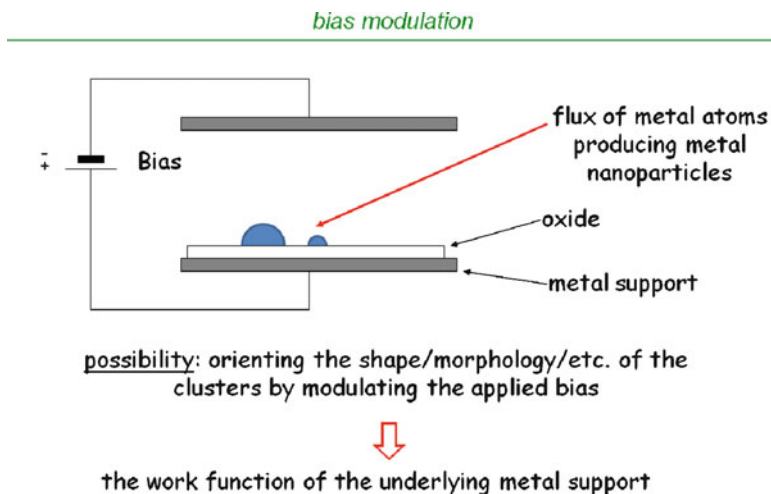


Fig. 2.20 Use of external electric fields to influence charge transfer effects at a metal/oxide interface and orient the physics and chemistry of adsorption

therefore believed that surface defects play a crucial role as trapping and nucleation centers. Defects can be distinguished into local and extended. Two examples of prototypical local defects that have been studied in great detail are the oxygen vacancy (or F_s -center) and the double vacancy (DV) on the MgO(100) surface. The F_s defect is obtained by removing a neutral oxygen atom from the surface, thus leaving behind a cavity filled with two electrons trapped by the Madelung potential created by the surface. It is usually chosen as an example of a neutral local defect, but charged F_s -centers obtained by removing one or both trapped electrons have also been studied [108]. The DV defect on the MgO(100) surface is instead obtained by removing a MgO neutral pair from the surface, thus leaving behind a larger cavity with no trapped electrons. Extended as opposed to local defects are for example step edges. Other possibilities include combinations of local defects with extended ones such as F_s -centers at steps, corners, kinks, etc. [39]. The importance of such defects on the properties of oxide surfaces as supports for the growth of metal clusters has been widely debated. Clearly, the way of preparing the surface plays a crucial role in determining the relative abundance of the various types of defects, and this may have a bearing on the adsorption properties of the oxide surface, and hence on the catalytic activity of metal nanoparticles supported on it, which might help explaining why heterogeneous catalysis is often considered as a kind of “black magic.” What can be certainly said at the theoretical level is the fact that the presence of a defect appreciably modifies the PES of metal atoms around the defect center [11, 106]. Let us consider for example the absorption of a single Au atom on the regular and defected MgO(100) surface. We fix the Au position in the plane parallel to the oxide surface and optimize its distance from the surface. Figure 2.21 shows the resulting absorption topography, that is, the equilibrium distance and absorption

defects on the MgO(100) surface: the F_s center

The oxygen vacancy: a prototype defect

Au- F_s topography

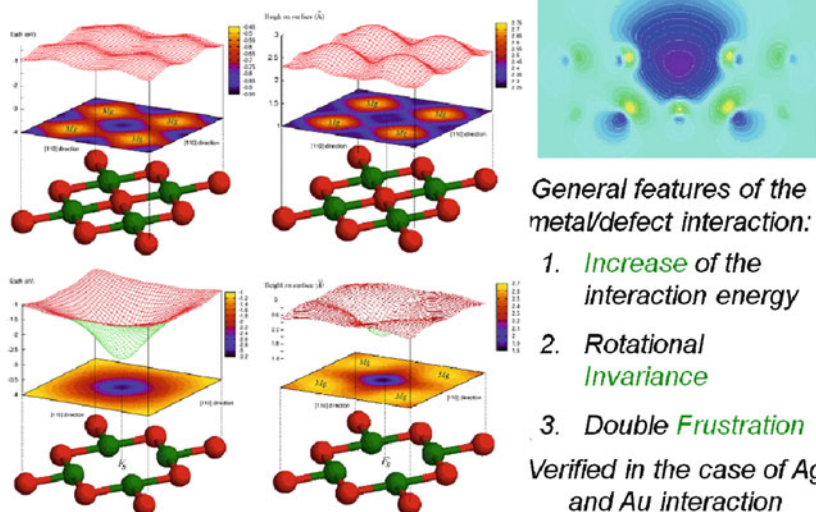


Fig. 2.21 Potential energy surface for adsorption of a single Au atom on the regular (*upper left and middle images*) and F_s -defected (*lower left and middle images*) MgO(100) surface. Plot of electron density at a F_s defect (*upper right image*). Reproduced with permission from [11]. Copyright 2006 American Chemical Society

energy as a function of the in-plane position, for both the regular (middle panel) and the defected (left-hand panel) surfaces [11]. A completely different energy and equilibrium distance landscape is immediately apparent in the two cases. On the regular surface, one finds a rather flat PES, exhibiting minima in correspondence of the oxygen atoms, maxima on the magnesium atoms, and saddle points on the hollow sites, with a maximum adhesion energy of 0.91 eV and energy barriers of about 0.2 eV for the diffusion between neighboring oxygen sites. Correspondingly, the equilibrium height exhibits minima at 2.30 Å on the oxygen sites, maxima at 2.71 Å on the magnesium sites, and saddle points at 2.40 Å on the hollow sites. The in-plane distance between the energy minima corresponds to the MgO lattice parameter of about 2.97 Å: this value is larger than the typical Au–Au distances (the Au–Au distance in the bulk is 2.885 Å, smaller distances are normally found in Au nanoclusters), thus inducing a frustration (mismatch) in the metal growth on the MgO(100) surface. The presence of the F_s defect completely alters this situation, with the resulting potential energy and equilibrium height surfaces exhibiting three major features:

- (a) The energy minimum in correspondence of the defect site is much deeper, with an adhesion energy of 3.07 eV.

- (b) A large basin of attraction is produced around the defect, with an adhesion energy of 1.62 eV on the magnesium atoms first-neighbors to the vacancy (to be compared to a value of 0.5 eV for the regular surface), extending its influence up to third neighbors, and exhibiting an approximate cylindrical symmetry: this is due to a strong perturbation of the electrostatic potential outside the surface with respect to the regular, undefected system, which affects the polarization and thus the adhesion characteristics of the metal atom.
- (c) There is a large difference between the equilibrium distance atop the defect (about 1.8 Å), strongly reduced with respect to the absorption onto the regular surface, and that atop the neighboring sites (2.65 Å on the magnesium and 2.59 Å on the oxygen sites first-neighbors to the vacancy, respectively), for which an increase in the absorption energy unexpectedly corresponds to an almost general increase in the equilibrium distance. The equilibrium distance then slowly relaxes to the values typical of the adsorption on the regular surface as the Au atom gets farther from the defect. The topography of the equilibrium distance as a function of the in-plane coordinates thus corresponds to a “crater” around the F_s center.

These three features determine the characteristics of the metal growth around the F_s defect:

- (a) Due to the strong interaction of gold with the oxygen vacancy, this defect can act as an efficient trapping center for the nucleation of metal clusters.
- (b) The approximate cylindrical symmetry of the adhesion energy around the defect site ensures the metal clusters a considerable rotational freedom, by which the clusters can rotate on the surface keeping the atom atop the defect fixed, as the adhesion energy to the surface is essentially determined by the distance of the site with which the metal atom is interacting from the defect, rather than by its chemical identity.
- (c) The strong variation of the equilibrium distance around the defect site finally entails that the growth of metal clusters is frustrated not only horizontally with respect to the surface, due to the mismatch between MgO and Au lattice parameters, but also vertically, due to the appreciable difference in the equilibrium height for the atom interacting directly with the F_s center and the neighboring atoms interacting with the surrounding sites, a feature which can be described as a “double frustration.”

In the right-hand-side of Fig. 2.21, the electron density contour of the HOMO orbital of the F_s -defected MgO(100) surface is shown [16]. The shape of this orbital, which lies in the band gap of the insulator oxide and presents a strong s -character, shows how the two electrons trapped in the cavity are not fully confined by the Madelung potential of the solid; their density, on the contrary, protrudes out of the cavity and extends also above the sites around the vacancy. This partially explains the strong perturbation to the metal/surface interaction associated with the presence of the defect.

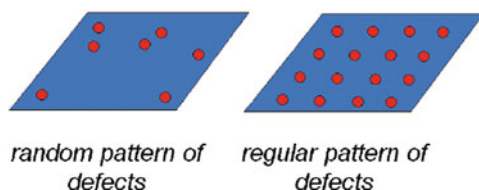
*nanopatterned oxide surfaces**nanopatterned vs random surfaces*

Fig. 2.22 Defects randomly distributed or organized according to a regular nanopattern on a surface

As the catalytic activity and in general all the properties of metal nanoparticles are strongly size dependent, reducing size dispersion is obviously an important goal. Furthermore, particle–particle distances are also important in determining the collective properties of an ensemble of metal nanoparticles. A lively line of the current research is thus concerned with metal oxide substrates used as templates for the growth of size-selected and ordered nanoparticle arrays [68]. In this connection and in relation with surface defects, this is tantamount to know whether the defects are randomly distributed over the surface or are organized in regular patterns, i.e., in other words, the topic of surface nanopatterning [34], see Fig. 2.22. The latter possibility is very intriguing as it has the advantage of automatically reducing the size dispersion [90] and allowing one to study cluster–cluster interaction [68]. It has been shown in fact both theoretically and experimentally that an ordered array of defect trapping centers can narrow the size distribution of metal particles growing on a support down to 5–10% with respect to 30–40% expected for random nucleation. Furthermore, new properties can arise when regular arrays of metal nanoparticles are created. In this case, a hierarchical material is obtained where the primary building blocks are organized to create a long-range-ordered secondary structure, a superlattice of the primary building blocks. In such a hierarchical material, nanoscale forces between the building blocks are active, which can generate new collective functionalities originated by the ensemble behavior of the metal particles [40, 144]. As an example, regular arrays of metal NPs allow to control the resonance frequency of the localized surface plasmon [37], and they are good candidates for sensors and extremely high-density data storage devices [149].

The adsorption of ligand molecules on supported metal clusters has finally been studied by DFT methods. We conclude this section with two such examples which are of interest in the field of catalysis. In Fig. 2.23, the optimal co-adsorption modes of an undissociated O_2 molecule or an O atom on small Ag clusters supported on a DV-defected MgO(100) surface are shown [14]. This system, which will

Ag_N/DV-defected/MgO(100): interaction with O and O₂

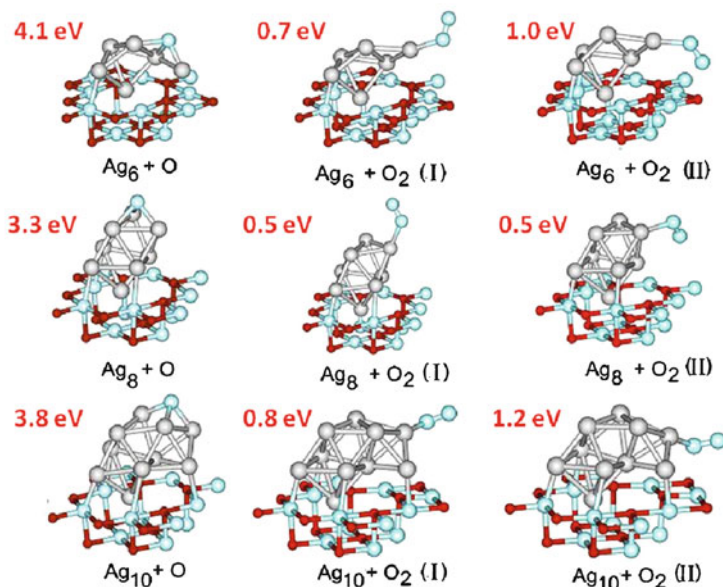


Fig. 2.23 Adsorption of atomic and molecular oxygen on DV-MgO(100) supported silver clusters. Adsorption energies (*in red*) in eV. Oxygen, magnesium, and silver atoms are represented by *light blue, red, and gray spheres*, respectively. Reproduced with permission from [14]. Copyright 2007 American Physical Society

be discussed in more detail in the next section, is also interesting to investigate whether being a surface magic cluster—Ag₈ on the DV-defected MgO(100) surface is one such clusters (see the next section)—can make a difference in the chemical properties of the metal particles. First, it can be seen from Fig. 2.23 that O binds preferentially to a triangular facet of the metal clusters, in agreement with the known behavior on crystal surfaces. Moreover, the peculiarity of Ag₈ is apparent, as its reaction energy with O is more than 0.5 eV smaller than that of the other clusters, due to both structural (shape of the cluster and exposed facets) and electronic effects. The results for the interaction with O₂ are in line with these findings and present an additional structural effect. O₂, in fact, can adsorb on Ag clusters interacting through a single O atom, with the second O atom pointing away from the MgO surface (mode I) or with the second O atom pointing toward the surface and interacting with a Mg ion (mode II). Both interaction modes are possible for Ag₆, Ag₈, and Ag₁₀, but it is interesting to observe that in the case of Ag₆ and Ag₈, the interaction energy with O₂ is larger by roughly 0.3–0.4 eV in interaction mode II with respect to interaction mode I, whereas in the case of Ag₈, modes I and II have practically the same interaction energy. This is due to the more compact structural arrangement of Ag₈, which does not present overhangs of metal atoms on the MgO(100) surface

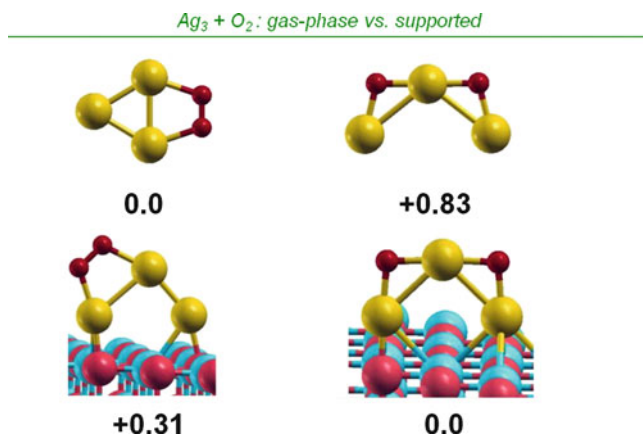


Fig. 2.24 Adsorption of an oxygen molecule on gas-phase and MgO(100)-supported silver trimers. Relative energies in eV

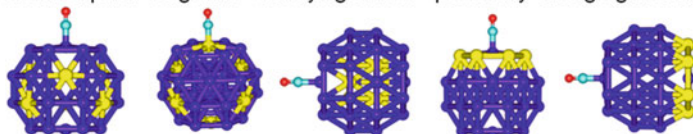
and thus does not favor the interaction of the O atom not directly bound to the metal cluster with the surface. This is interesting, as an interaction mode II connected with the presence of overhangs has been hypothesized to affect the catalytic activity of Au clusters [103]. Smaller interaction energies with incoming species could be useful when a fine-tuning of the cluster catalytic activity is sought for.

A clear example of the fact that the presence of the oxide surface can make a big difference on the chemical properties of supported metal clusters is presented in Fig. 2.24, where it is shown that according to DFT predictions the dissociation of an O₂ molecule is energetically unfavorable on a gas-phase Ag₃ cluster but becomes thermodynamically favored when Ag₃ is supported even on the regular undefected MgO(100) surface which is the classical example of an inert support. This is crucial on the chemical properties of supported Ag₃, as this can thus become an active oxidation catalyst [43]. A similar phenomenon occurs for Au₃ clusters, of particular interest as it is associated with the unexpected catalytic activity of Au nanoclusters.

Larger clusters can also be treated, see examples in Fig. 2.25. For example, the adsorption of ligands on metal nanoparticles and nanoalloys can be studied via DFT methods (Fig. 2.25a) and how this modifies the structure of the particles [30] or the chemical ordering (segregation) within an alloyed nanoparticle [151]. Ligands can in fact reshape the particles in reaction conditions, a phenomenon more and more often observed as the detail of experimental characterization improves [79] and which can be predicted at the theoretical level, see, e.g., [105] and Fig. 2.25b. Finally, one can take a further step and study reactions paths [109].

shape change in catalytic conditions: adsorption effects on structure

a chemisorption of ligands \Rightarrow alloying effect + possibility of segregation inversion



b partial oxidation of propene on Ag nanoparticles: a model study
chemisorption of $O_2 \Rightarrow$ reshaping + oxidation \Rightarrow reaction mechanism

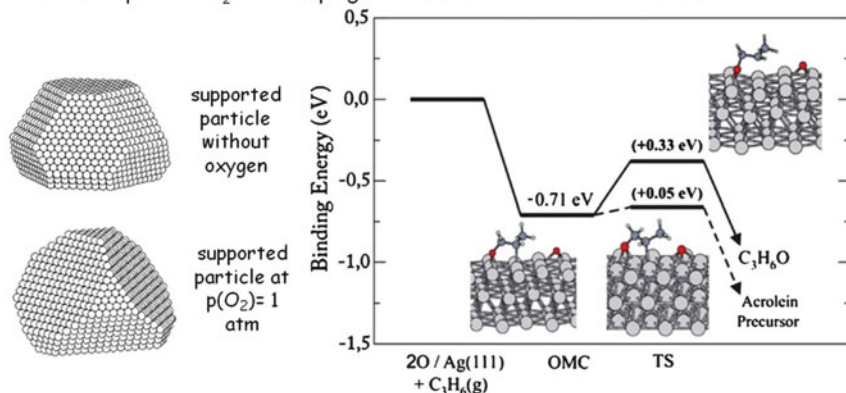


Fig. 2.25 Change in shape and chemical ordering in nanoparticles as a consequence of adsorption processes. **(a)** An fcc 38-atom model for studying adsorption of a CO molecule at the center of (111) facets of binary nanoalloys with different chemical environments, leading to tuning of adsorption energies by alloying and possible segregation inversion. **(b)** *Left*: reshaping of supported Ag nanoparticles as a consequence of oxygen adsorption at two O_2 pressures; *right*: reaction mechanism of propene on an oxidized Ag surface. Reproduced with permission from [105, 151]. Copyrights 2010 American Chemical Society and 2011 Elsevier

2.5 Three Examples

In the following, we will briefly discuss three illustrative examples of applications of DFT to the study of metal clusters, taken from the authors' own work. The aim is to provide test cases in which the concepts introduced in the previous sections can be exemplified.

As mentioned in a previous section, surface magic clusters are clusters exhibiting enhanced stability on a particular surface. The structure and energetics of Ag_N clusters both in the gas-phase and adsorbed on a defected MgO(100) terrace were studied using a DF-BH approach [14]. In this work, the search for the lowest-energy structures of small Ag_N ($N = 2-10$) clusters on a simple but realistic system—a MgO(100) terrace exhibiting a DV neutral local defect—was performed. The choice of a DV-defected MgO(100) terrace is justified by the fact that MgO(100) is one of the most studied oxide supports for the growth of model metal catalysts [78], that Ag clusters diffuse rapidly on the regular surface and are thus able to

Ag_N clusters: gas-phase and on a F_s-defected MgO(100) terrace

Structural transitions

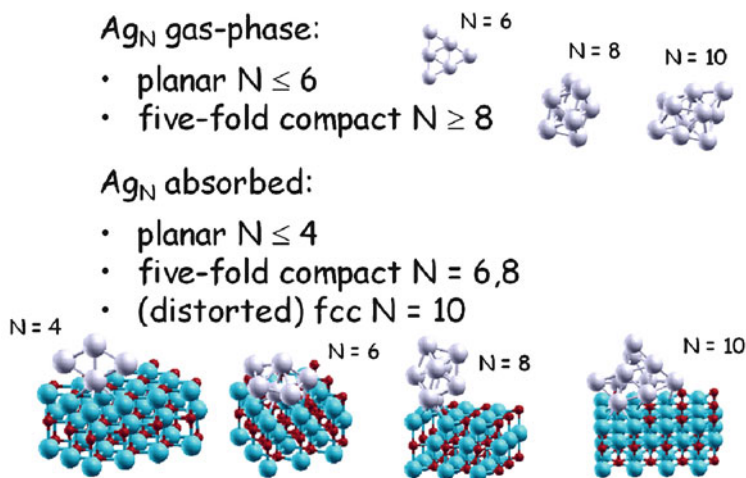


Fig. 2.26 Global minima of silver clusters both in the gas-phase and supported on an F_s -defected MgO(100) surface. Reproduced with permission from [12]. Copyright 2007 Wiley

reach surface defects which act as strong trapping centers, and that the DV is thought to be the most common neutral local defect on UHV-cleaved MgO(100) terraces [23]. A schematic view of the results is presented in Fig. 2.26. A single structural transition can be observed for gas-phase clusters: from planar to compact configurations at size 8 [106]. At variance, two different structural transitions can be observed for the supported clusters: from planar to compact at size 6 and from compact structures exhibiting fivefold symmetry axes to compact structures that are distorted pieces of an fcc lattice at size 10. The presence of the defected surface thus makes an appreciable difference on the structural properties of these small Ag clusters. Moreover, an analysis of the energetics of such clusters showed that Ag_8 has the highest incremental formation energy, while Ag_9 has the second lowest incremental formation energy, as for $PdAg_6$, see the inset in Fig. 2.11. In other words, the cluster/defected-surface interaction strongly reinforces the magic character of Ag_8 , thus producing a system with peculiar chemical and electronic properties: a substantially larger stability and a larger HOMO-LUMO gap than neighboring sizes. Additionally, Ag_8 exhibits a more compact structure with respect to the neighboring sizes, with no Ag atoms hanging over the MgO surface, and this has consequences on its chemical properties, as discussed in the previous section. The magic character of Ag_8 suggests the possibility of selectively producing it via a properly devised synthetic method, a possibility so far unfortunately unexplored.

Somewhat larger clusters can be investigated via a DF-EP approach, as discussed in the previous sections. Clusters containing few tens of atoms can present

structure of Pd clusters on regular MgO(100)

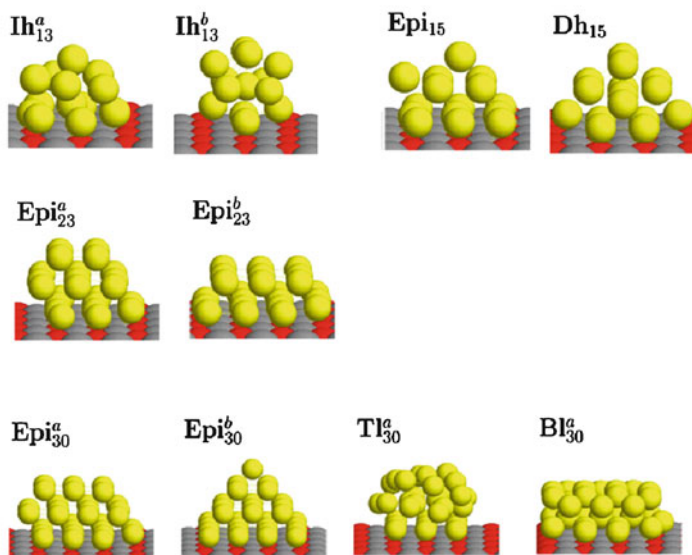


Fig. 2.27 Some structural motifs of small palladium clusters adsorbed on MgO(100) surface. Reproduced with permission from [15]. Copyright 2007 American Physical Society

nanofacets of different symmetries and orientations, edges between nanofacets, corners (in some cases truncated corners), and overhangs at the interface with the support, see Fig. 2.27. These nanoscale features give a variety of adsorption sites, with different symmetries and properties, confined in a very small region of space, which can be very important for applications. For example, this may originate low-energy pathways for chemical reactions, as in the case of the $\text{CO} + \text{NO}$ reaction on Pd clusters adsorbed on MgO, in which a low-temperature reaction mechanism is observed in small nanoclusters (below 30 atoms) but not in larger clusters or bulk surfaces [152]. It can be noted that overhangs in Au/MgO(001) clusters have been suggested to be very favorable sites for CO oxidation [104]. For Pd clusters on MgO(001), experimental evidence [78] indicates fcc structures in (001) epitaxy with the substrate for clusters of sizes $N \sim 100$ atoms and more. On the other hand, DFT calculations show that very small clusters, below ten atoms, present a different epitaxy, such as a tetrahedron for Pd₄, a square pyramid for Pd₅, and an octahedron for Pd₆. A transition to structures with (001) epitaxy must occur somewhere below 100 atoms, but the actual size is experimentally unknown. Empirical potentials are not fully informative, as they give different answers depending on the model, so that accurate DFT results are needed. These were obtained in [15], in which a systematic search for the lowest-energy structures of Pd clusters adsorbed on the regular MgO(001) surface was performed via a DF-EP approach [10, 13, 54]. Clusters were adsorbed on the flat regular oxide surface and not on surface defects, mimicking

deposition at low temperatures: deposition at sufficiently low temperatures or high fluxes may cause the growth of metal clusters on regular terrace sites. In the spirit of the DF-EP approach, the database of candidate structures to be re-optimized at the DFT level was constructed to include clusters belonging to several different structural families, and not simply the lowest-energy isomers of the prevailing family.

The results were interesting. Between 10 and 15 atoms, a competition among three main structural motifs was found: epitaxial (Epi), icosahedral (Ih), and decahedral (Dh) clusters, see Fig. 2.27. Epi clusters are epitaxial clusters obtained from the perfect square-basis pyramid of 14 atoms: an atom is added on a triangular facet of the pyramid to produce the cluster Epi_{15} . The Ih family comprises the perfect Mackay icosahedron of 13 atoms (Ih_{13}^b), and a distorted icosahedron (Ih_{13}^a), which presents a better matching with the substrate and a much lower energy. The Dh family is made of fragments of a decahedron presenting a fivefold axis which runs parallel to the MgO(001) surface, such as Dh_{15} , see Fig. 2.27. It was found that Epi structures clearly prevail for $N \geq 12$. As expected, metal–oxide interaction is not strong enough to cause a 2D cluster growth: the most stable cluster shapes are three dimensional. However, the metal–substrate interaction is crucial in determining the best cluster structures. In the gas phase, I_h and D_h clusters are much more stable than fcc truncated pyramids. However, this is not sufficient to counterbalance the better adhesion to the substrate of Epi clusters for $N \geq 12$. For example, at size $N = 13$, neither the undistorted icosahedron nor a buckled biplanar structure, which are favored in gas phase, can compete with the (001) epitaxy truncated pyramids. At $N = 30$, the most favorable Epi clusters are the perfect pyramid (Epi_{30}^b) and a structure presenting truncations and overhangs (Epi_{30}^a), while non-epitaxial structures can be classified as trilayers (TI) and bilayers (BI), see Fig. 2.27. The best TI structure (TI_{30}^a) has its bottom layer in good (001) epitaxy with the substrate, but the second and third layers do not continue this arrangement. Both BI structures present (111) facets in contact with the substrate. It can be noted that Epi structures are lower in energy at $N = 30$, with larger differences than for $N < 15$: (001) epitaxy is more and more favored as size increases. Moreover, overhangs are found to be already present for clusters in the size range $15 \leq N \leq 30$. A single overhanging atom is found in Epi_{15} . More significantly, well-developed overhanging atomic rows are present in Epi_{23}^a , which is clearly lower in energy than the structures without overhangs, and even in Epi_{30}^a , which is slightly better than the complete pyramid Epi_{30}^b , see Fig. 2.27, a particularly significant fact as Epi_{30}^b is a magic structure for the pyramidal motif. Structures with overhangs optimize metal–metal interactions at the expense of the adhesion with the substrate, since metallic bonding is improved by a more compact cluster shape, while adhesion suffers from the decrease of the number of atoms in the cluster basis. However, the “metal-on-top” effect partially compensates this decrease by an improvement of the adhesion energy per basal atom: basal atoms on an edge below an overhang better adhere to the substrate than other basal edge atoms. In summary, in [15] it was demonstrated that the transition toward fcc clusters in (001) epitaxy with the MgO substrate is taking place between sizes 11 and 13. At variance with the behavior of smaller clusters,

from these sizes on, the metal–substrate interaction becomes crucial, so that the best Pd/MgO(001) clusters are not only different from the best gas-phase Pd clusters but also grow in very good fcc (001) epitaxy with the underlying MgO lattice. The results for N around 30 show that the energy difference between epitaxial and non-epitaxial clusters becomes larger with increasing size, which supports the transition from non-epitaxial to epitaxial configurations. In epitaxial clusters, overhanging atomic rows are developed already at quite small sizes. Standard empirical potentials are unable to quantitatively predict the actual structures of the most stable clusters around $N = 13$ and the details of the shapes of larger clusters, such as preferential truncations and overhangs, due to the neglect of energy contributions such as the metal-on-top one effect.

As a last example we will consider a different environment: surfactant coating of metal nanoparticles in the homogeneous phase producing colloidal suspensions. Colloidal suspensions of transition metals are formed by metal nanoparticles which are stabilized by protective shells/layers to prevent coalescence phenomena [123]. The possibility of effectively stabilizing nanometric metallic particles with a high surface/volume ratio in solution allows for a quickly growing number of technological applications of such colloidal suspensions [26]. Bottom-up methods to produce these systems are based on the synthesis of metallic particles starting from elementary constituents, i.e., single atoms, ions, or small clusters. These methods primarily consist on the reduction of metal salts via chemical processes, the use of electrochemical techniques, the controlled decomposition of organometallic metastable compounds, or the aggregation of metallic species in low oxidation states. A large number of stabilizing species, donor ligands, polymers, and surfactants are used to control the growth of the freshly formed metallic particles and to protect the growing units from coalescence into the thermodynamic equilibrium phase (the bulk crystal). In this context, the use of olefinic complexes of metals in a low oxidation states proves to be a clean route for obtaining colloidal suspensions of mono- and bimetallic particles. Experimental evidence has in fact shown that in the presence of only the solvent molecules, the stability of these suspensions at room temperature is limited to a few days, while with the use of surfactants the stability of metal aggregates is extended to a few months. The effective mechanisms by which growth eventually takes place, however, are not known, and are difficult to investigate experimentally, due to the lack of proper characterization tools able to furnish information on reactive processes in situ and in real time. Computational approaches can provide a very useful support in this sense. In [18], such an enterprise was undertaken in the specific case of neutral small Pt clusters interacting with surfactants in which the ligand is based on unsaturated organic groups. In detail, a theoretical first-principles study of the $\text{Pt}_n(\text{ligand})_m$ ($n = 1, 3$) metallorganic complexes was performed, by varying the number of metal atoms and the nature and number of organic coordinate ligands (specifically, vinylic and arylc ligands), see Fig. 2.28. Several conclusions were drawn from such a study. First, the fact that the Pt/C=C interaction has a many-body character, i.e., the binding energy appreciably decreases with the number of interacting C=C units. Second, the weaker binding of aromatic species with respect to vinylic species, due

DF global optimization

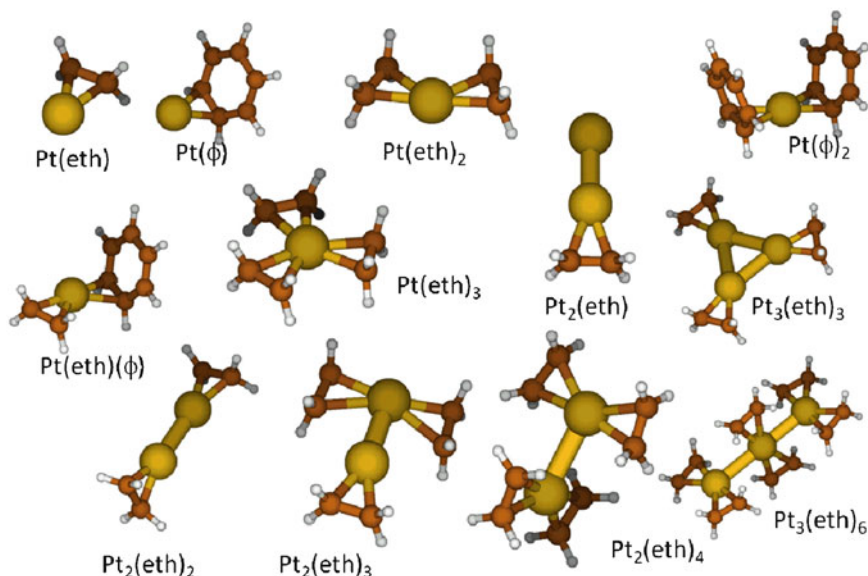


Fig. 2.28 Structures of $Pt_n(\text{ligand})_m$ ($n = 1, 3$) metallorganic complexes in the case of vinylic (eth = ethylene) and aryllic (Φ = benzene) ligands

to the need of disrupting π -electron conjugation, which makes that a third aromatic molecule does not bind to a doubly coordinated Pt center, thus leaving it free for further aggregation. Third, the relatively low values of the ligand detachment energy barriers from a fully coordinated Pt center that can be overcome at room or slightly higher temperatures. Fourth, the fact that two binding mechanisms between a small Pt cluster and a C=C bond: one involving the formation of σ bonds between Pt and C atoms (σ -interaction mode) and one in which the metal/ligand interaction takes place through a donation/back-donation mechanism (π -interaction mode). Additionally, two regimes could be distinguished in the growth of coated Pt clusters: a “coordinatively saturated” regime, in which the ratio among the number of ligands and the number of metal atoms is high and the ligand/organic π -interaction mode is preferred, and a “coordinatively unsaturated” regime, in which this ratio is low and the ligand/organic σ -interaction mode is preferred. The coordinative unsaturation typical of the latter regime favors more complicated, reactive processes, such as oxidative insertion of Pt atoms into a C–H bond. These conclusions were in tune with available experimental data, and suggested a positive role of theoretical simulations in the study of the nucleation and growth of metal clusters in the homogeneous phase in terms of accurate prediction of the energetics and of the kinetic growth parameters.

2.6 Growth

So far we have focused on static processes and structure prediction, and we have roughly described length-rescaling ideas. Kinetic processes such as diffusion and reaction have been simply mentioned, and the corresponding time-rescaling approaches have not been described [145]. However, it is known that length and time scales are intimately associated, in the sense that—very roughly—the interesting dynamics of larger systems become progressively slower. In this section, we will briefly touch upon this subject on which a huge literature is present.

At the lowest end, i.e., the fastest, of the time scales, it is possible to conduct first-principles MD simulations. In these simulations, both the electronic and the nuclear degrees of freedom can be simultaneously described. This implies a time step of the order of hundredths of femtoseconds (i.e., roughly 10^{-17} – 10^{-16} s). Considering that current simulations typically run for at most 10^6 steps, it derives that these simulations can cover a time span of at most tens of picoseconds. One of the most popular among these approaches is the Car–Parrinello method [35]. An important possibility is realized when the process of interest requires a description at the Quantum Mechanical level and occurs on a fast time scale but involves only a limited part of the system, with this part being coupled to a possibly complex environment (such as a solvent) whose evolution can be described classically. In such a case it is reasonable to describe the interesting part of the system at the Quantum Mechanical first-principles level, and the environment at the Classical or Molecular Mechanics level, giving rise to so-called QM/MM hybrid approaches [135]. These approaches fall within the general problem of embedding [82], i.e., the problem of setting up appropriate boundary conditions when attention is focused on a subset of a larger system whose behavior is supposed to be known and one aims at taking advantage of this to simplify and reduce the computational effort. Embedding techniques can be used both at the dynamical and at the static level: one popular embedding approach is the ONIOM protocol [60, 139].

A crucial issue using first-principles approaches in dynamical studies is whether it is possible to simulate time scales longer than few picoseconds. The answer can be affirmative if the process under study is an activated one. An activated process is one in which the system oscillates most of the time in the neighborhood of a given local minimum or inherent structure [137, 138], which is left by overcoming an energy barrier to jump into another local minimum, and so on. Several strategies can be devised to deal with this problem [145]. One strategy is to first single out all (or as many as possible) local minima in the PES, and then establish how they are connected via saddle points. Such information is often graphically summarized in terms of disconnectivity diagrams [148]. A complete knowledge of the topology and connectivity of the inherent structures would allow one to predict the system behavior as a function of temperature (both thermodynamics and kinetics: phase diagram and evolution), via, e.g., kinetic Monte Carlo simulations [127]. In these simulations one starts from a given local minimum, enumerates the possible paths leaving this minimum, and realizes the transition to one of them selected according

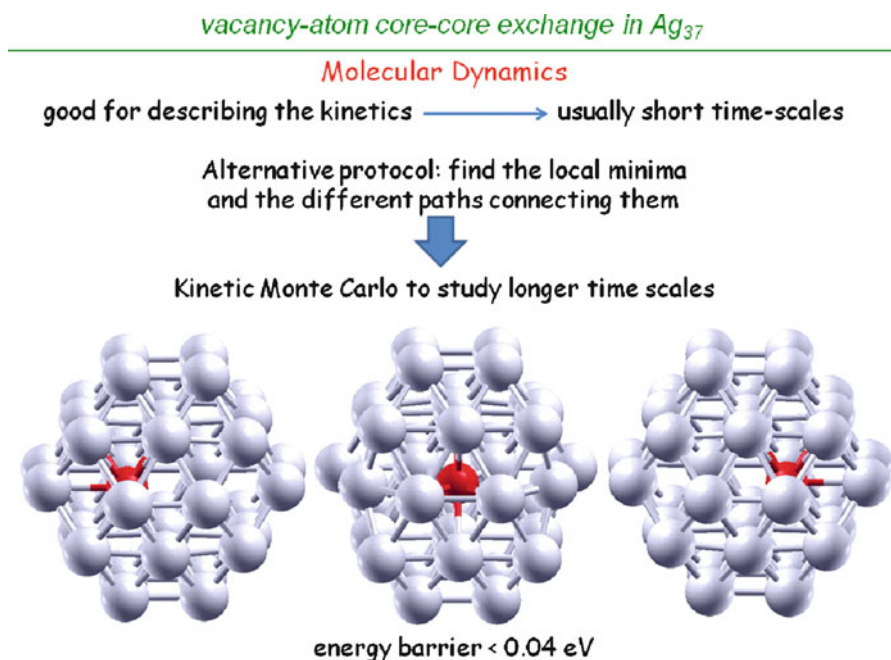


Fig. 2.29 Vacancy diffusion inside a Ag₃₇ cluster

to a Metropolis criterion. From a technical point of view, an exhaustive search of all the low-energy local minima at the first-principles level can be conducted via the global optimization algorithms discussed in previous sections. Saddle points and energy barriers can also be found using first-principles approaches. One can distinguish two cases, according to whether one has a knowledge of the initial and final configurations of the local minima to be connected or not. In the former case, the Nudged Elastic Band (NEB) method [102] is one of the most popular to find the reaction path between the two configurations and is implemented in many electronic structure codes, even though other methods have been proposed as numerically more robust [45]. If knowledge on the final configuration is lacking, then the search for the local minima connected to the starting structure can be conducted via several methods, see, e.g., [111]. To make a simple example, the process of diffusion of a vacancy (i.e., a vacancy-atom exchange) in the core of a truncated octahedral Ag₃₇ cluster is graphically shown in Fig. 2.29.

A phenomenon in the field of supported metal clusters that can be typically studied via this type of approaches is self-organization and growth by deposition of metal atoms from the gas-phase. The adsorption configurations that are the local minima of the system and the diffusion mechanisms connecting them can be singled out, and the corresponding energetics evaluated in detail. An interesting fact, already

diffusion of Pd, Ag, Au clusters on the regular MgO(100) surface

results of DF-NEB* diffusion energy barriers

(values in eV)	Pd	Au	Ag
<i>Monomer</i>	0.39	0.22	0.10
<i>Dimer</i>	0.39	0.62	0.22
<i>Trimer</i>	0.30	0.19	0.12
<i>Tetramer</i>	0.38	0.42	0.21
DFT \Rightarrow	~ 0.38	~ 0.20	~ 0.10

*interesting to note in passing: M_2 and M_4 for Ag and Au
diffuse more slowly than M_1 and M_3*

**DF-NEB (Density-Functional Nudged Elastic Band)*

Fig. 2.30 Diffusion energy barriers of small palladium, gold, and silver clusters diffusing on the regular MgO(100) surface

mentioned in the previous sections, which has been discovered via first-principles simulations [9, 107, 153] is that small metal clusters can diffuse on a regular oxide surface even faster than adatoms, see Fig. 2.30.

As the surface on which deposition occurs is usually composed of regular terraces and various kinds of defects, with the latter acting as trapping centers, the mobility of metal species is crucial in determining whether nucleation occurs preferentially at defects or on the flat surface. Fast diffusion causes nucleation at defects only, whereas slow diffusion allows nucleation also on flat terraces. Epitaxial relationships are important in determining cluster mobility. For metals on MgO(100), already dimers and trimers may not stay flat on the surface in their lowest-energy configuration due to the metal-on-top effect [8] mentioned in a previous section. For example, neutral copper, silver, and gold dimers prefer to stay vertical on regular MgO(001) terraces, even though the situation can be different on ultrathin films, where gold clusters can be charged. Palladium dimers stay horizontal, but palladium trimers adopt a vertical configuration. Due to these subtle epitaxial effects, small clusters can present a variety of interesting diffusion mechanisms. Due to the difficulty of directly measuring diffusion coefficients and of imaging diffusion processes in experiments, most of the available results in this field have been obtained in the domain of theory and simulations. However, information about the mobility of adatoms and small clusters can be inferred from the effects that such mobility has on quantities that can be more easily measured at the experimental level. At the theoretical level, it is found that the diffusion of metal adatoms and small clusters on the MgO(100) surface can occur via a variety of processes.

diffusion of Pd,Ag,Au clusters on the regular MgO(100) surface

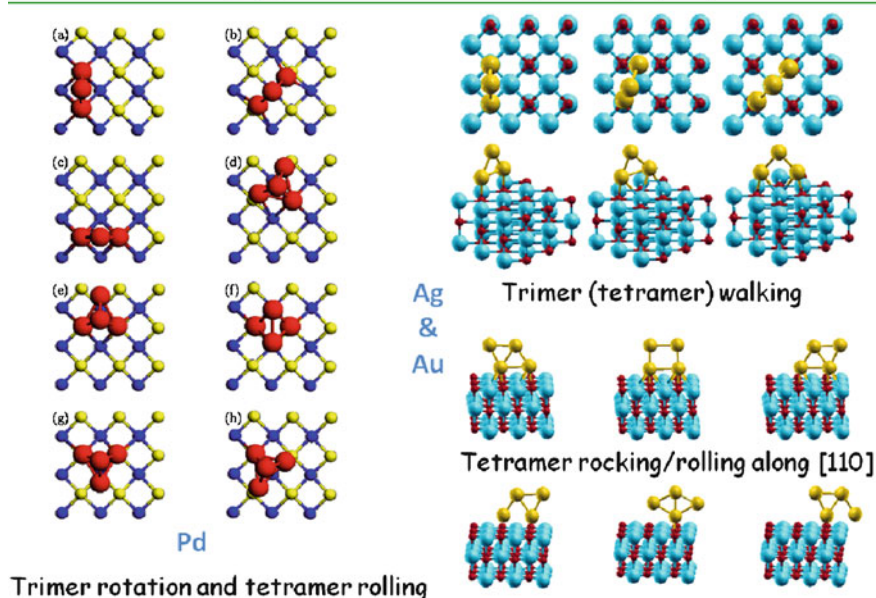


Fig. 2.31 Diffusion mechanisms of trimer and tetramer clusters on the regular MgO(100) surface. Reproduced with permission from [9, 17]. Copyrights 2005 American Physical Society and 2007 Institute of Physics

Apart from simple hopping between favorable adsorption sites, rotation, sliding, leapfrog, walking, concertina, flipping, twisting, rolling, and rocking mechanisms have been shown to take place, depending on the type of metal (i.e., the features of its interaction with the surface) and the size of the cluster [57], see Fig. 2.31. Moreover, it is also found that diffusion of small clusters and not only adatoms is crucial to reconcile theoretical predictions and experimental data, see Fig. 2.32. In an experiment that has stimulated much theoretical work [73], Pd adatoms were deposited on MgO(001) in a wide range of temperatures, from 200 to 800 K, and the temperature-dependent island density was measured. This density was found to be constant from 200 to about 600 K, and to drop suddenly down above this temperature. The constant island density until low temperature was an indication of nucleation at defects down to low temperatures, with a negligible proportion of terrace nucleation. The experimental estimate of the diffusion energy barrier was less than 0.3 eV, at variance with DFT calculations, predicting it to be 0.34–0.41 eV. The discrepancy between the experimental estimate and the calculations was solved by noting that small clusters, up to the tetramer, also strongly contribute to the mobility of palladium down to 200 K, as trimers or tetramers are in fact even more mobile than monomers. Therefore, in determining whether nucleation occurs either on terrace sites or at defects, the mobility of monomers and of small clusters must be taken into account.

diffusion of Pd,Ag,Au clusters on the regular MgO(100) surface

exp: deposition of Pd atoms on a cleaved highly defected MgO(100) surface



experimental evidence: **constant density** of Pd metal islands over a broad range of temperatures (200 – 600 K)



interpretation: Pd small clusters diffuse on the surface, reach the defects, are trapped there where islands nucleate and grow

results of Monte Carlo simulation of island nucleation where:

- only monomers diffuse
- small clusters up to the tetramer diffuse with 3 min postdeposition

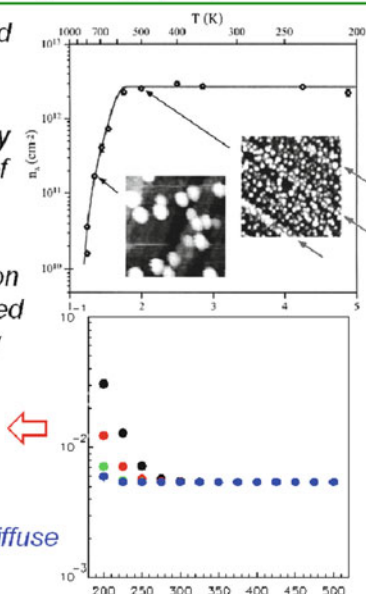


Fig. 2.32 Experiment-theory comparison in the case of small palladium clusters diffusing and growing on the MgO(100) surface. Reproduced with permission from [9, 73]. Copyrights 2000 and 2005 American Physical Society

This type of approaches can be employed for studying not only growth, but also other interesting dynamical phenomena, with heterogeneous catalysis being the most prominent, and is expected to become commonplace in a next future.

2.7 Summary and Perspectives

In this contribution, which is far from being exhaustive especially in terms of literature citation (and we apologize in advance with the colleagues whose important contributions have not been quoted mainly for reasons of space or needs of presentation), we have tried to present what in our opinion are the specific (sometimes unique) features of the chemical bond in metal nanoclusters and nanoalloys from the theoretical point of view. We have discussed some of the most advanced first-principles (especially DFT) techniques to model and simulate these systems, and pointed out their advantages and limitations. With an eye on a non-specialized audience, we have tried to make these methods understandable to nonexperts (experimentalists and students alike), making large use of pictorial representations and highlighting why and how these tools can be helpful. In particular, attention has also been focused on concepts and methods which can be

developed from a theoretical point of view which can help rationalizing the available data, provide a general framework for experimental investigations, and hopefully set the ground for a predictive computational science. We showed that interesting results have already been obtained in several cases and suggested that many more are likely to be expected in the next future, considering the increasing accuracy of first-principles methods, the advances in and the ever-increasing accessibility of computer hardware and software by which the application of first-principles approaches is becoming feasible in practice to a large set of users via commonly available computational resources. In particular in the field of the properties of metal nanoclusters and nanoalloys: catalytic, optical, magnetic, etc., we believe that computational methods are nowadays finally becoming able to treat realistic systems with sufficient accuracy and will give a decisive contribution to future advances in both basic and oriented research and industrial applications. We tried to limit the overlap with other contributions in this book, even though a certain amount of duplication is probably unavoidable, and not necessarily a serious drawback. Our hope is that this brief contribution will help bringing theory closer to experiment and promoting interdisciplinary research in this field.

Acknowledgments Financial support from the Italian CNR for the project SSA-TMN within the framework of the ESF EUROCORES SONS, and from European Community Sixth and Seventh Framework Programme for the projects GSOMEN (No. NMP4-CT-2004-001594) and SEPON (No. ERC-2008-AdG-227457) are gratefully acknowledged. Many of the DFT calculations here described were performed at the CINECA Supercomputing Center within an agreement with Italian CNR, and also at the CASPUR Supercomputing Center. The authors are indebted to Riccardo Ferrando, Giulia Rossi, Edoardo Aprà, Roy. L. Johnston, Lauro Oliver Paz-Borbon, Paul S. West, Francesca Baletto, Christine Mottet, Mauro Causà, Gaetano Granozzi, Claude Henry, Luca Gavioli, Stefan Vajda, Falko Netzer, Fabio R. Negreiros, Luca Sementa, and Iorwerth O. Thomas for very stimulating collaborations and/or many interesting discussions.

References

1. Abrikosov AI (2008) Rep Progr Phys 71:046501
2. Ahlrichs R, Elliott SD (1999) Phys Chem Chem Phys 1:13
3. Akola J, Walter M, Whetten RL, Hakkinen H, Grönbeck H (2008) J Am Chem Soc 130:3756
4. Altieri S, Finazzi M, Hsieh HH, Havekort MW, Lin HJ, Chen CT, Frabboni S, Gazzardi GC, Rot A, Valeri S (2009) Phys Rev B 79:174431
5. Anisimov VI, Zaanen J, Andersen OK (1991) Phys Rev B 44:943
6. Aprà E, Ferrando R, Fortunelli A (2006) Phys Rev B 73:205414
7. Baletto F, Ferrando R, Fortunelli A, Montalenti F, Mottet C (2002) J Chem Phys 116:3856
8. Barcaro G, Fortunelli A (2005) J Chem Theory Comput 1:972
9. Barcaro G, Fortunelli A, Nita F, Ferrando R (2005) Phys Rev Lett 95:246103
10. Barcaro G, Fortunelli A, Rossi G, Nita F, Ferrando R (2006) J Phys Chem B 110:23197
11. Barcaro G, Fortunelli A (2006) J Phys Chem B 110:21021
12. Barcaro G, Aprà E, Fortunelli A (2007) Chem Eur J 13:6408
13. Barcaro G, Fortunelli A (2007) J Phys Chem C 111:11384
14. Barcaro G, Fortunelli A (2007) Phys Rev B 76:165412
15. Barcaro G, Fortunelli A, Rossi G, Nita F, Ferrando R (2007) Phys Rev Lett 98:156101

16. Barcaro G, Causà M, Fortunelli A (2007) *Theor Chem Acc* 118:807
17. Barcaro G, Fortunelli A (2007) *New J Phys* 9:22
18. Barcaro G, Fortunelli A (2009) *Theor Chem Acc* 123:317
19. Barcaro G, Thomas IO, Fortunelli A (2010) *J Chem Phys* 132:124703
20. Barcaro G, Fortunelli A, Polak M, Rubinovich L (2011) *Nano Lett* 11:1766
21. Barcaro G, Sementa L, Negreiros F, Ferrando R, Fortunelli A (2011) *Nano Lett* 11:5542
22. Barone V, Bencini A, Cossi M, Di Matteo A, Mattesini M, Totti F (1998) *J Am Chem Soc* 120:7069
23. Barth C, Henry CR (2003) *Phys Rev Lett* 91:196102
24. Becke AD (1993) *J Chem Phys* 98:5648
25. Biswas A, Siegel D, Seidman DN (2010) *Phys Rev Lett* 105:076102
26. Bonnemann H, Richards RM (2001) *Eur J Inorg Chem* 2455
27. Booth GH, Alavi A (2010) *J Chem Phys* 132:174104
28. Paz-Borbon LO, Mortimer-Jones TV, Johnston RL, Posada-Amarillas A, Barcaro G, Fortunelli A (2007) *Phys Chem Chem Phys* 9:5202
29. Paz-Borbon LO, Johnston RL, Barcaro G, Fortunelli A (2007) *J Phys Chem C* 111:2936
30. Paz-Borbon LO, Johnston RL, Barcaro G, Fortunelli A (2009) *Eur Phys J D* 52:131
31. Paz-Borbon LO, Barcaro G, Fortunelli A, Levchenko SV (2012) *Phys Rev B* 85:155409
32. Born M, Oppenheimer JR (1927) *Ann Phys* 84:457
33. Broyer M, Cottancin E, Lermé J, Pellarin M, Del Fatti N, Valle F, Burgin J, Guillon C, Langot P (2008) *Faraday Discuss* 138:137
34. Brune H, Giovannini M, Bromann K, Kern K (1998) *Nature* 394:451
35. Car R, Parrinello M (1985) *Phys Rev Lett* 55:2471
36. Causà M, Colle R, Dovesi R, Fortunelli A, Pisani C (1988) *Phys Scripta* 38:194
37. Chan GH, Zhao J, Hicks EM, Schatz GC, Van Duyne RP (2007) *Nano Lett* 7:1947
38. Chen MS, Goodman DW (2007) *Top Catal* 44:41
39. Chiesa M, Paganini MC, Giamello E, Murphy DM, Di Valentin C, Pacchioni G (2006) *Acc Chem Res* 39:861
40. Claridge SA, Castleman AW Jr., Khanna SN, Murray CB, Sen A, Weiss PS (2009) *ACS Nano* 3
41. Cococcioni M, de Gironcoli S (2005) *Phys Rev B* 71:035105
42. Cohen-Tannoudji C, Diu B, Laloe F (2006) *Quantum mechanics*. Wiley-Interscience, Paris
43. Daniel C, Full J, Gonzalez L, Lupulescu C, Manz J, Merli A, Vajda S, Woste L (2010) *Science* 299:536
44. deHeer WA (1993) *Rev Mod Phys* 65:611
45. del Campo JM, Köster AM (2008) *J Chem Phys* 129:024107
46. Dirac PAM (1928) *Proc R Soc* 117:610
47. Dirac PAM (1930) *Proc Cambridge Phil Soc* 26:376
48. Dovesi R, Saunders VR, Roetti R, Orlando R, Zicovich-Wilson M, Pascale F, Civalleri B, Doll K, Harrison NM, Bush IJ, D'arco P, Llunel M CRYSTAL06. www.crystal.unito.it
49. Dunlap BI, Rosch N, Trickey SB (2010) *Mol Phys* 108:3167
50. Durante N, Fortunelli A, Broyer M, Stener M (2011) *J Phys Chem C* 115:6277
51. Durante N, Barcaro G, Fortunelli A, Broyer M, Stener M in preparation
52. Ertl G, Freund HJ (1999) *Phys Today* 52:32
53. Ferrando R, Fortunelli A, Rossi G (2005) *Phys Rev B* 72:085449
54. Ferrando R, Fortunelli A, Johnston RL (2008) *Phys Chem Chem Phys* 10:640
55. Ferrando R, Jellinek J, Johnston RL (2008) *Chem Rev* 108:845
56. Ferrando R, Rossi G, Nita F, Barcaro G, Fortunelli A (2008) *ACS Nano* 2:1849
57. Ferrando R, Fortunelli A (2009) *J Phys Condens Matter* 21:264001
58. Fortunelli A, Salvetti O (1991) *J Comp Chem* 12:36
59. Fortunelli A, Salvetti O (1991) *Chem Phys Lett* 186:372
60. Fortunelli A, Salvetti O, Villani G (1991) *Surf Sci* 244:355
61. Fortunelli A, Selmi M (1994) *Chem Phys Lett* 223:390
62. Fortunelli A, Velasco AM (1999) *J Mol Struct (THEOCHEM)* 487:251

63. Apra E, Fortunelli A (2000) *J Mol Struct* 501–502:251
64. Frank FC, Kasper JS (1959) *Acta Crystallogr* 12:483
65. Freund HJ (2002) *Surf Sci* 500:271
66. Freund LB, Suresh S (2003) *Thin film materials: stress, defect formation and surface evolution*. Cambridge University Press, Cambridge
67. Freund HJ, Pacchioni G (2008) *Chem Soc Rev* 37:2224
68. Gavioli L, Cavaliere E, Agnoli S, Barcaro G, Fortunelli A, Granozzi G (2011) *Progr Surf Sci* 86:59
69. Giannozzi P, Baroni S, Bonini N, Calandra M, Car R, Cavazzoni C, Ceresoli D, Chiarotti G, Cococcioni M, Dabo I, Dal Corso A, De Gironcoli S, Fabris S, Fratesi G, Gebauer R, Gerstmann U, Gougoussis C, Kokalj A, Lazzeri M, Martin-Samos L, Marzari N, Mauri F, Mazzarello R, Paolini S, Pasquarello A, Paulatto L, Sbraccia C, Scandolo S, Sclauzero G, Seitsonen AP, Smogunov A, Umari P, Wentzcovitch RM (2009) *J Phys Condens Matter* 21:395502
70. Goedecker S (1999) *Rev Mod Phys* 71:1085
71. Goniakowski J, Jelea A, Mottet C, Barcaro G, Fortunelli A, Kuntová Z, Nita F, Levi AC, Rossi G, Ferrando R (2009) *J Chem Phys* 130:174703
72. Grimme S (2006) *J Comput Chem* 27:1787
73. Haas G, Menck A, Brune H, Barth JV, Venables JA, Kern K (2000) *Phys Rev B* 61:11105
74. Haberlen OD, Chung SC, Stener M, Rosch N (1997) *J Chem Phys* 106:5189
75. Hakkinen H (2008) *Chem Soc Rev* 37:1847
76. Haunschild R, Scuseria GE (2010) *J Chem Phys* 132:224106
77. Heiz U, Landman U (eds) (2007) *Nanocatalysis series: nanoscience and technology*. Springer, New York
78. Henry CR (2005) *Prog Surf Sci* 80:92
79. Herzing AA, Kiely CJ, Carley AF, Landon P, Hutchings GJ (2008) *Science* 321:1331
80. Hohenberg P, Kohn W (1964) *Phys Rev* 136:864B
81. Honeycutt JD, Andersen HC (1987) *J Phys Chem* 91:4950
82. Huang C, Pavone M, Carter EA (2011) *J Chem Phys* 134:154110
83. Hubbard PS (1961) *Rev Mod Phys* 33:249
84. Hutchings GJ, Haruta M (2005) *Appl Catal A* 291:1
85. Jellinek J, Krissinel EB (1996) *Chem Phys Lett* 258:283
86. Johnston RL (2003) *Dalton Trans* 22:4193
87. Kittel C (1996) *Introduction to solid state physics*, 7th edn. Wiley, New York
88. Kohn W, Sham LJ (1965) *Phys Rev* 140:1133A
89. Kokalj A (2003) *Comp Mat Sci* 28:155
90. Lee C, Barabasi AL (1998) *Appl Phys Lett* 73:2651
91. Li Z, Scheraga HA (1987) *Proc Natl Acad Sci USA* 84:6611
92. Libuda J, Freund HJ (2005) *Surf Sci Rep* 57:157
93. Lin X, Nilius N, Freund HJ, Walter M, Frondelius P, Honkala K, Hakkinen H (2009) *Phys Rev Lett* 102:206801
94. Lopez N, Illas F, Rosch N, Pacchioni G (1999) *J Chem Phys* 110:4873
95. Mahan GD (2008) *Quantum mechanics in a nutshell*. Princeton University Press, Princeton
96. March NH, Stoddard JC (1968) *Rep Prog Phys* 31:53
97. Marks LD (1984) *Philos Mag A* 49:813
98. Matthey D, Wang JG, Wendt S, Matthiesen J, Schaub R, Laegsgaard E, Hammer B, Besenbacher F (2007) *Science* 315:1692
99. Matveev AV, Neyman K, Yudanov I, Rosch N (1999) *Surf Sci* 426:123
100. McWeeny R, Sutcliffe BT (1969) *Methods of molecular quantum mechanics*. Academic Press, London
101. McWeeny R (1980) *Coulson's valence*. Oxford University Press, Oxford
102. Mills G, Jonsson H (1994) *Phys Rev Lett* 72:1124
103. Molina LM, Hammer B (2004) *Phys Rev B* 69:155424
104. Molina LM, Hammer B (2005) *Appl Catal A* 291:21

105. Molina LM, Lee S, Fortunelli A, Lee B, Seifert S, Winans RE, Elam JW, Pellin MJ, Barke I, von Oeynhausen V, Lei Y, Meyer RJ, Alonso JA, Rodriguez AF, Kleibert A, Giorgio S, Henry CR, Meiwes-Broer KH, Vajda S (2011) *Cat Today* 160:116
106. Moseler M, Hakkinen H, Landman U (2002) *Phys Rev Lett* 89:176103
107. Musolino V, Selloni A, Car R (1999) *Phys Rev Lett* 83:3242
108. Neyman KM, Inntam C, Matveev AV, Nasluzov VA, Rosch N (2005) *J Am Chem Soc* 127:11652
109. Neyman KM, Lim KH, Chen ZX, Moskaleva LV, Bayer A, Reindi A, Borgmann D, Denecke R, Steinruck HP, Rosch N (2007) *Phys Chem Chem Phys* 9:3470
110. Olivier S, Conte R, Fortunelli A (2008) *Phys Rev B* 77:054104
111. Olsen RA, Kroes GJ, Henkelman G, Arnaldsson A, Jonsson H (2004) *J Chem Phys* 121:9776
112. Onida G, Reining L, Rubio A (2002) *Rev Mod Phys* 74:601
113. Pacchioni G, Giordano L, Baistrocchi M (2005) *Phys Rev Lett* 94:226104
114. Parker SC, Campbell CT (2007) *Top Catal* 44:3
115. Pauling L (1960) *The nature of the chemical bond*. Cornell University Press, New York
116. Pauwels B, Van Tendeloo G, Bouwen W, Theil Kuhn L, Lievens P, Lei H, Hou M (2000) *Phys Rev B* 62:10383
117. Perdew JP, Zunger A (1981) *Phys Rev B* 23:5048
118. Perdew JP (1985) *Phys Rev Lett* 55:1665
119. Perdew JP, Yue W (1986) *Phys Rev B* 33:8800
120. Perdew JP, Burke K, Ernzerhof M (1996) *Phys Rev Lett* 77:3865
121. Perdew JP, Ruzsinszky A, Tao J, Staroverov V, Scuseria G, Csonka G (2005) *J Chem Phys* 123:062201
122. Pettifor DG, Finnis MW, Nguyen-Manh D, Murdick DA, Zhou XW, Wadley HNG (2004) *Mat Sci Eng A* 365:2
123. Pileni MP, (2003) *C R Chimie* 6:965
124. Polak M and Rubinovich L (2000) *Surf Sci Rep* 38:127
125. Pyykkö P (2004) *Angew Chem Int Ed* 43:4412
126. Renaud G, Lazzari R, Revenant C, Barbier A, Noblet M, Ulrich O, Leroy F, Jupille J, Borensztein Y, Henry CR, Deville JP, Scheurer F, Mane-Mane J, Fruchart O (2003) *Science* 300:1416
127. Reuter K, Scheffler M (2006) *Phys Rev B* 73:045433
128. Ricci D, Bongiorno A, Pacchioni G, Landman U (2006) *Phys Rev Lett* 97:036106
129. Rossi G, Rapallo A, Mottet C, Fortunelli A, Baletto F, Ferrando R (2004) *Phys Rev Lett* 93:105503
130. Sahimi M, Hamzehpour H (2010) *Comp Sci Eng* 12:74
131. Schimka L, Harl J, Kresse G (2011) *J Chem Phys* 134:024116
132. Schrödinger E (1926) *Phys Rev* 28:1049
133. Scuseria GE (1999) *J Phys Chem A* 103:4782
134. Sementa L, Barcaro G, Negreiros F, Thomas IO, Netzer F, Ferrari AM, Fortunelli A (2012) *J Chem Theory Comput* 8:629
135. Shoemaker JR, Burggraf LW (1999) *J Phys Chem A* 103:3245
136. Slater JC (1972) Statistical exchange-correlation in the self-consistent field. In: Lowdin PO (ed) *Advances in quantum chemistry*. Academic Press, New York, p. 1
137. Stillingner FH, Weber TA (1984) *Science* 225:983
138. Stillingner FH (1995) *Science* 267:1935
139. Svensson M, Humbel S, Froese RDJ, Matsubara T, Sieber S, Morokuma K (1996) *J Phys Chem* 100:19357
140. Szabo A, Ostlund NS (1996) *Modern quantum chemistry*. Dover Publications, United States
141. Tao F, Grass ME, Zhang Y, Butcher DR, Renzas JR, Liu Z, Chung JY, Mun BS, Salmeron M, Somorjai GA (2008) *Science* 322:932
142. Tkatchenko A, Scheffler M (2009) *Phys Rev Lett* 102:073005
143. Tran F, Blaha P (2009) *Phys Rev Lett* 102:226401
144. Velev OD, Gupta S (2009) *Adv Mater* 21:1897

145. Voter AF, Montalenti F, Germann TC (2002) *Ann Rev Mater Res* 32:321
146. Wales DJ, Doye JPK (1997) *J Phys Chem A* 101:5111
147. Wales DJ, Scheraga HA (1999) *Science* 285:1368
148. Wales DJ (2004) *Energy landscapes: applications to clusters, biomolecules and glasses*. Cambridge University Press, Cambridge
149. Wang L, Shi X, Kariuki NN, Schadt M, Wang GR, Rendeng Q, Choi J, Luo J, Lu S, Zhong CJ (2007) *J Am Chem Soc* 129:2161
150. Weigend F, Kattannek M, Ahlrichs R (2009) *J Chem Phys* 130:164106
151. West P, Johnston RL, Barcaro G, Fortunelli A (2010) *J Phys Chem C* 114:19678
152. Worz AS, Judai K, Abbet S, Heiz U (2003) *J Am Chem Soc* 125:7964
153. Xu LJ, Henkelman G, Campbell CT, Jonsson H (2005) *Phys Rev Lett* 95:146103
154. Yacaman MJ, Ascencio JA, Tehuacanero S, Marin M (2002) *Top Catal* 18:167
155. Yulikov M, Sterrer M, Heyde M, Rust HP, Risse T, Freund HJ, Pacchioni G, Scagnelli A (2006) *Phys Rev Lett* 96:146804

Chapter 3

Closed-Shell Metal Clusters

René Fournier and Satya Bulusu

3.1 Introduction

Metal clusters are studied for many reasons, including modeling heterogeneous catalysts, understanding how physical properties and chemical reactivity evolve in the intermediate size regime between molecular species and solids, and trying to create building blocks for new materials [1]. The latter requires clusters, and cluster assemblies, that are stable under normal conditions. This is challenging. Taking the viewpoint of the solid state, metal clusters represent the ultra finely divided form of a solid, with an extremely high surface area and very large surface energy. They are inherently unstable [2]. So, one may ask, why go through the trouble of trying to make materials out of clusters, and how?

There are many known examples of clusters X_n with properties that are very different from their bulk counterparts and which sometimes vary abruptly with n . This includes atomic structure [3, 4], electronic structure [5], magnetism [6, 7], thermodynamic properties [8], optical properties [9, 10], and chemical reactivity [11–14]. Here are some examples. The energetically favored *atomic structure* of small Ru_n [15, 16], Rh_n [3], Os_n , and Ir_n [17] clusters is basically fragments of the simple cubic (sc) crystal, *not* fragments of fcc, hcp, or bcc crystals. Pt_n [4] clusters also have rather open structures. Further, many studies showed evidence of gold clusters with planar or cage structures [18]. Small clusters of Rh and Mn are *magnetic* [6, 7] (they have nonzero saturation magnetization) even though Rh(s) and Mn(s) are not ferromagnetic. Clusters usually melt at a lower temperature than the bulk, so their chemical reactivity in the liquid state can sometimes be investigated.

R. Fournier (✉)
Department of Chemistry, York University
e-mail: renef@yorku.ca

S. Bulusu
Department of Chemistry, Indian Institute of Technology Indore
e-mail: sbulusu@iiti.ac.in

The *reactivity* of Al_{100}^+ toward N_2 chemisorption was studied around the melting point of Al_{100}^+ (640 K). It was found that the activation barrier to N_2 chemisorption decreased sharply as temperature rose above 640 K [14]. Unlike most clusters, Sn_n ($n \approx 10\text{--}30$) clusters have a higher melting point than the bulk [8], and some of them do not melt—they sublime [19]. As it turns out, the geometric structure of Sn_n^- ($n = 18\text{--}25$) is also unique [20]. The *optical absorption* (plasmon resonance) of Ag_xAu_y clusters varies with composition and morphology [9] and can be tuned by laser irradiation annealing [10].

It has been noted that certain stable quasispherical clusters bear similarities to atoms. These so-called *superatoms* could open up new avenues for chemistry [21]. Interestingly, the general concept of superatom (or quasiatom) also applies, with some modifications, to excitons, impurities, and confined atoms [22].

On the other hand, individual atoms *in* a cluster X_n differ in many ways from atoms of the same element in the gas phase or condensed phase. Atoms *in clusters* (e.g., a Cu atom in Cu_3) could emulate another element (e.g., Rh(g) or Rh(s)) at specific cluster size [23]. If cluster nuclearity and structure can be controlled, this kind of “transmutation” can be exploited to create cheaper alternatives to costly catalytically active elements, or for designing alloy surfaces with properties intermediate between those of pure elements [24]. The selectivity and activity of bimetallic catalysts [25,26] is sometimes rationalized with similar concepts of active sites with specific geometric and electronic properties.

For all those reasons, clusters look like promising building blocks for a multitude of materials with unusual or extreme properties. Further, these properties could in principle be tuned by varying the size and composition, sometimes even by addition or removal of a single atom. There remains a crucial question: how could one possibly make stable materials out of inherently unstable building blocks?

There are two main strategies for stabilizing clusters. The *first* is to embed them, as quickly as they are formed, inside a host crystal [27, 28], for example, alumina [29] or a cryogenic Ne matrix [30] or a zeolite [31]. A similar idea is to deposit clusters on a support [32]. Sometimes thin films are made with a morphology that depends strongly on deposition energy [33]. If the goal is to isolate unperturbed clusters, low-energy deposition with a soft landing technique [34, 35] is ideal. On the other hand, one could take advantage of cluster–surface interactions to create entirely novel cluster structures [36]. The *second strategy* is to chemically modify the surface of clusters to make them inert [37, 38]. Essentially, a high surface energy material (the metal) gets coated with a low surface energy material which can be a simple ligand like CO [39], or an organic compound with a high metal affinity at one end so that it can bind to the metal cluster [40].

Two other things can help in addition to the two basic strategies. Firstly, one can downplay the stability aspect and shift efforts, instead, on creating conditions where clusters are formed *in situ* and get used immediately [41]. This is particularly useful in catalysis [25]. Secondly, one can start with metal clusters that are already stable relative to other metal clusters, in order to achieve better overall stability after embedding or passivation. This is where the concept of closed-shell metal clusters becomes especially relevant.

The words “closed shell” can mean two things for metal clusters. A n -atom cluster has closed *atomic* shells [42] if it is quasispherical in shape and has a relatively small surface area compared to the average of clusters of the same composition but with $(n + 1)$ and $(n - 1)$ atoms. It has a closed *electronic* shell if it has a large absolute hardness η , where η is half the difference between the ionization energy and the electron affinity, compared to the clusters with $(n + 1)$ and $(n - 1)$ atoms. In molecular orbital theory, a large η correlates with a large HOMO-LUMO gap. The electron count for such a cluster should correspond to a shell closing in a simplified model of electronic structure such as the jellium [43–45] (shell closings at 2, 8, 18, 20, 34, 40, ... electrons) or pseudo-atom (shell closings at $2n^2$ electrons). Generally, one expects that *closed atomic shells* would impart thermodynamic stability because of the smaller surface area (smaller surface energy), and impart kinetic stability because of the smaller number of distinct surface sites available for chemical reactions. Metal clusters with *closed electronic shells* should have thermodynamic and kinetic stability, for much the same reasons molecules with a “good Lewis structure” are stable. Quasispherical clusters with atomic closed shells are called *doubly magic clusters* (DMCs) if they simultaneously possess closed electronic shells. They are called *superatoms* if they are relatively stable, and their adjusted electron count ($N_e - N_e^*$) (N_e^* is the count for a closed shell), their properties, and their chemical behavior resemble those of an atom [21]. For example, Al_{13} and Al_{13}^- have quasispherical structures. With its 40 electrons, according to the jellium model, Al_{13}^- is a DMC (it could also be viewed as a “super-argon” atom), and with 39 electrons, Al_{13} is the superatom equivalent to a halogen atom (“superchlorine”). Indeed, the electron affinity [46] and chemistry [21] of Al_{13} were found to be similar to those of a Cl atom.

3.2 Atomic Shells

As a rule, geometric structures with closed atomic shells tend to be energetically favored because they often (but not always) have a high symmetry, high mean coordination, low surface area, and low strain. The most compact arrangements of n rigid atoms, with fixed nearest-neighbor (NN) distances, follow the sequence triangle, tetrahedron, trigonal bipyramid (TBP, two face-sharing tetrahedra), and face-capped TBP (three tetrahedra). This polytetrahedral (PT) sequence can continue only with the introduction of distortions [47]. Already, in the 7-atom pentagonal bipyramid (PBP), there are 2%–3% variations in NN distances, and in the 13-atom icosahedron, the central-to-surface NN distance is compressed by 5% relative to the surface-to-surface NN distance. Figure 3.1 shows some of the most stable LJ clusters below $n = 60$ ($n = 4, 7, 13, 19, 55$).

With minor variations, simple pair potentials have energy global minima (GM) that follow the PT sequence, often up to at least $N = 55$. The GM for the 6–12 Lennard–Jones (LJ) potential are PT up to $N = 30$, and mixed structures made of fused PT units (13-atom icosahedra) and centered pentagonal prism (13-atom CPP) units for $N \geq 31$ with two exceptions: the $N = 6$ and $N = 38$ GM which

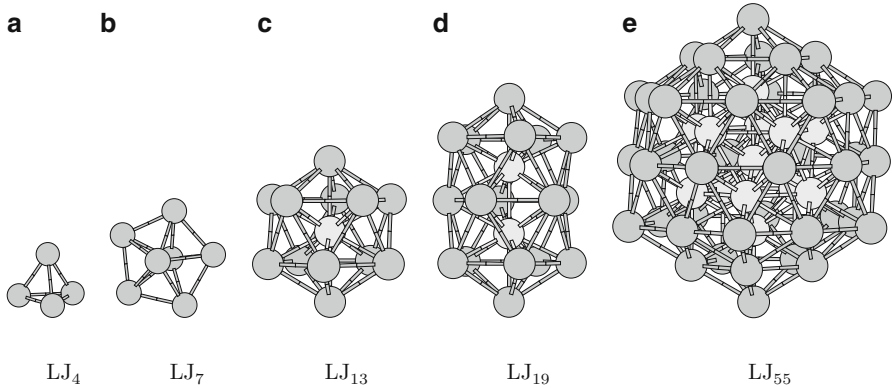


Fig. 3.1 Stable clusters in the Lennard–Jones global minima sequence

both have O_h symmetry structures. The PT structures are favored because they have a very large number of NN pair interactions N_{pairs} and nearly minimize surface area, A , and surface energy, E_s , while keeping bond strain to roughly 6% or less. Later, we will refer to the mean coordination c of a n -atom cluster: it is defined as $c = 2N_{\text{pairs}}/n$. The energetic disadvantage in PT is the strain energy, E_σ , associated with geometrical distortions at $N > 6$. In contrast, fragments of the fcc crystal structure have no strain: their pair distribution function $g(r)$ has only one sharp NN peak. The difference in E_s between PT and fcc-like structures grows roughly as the power two-thirds of the number of atoms, $n^{2/3}$. The difference in E_σ grows roughly as n . As a result, GM structures obtained from pair potentials are characterized by a transition from PT to fcc-like structures at some n that depends on details of the potential [48]. This value of n , usually larger than 100, depends a lot on the range of a pair potential. For $n \approx 10$ –100, very long-range potentials favor quasispherical highly strained disordered PT structures, intermediate range potentials favor icosahedral structures, and short-range potentials favor strain-free fcc fragments [49].

Generally speaking, there is correlation between cohesive energies, mean coordination c , and surface area A . We will take the LJ GMs [50] as a general purpose structural model and see how c and A evolve with size, keeping in mind that clusters of most elements adopt structures that are different from the LJ GMs. We calculate an effective surface area A for a cluster by considering overlapping spheres centered at the nuclear positions. Each sphere is assigned a radius $R_s = 1.72 \times R_{mn}/2$ where R_{mn} is the diatomic equilibrium distance. The combined surface area of the overlapping spheres is $N \times 4\pi R_s^2 \times f$, where f is the fraction of points on sphere j that is closer to nucleus j than any other nucleus, averaged over $j = 1, N$. The surface energy E_s for a metal cluster is modeled by a formula [51] using (a) the empirical fact that surface energies of metals are roughly 16% of their cohesive energies [52] and (b) a proportionality factor obtained by taking the surface area per atom calculated for a cluster and dividing it by the average of surface

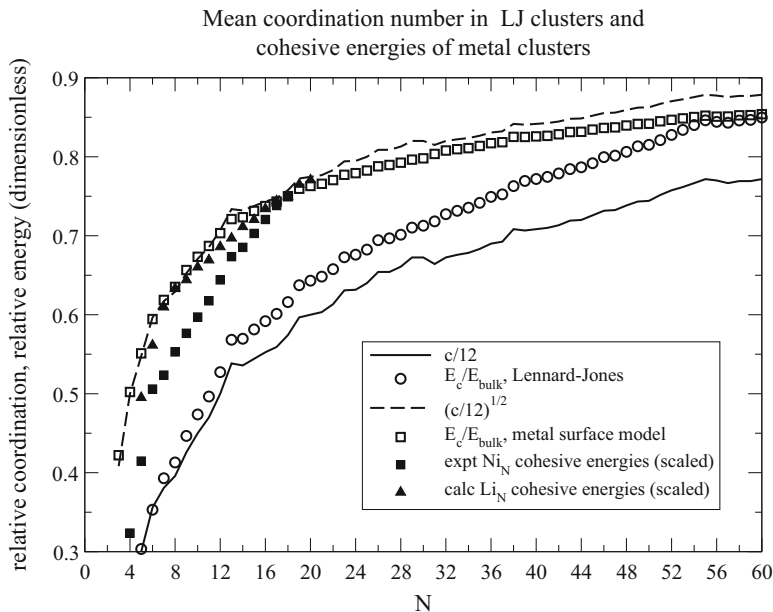


Fig. 3.2 Models of cluster cohesive energy

areas per atom calculated for fcc(100) and fcc(111) planar surfaces with the same overlapping spheres model. With this metal surface model (MSM), we calculate a cluster cohesive energy $E_c(n)$ and its dimensionless variant $E_c(n)/E_c(bulk) \leq 1$.

If one neglects long-range interactions and strain, and assuming that the maximum coordination is 12, the dimensionless cohesive energy $E_c(n)/E_c(bulk)$ of clusters governed by additive pair potentials is $c/12$. In metals, however, an atom's contribution to the total energy goes roughly as the square root of its coordination number [53], therefore, $E_c(n)/E_c(bulk) \approx \sqrt{c/12}$. Figure 3.2 shows $c/12$ and $\sqrt{c/12}$ calculated for the GM structure of LJ clusters, along with two models of dimensionless cohesive energies $E_c(n)/E_c(bulk)$: the empty circles are calculated directly with the LJ potential, and the empty squares are derived from our MSM. We also show experimental (collision-induced dissociation) Ni_n [54] binding energies that were scaled to intersect the $\sqrt{c/12}$ curve near $N = 18$ (filled squares) and density functional theory (DFT) Li_n energies [55] scaled in the same way (filled triangles). The way Ni_n and Li_n energies are scaled is not very important because we are interested primarily in the shapes of the curves in Fig. 3.2, not their absolute values.

The LJ curve (circles) is intermediate between the $c/12$ and $\sqrt{c/12}$ curves because long-range contributions make non-negligible positive contributions to $E_c(n)/E_c(bulk)$. These long-range interactions surely outweigh the short-range strain; otherwise, the GM of LJ clusters would be fcc-like. The MSM (squares) gives a curve that goes roughly as $\sqrt{c/12}$. This is not trivial because the square-root dependence of metal cohesive energies is obtained from consideration of electronic

energy levels [53], not geometry. The curves for the scaled Li_n DFT energies, and the scaled Ni_n experimental energies, are intermediate between $c/12$ and $\sqrt{c/12}$ but are closer to the latter. The relatively low cohesive energies of Ni_n are probably due to the nonzero promotion energy needed to bring triplet ground-state ($\dots 3d^8 4s^2$) Ni atoms to the hypothetical $\dots 3d^9 4s^1$ doublet (spin-unpolarized $4s^1$) configuration of a Ni atom in a Ni_n cluster. By comparison, promotion energy plays a minor role in Li_n . The second difference can also be used to examine the size evolution of a cluster property “ X ”:

$$\Delta_2 X(N) = X(N) - [X(N+1) + X(N-1)]/2.$$

It may not be clear from Fig. 3.2, but the biggest values in Δ_2 occur at these n : 4, (6), 13, (19), (23), (26), (29), (38), 55 for ($c/12$); and 4, (7), 13, (19), (23), (26), (29), (46), 55 for the Lennard–Jones (LJ) energy. These can be considered to be atomic shell closing in LJ clusters, with minor shell closing shown in parentheses. The MSM energy applied to those same LJ structures gives almost the same maxima in Δ_2 , with two interesting exceptions (underlined): $n = 4, 6, 13, 19, 23, 26, \underline{38}, \underline{43}, 55$. The $n = 38$ maximum helps explain an anomaly in the LJ sequence: aside from $n = 6$, $n = 38$ is the only LJ GM with a fcc-like structure.

We now consider closed shells in a strict geometric sense [42]. The number of atoms in an icosahedron with K closed shells is

$$N_K = (10/3)K^3 - 5K^2 + (11/3)K - 1$$

that is $N_K = 13, 55, 147, 309, 561, 923, \dots$. The cuboctahedra and truncated dodecahedra with K shells obey the same formula. Geometric shell closing for some of the other shapes occur at these numbers of atoms [42]:

$$N_K = (2/3)K^3 + (1/3)K \quad \text{octahedron (fcc)}$$

$$N_K = (1/6)K^3 + (1/2)K^2 + (1/3)K \quad \text{tetrahedron (fcc)}$$

$$N_K = 16K^3 - 33K^2 + 24K - 6 \quad \text{cuboctahedron, hexagonal faces (fcc)}$$

$$N_K = 4K^3 - 6K^2 + 4K - 1 \quad \text{rhombic, dodecahedron (bcc)}.$$

Some of the most stable clusters in the LJ and MSM series are indeed closed-shell in the geometric sense: tetrahedron ($n = 4$), octahedron ($n = 6$), and icosahedron ($n = 13, 55$). The $n = 38$ cluster is the $n = 44$ closed shell octahedron with its six lowest coordination atoms removed. The smallest among the other stable clusters ($n = 7, 19$) have large c and/or small surface area for other reasons: LJ_7 , a PBP, is a “half icosahedron” (one pentagonal ring) and LJ_{19} is a double icosahedron (three stacked pentagonal rings, and two central atoms). The $n = 23, 26, 29, 43$, and 46 cases are more complicated.

The second smallest closed-shell tetrahedral clusters at $n = 20$ is the observed form of Au_{20}^- [56]. In analogy to the octahedral structures $n = 44$ and $n = 38$ (LJ_{38}), one can make a rounder cluster by removing the four apex atoms of tetrahedral X_{20} .

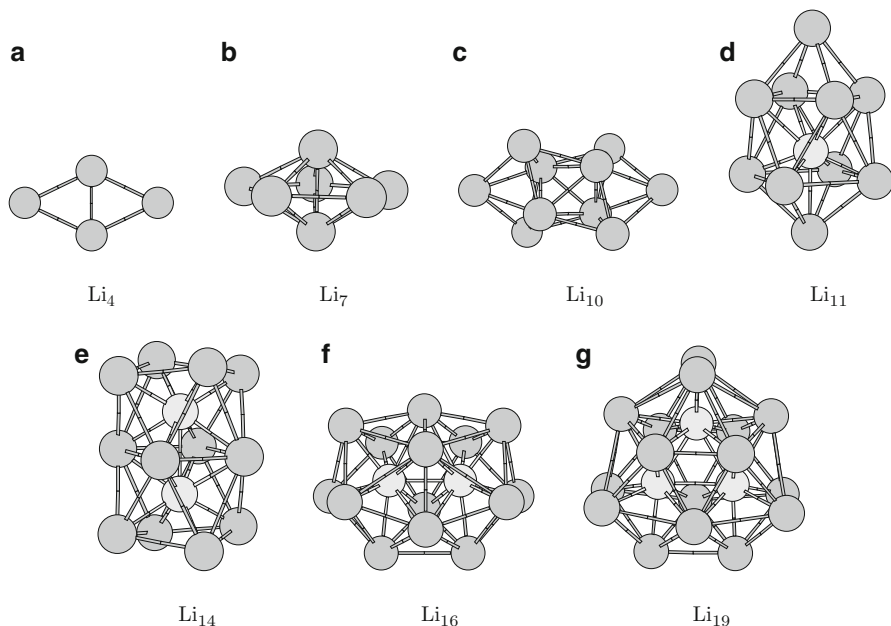


Fig. 3.3 Compact structures in the lithium clusters global minima sequence

This yields a 16-atom structure that was proposed on the basis of experiments and DFT calculations for gold clusters [18] and various bimetallic clusters [57].

The balance between E_s and E_σ is such that it favors PT and icosahedra for small clusters modeled by the LJ potential (and other potentials) and favors fcc-like structures in systems with more strain—larger clusters and elements governed by harder potentials [49] (this would seem to include the elements Tc, Re, and Pt [58]). Lithium, and maybe a few other elements, effectively has a *softer* potential than LJ. This gives rise to many highly strained (in a geometrical sense) Li_n structures [59] characterized by two or more peaks in the NN part of their pair distribution function [55]. These structures may be unique among elemental clusters, but they could be quite common in A_xB_y bimetallics where the size difference between atoms of A and B provides a mechanism for drastically decreasing E_σ . Figure 3.3 shows the Li_n structures that seem most relevant as possible GM for bimetallics. Strain is not a factor in the smaller clusters ($n = 4, 7, 10$), but we show them because they have been proposed for various metal clusters. The Li_{10} structure is a prolate combination of two PBP sharing four atoms. The Li_{11} , Li_{14} , and Li_{19} GM have 1, 2, and 3 interior atoms, respectively. In the LJ sequence, clusters with that many interior atoms are reached only at $N = 13, 19$, and 23 , respectively. At least one bimetallic equivalent to Li_{11} , CuSn_{10}^+ , has been characterized as a DMC [60,61]. The Li_{16} and Li_{19} structures are not spherical (Li_{16} is prolate, Li_{19} is slightly oblate), so it is unclear whether bimetallic DMC could be derived from them.

Figure 3.4 shows a few other compact quasispherical cluster geometries and three cage structures. The X_6 and X_{19} structures are O_h symmetry fragments of a close-

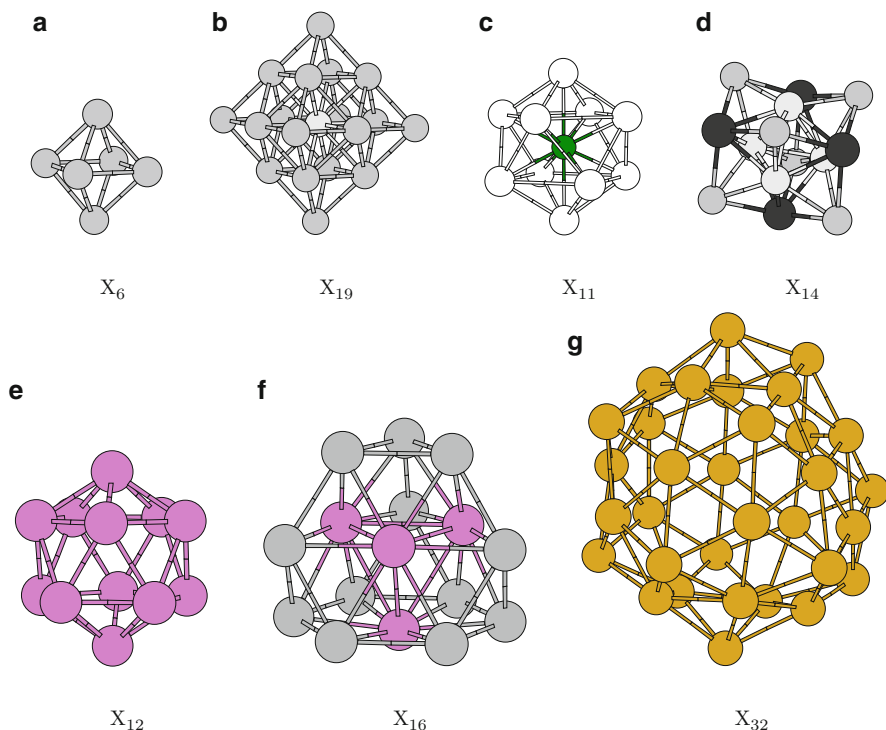


Fig. 3.4 Various closed-shell and cage cluster structures

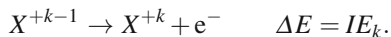
packed crystal structure, X_{11} is the D_{4d} symmetry equivalent of the icosahedron, and X_{14} is a PT structure made by capping the faces and edges of a tetrahedron. The icosahedral cage structure X_{12} is a low-energy isomer for Be_{12} [62], maybe even its GM. The 16-atom cage (Fig. 3.4f) is the experimentally determined structure of Au_{16}^- [18, 63, 64] and is the calculated GM for several A_4B_{12} bimetallic clusters that have a large HOMO-LUMO gap [57]. The 32-atom cage (Fig. 3.4g) was found as a GM candidate for Au_{32} (Zhang, private communication).

3.3 Electronic Shells

It is useful to think of a metal cluster M_n as being made of $n M^{+p}$ ions and np electrons. To a first approximation, the np electrons are delocalized over the whole cluster. A better description uses molecular orbitals to describe the np electrons with a set of distinct one-electron states. If we assume that the ionic charge $+np = Z$ is concentrated at the center, then we view the cluster as a *pseudo-atom* with one-electron states that are the familiar atomic orbitals—1s, 2s, 2p, 3s, 3p, 3d, ... The other extreme is to assume that the ionic charge $+np = Z$ is completely delocalized

over the volume $4\pi R^3/3$ of a sphere of radius R —this is the *spherical jellium model* (SJM). In that case, one finds one-electron states with radial distributions and energies qualitatively different from atomic orbitals. They are, in order of increasing energy, 1s 1p 1d 2s 1f ... Clearly, these two simplified models (pseudo-atom and SJM) lead to different electron counts for electronic shell closings. The pseudo-atom is rarely, if ever, applicable to metal clusters. But the SJM successfully explains a lot of data about metal clusters [44, 45]. However, other models, each with their own shell closing electron counts, become more relevant than the SJM when the structure of a cluster departs from that of a compact uniform sphere: the pseudo-atom model does not have predictive ability, but it gives a rationale for why shell closings occur at 18 but not 20 in doped metal clusters $A@B_n$ where the central ion A^{+q} has $q > 2$ [65–67]; the *ellipsoidal jellium model* (EJM) [43], a refinement of the SJM, can account for energy-shape trends in Ag_n and other metal clusters [80]; all-metal aromaticity has been invoked to rationalize the stability of some planar metal clusters [69–71], with $(4n + 2)$ electrons in closed-shell systems; “spherical aromaticity” may be relevant for some endohedrally doped clusters including the possibility of stable spdf-like 32-electron systems [72]; coincident electronic and nuclear shells (i.e., the spatial overlap of the radial distributions for nuclei and electrons) explain trends in calculated stabilities for A_4B_{12} bimetallic clusters [73].

Electronic shells can be defined for metal clusters as for atoms. The mean radius associated with one-electron states generally increases with energy. So the np electrons (more exactly, the np states that describe them) fall into shells. It is easier to look at shell structure through energy. Define the k 'th ionization energy IE_k of a cluster “X” as the energy difference between the ground states of X^{+k} and X^{+k-1} :



A plot of the IE_k 's of a cluster as a function of k will show a steady increase. More interestingly, it also shows comparatively large gaps at specific values k^* , indicating shell closing at $np - k^*$. In molecular orbital (MO) theory, one would see a larger gap in the energy vs charge curve when a completely filled set of degenerate orbitals loses one electron.

Experimental evidence for electronic shells comes from the IE 's (first ionization energies) of neutral clusters with different numbers of atoms [74]. A classical model for the charging of metal spheres gives a formula for IE vs cluster size that completely ignores shell closing effects [75]:

$$IE = W + e^2/2(R + a).$$

In this equation, R , the cluster's radius, is proportional to $N^{1/3}$, $(R + a)$ is the radial centroid of excess charge (a is normally between 1.1 and 1.4 bohr), and W is the bulk work function. By fitting experimental data to this formula, one gets a reference function $IE_{\text{fit}}(N)$. The differences $(IE_{\text{observed}}(N) - IE_{\text{fit}}(N))$ readily point to electronic shell closings: large positive values show shell closings, and large

negative values indicate that the np 'th electron is the single electron in a new shell (the cluster is analogous to an alkali atom). However, the most compelling experimental evidence for shells (atomic or electronic) is the relative abundance of clusters in mass spectra [76–78].

Electronic shells in metal clusters are normally explained with the EJM [43–45]. In the EJM, the jellium is bounded by an ellipsoid instead of a sphere, but orbitals still follow the energy order (filling order) $1s\ 1p\ 1d\ 2s\ 1f\ 2p\ 1g\ 2d\ 3s\ 1h\ \dots$ giving electron counts of 2, 8, 18, 20, 34, 40, 58, 68, 70, 92, ... Small changes in the potential felt by electrons (i.e., small changes in the assumed distribution of positive charge) changes the energy gap between states, or even their order. So, for instance, shell closings may be found for $n_e = 34$ but not $n_e = 40$ in some cases, or vice-versa, or for *both* $n_e = 34$ and $n_e = 40$. Also, in bimetallic systems where the two metals have very different electron densities (e.g., NaZn, KZn), jellium energy levels can get inverted and produce new electron counts at shell closings such as $n_e = 10$ [76, 79].

The EJM accounts quite well for the unusually high atomization and ionization energies in clusters of group 1, group 2, and group 11 and a few other elements. It also accounts for the energetically preferred shapes of some clusters [80]. At large cluster size, the energy minima of $E(n_e)$ (at $n_e = 2, 8, 20, 34, \dots$) caused by electronic shell display a supershell structure: the magnitude of shell closing effects becomes very small in the neighborhood of some values of n_e . In particular, the effect of shell closing on energy is almost zero in the range $n_e = 800$ to $n_e = 1,000$ but is very large in the range $n_e = 1,800$ to $n_e = 2,200$ [76].

Metal clusters that are very far from spherical, such as planar and cage structures, call for models completely different from the EJM. The stability of some planar (or strongly oblate) metal clusters has been explained by aromaticity [70, 81]. With the discovery of golden cages [18], it was realized that, in metal clusters constrained to a cage structure, the atomic and electronic magic numbers must be different from those of 3D structures. A doubly magic cage cluster, like Au_{32} , may turn out to be energetically favored over any 3D structure [82]. A stable DMC cage would be interesting because of the many ways it could be modified by inclusion of a central dopant atom or small molecule.

3.4 AB Ordering in Bimetallic Clusters

The atomic structure of bimetallic clusters A_xB_y ($x + y = n$) can be described by a X_n parent structure and a list of the x atomic sites being occupied by atoms of element A (homotop). If the parent structure X_n has no symmetry, there are $n!/(x!y!)$ possible homotops. These can have very different energies, and only one or a few of them are normally present in experiments on small clusters.

There are three limit types of atom ordering in A_xB_y clusters: maximally mixed (MM), left-right segregated (LRS), and core-shell (CS) structures. In a MM case, the cluster equivalent of a metal alloy, the number of A-B NN pairs is maximized or

nearly so: in a sense, the A/B interfacial area S_{AB} is maximized. In a LRS structure, there is a roughly circular dividing surface between atoms of A and atoms of B. This structure minimizes S_{AB} and can give rise to a significant electric dipole. In a CS structure, all atoms of A are closer to the center-of-mass than atoms of B. This minimizes S_{AB} under the condition that the surface area of A be zero. In a CS cluster where A and B have very different electronegativities, there could be significant radial charge separation and surface charge, but there is no net electric dipole. A fourth type of structure, “onion layers” (OL) [83, 84], has alternating concentric shells of A and B and may be viewed as a variation on the CS structure. The A_xB_y clusters that best fit the concept of closed atomic shells are those that (a) are derived from a closed atomic shell X_n parent structure and (b) are CS, or OL, or perfectly ordered MM structures.

It is possible to control the AB ordering by varying the method of preparation of clusters (kinetic control) [85–87]. For example, qualitatively different homotops of Ag_xAu_y were made by changing the sequence of Ag and Au deposition on an alumina substrate [88]. An important application of bimetallic CS clusters is biosensing [89].

Compared to elemental clusters, bimetallics offer many more possibilities for achieving multiple stability criteria. For instance, polyicosahedral clusters X_n may be favored because they maximize the number of NN pairs, but disfavored because of strain. In a CS polyicosahedral $A_x@B_y$ cluster, however, the strain could be greatly reduced by combining atoms of A that are smaller than atoms of B. This was shown theoretically to be the case for $Cu_x@Ag_y$ and $Ni_x@Ag_y$ ($(x,y)=(13,32), (8,30), (6,32), (7,27)$) [90], and experiments showed Ag-Ni clusters with CS structure [29].

At this point, it is useful to summarize structural principles that have been proposed by several authors over the years. Structural principles are used to design or rationalize clusters with special stability that satisfy two or more criteria (DMCs). Note that in the list below, for example, P1 and P3 cannot be satisfied simultaneously. We can rationalize the wide variety of observed cluster structures as being the result of competition between different principles (different physical effects) [91]. We refer the reader to earlier reviews and papers for detailed discussions [44, 45, 49, 76, 90–94].

- (P1) Surface area A — A tends to a minimum, and the mean coordination c to a maximum.
- (P2) Strain—structures with a single narrow peak in the pair distribution function $g(r)$ are favored, especially for elements with a large IE.
- (P3) Cage-forming tendency—The contribution of a metal atom j to binding energy goes roughly as $\sqrt{c_j}$. As a result, if we compare several structures having the same mean coordination c , the one where all atoms have nearly equal coordinations is favored. This effect is more pronounced in elements with a large IE (e.g., Be and Au).
- (P4) Square-forming tendency—high-cohesive energy elements with strong d - d bonding (e.g., Os and Ir) tend to favor 90-degree bond angles.

- (P5) EJM shapes—elements of groups 1, 2, and 11, as well as Al, are well described by the jellium model, and their clusters' overall shapes (spherical, oblate, or prolate) tend to conform to the EJM predictions.
- (P6) Magnetism-symmetry—there can be competition between high-spin, high-symmetry structures and low-spin Jahn-Teller distorted structures.

A consequence of P6 is that computational studies where cluster structure was *assumed* to have high symmetry (geometry optimization was ignored or incomplete) would often overestimate the spin magnetic moment.

Structural principles for AB ordering in bimetals A_xB_y are that A and B will have a tendency to:

- (P7) Mix if they have very different electronegativities.
- (P8) Segregate if they have very different surface energies.
- (P9) Segregate into a CS $A_x@B_y$ structure if R_B is significantly larger than R_A .
- (P10) Segregate if one element has a stronger interaction to the environment (support, ligand, or ambient gas).
- (P11) When the cluster's surface is made of A and B, the element with the lowest cohesive energy generally occupies the sites with lowest coordination.
- (P12) When the difference in cohesive energies ($E_{c,A} - E_{c,B}$) is large positive, the number of A–A bonds (not the total number of bonds) is maximized, and B atoms solvate A_x .

3.5 Examples of Closed-Shell Clusters

Here we simply show a collection, which is far from exhaustive, of closed-shell metal clusters. In each case, we give a label, “(e)” (experimental) or “(c)” (computational), references, and sometimes a comment. The next section will give more detailed descriptions for a few select clusters.

Examples of atomic shells [42] are found mainly among nonmetals [95]: Ar_n ($n=13, 19, 25, 55, 71, 87, 147$) (e) [96, 97]; Xe_n ($n=13, 19, 25, 55, 71, 87, 147$) (e) [98]; Xe_n^+ ($n=13, 16, 19, 23, 25, 29$) (e) [99] (the largest clusters investigated had 40 atoms). In what follows, we arranged closed-shell metal clusters into a few groups. A few references to met-cars and some Sn- and Pb-containing clusters are included even though they are not strictly metal clusters.

3.5.1 Atomic Shells

- Ba_n ($n=13, 19, 23, 26, 29, 32$) (e) [100] and (c) [101]: these clusters are believed to be weakly bound and adopt icosahedral structures.
- Au_n ($n=20, 32$) [102, 103].

3.5.2 Electronic Shells

- Na_n ($n = 8, 20, 40, 58, 92$) (ec) [92].
- Na_7^- , Na_{19}^- (ec) [104, 105]: observed and computed angle-resolved photoelectron spectra of metal cluster anions.
- Cu_n^+ , Ag_n^+ , $\text{Cu}_m\text{Ag}_{n-m}^+$ ($n_e = n - 1 = 8, 20$) (e) [106].
- Ag_8 (c) [107].
- Au_nX_m^+ ($\text{X} = \text{Cu}, \text{Al}, \text{Y}, \text{In}$) (e) [108]: several closed electronic shells are identified.
- Mg_n , Zn_n , Cd_n ($2n = 20, 36, 40, 56, 60, 64, 70, 92$ or $94, 108$ or $112, 124, 138$ or 140) (e) [109]: mass abundances.
- NbAl_4^- ($n_e = 18$) (e) [110]: unreactive toward O_2 .
- Al_4^{2-} (ce) [69, 71]: planar all-metal aromatic system.
- Al_n^- ($n = 13, 23, 37$) (e) [11]: these are unreactive toward O_2 .
- In_n^+ ($n_e = 3n - 1 = 8, 20$), Cu_nIn_m^+ ($(n, m) = (0, 3), (3, 2), (6, 1)$ or $n_e = 8$).
- Sn_{10} (ec) [20]: evidence that larger Sn clusters contain well-defined Sn_{10} and Sn_9 subunits.
- X_{12}^{2-} ($\text{X} = \text{Sn}, \text{Pb}$) (ec) [111, 112]: icosahedral cage.

3.5.3 Mixtures of Atomic and Electronic Shells

- Cu_nAl_m^+ ($(n, m) = (6, 5)$ or $n_e = 20$, and $(n, m) = (10, 11)$ or $n_e = 40$), Ag_6Al^+ (e) [106]: many other magic numbers were observed, not all of which are explainable with electronic shells.
- Pb_n^+ ($n = 7, 10, 13, 17, 19$) and Cu_nPb_m^+ ($(n, m) = (1, 6), (2, 5), (3, 5), (6, 1)$) (e) [106]: atomic structure is presumably the determining factor for these clusters, except for Cu_6Pb^+ ($n_e = 8$). The reason for the stability of Cu_3Pb_5^+ is unclear. It appears that stability is governed mainly by atomic structure in Pb-rich clusters and by electronic structure in Cu-rich clusters.
- Au_{32} (ec) [18, 63]: presumed to have a cage structure.

3.5.4 Doubly Magic Clusters

- Al_n^- ($n = 13$) (ec) [11, 21]
- $\text{X}@\text{Al}_{12}^-$ ($\text{X} = \text{Ge}, \text{Sn}, \text{Pb}$) (ec) [113]
- $\text{Cu}@\text{Al}_{12}^-$ (c) [114]
- BAl_{12}^- (e) [115] and $\text{B}_2\text{Al}_{11}^-$ (c) [116]
- $\text{Cu}@\text{Sn}_{10}^+$ (ec) [60, 61]
- Au_n ($n = 20$) [102, 103]
- $\text{W}@\text{Au}_{12}$ (c) [117]
- $\text{Al}@\text{Pb}_{10}^+$ (D_{4d} symmetry), $\text{Al}@\text{Pb}_{12}^+$ (I_h symmetry) (ec) [118]

3.5.5 *Singly Doped Clusters, AB_n*

- PbNa_6 (e) [119].
- MAl_{13} (M = H, Au, Li, Na, K, Rb, Cs) ($n_e = 40$) (ec) [120].
- LiAl_{13} (ec) [121–123].
- AgAl_{13} [124].
- BiAl_n ($n = 3, 5$) [70].
- $\text{XAl}_3, \text{XAl}_5$ (X = As, Sb) [81].
- CuAl_{22}^- (ec) [125]: this cluster is very unreactive toward O_2 . This was ascribed to its singlet ground state and large HOMO-LUMO gap. However, the large gap is *not* explained by the spherical jellium model but, instead, by an interplay between geometric and electronic structure akin to crystal field splitting.
- MSn_{12} (M = Pt, Pd), $\text{Bi}_2\text{Sn}_{10}$, $\text{Sb}_2\text{Sn}_{10}$ (c) [126].
- Mo@Cu_{12} [127].
- Sc@Cu_{16}^+ ($n_e = 18$) (ec) [66]: a truncated tetrahedron Cu cage with a central Sc atom, its calculated HOMO-LUMO gap is 2.05 eV s.
- $\text{Co@Ag}_{10}^+, \text{V@Ag}_{14}^+, \text{Ti@Ag}_{15}^+, \text{Sc@Ag}_{16}^+$ ($n_e = 18$) (ec) [128].
- M@Au_{12}^- (M = V, Nb, Ta) ($n_e = 18$) (ec) [129]: doped icosahedral gold cages.
- XAu_n^+ (X = Sc to Ni) (e) [130]: the observed electronic shell closings at different n for different dopant, and the jellium model, are used to make inferences about the number of itinerant electrons (3 for Sc, 4 for Ti, only 1 for Ni, etc.).
- AlPb_n^+ ($n = 9, 10, 12$) (c) [131].

3.5.6 *Other Bimetallics and Intermetallics*

- $\text{Pd}_2@\text{Ge}_{18}^{4-}$ (e) [132]: isolated as a salt and characterized by X-ray diffraction.
- $\text{Pd}_2@\text{Sn}_{18}^{4-}$ (e) [133]: isolated as a salt and characterized by X-ray diffraction.
- $\text{Pt}_2@\text{Sn}_{17}^{4-}$ (e) [134]: characterized by NMR and X-ray diffraction. This chapter has many references to earlier work on ligand-free “intermetalloid” clusters.
- A_4B_{12} (c) [73]: calculated (B3LYP) HOMO-LUMO gaps of 2.5 eV and 2.3 eV for T_d symmetry $\text{Mg}_4\text{Ag}_{12}$ and $\text{Mg}_4\text{Au}_{12}$, respectively.
- $\text{Al@Al}_{12}\text{Au}_{20}^-, \text{Al}_{12}\text{Au}_{20}^{2-}$ (c) [68]: icosahedral symmetry compound fullerene cages similar to Au_{32} .

3.5.7 *Passivated Metal Clusters*

- $[\text{Au}_{13}(\text{PMe}_2\text{Ph}_{10})\text{Cl}_2](\text{PF}_6)_3$ (e) [135]: this cluster has a Au_{13}^{5+} ($n_e = 8$) DMC core.

- $\text{Au}_{108}(\text{p-MBA})_{44}$ (p-MBA=p-mercaptobenzoic acid) (e) [40, 136]: it has 44 surface Au atoms that are “nonmetallic” (passivated with ligands) and a core of 58 Au atoms.
- $[\text{N}(\text{C}_8\text{H}_{17})_4][\text{Au}_{25}(\text{RS})_{18}]$ (R=CH₂CH₂Ph) (ec) [137, 138].

3.5.8 Metal-Carbon Compound Clusters

- M_8C_{12} (M=Ti, V, Zr, Nb) (e) [139–143]
- $\text{C}_{10}@\text{Au}_{18}$ (c) [144]

3.6 Description of Some Closed-Shell Clusters

3.6.1 Golden Pyramid (Au_{20}) and Golden Cages (Au_{16}^- , Au_{17}^-)

Gold in bulk form is often considered an inert metal (noble metal), and its importance in the field of catalysis and surface science has been overlooked. On the other hand, the isolation and detection of carbon-free hollow cages and nanotubes have attracted much interest in the field of nanoscience. But it was only in the late 1980s, when CO oxidation on supported gold Au/TiO_2 was reported [145], that the interest in the field of gold catalysts and gold nanostructures awakened. Since then, gold clusters and nanoparticles were the subject of intense research activity. They hold great promise for applications in catalysis, medical sciences, and sensors. More recently, it has been shown that gold clusters have unusual catalytic properties for selective oxidation of CO [146], are oxidation resistant [147], enable selective binding of DNA [148], and have potential applications in nanoelectronics [149, 150].

With the increase in atomic number, the electron’s relativistic mass becomes greater than the rest mass. As a result, the effective Bohr radius decreases for inner electrons with large speeds. The direct consequences of relativistic effects are the radial contractions of *s*-type orbitals, spin-orbit splitting effects, and relativistic expansion of *d*-type and *f*-type orbitals [151]. Due to relativistic effects, gold exhibits unusual properties compared to copper and silver. In gold, 6*s* orbital contraction and 5*d* orbital expansion reduce the energy gap between the 6*s* and 5*d* orbitals. This leads to an outer electronic configuration $^2D_{5/2}$ (d^9s^2) instead of $^2S_{1/2}$ ($d^{10}s^1$). This, in turn, means that the participation of *d* electrons in bonding is more pronounced in gold. So, in gold clusters, we can expect some directionality in the bonding due to the participation of *d* orbitals. This contrasts with copper and silver clusters where *s*-type metallic bonding dominates. These relativistic effects lead to very surprising results. For example, small copper and silver clusters favor 3D shapes, like most metal clusters, but small neutral gold clusters exhibit planar structures. The medium-sized gold clusters exhibit a variety of structures including flat, cage, pyramidal, and tubular structures.

The Au₂₀ cluster has been characterized as a small tetrahedral piece of fcc gold, with a small relaxation [102]. Each of the four faces represents a (111) surface. This cluster has a very high surface area because all the atoms are on the cluster surface and a large fraction are at corner sites with low coordination. There are three different kinds of atoms in the T_d structure: 4 at the apexes, 4 at the center of each face, and 12 along the edges. They have different coordination environments and may be viewed as different surface sites for binding molecules (such as CO, O₂, CO₂) for catalysis. The large HOMO-LUMO gap of Au₂₀ suggests that it is a highly inert and stable molecule and may possess novel chemical and physical properties.

A combined theoretical and experimental study of the structures of Au_{*n*}⁻ in the medium size range ($n=15-20$) has shown that clusters with $n=16-18$ possess unprecedented cage structures [18, 64]. In particular, Au₁₆⁻ has an interesting tetrahedral structure (see Fig. 3.4f) with an inner diameter of about 5.5 Å and has been compared to a fullerene. The cage structures of Au₁₆⁻ and Au₁₇⁻ have been confirmed by electron diffraction studies [63], and thus, they are the first experimentally confirmed, and smallest possible, gold cages. The large empty space inside these cage clusters immediately suggested that they can be doped with a foreign atom to produce a new class of endohedral gold cages analogous to endohedral fullerenes. A gold cage containing a central atom was first predicted for a series of icosahedral clusters M@Au₁₂ (M=W, Ta, Re⁺) based on the 18-electron rule [117, 152] and was subsequently confirmed experimentally [129, 153]. However, since Au₁₂ itself does not possess a cage structure, the dopant atom with the appropriate electron count must play an essential role in holding the cage together. Following the discovery of the hollow gold cages, Au₁₆⁻ and Au₁₇⁻, many different types of atoms could be used as dopants to form new endohedral gold clusters. Copper atom-doped Au₁₆⁻ and Au₁₇⁻ have been observed and characterized using photoelectron spectroscopy (PE) and DFT calculations. The similarity in the PE spectra of Au₁₆⁻ and Cu@Au₁₆⁻ species suggests that the Cu doping does not alter the geometric and electronic structures of the Au₁₆⁻ cluster anion significantly, which is only possible if Cu is trapped inside the Au₁₆⁻ cage. The Au₁₆⁻ cluster anion itself is unique in that its PE spectrum does not exhibit an energy gap similar to that for other even-sized gold clusters in this size range. The high electron binding energies and the lack of an energy gap suggest that neutral Au₁₆ is open shell, probably in a triplet ground state. This means that two extra electrons would be required to reach a closed-shell 18-electron Au₁₆²⁻ ion. Because of the high electron affinity of Au, the Cu atom can be viewed as donating an electron to the gold cage, effectively giving Cu⁺@Au₁₆²⁻ which has a stable closed-shell Au₁₆²⁻ dianion. The spectrum of the doped cluster anion Cu@Au₁₇⁻ is also very similar to that of the parent gold cluster Au₁₇⁻ except that there is one low binding energy peak followed by a large energy gap in the spectrum of the Cu-doped cluster. The new peak will arise because Au₁₇⁻ is a closed-shell species with 18 valence electrons; therefore, the extra electron is expected to enter its LUMO and give rise to the low binding energy peak in the PE spectrum of the Cu@Au₁₇ cluster anion. The spectral similarity again suggests that the Cu dopant induces very little structural change in the Au₁₇⁻ cage except

that it donates one electron. All these observations again imply that Cu stays in the center of the Au_{17} anion cage ($\text{Cu}^+ @ \text{Au}_{17}^{2-}$) and does not perturb the electronic and geometric structures of the cage significantly.

3.6.2 Ligand-Protected Gold Clusters

Stability of metal clusters in the gas phase can be explained using concepts of electron shell closing and atomic shell closing. But even the most stable clusters made in the gas phase have the tendency to coalesce and are short lived. One way to protect clusters from coalescing is to attach ligands to their surface. The ligands form a protective layer and stabilize the cluster electronically by withdrawing the delocalized electrons from the surface. Halides (Cl^-) and substituted thiols (SR) are electron-withdrawing ligands commonly used to stabilize clusters. $\text{Au}_{102}(\text{SC}_7\text{O}_2\text{H}_5)_{44}$ is a prime example of a ligand-protected cluster that has been well characterized both experimentally [40] and by DFT calculations [136]. The details of synthesis and crystallization methods can be obtained from Jadzinsky et al. [40]. The structure of the cluster was obtained by X-ray crystallography. The questions now arise of how to interpret the stability of the cluster. Large-scale DFT calculations were used to solve the electronic structure of this cluster [136]. Just as in the case of pure metallic clusters, electron shell closing can be used to explain the stability of ligand-protected clusters both in the gas phase and in solution. According to this theory, stability is associated to a total valence electron count $n_e = 2, 8, 18, 34, 58, 92, 138$, and so on. With electron-withdrawing ligands, the stability criterion has to be modified slightly so that n_e is calculated with the equation $n_e = NV - L - Q$. In that equation, N is the number of core metal atoms, V is their atomic valence, L is the number of electron-withdrawing ligands, and Q is the total charge on the complex. For the Au_{102} passivated cluster, $n_e = 58$ which satisfies the total electron count required for the stability. The 102 Au atoms can be divided into two groups: 79 core atoms and 23 atoms that bind to ligands. The 79-atom metallic core has a D_{5h} symmetry structure, while the 23 other Au atoms form RS–Au–SR units. The calculated HOMO-LUMO gap is 0.5 eV. This is relatively large for a metal cluster of this size and partly explains the stability of that cluster. The detailed examination of the DOS profiles showed that the 79 metal core atoms are in a neutral state and the 23 surface Au atoms are in an oxidized state. It can be concluded from this observation that the 79 core atoms are fully covered by the RS–Au–RS units with each surface Au atom covalently bonded to at least one sulfur atom. The superatom concept holds good to explain stabilities of ligand-protected gold clusters of different sizes that were observed experimentally. For example, $\text{Au}_{39}(\text{PPh}_3)_{14}\text{Cl}_6$ [154] in its anionic state has $n_e = 34$. In order to get this electron count, one considers that the PPh_3 is a weak ligand and should not be used in calculating n_e with the above formula. Therefore, out of 40 electrons (39 Au atoms and a minus charge), 6 participate in bonding with the 6 chlorine atoms:

the remaining 34 electrons on the Au₃₉ core are responsible for the shell closings. The calculated (DFT) HOMO-LUMO gap is 0.8 eV [154], consistent with the stability of this cluster.

3.6.3 Superatoms

A *superatom* is a stable quasispherical cluster with physical and chemical properties similar to those of an atom isovalent to it. Al₁₃⁻ is a good example of a superatom because it satisfies both atomic shell closing and electronic shell closing rules. It has an icosahedral geometry which is considered to be one of the most stable atom packing geometries. With 40 electrons, its electron configuration in the jellium model is 1s² 1p⁶ 1d¹⁰ 2s² 1f¹⁴ 2p⁶. Shell closing occurs after filling the second *p*-type subshell which makes Al₁₃⁻ isovalent to a halogen anion and closest, in a sense, to Cl⁻. Likewise, Al₁₃ may be viewed as a chlorine superatom. However, it should be noted that Al₁₃ is not particularly stable and that it is strongly distorted relative to the I_h icosahedron. Therefore, it is maybe more correct to view Al₁₃ as a “superchloride ion precursor” rather than a “superchlorine atom.”

Al₁₃⁻ was produced by laser vaporization and characterized by mass spectrometry [155]. Similar to a halide ion, Al₁₃⁻ was predicted to form ionic bonds with electropositive elements of the periodic table and covalent bonds with alkyl groups analogous to haloalkanes. When Al₁₃⁻ was reacted with iodine or HI, it acted as a superhalogen [155]. The mass spectral analysis showed the formation of Al₁₃I⁻. The structure of this complex, obtained by quantum chemical calculations, showed that the I atom is attached to one end of the icosahedral Al₁₃ while the negative charge resided on the opposite end. It is clear, in this reaction, that the superatom does not get distorted even in the presence of highly reactive iodide. This is because the electron affinity of Al₁₃ is roughly 3.4 eV while that of I is 3.05 eV, so the Al₁₃⁻ unit is conserved. At higher iodine concentration, the reaction produces a series of Al₁₃I_x⁻ compounds where *x* is even [156]. It is known that an odd number of iodine atoms are involved in the formation of polyhalides. So one can rationalize Al₁₃I_x⁻ (*x* even) compounds by considering Al₁₃ itself as a halogen atom (or superatom). This is confirmed both by mass spectroscopic analysis and ab initio calculations [155].

3.7 Concluding Remarks

Small metal clusters are fascinating because they often display unique properties and chemical reactivity not seen in condensed phases. Whichever way one looks (structure, magnetism, thermodynamic properties, chemical reactivity, etc.), the physics and chemistry of clusters are full of surprises. The unusual properties of some of the clusters derive from their small size itself. Others stem from the low atomic coordinations (high surface area) found in clusters. Others, yet, can be

attributed to electronic shell effects which are important, in a relative sense, only in small ($N \lesssim 100$) clusters. Low coordination and electronic shell effects in clusters often create geometrical structures totally different from fragments of the bulk and that, in turn, impacts all other properties.

But what makes clusters interesting is often also what makes them unstable. Simple considerations of surface area and surface energies show that X_n metal clusters ($n \lesssim 1000$) have a strong tendency to coalesce into larger particles. Therefore, an important challenge is to make relatively stable X_n or A_xB_y metal clusters and, concurrently, understand principles that govern their stability in order to guide the search for additional stable clusters. It is generally found that the most stable clusters are those that simultaneously satisfy two or more criteria (doubly magic clusters, DMCs), in particular, atomic and electronic shell closings. The chemistry of metalloids and Zintl ions is inspiring searches for stable clusters at the boundary of metallic and main group elements.

Another challenge, which we only briefly mentioned in this chapter, is to protect clusters by trapping them inside a matrix, or on a support, or by passivating their surface with ligands. In principle, there is a danger that, in the process of protecting metal clusters, one may lose some or all of the unique properties that made them interesting in the first place. However, the literature on DMCs and cluster-assembled materials gives ample evidence that protected clusters remain a fascinating new class of chemical species.

Small clusters have been studied in the gas phase for over 30 years, and finely divided metals and supported clusters have a longer history still. But from a synthetic chemistry and applications perspective, clusters are still relatively new. The field of fullerenes, nanotubes, graphenes, and generally, carbon-based nanomaterials and their analogs is evolving very fast, with many actual and potential applications. Likewise, in the bottom-up approach to metal clusters, there is a realistic hope that completely new avenues will open up in chemistry and materials, along with important applications. This should happen as more and more metal cluster building blocks get discovered—superatoms, passivated superatoms, cage clusters, high-symmetry endohedrally doped clusters, core-shell bimetallics, other high-symmetry bimetallics, Zintl-like clusters—and as the methods for making, protecting, and assembling them get better.

References

1. Castleman AW Jr., Khanna SN, Sen A, Reber AC, Qian M, Davis KM, Peppernick SJ, Ugrinov A, Merritt MD (2007) *Nano Lett* 7:27342741
2. Häkkinen H, Manninen M (1996) *Phys Rev Lett* 76:1599–1602
3. Bae Y-C, Kumar V, Osanai H, Kawazoe Y (2005) *Phys Rev B* 72:125427
4. Xiao L, Wang L (2004) *J Phys Chem A* 108:8605
5. de Heer WA, Knight WD, Chou MY, Cohen ML (1987) *Solid State Phys* 40:93
6. Cox AJ, Louderback JG, Bloomfield LA (1993) *Phys Rev Lett* 71:923
7. Knickelbein MB (2001) *Phys Rev Lett* 86:5255

8. Shvartsburg A, Jarrold MF (2000) *Phys Rev Lett* 85:2530–2532
9. Wilcoxon JP, Provencio PP (2004) *J Am Chem Soc* 126:6402–6408
10. Hodak JH, Henglein A, Giersig M, Hartland GV (2000) *J Phys Chem B* 104:11708–11718
11. Leuchtner RE, Harms AC, Castleman AW Jr. (1989) *J Chem Phys* 91:2753
12. Riley SJ, Bunsenges B (1992) *Phys Chem* 96:1104
13. Knickelbein MB (1999) *Annu Rev Phys Chem* 50:79
14. Cao B, Starace AK, Judd OH, Jarrold MF (2009) *J Am Chem Soc* 131:2446–2447
15. Zhang W, Zhao H, Wang L (2004) *J Phys Chem B* 108:2140
16. Li S, Li H, Liu J, Xue X, Tian Y, He H, Jia Y (2007) *Phys Rev B* 76:045410
17. Zhang M, Fournier R (2009) *Phys Rev B* 79:043203
18. Bulusu S, Wang L-S, Zeng XC (2006) *Proc Natl Acad Sci* 103:8326
19. Breaux GA, Neal CM, Cao B, Jarrold MF (2005) *Phys Rev B* 71:073410
20. Lechtken A, Drebov N, Ahlrichs R, Kappes MM, Schooss D (2010) *J Chem Phys* 132:211102
21. Castleman AW Jr., Khanna SN (2009) *J Phys Chem C* 113:2664–2675
22. Connerade J-P (2003) *Physica Scripta* 68:C25–32
23. Fournier R (1995) *J Chem Phys* 102:5396–5407
24. Stamenkovic V, Mun BS, Mayrhofer KJJ, Ross PN, Markovic NM, Rossmeisl J, Greeley J, Nørskov JK (2006) *Angew Chem Int Ed* 45:2897–2901
25. Sinfelt JH (1999) *Catal Today* 53:305
26. Alexeev OS, Gates BC (2003) *Ind Eng Chem Res* 42:1571–1587
27. Liu P, Huang Y, Zhang Y, Bonder MJ, Hadjipanayis GC, Vlachos D, Deshmukh SR (2005) *J Appl Phys* 97:10J303
28. Hillenkamp M, Domenicantonio D, Félix C (2006) *Rev Sci Instrum* 77:025104
29. Gaudry M, et al. (2003) *Phys Rev B* 67:155409
30. Lecoultre S, Rydlo A, Félix C, Buttet J, Gilb S, Harbich W (2011) *J Chem Phys* 134:074302; *ibid.* 074303
31. Bein Th, Jacobs PA, Schmidt F (1982) In: Jacobs PA (ed) *Metal microclusters in zeolites*. Elsevier, Amsterdam
32. Thomas JM, Johnson BFG, Raja R, Sankar G, Midgley PA (2003) *Acc Chem Res* 36:20–30
33. Binns C (2001) *Surf Sci Rep* 44:1
34. Heiz U, Vanolli F, Trento L, Schneider W-D (1997) *Rev Sci Instrum* 68:1986
35. Heiz U, Bullock EL (2004) *J Mater Chem* 14:564
36. Ferrando R, Barcaro G, Fortunelli A (2009) *Phys Rev Lett* 102:216102
37. Ozin GA, Arsenault AC (2005) *Nanochemistry, a chemical approach to nanomaterials*. RSC Publishing, Cambridge
38. Shevchenko EV, Talapin D, Rogach AL, Kornowski A, Haase M, Weller H (2002) *J Am Chem Soc* 124:11480–11485
39. Femoni C, Iapalucci MC, Longoni G, Svensson PH (2001) *Chem Commun* 1776
40. Jadzinsky PD, Calero G, Ackerson CJ, Bushnell DA, Kornberg RD (2007) *Science* 318:430
41. Okumura K, Matsui H, Sanada T, Harao M, Honma T, Hirayama S, Niwa M, *Catal J* (2009) 265:89–98
42. Martin TP (1996) *Phys Rep* 273:199–241
43. Clemenger K (1985) *Phys Rev B* 32:1359
44. DeHeer WA (1993) *Rev Mod Phys* 65:611;
45. Brack M (1993) *Rev Mod Phys* 65:677
46. Li X, Wu H, Wang X-B, Wang L-S (1998) *Phys Rev Lett* 81:1909
47. Farges J, de Feraudy MF, Raoult B, Torchet J (1988) *Adv Chem Phys* 70:45
48. Smirnov BM, Strizhev AY, Berry RS (1999) *J Chem Phys* 110:7412–7420
49. Doye JPK, Wales DJ, Berry RS (1995) *J Chem Phys* 103:4234–4249
50. Wales DJ, Doye JPK, Dullweber A, Hodges MP, Naumkin FY, Calvo F, Hernandez-Rojas J, Middleton TF. The Cambridge cluster database. <http://www-wales.ch.cam.ac.uk/CCD.html>
51. Fournier R, Zamiruddin S, Zhang M (2009) *Can J Chem* 87:1013–1021
52. Somorjai GA (1994) *Introduction to surface chemistry and catalysis*. Wiley, New York
53. Methfessel M, Hennig D, Scheffler M (1992) *Appl Phys A* 55:442

54. Lian L, Su C-X, Armentrout PB (1992) *J Chem Phys* 96:7542
55. Fournier R, Cheng JBY, Wong A (2003) *J Chem Phys* 119:9444–9454
56. Li J, Li X, Zai H-J, Wang L-S (2003) *Science* 299:864
57. Sun Y, Fournier R (2007) *Phys Rev A* 75:063205
58. Sun Y, Zhang M, Fournier R (2008) *Phys Rev B* 77:075435
59. Sung M-W, Kawai R, Weare JH (1994) *Phys Rev Lett* 73:3552
60. Breaux GA, Hillman DA, Neal CM, Jarrold MF (2005) *J Phys Chem A* 109:8755–8759
61. Fournier R (2010) *Can J Chem* 88:1071–1078
62. Sun Y, Fournier R (2005) *Comp Lett* 1:210–219
63. Xing XP, Yoon B, Landman U, Parks JH (2006) *Phys Rev B* 74:165423
64. Wang L-M, Bulusu S, Zhai H-J, Zeng X-C, Wang L-S (2007) *Angew Chem Int Ed* 46:2915
65. Bouwen W, Vanhoutte F, Despa F, Bouckaert S, Neukermans S, Kuhn LT, Weidele H, Lievens P, Silverans RE (1999) *Chem Phys Lett* 314:227–233
66. Veldeman N, Hóltzl T, Neukermans S, Veszprémi T, Nguyen MT, Lievens P (2007) *Phys Rev A* 76:011201
67. Gao Y, Bulusu S, Zeng XC (2005) *J Am Chem Soc* 127:156801
68. Kumar V (2009) *Phys Rev A* 79:085423
69. Li X, Kuznetsov AE, Zhang H-F, Boldyrev AI, and Wang L-S (2001) *Science* 291:859
70. Castleman AW Jr. (2008) *J Phys Chem A* 112:13316
71. Boldyrev AI, Wang L-S (2005) *Chem Rev* 105:3716
72. Dognon J-P, Clavaguéra C, Pyykkö P (2007) *Angew Chem Intl Ed* 46:1427–1430
73. Sun Y, Fournier R (2007) *Phys Rev A* 75:063205
74. Kappes MM, Schar M, Radi P, Schumacher E (1986) *J Chem Phys* 84:1863
75. Perdew JP (1988) *Phys Rev B* 37:6175–6180
76. Alonso JA (2005) *Structure and properties of atomic nanoclusters*. Imperial College Press, London, and references therein
77. Näher U, Hansen K (1994) *J Chem Phys* 101:5367
78. Hansen K, Näher U (1999) *Phys Rev A* 60:1240
79. Baladron C, Alonso JA (1988) *Physica B* 154:73–81
80. Fournier R (2001) *J Chem Phys* 115:2165–2177
81. Melko JJ, Clayborne PA, Jones CE Jr., Reveles JU, Gupta U, Khanna SN, Castleman AW Jr. (2010) *J Phys Chem A* 114:2045
82. Pyykkö P (2007) *Nature Nanotech* 2:273–274
83. Ferrer D, Torres-Castro A, Gao X, Sepúlveda-Guzmán S, Ortiz-Méndez U, José-Yacamán M (2007) *Nano Lett* 7:1701–1705
84. Baletto F, Mottet C, Ferrando R (2003) *Phys Rev Lett* 90:135504
85. Goia DV, Matijević E (1998) *New J Chem* 22:1203
86. Mizukoshi Y, Fujimoto T, Nagata Y, Oshima R, Maeda Y (2000) *J Phys Chem B* 104:6028–6032
87. Park JI, Kim MG, Jun YW, Lee JS, Lee WR, Cheon J (2004) *J Am Chem Soc* 126:9072
88. Bente W, Nilus N, Ernst N, Freund H-J (2005) *Phys Rev B* 72:045403
89. Rosi NL, Mirkin CA (2005) *Chem Rev* 105:1547–1562
90. Rossi G, Rapallo A, Mottet C, Fortunelli A, Baletto F, Ferrando R (2004) *Phys Rev Lett* 93:105503
91. Sun Y, Zhang M, Fournier R (2008) *Phys Rev B* 77:075435
92. Knight WD, Clemenger K, deHeer WA, Saunders WA, Chou YM, Cohen ML (1984) *Phys Rev Lett* 52:2141–2143
93. Rapallo A, Rossi G, Ferrando R, Fortunelli A, Curley BC, Loyd LD, Tarbuck GM, Johnston RL (2005) *J Chem Phys* 122:194308
94. Ferrando R, Jellinek J, Johnston RL (2006) *Chem Rev* 108(3):845–910
95. Echt O, Kandler O, Leisner T, Miehe W, Recknagel E (1990) *J Chem Soc Faraday Trans* 86:2411–2415
96. Farges J, de Feraudy MF, Raoult B, Torchet J (1983) *J Chem Phys* 78:5067
97. Farges J, de Feraudy MF, Raoult B, Torchet J (1986) *J Chem Phys* 84:3491

98. Echt O, Sattler K, Recknagel E (1981) *Phys Rev Lett* 47:1121
99. Wei S, Shi Z, Castleman AW Jr. (1991) *J Chem Phys* 94:8604
100. Rayane D, Melinon P, Cabaud B, Hoarau P, Tribollet B, Broyer M (1989) *Phys Rev A* 39:6056–6059
101. Wang Q, Sun Q, Yu J-Z, Gu B-L, Kawazoe Y, Hashi Y (2000) *Phys Rev A* 62:063203
102. Li J, Li X, Zhai H-J, Wang LS (2003) *Science* 299:864
103. Johansson MP, Sundholm D, Vaara J (2004) *Angew Chem Int Ed* 43:2678
104. Bartels C, Hock C, Huwer J, Kuhnen R, Schwobel J, von Issendorff B (2009) *Science* 323:1323
105. Solov'yov AV, Polozkov RG, Ivanov VK (2010) *Phys Rev A* 81:021202
106. Yamada Y, Castleman AW Jr. (1992) *J Chem Phys* 97:4543–4548
107. Lisinetskaya PG, Mitrić R (2011) *Phys Rev A* 83:033408
108. Bouwen W et al. (1999) *Chem Phys Lett* 314:227–233
109. Diederich Th, Döppner T, Fennel Th, Tiggesbäumker J, Meiwes-Broer K-H (2005) *Phys Rev A* 72:023203
110. Harms AC, Leuchtner RE, Sigsworth SW, Castleman AW Jr. (1990) *J Am Chem Soc* 112:5673
111. Cui LF, Huang X, Wang LM, Zubarev DY, Boldyrev AI, Li J, Wang L-S (2006) *J Am Chem Soc* 128:8390
112. Cui LF, Huang X, Wang LM, Wang L-S (2006) *J Phys Chem A* 110:10169–10172
113. Li X, Wang L-S (2002) *Phys Rev B* 65:153404
114. Rao BK, Khanna SN, Jena P (2001) *J Chem Phys* 115:778
115. Nakajima A, Sugioka T, Kishi T, Kaya K (1992) In: Jena P et al. (ed) *Physics and chemistry of finite systems: from clusters to crystals*, vol. 1. Kluwer Academic, The Netherlands
116. Wan J, Fournier R (2003) *J Chem Phys* 119:5949–5954
117. Pyykkö P, Runeberg N (2002) *Angew Chem Int Ed* 41:2174
118. Neukermans S, Janssens E, Chen ZF, Silverans RE, Schleyer PvR, Lievens P (2004) *Phys Rev Lett* 92:163401
119. Yerezian C, Röthlisberger U, Schumacher E (1995) *Chem Phys Lett* 237:334–338
120. Ko YJ, Shakya A, Wang H, Grubisic A, Zheng W, Götz M, Ganteför G, Bowen KH, Jena P, Kiran B (2010) *J Chem Phys* 133:124308
121. Khanna SN, Jena P (1995) *Phys Rev B* 51:13705
122. Thomas OC, Zheng W-J, Lippa TP, Xu S-J, Lyapustina SA, Bowen KH Jr. (2001) *J Chem Phys* 114:9895–9900
123. Khanna SN, Rao BK, Jena P (2002) *Phys Rev B* 65:125105
124. Kumar V, Kawazoe Y (2001) *Phys Rev B* 64:115405
125. Roach P, Woodward WH, Reber AC, Khanna SN, Castleman AW Jr. (2010) *Phys Rev B* 81:195404
126. Zdetsis AD (2009) *J Chem Phys* 131:224310
127. Sun Q, Gong XG, Zheng QQ, Sun DY, Wang GH (1996) *Phys Rev B* 54:10896
128. Janssens E, et al. (2005) *Phys Rev Lett* 94:113401
129. Zhai H-J, Li J, Wang L-S (2004) *J Chem Phys* 121:8369–8374
130. Neukermans S, Janssens E, Tanaka H, Silverans RE, Lievens P (2003) *Phys Rev Lett* 90:033401
131. Chen D-L, Tian WQ, Sun C-C (2007) *Phys Rev A* 75:013201
132. Goicoechea JM, Sevov SV (2005) *J Am Chem Soc* 127:7676–7677
133. Sun Z-M, Xiao H, Li J, Wang L-S (2007) *J Am Chem Soc* 129:9560–9561
134. Kesanli B, Halsig J, Zavaliy P, Fettinger JC, Lam YF, Eichhorn BW (2007) *J Am Chem Soc* 129:4567–4574
135. Briant CE, Theobald BRC, White JW, Bell LK, Mingos DMP, Welch AJ (1981) *J Chem Soc Chem Commun* 201
136. Walter M, Akola J, Lopez-Acevedo O, Jadzinsky PD, Calero G, Ackerson CJ, Whetten RL, Grönbeck H, Häkkinen H (2008) *Proc Nat Acad Sci* 105:9157
137. Heaven MW, Dass A, White PS, Holt K, Murray RW (2008) *J Am Chem Soc* 130:3754

138. Akola J, Walter M, Whetten RL, Häkkinen H, Grönbeck H (2008) *J Am Chem Soc* 130:3756
139. Guo BC, Kerns KP, Castleman AW Jr. (1992) *Science* 255:1411
140. Guo BC, Wei S, Purnell J, Buzza SA, Castleman AW Jr. (1992) *Science* 256:515
141. Wei S, Guo BC, Purnell J, Buzza SA, Castleman AW Jr. (1992) *J Phys Chem* 96:4166
142. Kerns KP, Guo BC, Deng HT, Castleman AW Jr. (1994) *J Chem Phys* 101:8529–8534
143. Pilgrim JS, Duncan MA (1993) *J Am Chem Soc* 115:6958
144. Naumkin FY (2008) *Chem Phys Lett* 466:44–49
145. Haruta M (1997) *Catal Today* 36:153
146. Lopez N, Nørskov JK (2002) *J Am Chem Soc* 124:11262
147. Boyen H-G et al. (2002) *Science* 297:1533
148. Elghanian R, Storhoff JJ, Mucic RC, Letsinger RL, Mirkin CA (1997) *Science* 277:1078
149. Chen S, et al. (1998) *Science* 280:2098
150. Whetten RL, et al. (1999) *Acc Chem Res* 32:397
151. Pyykkö P (2004) *Angew Chem* 114:2278
152. Pyykkö P (2006) *J Organomet Chem* 691:4336
153. Li X, Kiran B, Li J, Zhai H-J, Wang L-S (2002) *Angew Chem Int Ed* 41:4786
154. Teo BK, Shi X, Zhang H (1992) *J Am Chem Soc* 114:2743
155. Bergeron DE, Castleman AW Jr., Morisato T, Khanna SN (2004) *Science* 304:84
156. Bergeron DE, Roach PJ, Castleman AW Jr., Jones NO, Khanna SN (2005) *Science* 307:231

Chapter 4

Optical Properties of Metal Nanoclusters from an Atomistic Point of View

Christian F.A. Negre and Cristián G. Sánchez

4.1 Introduction

Optical properties of metal nanoclusters are related to their great capacity of absorbing light in the visible region, and they are among the most important properties concerning these clusters. Following light absorption, there is a collective electronic excitation of electrons which is known as a *plasmon* excitation [1–3]; the electric field of the incident photon produces a coherent oscillation of the metal conduction electrons. This situation can be represented with the scheme of Fig. 4.1. When the electron cloud is displaced with respect to the nuclei, a restorative force arises from the Coulombic interaction between electrons and nuclei, creating the oscillatory motion. This is, in general, a dipolar oscillation if the nanoparticle (NP) is much smaller than the wavelength of the incident light. The latter is known as the quasistatic approximation. Under this condition, the incident field is uniform inside the NP and the interactions can be treated by means of simple electrostatic considerations.

On the other hand, if NPs are larger than the wavelength of the incident light, multipolar oscillations can occur. For quadrupolar modes, for example, half of the electrons are oscillating parallel to the incident field vector, while the other half oscillates perpendicular to the field. This mode produces no net change in the dipole moment. Collective electronic oscillations are also present in the bulk material, but in the case of NPs the degree of confinement and the large surface to volume ratio decrease the plasmon resonance energy from UV to the visible range and make absorption features extremely sensitive to shape, size, and surface condition [1,4–6].

C.F.A. Negre (✉) • C.G. Sánchez

Departamento de Matemática y Física, Facultad de Ciencias Químicas, INFIQC,
Universidad Nacional de Córdoba, Ciudad Universitaria, Córdoba, Argentina
e-mail: christianfannegre@gmail.com

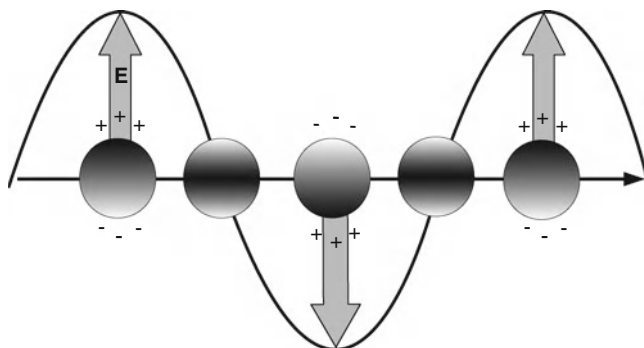


Fig. 4.1 Scheme showing plasmonic excitation in tune with an oscillating incident field

Plasmonic excitations have been observed in both large-size clusters, with a few tens of nanometers radius, and very small clusters formed by a few hundred atoms. Regarding large clusters and bulk material, surface plasmons are well described in terms of the Mie¹ electrodynamic theory [1,3–5]. Theoretical calculations using this theory have revealed, for example, that peak widths in absorption spectra vary with $\frac{1}{R}$, where R is the particle radius [7]. Small clusters, on the other hand, exhibit a more complex behavior with a high degree of UV-VIS peak fragmentation, and the relation of peak width with $\frac{1}{R}$ is no longer valid, due to quantum scattering. There is currently no theory or simulation method that can cover all NP sizes, and ab initio methods apply only to very small particles [8].

Mie theory does not apply to nanoclusters of any shape and size, but this is not the case of the DDA (discrete dipole approximation) electrodynamic method [9]. In this method, the object of interest is represented through a cubic grid of N polarizable elements. The cluster being treated can occupy any point in the cubic space, which implies that any particle shape can be handled with this method. Each element of the discretized space behaves as a dipole, whose polarizability depends on the material through the dielectric function of the metal [2, 10]. This strategy allows the calculation of the induced cluster polarization by the presence of an oscillating external electric field. Although this method yields results that in many cases match experimental data, it has three main drawbacks: (a) It does not account explicitly for atomic structure; (b) In many cases, the result may depend on the discretization degree; (c) Finally, topological problems regarding to the limit of the metallic surface in particles having surface defects are introduced [9]. The latter can produce unphysical results.

In order to overcome these disadvantages, methods for calculating optical properties of small particles must be based on models in which the atomistic nature

¹In 1908, Mie proposed a solution of Maxwell equations to describe the extinction spectra of spherical particles of arbitrary size.

of matter is addressed. For the case of metals such as Au, the frequency of the plasmon resonance is influenced by electrons in the d band. This fact introduces serious problems when trying to implement a quantum method to calculate optical properties. These problems are due to the difficulty of representing interband transitions of conducting electrons [1]. Hence, a high detail of valence orbitals in transition metals must be taken into account when implementing quantum descriptions. In classical methods, the effect of d electrons is implicitly included in the metal dielectric function [11].

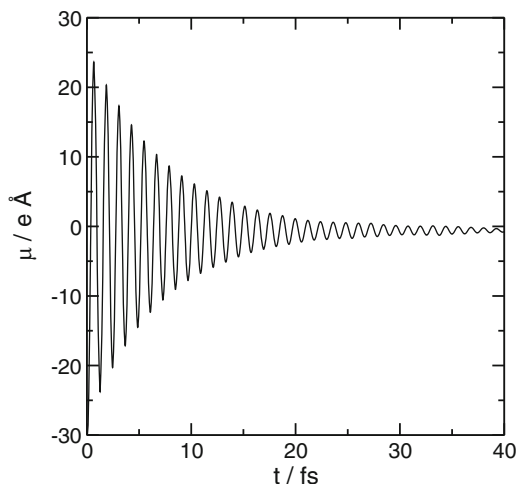
Experimentally, the study of plasmon dynamics is performed with different techniques that allow the determination of absorption spectra [7, 12–14] and the decay of excitations [15–17] of individual particles. The latter are based on double pulse techniques which permit independent resolution of relaxation times, of both electronic and vibrational modes [18, 19]. The most advanced experimental techniques allow, for example, the study of the interaction of individual NPs with single molecules [20, 21] and the mutual influence exerted on their optical properties.

UV-VIS spectroscopy is an essential tool to study the optical properties of metal nanoclusters. Spectral features of large NPs are characterized by two parameters that describe the main peak of the absorption spectra. These parameters are: the wavelength (or energy) of the surface plasmon resonance (SPR), at which the maximum of the absorption takes place, and the peak width. The peak width is closely related to the lifetime of the plasmonic excitation. High values of peak width correspond to a collective excitation of electrons that rapidly decays when the incident field is suddenly turned off.

According to the usual interpretation, the plasmon relaxation (coherent oscillation decay) occurs in two stages. The first decay is due to the decoherence of electrons which are part of the plasmon excitation, a process known as *Landau damping* [1, 22]. This process occurs at intrinsic electronic speeds (Fermi velocity); it is therefore ultrafast and takes place at times of the order of femtoseconds (see Fig. 4.2). After the end of the first decay step, the result is a *sea of hot electrons* with random movement, that can transfer energy to nuclear motion (through electron–phonon interaction). The ability to produce NPs with particular spectral features requires a deep understanding of the decaying processes. The initial plasmon damping is the responsible for the homogeneous broadening of plasmon absorption peaks. Analytical applications such as surface-enhanced Raman spectroscopy (SERS) require the maximization of excitation lifetimes in order to increase local field effects [15].

Factors that produce peak broadenings can be classified into two groups: homogeneous and inhomogeneous broadenings. Factors that have to do strictly with intrinsic properties of individual NPs, such as shape and surface condition, are known as homogeneous broadening [7]. Most of the optical experiments require clusters to be embedded in a nonmetallic matrix in order to stabilize them in solution. A homogeneous broadening is produced by the interaction of the metal with the protective matrix. On the other hand, spectra determined when dealing with a mixture of NPs of different shapes have a broadened peak as a result of the

Fig. 4.2 Dipole moment as a function of time for the case of an icosahedral particle of 3,871 Au atoms after an initial perturbation in a shape of a step. Reprinted with permission from J. Chem. Phys. **129**, 034710 (2008). Copyright (2008) American Chemical Society



average over every individual spectrum associated with each shape. The latter is a key contributing factor to what is known as inhomogeneous broadening [23].

For small NPs, electronic excitations resemble more the scenario found in molecular systems, in which discrete electronic transitions are related to peak positions. The smaller the aggregate, the more fragmented the absorption spectrum. When the particle becomes large, the definition of a resonant plasmonic peak is the result of a kind of correspondence principle, since in this case the electrons behave *classically*.

The energy contained in the plasmonic excitation is finally dissipated to the surrounding environment. The direct mechanism of dissipation is the coupling with phonons in which the nuclear lattice becomes vibrationally excited. The heat stored in the NP finally dissipates to the environment molecules. This principle has powerful applications, such as, for example, to propose treatments to remove tumor tissue in cancer therapies when particles are adequately functionalized. The other way of dissipating energy is a radiation mechanism where the involved NP behaves as an *antenna* emitting electromagnetic waves as a consequence of electron movement. This mechanism can be very significant in large NPs, greater than 50 nm [1, 2]. Every relaxation mechanism yields, as a consequence, a broadened peak in the absorption spectra. Broadenings produced by energy dissipation pertain to the classification of homogeneous. On the other hand, without any dissipation, Landau damping also produces homogeneous broadening. Whenever the cluster is small, the electronic dissipation is smaller and the peak widths become very narrow, coming to resemble spectral lines [8].

As mentioned above, models that use continuous electrodynamics do not take into account the atomistic nature of matter [2, 10] and are only suitable for large particles in which the approximation of a continuum metallic model is reasonable. First-principle calculations, such as time-dependent density functional theory [24]

(TDDFT), are limited to the study of particles formed by several tenth of atoms [25–28]. Only by representing the metal as a *jellium* it is possible to treat larger NPs within the TDDFT [29] formalism, underlying the drawback that it is not possible to represent the metal atomic structure.

The method that will be presented here represents an intermediate step between first-principle calculations and continuum electrodynamics. We will explain the use of a self-consistent tight-binding (TB) Hamiltonian and the formalism of quantum dynamics to allow a fully quantum description of electrons and the inclusion of atomistic structure of matter in order to study the plasmon dynamics. Depending on the degree of detail of the TB description, this method has the advantage of being able to address systems with thousands of atoms, reaching experimental sizes.

The purpose of this chapter is to show an alternative tool for studying the absorption spectra of metallic NPs considering the influence of the shape, size, and surface so as to kick-start towards understanding the influence of the atomistic structure in the absorption spectra of metallic NPs.

4.2 Tight-Binding Method

The *tight-binding* method (TB) is one of the most widely used electronic structure calculation methods in condensed matter. It has been applied to a wide range of systems, going from semiconductors to transition metals. In quantum chemistry, the most exact results are provided by *ab initio* methods, in which the only approximation is given by the use of an incomplete basis and the choice of the exchange correlation functionals in the case of DFT. However, one of the strong disadvantages regarding the application of these methods is the impossibility of treating extended systems formed by several thousand of atoms. TB methods give the possibility of treating larger systems with a great quantity of atoms, or to study the behavior of a system during longer periods of time when performing a dynamical study [30].

There is no single model or theory to describe the method of TB; it is only a variation and modification of the usual quantum mechanical methods, i.e., DFT. We usually have energy sites $\langle \phi_i | \hat{H} | \phi_i \rangle = \epsilon_i$ and couplings or *hoppings* $\langle \phi_i | \hat{H} | \phi_j \rangle = V_{ij}$ of the Hamiltonian matrix H , and through the latter, we can represent the electronic structure of interest. This coupling parameters that enter in the H matrix give a very tangible idea of the bond constitution. Widely speaking, using a TB method involves modeling electronic properties of a system using *couplings* and *on-site energies* no matter what basis was used or how they were derived.

The Hückel method, for example, is only a TB method where the onsite and coupling parameters α and β act as ϵ and V . In general, if each site is associated with a particular atom, couplings between a minimal basis of localized atomic orbitals, constituted by one “s” orbital, three “p” orbitals, and five “d” orbitals per atom, are used. The valence wave function constructed with these atoms is part

of the chemical bonds in most materials. Transition metals are characterized by being bonded by “s” or “d” orbitals. Most of materials that are not constituted by transition elements (insulators or semiconductors) possess bonds constituted principally by the overlap of a linear combination of “s” and “p” atomic orbitals. The latter suggests that the TB method is closely related with *linear combination of atomic orbitals* (LCAO) [31] which is principally focused on the atomic orbitals (shape and symmetry) rather than the constitution of the H matrix as it is the case of the TB method.

The reliability of TB methods depends on the approximations that are made. The need to reduce computational cost is satisfied by further approximations such as the following: to ignore the two- and three-center integrals, assume that atomic orbitals are orthogonal, etc. One of the factors that contribute to the quality of TB models is what is known as *transferability*. This means that the aforementioned model could be transferred to other situations or systems without lowering its original predictive power. The numerical complexity of TB methods increases, usually with N^3 , N being the number of the atomic orbitals of the system. The *order* of the method, in this case, is the power with which the numerical complexity varies. For the case of metallic systems, it is difficult to reduce the order of the method; this is because the Hamiltonian matrix elements that are found outside the main diagonal (responsible of the electron delocalization) have significant values [32].

In the following section, we will see how it is possible to determine TB parameters from considering the Hamiltonian H in a localized atomic basis. Finally, we will show how to deduce TB parameters from a full DFT framework in order to obtain the DFTB method.

4.2.1 Two- and Three-Center Integrals

Let $\{I, J, \dots\}$ be a set of atomic center positions and $\{\mu, \nu, \dots\}$ a set of localized atomic orbitals in each of the previous atomic positions. We know that:

$$H_{I\mu J\nu} = \langle I\mu | \hat{H} | J\nu \rangle = \langle I\mu | \hat{T} | J\nu \rangle + \langle I\mu | \hat{V}_{\text{ef}} | J\nu \rangle, \quad (4.1)$$

where

$$\langle I\mu | \hat{T} | J\nu \rangle = \int \langle I\mu | r \rangle \left\{ \frac{-\nabla^2}{2} \right\} \langle r | J\nu \rangle dr \quad (4.2)$$

and $\langle I\mu | r \rangle = \phi_{I\mu}(r - R_I)$ is the wave function that represents the orbital μ located at I and r is the spatial coordinate. $\frac{-\nabla^2}{2}$ is the kinetic energy operator written in atomic units. We see that the integral of the right-hand side of (4.2) is a two-center integral because the result depends on the positions of both I and J atoms.

The \hat{V}_{ef} operator is an addition of other operators: $\hat{V}_{\text{ef}} = \sum_K \hat{V}_{\text{ef},K}$; therefore, $V_{\text{ef}}(r) = \sum_K V_{\text{ef},K}(r - R_K)$, which is the effective potential that an electron would

feel at position r . For evaluating $\langle I\mu | \hat{V}_{\text{ef}} | J\nu \rangle$, it is necessary to solve two- and three-center integrals:

$$\langle I\mu | \hat{V}_{\text{ef}} | J\nu \rangle = \langle I\mu | \sum_K \hat{V}_{\text{ef}}^{(K)} | J\nu \rangle = \langle I\mu | \hat{V}_{\text{ef}}^{(I)} | J\nu \rangle + \langle I\mu | \hat{V}_{\text{ef}}^{(J)} | J\nu \rangle + \underbrace{\langle I\mu | \sum_{K \neq I, J} \hat{V}_{\text{ef}}^{(K)} | J\nu \rangle}_{\text{Three-center integral}} \quad (4.3)$$

in which the last term of the right-hand side is called a three-center integral. When the orbitals are situated at the same atom, the latter expression is composed by two- and one-center integrals:

$$\langle I\mu | \hat{V}_{\text{ef}} | I\nu \rangle = \langle I\mu | \sum_K \hat{V}_{\text{ef}}^{(K)} | I\nu \rangle = \underbrace{\langle I\mu | \hat{V}_{\text{ef}}^{(I)} | I\nu \rangle}_{\text{One-center integral}} + \underbrace{\langle I\mu | \sum_{K \neq I} \hat{V}_{\text{ef}}^{(K)} | I\nu \rangle}_{\text{Two-center integrals}} \quad (4.4)$$

The TB method neglects three-center integrals, and two-center integrals are not calculated explicitly, but they are parameterized. This means that the functional form of a particular orbital is not taken into account, but the matrix elements are modeled directly as a function of the atomic positions. For the case of extended systems, the functional form of the matrix elements is fitted to bulk properties such as the filling of the s band, the lattice parameter, the binding energy, etc. [32]. Those methods that parameterize the coupling integrals using experimental data are known as semiempirical TB methods. However, there is no guarantee that parameters adjusted empirically are transferable to other physical systems. Transferability is only guaranteed if the meaning of the parameters and their relation are well known and if there is a way to calculate them in a direct way within a theoretical formalism. The theoretical formalism used for this purpose is DFT, whose relation with TB methods will be explained in the following section.

4.2.2 DFT-Based TB

As it was mentioned in the previous section, in TB methods, the matrix elements are usually parameterized to the band structure of a reference system. As a consequence, many-body effects are contained in the matrix elements. The transferability of the TB methods can be improved by taking into account mainly two modifications: the use of nonorthogonal basis sets and the implementation of a self-consistent method. These improvements are taken into account in the TB method based in first-principle formalisms. The TB method based in DFT, known as DFTB (density functional tight-binding), is a method based on the second-order expansion of the Kohn-Sham (KS) functional with respect to charge fluctuations. This procedure

ensures a proper distribution of charge and satisfies the electro-neutrality condition. Improved self-consistent versions work better for both metals and molecules than the primitive non-self-consistent versions [33].

The DFTB method can be seen as an intermediate step between a simple semiempirical TB and DFT itself. A DFT implementation can be found in the DFTB+ code which is a program based on the sparsity of the Hamiltonian matrix for efficiently calculating the electronic structure [34, 35]. This code was used for finding the initial ground state (GS) that is used as an input in quantum dynamics for studying plasmon dynamics in NPs. In this section, we will develop the self-consistent DFTB method from a second order expansion of the KS functional. This procedure was developed by Frauenheim et al. and the details of it can be found in [36, 37].

After some algebra, the KS functional can be rewritten as [38]:

$$E^{\text{KS}}[n(r)] = \sum_i f_i \langle \psi_i | T + V_{\text{eff}} | \psi_i \rangle - \frac{1}{2} \int n(r) V_H(r) dr - \int n(r) V_{\text{ext}}(r) dr + E_{\text{xc}}[n(r)], \quad (4.5)$$

where $n(r)$ is the electron density at position r with $V_{\text{eff}} = V_H(r) + V_{\text{xc}}(r) + V_{\text{ext}}(r)$. $V_H(r)$ is the Hartree potential which takes into account the electron–electron interaction for independent particles; $V_{\text{xc}}(r)$ is the exchange correlation potential, and $V_{\text{ext}}(r)$ is the external potential which gives the nuclear–electron interactions. The second term of the right-hand side of (4.5) corrects for the double counting produced by the term V_{eff} .

Replacing n by $n_0 + \delta n^2$ and expanding $E_{\text{xc}}[n(r)]$ around n_0 to second order, we have:

$$E^{\text{KS}}[n(r)] = \sum_i f_i \langle \psi_i | T | \psi_i \rangle - E_H^0 - \int n^0(r) V_{\text{xc}}[n^0(r)] dr + E_{\text{xc}}[n^0(r)] + \frac{1}{2} \int \int C(r, r') \delta n(r) \delta n(r') dr dr' \quad (4.6)$$

with:

$$C(r, r') = \frac{1}{|r - r'|} + \frac{\delta^2 E_{\text{xc}}}{\delta n(r) \delta n(r')_{n_0}} \quad (4.7)$$

Here, n_0 is the electron density function over the isolated atoms when they are not forming bonds in a molecular system. Linear terms in δn vanish for each density n^0 . Thus, it is possible to separate what comes from the self-consistent system in

²This is a standard mathematical approach used to express the functional around n_0 for small charge fluctuations, such as those arising from bonding.

two terms: one depending on n^0 and other that depends only on δn . The term that depends only on n^0 together with the nuclear repulsion, enters in E_{rep} (a repulsive pair potential).

$$E_{\text{rep}} = -E_H^0 - \int n^0(r) V_{\text{xc}}[n^0(r)] dr + E_{\text{xc}}[n^0(r)] \quad (4.8)$$

This quantity only raises the total energy of the system and is independent of charge fluctuations, thus, it will not contribute to an eventual quantum dynamics (constant terms contribute with zero to the Liouville equation).

The term of (4.6) that depends on δn is responsible for the variation of energy with the fluctuations of charge and, in consequence, it is the most important term in a self-consistent TB method. The common non-self-consistent DFTB method simply neglects this term:

$$E_{\text{TB}} = \sum_i^{\text{occ}} \langle \psi_i | H_0 | \psi_i \rangle + E_{\text{rep}} \quad (4.9)$$

Therefore, for the non-self-consistent case, the KS equations are solved in a basis of localized atomic orbitals. For this purpose, a Slater orbital basis is chosen. Elements of $H_{\mu,\nu} = \langle \mu | H_0 | \nu \rangle$ for obtaining the Hamiltonian matrix within this basis are calculated after solving KS equations.

Going back to the self-consistent case, when an atomic basis is employed, the fifth term of the right-hand side of (4.6) is parameterized analytically as a function of the distance between orbitals $\gamma_{AB}(|R_A - R_B|)$ and orbital charges $\Delta q_{A/B}$:

$$\begin{aligned} \frac{1}{2} \int \int C(r, r') \delta n(r) \delta n(r') dr dr' &= \frac{1}{2} \sum_{AB} \int \int C(r, r')_{AB} \delta n_A(r) \delta n_B(r') dr dr' \\ &= \frac{1}{2} \sum_{AB} \gamma_{AB}(|R_A - R_B|) \Delta q_A \Delta q_B \end{aligned}$$

Therefore, for the self-consistent case, we have:

$$E_{\text{TB}}[n(r)] = \sum_i^{\text{occ}} \langle \psi_i | H_0 | \psi_i \rangle + \frac{1}{2} \sum_{AB} \gamma_{AB} \Delta q_A \Delta q_B + E_{\text{rep}}. \quad (4.10)$$

In the large distance limit, the exchange correlation term contained in γ_{AB} goes to zero and only the part of Coulombic interaction between the two charges Δq_A and Δq_B remains nonzero. On the other hand, when both orbitals lay in the same site, the parameter $\gamma_{AA} = U_A$ can be approximated as the difference between the ionization energy and the electron affinity. As in the simple non-self-consistent TB, the latter is related to the chemical hardness of the atom.

If we now introduce a localized Slater orbital base and apply the variational principle to functional of (4.10), we finally have the following generalized eigenvalue equation:

$$\sum_{\nu I} C_{\nu I} (H_{\mu\nu} - \epsilon_I S_{\mu\nu}) = 0 \quad (4.11)$$

with

$$H_{\mu\nu} = \langle \phi_\mu | \hat{H}_0 | \phi_\nu \rangle + \frac{1}{2} S_{\mu\nu} \sum_X (\gamma_{AX} + \gamma_{BX}) \Delta q_X. \quad (4.12)$$

$S_{\mu\nu} = \langle \mu | \nu \rangle$ being the overlap matrix elements between orbital basis elements. Elements of H , S and γ are parameterized as a function of the inter-orbital distance (atomic sites distances). We have to remark the fact that the many body interacting contribution of electrons (electron interaction at the DFT level) is implicit in the γ and U parameters:

$$\gamma_{AB} = \gamma_{AB}(U_A, U_B, |\vec{R}_A - \vec{R}_B|) \quad (4.13)$$

Charge fluctuations $\Delta q_X = q_X - q_X^0$ are obtained from Mulliken analysis. For the case of non orthogonal orbitals these are:

$$q_X = \frac{1}{2} \sum_i^{\text{occ}} n_i \sum_{\mu \in X} \sum_{\nu} (C_{\mu i}^* C_{\nu i} S_{\mu\nu} + C_{\nu i}^* C_{\mu i} S_{\nu\mu}), \quad (4.14)$$

where n_i is the population of the $|\psi_i\rangle$ molecular orbital and N is the total number of orbitals.

The self-consistent DFTB method is suitable when bonds with a great redistribution of charge between the two bound atomic species are present, particularly in heteronuclear molecules and polar semiconductors [36, 37]. In this case, \hat{H} is a function of the density matrix $\hat{\rho}$ ($\hat{H} = f(\hat{\rho})$), or more precisely:

$$H_{ij} = H_{ij}^0 + \frac{1}{2} U_i \Delta q_i \delta_{ij} + \sum_{j \neq i} \gamma_{ij} \Delta q_j \quad (4.15)$$

The second term of the right-hand side of (4.15) can be interpreted as the correction of the energy of orbital $|i\rangle$ by the excess of population in this orbital. The third term corrects for the on-site energy due to the charge distribution in the rest of the orbitals. The first approximation to parameter γ_{ij} for the case of an orthogonal TB model is $\gamma_{ij} = \frac{1}{4\pi\epsilon_0 R_{ij}}$; this is just the Coulombic interactions between different on-sites charges. This equation is the same as (4.12), with the only difference that in the first one we have considered an orthogonal system to achieve a direct physical interpretation of γ_{ij} factors.

4.2.3 Semiempirical TB for Noble Metals

In many cases, it is possible to use a simple orthogonal TB method to describe the electronic structure of noble metals. We will briefly describe the TB model developed by Sutton et al. [39]. This model allows to calculate properties of

metals such as Au, Ag, and Cu. It is orthogonal and self-consistent and has only one orbital per site (atom), which makes it appropriate for systems with large numbers of atoms³ [32,40,41]. The Hamiltonian possess exactly the shape of (4.15). Where $\Delta q_i = 2(\rho_{ii} - 1/2)$ is the Mulliken charge on each site. γ_{ij} is a function of the interatomic distance $\gamma_{ij} = K/\sqrt{R_{ij}^2 + K^2/U^2}$, with $K = e^2/4\pi\epsilon_0$ interpolating smoothly between on-site interaction U and the Coulombic interaction at largest separations. The parameter U , as in the case of DFTB, is related with the chemical hardness of the atomic species and corresponds to the difference between its ionization energy and electronic affinity. The matrix elements $H_{ij}^0 = H^0(R_{ij})$ are function of the distance between atoms. The functional form of the matrix elements is the following [39]:

$$H_{ij}^0 = -\frac{\epsilon c}{2} \left(\frac{a}{R_{ij}} \right)^q \quad (4.16)$$

where i and j underscripts designate atomic sites at different separations R_{ij} , ϵ is an energy scale factor, a is a characteristic length (usually the lattice parameter), and c and q are just constants that control the shape of the hopping distance dependence. These parameters are fitted to reproduce several properties of the bulk metal such as lattice parameter and compressibility.

For a periodic structure, the diagonal elements of ρ are all the same and have a value between zero and one that corresponds to the s band filling of the specie. Partial fillings obtained in Sutton's work are related with a rehybridization between s , p , and d orbitals [39].

4.3 Time Evolution of the Density Matrix

The time evolution of the density matrix is governed by the following equation:

$$\frac{\partial \hat{\rho}}{\partial t} = -\frac{i}{\hbar} [\hat{H}, \hat{\rho}] \quad (4.17)$$

This expression is known as the Liouville–von Neumann equation, and is nothing but a representation of the well-known time-dependent Schrödinger equation [42, 43].

If we consider a basis $B = \{\mu, \nu, \dots\}$ of localized orbitals, then $(\frac{\partial \rho}{\partial t})_{\mu\nu} = \langle \mu | -\frac{i}{\hbar} [\hat{H}, \hat{\rho}] | \nu \rangle = -\frac{i}{\hbar} [H, \rho]_{\mu\nu}$, where H and ρ are the respective matrix representations in the basis B for the corresponding operators.

The time evolution of the ρ matrix is obtained by means of a numerical integration of (4.17). With respect to the integration algorithm, the following simple

³For the case of DFTB, we need nine orbitals per site (one s orbital, three p orbitals, and five d orbitals) in order to represent metals such as Ag, Au, and Cu.

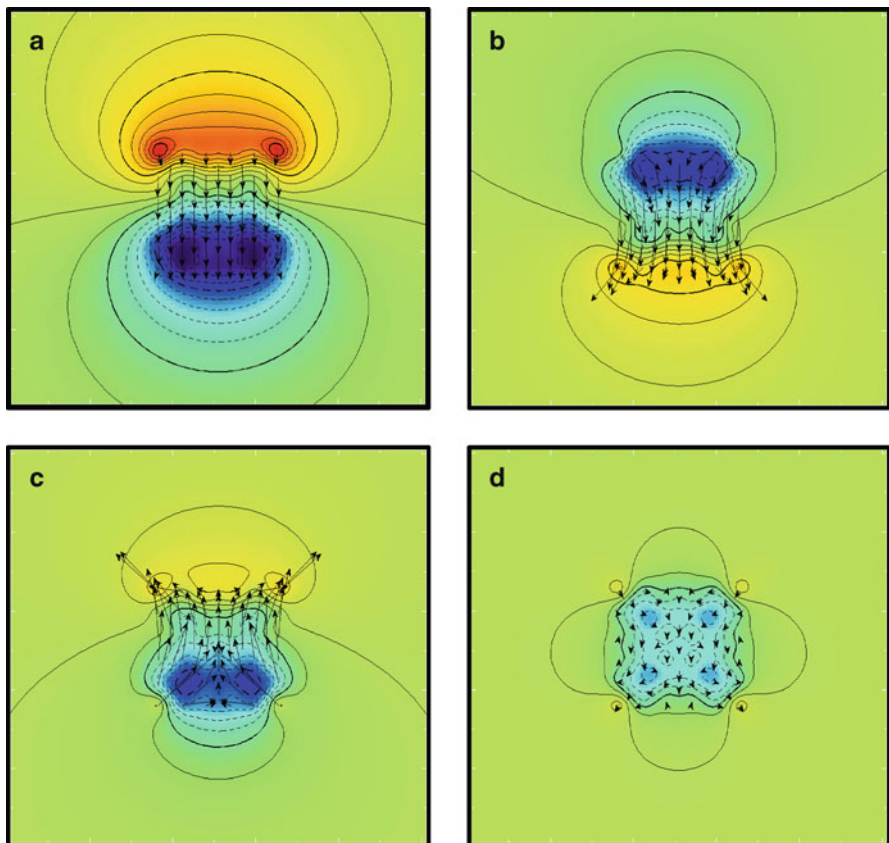


Fig. 4.3 Electronic current evolution between atoms for a 561 gold cuboctahedral NP, calculated with the time-dependent density matrix after the application of a perturbation in a shape of a step. (a) $t = 0.0$ fs. (b) $t = 0.2$ fs. (c) $t = 0.5$ fs. (d) $t = 20.0$ fs. The figure shows the current vectors (*dark arrows*) calculated for each pair of neighbors in a transversal section of the NP

scheme is used, because it preserves the trace of ρ (which is a constant of motion) all over the dynamics:

$$\rho(t + \Delta t) = \rho(t - \Delta t) + 2\Delta t \frac{\partial \rho}{\partial t}(t) \quad (4.18)$$

Δt being the integration time step. With the time evolution of the density matrix, it is possible to determine the evolution of any expectation value A as $A(t) = \text{tr}(\hat{\rho}\hat{A})$.

As an example of the results obtained from the numerical integration of the density matrix equation of motion after the application of an external perturbation, Fig. 4.3 shows the evolution of current vectors between interatomic bonds of neighboring atoms for a transversal section of a gold NP. Together with the

current, the potential generated by the charge fluctuation is also shown. Electronic movements in metallic NPs have a strong resemblance to classical fluids dynamics. This resemblance becomes stronger the larger the system [44].

4.3.1 Dipole Moment and Expectation Values

Given the dynamics of the density matrix, it is possible to determine the time evolution of the expectation value of a given operator. For studying plasmon dynamics, we will be interested in Mulliken charges, eigenvalues, dipole moments, electric currents in molecular bonds, the electric field,⁴ and interatomic forces. The first two properties of the list above are trivially obtained from the density matrix at each time step. For example, Mulliken charges in an orthogonal tight-binding representation are calculated as:

$$q_I = Z_I - \sum_{\mu \in I} [\rho^{\text{OA}}]_{\mu\mu}, \quad (4.19)$$

where q_I is the on-site charge at atom I , Z_I is the effective nuclear charge associated with each site⁵ and the set $\{\mu\}$ is the set of atomic orbitals on site I . Moreover, the energy levels of the system are calculated directly as they are given by the eigenvalues of the Hamiltonian matrix.

When considering optical properties, the most important expectation value is the dipole moment, since, as we will show below, it is necessary to obtain the absorption spectra of a metallic cluster. In order to obtain the time evolution of the dipole moment, it is only necessary to apply the classical dipole moment formula at each time step:

$$\langle \mu(t) \rangle = \sum_I \mathbf{r}_I q_I(t) \quad (4.20)$$

where charges $q_I(t)$ are obtained from applying (4.19) and \mathbf{r}_I is the vector position of the atom I .

4.3.2 Optical Properties

In this section, we will discuss about the interaction of matter with external electric fields under the linear response regime, and how to use the information contained in the time evolution of the dipole moment in order to obtain spectroscopic information of the system.

⁴This is important when studying near-field effects as it is explained in Sect. 4.8.

⁵The formula for calculating the on-site charges, in general, depends on the TB model.

When incident electric fields are much smaller than the internal fields of the system, the latter is considered to be in the linear response regime [45, 46]. The time evolution of the expectation value of any operator \hat{O} , can be expressed as a convolution between the applied perturbation and the response function of the system:

$$\langle O(t) \rangle = \langle O(0) \rangle + \int_{-\infty}^{\infty} \chi(t - \tau) V(\tau) \Theta(t - \tau) d\tau = \langle O(0) \rangle + \chi(t) * V(t) \quad (4.21)$$

where $\chi(t)$ is the system response function and V is an applied external perturbation. The Heaviside function ($\Theta(t - \tau)$) serves to enforce the causality principle.⁶ Equation (4.21) can be read as: the *response* $\langle O(t) \rangle$ is linear with respect to the *impulse force* $V(t)$, with the response function $\chi(t)$ as *coefficient of proportionality* [45].

In particular, for the case of the dipole moment, we have:

$$\langle \mu(t) \rangle = \int_{-\infty}^{\infty} \alpha(t - \tau) E(\tau) \Theta(t - \tau) d\tau, \quad (4.22)$$

where $E(\tau)$ is the electric field used to apply a perturbation over the system and $\alpha(t - \tau)$ is the polarizability. Written in the frequency domain, after using the convolution theorem, the last expression can be expressed as follows [47]:

$$\langle \mu(\omega) \rangle = \alpha(\omega) E(\omega). \quad (4.23)$$

From the knowledge of the time evolution operator of the system, it is possible to obtain an analytic expression of $\langle \mu(t) \rangle$ after applying the *Kubo* formula⁷:

$$\langle \mu(t) \rangle = \int_{-\infty}^{\infty} -\frac{i}{\hbar} \langle [\mu_H(t - \tau), \mu] \rangle E(\tau) d\tau, \quad (4.24)$$

where $\mu_H(t - \tau)$ is the operator μ in the Heisenberg picture [48]. From the last formula, we can immediately recognize that $\alpha(t - \tau) = -\frac{i}{\hbar} \langle [\mu_H(t - \tau), \mu] \rangle$, which gives a formula to express the polarizability [45].

The fact that the electric field has three components suggests that the polarizability should be expressed as a matrix so as to make the induced dipole moment dependent on the direction of the applied field. In other words, the polarizability is in general an anisotropic magnitude and must be written as a tensor [49]. Thus we have:

⁶The causality principle states that the effect is followed by the cause and not the reverse. It can be seen that for τ larger than t (cause before effect) the function $\Theta(t - \tau)$ is 0. The advantage of introducing the function $\Theta(t - \tau)$ is that it allows to extend the limits of the integral of (4.21) to infinity.

⁷This expression is also valid for a generic operator $O(t)$ where we have: $\langle O(t) \rangle = \int_{-\infty}^{\infty} -\frac{i}{\hbar} \langle [O_H(t - \tau), O] \rangle V(\tau) d\tau$.

$$\begin{pmatrix} \mu_x(\omega) \\ \mu_y(\omega) \\ \mu_z(\omega) \end{pmatrix} = \begin{pmatrix} \alpha_{xx}(\omega) & \alpha_{xy}(\omega) & \alpha_{xz}(\omega) \\ \alpha_{yx}(\omega) & \alpha_{yy}(\omega) & \alpha_{yz}(\omega) \\ \alpha_{zx}(\omega) & \alpha_{zy}(\omega) & \alpha_{zz}(\omega) \end{pmatrix} \begin{pmatrix} E_x(\omega) \\ E_y(\omega) \\ E_z(\omega) \end{pmatrix} \quad (4.25)$$

By diagonalizing the α matrix, we obtain three eigenvectors that indicate the direction of the principal axes of polarizability (v_1 , v_2 , and v_3). This makes it possible to determine the direction of maximum polarizability corresponding to the axis having the largest associated eigenvalue. The average polarizability is defined as: $\bar{\alpha} = (\alpha_{v_1} + \alpha_{v_2} + \alpha_{v_3})/3$, where α_{v_1} is the polarizability along v_1 and thus for the other two terms.

The imaginary part of the average polarizability $\bar{\alpha}$ represents a measurable quantity related with the photoabsorption cross section [50]:

$$\sigma(\omega) = \frac{4\pi\omega}{c} \Im(\bar{\alpha}), \quad (4.26)$$

where c is the speed of light.

4.4 Initial Perturbation

In order to make the density matrix evolve in time, it is necessary to apply an initial perturbation to the system. This perturbation moves the system from its initial ground state. The new state is no longer an eigenstate of the Hamiltonian, and thereafter, it evolves along a trajectory described by the integration of (4.17) [45].

The perturbation enters directly into the Hamiltonian of the system as an additional time-dependent matrix, i.e.:

$$H(t) = H_0 + V(t). \quad (4.27)$$

As a consequence, the electrons *feel* the influence of an external potential $V(t)$ and respond to it according to the time-dependent Schrödinger equation. The Hamiltonian constructed in (4.27) is quite general and describes the situation of atoms, molecules, and solids under the action of, for example, a time-dependent electric field [51].

The shape and duration of the perturbation depends on the phenomenon to be simulated. For example, if some information about electronic excitations of the system is needed, a perturbation in the shape of a Dirac delta must be used, in order to excite all the system frequencies [26]. It is also possible to reproduce the effect of an oscillating electric field generated by the effect of a laser [51] over an irradiated system.

The most useful ways to induce a perturbation V for studying plasmon dynamics are the following: the pulse-type perturbation, which excites all the system frequencies; the step-type perturbation, used to suddenly apply an external electric field;

and the laser-type perturbation, used to apply an oscillating field so as to represent an electromagnetic wave.

In the case of using an orthogonal basis to represent the electronic structure of the system (orthogonal TB), the effect of the perturbation $V(t)$ is nothing but an on-site energy shift. As a consequence, $V(t)$ will have a diagonal representation $f(t)$, where $f_i(t)$ is the variation of the *site energy* of the i -th orbital. For a general nonorthogonal case (with nonzero interorbital overlap), we have:

$$H = H_0 + \frac{1}{2}(Sf + fS), \quad (4.28)$$

where $S_{\mu,\nu} = \langle \mu | \nu \rangle$, is the overlap matrix. Equation (4.28) is reduced to (4.27) for $S = I$, where I is the identity operator.

The most natural way to perturb the electronic structure of a system is by the action of an electric or magnetic field. For the case of homogeneous electric fields, it is known from classic electrostatics that the potential at the site i is calculated as: $V_i = -e\mathbf{F} \cdot \mathbf{r}_i$. This suggests that if the electric field is uniform throughout the system for each time coordinate, that is, $\mathbf{F}(\mathbf{r}_i, t) = \mathbf{F}(\mathbf{r}_j, t)$ for every coordinate \mathbf{r}_i and \mathbf{r}_j , (4.27) can be rewritten as:

$$\hat{H}(t) = \hat{H}_0 - e\mathbf{E}(t)\hat{r} = \hat{H}_0 + \mathbf{E}(t)\hat{\mu} \quad (4.29)$$

The latter is known as the dipole approximation and comes from considering that the system is too small to perceive changes in the electric field on the spatial coordinates [1].

4.5 Absorption Spectra

In this section, we will describe the method used to obtain the absorption spectrum for both molecular and metal nanoclusters systems. First, the ground state of the system is found by using the most appropriate model to represent the electronic structure. Then we perform a quantum dynamical simulation preceded by the application of an initial perturbation that excites all frequencies of the system (see Sect. 4.4). The coupling with the external field of the initial perturbation is included in the Hamiltonian via the dipole approximation, as shown in (4.29). Both pulse and step perturbations can be used for this purpose.

From the time evolution of the density matrix, we can obtain the evolution of the dipole moment, which is the expectation value needed to determine the polarizability. The duration of the simulation is regulated based on the following two considerations: on the one hand, the size of the system to deal with, which depends mainly on available computational power, and on the other hand, the frequency range of interest. For the latter, if the information required is at low frequency, long

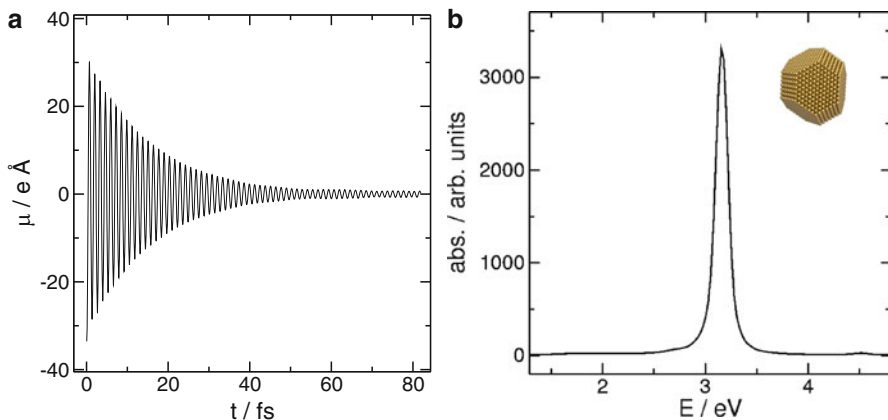


Fig. 4.4 (a) Dipole moment as a function of time for a truncated octahedron of 4,033 Au atoms following the application of an initial perturbation in a shape of a step. (b) Absorption spectrum. Here, abscissa axis is in eV. $x(\text{nm}) = \frac{1239.84}{x(\text{eV})}$

times should be simulated with a large integration step. If the information needed is at high frequency, short times should be simulated with a small integration step. The longer the simulation time and the smaller the integration step used, the better the resolution of the peaks of the absorption spectrum.

Once the dynamics are obtained, a numerical Fourier transformation of $\mu(t)$ is performed. From (4.23) we can solve for the frequency-dependent polarizability, the imaginary part of which is proportional to the absorption spectrum [26]. The latter is nothing but the deconvolution of the applied initial perturbation:

$$\alpha(\omega) = \frac{\mu(\omega)}{E(\omega)}. \quad (4.30)$$

Function $E(\omega)$ is obtained from the analytical Fourier transforms of $E(t)$ which, in the case of the pulse and step, are $E(\omega) = E_0$ and $E(\omega) = \frac{iE_0}{\omega}$, respectively. We will show some results found with this procedure in Sects. 4.6 and 4.7 for spectral calculation purposes.

In Figs. 4.4 and 4.5, we can see the dipole moment evolution, together with the absorption spectra for a metallic cluster and an organic molecule, respectively, after the application of a pulse-shaped perturbation. For the organic molecule, we can observe that the dipole moment does not decay in time; this is not the case of metallic clusters for which the plasmon excitation has an intrinsic electronic lifetime. For the case of a molecular system, it is necessary to include an external artificial width by multiplying $\mu(t)$ by an exponential decaying function before performing the Fourier transform in order to compensate for the finite length of the dynamics.

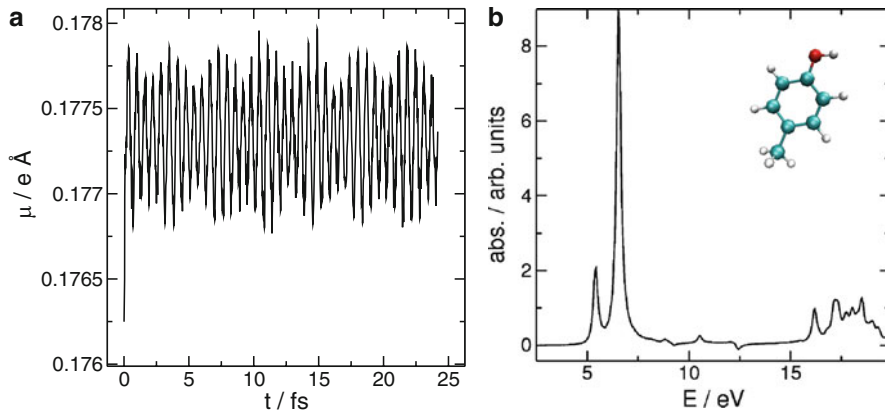


Fig. 4.5 (a) Dipole moment as a function of time for a p-cresol molecule following the application of an initial perturbation in a shape of a step. (b) Absorption spectrum

4.6 Some Results Concerning Metal Nanoclusters

The scope of this section is to study the absorption spectra of metallic NPs by considering the influence of shape, size, and surface condition with atomistic detail. The latter may be the first step towards a sharp understanding of the atomic level structure influence on optical properties. In this section, we will show some results concerning the absorption spectra of NPs of different size and shapes as those shown in Fig. 4.6. We have studied spheres and spheroids varying the aspect ratio, as well as polyhedral solids.

The electronic structure of these gold NPs is represented through a TB Hamiltonian as the one detailed in [32, 40, 41] for which the main characteristics were explained in Sect. 4.2.3. Spectral features are determined by the procedure previously described in Sect. 4.5. In this case, a step-shaped perturbation is used with $E_0 = 0.01 \text{ eV/\AA}$. The average polarizability over the three main axes is used for all the results shown here. Absorption spectra were verified to be independent of the applied initial field intensity, meaning that simulations were performed under the linear response regime for which the frequency-dependent polarizability can be extracted from the dipole moment by using (4.30).

4.6.1 Estimation of Au^+ Permittivity

It was found that, by using the vacuum dielectric constant ($\epsilon_r = 1$) for the Coulombic expression in (4.16), the plasmon resonance energies are too high when compared with experimental data. Instead of $\epsilon_r = 1$, a value of $\epsilon_r = 6.96$ was used to obtain the results that are shown below. This ϵ_r value was fitted to obtain the plasmon

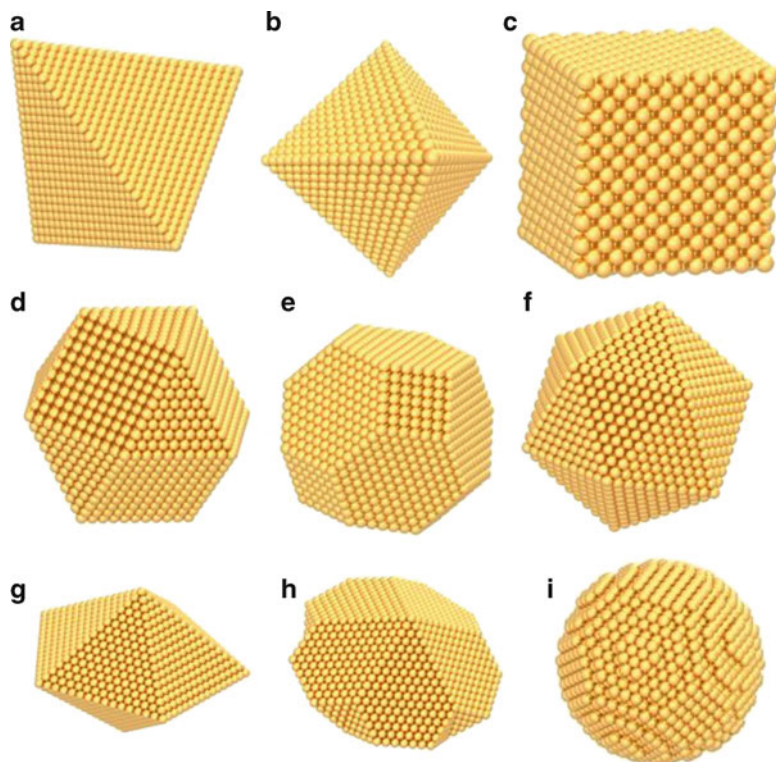


Fig. 4.6 Different kinds of aggregates: (a) tetrahedron, (b) octahedron, (c) cube, (d) cuboctahedron, (e) truncated octahedron, (f) icosahedron, (g) decahedron, (h) Marks decahedron, (i) sphere. Reprinted with permission from *J. Chem. Phys.* **129**, 034710 (2008). Copyright (2008) American Chemical Society

resonance energy of a large radius particle as the one predicted by Mie theory for a Au sphere in the dipole approximation [4, 11]. Within the TB model, ϵ_r can be interpreted as the relative permittivity of the medium given by the cores, including d electrons. The fitted value corresponds to a polarizability that is in between the one of a Au^+ ion and a neutral Au atom and therefore within a reasonable physical range. Electrons of the d shell in metallic atoms make s electrons to *see* an ϵ_r value higher than the one for vacuum due to their intrinsic polarizability. The vacuum permittivity, expressed in units of eV, fs, and Å, is 5.52×10^{-3} . Moreover, according to the classical Clausius–Mossotti equation [3], we have that the local polarizability as a function of the permittivity for a metallic sphere is:

$$\alpha = \frac{3}{4\pi\rho_N} \left(\frac{\epsilon - 1}{\epsilon + 2} \right) \quad (4.31)$$

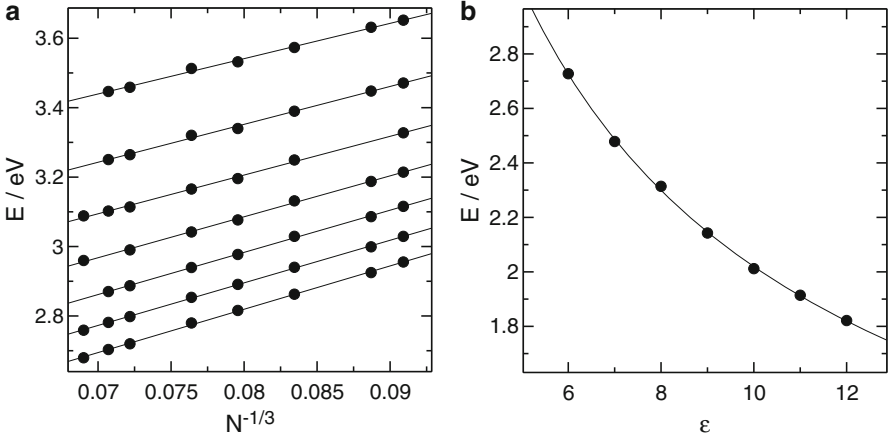


Fig. 4.7 (a) Variation of E vs. $N^{-1/3}$ for each ϵ value. In this case, the larger the ϵ value, the lower the intercepts of the linear fits obtained in the graphs. We have chosen seven ϵ values between 6 and 12, and they correspond to the points shown in graph b. (b) Variation of the intercept of the graphs of (a) with varying ϵ values. Points in the graph are fitted to the function: $E(\epsilon) = 8.056\epsilon^{(-0.66)} + 0.256$

where the density ρ_N calculated for the case of Au fcc with a lattice parameter of 4.08 \AA is 0.005889 1/cm^3 . Finally, formula (4.31) is rewritten as:

$$\alpha = 4.053829 \left(\frac{\epsilon - 1}{\epsilon + 2} \right) \quad (4.32)$$

This expression allows to obtain an approximation to the local polarizability in function of the ϵ value. In this equation, α units are expressed in \AA^3 .

Numerical calculations determining the energy of the plasmon resonance for different values of ϵ were performed for a series of metallic spheres with N ranging from 1,400 to 3,000 in order to obtain an extrapolated value when N tends to infinity (E_∞)(very large clusters). In Fig. 4.7a, we show graphs of E vs. $N^{-1/3}$ for different ϵ values varied from 6 to 12.

By plotting the intercepts as a function of ϵ , we obtain a power law that allows for interpolation and further determination of the ϵ value for a plasmon resonance energy of 2.5 eV (see Fig. 4.7b). The latter value is the one predicted by classic electrodynamics for a large Au sphere within the quasi-static approximation [11]. From this procedure, the ϵ value that produces the correct plasmon energy for a large sphere is 6.9628 .⁸ Using this value in (4.32) gives a local polarizability of about 2.7 \AA^3 . Polarizability values calculated from DFT are of 1.4 \AA^3 for Au^+ and 5.48 \AA^3 for Au. Free electrons in plasmonic excitations would be *feeling* an intermediate polarizability.

⁸The same procedure was carried out for Ag yielding a value of $\epsilon = 3.015$.

If we think of a *Drude* model, in which the metal is nothing but a *sea of electrons* embedding positively charge cores, it would be reasonable to think of electrons seeing an electric permittivity induced only by Au^+ cations. From a less naive point of view, we could think that if Au^+ cations are embedded in *s* electrons, they get *softer* making the medium more polarizable. Our model should respond with a local polarizability generated by *d* electrons partially perturbed by the presence of *s* electrons. The latter situation can be found in a Hg^+ ion, which yields a DFT polarizability value of 3.4 \AA^3 , which is closer to the value obtained for our method.

4.6.2 Spectral Features

As it can be seen from Fig. 4.2, the decay time of the plasmon oscillation is of several femtoseconds. The density matrix dynamics, obtained from the Liouville equation integration, does not have any external dissipation mechanism (there is no electron–phonon interaction); however, the induced dipole moment evolution finally decays. This decay mechanism can be explained from both quantum and classical considerations. The plasmon excitation can be viewed as a superposition of many excitations which are oscillating phase coherently at early stages. As the dynamics proceeds, the excitations begin to dephase from each other and the oscillation is destroyed (Fig. 4.8). This phenomenon is known as Landau damping. As it will be seen later, each physical defect at cluster surface acts as a *scatterer*, which deviates the collective motion of electrons and finally destroys the dipole signal.

The decay time is much shorter than characteristic atom vibrations and, in consequence, plasmon decay proceeds as if the atoms of the nuclear lattice were frozen at their equilibrium positions. Absorption spectra for different cluster families were calculated, reaching sizes up to 4,000 atoms (4-nm diameter) [52].

4.6.3 Spherical Particles

Spheres are constructed by cutting a spherical piece of metal centered at an atom of an fcc lattice. The absorption spectra for spherical clusters show a Lorentz-like functional shape, for which the maximum absorption peak reveals a linear dependence with respect to the surface to volume ratio. This relation is given by $N^{-1/3}$, N being the number of atoms in the particle (see Fig. 4.9).

The peak shifts bathochromically with increasing cluster size, which is in good agreement with experimental observations [1]. Peak intensity grows with the volume of the solid, as it is expected for an increasing polarizability given by the linear growth in the number of electrons with increasing particle size.

The perfectly defined Lorentzian shape of the absorption peak is attributed to the lack of surface defects on the sphere surface. Among these accidents, we can mention the vertex and edges always presented in polyhedral particles, which

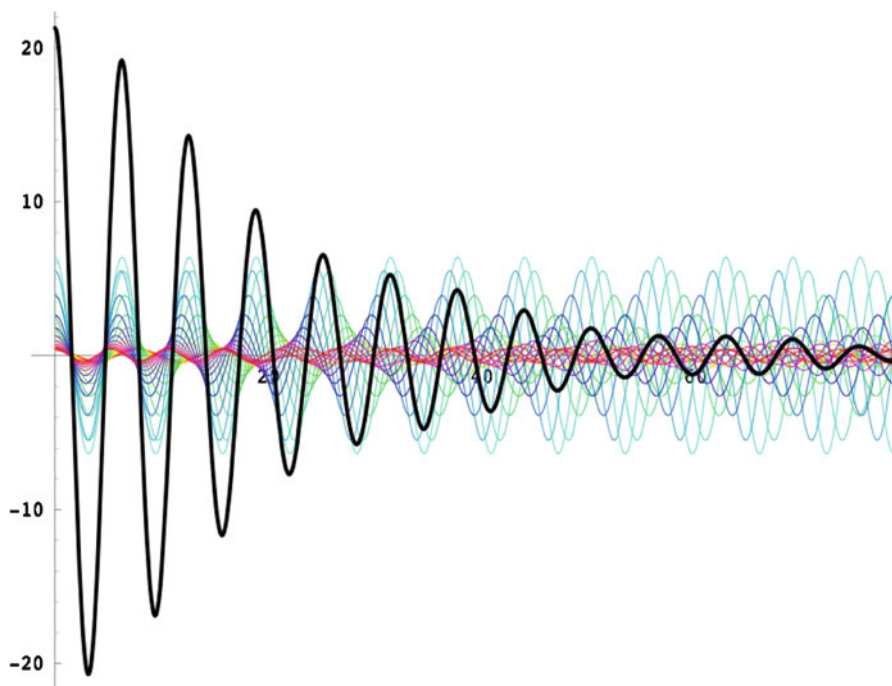


Fig. 4.8 Picture depicting the dephasing of initially in phase waves with different Lorentzian distributed frequencies as a function of time

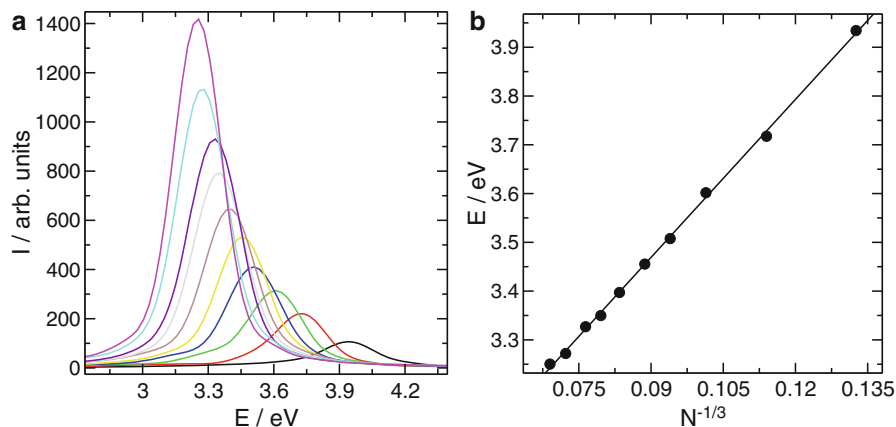
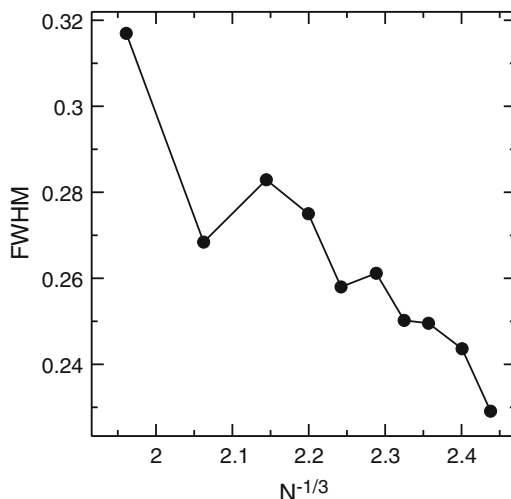


Fig. 4.9 (a) Absorption spectra for a series of spherical aggregates going from 429 to 3,043 atoms. The plasmon peak red shifts with the increase of size. Peak intensity grows linearly with particle size. (b) Plasmon resonance energy as a function of the inverse cube root of the atom number together with its corresponding linear fits. Reprinted with permission from *J. Chem. Phys.* **129**, 034710 (2008). Copyright (2008) American Chemical Society

Fig. 4.10 Full width at half maximum as a function of the inverse of the cube root of the atom numbers in the particle. Reprinted with permission from *J. Chem. Phys.* **129**, 034710 (2008). Copyright (2008) American Chemical Society



are main contributing factors to plasmon dephasing. Full width at half maximum (FWHM) possesses an oscillatory dependence with respect to the surface to volume ratio, but the average follows a linear trend, as it can be seen in Fig. 4.10 [53].

4.6.4 Prolates and Oblate Spheroids

With the aspect ratio⁹ being different to one, particles become spheroid-like shaped [54,55]. We have studied prolates and oblates cut from an fcc atom-centered lattice. These shapes possess two principal axes that are equal and a third which is different from the others. In the case of prolates, the third axis is longer than the others and the inverse is true for the case of oblates. All aggregates considered here have in average 2,000 atoms, and the spectra were calculated by only changing the aspect ratio from oblate to prolate.

Spectra observed in Fig. 4.11 are bimodal, and each peak can be associated to the collective oscillation of the electrons in the direction of some principal axis of the particle (two of them are equal in length, so, only two peaks are observed). The resonance at larger frequencies corresponds to shorter axes. The peak intensity grows with the length of the corresponding axis, in a similar fashion to the trends observed with respect to the behavior of the intensity with the particle size, shown before. The peak energy, however, becomes smaller with increasing the length of the corresponding axis. The relative intensities of the two resonances are the result

⁹The aspect ratio of a molecular system, in general, is defined by Bonnett et al. as the ratio between the longest and shortest vertex of a regular parallelepiped of minimum volume, that can host the whole molecular system [54].

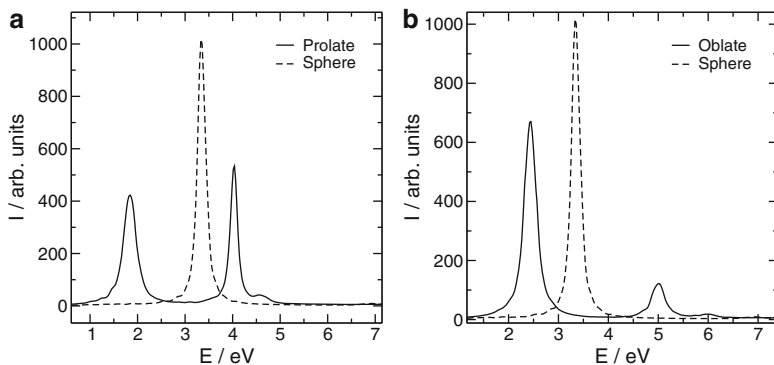


Fig. 4.11 Spectra for the case of prolates (**a**) and oblate (**b**) spheroids with aspect ratios of 3 and 1/3, respectively. Spectra for the case of spheres with the same quantity of atoms are included as a reference. Both peaks correspond to z and x (or y) polarization directions. The x -axis is different from the others. Reprinted with permission from *J. Chem. Phys.* **129**, 034710 (2008). Copyright (2008) American Chemical Society

of different causes: the increase in intensities when the axis of polarization becomes larger and the degeneration produced by the fact that two axes are of equal length. Oblate spheroids show a higher intensity for the peak that correspond to smaller energies, because this resonance is degenerate and corresponds to longer axes. In the case of prolates, the effect produced by enlarging the mayor axis eventually overcomes the degeneracy, and dominates the spectra.

Figure 4.12 shows how the two resonances corresponding to different axis are split as the z/x differs from one. Lines in plots correspond to a fit with a power law in the shape of $ax^\alpha + b$. There is a quantitative agreement between the energy shifts as a function of the aspect ratio shown here and those from Lance Kelly et al. in [2]. In the oblate case, the lowest resonance peak corresponds to a polarization along x and y axes. For the extreme cases, the lowest energy peak dominates the spectra because those of higher energy, corresponding to shortest axes, eventually become negligible in intensity. Particles in the shape of disks or needles have only one resonance energy peak. In both cases, there is a very small axis which does not contribute to the absorption spectra. Average absorption spectra¹⁰ are shifted bathochromically (to lower energies or longer wavelengths) when the aspect ratio is increased and a monotonic relation exists between the observed shifts and the structural deviation respect to a sphere define as $\zeta = \frac{b-a}{a}$, where b and a corresponds to the mayor and minor axes, respectively [55], as can be seen in Fig. 4.12b. As shown below, the same is observed for polyhedral particles. In comparison with the energy shift caused by the particle size, a change in shape has a greater influence in determining the plasmon energy. Researchers engaged to tune the resonance frequency must be focused in controlling particle shape.

¹⁰This is a weighted average by the peak intensity.

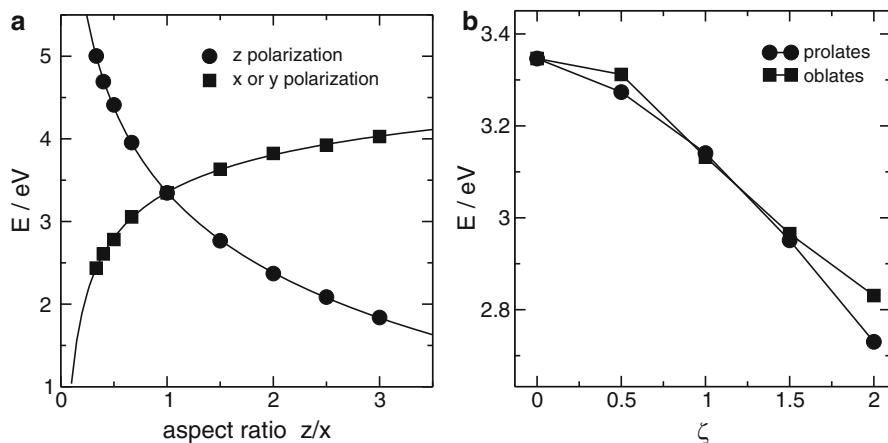


Fig. 4.12 (a) Peak position as a function of the aspect ratio for a series of spheroids for polarizations z and x directed. Oblates correspond to aspect ratios smaller than one, and the inverse is true for prolates. (b) Weighted average of the peak position as a function of the spherical deviation. Reprinted with permission from J. Chem. Phys. **129**, 034710 (2008). Copyright (2008) American Chemical Society

4.6.5 Surface Condition

The surface condition of a particular cluster is an important factor in determining both the energy and the lifetime of the plasmon excitation. For determining the influence of the surface condition, spectra for a series of spherical particles with different concentration of surface defects were calculated. These defects were introduced as adsorbed atoms with a low coverage degree. Spheres of about 2,000 atoms were used. In Fig. 4.13, the influence of the concentration of surface defects both in the absorption energy and width is observed.

The strong influence of adsorbates on the plasmon resonance features, particularly in the lifetimes of the excitation, can be explained by the fact that the plasmon is a surface phenomenon. Accidents present on the cluster surface act as a source of *friction* for electrons, making the energy of the oscillation to decrease and the coherence to be drastically attenuated. The term friction has been used in a loose sense since no dissipation mechanism was introduced in the model. Electrons dispersed by defects slow down their speed component in the direction of the plasmon propagation, producing a net decrease of the collective velocity and in consequence, decreasing the resonance energy. This result shows qualitatively that any attempt to predict the plasmonic lifetime must take into account the details of the surface condition. In Sect. 4.7, we will see that even the presence of stabilizers adsorbed onto the particle surface has a great influence on plasmon lifetime. The phenomenon described above cannot be studied with classical electrodynamic methods; this is a strong advantage of using the tools introduced here.

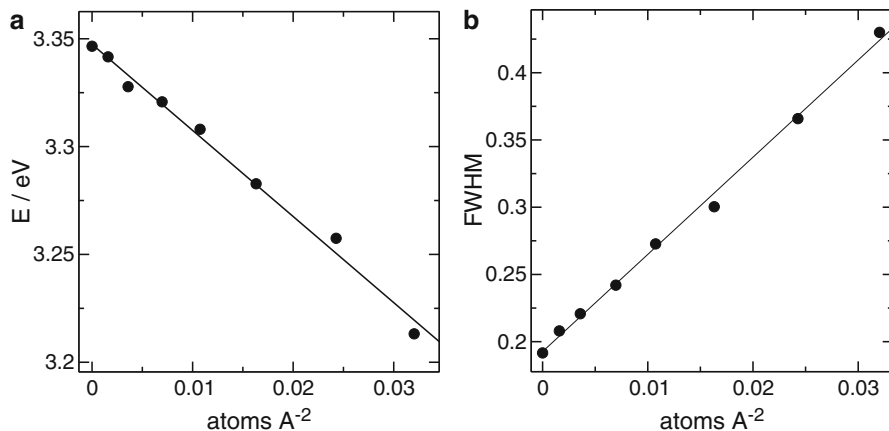


Fig. 4.13 Peak position (a) and peak width (b) as a function of surface defect concentration. The surface defects were introduced by adding adatoms onto a 2,000-atom particle surface. Reprinted with permission from *J. Chem. Phys.* **129**, 034710 (2008). Copyright (2008) American Chemical Society

4.6.6 Polyhedral Particles

There is clear experimental evidence that NPs have a well-defined symmetry and that are not necessarily an amorphous conglomerate of atoms [56, 57]. Some aggregates are characterized by having a quantized growth, where only certain number of atoms are permitted for each size for a given shape [58]. In this way, it is possible to obtain a whole family of clusters (with different sizes but equal shapes) in an iterative way by adding atoms onto the surface of one of them to obtain the subsequent in size. In this way, for example, for cuboctahedral clusters¹¹ (see Fig. 4.14), we have that $N = \frac{1}{3}(10n^3 + 15n^2 + 11n + 3)$, where N is the number of atoms of the cluster and n is the order occupied within the family [59].

Polyhedral families studied here are: tetrahedra, octahedra, cubes, cuboctahedra, truncated octahedra, icosahedra, decahedra and Marks decahedra (see Fig. 4.6). As an example, in Fig. 4.15, we show spectra for a series of cuboctahedra, and Marks decahedra. Cuboctahedra show only one absorption peak, which is red shifted with increasing the particle size. This peak is not perfectly Lorentzian as was the case for spherical particles. Marks decahedra, on the other hand, show bimodal spectra similar to those observed for an oblate spheroid. In general, we observe that the shape of the peak is deviated from a purely Lorentzian shape for every studied geometry and it depends on the shape of the cluster; however, it is always possible to identify a principal absorption peak. This principal absorption peak was used for further characterizations.

¹¹This function also applies for icosahedral particles.

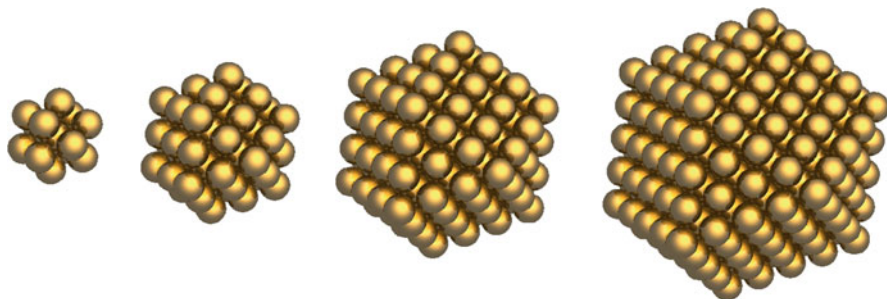


Fig. 4.14 First members of cuboctahedral family. From *left to right*: $N = 13, 55, 147,$ and 309

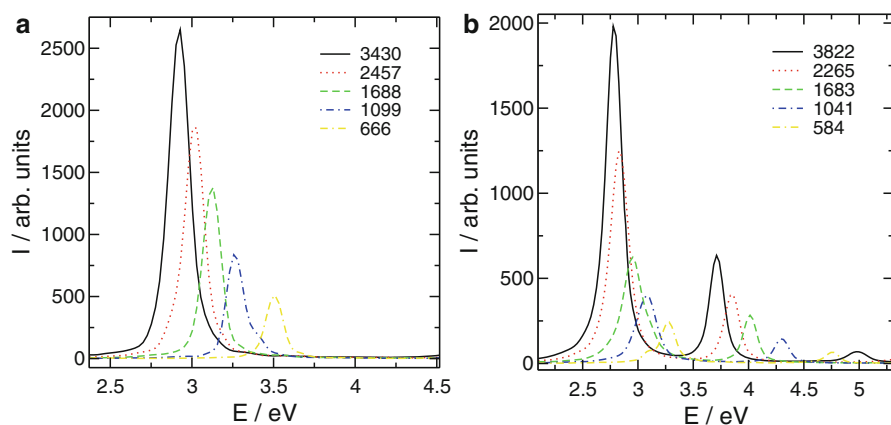


Fig. 4.15 Spectra for a series of cuboctahedra (a) and Marks decahedra (b). As in the case of spheres, the main resonance peak is shifted towards smaller energies when the atom number is increased, while the peak intensity is increased due to increasing volume. Reprinted with permission from *J. Chem. Phys.* **129**, 034710 (2008). Copyright (2008) American Chemical Society

In Fig. 4.17 we have plotted the principal peak energy as a function of the inverse of the cube root of the atom numbers subtracting the extrapolation to infinite size (E_∞) with the purpose of emphasizing slope differences. The linear dependence and the surface to volume ratio observed for spheres are also verified in polyhedral particles. The slope of the linear dependence is smaller for spherical particles, while for less spherical particles, this dependence is more pronounced. The dependence of the frequency with surface to volume ratio has been observed experimentally and theoretically and predicted from other models [1]. The novel aspect presented here is the dependence of the slope with the shape. The spherical deviation can be characterized from a single parameter ζ as follows:

$$\zeta = \frac{r_b - r_a}{r_a} \quad (4.33)$$

Fig. 4.16 2D scheme that shows a polyhedral figure with two circumferences of radii r_a and r_b that represent the contained and containing sphere, respectively

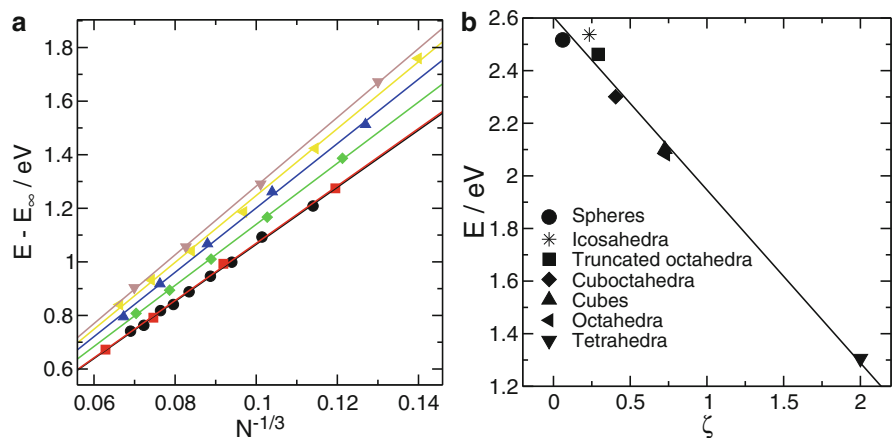
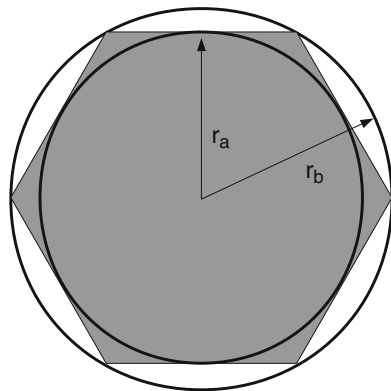


Fig. 4.17 (a) $E - E_\infty$ as a function of the inverse of the cube root of the atom number in the particle, for a series of polyhedral particles. Here, E is the peak resonance energy. (b) $E(E_\infty)$ as a function of the spherical deviation. Cubes and octahedra have the same value of ζ . The same symbols were used for representing the points corresponding to each cluster shape in both graphs. Reprinted with permission from J. Chem. Phys. **129**, 034710 (2008). Copyright (2008) American Chemical Society

where r_a and r_b are the internal and external radii of the convex solid, corresponding to the radius of the contained sphere and the containing sphere, respectively (see Fig. 4.16). This quantity is the same as the one defined for spheroids where $b = r_b$ and $a = r_a$.

Slopes of the linear fits in Fig. 4.17 increase in a monotonous way with ζ , being the sphere-shaped cluster the one showing the smaller dependence of the resonance energy with the solid size.

The resonance energy extrapolated to infinite size (E_∞) shows a linear dependence with the spherical deviation as shown in Fig. 4.17b. Due to the linear relation with the surface to volume ratio, a change in size for large particles produces a small

change in the plasmon resonance energy which is principally determined by the particle shape. Less spherical particles will have resonances at lower energies with the sphere as an upper bound. As it was emphasized for the case of the spheroids, shape control provides a more sensitive mechanism than size to control the energy of the main absorption peak. In the case of very small particles ($N < 1,000$), small changes in the number of atoms will produce big changes in the surface to volume ratio, making the size to be an important factor only for small particles. Values of E_{∞} cover an energy range of about 1 eV, showing that the shape can have a determining influence in the plasmon resonance energy.

The fact that the sphere is an upper bound for the resonance energy and that this energy is lower for less spherical particles can be understood by analogy with spheroids. For the spheroid case, the resonance energy corresponding to the longest polarization axis is shifted to lower energies with increasing aspect ratio. In the case of polyhedral particles, radii of the contained and containing spheres are different and, the same as in the spheroids case, there are two characteristic lengths. Whenever, one of the characteristic lengths grows at the expense of the other, the resonance energy is therefore shifted to lower values. On top of this, surface structure, such as edges act in a similar way to the case of adsorbates, lowering the resonance energy.

Excitation lifetimes characterized through the peak width of the principal resonance are hard to define for non-spherical aggregates because in these cases peaks are not purely Lorentzian. No systematic trends of the width with the shape or size were found. Excitation lifetimes of polyhedral particles possess an oscillatory dependence with particle size and show significant differences between different shapes. Hence, it is not possible to identify a systematic trend within the data. This results can be explained in terms of the presence of surface imperfections. Surface defects such as edges lower the resonance energy and the lifetime. Different shapes have different surface structures, and this is the reason of the lack of a universal characterization of the resonance lifetime. It is important to note that the latter is a quantum effect produced by electron scattering within the cluster surface.

In the above analysis, Marks decahedra, decahedra, and icosahedra were not included. The reason for this is that these solids do not follow the trends found for regular polyhedra. In the case of decahedra, most of the spectral features can be interpreted as the one of an oblate spheroid. Values of peak energy, however, differ due to the presence of polyhedral faces. Icosahedra are a special case of regular solids as they are formed by the aggregation of 20 tetrahedra with fcc internal structure (the same is true for decahedra) [60] but do not have fcc structure as a whole. Significant deviations of the trends were observed for icosahedra with respect to regular solids; however, the slope and the intercept of the linear fit in function of $N^{-1/3}$ are similar to those found for the tetrahedra and spheres, respectively.

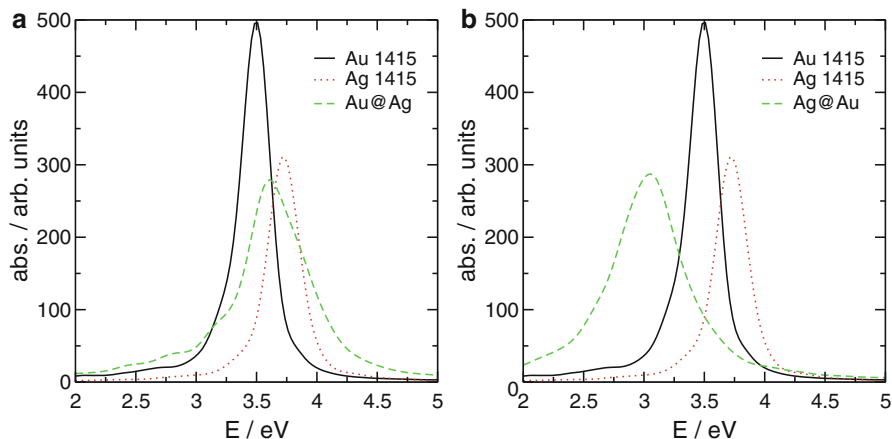


Fig. 4.18 (a) Spectrum of a 1,415 Au atoms icosahedral NP with a monolayer of Ag (Au@Ag), together with the corresponding spectra for Au and Ag NPs of the same size and shape of the core as a reference. (b) Spectrum of a 1,415 Ag atoms icosahedral NP with a monolayer of Au (Ag@Au), together with the corresponding spectra for Au and Ag NPs of the same size and shape of the core as a reference

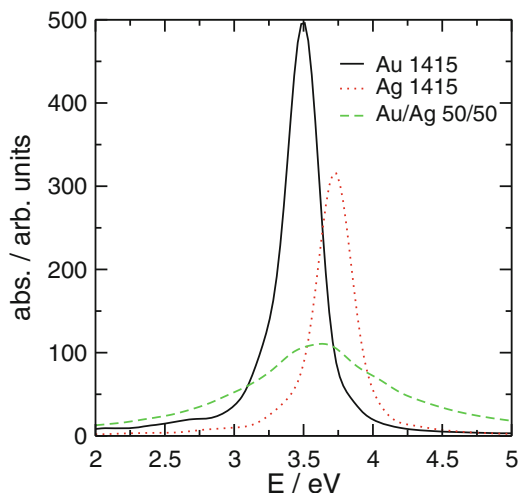
4.6.7 Bimetallic Nanoparticles

Bimetallic nanoparticles, in particular, *core@shell* NPs, possess very special optical properties. Great variations of their spectral features are obtained with their structural and composition modification. The relative modification of the radii of the *core* and the *shell* produces spectral shifting in very wide ranges that are sometimes even as important as the morphological modification in a one-component NP [61]. Both shifting and spectral width are hard to predict with classical methods, in particular when sizes are smaller than 3-nm diameter [62], where quantum effects are more important.

This section deals with the calculation of the spectral features of a series of bimetallic NP from dynamical simulations of the plasmonic excitation using the TB model explained in (4.2.3). In this case, we have employed the TB parameters of silver detailed in [39] with $\epsilon_r = 3.015$ following the procedure described in (4.6.1). For calculating the matrix elements between orbitals of different metals, we have utilized the average of the parameters for the semiempirical TB description of both metals. This is a rough way of having an approximation of the polarizability of the alloy. A difference in orbital energy sites was introduced according to the difference in metal work functions.

In Fig. 4.18a, we show the result of adding a monolayer of Ag onto a 1,415 icosahedral Au particle (Au@Ag). We observe that the incorporation of even a single layer of Ag makes the resonance energy shift to higher values, resembling the situation found for Ag with respect to spectral features [62]. In this case, two effects are in opposite directions. These are the bathochromic shift due to the increase in

Fig. 4.19 (a) Spectra of an icosahedral 1,415 NP composed by 50% N/N of Ag and Au atoms randomly distributed



size that occurs when adding a new metal layer and the hypsochromic shift due to the addition of a metal with a higher resonance energy. Adding an Ag extra layer does not cause further changes in the peak energy because the effect of size becomes dominant.

For the case of the addition of Au onto an icosahedral particle of Ag (Ag@Au), a synergistic effect is observed between the size effect and the metal shell effect. Surprisingly, the plasmon resonance peak appears at energies even lower than the ones obtained for the naked Au NP.

The same procedure was applied to a 50/50 Au/Ag NP alloy. Atoms in this NPs were randomly distributed so as to have a good mix of both types of atoms. According to these calculations, the result of having an alloy is the formation of a very broad resonance peak with an energy that remains between the energy of the two metals separately. This behavior cannot be predicted from classical models as in these calculations a dielectric function for the alloy must be introduced regardless of atomistic detail. The latter makes the peaks of the alloys to be narrower than real ones [63] due to the neglect of internal electron scattering in the disordered system which has a very strong effect on plasmon dephasing (see Fig. 4.19).

4.6.8 Some Conclusions

The plasmon oscillation decay and its fundamental frequency are determined by the cluster shape and size. The frequency of this fundamental oscillation shows a linear dependence with the surface to volume ratio for particles of the same size, for which their slopes depend in a monotonous way with the sphericity. For similar-sized particles, those that are less spherical possess lower resonance energies.

Shape has an important influence in the absorption spectra of a metallic particle; thus, significant control of the resonance energy can be exerted by controlling the atomistic shape of the cluster or its aspect ratio (sphericity).

Surface condition also has a great influence over spectral features, principally, on the excitation lifetime. Surface defects act as scatterers lowering electron speed due to friction (in the sense explained above) increasing plasmon dephasing. The complex surface structure of the polyhedral cluster makes the spectra to strongly deviate from the purely Lorentzian shape observed for spherical particles .

As a main conclusion of this section, we have the fact that the shape of the cluster at the atomic level has a great influence on the absorption spectra of metal NPs. Because of the latter, new models that could include the atomistic details and provide quantitative information as well, are needed in order to help to the fabrication of materials with desired optical properties.

4.7 Effect of Molecular Adsorbates

In this section, we will address a brief study, the main characteristics of the influence of molecular adsorbates (capping agent) on the absorption spectra of spherical NPs by means of a simple TB model. We have built a special TB model to include the coupling to the cluster surface of a general molecule represented by a two level system characterized by its HOMO-LUMO gap. We will see how the presence of adsorbates can shift and widen the plasmon resonance peaks. For strong couplings, a splitting of the main resonance peak is achieved and the two resultant resonances are localized in different regions of the capped nanoparticle.

4.7.1 Introduction

It is well known from experimental results that for preparing NP colloidal suspensions, it is necessary to employ some stabilizing agent to prevent the aggregation and further precipitation [64, 65]. Stability of the colloidal suspension can be achieved by several ways: a chemical one, where stabilizing agents are bonded to the particle with strong covalent bonds through functional groups such as $-SH$, $-SeH$, or $-COOH$; an electrostatic mechanism which works by controlling the width of the electric double layer that surrounds the particle, thus preventing coalescence; and finally, a steric method which employs organic polymers to prevent particle aggregation [66]. The adsorbates can also be used as a way to identify specific compounds, as vectors to deliver therapeutic agents or to bind the NPs to a potential electronic circuit [67, 68]. Adsorbates that have acid-base character can also make the plasmon resonance to be sensitive to the pH of the solvent [69].

It is well known that the surrounding medium influences the optical properties of NPs suspensions [1]. In a simple description, the surrounding medium acts as

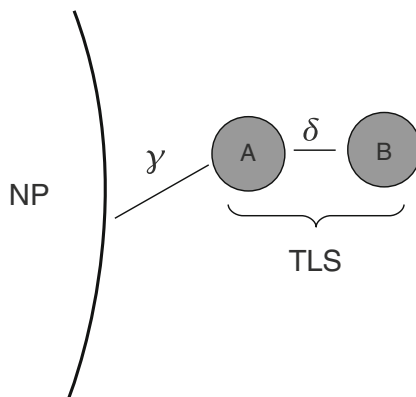
a dielectric material, decreasing the plasmon excitation energy by means of the stabilizing surface charge oscillations on NPs [3]. The effects on the excitation lifetimes are more difficult to describe using simple electrostatic models that cannot capture the effect of adsorbates on the underlying electron dynamics [71]. Mie theory allows to calculate the plasmon resonance energy by including the effect of adsorbates as a dielectric shell [72]; however, the influence of the adsorbates is also important at low coverages (less than a monolayer) where both a dielectric function and a suitable layer width are difficult to define. An atomistic description that takes into account the electronic structure of the particle and the adsorbates as a whole is mandatory in the description of the entire problem. Some of the effects produced by the adsorbates on the resonance width can be qualitatively described with the decaying mechanism through the chemical interface, commonly known as *chemical interface damping* [73, 74]. According to this model, electrons being part of the plasmon excitation can tunnel in or out from the states of the adsorbate that are near the Fermi level, losing coherence in this process and thus, making the plasmon excitation lifetime to decrease. This image has been useful to qualitatively describe the effects produced by the surrounding medium to the width of the plasmon excitation [18, 73, 75]. Adsorbates can also transfer charges to the particle modifying the plasmon resonance energy and its width [74, 76]. Although this scheme is attractive from the physical point of view because (through modifications of the classical theory) it can successfully describe some effects that surface modification produces [76], it cannot explain the complex interaction between molecules and plasmon excitations. The latter is due to the fact that a great energy resonance shift can be produced when the molecular excitations of adsorbates are in resonance with plasmon excitation [21], yielding a splitting of the peak into two distinct resonances [77]. This scheme cannot describe the relationship between the decay and the chemical nature of adsorbates [78]. In Sect. 4.6 we have shown that the presence of simple adsorbates as metallic atoms of the same nature of those of the cluster possesses a significant effect both in the energy and resonance width [52] that are linear with the surface concentration.

In sections below, we will show how the TB model used in Sect. 4.6 can be adapted to describe the adsorbed molecule modeled within a simple molecular adsorbate. With this strategy, it is possible to describe the effects of adsorbates on spectral features with special attention on its dependence with the molecules HOMO-LUMO difference and the coupling strength to the particle surface.

4.7.2 Model and Simulation Method

The electronic structure of the system is represented by using the same TB model as the one of Sect. 4.6. The electronic structure of adsorbates is presented via a two-level system Hamiltonian (TLS) characterized by two parameters, the coupling with surface (NP), given by parameter γ and the coupling between sites of TLS characterized by the δ matrix element (Fig. 4.20). The atom of the adsorbed

Fig. 4.20 Schematic representation of the system Hamiltonian: $\delta = H_{ij}$ (atom–atom). $\gamma = H_{ij}$ (atom–metal). Reprinted with permission from [70]



molecule which is near the metallic surface (atom A) is located in an fcc site of the particle lattice chosen at random and the second atom (atom B) is located so as to make the diatomic molecular axis perpendicular to the particle surface. The Hubbard parameter U for the adsorbate was chosen to be 10 eV, which is approximately what corresponds for C atoms. The ground state density matrix evolves after applying an electric field as the case for bare metallic clusters (see Sect. 4.6). The absorption spectra is calculated in the same way that for the case of Sect. 4.6.

4.7.3 Some Results

All the calculations shown below were performed for a spherical particle of 1,985 Au atoms of approximately 20 Å radius extracted from an fcc Au lattice. Four hundred and eighty (24%) of the NP atoms are located at the surface. Seventy-five diatomic molecules were adsorbed randomly covering approximately 17% of the cluster surface (Fig. 4.21). Calculations were repeated for a coverage of 36%, and results for this calculation will be compared when significant differences from the low coverage situation are encountered. This cluster possess a plasmon resonance frequency at 370 nm with a peak width of 27.62 nm when no adsorbates are present at the surface. Figures 4.22 and 4.23 show contour maps of the peak width and resonance energy for a range of values of parameters γ and δ . This parameters are related with the surface interaction and the HOMO-LUMO gap of the diatomic molecule, respectively, as shown in Fig. 4.21. Plasmon resonance energy is influenced by the presence of molecular adsorbates which produce resonances to shift their frequency, widening peaks (making changes on plasmon lifetimes) and splitting the main resonance into two different excitations depending on the value of the aforementioned parameters.

Parameter δ can be easily related with the HOMO-LUMO difference of the adsorbate, if the molecule behaves ideally as a TLS $|\delta| \approx (LUMO - HOMO)/2$.

Fig. 4.21 Nanoparticle of 1,985 Au atoms, partially recovered with 75 diatomic adsorbates. Reprinted with permission from [70]

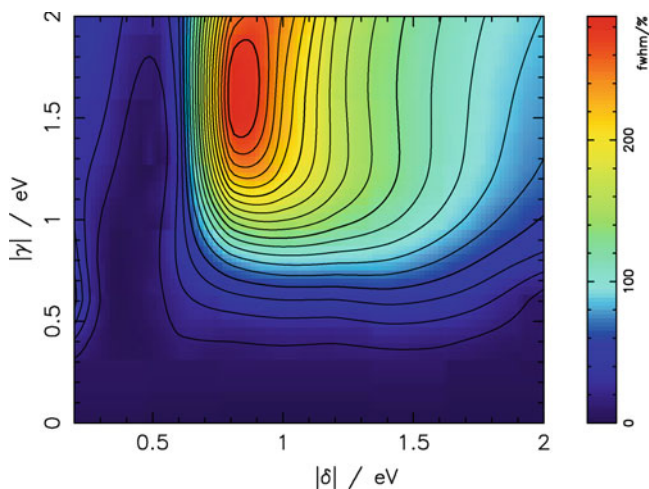
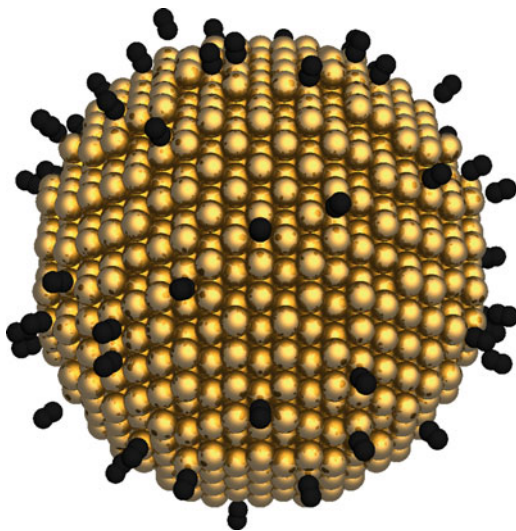


Fig. 4.22 Peak width dependence on Hamiltonian parameters which describes the interaction with surface (γ) and the coupling between sites of the TLS in the diatomic molecule (δ). Changes are expressed as a percentage of the resonance width for the bare sphere. Values shown in this map correspond to the plasmon excitation even for the case of two resonances. Reprinted with permission from [70]

We will derive an expression that can be useful to establish the strength of the adsorption in terms of the coupling to surface parameters. We know from [32] that the energy for a TB model can be calculated as $E = \text{Tr}(\rho H) + V_N^{\text{eff}}$. Where ρ is the system density matrix, H is the Hamiltonian matrix and V_N^{eff} is the effective potential that accounts for Coulombic interactions and repulsion between internal

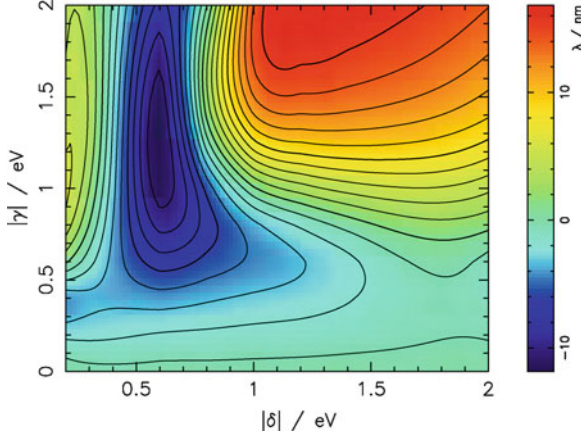


Fig. 4.23 Resonance energy dependence on Hamiltonian parameters: The interaction with surface (γ) and the coupling between sites of the TLS in the diatomic molecule (δ). Contours correspond to the difference between the resonance wavelength for the capped sphere and the bare sphere expressed in nm. Values shown in this map correspond to plasmon excitation even for the case of two resonances. Reprinted with permission from [70]

cores. The force is then calculated by taking the derivative of the latter expression: $F(r) = -\frac{\partial \text{Tr}(\rho H)}{\partial r} - \frac{\partial V_N}{\partial r}$. If we integrate the work differential from the equilibrium distance r_0 to infinity, we obtain the value for the adsorption energy:

$$|E_{\text{ads}}(r)| = \left| \int_{r_0}^{\infty} \left(\frac{\partial \text{Tr}(\rho H)}{\partial r} + \frac{\partial V_N}{\partial r} \right) dr \right|$$

If conditions are favorable for adsorption and both systems are neutral, the above expression can be rewritten as:

$$|E_{\text{ads}}(r)| = \left| \int_{r_0}^{\infty} \frac{\partial \text{Tr}(\rho H)}{\partial r} dr \right| - \left| \int_{r_0}^{\infty} \frac{\partial V_N}{\partial r} dr \right|$$

Therefore,

$$|E_{\text{ads}}(r)| \leq \left| \int_{r_0}^{\infty} \frac{\partial \text{Tr}(\rho H)}{\partial r} dr \right|$$

By rewriting $\text{Tr}(\rho H)$ for the sites involved in the interaction, i.e., atom A and the atom which is closer to the surface (S), we have:

$$|E_{\text{ads}}(r)| \leq \left| \int_{r_0}^{\infty} 4\Re(\rho_{A,S}) \frac{\partial \gamma}{\partial r} dr \right| \leq \left| \int_{r_0}^{\infty} 4 \frac{1}{2} \frac{\partial \gamma}{\partial r} dr \right|$$

Finally, solving the integral, the last expression yields:

$$|E_{\text{ads}}| \leq |2\gamma| \quad (4.34)$$

We can consider this in order to have an upper bound for the adsorption energy. If we think of thiol molecules adsorbed onto a Au surface (having an absorption energy $E_{\text{ads}} \approx -2$ eV) as a reference, the formula above tells us that the γ parameter to be used to model a S–Au bond is larger in absolute value than 1.0 eV. This means that if the γ parameter is smaller than 1 eV, we will be representing molecules with weaker bonds than for the case of S–Au. This divides the map of Figs. 4.23 and 4.22 into two regions, of weak and strong adsorption zones if $|\gamma|$ values are lower or higher than 1.0 eV, respectively.

For the weak adsorption regime, corresponding to $|\gamma|$ values lower than 1 eV, the effect of the adsorbates in the plasmon resonance features influences mainly the width of the resonance that can be even twice the value for the particle without adsorbates. The resonance frequency, however, is shifted to higher values not exceeding 10 nm. The effect of the resonance width can be interpreted by the fact that adsorbates act as surface impurities that interfere with the electron path, decreasing coherence and increasing Landau damping [52], an effect that is present even at lower values of the coupling parameter $|\gamma|$. The *scattering* effect is originated from both charge transfer entering molecular adsorbates and changes of the local electronic structure of the surface atoms, due to changes in bond orders and the local density of states at energies near the Fermi level. Within this regime which corresponds roughly to the lower third of the $\gamma - \delta$ plane of Figs. 4.22 and 4.23, the total dependence on δ is small and monotonic; this is not the case for strong surface couplings, where there is a great influence of adsorbates on spectral characteristics. When coupling to the surface (given by parameter γ) is increased, scattering effects are more pronounced, causing a monotonic increase of the resonance width, which depends in a non-monotonic manner with the inter-site adsorbate coupling (given by δ).

The effect of decoherence caused by adsorbates is reflected on the values of peak width. High values of peak width imply stronger decoherence. This decoherence effect has a maximum efficiency at a value of γ of about -1.6 eV at 17% coverage regardless of inter-site coupling. For higher coverage, the maximum effect on the width of the resonance occurs at lower values of $|\gamma|$ (-1.1 eV at 36% coverage). The effect on the resonance energy is much less pronounced than in the case of the resonance width. For the case we have explored, changes in plasmonic frequency are usually smaller than a few nm; however, the width of the resonance can be increased by more than 200%. As in the case of the resonance width, for the weak absorption regime, adsorbates produce a small effect in the resonance energy. When $|\gamma|$ is higher than 1 eV, however, both bathochromic and hypsochromic shifts are observed, depending on the value of the parameter δ . For small HOMO-LUMO gap values, adsorbates cause a blue shift, a tendency which is reverted when the HOMO-LUMO gap is increased. The results of this study are qualitatively similar to those found in literature for environments or adsorbates that interact weakly with the metal surface such as SO_2 [73] or tetraalkylammonium [78, 79] and those for particles prepared by the citrate method [75]. In these cases, the adsorbates cause a significant broadening of the resonance. Quantitative comparisons however, are difficult to accomplish due to the lack of structural details reported on the

experimental systems. The experimental results show that thiol-coated NPs have a significant widening in their resonances, which can be large to the point of making the resonance undetectable [78, 79].

This is consistent with our findings for large values of $|\delta|$ (corresponding to a large HOMO-LUMO difference such as for alkane chains) and large coupling with surface via S–Au bonds (corresponding to large $|\gamma|$ values). For strong couplings to the surface and small enough values of $|\delta|$, the molecular resonance approaches the plasmon energy from above (from higher energy). When the two excitations are close in energy, the plasmon resonance peak widens significantly and shifts to the blue. The latter corresponds to the region of the maximum (red area) in Fig. 4.22. Similar effects to those described here have been observed experimentally for molecular excitations in resonance with the plasmon excitations on coated silver nanoparticles [21]. When adsorbates excitations become lower than the plasmon resonance energy, the peak is split into two different excitations. This effect can be observed in detail in Fig. 4.24 where we have plotted the absorption spectra for fixed values of $\gamma = -1.4$ eV and a series of δ values that goes from -0.2 to -1.2 eV. In Figs. 4.23 and 4.22, only the spectral features for the highest energy (purely plasmonic) resonance are plotted.

The nature of these two excitations can be determined by applying an electric field oscillating in tune with each one of these resonances. Figure 4.25a shows the dipole moment of the particle as a function of time when illuminating at plasmon resonance energy (for $\delta = -0.2$ eV and $\gamma = -2.0$ eV). As shown in the figure, the electronic system reaches a quasi-steady state after 20 fs of constant illumination due to the finite lifetime of the plasmon excitation. Figure 4.25b shows the standard deviation of atomic charges with respect to their values in the ground state caused by excitations, as a function of the distance to the NP center.

The lower energy excitation is localized on the adsorbates. Through a detailed analysis of charge distribution, we can see that the lowest energy resonance corresponds to an in-phase oscillation of molecular dipoles located on opposite sides of the NP. Molecular excitations are coupled through the NP via the conduction electrons. Therefore, the coupling of molecular excitations only occurs when the energy of these excitations is smaller than the plasmon energy. These new excitations resemble a dimer exciton, in which the oscillations of molecular dipole moments are coupled in phase. However, in this case, the electrostatic coupling between the molecular dipoles occurs via the NP, allowing significant coupling through long distances. The cross section of these exciton oscillation is orders of magnitude higher than that of molecular adsorbates, due to the great distance involved. Similar couplings of molecular excitons have been observed experimentally [80].

4.7.4 Conclusions

As a first step in developing a better understanding of the effect of surface chemistry on the spectral characteristics of metal nanoparticles, we have built a simple model

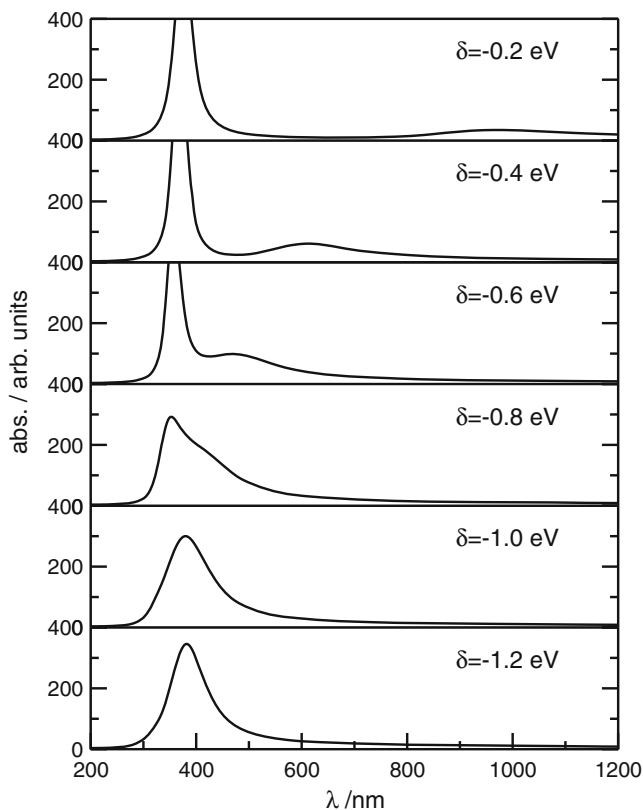
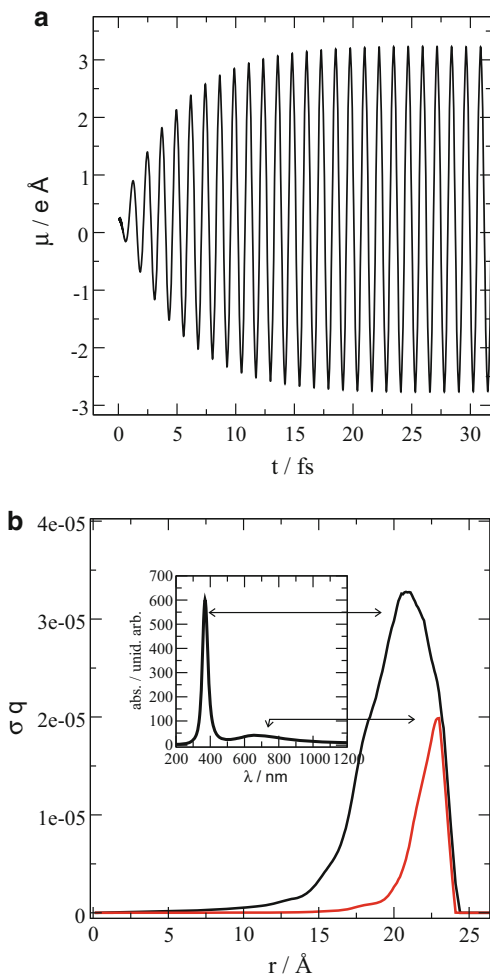


Fig. 4.24 Splitting of the plasmon resonance as a function of the diatomic coupling parameter δ for a fixed value of the coupling to the particle of $\gamma = -1.4$ eV. The highest energy peak corresponds to pure plasmon excitation, while the lowest excitation is located on the adsorbates layer. Reprinted with permission from [70]

that can encompass a wide range of adsorbates and couplings to the surface. The adsorbates can produce peak broadening without altering the resonance energy even if couplings with surface are weak. When increasing the coupling with the NP surface, the peak width becomes larger, although the molecular excitation energies differ from the SPR. When the molecular excitation is in resonance with the plasmon excitation, the effects are most important. Adsorbates with excitations below the SPR excitation can produce new spectral features due to exciton coupling between adsorbates, mediated by the metal NP. Due to its extreme simplicity, this model can only give qualitative descriptions of possible trends. A more precise understanding of the complexity of the phenomena promoted by surface adsorbates on plasmon resonance requires a more sophisticated model of the electronic structure of the system, such as those provided by DFTB [36].

Fig. 4.25 (a) Variation of the dipole moment with time for a NP as a response to a laser field in resonance with plasmonic excitation. (b) Standard deviation of atomic charges caused by the excitation energies corresponding to the two absorption peaks in the inset. Here, $\delta = -0.2$ eV and $\gamma = -2.0$ eV. Reprinted with permission from [70]



4.8 Near Field Properties

4.8.1 Introduction

In this section, near-field properties arising from surface plasmon dynamics are described by means of quantum dynamics simulations using the method detailed above [81]. Unlike far-field properties, studied by means of the evolution of the dipole moment, in this section, we will study local details of the magnitude and distribution of the electrodynamic field generated around a metallic particle during plasmon excitation. Influence of shape and surface condition on the surface electric field distribution will be addressed. It also highlights the importance of the effects of

the tunneling current in diminishing the enhancement in the inter-particle region of metal dimers. Finally, we make a direct comparison with calculations from classic electrodynamics. The importance of atomistic structure in the shape of *hot spots* (zones with high enhancement values) is also highlighted as well as and the solution of the border problems found in classical methods [82]. The importance of the study of field enhancement induced by plasmon dynamics is related with Raman spectroscopy. Raman effect is a low-intensity scattering process where a small part of incident photons are dispersed with a different energy when interacting with molecules [83]. The fraction of light that is involved in this process is very low. Only one of each 10^7 photons is scattered in this manner. When molecules are adsorbed on a metallic surface, the intensity of the Raman signal is amplified by a factor of about 6 orders of magnitude [84]. This phenomenon was first observed in 1974 on 6G Rhodamine molecules adsorbed on a silver electrode [85]. The spectroscopic technique derived from this phenomenon is known as SERS [86]. Employing this analytic technique enables the observation of Raman spectra of very dilute solutions and allows, for example, single-molecule detection [87,88]. Despite the advances in the experimental application of this phenomenon, there is no clear explanation of the mechanism that governs the amplification of the Raman signal that gives rise to SERS [82]; however, it has been suggested that two contributions are responsible for this effect: one of chemical origin, given by the changes in the polarizability of the adsorbed molecule [84] upon adsorption, and another purely electromagnetic (or physical), given by the local electric field in which the molecule is immersed when adsorbed. The physical mechanism is explained by the fact that electric fields generated by the plasmons of the irradiated metal surface cause the adsorbed species to “feel” an oscillating electric field of higher intensity, resulting into a Raman signal amplification [82]. In some experiments, this phenomenon depends strongly in the molecule involved [84]. Therefore, the differences of the chemical species must be taken into account and represent the chemical contribution of the SERS phenomenon. This chemical effect is less intense than the physical one, but both contribute to Raman amplification. Classical calculations have shown that using some particular arrangements of metal nanoclusters, the square of the local field is amplified in seven orders of magnitude without taking into account the chemical contribution [89]. The intensity and energy of the plasmon oscillation in metal nanoclusters strongly depend on the shape of the aggregate and surface condition [2,52]; therefore, these structural aspects must be taken into account when studying near-field properties. Stronger enhancement effects are observed when the metallic surface is more complex [90].

Most of the actual calculations of local electric field enhancements values are exploratory and qualitative. There are no systematic studies showing general field trends up to now; nevertheless, Perassi et al. have developed a technique to characterize the enhancement based on the variation of the trapped volume (VTV) [91]. Since the electric field distribution around an illuminated particle is highly inhomogeneous, it is not possible to assign a single value to the enhancement in order to characterize a particular nanocluster.

Here, we show results of the influence of the shape and surface structure of a silver metallic aggregate on the amplification of the local electric field in order to determine which are the most important structural aspects that influence its amplification and compare them with classical results. We show that in some cases remarkable differences exist between classical and quantum near-field distribution results.

In this section, we focus on the influence of shape and surface structure of metallic aggregate on the amplification of the local electric field from a quantum point of view, with perspectives to a further systematization of the results and the possibility of studying smaller systems. As far as we know, this is the first direct quantum and classical comparison of electric field enhancement in metal clusters conformed by hundred of atoms.

4.8.2 *Electronic Structure*

In this section, we will show results from calculations employing two types of TB methods. One of this is the one used in Sect. 4.6 for determining optical properties of metal nanoparticles. The other Hamiltonian we have used is that of DFTB explained in Sect. 4.2.2 that allows for a more detailed description of the electronic structure since it includes all valence electrons. For the first simple TB description, we have studied gold nanostructures larger than 500 atoms, while for the case of DFTB, we employ Ag NPs smaller than 500 atoms, due to the higher computational cost of this method. Employing Au or Ag particles produces different result for the electric field values, but this does not affect the general conclusions drawn from the results.

4.8.3 *Simulation Method*

The density matrix of the particle ground state in the presence of a static electric field is determined first. At $t > t_0$, the field is removed in a short period of time, and the particle, which is no longer in a stationary state, evolves in time following the Liouville equation, which can be numerically integrated as explained in Sect. 4.3. Electric field used for the initial applied perturbation is the same as those for Sect. 4.6, which are small enough ($E_0 = 0.01 \text{ eV}/\text{\AA}$) to ensure the system to be in the linear response regime. The induced electric field due to the electronic motion as a function of time can be calculated in any point of the space (over the NP surface) from the following equation:

$$\mathbf{E}(\mathbf{r}, t) = \sum_i \frac{q_i(t)}{4\pi\epsilon^0\epsilon} \frac{(\mathbf{r}_i - \mathbf{r})}{\|\mathbf{r}_i - \mathbf{r}\|^3} \quad (4.35)$$

$q_i(t)$ being the charge on atomic site i . Applying a Fourier transform, we can obtain the value of \mathbf{E} in the frequency domain. This is:

$$\mathbf{E}(\mathbf{r}, \omega) = \text{Ft}(\mathbf{E}(\mathbf{r}, t)). \quad (4.36)$$

The quantity of interest is: $|\mathbf{E}|^2(\mathbf{r}, \omega) = \mathbf{E}(\mathbf{r}, \omega) \cdot \mathbf{E}^*(\mathbf{r}, \omega)$. Finally, the electric field enhancement factor is calculated as:

$$\Gamma = \frac{|\mathbf{E}|^2(\mathbf{r}, \omega)}{|\mathbf{E}_{step}|^2(\mathbf{r}, \omega)} \quad (4.37)$$

where $\mathbf{E}_{step}(\mathbf{r}, t) = (1 - \Theta(t))\mathbf{E}^0$ is the applied initial perturbation. From now on, the term *field* will be used to refer to the field enhancement factor Γ .

The field enhancement factor can be calculated at any point at or above the particle surface. For the case of the present work, the field was calculated over a transversal section that passes through the center of mass of the NP. This has been used for both TB representations explained above. The problem associated with the utilization of the semiempirical TB is that it implies the introduction of a dielectric constant for the d electrons in the metal. If a charge is located at a point near the metallic surface, the electric field generated by the atoms immediately close to the surface must be calculated taking into account the vacuum permittivity. On the other hand, the electric field generated by the atoms inside the metal must be calculated taking into account the permittivity imposed by the internal electrons of the metal.

Here, we make the following approximation: if a charge is located near the surface, the field generated by metallic atoms would have to be calculated taking into account the relative permittivity, different from vacuum. For the Au atoms in the semiempirical TB method, we have employed $\epsilon_r = 6.98$ (see Sect. 4.6). This approximation is valid whenever the charge is close to the metallic surface. For points located far from the metallic surface, there exists artificial shielding coming from considering the presence of the metal instead of vacuum, making fields to be less intense that they would have to be. Within the DFTB method, since d electrons are taken explicitly into account, we do not have a different permittivity inside the metal, and the latter problem does not exist, which gives more reliable values of local field enhancement but restricts the analysis to small clusters.

The field enhancement factor is a function of the incident photon frequency. Moreover, the enhancement factor is a function of both the position and frequency $\Gamma = \Gamma(\omega, r)$. For all cases analyzed here, the enhancement factor was calculated at the frequency of maximum enhancement. In Fig. 4.26, we observe that plots of $\Gamma(\omega)$ coincide in shape and position with the absorption spectra of the nanocluster, but a slight frequency shift can be seen. In this case, the frequency of the maximum of $\Gamma(\omega)$ is slightly higher than the frequency of plasmon oscillation. This difference is mainly due to the fact that the field enhancement factor is a local property, and this is not true for the dipole moment.

Fig. 4.26 Comparison between plots for the enhancement Γ as a function of frequency together with the imaginary part of the polarizability α for a sphere of 1,985 gold atoms in the area of maximum enhancement

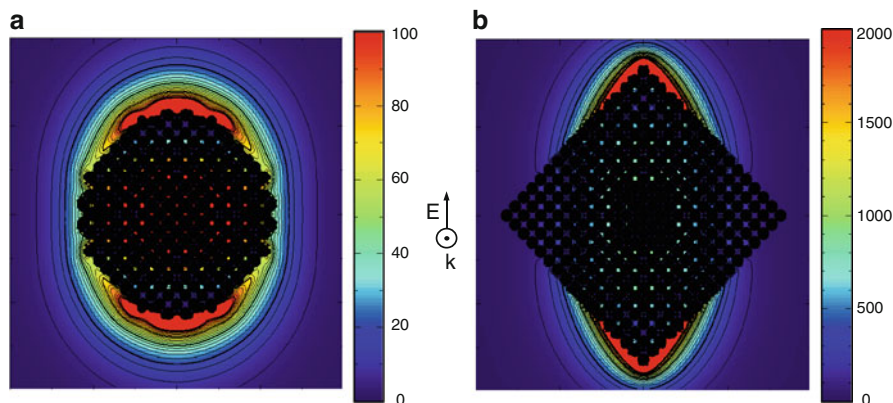
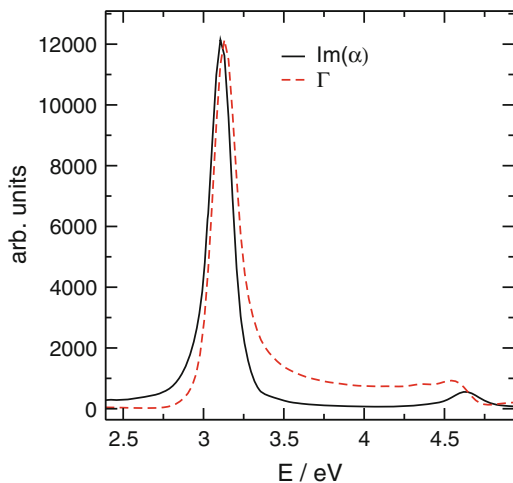


Fig. 4.27 (a) Cross section for a 3,043 Au atoms sphere that shows Γ distribution. (b) Cross section for a 3,281 Au atoms octahedra. We observe that the electric field is accumulated at the corners. The square section of both figures have $80.0 \times 80.0 \text{ \AA}^2$

4.8.4 Semiempirical TB

Employing the TB semiempirical model, we have calculated the local field enhancement for a transversal section of two metallic NPs of different shapes (sphere and octahedra). In Fig. 4.27 a, the distribution of the field enhancement factor over a transversal NP section can be seen. We see that the highest field intensity is distributed in a dipolar fashion, aligned with the polarization vector \mathbf{E} .

Black circles observed in Fig. 4.27 have 1.4 \AA radius, (approximately the van der Waals radii for Au and Ag) and serve to identify the position of the Au atoms in the

cross section. The electric field inside the metal is not taken into account as it has very high values compared to the external ones and it is not physically relevant.

In the case of the octahedral NP, electric fields are accumulated at the tips. In this case, the amplification factor is an order of magnitude larger than in the case of the sphere. This result looks familiar, because it is well known from electrostatics that charges are concentrated at the surface; thus, intensifying the electric field. If the surface has defects like edges or sharp tips, the electric field enhancement will be higher. The latter is nothing but the phenomenon known as electrostatic tip effect, discovered by Franklin in 1753, which states that the charge density increases when the convexity of the solid surface containing this charges is greater [92].

We have also performed some calculations on prolate and oblate spheroids. It was noted that if we have an oblate shape and the external field is applied along the minor axis direction, the generated field is distributed over a large area of low convexity, making fields lower. When the shape is prolate and the polarization direction is along the major axis, the charge must be accumulated in a smaller area of high convexity resulting in a larger field enhancement.

One of the fundamental problems in the calculation of Γ factors is to delimit the metallic border. It is very difficult to determine where to locate the metal-vacuum delimitation in a classical method since for the classical calculations the amplification factor increases as we approach the surface and, therefore, it is not possible to assign a value to characterize the near-field properties of a given NP [82]. As mentioned in the introduction, Perassi et al. solved this problem by informing the volume contained in a field isosurface¹² [91]. In the case of the calculations shown here, it is observed that the assignment of atomic radius trivially solves this problem because a given metal is characterized by the maximum field that is situated beyond the atomic radius of the atoms of the metal surface.

In Fig. 4.28, we observe the local field dependence for the interparticle region in dimers formed by spherical NPs of 1,205 Au atoms. Both the polarization axis and the direction of plasmon-induced oscillation are collinear to the main axis that binds the particle. The first thing to stress is the magnitude of the emerging field that is a 100 times higher ($\Gamma = 10,000$) than the incident field, which agrees with the findings of [93].

When there is a current between the two plates of a capacitor, the emerging field inside, it is reduced [92]. By analogy with the short-circuited capacitor, it is natural to find that fields are smaller when the NPs are very close together (Fig. 4.29). This can be explained by the fact that when NPs are sufficiently close together, the matrix elements connecting orbitals from one to the another are not zero, and therefore, there is a charge transfer during plasmon oscillation. In the case of Fig. 4.28a, NPs are at a distance of first neighbors, which is equivalent to say that they are in a direct contact. Therefore, the electronic transfer is so intense that the enhancement is zero. The latter is consistent with the experimental results obtained by Novotny et al. in [94] and simulations performed by Northlander et al. employing TDDFT [93]

¹²The field isosurface is the surface for which we have a constant value for the amplification factor.

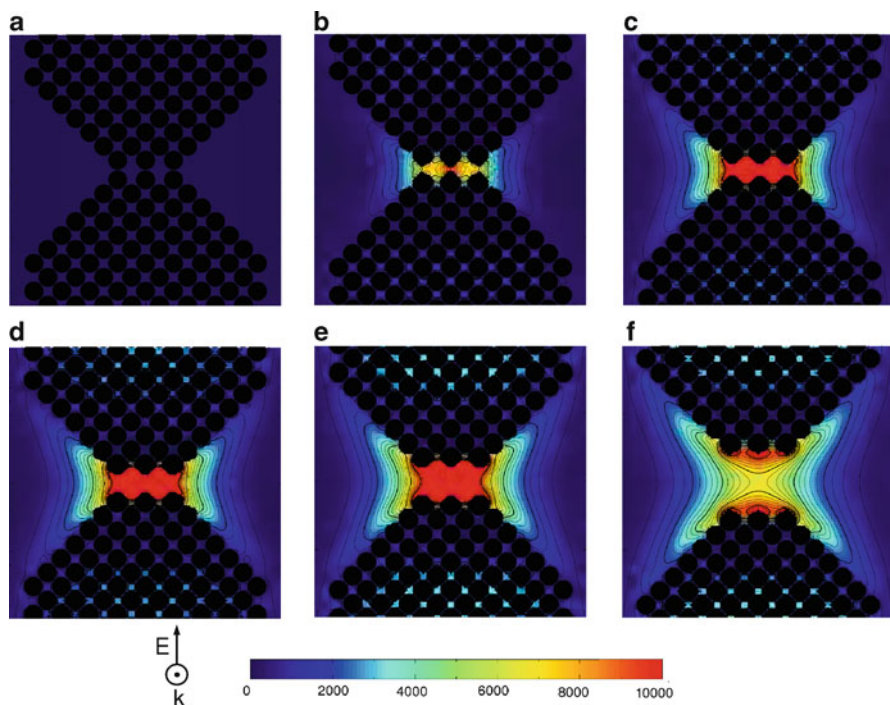
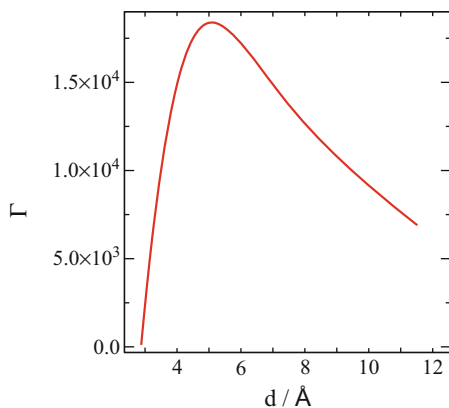


Fig. 4.28 Local field enhancement for a cross section in NP dimers of 1,205 Au atoms, with d (a), $1.5d$ (b), $2.0d$ (c), $2.5d$ (d), $3.0d$ (e), $3.5d$ (f), where d is the first neighbor distance that for the case of Au fcc is 2.88 \AA . The square of these figures has $40.0 \times 40.0 \text{ \AA}^2$

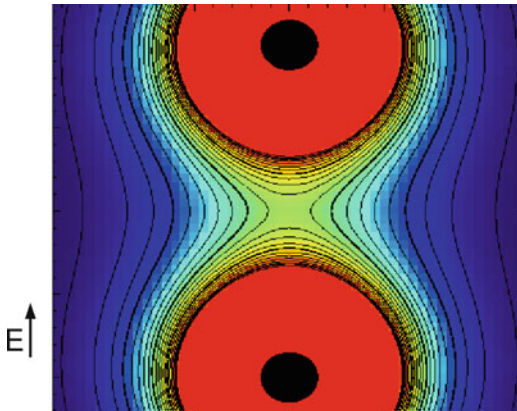
Fig. 4.29 Field enhancement factor as a function of the inter-particle distance for the case of the dimers of Fig. 4.28. A maximum at about 5.5 \AA inter-particle distance is observed



for jellium sphere dimers. The phenomenon of interparticle charge transfer not only affects near-field properties, but in general, all optical properties are affected [95].

On the other hand, at large distances, field enhancement also decays, but in this case, the decay is attributed to a purely Coulombic effect. Moreover, we observe that

Fig. 4.30 Contour plot for the function $E^2(x,y)$ for a point dipole. In this case, units are arbitrary



hot spot size increases considerably, indicating that the field that at shorter distances was concentrated in a very small region, is now spread over a larger area.

The lines of *isofield* have the same behavior as the one expected for the field emerging from the inter-site region of an electric dipole as it is shown in Fig. 4.30. When the aggregates are smaller, the situation differs from the electrostatic case as shown in Fig. 4.31.

The U parameter for the chosen TB Hamiltonian description, acts as a force that prevents charges from accumulating at atomic sites. This parameter accounts for the compressibility of electron gas and therefore can be used as a measure of it.

The electron gas compressibility influences the intensification of the electric field. In Fig. 4.32, we show the decay of Γ in the zone of maximum enhancement, and the point at which the field is calculated is separated from the border of the cluster. This suggests that the inertia of the moving charges forces them to compress at the end of the oscillation pathway. If the surface has sharp tips (areas of high convexity), the effect of charge compression coerces with the effect of the tip making large fields. If the above reasoning is correct and the electronic front wave has a certain *inertia*, we should expect much more intense fields for larger clusters. This behavior is depicted in Fig. 4.33.

4.8.5 DFTB Hamiltonian

Using this TB Hamiltonian, it is possible to have a more specific detail of the electronic structure of the system. We do not have the problem of whether or not to use a different permittivity because the effect of d electrons is explicitly taken into account in the Hamiltonian. The main disadvantage of using this Hamiltonian is that it only covers small systems with less than 500 atoms because of its higher computational cost. In this work, we have compared our quantum calculations with results arising from classic electrodynamics.

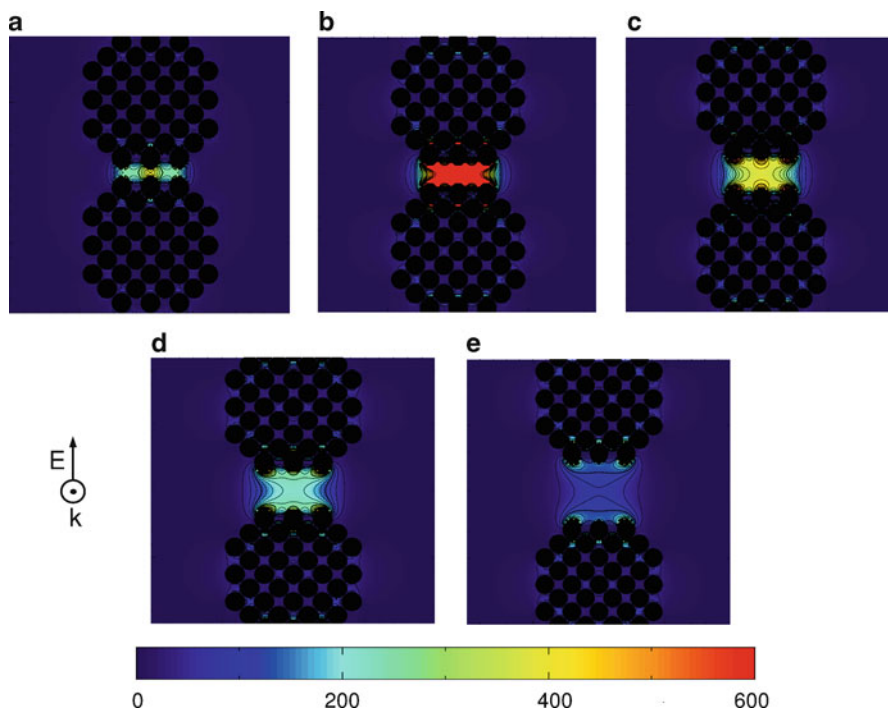


Fig. 4.31 Local field enhancement for a cross section in NP dimers formed by truncated octahedra of 201 Ag atoms, separated at $1.5d$ (a), $2.0d$ (b), $2.5d$ (c), $3.0d$ (d), $4.0d$ (e), where d is the first neighbor distance that for the case of Ag is 2.89 \AA . The square of these figures has $40.0 \times 40.0 \text{ \AA}^2$

Classical simulations were done by using the DDA method¹³ (*discrete dipole approximation*) because it is particularly efficient for small aggregates or isolated NPs embedded in an environment with different dielectric properties and can be applied to various shapes of metallic clusters. In this method, the object of interest is an array of N cubic polarizable volumes [9]. The optical resonance for this arrangement is determined in a self-consistent manner, solving the induced dipole moment in each volume element. The result of this procedure can be used to determine the far-field properties (extinction coefficient or dispersion) as well as near-field properties, like the electromagnetic field near an aggregate surface. It has the disadvantage that the value of field strength near the edge of the metal depends on the space discretization [96].

Figure 4.34 shows a comparison made on a 309 atoms cuboctahedron for the classical (a) and quantum mechanical method (b). Beyond the differences in the details of the field distribution, the overall distribution is very similar and

¹³These simulations were performed by E. Perassi and E. Coronado of the Physical Chemistry Department, Faculty of Chemistry, UNC, as part of a collaborative work.

Fig. 4.32 Comparison of two profiles of Γ as a function of the distance to the vertex of an 2,255 Au octahedra for two different values of parameter U

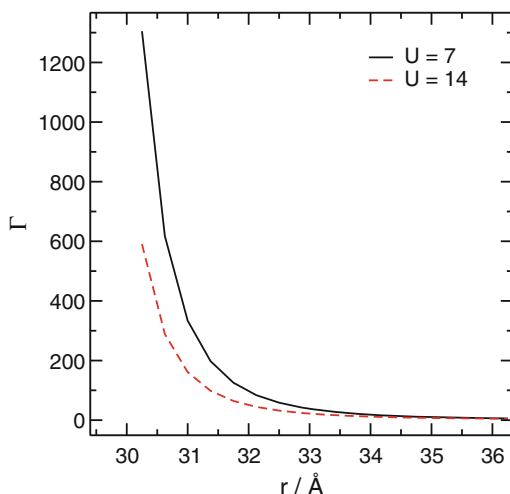
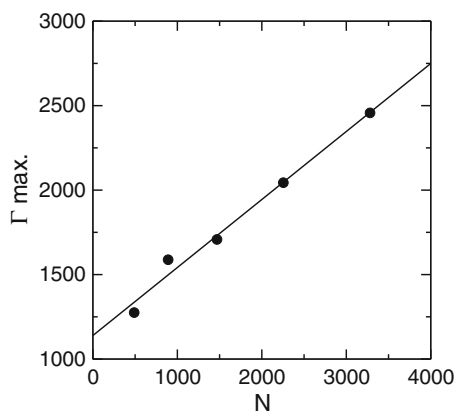


Fig. 4.33 Γ max values for different particle sizes. We have employed clusters in a shape of octahedra, and the Γ max value is calculated at 1.41 Å (Au atomic radii) from the last atom from the vertex pointing towards the polarization direction



magnitudes of the fields are approximately equal. We can also notice that the quantum calculation shows more detail at the atomistic level than the classical calculation. This is the case of the nodes that can be seen at the particle corners for the quantum case.

When the figure of the aggregate becomes more complex (i.e., it has tips), classical and quantum fields differ both in magnitude and distribution. The quantum calculation shows a drastic enhancement of the field at the end of the octahedron vertex in Fig. 4.35b, while for the classical calculation, there is a different distribution, resembling the situation of Fig. 4.27b for a cuboctahedron 10 times larger. We can also observe that the hot spot size is much larger in the quantum case, which means that it is enough to have sharp tips for having a great enhancement zone even if these solids are small.

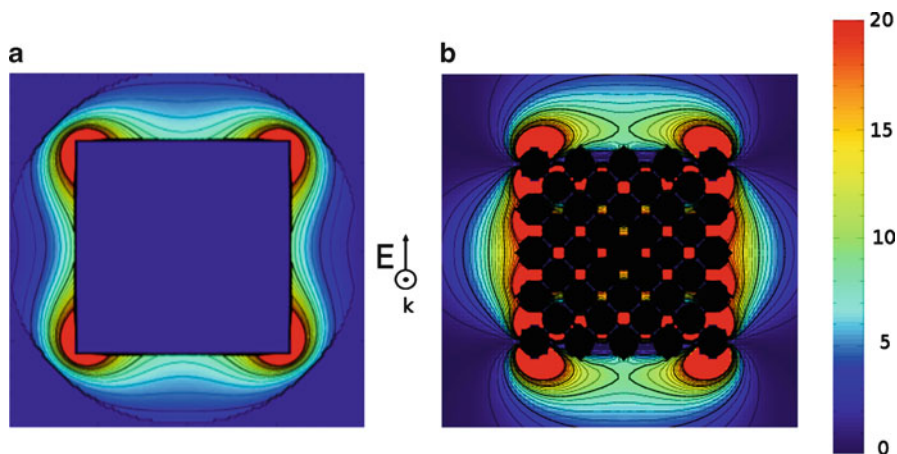


Fig. 4.34 Comparison between classical and quantum simulations for a 309 atoms Ag cuboctahedron: (a) classical simulation using DDA. (b) quantum simulation using a DFTB Hamiltonian. The square of these figures has $40.0 \times 40.0 \text{ \AA}^2$

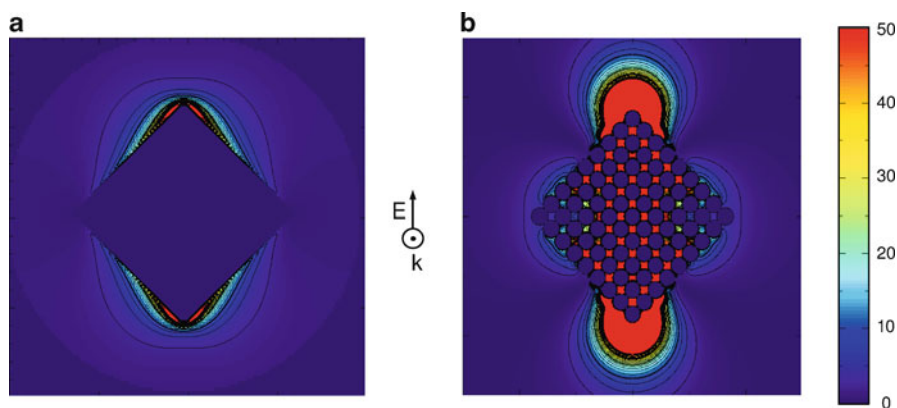


Fig. 4.35 Comparison between classical and quantum simulations for a cuboctahedron of 489 Ag atoms: (a) classical simulation using DDA. (b) quantum simulation using DFTB Hamiltonian. The square of these figures has $40.0 \times 40.0 \text{ \AA}^2$

4.8.6 Conclusions

The method presented here offers a quantum alternative to calculate the local electric field enhancement in metal nanoclusters. It has the advantage of including the atomistic structure of the NP, solving the problem of borders mentioned at the introduction. Field values calculated using either electronic structure methods give similar results to those found by classical methods. The distribution of the fields, however, widely differs from the classical results when particles are small and have

surface defects. Surface features such as corners make the quantum field much more intense than what is observed for classical results. When the electron gas compressibility is larger, higher electric field amplifications can occur. In the area between two particles, the field is very intense and there is an optimal distance where it reaches a maximum value. For longer distances, the field decays by electrostatic effects, and at shorter distances, charge transfer effect makes the fields to be less intense. The amplification factor increases approximately linearly with the size of the particle.

References

1. Kreibig U, Volmer M (1995) Optical properties of metal clusters. Springer, New York
2. Kelly LK, Coronado E, Zhao LL, Schatz GC (2003) *J Phys Chem B* 107:668–677
3. Bohren CF, Huffman DR (1983) Absorption and scattering of light by small particles. Wiley, New York
4. Link S, El-Sayed MA (2000) *Int Rev Phys Chem* 19:409
5. Link S, El-Sayed MA (2004) *Annu Rev Phys Chem* 54:331
6. Lee K, El-Sayed MA (2006) *J Phys Chem B* 110:19220
7. Berciaud S, Cognet L, Tamarat P, Lounis B (2005) *Nano Lett* 5:515
8. Aikens CM, Li S, Schatz GC (2008) *J Phys Chem C* 112:11272–11279
9. Yurkin MA, Hoekstra AG (2007) *J Quant Spectros Radiative Tran* 106:558–589
10. Jain PK, Lee K, El-Sayed IH, El-Sayed MA (2006) *J Phys Chem B* 110:7238
11. Johnson PB, Christy RW (1972) *Phys Rev B* 6:4370–4379
12. Hu M, Petrova H, Sekkinen AR, Chen J, McLellan JM, Li ZY, Marquez M, Li X, Xia Y, Hartland GV (2006) *J Phys Chem B* 110:19923
13. Sherry LJ, Jin R, Mirkin CA, Schatz GC, Van Duyne RP (2006) *Nano Lett* 6:2060
14. Van Dijk MA, Tchebotareva AL, Orrit M, Lippitz M, Berciaud S, Lasne D, Cognet L, Lounis B (2006) *Phys Chem Chem Phys* 8:3486
15. Sönnischen C, Franzl T, Wilk T, Von Plessen G, Feldman J (2002) *Phys Rev Lett* 88:077402
16. Arbouet A, Christofilos D, Del Fatti N, Vallée F, Huntzinger JR, Arnaud L, Billaud P, Broyer M (2004) *Phys Rev Lett* 93:127401
17. Klar T, Perner M, Grosse S, Von Plessen G, Sprinkl W, Feldmann J (1998) *Phys Rev Lett* 80:4249
18. Bosbach J, Hendrich C, Stietz F, Vartanyan T, Träger F (2002) *Phys Rev Lett* 89:257404
19. Muskens OL, Del Fatti N, Vallee F (2006) *Nano Lett* 6:552
20. Kuhn S, Hakanson U, Rogobete L, Sandoghdar V (2006) *Phys Rev Lett* 97:017402
21. Haes AJ, Zou S, Zhao J, Schatz GC, Van Duyne RP (2006) *J Am Chem Soc* 128:10905
22. Watanabe K, Menzel D, Nilius N, Freund HJ (2006) *Chem Rev* 106:4301
23. Qiu L, Larson TA, Smith D, Vitkin E, Modell MD, Korgel BA, Sokolov KV, Hanlon EB, Itzkan I (2008) *App Phys Lett* 93:1–3
24. Runge E, Gross EKV (1984) *Phys Rev Lett* 52:997
25. Tsolakidis A, Sánchez-Portal D, Martin RM (2002) *Phys Rev B* 66:235416
26. Yabana K, Bertsch GF (1996) *Phys Rev B* 54:4484–4487
27. Castro A, Marques MAL, Alonso JA, Rubio A (2004) *J Comp Theor Nanoscience* 1:1057
28. Blase X, Ordejón P (2004) *Phys Rev B* 69:085111
29. Baer R, Neuhauser D, Weiss S (2004) *Nano Lett* 4:85
30. Paxton AT (2009) *Multiscale Simul Methods Mol Sci* 42:145–176
31. Levine IN (2000) *Quantum Chemistry*, 5th ed. Prentice Hall.

32. Finnis MW (2004) Interatomic forces in condensed matter. Oxford series on materials modelling. Oxford University Press, Oxford
33. Porezag D, Frauenheim Th, Köhler Th, Seifer G, Kaschner R (1995) Phys Rev B 51:12947–12957
34. Aradi B, Hourahine B, Frauenheim Th (2007) J Phys Chem A 111:5678–5684
35. DFTB + Version 1.1 USER MANUAL. <http://www.dftb-plus.info/>
36. Elstner M, Porezag D, Jungnickel G, Haugk M, Frauenheim Th, Suhai S, Seifer G (1998) Phys Rev B 58:7260–7267
37. Frauenheim Th, Seifert G, Elstner Th, Köhler C, Amkreutz M, Stenberg M, Hajmal Z, Di Carlo A, Suhai S (2002) J Phys Cond Matt 14:3015–3047
38. Foulkes W, Haydock R (1989) Phys Rev B 39:12520–12536
39. Sutton AP, Todorov TN, Cackewell MJ, Hoekstra J (2001) Phyl Mag A 81:1833
40. Todorov TN (2001) J Phys Cond Matt 13:10125–10148
41. Finnis MW, Paxton AT, Methfessel M, van Schilfgaarde M (1998) Phys Rev Lett 81:5149
42. Schlosshauer M (2007) Decoherence, and the quantum to classical transition Springer, Berlin
43. Breuer HP, Petruccione F (2002) The theory of open quantum systems Oxford University Press, Oxford
44. Bushong N, Gamble J, Di Ventra M (2007) Nano Lett 7:1789–1792
45. Mukamel S (1995) Principles of nonlinear optical spectroscopy. Oxford series in optical and imaging sciences. Oxford University Press, New York
46. Gerry CC, Knight PL (2005) Introductory quantum optics. Cambridge university press, Cambridge
47. Bracewell RN (2000) The fourier transform and its applications. McGraw-Hill, New York
48. Merzbacher E (1998) Quantum mechanics. Wiley, New York
49. Miller KJ (1990) J Am Chem Soc 112:8543–8551
50. Sottile F (2003) Response functions of semiconductors and insulators: from the Bethe-Salpeter equation to time-dependent density functional theory. Tesis Doctoral, École polytechnique, Palaiseau, France
51. Fiolhais C, Nogueira F, Marques M (2003) A primer in density functional theory. Springer, Berlin, Heidelberg
52. Negre CFA, Sánchez CG (2008) J Chem Phys 129:034710
53. Molina RA, Weinmann D, Jalabert RA (2002) Phys Rev B 65:155427
54. Wise SA, Bonnet WJ, Guenther FR, May WE (1981) J Chromatogr Sci 19:248
55. Tedeschini R, Consinni V (2009) Molecular descriptors for Chemoinformatics. Methods and principles in Medicinal Chemistry, Series editions, vol. 41, WILEY-VCH Verlag GmbH & Co. KgaA, Weinheim.
56. Ahrenkile SP, Yu PR, Murphy JE (2008) J Microsc 230:382–387
57. Xu X, Saghi Z, Gay R, Möbus G (2007) Nanotechnology 18:1–8
58. Martin TP (1996) Phys Rep 273:199–241
59. Wales D (2003) Energy landscapes: applications to clusters, biomolecules and glasses. Cambridge University Press, Cambridge
60. Wales D (2004) Energy landscapes: applications to clusters, biomolecules and glasses. Cambridge University Press, Cambridge
61. Hubenthal F, Ziegler T, Hendrich C, Alschinger M, Trager F (2005) J Phys Chem 34:165–168
62. Zhang J, Tang Y, Weng L, Ouyang M (2009) Nano Lett 9:4061–4065
63. F. Hubenthal, N. Borg and F. Träger, Appl Phys B (2008) 93: 39–45
64. Mariscal M, Dassie SA (eds) (2007) Recent advances in nanoscience. Research Signpost, Trivandrum, India
65. Daniel M-C, Astruc D (2004) Chem Rev 104:293–346
66. Nagarajan R, Hatton TA (eds) (2008) Nanoparticles synthesis, stabillization, passivation and functionalization (Acs Symposium Series). Oxford University Press, USA, Washington, DC
67. Alivisatos P (2004) Nature Biotech 22:47–52
68. Brust M, Fink J, Bethell D, Schiffrin DJ, Kiely C (1995) J Chem Soc Chem Comm 16: 1655–1656

69. Templeton AC, Chen S, Gross SM, Murray RW (1999) *Langmuir* 15:66–76
70. Negre CFA, Sánchez CG (2010) *Chem Phys Lett* 494:255–259
71. Hövel H, Fritz S, Hilger A, Kreibig U, Vollmer M (1993) *Phys Rev B* 48:18178–18188
72. Leroux Y, Lacroix JC, Fave C, Trippe G, Flidj N, Aubard J, Hohenau A, Krenn JR (2008) *ACS Nano* 2:728–732
73. Hendrich C, Bosbach J, Stietz F, Hubenthal F, Vartanyan T, Träger F (2003) *Appl Phys B Laser Optic* 76:869
74. Kreibig U (2008) *App Phys B* 93:79–89
75. Hubenthal F (2007) *Prog Surf Sci* 82:378–387
76. Lica GC, Zelakiewicz BS, Constantinescu M (2004) *J Phys Chem B* 108:19896–19900
77. Su YH, Chang S-H, Teoh LG, Chu W-H, Tu S-L (2009) *J Phys Chem C* 113:3923–3928
78. Guerrero E, Muñoz Márquez MA, García MA, Crespo P, Fernández-Pinel E, Hernando A, Fernández A (2008) *Nanotechnology* 19:175701
79. Garcia M, de La Venta J, Crespo P, LLopis J, Penadés S, Fernández A, Hernando A (2005) *Phys Rev B* 72:2–5
80. Wiederrecht GP, Wurtz GA, Hranisavljevic J (2004) *Nano Lett* 4:2121–2125
81. Novotny L, Hecht B (2006) *Principles of nano-optics*, Cambridge University Press
82. Schatz GC, Young MA, Van Duyne RP (2006) *Topics Appl Phys* 103:19–46
83. Ferraro JR, Nakamoto K (1994) *Introductory Raman spectroscopy*, Elsevier Science
84. Michaels AM, Nirmal M, Brus LE (1999) *J Am Chem Soc* 121:9932–9939
85. Fleischmann MP, Hendra J, McQuillan AJ (1974) *Chem Phys Lett* 26:163–166
86. Otto A (2002) *J Ramman Spec* 33:593–598
87. Polubotko AM (1999) *J Optic A Pure Appl Optic* 1:L18–L20
88. Yoshihiro M, Ishikawa M, Futamata M (2001) *Anal Sci Jpn Soc Anal Chem* 17:1181–1183
89. Zou S, Schatz GC (2005) *Chem Phys Lett* 403:62–67
90. Sherry LJ, Mirkin CA, Schatz GC, Van Duyne RP (2006) *Nano Lett* 6:2060–2065
91. Perassi EM, Canali LR, Coronado EA (2009) *J Phys Chem C* 113:6315–6319
92. Serway RA (1999) *Principles of physics*, 6th edn., vol. II. Thomson Learning ISBN 10: 0030206693 / 0-03-020669-3 ISBN 13: 9780030206696
93. Zuloaga J, Prodan E, Nordlander P (2009) *Nano Lett* 9:887–891
94. Danckwerts M, Novotny L (2007) *Phys Rev Lett* 98:2614
95. Marhaba S, Bachelier G, Bonnet C, Broyer M, Cottacin E, Grillet N, Lermé J, Vialle J-L, Pellarin M (2009) *J Phys Chem C* 113:4349–4356
96. Hao E, Schatz GC (2004) *J Chem Phys* 120:357–366

Chapter 5

Spin-Fluctuation Theory of Cluster Magnetism

R. Garibay-Alonso, J. Dorantes-Dávila, and G.M. Pastor

5.1 Introduction

The magnetism of small clusters, nanoparticles, and nanostructures is the subject of a very intense research activity driven by strong fundamental and technological interests. On the one side, one would like to understand how the properties of the electrons of an atom changes as they become part of a cluster of increasing size and how their magnetic behavior changes with the system dimensions. On the other side, small magnetic clusters can be used to store information in high-density recording media as well as in spintronic devices.

Transition-metal (TM) clusters in particular have been investigated with a variety of experimental techniques many of which originate from related disciplines such as molecular, surface, and solid-state physics [1–19]. Stern–Gerlach (SG) deflection measurements on size-selected cluster beams have provided information on the average magnetization per atom $\bar{\mu}_N(T)$ of isolated clusters as a function of the nozzle temperature T . Remarkable temperature dependencies of $\bar{\mu}_N$ have been thus reported for different magnetic TMs [6–11, 17]. For example, the experiments on Ni_N with $40 \leq N \leq 600$ atoms show that the magnetization curves are qualitatively

R. Garibay-Alonso
Facultad de Ciencias Físico Matemáticas, Universidad Autónoma de Coahuila,
CU Camporredondo, 25000 Saltillo, Mexico
e-mail: raul.garibay@uadec.edu.mx

J. Dorantes-Dávila
Instituto de Física, Universidad Autónoma de San Luis Potosí, Alvaro Obregón 64,
78000 San Luis Potosí, Mexico
e-mail: jdd@ifisica.uaslp.mx

G.M. Pastor (✉)
Institut für Theoretische Physik, Universität Kassel, Heinrich Plett Straße 40,
34132 Kassel, Germany
e-mail: pastor@uni-kassel.de

similar to the bulk, except for an important finite-size broadening of the transition Curie temperature T_C beyond which paramagnetic behavior is observed [7, 9]. In the case of Co_N , one observes that $\bar{\mu}_N(T)$ is about $0.1\text{--}0.5 \mu_B$ ¹ larger than the bulk magnetization $M(T)$ for $50 \leq N \leq 600$ and $100 \text{ K} \leq T \leq 1,000 \text{ K}$ [7, 17]. Moreover, at low temperatures, $100 \text{ K} \leq T \leq 500 \text{ K}$, the magnetization per atom is found to increase slightly with T . This is an unusual effect that is not observed in the solid. In Fe clusters, the temperature dependence derived from experiment is qualitatively different from that of Ni or Co clusters. For $250 \leq N \leq 600$, one observes a rapid, almost linear decrease of $\bar{\mu}_N(T)$ with increasing T ($T \leq 500\text{--}600 \text{ K}$). For $T \geq 300 \text{ K}$, $\bar{\mu}_N(T)$ is significantly smaller than the bulk $M(T)$, even though at $T = 0$ it was larger [$T_C(\text{Fe bulk}) = 1,043 \text{ K}$]. As the cluster size increases ($250 \leq N \leq 600$), $\bar{\mu}_N(T)$ decreases, further making the difference between cluster and bulk magnetizations even larger [7]. This trend is expected to change for larger Fe clusters, although no experimental evidence seems to be available so far.

From the point of view of theory, mean-field electronic calculations of ground-state properties have been quite successful in predicting a large variety of experimental results on the magnetic behavior of clusters at low temperatures [20–31]. This includes in particular the determination of average magnetic moments per atom [21–28], the spin and orbital contributions [29], the magnetic order within the cluster, the magnetic anisotropy energies [30], etc. In contrast, studies of cluster magnetism at finite temperatures in the framework of electronic theories remain far more scarce [32–34]. This is quite remarkable since a correct description of the temperature dependence of the magnetic properties is crucial for understanding the physics of the underlying many-body problem as well as for controlling the behavior of magnetic clusters in view of technological applications such as high-density storage media and memory devices. It is the purpose of this chapter to review some of the recent progress made in this field by applying functional-integral methods to realistic many-body Hamiltonians.

One of the major current challenges for the theory of magnetism is to understand how the stability of the magnetic order at finite temperatures depends on the size, composition, and dimensionality of nanostructures. Simple trends—for example, in the size dependence of the “Curie” temperature $T_C(N)$, above which the spin correlations are destroyed within clusters—seem very difficult to infer a priori. On the one side, taking into account the enhancement of the ground-state local magnetic moments μ_l^0 and d -level exchange splittings $\Delta\epsilon_{Xl}^d = \epsilon_{l\downarrow}^d - \epsilon_{l\uparrow}^d$ between minority and majority-spin states, one could expect that $T_C(N)$ should be larger and that the ferromagnetic (FM) order should be more stable in small clusters than in the bulk. However, on the other side, the local coordination numbers are smaller at the cluster surface, and therefore, it should be energetically easier to disorder the local magnetic moments by flipping or canting them. If the latter effect dominates, $T_C(N)$ should decrease with decreasing coordination or N . In addition, possible changes or fluctuations of the cluster structure may also affect significantly the temperature

¹As usual, $\mu_B = e\hbar/2mc = 5.79 \times 10^{-5} \text{ eV/T}$ stands for the Bohr magneton.

dependence of the magnetization [35–39], in particular for systems like Fe_N and Rh_N which show a remarkable structural-dependent magnetic behavior already at $T = 0$ [24, 25, 40–44].

The well-known strong sensitivity of the d -electron properties on the local environment of the atoms suggests that reliable conclusions on cluster magnetism at finite T must be based on an electronic theory that takes into account, not only the fluctuations of the magnetic degrees of freedom, but also the itinerant character of the d -electron states. Moreover, the theoretical description of finite T should recover the ground-state limit and its wide diversity of behaviors as a function of size, structure, bond length, etc. Only in this way one may hope to be able to understand even more challenging and technologically important phenomena such as the temperature dependence of orbital moments and magnetic anisotropy energy which measures the stability of the magnetization direction. Simple localized-spin models, for example, based on the Heisenberg or Ising model [45], are not expected to be predictive unless they incorporate the electronic effects responsible for the size dependence of the local magnetic moments and of their exchange couplings. In fact, previous studies of itinerant magnetism in clusters, films, and surfaces have already shown that the effective exchange interactions J_{lm} between nearest neighbor (NN) moments μ_l and μ_m depend quite strongly on the local environment of the atoms [32, 46–48].

In this chapter, we review the formulation and application of a functional-integral theory of cluster magnetism that incorporates the environment dependence of the electronic structure of itinerant d -electrons as well as the temperature-induced fluctuations of the spin degrees of freedom. Section 5.2 presents the theoretical background starting from a realistic d -band many-body Hamiltonian and deriving the expressions for the relevant observable properties by using a functional-integral approach to electron correlations and spin fluctuations. The model extends Hubbard and Hasegawa’s bulk electronic theory of itinerant magnetism [49–55] in several respects: (a) it incorporates the local-environment dependence of the electronic structure, which is central to nanostructures (Pastor (1989) PhD. Thesis, Freie Universität Berlin, unpublished), (b) it allows to quantify the effect of local fluctuations of the exchange fields, thereby revealing a remarkable environment dependence of the cluster spin-fluctuation energies; and (c) it takes into account the collective fluctuations of all the local magnetic moments in the cluster, which removes completely any of the usual single-site approximations. This is particularly important when the size of the cluster is comparable to or smaller than the extent of short-range magnetic correlations [56]. Sections 5.3–5.4 are concerned with representative applications, giving particular emphasis to the environment dependence of the magnetic behavior as a function of size, structure, and interatomic distances. In Sect. 5.3, the low-temperature limit of the local spin-fluctuation energies $\Delta F_l(\xi)$ at different atoms l is analyzed as a function of the exchange fields ξ . The interplay between fluctuations of the module and of the relative orientation of the local magnetic moments is discussed. A remarkable dependence of the spin-excitation spectrum on the local atomic environment is thereby revealed. Section 5.4 is concerned with the stability of short-range magnetic order (SRMO)

in TM clusters at finite temperatures. A simple relation between the low- and high-temperature values of the average magnetic moment per atom is derived from which an important degree of SRMO is inferred in Fe_N and Ni_N even at temperatures above T_C . In Sect. 5.5, the results of Monte Carlo simulation on Fe clusters are discussed including the temperature dependence of the average magnetization per atom, local magnetic moments, and spin-correlation functions. Finally, Sect. 5.6 summarizes the main conclusions by pointing out some interesting future research perspectives.

5.2 Theoretical Background

The Hamiltonian describing the magnetic properties of TM nanostructures can be written in the form

$$\hat{H} = \hat{H}_0 + \hat{H}_I, \quad (5.1)$$

where the first term

$$\hat{H}_0 = \sum_{l,\alpha,\sigma} \varepsilon_l^0 \hat{n}_{l\alpha\sigma} + \sum_{\substack{l \neq k \\ \alpha,\beta,\sigma}} t_{lk}^{\alpha\beta} \hat{c}_{l\alpha\sigma}^\dagger \hat{c}_{k\beta\sigma} \quad (5.2)$$

describes the single-particle electronic structure of the valence d -electrons in the tight-binding approximation [24, 25].² The contributions of s and p electrons are neglected here for simplicity since they are expected to affect both spin directions essentially in the same way. As usual, $\hat{c}_{l\alpha\sigma}^\dagger$ ($\hat{c}_{l\alpha\sigma}$) refers to the creation (annihilation) operator of an electron with spin σ at the orbital α of atom l ($\alpha \equiv xy, yz, zx, x^2 - y^2$, and $3z^2 - r^2$), and $\hat{n}_{l\alpha\sigma} = \hat{c}_{l\alpha\sigma}^\dagger \hat{c}_{l\alpha\sigma}$ is the corresponding number operator. ε_l^0 stands for the bare d -orbital energy of the isolated atom and $t_{lk}^{\alpha\beta}$ for the hopping integrals between atoms l and k . The second term

$$\hat{H}_I = \frac{1}{2} \sum_{\substack{l,\alpha,\beta \\ \sigma,\sigma'}} ' U_{\sigma\sigma'} \hat{n}_{l\alpha\sigma} \hat{n}_{l\beta\sigma'} \quad (5.3)$$

approximates the interactions among the electrons by an intra-atomic Hubbard-like model, where $U_{\sigma\sigma'}$ refers to the Coulomb repulsion between electrons of spin σ and σ' . The prime in the summation indicates that the terms with $\alpha = \beta$ and $\sigma = \sigma'$ are excluded. $U_{\uparrow\downarrow} = U_{\downarrow\uparrow} = F^{(0)}$ is the average direct Coulomb integral and $U_{\uparrow\uparrow} = U_{\downarrow\downarrow} = U_{\uparrow\downarrow} - J$, where $J = (F^{(2)} + F^{(4)})/14$ is the average exchange integral. The $F^{(i)}$ stands for the radial d -electron Coulomb integrals allowed by atomic symmetry [57]. These are obtained by taking the ratios $F^{(0)}/F^{(2)}$ and $F^{(4)}/F^{(2)}$ from atomic calculations (Mann, Los Alamos Sci. Lab. Report LA-3690,

²For the sake of clarity, a *hat* (^) is used to distinguish operators from numbers.

1967 (unpublished)) and by fitting the value $F^{(2)}$ to reproduce the bulk Fe spin moment at zero temperature. For simplicity, we neglect in Eqs. (5.2) and (5.3) the dependence of the d -level energies and Coulomb integrals on the orbital α , retaining the dominant spin dependence due to exchange. Notice that Eq. (5.3) does not respect spin-rotational symmetry since the exchange terms of the form $\hat{H}_{xy} = -\sum_{l,\alpha<\beta} J_{\alpha\beta} (\hat{S}_{l\alpha}^- \hat{S}_{l\beta}^+ + \hat{S}_{l\alpha}^+ \hat{S}_{l\beta}^-)$ have been dropped (see also Eq. (5.4)) [58]. Nevertheless, this is not expected to be a serious limitation in the present work, since we are interested in studying the effects of spin fluctuations on broken-symmetry FM ground states.

5.2.1 Partition Function and Derived Properties

The finite-temperature magnetic properties of clusters are derived from the canonical partition function $Q = \exp\{-\beta\hat{H}\}$, where \hat{H} stands for the many-body Hamiltonian given by Eqs. (5.1)–(5.3) and $\beta = 1/k_B T$. In the case of isolated clusters, the temperature T refers to that of the cluster source that defines the macroscopic thermal bath with which the small clusters are in equilibrium before expansion [16]. Thermal average refers then to the ensemble of clusters in the beam. For deposited clusters the temperature is defined by the support. Keeping the number of atoms N and the number of electrons n_d , fixed (canonical ensemble) corresponds to the experimental situation found in charge- and size-selected beams or at inert (insulating) supports.

The partition function is solved by extending the functional-integral formalism developed by Hubbard and Hasegawa for periodic solids [49–55] to the case of finite systems with arbitrary symmetry (Pastor (1989) PhD. Thesis, Freie Universität Berlin, unpublished) [32]. To this aim, we rewrite the many-body interaction \hat{H}_I as

$$\hat{H}_I = \sum_l \left(\frac{U}{2} \hat{N}_l^2 - J \hat{S}_{lz}^2 \right), \quad (5.4)$$

where $\hat{N}_l = \sum_{\alpha\sigma} \hat{n}_{l\alpha\sigma}$ is the number operator at atom l , $\hat{S}_{lz} = (1/2) \sum_{\alpha} (\hat{n}_{l\alpha\uparrow} - \hat{n}_{l\alpha\downarrow})$ is the z component of the local spin operator, and $U = (U_{\uparrow\downarrow} + U_{\uparrow\uparrow})/2$. Note that Eq. (5.4) includes the self-interaction terms $U_{\uparrow\uparrow} \hat{n}_{l\alpha\sigma}^2/2 = U_{\uparrow\uparrow} \hat{n}_{l\alpha\sigma}/2$ which are canceled out by redefining the d -energy levels as $\varepsilon_l^0 - U_{\uparrow\uparrow}/2$. For the calculation of the canonical partition function Q , the quadratic terms in Eq. (5.4) are linearized by means of a two-field Hubbard–Stratonovich transformation within the static approximation [59, 60]. Thus, a charge field η_l and an exchange field ξ_l are introduced at each cluster site l , which describe the finite-temperature fluctuations of the d -electron energy levels and local exchange splittings, respectively. Using the notation $\xi = (\xi_1, \dots, \xi_N)$ and $\eta = (\eta_1, \dots, \eta_N)$, Q is given by

$$Q \propto \int d\eta d\xi \exp\{-\beta F'(\xi, \eta)\}, \quad (5.5)$$

where the free energy F' associated with the exchange fields ξ and η is given by

$$F'(\xi, \eta) = \frac{1}{2} \sum_l \left(U \eta_l^2 + \frac{J}{2} \xi_l^2 \right) - \frac{1}{\beta} \ln \{ \text{Tr} [\exp \{ -\beta \hat{H}' \}] \}. \quad (5.6)$$

The effective Hamiltonian

$$\hat{H}' = \sum_{l, \alpha, \sigma} \epsilon'_{l\sigma} \hat{n}_{l\alpha\sigma} + \sum_{\substack{l \neq k \\ \alpha, \beta, \sigma}} t_{lk}^{\alpha\beta} \hat{c}_{l\alpha\sigma}^\dagger \hat{c}_{k\beta\sigma} \quad (5.7)$$

describes the dynamics of the d -electrons as if they were independent particles moving in a random alloy with energy levels $\epsilon'_{l\sigma}$ given by

$$\epsilon'_{l\sigma} = \epsilon_l^0 + U i \eta_l - \sigma \frac{J}{2} \xi_l. \quad (5.8)$$

The thermodynamic properties of the system are obtained as a statistical average over all possible distributions of the energy levels $\epsilon'_{l\sigma}$ throughout the cluster. The approach is known as the static approximation, which is exact in the atomic limit ($t_{lm}^{\alpha\beta} = 0, \forall l \neq m$) where no fluctuations are present, and in the noninteracting limit ($U_{\sigma\sigma'} = 0$).

For $T \rightarrow 0$, the dominating field configuration (ξ^0, η^0) corresponds to the saddle point in the free energy $F'(\xi, \eta)$. This is determined from the self-consistent equations

$$\left. \frac{\partial F'}{\partial \xi_l} \right|_0 = \frac{J}{2} (\xi_l^0 - 2 \langle \hat{S}_{lz} \rangle') = 0 \quad (5.9)$$

and

$$\left. \frac{\partial F'}{\partial \eta_l} \right|_0 = U (\eta_l^0 + i \langle \hat{N}_l \rangle') = 0, \quad (5.10)$$

where $\langle \dots \rangle'$ indicates average with respect to the single-particle Hamiltonian H' . Replacing Eqs. (5.9) and (5.10) in Eq. (5.8) yields the known mean-field approximation to the energy levels $\epsilon'_{l\sigma}$ [24, 25]. The present approach provides therefore a proper finite-temperature extension of the self-consistent tight-binding theory developed in [24, 25] for the ground state.³

In this work, we are interested in the temperature dependence of the magnetic properties which are dominated by the low-lying spin fluctuations. Moreover, $J \ll U$, which implies that the energy involved in local charge fluctuations is much larger

³Recent applications of the mean-field approach to TM clusters and nanostructures at $T = 0$ may be found, for example, in [29] and [61–63], and in references therein.

than the spin-fluctuation energies. Therefore, it is reasonable to neglect the thermal fluctuations of the charge fields η_l . For each exchange-field configuration ξ , we set η_l equal to the saddle point of $F'(\xi, \eta)$ which is given by $i\bar{\eta}_l = v_l = \langle \hat{N}_l \rangle'$. Physically, this means that the charge distribution $v_l = \langle \hat{N}_l \rangle'$ is calculated self-consistently for each exchange-field configuration ξ . Since the v_l are implicit functions of ξ , one may write

$$Q \propto \int d\xi \exp\{-\beta F'(\xi)\}, \quad (5.11)$$

where the free energy

$$F'(\xi) = -\frac{1}{2} \sum_l \left(U v_l^2 - \frac{J}{2} \xi_l^2 \right) - \frac{1}{\beta} \ln \{ \text{Tr}[\exp\{-\beta \hat{H}'\}] \} \quad (5.12)$$

associated with ξ depends only on the exchange variables ξ_l that describe the relevant fluctuations of the spin degrees of freedom. Notice that $F'(\xi)$ in Eqs. (5.11) and (5.12) is actually a shorthand for $F'(\xi, \bar{\eta}(\xi))$ where $\bar{\eta}(\xi)$ refers to the saddle-point value of η for the exchange configuration ξ . The integrand in Eq. (5.11) is proportional to the probability $P(\xi) = [\exp\{-\beta F'(\xi)\}]/Q$ of the exchange-field configuration ξ .

The thermodynamic properties are obtained by averaging over all possible ξ with $\exp\{-\beta F'(\xi)\}$ as weighting factor. For example, the local spin magnetization $m_l = 2\langle \hat{S}_{lz} \rangle$ at atom l is given by

$$m_l(T) = \frac{2}{Q} \int d\xi \exp \left\{ \frac{\beta}{2} \sum_l \left(U v_l^2 - \frac{J}{2} \xi_l^2 \right) \right\} \text{Tr}[\hat{S}_{lz} \exp\{-\beta \hat{H}'\}] \quad (5.13)$$

$$= \frac{2}{Q} \int d\xi \langle \hat{S}_{lz} \rangle' e^{-\beta F'(\xi)}, \quad (5.14)$$

where $\langle \hat{S}_{lz} \rangle'$ is the average spin moment at atom l according to the effective single-particle Hamiltonian \hat{H}' , which depends on the fluctuating ξ . Taking into account that

$$\partial F / \partial \xi_l = \frac{J}{2} (\xi_l - 2\langle \hat{S}_{lz} \rangle'), \quad (5.15)$$

one may rewrite Eq. (5.14) as

$$m_l(T) = \frac{1}{Q} \int d\xi \xi_l e^{-\beta F'(\xi)}. \quad (5.16)$$

Thus, the local magnetization at atom l is equal to the average of the exchange field at the same atom. Equation (5.16) justifies the intuitive though not quite rigorous association between the fluctuations of the local moment $2\langle \hat{S}_{lz} \rangle$ at atom l and those of the exchange field ξ_l . Notice that in Eqs. (5.14) and (5.16), the restriction $\sum_l \xi_l \geq 0$ or positive total cluster moment $\sum_l \langle \hat{S}_{lz} \rangle \geq 0$ must be enforced in

order to avoid trivially vanishing results for the average magnetization due to time-inversion symmetry. This applies to any finite-system calculation and correspond to the experimental situation where the cluster moment is aligned along an external magnetic field. We therefore compute the local magnetizations from

$$m_l(T) = \frac{1}{Q} \int d\xi \operatorname{sgn}(\sum_l \xi_l) \xi_l e^{-\beta F'(\xi)}. \quad (5.17)$$

The cluster magnetization per atom \bar{m}_N is determined by averaging the z component of the total spin operator $\hat{S}_z = \sum_l \hat{S}_{lz}$ under the constraint $\langle \hat{S}_z \rangle' \geq 0$. This is given by

$$\bar{m}_N(T) = \frac{2}{N} \langle |\hat{S}_z| \rangle = \frac{1}{N} \sum_l m_l(T), \quad (5.18)$$

which corresponds to the cluster average of the local magnetizations m_l . The previous definitions of local and average magnetizations are equivalent to the constraint of positive magnetization used in Monte Carlo simulations of phenomenological spin models like the Ising model [64]. In this way, the local magnetizations $m_l(T)$ can be determined for different local environments in analogy to the layer by layer magnetizations in thin films.

An alternative definition of the average magnetic moment per atom is provided by

$$\bar{\mu}_N(T) = \frac{2}{N} \sqrt{\langle \hat{S}_z^2 \rangle}, \quad (5.19)$$

where

$$\langle \hat{S}_z^2 \rangle = \frac{1}{Q} \int d\xi \langle \hat{S}_z^2 \rangle' e^{-\beta F'(\xi)} \quad (5.20)$$

denotes the average of the square total spin. Using Eq. (5.15), one can express $\langle \hat{S}_z^2 \rangle$ in terms of the exchange-field averages as [49–52]

$$4\langle \hat{S}_z^2 \rangle = -\frac{2N}{\beta J} + \frac{1}{Q} \int d\xi \xi^2 e^{-\beta F'(\xi)}, \quad (5.21)$$

where $\xi^2 = (\sum_l \xi_l)^2$. The first term in Eq. (5.21) cancels the trivial contribution to $\langle \xi^2 \rangle$ that is present even if H' is independent of ξ . The magnetic order within the cluster and its stability at finite T are characterized by the correlation functions

$$\gamma_{lk} = 4\langle \hat{S}_{lz} \hat{S}_{kz} \rangle = -\frac{2}{\beta J} \delta_{lk} + \frac{1}{Q} \int d\xi \xi_l \xi_k e^{-\beta F'(\xi)} \quad (5.22)$$

between the magnetic moments at atoms l and k . Notice that $4\langle \hat{S}_z^2 \rangle = \sum_{lk} \gamma_{lk}$. Positive (negative) values of γ_{lk} for $l \neq k$ indicate ferromagnetic (antiferromagnetic) correlations which tend to enhance (reduce) the total magnetization per atom $\bar{\mu}_N(T)$. The diagonal elements of γ_{lk} are related to the local magnetic moments

$$\mu_l = 2\sqrt{\langle \hat{S}_{I_z}^2 \rangle} = \sqrt{\gamma_{ll}} \quad (5.23)$$

at atom l . It should be noted that temperature fluctuations in itinerant-electron magnets not only affect the spin-spin-correlation functions, for example, by destroying the ground-state FM order in Fe_N , but can also modify the size of the local spin polarizations μ_l . This contrast, with localized magnetism where spin and charge degree of freedoms are well separated. In the applications, it is interesting to investigate the different temperature scales yielding changes of the various γ_k , in order to infer which local moments fluctuate more or less easily and which are the moments that trigger the breakdown of the cluster magnetic order.

5.3 Low-Temperature Spin-Fluctuation Energies

The free-energy difference

$$\Delta F(\xi) = F(\xi) - F(\xi^0) \quad (5.24)$$

with respect to the minimum or ground-state value $F(\xi^0)$ determines the probability that the exchange-field fluctuation $\Delta\xi = \xi - \xi^0$ is realized at a given T . $\Delta F(\xi)$ can be regarded as the spin-fluctuation energy associated with ξ since the fluctuations of ξ are responsible for the fluctuations of the spin moments $\langle S_{I_z} \rangle'$. In clusters and other non-periodic systems, it is very interesting to analyze the spin-fluctuation energies $\Delta F(\xi)$ from a local point of view and to clarify the relation between the local contributions to $\Delta F(\xi)$ and the temperature dependence of the spin moments μ_l . It is then useful to introduce the probability

$$P_l(\xi) = \frac{1}{Q} \int \prod_{m \neq l} d\xi_m \exp\{-\beta F(\xi_1, \dots, \xi_{l-1}, \xi, \xi_{l+1}, \dots, \xi_N)\} \quad (5.25)$$

$$= \frac{1}{Q} \exp\{-\beta F_l(\xi)\} \quad (5.26)$$

of having the value ξ for the exchange field at atom l , since in terms of $P_l(\xi)$, one may write

$$\mu_l(T) = \int \xi P_l(\xi) d\xi. \quad (5.27)$$

Thus, the temperature-dependent local spin magnetization is equal to the average of the local exchange field. Equation (5.27) justifies the intuitive association between the fluctuations of the local moment $\mu_l = 2\langle \hat{S}_{I_z} \rangle'$ at atom l and those of the exchange field ξ_l . The local free energy $F_l(\xi)$ is obtained by averaging over all possible values of ξ_m for $m \neq l$ [see Eqs. (5.25) and (5.26)]. Notice that the temperature dependence of $F_l(\xi)$ is in general far more complex than that of $F(\xi)$

since the local $F_l(\xi)$ involves averaging over the fluctuations of fields at all other sites m , in particular at the NNs of l which are sensitive to SRMO.

A first insight on the magnetic behavior of $3d$ transition-metal clusters at $T > 0$ can be obtained by considering the low-temperature limit of $F_l(\xi)$. For $T \rightarrow 0$, the integration in Eq. (5.25) may be simplified by setting $\xi_m = \xi_m^0$ for $m \neq l$ [see Eq. (5.9)]. The local free-energy difference

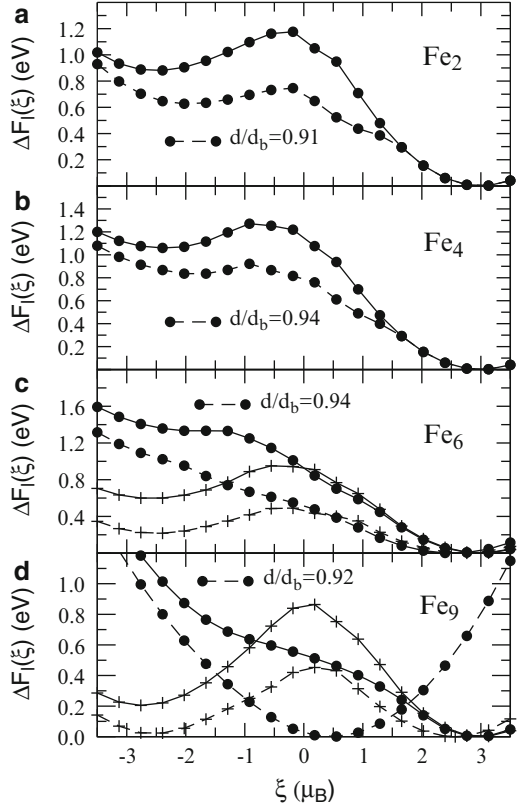
$$\Delta F_l(\xi) = F_l(\xi) - F_l(\xi_l^0), \quad (5.28)$$

with $\xi_l^0 = \mu_l^0$ being the local moment of atom l at $T = 0$, represents the energy involved in an exchange-field fluctuation at atom l above the Hartree–Fock ground state. $\Delta F_l(\xi)$ determines the probability of the fluctuation $\Delta\xi = \xi - \xi_l^0$ and thus conditions the stability of the ground-state magnetic order within the cluster at finite T . As it will be discussed below, $\Delta F_l(\xi)$ has often two minima at $\xi^+ = \xi_l^0$ and $\xi^- \simeq -\xi_l^0$. At $T > 0$, the FM order is reduced by spin fluctuations involving transitions between these two minima and by more or less asymmetric Gaussian-like fluctuations around them. For small clusters, the directional fluctuations of the local moments are expected to dominate since the reduction of coordination number should enhance the local character of the spin excitations. As the cluster size increases, the fluctuations of the amplitude of μ_l or ξ_l should also become important, particularly for the case of Ni clusters, which indicates a crossover to a more itinerant behavior. In the following, we present and discuss representative results for low-temperature limit of the local free energies $F_l(\xi)$ and the resulting spin-fluctuation energies $\Delta F_l(\xi)$ in Fe_N and Ni_N clusters with $N \leq 51$ atoms [see Eq. (5.28)]. Comparing the $\Delta F_l(\xi)$ for different sizes, interatomic distances, and atoms l within the cluster provides useful information on the stability of the local magnetizations and its environment dependence. In particular, it allows us to identify the atoms which trigger the decrease of the magnetization at low T (see [32]).

5.3.1 Fe_N Clusters

In Fig. 5.1, results are given for $\Delta F_l(\xi)$ in small Fe clusters: Fe_2 , Fe_4 tetrahedron, Fe_6 square bipyramid, and Fe_9 with bcc-like structure [24, 25]. The corresponding structures are illustrated in Fig. 5.2. First of all, one observes that $\Delta F_l(\xi) > 0$ for all $\xi \neq \mu_l^0$, which indicates, as expected, that in these clusters the FM order is stable at low temperatures. For the smallest clusters, i.e., Fe_2 and Fe_4 , $F_l(\xi)$ shows two minima located at the exchange fields $\xi^+ = \mu_l^0$ and $\xi^- \simeq -\mu_l^0$, where μ_l^0 refers to the ground-state magnetic moment. This double-minimum structure indicates that the dominant magnetic excitations are flips of the magnetic moments, keeping their amplitude approximately constant. In fact, at finite T , the probability $P_l(\xi) \propto \exp\{-\beta\Delta F_l(\xi)\}$ has two maxima at ξ^+ and ξ^- . It is thus more probable to

Fig. 5.1 Local spin-fluctuation energy $\Delta F_l(\xi) = F_l(\xi) - F_l(\xi_l^0)$ as a function the exchange field ξ at different atoms l of Fe_N clusters: (a) Fe_2 , (b) Fe_4 (tetrahedron), (c) Fe_6 (square bipyramid), and (d) Fe_9 (bcc-like) as illustrated in Fig. 5.2. Results are given for bulk NN distances $d/d_b = 1$ (full curves) and for relaxed NN distances (dashed curves). In (c) and (d) the dots refer to the atom $l = 1$ with the largest local coordination number (i.e., the central atom for Fe_9) and the crosses to one of the surface atoms, $l = 2$ (see Fig. 5.2c and d)



find $\xi \simeq -\mu_l^0$ than $\xi \simeq 0$. In the case of Fe_6 and Fe_9 , $F_l(\xi)$ also shows two minima for the lowest coordinated atoms $l = 2$, which have the largest local magnetic moments μ_l^0 at $T = 0$. In these cases, as in Fe_2 and Fe_4 , only moderate or small fluctuations $\Delta\xi = \xi - \mu_l^0$ are possible with an excitation energy $\Delta F_l(\xi)$ smaller than the energy $\Delta F_l(\xi^-) = F_l(\xi^-) - F_l(\xi^+)$ required to flip the local moment. In contrast, for the most coordinated atoms which have smaller μ_l^0 (e.g., the central atom in bcc-like Fe_9), one observes a single minimum in $F_l(\xi)$, which implies that the fluctuations of the amplitude of the local moments dominate.

The fact that very small clusters and in particular the atoms having the smallest local coordination numbers z_l show such a Heisenberg- or Ising-like behavior should not be surprising. On the one side, the kinetic-energy loss ΔE_K caused by flipping a local magnetic moment ($\xi \simeq \mu_l^0 \rightarrow \xi \simeq -\mu_l^0$) decreases with decreasing z_l since the perturbation introduced by flipping ξ_l is in general less important when l has a small number of neighbors and since the contribution of atom l to E_K is approximately proportional to $\sqrt{z_l}$ (second-moment approximation). On the other side, the exchange energy $\Delta E_X = (J/4) \sum_l \mu_l^2$ is basically a local property which is

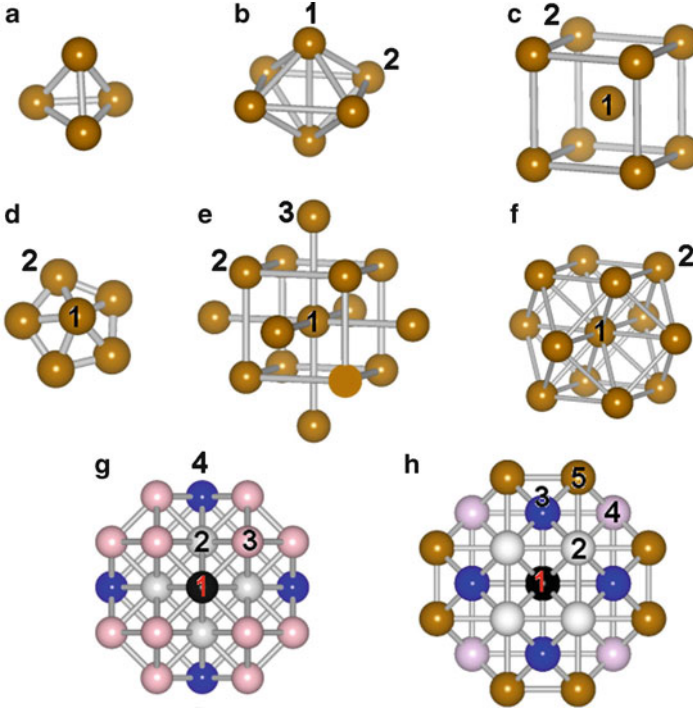
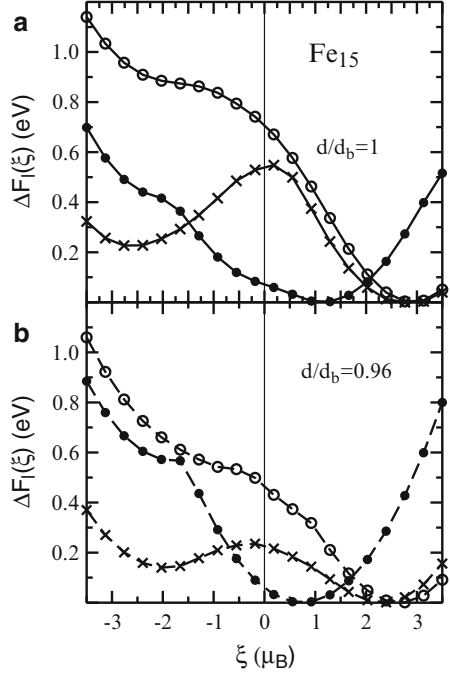


Fig. 5.2 (Color online) Illustration of the structures considered in the calculations for Fe_N and Ni_N clusters: (a) tetrahedron, (b) square bipyramid, (c) bcc_9 , (d) pentagonal pyramid, (e) bcc_{13} , (f) fcc_{13} , (g) fcc_{43} , and (h) bcc_{51} . Notice that in the case of fcc_{43} and bcc_{51} , a symmetrical transversal cut is shown for the sake of clarity

much less affected by the change of sign of ξ . Thus, when z_l is reduced, the local character is enhanced and it becomes energetically more favorable to have $\xi \simeq -\mu_l^0$ than $\xi \simeq 0$. At this point, one may anticipate that at finite T , when statistically some of the fields ξ_m at NNs of l have negative values, $F_l(\xi)$ should tend to develop a second minimum close to $\xi^- \simeq -\mu_l^0$. Such a behavior has already been observed in bulk and thin-film calculations [48–53].

$\Delta F_l(\xi)$ depends strongly on the local environment of the different atoms within the cluster, as clearly illustrated by the results for Fe_{15} shown in Fig. 5.3. Besides the central atom and its first NNs, which show similar behaviors as in Fe_9 , one observes that the FM order is particularly stable at the outermost shell $l = 3$. The larger spin-flip energy $\Delta F_3(-\xi_3^0)$ is favored by the larger local moment μ_3^0 found at these atoms, which in this case compensates the reduction of local coordination number z_l at the cluster surface (for $l = 3$, there are four first NNs and one second NN). However, notice that this trend is not always followed. For example, the atoms at the second shell (crosses in Fig. 5.3) show a much smaller $\Delta F_l(-\xi_l^0)$, despite having similar μ_l^0

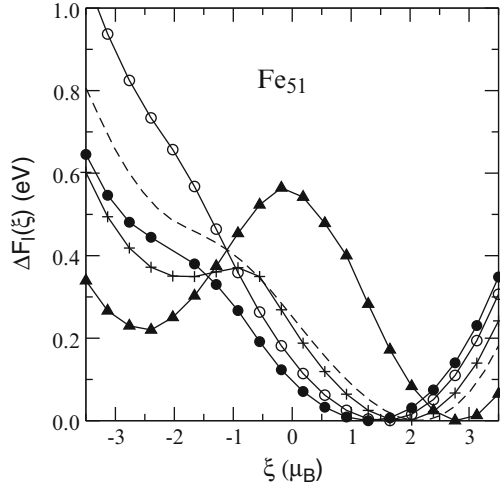
Fig. 5.3 Local spin-fluctuation energy $\Delta F_l(\xi) = F_l(\xi) - F_l(\xi_l^0)$ as a function of the exchange field ξ at different atoms l of Fe_{15} with bcc-like structure. *Dots* refer to the central atom ($l = 1$), *crosses* to the first NN shell ($l = 2$), and *open circles* to the outermost shell ($l = 3$). The numbers l are the same as labeled in Fig. 5.2e. Results are given for (a) bulk NN distance $d/d_b = 1$ and (b) relaxed NN distance $d/d_b = 0.96$. The *dashed curve* in (a) refers to bulk bcc Fe



and similar z_l as the atoms in the outermost shell (for $l = 2$, there are four first NNs and three second NNs). A remarkable environment dependence of $\Delta F_l(\xi)$ is also found in smaller clusters, for example, in Fe_6 and Fe_9 , as shown in Fig. 5.1.

It is also interesting to determine how $\Delta F_l(\xi)$ depends on the interatomic distances in order to infer the effects of structural distortions on the cluster magnetization curves. If the ground-state energy is optimized by changing the NN distances keeping the cluster symmetry unchanged (uniform relaxation), a bond-length contraction is usually obtained in TM clusters ($d < d_b$) [24, 25]. In Fig. 5.1, results are given for Fe_9 using $d/d_b = 0.92$ [24, 25]. In this case, one finds strong quantitative changes in $F_l(\xi)$ as a function of ξ . First, one observes shifts of the positions of the minima at ξ_l^0 that reflect the reduction of the local magnetic moments at $T = 0$. Moreover, there is an important reduction (about a factor 10 for $l = 2$ in Fe_9) of the free energy $\Delta F_l(-\xi_l^0) = F_l(-\xi_l^0) - F_l(\xi_l^0)$ required to flip a local magnetic moment at the surface atoms. A similar large reduction of the ‘‘Curie’’ temperature $T_C(N)$ is expected to occur upon relaxation since in first approximation, $T_C(N)$ should be proportional to $\langle \Delta F_l(-\xi_l^0) \rangle_l$. Conversely, if the exchange integral J is increased or if the NN distances are expanded, one obtains an enhancement of the local moments μ_l^0 as well as an increase of the local spin-fluctuation energies. At the same time, a more pronounced double minimum is found in $\Delta F_l(\xi)$, particularly at the cluster surface, which is characteristic of the localized regime. The larger stability of FM order with increasing ratio J/W , between the exchange

Fig. 5.4 Local spin-fluctuation energy $\Delta F_l(\xi)$ as a function of the exchange field ξ at different atoms l of Fe_{51} with bcc-like structure and bulk NN distances ($d/d_b = 1$). Dots refer to the central atom ($l = 1$), crosses to the first NN shell ($l = 2$), open circles to the second NN shell ($l = 3$), and triangles to the outermost shell ($l = 5$) as labeled in Fig. 5.2h. The dashed curve refers to bulk bcc Fe



interaction J and the effective d -band width W , is qualitatively in agreement with exact-diagonalization studies of finite-temperature properties of clusters using the single-band Hubbard model [38, 39].

In Fig. 5.4, results are given for Fe_{51} with bcc-like structure. In this case, we also observe a tendency to spin reversals at the surface atoms $l = 5$ and the typical two-minimum form of $\Delta F_5(\xi)$. At inner atoms, the amplitude fluctuations $\Delta\xi = \xi - \mu_l^0$ around the Hartree–Fock minimum are energetically more favorable, at least in the present low-temperature limit. This is probably related to the smaller values of μ_l^0 and to the larger coordination numbers of inner atoms. Notice that the form of $\Delta F_l(\xi)$ depends significantly on l . For the central atom ($l = 1$), the behavior is similar to that of the bulk. Other sites ($l = 2$ and 5) tend to favor spin reversals, while for $l = 3$, flipping a spin requires a much higher energy than in the solid. Therefore, a very interesting site dependence of $\mu_l(T)$ can be expected. Nevertheless, it should be noted that the trends in $\Delta F_l(\xi)$ are likely to change at finite temperatures since the inner atoms will be affected by the fluctuations of the surrounding surface sites and vice versa.

The results shown in Figs. 5.1 and 5.4 reflect the strong sensitivity of the magnetic properties of $3d$ TM clusters to the local environment of the atoms. $\Delta F_l(\xi)$ is actually much more sensitive to size and structure than the magnetic moments at $T = 0$. The effect is most clear in small clusters where the local magnetic moments are nearly saturated and therefore depend weakly on the site l or on precise cluster geometry. The strong environment dependence of the spin-fluctuation energies suggests that temperature-induced structural fluctuations could also play a role on the magnetic behavior at finite T . In fact, recent calculations including correlations effects exactly within the single-band Hubbard model have revealed the importance of structural changes and structural fluctuations to the temperature dependence of the magnetic properties of clusters [35–39]. Comparing

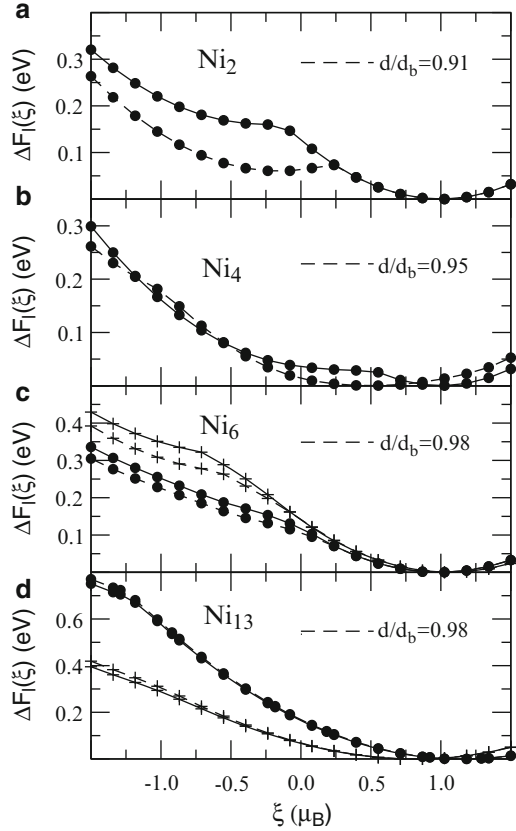
results for different l , one finds that the spin-flip energy $\Delta F_l(-\xi_l^0)$ does not scale simply with the local coordination number z_l (see Figs. 5.1 and 5.4). This implies that the effective exchange couplings between local magnetic moments cannot be transferred straightforwardly from one environment to another. Electronic structure effects due to the itinerant character of the d -electrons are therefore important, as already found near the surfaces of macroscopic TMs [46, 47]. The present results for $\Delta F_l(\xi)$ may be used to infer which are the atoms that trigger the decrease of the average magnetization of the cluster with increasing T . For example, in Fe_9 and Fe_{51} , the local magnetization $\mu_l(T)$ should decrease most rapidly at the outermost shells $l = 2$ and $l = 5$, respectively (see Figs. 5.1d and 5.4). In contrast, $\mu_3(T)$ at the outermost shell of Fe_{15} should depend more weakly on T since $\Delta F_3(\xi)$ is larger.

5.3.2 Ni_N Clusters

In Figs. 5.5 and 5.6, results are given for Ni_N clusters having $N \leq 43$ atoms. For the smallest sizes, the considered structures are the tetrahedron ($N = 4$) and the pentagonal pyramid ($N = 6$). For $N \geq 13$, the cluster have fcc-like structures formed by a central atom and the successive shells of its nearest neighbors. The corresponding structures are illustrated in Fig. 5.2. In contrast to Fe clusters, the dominant spin excitations in Ni_N involve mainly amplitude fluctuations of the local exchange fields around the Hartree–Fock moments, which are characterized by a single minimum in $\Delta F_l(\xi)$. The same type of behavior is also observed in the case of bulk Ni (see Fig. 5.6). This is probably due to the fact that the magnetic moments at $T = 0$ are much smaller in Ni than in Fe. Let us recall that $\Delta F_l(\xi)$ also shows a single minimum in Fe_N when the local moments at $T = 0$ are small (e.g., at the central atom in Fe_9). Only in Ni_2 one observes that negative values of $\xi \simeq -\mu_l^0$ are, if not more probable, at least as probable as $\xi = 0$. The dimer behavior can be interpreted as an enhancement of the local character of the spin fluctuation in very small Ni clusters due to the strong reduction of the local coordination number and of the kinetic energy of the d -electrons.

As in the case of Fe, $\Delta F_l(\xi)$ is much more sensitive to cluster size and to changes in the interatomic distances than the magnetic moments at $T = 0$. For example, in small Ni_N , the magnetic moments are saturated and are thus nearly independent of cluster structure and local atomic environment. Nevertheless, $\Delta F_l(\xi)$ presents significant quantitative changes as a function of l and N (see Fig. 5.5) which let us expect interesting changes in the temperature-dependent properties. Notice, moreover, that bond-length contractions ($d < d_b$) usually result in a reduction of $\Delta F_l(\xi)$ even if μ_l^0 remains unchanged. Comparing surface and inner atoms, it is interesting to observe that the spin-fluctuations energies are in general smaller at the cluster surface, i.e., as the local coordination number is smaller (see Figs. 5.5 and 5.6). Thus, one expects that in Ni clusters, the surface atoms should drive the decrease of the average magnetization per atom as T increases.

Fig. 5.5 Local spin-fluctuation energy $\Delta F_l(\xi) = F_l(\xi) - F_l(\xi_l^0)$ as a function of the exchange field ξ at different atoms l of Ni_N clusters: **(a)** Ni_2 , **(b)** Ni_4 (tetrahedron), **(c)** Ni_6 (pentagonal pyramid), and **(d)** Ni_{13} (fcc-like structure). Results are given for bulk NN distances $d/d_b = 1$ (full curves) and for optimized NN distances (dashed curves). In **(c)** and **(d)**, dots refer to the atom $l = 1$ with the largest local coordination number (i.e., the central atom for Ni_{13}) and the crosses to one of the surface atoms $l = 2$ (see Fig. 5.2d and f)



5.3.3 Discussion

The low-temperature limit of the local spin-fluctuation energies $\Delta F_l(\xi)$ at different atoms l in Fe_N and Ni_N clusters has revealed a variety of new interesting behaviors concerning the dependence of $\Delta F_l(\xi)$ on the atomic site l , on the cluster structure and interatomic distances, as well as qualitative differences between the Fe and Ni clusters. This certainly encourages further investigations. However, the low-temperature limit of $\Delta F_l(\xi)$ cannot be taken as a straightforward means of estimating the temperature $T_C(N)$ above which the FM order is lost within the cluster. Notice that the Curie temperature is not the energy necessary to flip a spin at $T = 0$ but rather the temperature at which it costs no free energy to flip one [49–52]. In other words, collective fluctuations of $\xi_m \neq l$ modify the effective spin-excitation energies, thereby reducing the stability of the FM order. Moreover, the low-temperature limit of $\Delta F_l(\xi)$, where all but one field ξ_l are kept equal to the $T = 0$ value, ignores that the local exchange fields at different sites fluctuate in some correlated fashion showing some degree of SRMO. Fluctuations of the

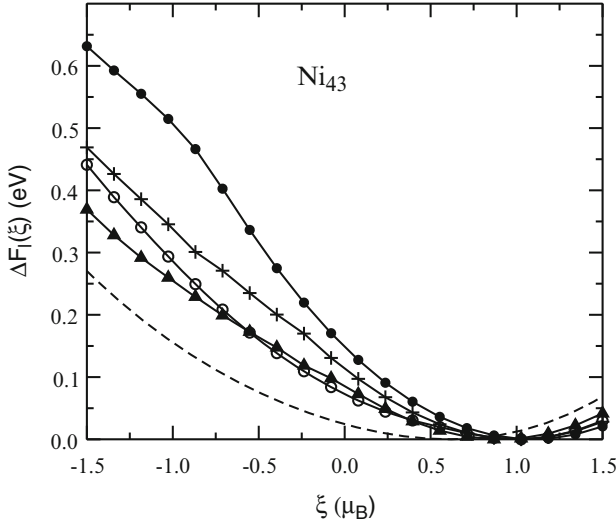


Fig. 5.6 Local spin-fluctuation energy $\Delta F_l(\xi)$ as a function of the exchange field ξ at different atoms l of Ni_{43} with fcc-like structure. *Dots* refer to the central atom ($l = 1$), *crosses* to the first NN shell ($l = 2$), *open circles* to the second NN shell ($l = 3$), and *triangles* to the outermost shell ($l = 4$), as labeled in Fig. 5.2g. The *dashed curve* refers to bulk fcc Ni

ensemble of exchange fields modify the magnetic environment at which individual spin fluctuations occur and should be therefore taken into account in quantitative studies at finite T .

Besides the temperature $T_C(N)$, one is interested in the size dependence of the temperature $T_{\text{SR}}(N)$ above which thermal fluctuations destroy the short-range correlations between the local magnetic moments, for example, between NN μ_i . A significant degree of SRMO is observed in the bulk and near the surfaces of Fe, Co, and Ni [46, 47, 65, 66]. This holds even for $T > T_C$, i.e., after the average magnetization $M(T)$ vanishes [$T_{\text{SR}}(b) > T_C(b)$]. For small clusters having a radius R smaller than the range of SRMO, it is no longer possible to increase the entropy without destroying the energetically favorable local magnetic correlations. In addition, the degree of SRMO is likely to depend on the details of the electronic structure and on cluster size [56]. The single-site spin fluctuations considered in this chapter ignore short-range magnetic correlations among the local magnetic moments. In the framework of the previous functional-integral theory, SRMO manifests itself as correlations between the exchange fields at neighboring sites. For example, in the FM case, $\langle \xi_i \xi_m \rangle > \langle \xi_i \rangle \langle \xi_m \rangle$ for NN atoms i and j . Therefore, it is worth to perform systematic temperature-dependent simulations by treating the fluctuations of all spin degrees of freedom on the same footing. In the following Sect. 5.4, the importance of SRMO is analyzed, while the results of Monte Carlo simulations are reviewed in Sect. 5.5.

5.4 Short-Range Magnetic Order in Transition-Metal Clusters

The experimental results for the temperature dependence of the magnetization per atom $\bar{\mu}_N(T)$ of Fe_N ($25 \leq N \leq 700$, $100 \text{ K} \leq T \leq 1,000 \text{ K}$) and Ni_N ($40 \leq N \leq 600$, $100 \text{ K} \leq T \leq 700 \text{ K}$) [6, 7] show that for all studied sizes, $\bar{\mu}_N(T)$ decreases with increasing T , reaching an approximately constant value above a characteristic size-dependent temperature $T_C(N)$, which corresponds to a magnetically disordered state [45]. The magnetization above $T_C(N)$, $\bar{\mu}_N(T > T_C)$, was found to be significantly larger than $\bar{\mu}_N(T=0)/\sqrt{N}$, the value corresponding to N randomly oriented *atomic* magnetic moments [6, 7]. This is a very interesting and a priori puzzling finding since the results for randomly oriented moments should be independent of the details of the interactions between the local moments or, in other words, independent of the underlying Hamiltonian. It is the purpose of this section to analyze the observed large values of $\bar{\mu}_N(T > T_C)$ by taking into account the existence of a certain degree of SRMO in these clusters above $T_C(N)$, which is similar to the one observed in the bulk and near surfaces. In this way, the results for $\bar{\mu}_N(T)$ at low and high temperatures can be brought into agreement with model independent predictions (see [56]).

The degree of SRMO within the cluster can be characterized by the average number of atoms ν involved in a SRMO domain. The magnetization per atom of a N -atom cluster at $T > T_C(N)$ is then approximately given by

$$\bar{\mu}_N(T > T_C) \simeq \bar{\mu}_N(T=0) \sqrt{\nu/N}, \quad (5.29)$$

which represents the average $\sqrt{\langle \mu^2 \rangle}$ of N/ν randomly oriented SRMO domains, each carrying a magnetic moment $\nu \bar{\mu}_N(T=0)$. The disordered-local-moment picture, i.e., the situation without SRMO, corresponds thus to $\nu = 1$. The actual value of ν for $3d$ TM can be estimated first from known bulk and surface results [46, 47, 65, 66]. For bulk Fe, Haines et al. [66] have retrieved a range of SRMO near T_C of about 5.4 \AA (at least 4 \AA), which corresponds to $\nu \simeq 15$ (up to next nearest neighbors). Similar values are obtained in calculations of SRMO in Fe bulk and Fe surfaces [46, 47]. For Fe_N clusters, one finds a particularly high stability of ferromagnetism for $N \simeq 15$. The energy gain associated with the development of the magnetic moments, $\Delta E(N) = E(\mu) - E(\mu=0)$, is quite large around this size: $\Delta E(15) - \Delta E(\text{bulk}) \simeq 0.3 \text{ eV}$ [24, 25]. Furthermore, the energy involved in flipping a single local magnetic moment within Fe_{15} —as calculated by extending Hubbard–Hasegawa’s spin-fluctuation theory of itinerant magnetism [49–52] to finite clusters—is about 0.1 eV larger than for the bulk [32]. Therefore, $\nu = 15$ seems a reasonable estimation of the degree of SRMO in Fe clusters. For Ni, the SRMO is generally expected to be stronger than for Fe [65].

Table 5.1, summarizes our results for $\bar{\mu}_N(T > T_C)$. The comparison between experiment and the results neglecting SRMO (i.e., with $\nu = 1$) is very poor. The root mean square deviation σ amounts to $\sigma = 0.75 \mu_B$ for Fe_N and $\sigma = 0.21 \mu_B$ for Ni_N .

Table 5.1 Average magnetization per atom (in μ_B) of Fe_N and Ni_N clusters at high temperatures [$T > T_C(N)$] as calculated from Eq. (5.29), where ν refers to the size of the SRMO domain. For Fe $\nu_{\text{srmo}} = 15$, and for Ni $\nu_{\text{srmo}} = 19\text{--}43$. The experimental results are estimated from [6, 7]

	N	$\nu = 1$	$\nu = \nu_{\text{srmo}}$	Expt.
Fe_N	50–60	0.47–0.38	1.61–1.48	1.6 ± 0.2
	82–92	0.33–0.31	1.26–1.20	1.2 ± 0.2
	120–140	0.27–0.25	1.05–0.97	0.9 ± 0.1
	250–290	0.16–0.15	0.63–0.59	0.4 ± 0.05
	500–600	0.10–0.09	0.38–0.36	0.4 ± 0.05
Ni_N	140–160	0.06–0.05	0.39–0.24	0.36 ± 0.16
	200–240	0.05–0.04	0.33–0.20	0.24 ± 0.16
	550–600	0.03–0.02	0.17–0.11	0.11 ± 0.08

This rules out the disorder-local-moment picture for Fe and Ni clusters, as it is also the case for the bulk and for plane surfaces [46, 47, 65, 66]. On the contrary, the results including SRMO are in very good agreement with experiment for both Fe_N , with $\nu = 15$, and Ni_N , with $\nu = 19\text{--}43$ [$\sigma(\text{Fe}_N) = 0.12\mu_B$ and $\sigma(\text{Ni}_N) = 0.06\mu_B$, see Table 5.1]. These values of σ are of the order of the experimental uncertainties (about 7% [6, 7]). One concludes that the low- and high-temperature measurements of $\bar{\mu}_N(T)$ of Fe and Ni clusters [6, 7] are in accord and that the large observed values of $\bar{\mu}_N(T > T_C)$ provide a clear evidence for the existence of SRMO in these clusters above $T_C(N)$. These conclusions are also consistent with known surface and bulk properties of itinerant magnetism [46, 47, 65, 66].

Equation (5.29) can also be used to infer the degree of SRMO in clusters from the experimental results for $\bar{\mu}_N(T=0)$ and $\bar{\mu}_N(T > T_C)$. For example, assuming that ν is independent of N , the value of ν which minimizes the mean square deviations between the outcome of Eq. (5.29) and the experimental results for Fe_N ($25 \leq N \leq 700$) is $\nu = 13\text{--}15$. Two reasons should be mentioned, however, which indicate that from Eq. (5.29), one should tend to *underestimate* ν to a certain extent. First, in 3d TM, there is a reduction of the local magnetic moments as we go from $T = 0$ to $T = T_C$, which is a consequence of the itinerant character of the d -electrons and which amounts to about 10–15% in the solid [46, 47, 49–52]. Second, the statistical averages $\langle |\mu| \rangle$, which is the experimentally relevant one, and $\sqrt{\langle \mu^2 \rangle}$, which is the one used for deriving Eq. (5.29), differ: $\langle |\mu| \rangle \leq \sqrt{\langle \mu^2 \rangle}$ with $\langle |\mu| \rangle \propto \sqrt{\langle \mu^2 \rangle}$ (see [45]). Taking this into account, the degree of SRMO that one derives for the clusters might result to be somewhat larger than what is generally accepted in the corresponding solids, which could be related to the increase of the local magnetic moments and exchange splittings as calculated for $T = 0$ [21–25]. Clearly, the existence of SRMO *alone* cannot explain the full temperature dependence of $\bar{\mu}_N(T)$. As in the solid, there are many element-specific features to consider, such as the details of the electronic densities of states, the d -band filling, the Coulomb interaction strengths, and so on. These challenging questions are investigated in the following section.

5.5 Monte Carlo Simulations of Finite-Temperature Properties

The calculation of the partition function and derived magnetic properties involves two averages. The first one concerns the electronic degree of freedom of the effective single-particle Hamiltonian \hat{H}' and the second one the functional integration over the spin degrees of freedom. In practice, the averages over \hat{H}' are performed by using a grand-canonical ensemble with a ξ -dependent chemical potential that yields the appropriate fixed total number of electron electrons for all ξ . The average occupation of the eigenstates of \hat{H}' are given by the Fermi function $f(\varepsilon)$. Thus, the charge distribution and local spin moment for each exchange-field configuration are obtained straightforwardly by integrating the local densities of states (DOS) $\rho_{l\alpha\sigma}(\varepsilon)$ of \hat{H}' as

$$v_l = \langle \hat{N}_l \rangle' = \int_{-\infty}^{+\infty} \sum_{\alpha\sigma} \rho_{l\alpha\sigma}(\varepsilon) f(\varepsilon) d\varepsilon \quad (5.30)$$

and

$$\langle \hat{S}_{lz} \rangle' = \frac{1}{2} \int_{-\infty}^{+\infty} \sum_{\alpha\sigma} \sigma \rho_{l\alpha\sigma}(\varepsilon) f(\varepsilon) d\varepsilon. \quad (5.31)$$

The local DOS can be efficiently computed by using Haydock–Heine–Kelly’s recursion method [67].

In order to determine the relevant magnetic properties of an N -atom cluster, one needs to evaluate integrals over N exchange fields where each point involves an electronic calculation that is almost as involved as a ground-state one. The integration procedure must be therefore efficient and unbiased. In this context, the simple Metropolis Monte Carlo (MC) method [68] very often fails or needs far too long ergodicity times, if the energy landscape is complex, showing numerous local minima separated by large barriers. As shown in Sect. 5.3, this is the case for the free energy $F'(\xi)$ of Fe clusters since the magnetic states of positive and negative fields are in general separated by significant barriers. Several improvements have been proposed to overcome this difficulty [69–74]. The ergodicity times can be drastically reduced if several simulations are performed at different temperatures in a parallel way, enabling the exchange of configurations between the various temperatures [74]. In the exchange MC method, one considers many replicas of the system of interest, each of which is simulated simultaneously and independently at a different temperature using a conventional Metropolis MC algorithm. In addition to the usual local updates of the spin configurations ξ , one allows the exchange of configurations at nearby temperatures according to a Metropolis criterion, taking into account the involved energy difference between the configurations. This introduces additional nonlocal Markov steps by which a simulation at low temperature can escape from local minima. Further details of the parallel-tempering MC method may be found in [74], while specific applications in the context of the spin fluctuation of itinerant magnetism are discussed in [75]. In the following, we discuss results for the

temperature dependence of the average magnetizations, $\bar{\mu}_N(T)$ and $\bar{m}_N(T)$, local magnetic moments μ_l , and pair-correlation functions γ_k for Fe_N clusters having $N \leq 24$ atoms.

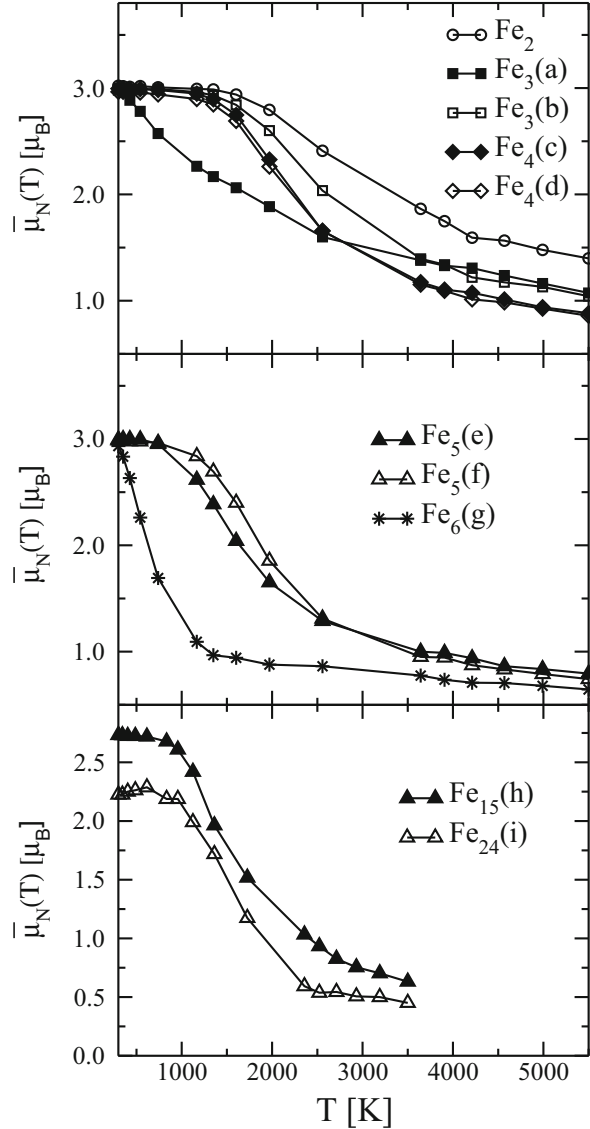
5.5.1 Average Magnetization

The results for temperature dependence of the average magnetization $\bar{\mu}_N$ given by Eq. (5.19) are shown in Fig. 5.7. Among the general common features of all curves, we observe the low-temperature saturation of $\bar{\mu}_N$ for small clusters [$\bar{\mu}_N(T \rightarrow 0) \simeq 3.0\mu_B$ for $N \leq 6$] and the enhancement of $\bar{\mu}_N(0)$ with respect to the bulk for $N = 15$ and 24. In the other extreme, at high temperatures ($T \gtrsim 4,000$ K), $\bar{\mu}_N$ is approximately constant as expected for a randomly disordered magnetic state. Notice that the high-temperature values are somewhat smaller than $\bar{\mu}_N(0)/\sqrt{N}$, which would be the result predicted by a simple localized Ising-like model.⁴ This reflects a moderate though significant reduction of the local magnetic moments μ_l , which can be ascribed to the delocalized character of the d -states. Notice that the high-temperature limit of $\bar{\mu}_N$, as well as of the local moments μ_l to be discussed below, is essentially independent of the details of the electronic structure and of the cluster geometry. It is mainly a statistical local effect. The temperature dependence linking the low and high T limits is not universal, i.e., it depends strongly on the cluster geometry and on the details of the single-particle spectrum. Remarkably, a strong structural dependence of $\bar{\mu}_N(T)$ is found, even in situations where the ground-state moments are saturated and therefore do not depend significantly on structure (e.g., in small clusters). The differences in $\bar{\mu}_N(T)$ are found to be very important in Fe_3 and to lesser extent in Fe_4 and Fe_5 (see Fig. 5.7). However, notice that at high temperatures, in the disordered-local-moment regime, the differences in $\bar{\mu}_N$ or \bar{m}_N among different isomers disappear completely even in cases where the deviations at low and intermediate temperatures are important (e.g., Fe_3 chain and triangle, or Fe_5 bipyramid and trust). This occurs for $T \simeq 2,500$ – $3,000$ K, where the pair-correlation functions essentially vanish.

The stability of cluster ferromagnetism can be quantified by the size-dependent temperature $T_C(N)$ corresponding to the inflection point in $\bar{\mu}_N(T)$. In the thermodynamic limit, $T_C(N)$ should converge to the bulk Curie temperature [45]. However, the physics behind $T_C(N)$ in small clusters should be different from the behavior expected in large nanoparticles and solids. In large systems, T_C defines naturally the temperature above which the long-range magnetic order disappears. Nevertheless, as discussed in Sect. 5.4, there is clear experimental evidence for a significant degree of SRMO in TM clusters above T_C [6, 56]. The size of the SRMO domains near T_C has been estimated to be $\nu = 15$ – 19 atoms [56]. For clusters that are smaller than the range of SRMO, it is no longer possible to increase the

⁴As in an N -step random walk the root mean square average of the total magnetic moment per atom of a cluster having N uncorrelated local moments of size μ_0 is μ_0/\sqrt{N} .

Fig. 5.7 Temperature dependence of the average magnetic moment per atom $\bar{\mu}_N(T)$ of Fe_N clusters [see Eqs. (5.19) and 5.20)]. The labels (a)–(i) refer to different structures (after [75])



entropy without destroying the energetically favorable local magnetic correlations. Therefore, the cluster “Curie” temperature in the limit of $N \lesssim v$ should tend to a higher temperature $T_{\text{SR}}(N)$ above which thermal fluctuations destroy the short-range correlations between the local magnetic moments, for example, between NN μ_l . This is probably the reason for the relatively large values of $T_C(N)$ derived from our calculations: $T_C(N) \simeq 1,500\text{--}2,500\text{ K}$ except for linear Fe_3 [$T_C(3) \simeq 750\text{ K}$] and square pyramid Fe_6 [$T_C(6) \simeq 750\text{ K}$].

Larger clusters like Fe_{15} and Fe_{24} have their own special interest since the present non-saturated spin moments, in contrast to the already discussed smaller ones. Moreover, 15–20 atoms is the typical size of a SRMO domain in Fe. For Fe_{15} , the average magnetic moment at very low temperatures is $\bar{\mu}_{15}(0) = 2.75\mu_{\text{B}}$ and $\bar{\mu}_{24}(0) = 2.25\mu_{\text{B}}$. These values are in agreement with previous works [24, 25, 76–79]. As T increases, $\bar{\mu}_N(T)$ remains close to the ground-state magnetization up to $T \simeq 800\text{--}1,000\text{ K}$. Here it starts a rapid decrease, reaching the disordered-local-moment limit for $T \simeq 2,500\text{ K}$, where $\bar{\mu}_N \simeq \bar{\mu}_N(0)/\sqrt{N}$. The fact that at these temperatures $\bar{\mu}_N$ is close to the average of randomly oriented local moments indicates that these clusters are completely disordered without any significant SRMO being left ($N = 15$ and 24 at $T \simeq 2,500\text{ K}$). This is in agreement with our previous discussion suggesting that $T_{\text{C}}(N) \simeq T_{\text{SR}}(N)$ for $N \lesssim \nu$, and is confirmed by more detailed calculations of the correlation functions γ_{lk} . From the inflection point of $\bar{\mu}_N(T)$, we obtain $T_{\text{C}} \simeq 1,500\text{ K}$ which is not far from the bulk value $T_{\text{C}}^{\text{CPA}}(\text{bulk}) = 1,600\text{ K}$ calculated using the same model and the coherent potential approximation (CPA) [48]. Interestingly, in the case of Fe_{24} , we find a slight low-temperature increase of $\bar{\mu}_{24}(T)$ with respect to $\bar{\mu}_{24}(0)$ (see Fig. 5.7). This unusual behavior reflects temperature-induced changes in the local electronic structure corresponding to the occupations of higher-spin states. A similar effect has been observed experimentally on large Co clusters [6, 17].

It is interesting to compare the temperature dependence of $\bar{\mu}_N$ for the most compact and highly symmetric clusters ($N = 2\text{--}5$) since the coordination numbers increase here very fast, almost linear with N . Remarkably, the calculations show that as N increases, $\bar{\mu}_N(T)$ decreases more rapidly with T (see Fig. 5.7). This means that at $T > 0$, the ferromagnetic order becomes comparatively less stable as N and the coordination number z increases. This trend is strictly opposite to the predictions of simple spin models (for instance, the Ising model). In fact, if one would attempt to derive an effective Ising or Heisenberg NN exchange coupling constant J by fitting our electronic calculations, one would conclude that J decreases rapidly with N or z (like $1/z$ or faster). Obviously, this surprising behavior has to be ascribed to the itinerant character of the d -states. As z increases, the d -band width increases and with it the relative importance of the kinetic energy as compared to the local exchange energy. This effect appears to be so strong in the case of small Fe clusters that it overcomes the fact that with increasing z the perturbation introduced by the fluctuations of an exchange field ξ_l affects a larger number of atoms and should thus imply a higher excitation energy.

5.5.2 Local Moments and Spin Correlations

The temperature dependence of the magnetic order within the cluster can be analyzed in more detail by considering the spin-correlation functions γ_{lk} [see Eq. (5.22)]. Comparing the various local moments $\mu_l = \sqrt{\gamma_{ll}}$ and interatomic γ_{lk}

allows us to understand the behavior of $\bar{\mu}_N = \sqrt{\sum_{lk} \gamma_{lk}}$ from a local perspective and at the same time gain a useful insight on the environment dependence of finite-temperature cluster magnetism. Figures 5.8 and 5.9 show our results for the pair-correlation functions and for the square of the local magnetic moments $\mu_l^2 = \gamma_{ll}$ of Fe_N clusters. The suffixes of γ_{lk} correspond to different nonequivalent atoms or pairs of atoms. An important feature common to all considered clusters is the remarkable stability of the local moments μ_l^2 at finite temperatures, which are reduced by at most 20–30% with respect to the ground state, even at the highest considered temperatures. Similar results are found in thin films and bulk Fe [48]. This simplifies the analysis of the temperature-dependent properties, at least to some extent, since in first approximation we may consider that the fluctuating moments have a fixed size. Thus, the magnetic moments preserve a local character despite the fact that the d -electrons are delocalized. This is physically quite plausible since the formation of local moments involves an energy of the order of $J\mu_l^2/4$ that is much larger than the typical spin-fluctuation energies. In addition, the narrowing of the d -band in clusters reduces the kinetic or band energy and tends to enhance the localized or directional character of spin fluctuations [24, 25]. The only exception we found to these trends is the moment at the center of a bcc-like Fe_{15} cluster. As will be discussed below, this is related to the fact that the $T = 0$ local moments are not saturated at this atom.

The temperature dependence of γ_{12} for Fe_2 and Fe_3 (triangle) follows the behavior of the corresponding $\bar{\mu}_N(T)$ curves as expected for highly symmetric clusters having local moments μ_l that depend weakly on temperature. One observes that the ground-state ferromagnetic coupling is almost fully preserved up to a relatively high temperature $T \simeq 1,500$ K. Above this temperature, γ_{12} decreases monotonically, remaining positive and approaching zero ($\gamma_{12} \ll \gamma_{11}$) at approximately $T \simeq 4,000$ K. For $T \gtrsim 4,000$ K the local moments fluctuate in an uncorrelated way and $\bar{\mu}_N \simeq \mu_l/\sqrt{N}$. As a first example of the role of cluster structure, it is interesting to compare the triangle with the linear chain. In linear Fe_3 , the ground state is ferromagnetic with saturated moments $\mu_l(0) \simeq 3\mu_B$, and therefore, the first NN and second NN correlation functions at $T = 0$ are $\gamma_{12}(0) \simeq \gamma_{13}(0) \simeq 9$. However, in this case, γ_{12} and γ_{13} decrease very rapidly, almost linearly in T already at very low temperatures (see Fig. 5.8c). Moreover, γ_{13} changes sign at $T \simeq 1,500$ K, showing weak antiferromagnetic (AF) correlations between second NNs ($\gamma_{13} < 0$). These antiferromagnetic correlations together with the fast decrease of the ferromagnetic NN γ_{12} are responsible for the rapid decrease of $\bar{\mu}_N(T)$ with increasing T . It is interesting to analyze the origin of the second NN antiferromagnetic correlations since they are also found in other clusters ($N = 4-6$) and since they provide some insight into the nature of the dominant spin fluctuations. First of all, one should notice that a negative γ_{13} cannot be understood in terms of uncorrelated local spin fluctuations or unconditional probabilities $p_+(i)$ and $p_-(i) = 1 - p_+(i)$ of having up and down moments at different sites i . In fact, in this case, one would have, using for simplicity a spin-1/2 Ising model, $\gamma_{13} = 1 - 4p_+^2(1 - p_+) > 0$ for all p_+ . Intuitively, in absence of any special correlations, it is clear that positive γ_{12} and γ_{23} should imply a positive γ_{13} . However, if one considers the correlated probabilities

Fig. 5.8 (Color online) Local magnetic moments μ_l and pair-correlation functions γ_{lk} in small Fe_N clusters having $N \leq 4$ atoms [see Eqs. (5.22) and (5.23)]. The numbers refer to the different atoms l or pairs of atoms lk as labeled in the inset figure

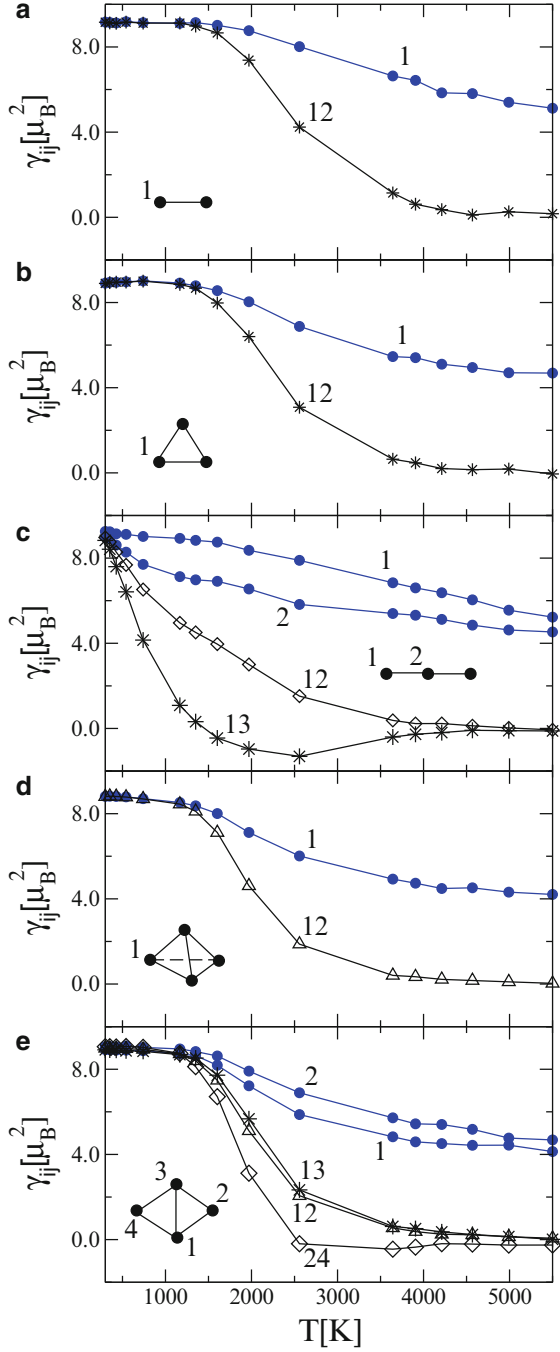
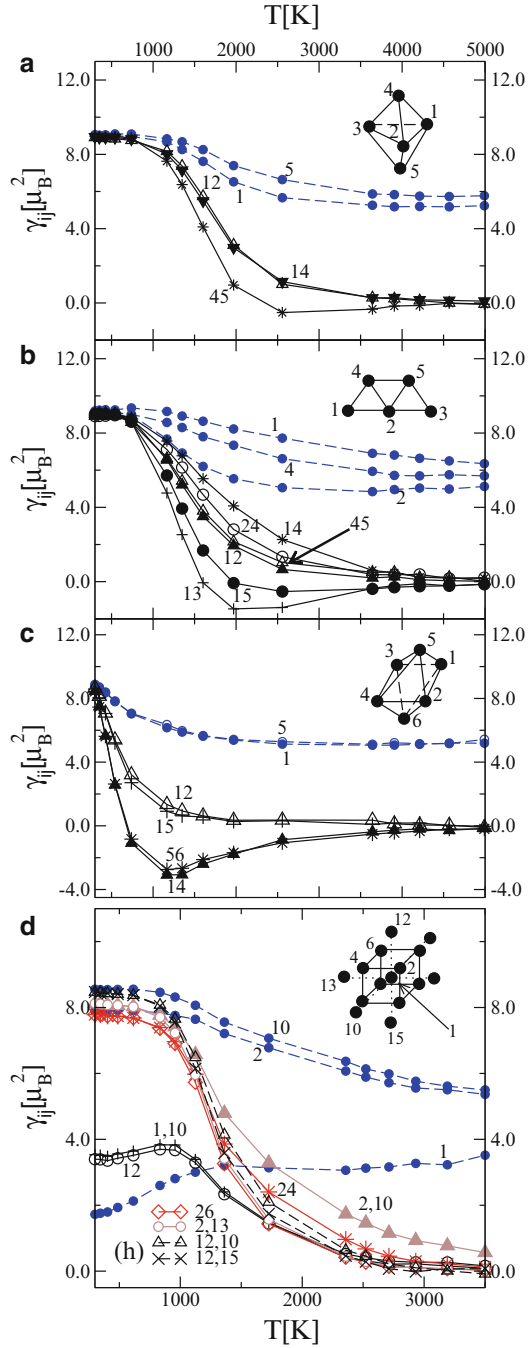


Fig. 5.9 (Color online)
Local magnetic moments μ_i
and pair-correlation functions
 γ_{ij} in Fe_N clusters having
 $5 \leq N \leq 15$ atoms [see
Eqs. (5.22) and (5.23)]. The
numbers refers to the
different atoms l or pairs of
atoms lk



$p_1 = p_{+++}$, $p_2 = p_{++-} = p_{-++}$ and $p_3 = p_{+-+}$ of all different configurations on a linear trimer ($\sum_i \xi_i \geq 0$), it is easy to show that $\gamma_{13} = 1 - 4p_2$. This is negative provided that p_3 does not increase significantly when p_1 decreases with increasing T [$\gamma_{13} < 0 \Leftrightarrow p_2 > (p_1 + p_3)/2$]. In other words, $\gamma_{13} < 0$ indicates that the dominant spin fluctuations in the linear trimer take place at the extremes of the chain, while spin flips at the central site are much less frequent. As we shall see, a similar analysis applies to larger clusters where the fluctuations at the lowest coordinated sites also dominate over those at the highest coordinated ones (e.g., the rhombus Fe_4 , trust Fe_5 , and square bipyramid Fe_6).

The pair-correlation functions of the Fe_4 clusters having rhombohedral and tetrahedral geometry are shown in Fig. 5.8c and d. Qualitatively, the tetrahedron resembles the triangle, while the rhombus shows the same main features as the linear trimer with ferromagnetic coupling between first NNs and antiferromagnetic coupling between second NNs above a certain T (see Fig. 5.8e for γ_{13} and γ_{24} , respectively). As before, the antiferromagnetic correlations result in a faster decrease of the average magnetization with increasing temperature.

Figure 5.9 shows the pair-correlation functions of Fe_N for $5 \leq N \leq 15$. For Fe_5 , we always find ferromagnetic-like correlations between NNs ($\gamma_{ij} > 0$), both for the bipyramid (Fig. 5.9a) and for the trust (Fig. 5.9b). In contrast, the second NNs correlations are antiferromagnetic-like above a temperature $T \simeq 1,500\text{--}2,500\text{ K}$, depending on the structure and pair of sites. This can be qualitatively understood by analogy with the linear trimer as an indication that the spin fluctuations at the atoms lying at the extremes of the cluster (e.g., $i = 4$ and $j = 5$ in the bipyramid, and $i = 1$ and $j = 3$ or 5 in the trust) are much more frequent than the fluctuations of the inner atoms. Notice that negative γ_{ij} are only possible when the average magnetic moments have significantly decreased. Comparing the various γ_{ij} of the two considered Fe_5 isomers, one first of all notes the larger dispersion of the results for the trust, a logical consequence of its lower symmetry. Moreover, one observes that the correlations in the trust decrease in general more rapidly than in the bipyramid. This is consistent with the idea that spin fluctuations are more frequent in weakly coordinated environments. However, for some particular pairs of atoms in the trust (e.g., $i = 1$ and $j = 4$), the FM correlations are systematically stronger than for any pair of atoms in the bipyramid. In the case of Fe_6 , the pair-correlation functions decrease much faster with increasing T than in any of the previously discussed clusters (see Fig. 5.9c). Moreover, the AF correlations between second NNs are particularly strong here (γ_{14} and $\gamma_{56} < 0$). They set in at about $T = 700\text{ K}$ and vanish only above $T = 3,000\text{ K}$. In contrast, the FM-like correlations γ_{12} and γ_{15} are rather weak and disappear above $T = 1,000\text{ K}$. The conjunction of these effects explains the very rapid decrease of $\bar{\mu}_N(T)$ and $\bar{m}_N(T)$ in this cluster (see Fig. 5.7).

The characteristic behavior found in very small low-symmetry clusters, i.e., FM correlations for first NNs and AF correlations for second NNs above $T \simeq 1,500$, no longer applies to Fe_{15} . In this case, all the correlation functions are positive (see, in particular, $\gamma_{1,10}$ and γ_{24} in Fig. 5.9c). Furthermore, the correlation functions between the pairs involving the central atom $i = 1$ (γ_{12} and $\gamma_{1,10}$) as well as the central local moment μ_1 show an unusual temperature dependence. They start from rather small

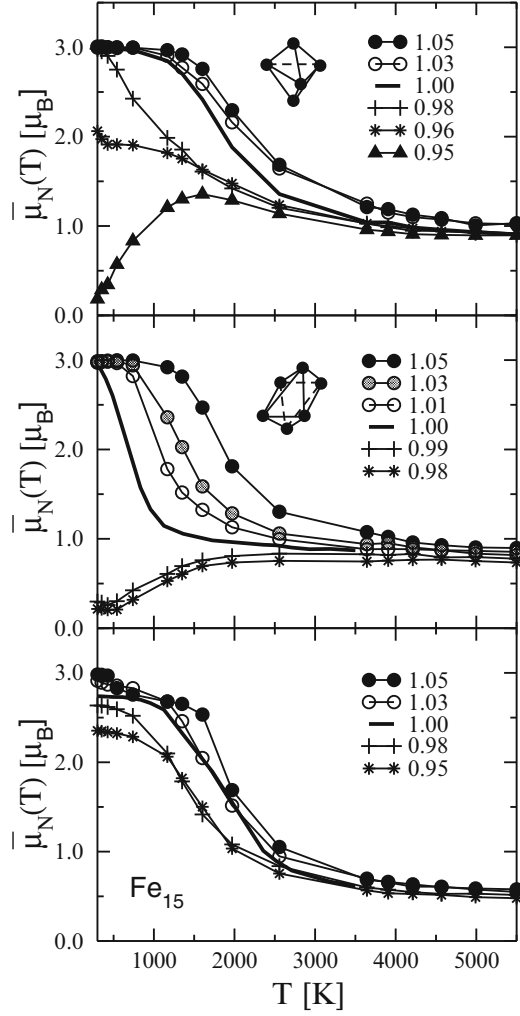
values at $T = 0$, and then *increase* with increasing T , as if they were driven by the still strong FM correlations between all the other atoms in the cluster (see Fig. 5.9c). A change of trend and a decrease of γ_{12} and $\gamma_{1,10}$ are only observed when the fluctuations are so important that the correlations between the atoms $i = 2-15$ start to decrease. This effect is most probably due to changes in the local electronic structure with temperature. It suggests that low-energy states with higher spin are occupied at $T > 0$. A similar behavior has been found in other clusters showing non-saturated ground-state moments including fully correlated exact-diagonalization studies of Hubbard clusters (López-Urías and Pastor, unpublished).

5.5.3 Bond-Length Relaxation Effects

The effects of structural relaxations local environment on the magnetic properties of Fe_N clusters have been investigated by varying the NN distance r . In this way, the interplay between kinetic and Coulomb energies can also be explored since r controls the d -band width and the energy associated with electron delocalization through the distance dependence of the hopping integrals t_{ij} [80–82]. In this work, we apply the relation $t_{ij} \sim r^{-5}$ as derived in [80–82]. As a result, the effective coupling constants between the local moments can be manipulated. In Fig. 5.10, the average magnetization curves $\bar{\mu}_N(T)$ of Fe_5 , Fe_6 , and Fe_{15} are given for different values of r . Before discussing the temperature dependence of $\bar{\mu}_N(T)$, a few comments on the ground-state moments $\bar{\mu}_N(0)$ are due. For large interatomic distances, one obtains saturated $\bar{\mu}_N(0) = 3\mu_B$, as expected for a very narrow d -band width. As r decreases, $\bar{\mu}_N(0)$ remains first saturated until r lies below a critical value that depends on size and structure [24, 25] (see Fig. 5.10). Finally, for very short r , the ground-state ferromagnetic order breaks down, and $\bar{\mu}_N(0) \rightarrow 0$. Notice that the changes in $\bar{\mu}_N(0)$ with r are very abrupt in small clusters due to the extreme discreteness of the single-particle spectrum.

At finite temperatures, one observes very different behaviors depending on the values of r . Let us first consider large distances where the ground-state moments are saturated. For the considered values of r ($r/r_b = 1.00-1.05$), $\bar{\mu}_N(T)$ decreases faster with increasing T when the NN distances are shorter. This is consistent with the trends found in smaller compact clusters, where a larger size or higher coordination number implies a reduction of the cluster “Curie” temperature. In this range of NN distances, magnetism is more stable when the delocalization or band energy is smaller (larger r/r_b). Notice that all the curves start at the same saturated magnetization per atom $\bar{\mu}_N(0) = 3\mu_B$. Therefore, the higher $T_C(N)$ cannot be ascribed to an enhancement of the local moments. If one attempts to interpret these results in the framework of an Ising or Heisenberg model, one must conclude that the effective exchange coupling between local moments J_{lk} *increases* with increasing NN distance. Of course, this trend cannot hold in the limit of very large r . One actually observes that the effective J_{lk} goes over a maximum and then decreases

Fig. 5.10 Bond-length dependence of the magnetization curves $\bar{\mu}_N(T)$ of Fe clusters [see Eqs. (5.19) and (5.20)]. Results are given for Fe₅ (*triangular bipyramid*), Fe₆ (*square bipyramid*), and Fe₁₅ (see Fig. 5.2e). The numbers indicate the ratio r/r_b between the NN distance r in the cluster and the bulk value r_b



if r is further increased. A similar distance dependence of T_C has been found in thin Fe films [48].

A more interesting temperature dependence of $\bar{\mu}_N(T)$ is found at smaller NN distances, where the $T = 0$ moments are not saturated and eventually almost vanish for very small r due to strong d -band broadening. Here, we observe a remarkable enhancement of $\bar{\mu}_N(T)$ with increasing T that indicates, as already mentioned before, the presence of higher-spin states that are populated at finite temperatures. At the same time, the local magnetic moments μ_l also increase with T . A similar effect is most probably at the origin of the finite-temperature increase of the magnetic moments observed in beam experiments on large Co clusters [6, 17]. Notice, moreover, that the simple relation for randomly orientated spins, $\bar{\mu}_N(T > T_C) = \bar{\mu}_N(0)/\sqrt{N}$,

is no longer valid in this range of NN distances. These results illustrate very clearly the important interplay of spin fluctuations and electronic structure and the subtle competition between localized and itinerant aspects of d -electron magnetism.⁵

5.6 Discussion

The finite-temperature magnetic properties of Fe_N clusters have been determined in the framework of a spin-fluctuation functional-integral theory and a parallel-tempering Monte Carlo simulation approach. In this way, both the cluster-specific electronic structure and the collective fluctuations of the magnetic degrees of freedom at all atoms are treated on the same footing. This is an important improvement with respect to single-site approximations [32, 48–53], which allows us to take into account and quantify the degree of SRMO in clusters. The study has revealed a variety of new interesting behaviors concerning the dependence of the finite-temperature magnetic properties of clusters as a function of size, structure, and interatomic distances. A remarkable non-monotonous temperature dependence of the average and local magnetizations has been found. The role of the local atomic environment has been studied by means of the interatomic spin-correlation functions and by varying the NN bond lengths. We have shown that simple Heisenberg or Ising models are not applicable straightforwardly to Fe clusters, since the electronic structure contributions and the itinerant character of the d -electrons are crucial for determining the magnetic behavior at finite temperatures.

A few comments should be made concerning the possible role of fluctuations of the cluster structure that can be induced by temperature and that could coexist with spin fluctuations of electronic origin considered in this chapter. Previous exact-diagonalization studies on the single-band Hubbard model have shown that the isomerization energies of magnetic clusters are often comparable to the spin-excitation energies (López-Urías and Pastor, unpublished). Although we expect the stability of ground-state structures to be higher in realistic d -band calculations, it is also true that the contributions of structural fluctuations to the temperature dependence cannot be excluded a priori. The effect could be particularly significant in weak unsaturated ferromagnets like Fe_N , which magnetic moments are known to be very sensitive to structure already for $T = 0$ [24, 25]. Moreover, as shown in this chapter, the stability of ferromagnetism at finite T also depends on cluster geometry. Therefore, the population of low-energy isomers can modify $\bar{\mu}_N(T)$, even

⁵From Fig. 5.10 it is possible to infer the distance dependence of cluster “Curie” $T_C(N)$. Despite changes as a function of size and structure, $T_C(N)$ always remains of the same order of magnitude as in the bulk. The actual value of T_C is the result of an interplay between two effects directly related to the reduction of the coordination numbers: the enhancement of local magnetic moments and the reduction of the number of NN couplings. For some clusters, this may lead to incidental compensations and to values of $T_C(N)$ close to the bulk one. However, in most cases one of the contributions dominates over the other (see Fig. 5.10).

if the $T = 0$ moments of the excited isomers are nearly the same as for the optimal geometry. In strong ferromagnets, the excited isomers are usually quite disordered magnetically when one reaches the temperatures at which they are significantly populated. In this case, their contribution to the ensemble average leads to a more rapid decrease of $\bar{\mu}_N(T)$. However, in systems with unsaturated moments, it is also conceivable to find excited isomers for which ferromagnetism is stronger and comparatively more stable. In such a situation, an increase of $\bar{\mu}_N(T)$ is possible. More detailed investigations taking into account electronic spin fluctuations and structural rearrangement on the same footing are certainly most interesting.

The results discussed in this chapter encourage further theoretical developments. The present functional-integral approach to spin fluctuations and the local method of calculations of the electronic structure are well suited to investigate more complex systems with reduced symmetry, such as clusters and nanostructures on surfaces or substrate effects on thin films. In particular, another interesting extension concerns the effects of the interactions at interfaces with nonmagnetic substrates in order to achieve a more realistic comparison with experiments on clusters deposited on surfaces. In addition, a number of methodological improvements seem worthwhile. The spin rotational symmetry of the effective Hamiltonian H' could be restored by introducing vector exchange fields ξ_i at each atom i . Thus, noncollinear magnetic order and transversal fluctuations of the exchange fields could be taken into account. These are likely to affect the magnetization curves and probably reduce the calculated values of T_C . As already discussed, incorporating structural fluctuations in the statistical average process is also desirable. Last but not least, the model can be readily extended to take into account spin-orbit interactions [30], and dipole-dipole interactions that are responsible for magnetic anisotropy and for spin reorientation transitions (SRT). In fact, temperature-driven SRT in thin films have been observed since long time ago [83–87]. The reorientation transitions are often interpreted phenomenologically in terms of competition between magnetic anisotropy free energy (MAFE) and dipole-dipole anisotropy. The theory presented in this work, should serve as a starting point to characterize the dominant electronic contributions and to reveal the microscopic mechanisms underlying such a remarkable phenomenon.

Acknowledgements This work was supported in part by CONACyT-Mexico (grant No. 62292), by the Deutsche Forschungsgemeinschaft, and by the Mexico-Germany exchange program PROALMEX. The authors (RGA and JDD) would like to acknowledge the kind hospitality and support of the University of Kassel.

References

1. Cox DM, Trevor DJ, Whetten RL, Rohlfing EA, Kaldor A (1985) Phys Rev B 32:7290
2. de Heer WA, Milani P, Châtelain A (1990) Phys Rev Lett 65:488
3. Bucher JP, Douglass DC, Bloomfield LA (1991) Phys Rev Lett 66:3052
4. Douglass DC, Cox AJ, Bucher JP, Bloomfield LA (1993) Phys Rev B 47:12874
5. Douglass DC, Bucher JP, Bloomfield LA (1992) Phys Rev B 45:6341

6. Billas IML, Becker JA, Châtelain A, de Heer WA (1993) *Phys Rev Lett* 71:4067
7. Billas IML, Châtelain A, de Heer WA (1994) *Science* 265:1682
8. Gerion D, Hirt A, Billas IML, Châtelain A, de Heer WA (2000) *Phys Rev B* 62:7491
9. Apse SE, Emmert JW, Deng J, Bloomfield LA (1996) *Phys Rev Lett* 76:1441
10. Knickelbein MB (2001) *J Chem Phys* 115:1983
11. Knickelbein MB (2007) *Phys Rev B* 75:014401
12. Binns C (2001) *Surf Sci Rep* 44:1
13. Zitoun D, Respaud M, Fromen M-C, Casanove MJ, Lecante P, Amiens C, Chaudret B (2002) *Phys Rev Lett* 89:037203
14. Lau JT, Föhlisch A, Nietubyc R, Reif M, Wurth W (2002) *Phys Rev Lett* 89:057201
15. Gambardella P, Rusponi S, Veronese M, Dhessi SS, Grazioli C, Dallmeyer A, Cabria I, Zeller R, Dederichs PH, Kern K, Carbone C, Brune H (2003) *Science* 300:1130
16. Bansmann J, Baker SH, Binns C, Blackman JA, Bucher J-P, Dorantes-Dávila J, Dupuis V, Favre L, Kechrakos D, Kleibert A, Meiwes-Broer K-H, Pastor GM, Perez A, Toulemonde O, Trohidou KN, Tuaille J, Xie Y (2005) *Surf Sci Rep* 56:189
17. Xu X, Yin S, Moro R, de Heer WA (2005) *Phys Rev Lett* 95:237209
18. Yin S, Moro R, Xu X, de Heer WA (2007) *Phys Rev Lett* 98:113401
19. Gruner ME, Rollmann G, Entel P, Farle M (2008) *Phys Rev Lett* 100:087203
20. See, for instance, Pastor GM (2001). In: Guet C, Hobza P, Spiegelman F, David F (eds) *Atomic clusters and nanoparticles, Lectures Notes of the Les Houches Summer School of Theoretical Physics*. EDP Sciences, Les Ulis/Springer, Berlin, p. 335ff
21. Lee K, Callaway J, Dhar S (1984) *Phys Rev B* 30:1724
22. Lee K, Callaway J, Kwong K, Tang R, Ziegler A (1985) *Phys Rev B* 31:1796
23. Lee K, Callaway J (1993) *Phys Rev B* 48:15358
24. Pastor GM, Dorantes-Dávila J, Bennemann KH (1988) *Phys B* 149:22
25. Pastor GM, Dorantes-Dávila J, Bennemann KH (1989) *Phys Rev B* 40:7642
26. Castro M, Jamorski Ch, Salahub D (1997) *Chem Phys Lett* 271:133
27. Reddy BV, Nayak SK, Khanna SN, Rao BK, Jena P (1998) *J Phys Chem A* 102:1748
28. Diéguez O, Alemany MMG, Rey C, Ordejón P, Gallego LJ (2001) *Phys Rev B* 63:205407
29. Guirado-López RA, Dorantes-Dávila J, Pastor GM (2003) *Phys Rev Lett* 90:226402
30. Pastor GM, Dorantes-Dávila J, Pick S, Dreyssé H (1995) *Phys Rev Lett* 75:326
31. Rollmann G, Gruner ME, Hucht A, Meyer R, Entel P, Tiago ML, Chelikowsky JR (2007) *Phys Rev Lett* 99:083402
32. Pastor GM, Dorantes-Dávila J, Bennemann KH (2004) *Phys Rev B* 70:064420
33. Andriotis AN, Fthenakis ZG, Menon M (2006) *Europhys Lett* 76:1088
34. Polesya S, Siper O, Bornemann S, Minár J, Ebert H (2006) *Europhys Lett* 74:1074
35. Pastor GM, Hirsch R, Mühlischlegel B (1994) *Phys Rev Lett* 72:3879
36. Pastor GM, Hirsch R, Mühlischlegel B (1996) *Phys Rev B* 53:10382
37. López-Urías F, Pastor GM (1999) *Phys Rev B* 59:5223
38. López-Urías F, Pastor GM, Bennemann KH (2000) *J Appl Phys* 87:4909
39. López-Urías F, Pastor GM (2005) *J Magn Mater* 294:e27
40. Jinlong Y, Toigo F, Kelin W (1994) *Phys Rev B* 50:7915
41. Jinlong Y, Toigo F, Kelin W, Manhong Z (1994) *Phys Rev B* 50:7173
42. Wildberger K, Stepanyuk VS, Lang P, Zeller R, Dederichs PH (1995) *Phys Rev Lett* 75:509
43. Nayak SK, Weber SE, Jena P, Wildberger K, Zeller R, Dederichs PH, Stepanyuk VS, Hergert W (1997) *Phys Rev B* 56:8849
44. Villaseñor-González P, Dorantes-Dávila J, Dreyssé H, Pastor GM (1997) *Phys Rev B* 55:15084
45. Binder K, Rauch R, Wildpaner V (1970) *J Phys Chem Solids* 31:391
46. Dorantes-Dávila J, Pastor GM, Bennemann KH (1986) *Solid State Commun* 59:159
47. Dorantes-Dávila J, Pastor GM, Bennemann KH (1986) *Solid State Commun* 60:465
48. Garibay-Alonso R, Dorantes-Dávila J, Pastor GM (2006) *Phys Rev B* 73:224429
49. Hubbard J (1979) *Phys Rev B* 19:2626
50. Hubbard J (1979) *Phys Rev B* 20:4584
51. Hasegawa H (1980) *J Phys Soc Jpn* 49:178

52. Hasegawa H (1980) *J Phys Soc Jpn* 963
53. Kakehashi Y (1981) *J Phys Soc Jpn* 50:2251
54. Moriya T (ed) (1981) *Electron correlation and magnetism in narrow-band systems*, vol. 29. Springer series in solid state sciences. Springer, Heidelberg
55. Vollhardt D et al. (1999) *Advances in solid state physics*, vol 38. Vieweg, Wiesbaden, p. 383
56. Pastor GM, Dorantes-Dávila J (1995) *Phys Rev B* 52:13799
57. Slater JC (1960) *Quantum theory of atomic structure*, vols. I and II. McGraw-Hill, New York
58. Mühlischlegel B (1968) *Z Phys* 208:94
59. Stratonovich RL (1958) *Sov Phys Dokl* 2:416
60. Hubbard J (1959) *Phys Rev Lett* 3:77
61. Nicolas G, Dorantes-Dávila J, Pastor GM (2006) *Phys Rev B* 74:014415
62. Muñoz-Navia M, Dorantes-Dávila J, Zitoun D, Amiens C, Chaudret B, Casanove M-J, Lecante P, Jaouen N, Rogalev A, Respaud M, Pastor GM (2008) *Faraday Discuss* 138:181
63. Muñoz-Navia M, Dorantes-Dávila J, Zitoun D, Amiens C, Jaouen N, Rogalev A, Respaud M, Pastor GM (2009) *Appl Phys Lett* 95:233107
64. Landau DP, Binder K (2005) *A guide to Monte Carlo simulations in statistical physics*, 2nd edn. Cambridge University Press, Cambridge
65. Korenman V, Prange RE (1984) *Phys Rev Lett* 53:186
66. Haines EM, Clauberg R, Feder R (1985) *Phys Rev Lett* 54:932
67. Haydock R (1980) In: Ehreinreich H, Seitz F, Turnbull D (eds) *Solid state physics*, vol. 35. Academic, New York, p 215
68. See for example, Newman MEJ, Barkema GT (1999) *Monte Carlo methods in statistical physics*. Oxford University Press, Oxford
69. Swendsen RH, Wang JS (1987) *Phys Rev Lett* 58:86
70. Wolff U (1989) *Phys Rev Lett* 62:361
71. Berg BA, Neuhaus T (1991) *Phys Lett B* 267:249
72. Berg BA, Neuhaus T (1992) *Phys Rev Lett* 68:9
73. Marinari E, Parisi G (1992) *Europhys Lett* 19:451
74. Hukushima K, Nemoto K (1996) *J Phys Soc Jpn* 65:1604
75. Garibay-Alonso R, Dorantes-Dávila J, Pastor GM (2009) *Phys Rev B* 79:134401
76. Guevara J, Parisi F, Llois AM, Weissmann M (1997) *Phys Rev B* 55:13283
77. Vega A, Dorantes-Dávila J, Balbás LC, Pastor GM (1993) *Phys Rev B* 47:4742
78. Postnikov AV, Entel P, Soler JM (2003) *Eur Phys D* 25:261
79. Sipr O, Kosuth M, Ebert H (2004) *Phys Rev B* 70:174423
80. Heine V (1967) *Phys Rev* 153:673
81. Harrison WA (1983) *Phys Rev B* 27:3592
82. Moruzzi VL, Marcus PM (1988) *Phys Rev B* 38:1613
83. Pappas DP, Kämper K-P, Hobster H (1990) *Phys Rev Lett* 64:3179
84. Allenpasch R, Bischof A (1992) *Phys Rev Lett* 69:3385
85. Qiu ZQ, Pearson J, Bader SD (1993) *Phys Rev Lett* 70:1006
86. Arnold CS, Pappas DP, Popov AP (1999) *Phys Rev Lett* 83:3305
87. Kukunin A, Prokop J, Elmers HJ (2007) *Phys Rev B* 76:134414

Part III
Thermodynamics and Kinetics
Using Semiempirical Approaches

Chapter 6

Global Optimization of Free and Supported Clusters

Riccardo Ferrando

6.1 Introduction

Aggregates of atoms of nanometric sizes (denoted as clusters or nanoparticles in the following) have been widely studied in the last decades due to their intriguing properties. In many cases, these properties depend on the nanoparticle structure, which in turn depends on size and, in the case of multi-component systems, on composition. For this reason, considerable efforts have been devoted to the determination of nanoparticle structures, both by experiments and calculations (see, e.g. [1]).

From the computational point of view, the problem is to determine the lowest-energy structure of a nanoparticle, starting from the knowledge of its size and composition. This is a highly non-trivial task, due to the enormous number of possible structures that a nanoparticle of given size and composition can assume. These structures belong to a large variety of structural motifs. These motifs comprise fragments of the bulk crystal structure (*crystalline motifs*) and structures that have no counterpart in the bulk crystal (*noncrystalline motifs*) such as icosahedra, decahedra and polyicosahedra [1, 2]. The noncrystalline motifs are possible because the constraint of lattice periodicity does not apply to nanoparticles, so that a much larger variety of structures is possible than in the bulk case.

For bi- and multi-component systems, the geometric structure is not the only important feature of the nanoparticle that has to be determined. In fact, it is important also to determine the way in which the different species are arranged within the nanoparticle, i.e. to determine its *chemical ordering*. Restricting to bi-component nanoparticles, we can identify several chemical ordering patterns, such as the core-shell, multi-shell, randomly intermixed, phase-ordered, and quasi-Janus

R. Ferrando (✉)

Dipartimento di Fisica dell'Università di Genova, via Dodecaneso 33, 16146, Genova, Italy
e-mail: ferrando@fisica.unige.it

patterns [3–11]. The number of possible chemical ordering patterns is enormous even for a given fixed geometric structure [12].

The possible structure of a nanoparticle of given size and composition can be identified with the stability points, i.e. with the *local minima* of its potential energy surface (PES) [13]. The PES is a function of the coordinates of all atoms of the nanoparticle and is denoted as $E(\{\mathbf{r}\})$. In the following, we assume that $E(\{\mathbf{r}\})$ is known and focus on the methods that are currently used to explore it and to search for its low-energy minima. The search for the lowest minimum on the PES is usually known as *global optimization* of the PES.

In practical cases, the form of $E(\{\mathbf{r}\})$ is determined either by first-principle methods (of which the most popular is density functional theory (DFT) [14]) or by atomistic interaction potentials, such as embedded atom method (EAM) potentials [15], or second-moment approximation tight-binding (SMATB) potentials [16–18].

First-principle methods are of general applicability, and in many cases, they are of great accuracy. Their main drawback is that they are very demanding from the computational point of view. This poses rather severe limits on the system sizes that can be actually treated and that are of a few ten atoms for single-element nanoparticles [19, 20]. And also for these small-size clusters, a true thorough exploration of the PES can be extremely cumbersome.

On the other hand, also atomistic approaches suffer from several drawbacks. In fact, the validity of an atomistic potential must be carefully checked for each system separately, because the approximations involved in atomistic modeling are not easily controllable a priori. Moreover, atomistic potentials miss specific quantum effects such as the electronic shell closure effect, which is important for clusters of small sizes (see [21] for a discussion of the interplay between geometric and electronic shell closure in AgCu and AuCu clusters of 40 atoms). For these reasons, the validity of atomistic approaches is strongly system dependent. However, atomistic approaches present several advantages. In fact, once an atomistic potential is validated, it allows an efficient and thorough exploration of the PES of large systems, containing hundreds of atoms [22]. Moreover, an atomistic potential can be used for studying many important processes well beyond the determination of low-energy structures. In fact, it allows the simulation of melting, growth, collision and coalescence of nanoparticles on long, experimentally relevant time scales [4, 5, 7, 23–26] that are not at all accessible to first-principle methods even for small clusters.

In order to overcome the drawbacks of first-principle and of atomistic potential modeling, a hybrid approach has been adopted by several groups [3, 6, 22, 27–39]. This approach consists of two steps. In the first step, an atomistic PES is defined and searched for by some global optimization procedure. The significant structural motifs are singled out, and a structural database is constructed in such a way that it contains the lowest minima of each structural motif. In the second step, the lowest minima of each motif are locally relaxed by first-principle methods, usually by DFT. After this relaxation, the results of the atomistic model can be compared to those resulting from the first-principle relaxation. If necessary, an effort can be made in trying to improve the atomistic potential parameterization, and the procedure can be iterated from the first step.

In the following chapters, we assume that the method for calculating the PES (either atomistic or first-principle) has been already chosen, so that we can focus on the global optimization procedures for exploring the PES and finding its low-energy minima. Applications to specific cases are discussed, both for gas-phase and substrate-supported nanoparticles.

6.2 Global Optimization Methods

The complexity of the problem of finding the lowest minimum of a function of many variables, such as the PES, is due to the large number of minima that such a function can present. In fact, we should expect an exponential increase of the number of local minima with size, as follows from a simple argument [40–43]. Let us divide the nanoparticle into n_s equivalent subsystems of N atoms each. Under the rather crude approximation that every subsystem has independent stable configurations, we find:

$$n_{\min}(n_s N) = [n_{\min}(N)]^{n_s}, \quad (6.1)$$

whose solution is an exponential

$$n_{\min}(N) = e^{cN}, \quad (6.2)$$

where the constant c depends on the system. As an example of the explosive growth of the number of minima with size, it has been estimated that in Lennard–Jones clusters, the number of minima increases from about 1,500 for size 13 to at least 10^{40} for a cluster of 40 atoms [44].

The complexity of global optimization drastically increases when considering bi- or multi-component systems. Let us consider a binary cluster of a given geometric structure. For a single-component system, this corresponds to a single local minimum. For a binary system, we can think of exchanging the positions of atoms of different species, thus obtaining new structures which share the same geometry (apart from some local relaxation) but with different chemical ordering. Isomers sharing the same geometry but differing in chemical ordering are known as *homotops*, a term that has been introduced by Jellinek and Krissinel [45]. In a $A_m B_n$ binary cluster, the number of homotops is given by

$$N_{\text{homotops}} = \frac{(n+m)!}{n!m!}. \quad (6.3)$$

Many of these homotops can be symmetry equivalent, but N_{homotops} is easily a huge number, with a factorial increase with system size.

From these considerations, one may deduce that the problem of finding the global minimum for PES of interest cannot be solved in practical cases. Indeed, the rigorous solution of this problem would imply to sample *all* minima of the PES

and compare their energies. This is clearly impossible for sizes exceeding a few atoms. For this reason, we note that all structures that will be denoted as “global minimum” (GM) in the following have to be intended as a *putative* global minima.

However, one must keep in mind that the practical scope of global optimization is to sample the low-energy part of the PES, i.e. the part of the PES whose statistical weight is important at low temperatures, and not to find of a single deep minimum. For example, it is not really important to find the best homotop out of an enormous number of them, but to single out the typical low-energy chemical ordering pattern, which usually corresponds to a large number of similar homotops that are in the same energy range.

Keeping this in mind, there are some features of nanoparticle PES that render global optimization feasible in most cases. Nanoparticle PES are usually organized in *funnels* [13, 46, 47]. A funnel is a region of the PES in which the pathways to its absolute minimum are sequences of monotonically decreasing minima separated by low-energy barriers. Within a given funnel, it is rather easy to develop an algorithm which quickly leads to its bottom. Minima belonging to the same funnel usually present similar structures. We can, for example, single out icosahedral funnels, decahedral funnels etc., on the same PES.

When the PES is organized in funnels, the main difficulty of its global optimization is finding all of them. In practical cases, funnels are usually separated by huge energy barriers, so that it is quite common that a search procedure remains trapped in the funnel that is encountered first. Another difficulty is that, when the nanoparticle size is large, even exploring a single funnel may become cumbersome.

In summary, a good global optimization algorithm should be able first to explore different funnels without being trapped forever in the initial one and then to reach quickly the minima at the bottom of each funnel. Several types of global optimization algorithms have been developed and applied to nanoparticles and nanoalloys.

Several algorithms have been developed in recent years and widely applied to the global optimization of nanoparticles. These comprise simulated annealing (see [48, 49] and references therein), genetic algorithms [50–52], minima hopping [53] and basin hopping (BH) [54]. In the following, we focus on the BH algorithm.

6.3 Basin Hopping

In this section, we concentrate on the BH algorithm, which has proved to be a very efficient global optimization tool. The structure of the BH algorithm is simple. It is a Monte Carlo algorithm with local minimization. However, its efficiency strongly depends on which moves are adopted to generate new configurations in the Monte Carlo procedure. For this reason, we concentrate in some details on the description of the main types of moves used in the simulations. Finally, we focus on two different algorithms, the parallel excitable walkers (PEW) and the HISTO algorithm, which have been developed as possible improvement of the BH algorithm.

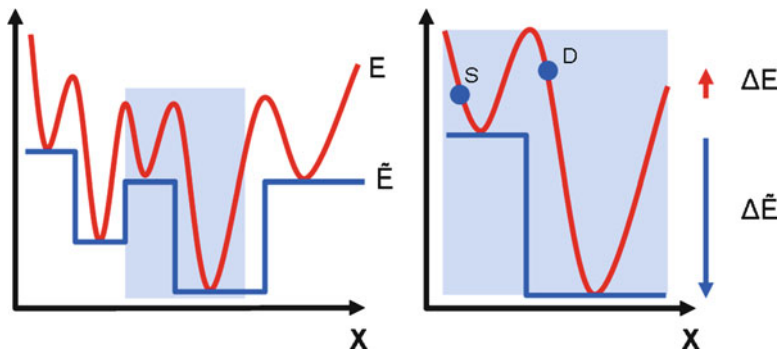


Fig. 6.1 Schematic one-dimensional representation of the transformation of a PES (red line) into a staircase function (blue line). From the right panel, it is evident that this transformation favours those points in configuration space that belong to basins of low-energy minima. Before the transformation, point D has a higher energy than point S . After the transformation, the opposite is true, with an exponential gain in the probability of sampling point S in an equilibrium simulation (from [43])

6.3.1 Structure of the BH Algorithm

The BH algorithm [54] is based on the thermal equilibrium sampling of a modified PES. In fact, the PES is transformed by associating at each point $\{\mathbf{r}\}$ the energy of the closest local minimum, i.e. the energy that is reached by a local minimization procedure starting at $\{\mathbf{r}\}$. In this way, the PES $E(\{\mathbf{r}\})$ is transformed into a staircase function $\tilde{E}(\{\mathbf{r}\})$, as schematically shown in Fig. 6.1. The transformed PES is then sampled by a Metropolis Monte Carlo procedure at a given simulation temperature T . This temperature is a parameter chosen in order to maximize the efficiency of the simulation.

As shown in Fig. 6.1, the transformation to \tilde{E} exponentially increases the probability of sampling the basins of low-energy minima. In order to understand this, consider two points in configuration space $\{\mathbf{r}_S\}$ and $\{\mathbf{r}_D\}$, belonging to different basins (as in Fig. 6.1) with $\Delta E = E(\{\mathbf{r}_D\}) - E(\{\mathbf{r}_S\}) > 0$. In an equilibrium simulation on E , the probability of visiting D is smaller than the probability of visiting S by a factor $\exp[-\Delta E/(k_B T)]$. However, after the transformation to \tilde{E} , the energy of D becomes lower than the energy of S because D belongs to the basin of a deeper local minimum. In this case, the probability of visiting D becomes larger than the probability of visiting S by the factor $\exp[\Delta \tilde{E}/(k_B T)]$, where $\Delta \tilde{E} > 0$ is the energy difference between the two local minima. It is also important to note that the transformation to \tilde{E} lowers the barriers between different local minima to the maximum possible extent, while keeping the energies of the local minima unaltered. However, this transformation does not eliminate the energy barrier between different funnels.

The structure of a BH search is quite simple. In a *unseeded* search, the initial configuration is generated by choosing randomly the coordinates of the cluster

atoms within a given (usually cubic or spherical) box. This random configuration is locally minimized. After this first local minimization, which gives \tilde{E}_0 , a loop is started. At step n in the loop, the locally minimized structure obtained at step $n - 1$ (of energy \tilde{E}_{n-1}) is perturbed by some kind of elementary *move* (see below for the description of typical moves), whose scope is to drive the cluster outside the basin of its present local minimum. After the move, local minimization is applied, so that the energy of a new trial local minimum, \tilde{E}_n^t , is obtained. If $\tilde{E}_n^t \leq \tilde{E}_{n-1}$, the transition to the new minimum is always accepted, putting $\tilde{E}_n = \tilde{E}_n^t$. If $\tilde{E}_n^t > \tilde{E}_{n-1}$, the move is accepted, with probability $\exp[-(\tilde{E}_n^t - \tilde{E}_{n-1})/k_B T]$. When the move is accepted $\tilde{E}_n = \tilde{E}_n^t$; if it is refused, $\tilde{E}_n = \tilde{E}_{n-1}$. Each time the simulation reaches a local minimum which is lower than all minima that were previously visited, the putative global minimum is updated. In a *seeded* search, the initial configuration is not chosen randomly, but it is some already known local minimum. From this seed, the simulation proceeds in the same way as an unseeded simulation.

The simulation temperature T is the only parameter that can be tuned in order to achieve the best efficiency of the algorithm. This is a very attractive feature of the BH algorithm, which does not require elaborate tuning procedures to achieve a good degree of efficiency. However, the choice of T may sometimes become problematic because conflicting needs are to be satisfied. In fact, when exploring a single funnel, the choice low T is more efficient, because it does not allow moves leading to energy increases, and therefore, the simulation is likely to arrive quite fast at the funnel bottom. On the other hand, if the simulation needs to explore different funnels, a high T is more appropriate, because the barriers separating the funnels are high and are not significantly lowered by the transformation to \tilde{E} . As we will see in the following, the optimal temperature may also depend on the type of move which is adopted in the simulation.

6.3.2 Elementary Moves

In the BH algorithm, the choice of appropriate elementary moves is crucial for the efficiency of the search. Generally speaking, a move is a perturbation of a local minimum structure. This perturbation should take into account two contrasting needs. First, the perturbation should be strong enough to lead the system outside the basin of its present local minimum. In fact, after a weak perturbation, local minimization drives the system back to the same configuration. In this case, the move is accepted by the Monte Carlo rule, but this does not produce a true change of configuration. However, the perturbation cannot be too strong, because a very strong perturbation is likely to drive to a very-high-energy local minimum which would not be accepted by the Monte Carlo rule. This would lead to very low acceptance rates giving an inefficient sampling of the PES. Depending on the system, a move must thus be tuned in order to achieve a reasonable acceptance rate of true configuration changes.

Here below follows a list of the most common moves used in BH searches.

6.3.2.1 Shake Move

Each atom is displaced from its present position within a sphere of radius r_s (of within a cube of given size [54]). The efficiency of the shake move is quite sensitive to the choice of r_s . Typical values of r_s are close to half of the nearest-neighbour distance between atoms. Smaller r_s are usually not sufficient to drive the cluster out of a local minimum. Larger r_s are likely to produce very low acceptance rates. The value of r_s can also be adjusted on the fly to achieve a target acceptance rate. Variants of the shake move displace only a fraction of the cluster atoms (even a single atom) or displace surface atoms by larger amounts than inner atoms.

6.3.2.2 Brownian Move

A short molecular-dynamics (or Langevin) simulation is run at high temperature T_B . Compared to the shake move, the Brownian move takes into account the features of the PES, so that it is less likely to produce unphysical configurations leading to very-high-energy minima, at the same time allowing strong rearrangements of the cluster. Moreover, it has been shown that molecular dynamics is very efficient in finding quickly low-lying saddle points that are likely to be connected to low-energy minima [55]. A disadvantage of this move with respect to the shake move is that the move itself is a short simulation run, which however requires several steps needing need computer time. This may slow down the search procedure by a non-negligible amount.

6.3.2.3 Shell Move

It is designed to improve the arrangement of the cluster surface. A single surface atom is displaced to a random position within a spherical shell which roughly corresponds to the external atomic layer of the cluster. The choice of the surface atom to be displaced can be made by assigning a probability depending on coordination, in order to move undercoordinated atoms and help them to find more favourable positions.

6.3.2.4 Exchange Move

This move is specific to bi- or multi-component systems. The positions of two atoms of different species are exchanged. This move is very important for optimizing chemical ordering in nanoalloys. Variants of this move include tailored exchanges [22]. For example, in a system which is known to segregate element B to the cluster surface, a tailored exchange can be defined as an exchange which involves only surface atoms of species A and inner atoms of species B .

An important point that has to be taken into account is that the optimal BH temperature T (not to be confused with the temperature of the Brownian move T_B) can depend on the specific move. As an example, let us consider the case of a binary system like AgPd, which shows a rather strong tendency to intermixing of the two species, producing however randomly intermixed configurations [38] in the interior part of the nanoparticles. In a BH search with shake moves, optimal temperatures for AgPd are above 1,000 K. These temperatures are necessary in order to obtain a good acceptance rate for moves producing significant changes in the geometric structure of the cluster. The same applies to the Brownian moves. On the contrary, in a BH search with exchange moves, the optimal temperatures are as low as 100 K. This is due to the fact that the energy difference between homotops can be very small, so that high T leads to the acceptance of high-energy homotops, with a worse optimization of chemical ordering. Because of this temperature difference, it is usually more efficient to run first a simulation with shake (or Brownian) moves, which serves to optimize the geometric structure. Then, seeded simulations at low T are run to optimize the chemical ordering of the significant geometries. Another way to overcome this problem is to assign different temperatures T to the different moves within the same simulation.

6.3.3 *Parallel Excitable Walkers Algorithm*

As explained previously, the transformation of the PES into a staircase function eliminates all energy barriers between minima belonging to a descending sequence. However, barriers between different funnels are not in such kind of a sequence, so that they are essentially unaltered by the PES transformation. As a consequence, a BH run can easily remain trapped inside the funnel to which its initial configuration belongs. To avoid this trapping, high-simulation temperatures may be used, but this could deteriorate the efficiency of sampling the funnel bottoms.

An approach that tries to combine the efficiency of BH in sampling the low-energy parts of funnels with an increased probability of exploring several different funnels is the PEW algorithm [56]. In the PEW algorithm, n_w Monte Carlo walkers perform BH searches of the PES in parallel. These walkers interact with each other by a rule based on an order parameter. The order parameter $p(\{\mathbf{r}\})$ should be chosen in such a way that different funnels are associated with different intervals of p .

A neighbouring relation between walkers is defined in the order parameter space. Given a distance δ , walkers a and b are neighbours if they satisfy

$$|p(\{\mathbf{r}_a\}) - p(\{\mathbf{r}_b\})| \leq \delta. \quad (6.4)$$

Another quantity which defines the PEW algorithm is the excitation energy E^* , which is used to facilitate the moves of walkers that have neighbours. The algorithm is structured as follows. At each step of the simulation, one walker is randomly chosen. If this walker has no neighbours, its move is either accepted or refused

according to the usual Metropolis criterion applied to $\Delta\tilde{E}$, exactly as in standard BH. If this walker has at least one neighbour, the Metropolis criterion is applied to $\Delta\tilde{E} - E^*$, where E^* is the excitation energy. This amounts to increasing the energy of the initial local minimum of the walker by the quantity E^* . Walkers with neighbours have thus much larger probability of having their moves accepted, so that they are likely to escape away from their neighbours. This procedure has proven to be efficient in exploring multiple-funnel PES [56], in both single-element nanoparticles and in nanoalloys. Typical values of E^* are in the range of 0.5 eV for transition metal nanoparticles. The distance δ is chosen in such a way that $2n_w\delta$ is about half of the variation range of p . The use of the excitation energy allows to employ low-simulation temperatures (in the range 100–500 K), so that walkers with no neighbours are very efficient in arriving at the bottom of their funnels.

The efficiency of the PEW algorithm depends on the choice of the order parameter. An order parameter is well chosen if it associates well-separated intervals to different funnels. Parameters deriving from the common neighbour analysis [57] have proven to be effective since they are able to distinguish crystalline structures, decahedra, icosahedra and polyicosahedra. Also, parameters measuring the degree of intermixing, such as the percentage of heterogeneous nearest-neighbour bonds, can be quite useful.

A good feature of the PEW algorithm is that it is robust against a bad choice of the order parameter (typically, a choice of an order parameter which associates the same range of values to different structural motifs). In fact, with a good choice of the order parameter, the PEW algorithm can achieve relevant improvements over pure BH. With a bad choice of the order parameter, the performance of PEW is essentially as good as that of BH [43, 56].

6.3.4 Basin Hopping with Memory: HISTO Algorithm

Another approach which may improve BH takes into account the history of the simulation, i.e. the memory of previously visited minima. In fact, while searching the PES for lower and lower minima, it may seem useless to explore again those regions which have been already visited. The HISTO algorithm uses the order parameter p to build up a coarse-grained memory of the regions of the PES that have already been visited. This algorithm adopts the same kind of approach of the energy landscape paving (ELP) algorithm of Hansmann and Wille [58] and of the metadynamics of Laio and Parrinello [59]. The main difference with respect to the ELP is that the HISTO algorithm samples the transformed PES after local minimization. On the other hand, the metadynamics is a molecular-dynamics procedure.

In the HISTO algorithm, a normalized histogram H is constructed on the fly by reporting the frequencies of visited minima which belong to different intervals of the order parameter space. The quantity E^* is defined by

$$\tilde{E}^* = \tilde{E} + wH(p), \quad (6.5)$$

where w is a positive weight and $H(p)$ is the height of the histogram for the value p of the order parameter which is associated with the minimum of energy \tilde{E} . The Metropolis criterion is applied to $\Delta\tilde{E}^*$:

$$\Delta\tilde{E}^* = \tilde{E}_2 - \tilde{E}_1 + w[H(p_2) - H(p_1)]. \quad (6.6)$$

If the order parameter interval of minimum 1 has been more frequently visited than the interval of minimum 2 one has, $H(p_1) > H(p_2)$, and therefore $\Delta\tilde{E}^* < \Delta\tilde{E}$. This means that the memory term increases the acceptance probability of moves to configuration 2. On the contrary, if $H(p_2) > H(p_1)$, the move is hindered.

The efficiency of the HISTO algorithm has been checked against BH and PEW in several examples [43,56]. The HISTO algorithm is more sensitive to the choice of the order parameter than PEW. If the choice is appropriate, improvements over BH can be more spectacular than in PEW. On the contrary, if the choice of p is such that different funnels are not mapped to different intervals, the performance of HISTO easily deteriorates. This is due to the following reason: If the order parameter assigns overlapping intervals to structures belonging to different funnels, to avoid revisiting order parameter regions which have been already explored can lead to an incomplete sampling of parts of the PES which may contain low-energy minima.

6.4 Global Optimization of Free Nickel Clusters

In this section, we consider the global optimization of pure Ni nanoparticles in gas phase. The PES of the nanoparticle is given by an atomistic SMATB interaction potential [60]. The results shown in this section are to be compared to those reported in the following about the structures of oxide-supported Ni nanoparticles.

6.4.1 Atomistic Model

In the atomistic model for Ni, the total potential energy E of the nanoparticle is written as the sum of single-atom contributions E_i , i.e. $E = \sum E_i$. E_i is a many-body term which depends on the ensemble $\{\mathbf{r}\}$ of the coordinates of all Ni atoms. Its functional form is derived within the second-moment approximation to the tight-binding model [16, 17] and reads:

$$E_i = E_i^b + E_i^r \quad (6.7)$$

with

$$E_i^r = \sum_{j \neq i, r_{ij} < r_c} A \exp \left[-p \left(\frac{r_{ij}}{r_0} - 1 \right) \right]; \quad (6.8)$$

$$E_i^b = - \left\{ \sum_{j \neq i, r_{ij} < r_c} \xi^2 \exp \left[-2q \left(\frac{r_{ij}}{r_0} - 1 \right) \right] \right\}^{\frac{1}{2}}, \quad (6.9)$$

where r_{ij} is the distance between atoms i and j and $r_0 = 2.49 \text{ \AA}$ is the nearest-neighbour distance in bulk Ni. r_c is the cut-off radius, which is usually chosen to include a few shells of neighbours [60]. The parameters (A, ξ, p, q) are usually fitted to experimental bulk quantities. In this case, we use the values $p = 11.73$, $q = 1.93$, $A = 0.084470 \text{ eV}$ and $\xi = 1.404973 \text{ eV}$ and a cutoff radius extending to the fifth-neighbour distance. This parameter set has been shown to reproduce well the experimentally observed structures for Ni nanoparticles adsorbed on magnesium oxide [37].

6.4.2 Results for Free Ni Clusters

We consider the size range from 38 up to about 100 atoms. The global optimization searches have been performed by means of BH and PEW algorithms [60]. Both algorithms perform well in this size range, which does not require huge computational efforts.

The global optimization searches show that the dominant motif in this size range is icosahedral because most of global minima are either incomplete icosahedra (below size 55, which is the geometric magic size for a perfect icosahedron) or icosahedra with an atomic island on its surface (above 55 atoms). In Fig. 6.2, we report the lowest-energy structure found for $N = 65$. This consists of the magic icosahedron of 55 atoms capped by an island with anti-Mackay stacking [61], which means that the island is adsorbed on hcp-like sites instead of fcc-like sites. With increasing size, the best islands shift to the usual Mackay fcc stacking. Exceptions to the predominance of icosahedra are size 38, which is a magic size for the fcc truncated octahedron, and sizes around 75 and 101, where we find Marks decahedra (see Fig. 6.2).

As we will see in the following, the interaction with the MgO substrate will strongly modify the preferential structures of Ni nanoparticles.

6.5 Global Optimization of Oxide-Supported Metallic Clusters: Ni, Ag and Au on MgO(001)

In this section, we focus on some applications of global optimization algorithms to the search for the low-energy structures of oxide-supported metallic nanoparticles. In the following examples, we consider the same substrate, the (001) surface of magnesium oxide and three different metals, nickel, silver and gold. The MgO(001) substrate presents a checkerboard arrangement of O and Mg sites. For Ni, Ag and

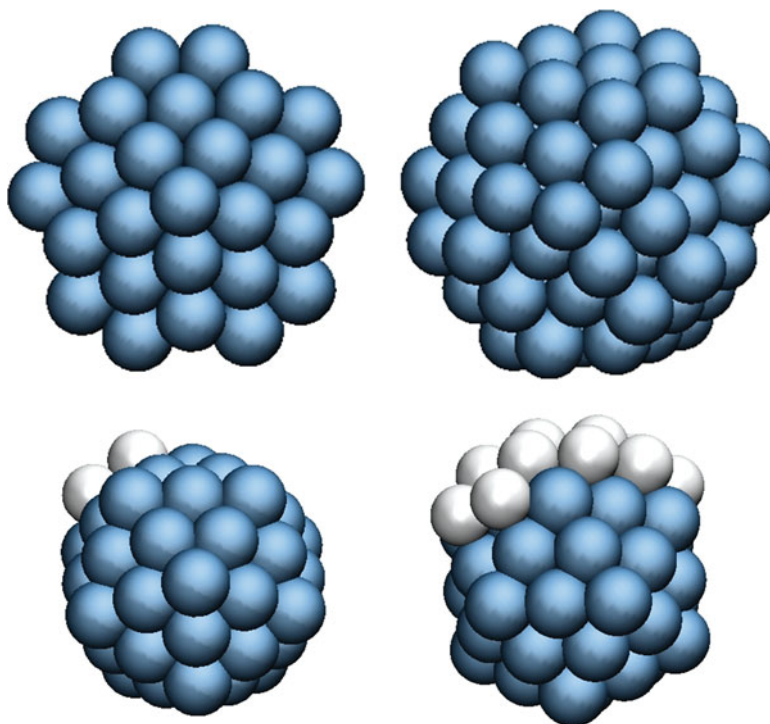


Fig. 6.2 Structures of gas-phase clusters. *Top row*: decahedral lowest-energy structures for sizes 75 (*left*) and 101 (*right*). *Bottom row*: two views of the lowest-energy structure at size 65. It is a 55-atom icosahedron capped by an island in anti-Mackay stacking. Atoms of the island are depicted in *light grey*. From [60]. Reproduced by permission of the PCCP Owner Societies

Au, the preferred adsorption sites are on top of oxygen atoms [37, 60, 62, 63]. Therefore, the lattice of adsorption sites is of square symmetry, with a distance between nearest-neighbour oxygen sites of about 2.98 Å.

Qualitative considerations show that we can expect that these metals may produce quite different structures on the MgO(001) substrate. In fact, Ni is characterized by a large lattice mismatch with the substrate. In bulk Ni, the distance between nearest neighbours is of 2.49 Å, which is much smaller than the distance between oxygens. On the other hand, Au and Ag present a much smaller lattice mismatch since their bulk nearest-neighbour distances are of 2.89 and 2.88 Å, respectively. These metals differ also with respect to the intensity of the interaction with the substrate: Ag interacts weakly, Ni interacts strongly and Au is intermediate [37, 62].

6.5.1 Atomistic Model for the Metal-Substrate Interactions

The PES of the oxide-supported nanoparticles is modeled as follows. The binding energy E of the adsorbed nanoparticles is written as a sum of two contributions:

$$E = E_{\text{met}} + E_{\text{sub}}, \quad (6.10)$$

where E_{met} is the metal–metal part, which is modeled by a SMATB potential as in the case of free nanoparticles and E_{sub} represents the metal–substrate interaction. E_{sub} is written as a sum of single-atom terms:

$$E_{\text{sub}} = \sum_i E_{\text{sub}}^i, \quad (6.11)$$

where the sum is on all atoms of the nanoparticle.

For E_{sub}^i , a many-body PES for metal–MgO(001) interactions is fitted on first-principles calculations in order to take into account the main features of the metal–MgO interaction [64]. This is a weak metal–oxide interaction, with no interdiffusion and small interfacial charge transfer, which is due principally to polarization and van der Waals interactions, with only a small contribution from covalent metal–oxygen bonds. This interaction is of many-body character, i.e. it depends on the metal coverage, so that a metal atom surrounded by other metal atoms has a weaker interaction with the substrate than an isolated adatom. A rigid substrate is assumed. The dependence of the interaction of a metal atom on the distance from the substrate (z) is reproduced via a Morse-like function, whereas a cosine function is used to model the dependence of the interaction energy on x and y coordinates. The functional form of E_{sub}^i is [65]:

$$E_{\text{sub}}^i(x_i, y_i, z_i, Z_i) = a_1(x_i, y_i, Z_i) \times \left\{ e^{-2a_2(x_i, y_i, Z_i)[z_i - a_3(x_i, y_i, Z_i)]} - 2e^{-a_2(x_i, y_i, Z_i)[z_i - a_3(x_i, y_i, Z_i)]} \right\},$$

with

$$a_j(x_i, y_i, Z_i) = b_{j1}(x_i, y_i) + b_{j2}(x_i, y_i)e^{-Z_i/b_{j3}(x_i, y_i)}$$

and

$$b_{jk}(x_i, y_i) = c_{jk1} + c_{jk2} \{ \cos(\chi x_i) + \cos(\chi y_i) \} + c_{jk3} \{ \cos(\chi(x_i + y_i)) + \cos(\chi(x_i - y_i)) \}.$$

Z_i is the number of metal nearest neighbours of atom i and $\chi = 2\pi/a$, with a the oxygen–oxygen distance in the substrate. The x and y coordinates are parallel to the $\langle 110 \rangle$ directions. Z_i is calculated including all neighbours within $1.25 r_0$, with r_0 the nearest-neighbour distance in the bulk metal. The metal–substrate interaction

has thus 27 parameters c_{jkl} that must be fitted. To some extent, the specific details of the fitting procedure are metal dependent. A more complete description of the fitting procedure can be found in [62, 65].

6.5.2 Global Optimization Results for Ni, Ag and Au on MgO(001)

6.5.2.1 Ni/MgO(001)

Ni/MgO(001) is a system characterized by a huge lattice mismatch between the nearest-neighbour distance in solid Ni and the lattice of adsorption sites on MgO. Moreover, the interaction of Ni with the substrate is rather strong. Because of the lattice mismatch, we expect that Ni will not accommodate easily in the cube-on-cube epitaxy which would continue naturally the substrate lattice. On the other hand, the strong interaction with the substrate indicate that adsorption is likely to produce major structural changes compared to the gas-phase structures shown in the previous section.

This is indeed the case. The global optimization results show that, for sizes below 40 atoms, there is no indication in favour of a preferential motif. However, when size increases above 40 atoms, a clear preference for hcp clusters is evident. In fact, almost all global minima found in the range 40–100 atoms belong to the hcp motif [60]. The preferential stability of hcp structures is confirmed also by DFT calculations on selected motifs for different sizes in this range [37]. We note that bulk Ni is an fcc crystal and that small Ni clusters are icosahedral in this range; therefore, the interaction with the substrate is crucial in stabilizing the hcp motif. In fact, in the hcp clusters, the close-packed planes (which alternate in ABABAB stacking) are perpendicular to the substrate and oriented in such a way that the c -axis of the hcp lattice coincides with either the (100) or the (010) direction of the substrate, as shown in Fig. 6.3.

For sizes larger than 100 atoms, global optimization becomes more and more difficult, but still feasible up to sizes of 500 atoms. For these large sizes, we have noted a better efficiency of the PEW algorithm with respect to BH and HISTO. The global minima still belong to the hcp motif. However, stacking faults begin to appear in the nanoparticles, i.e. in some parts of the cluster, some ABC sequence of close-packed planes can be seen [37].

When nanoparticle size increases further, we expect that a transition to the bulk fcc structure will take place. Unfortunately, the transition size is too large for being investigated by means of global optimization tools. In order to find this transition, hcp and fcc clusters have been built up for geometric magic sizes, locally relaxed and compared [37]. These calculations have shown that the transition from hcp to fcc clusters takes place in the size range between 2,000 and 2,500 atoms, corresponding to nanoparticle diameters of 4.5 nm in the surface plane.

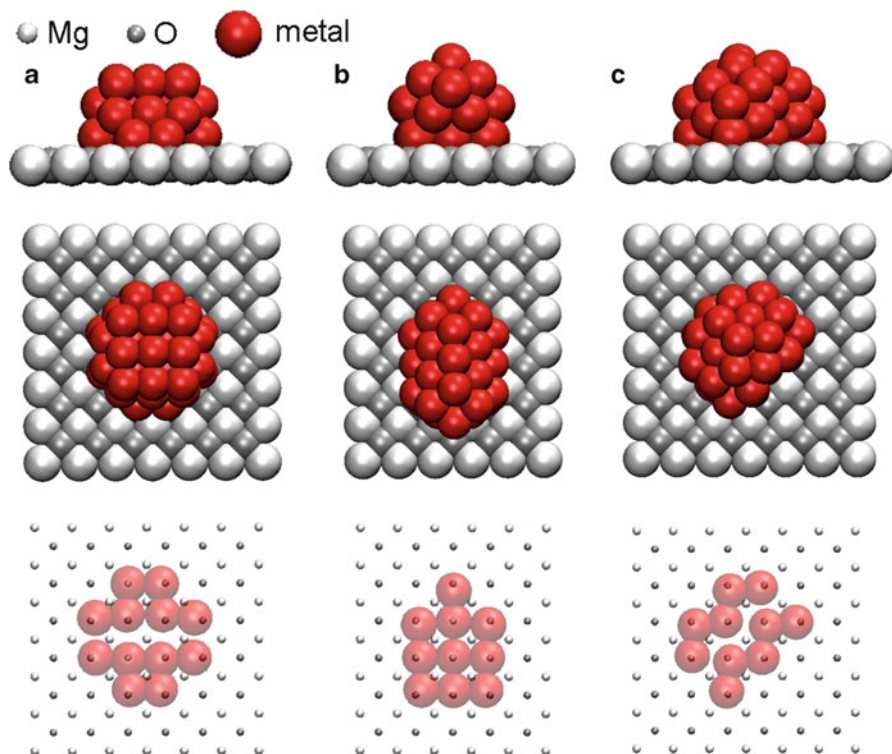


Fig. 6.3 Representative structures of the three significant structural motifs of 40-atom Ni nanoparticles on MgO: (a) fcc(001) motif, (b) fivefold motif, (c) hcp motif. From top to bottom, side, top and bottom views of the dots. The bottom view shows only the atoms that are in contact with the substrate. The fcc cluster presents a bad matching with the substrate already for small sizes. The fivefold motif is a decahedral fragment whose fivefold axis is parallel to the substrate surface. The hcp cluster presents a typical zigzag pattern at the interface with the substrate. This pattern matches the lattice of adsorption sites quite well. Reprinted with permission from [37]. Copyright 2008 American Chemical Society

These results are in good agreement with the experimental observations. This system has been studied experimentally by Tian et al. [66], who observed hcp Ni nanoparticles on MgO(001) for diameters below 5 nm and a transition to fcc structures for larger sizes. Moreover, they observed also the presence of more and more fcc stacking faults in the hcp nanoparticles as size increases.

6.5.2.2 Ag/MgO(001)

Ag presents a rather small lattice mismatch with MgO(001), and its interaction with the substrate is weaker than for Ni. We expect that the small size mismatch would favour a fcc cube-on-cube epitaxy. This is indeed the case. The global optimization searches show that three structural motifs are in competition for sizes

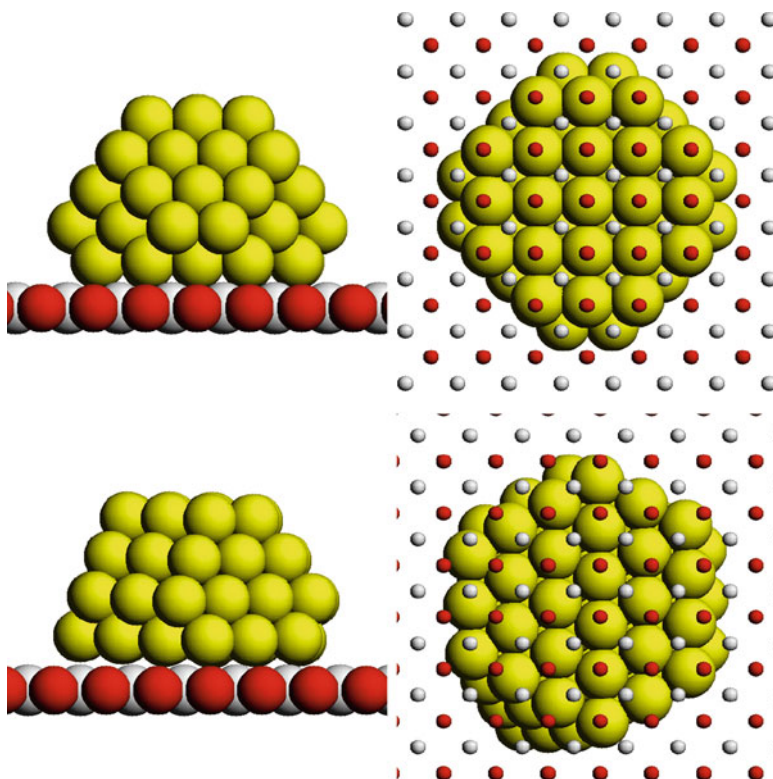


Fig. 6.4 Nanoparticles in fcc(001) and fcc(111) epitaxy (*left and right columns, respectively*). In the *bottom row*, we show the facet in contact with the substrate. Reprinted with permission from [62]

from 40 atoms on. Two motifs are fcc clusters, which differ by the type of epitaxy. The first motif is denoted as the fcc(001) motif because clusters belonging to this motif are in cube-on-cube epitaxy and present a (001) facet in contact with the substrate. The second motif is denoted as the fcc(111) motif because the clusters present a (111) facet in contact with the substrate, as shown in Fig. 6.4. A (111) facet has a worse matching with the square MgO(001) surface; however, it is possible to build up clusters with a larger contact area in this way, and this may compensate for the weaker adhesion per unit area. The third motif is decahedral, being made of decahedral fragments with the fivefold axis running parallel to the substrate.

According to the global optimization results, the fcc(001) motif is the most favourable in the size range up to 300 atoms [62] (the maximum size at which global optimization has been performed for this system). The lowest-energy clusters for size 90 are shown in Fig. 6.5. The second motif is the decahedral one, and the least favourable is the fcc(111) motif. Note that according to the same atomistic model, gas-phase clusters would not adopt fcc structures, but icosahedral or decahedral

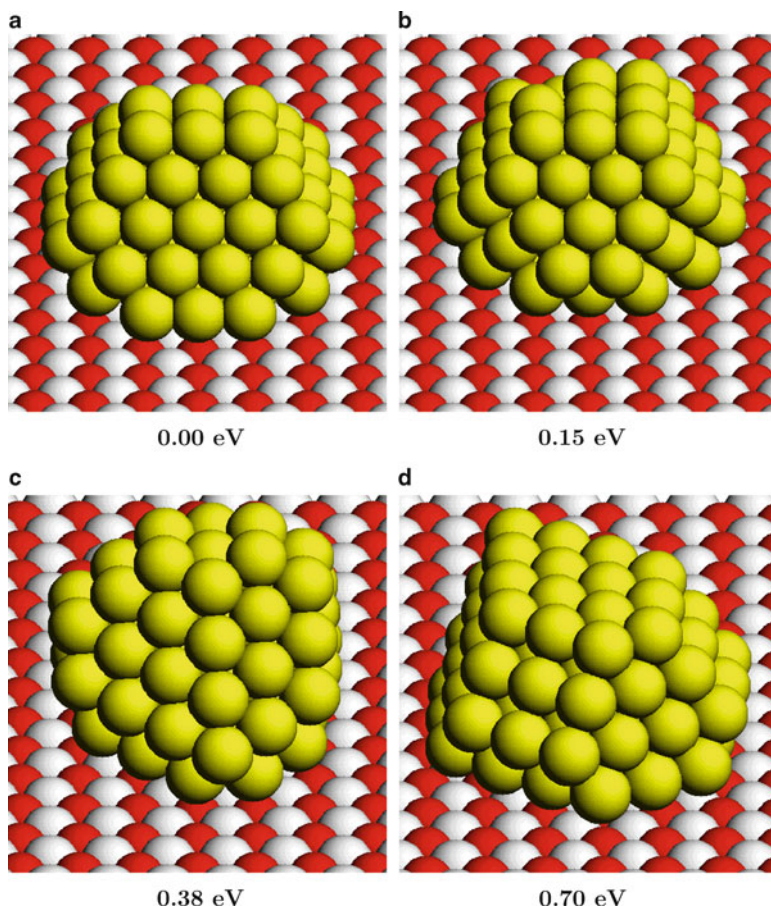


Fig. 6.5 Lowest-energy isomers for Ag/MgO(001) at size 90. Two fcc(001) clusters (*top row*), a decahedral and a fcc(111) cluster are shown, together with their energy difference from the global minimum, which is the structure in the *top left panel*. Reprinted with permission from [62]

ones, in this size range [23, 24, 67]. The interaction with the substrate is thus crucial in determining the nanoparticle structure. At variance with Ni/MgO, Ag nanoparticles adopt the same structure as bulk Ag, which is fcc.

It is interesting to study the competition of these motifs for sizes larger than 300 atoms. In fact, the Wulff–Kaischew construction [68, 69] predicts a transition from the fcc(001) to the fcc(111) epitaxy in the limit of large sizes [62], in which the fcc(111) epitaxy should be slightly favoured. The competition between fcc(001) and fcc(111) clusters has thus been investigated by building up structures at geometric magic sizes, finding that the fcc(001) motif prevails at least up to 3,000 atoms.

Also, for Ag/MgO(001), our results compare favourably with the experiments. In fact, fcc(001) structures are experimentally observed for all sizes [70, 71]. Moreover,

the aspect ratio (i.e. the ratio between the diameter in the $x - y$ plane and the height of the cluster) of these experimental fcc(001) clusters is close to the aspect ratio of the optimal clusters obtained in the simulations [62].

6.5.2.3 Au/MgO(001)

The lattice mismatch between Au and MgO is small as in the case of Ag, but the interaction with the substrate is stronger. The global optimization searches single out the same motifs as in Ag for sizes between 40 and 300 atoms [62]. Note that, for smaller sizes, DFT calculations indicate that the lowest-energy structures are either two-dimensional leaflets or empty cages [63, 72]. For sizes above 40 atoms, the lowest-energy motif is fcc(001), as in Ag. At variance with Ag, the second motif is fcc, and the third is decahedral. Indeed, fcc(001) and fcc(111) motifs are in rather close competition. This suggests that there could be a crossover with increasing size, also because the Wulff–Kaischew construction indicates that the fcc(111) epitaxy should be clearly lower in energy in the limit of macroscopic crystals. For this reason, the energetics of fcc(001) and fcc(111) nanoparticles have been investigated for sizes above 300 by building up perfect structures at geometric magic numbers. It turns out that there is a crossover towards the fcc(111) epitaxy for sizes above 1,200 atoms [62].

Let us compare these findings with the experimental results. The results by Pauwels et al. [73] show that Au/MgO(001) nanoparticles of sizes up to about 1,000 atoms are fcc nanocrystals in (001) epitaxy. This is consistent with our findings of a crossover above 1,000 atoms. Moreover, the aspect ratios of our optimal clusters fall in the interval of the experimentally measured aspect ratios that are however covering a rather wide interval, while the simulated aspect ratios fall in a narrower interval. The experiments confirm also that a crossover to fcc(111) epitaxy should take place, even though the crossover size is not yet determined. In fact, the observation of much larger nanocrystals (diameter of 10 nm and more) shows a majority of fcc(111) structures [69].

6.6 Conclusions

In conclusion, we have shown that global optimization techniques are reliable tools for searching for the low-energy structures of nanoparticles for systems and sizes of interest in experiments. The global optimization searches are often able to single out unexpected nanoparticle structures, both for free gas-phase clusters and for supported clusters. The results of these searches can be readily compared with experimental results. Moreover, the knowledge of low-energy minima is the starting point from which the statistical mechanics of a nanoparticle can be studied on a firm basis. For these reasons, we believe that the development of more and more efficient algorithms to deal with systems and models of increasing complexity is a very important field in nanoscience.

References

1. Baletto F, Ferrando R (2005) *Rev Mod Phys* 77:371
2. Marks LD (1994) *Rep Prog Phys* 57:603
3. Ferrando R, Jellinek J, Johnston RL (2008) *Chem Rev* (Washington, DC) 108:845
4. Baletto F, Mottet C, Ferrando R (2002) *Phys Rev B* 66:155420
5. Baletto F, Mottet C, Ferrando R (2003) *Phys Rev Lett* 90:135504
6. Rossi G, Rapallo A, Mottet C, Fortunelli A, Baletto F, Ferrando R (2004) *Phys Rev Lett* 93:105503
7. Mariscal MM, Dassie SA, Leiva EPM (2005) *J Chem Phys* 123:184505
8. Fromen MC, Morillo J, Casanove MJ, Lecante P (2006) *Europhys Lett* 73:885
9. Cheng DJ, Wang WC, Huang SP (2006) *J Phys Chem B* 11:16193
10. Ferrer D, Torres-Castro A, Gao X, Sepulveda-Guzman S, Ortiz-Mendez U, Jose-Yacamán M (2007) *Nano Lett* 7:1701
11. Parsina I, Baletto F (2010) *J Phys Chem C* 114:1504
12. Lordeiro RA, Guimaraes FF, Belchior JC, Johnston RL (2003) *Int J Quantum Chem* 95:112
13. Wales DJ (2003) *Energy landscapes*. Cambridge University Press, Cambridge
14. Martin RM (2004) *Electronic structure: basic theory and practical methods* Cambridge University Press, Cambridge
15. Daw MS, Baskes MI (1984) *Phys Rev B* 29:6443
16. Cyrot-Lackmann F, Ducastelle F (1971) *Phys Rev B* 4:2406
17. Gupta RP (1985) *Phys Rev B* 23:6265
18. Rosato V, Guillopé M, Legrand B (1989) *Philos Mag* A59:321
19. Aprà E, Ferrando R, Fortunelli A (2006) *Phys Rev B* 73:205414
20. De S, Ghasemi SA, Willand A, Genovese L, Kanhere D, Goedecker S (2011) *J Chem Phys* 134:124302
21. Barcaro G, Fortunelli A, Rossi G, Nita F, Ferrando R (2006) *J Phys Chem B* 110:23197
22. Bochicchio D, Ferrando R (2010) *Nano Lett* 10:4211
23. Baletto F, Mottet C, Ferrando R (2000) *Phys Rev Lett* 84:5544
24. Baletto F, Mottet C, Ferrando R (2001) *Phys Rev B* 63:155408
25. Toai TJ, Rossi G, Ferrando R (2008) *Faraday Discuss* 138:49
26. Paz SA, Leiva EPM, Jellinek J, Mariscal MM (2011) *J Chem Phys* 134:094701
27. Garzon IL, Michaelian K, Beltran MR, Posada-Amarillas A, Ordejon P, Artacho E, Sanchez-Portal D, Soler JM (1998) *Phys Rev Lett* 81:1600
28. Wales DJ, Hodges MP (1998) *Chem Phys Lett* 286:65
29. Calvo F, Tran S, Blundell SA, Guet C, Spiegelmann F (2000) *Phys Rev B* 10394:62
30. Soler JM, Beltrán MR, Michaelian K, Garzón IL, Ordejón P, Sanchez-Portal D, Artacho E (2000) *Phys Rev B* 61:5771
31. Hartke B (2002) *Angew Chem Intl Ed* 41:1468
32. Paz-Borbón LO, Johnston RL, Barcaro G, Fortunelli A (2007) *J Phys Chem C* 111:2936
33. Paz-Borbón LO, Johnston RL, Barcaro G, Fortunelli A (2008) *J Chem Phys* 128:134517
34. Paola CD, Baletto F (2011) *Phys Chem Chem Phys* 13:7701
35. Ferrando R, Fortunelli A, Johnston RL (2008) *Phys Chem Chem Phys* 10:640
36. Barcaro G, Fortunelli A, Rossi G, Nita F, Ferrando R (2007) *Phys Rev Lett* 98:156101
37. Ferrando R, Rossi G, Nita F, Barcaro G, Fortunelli A (2008) *ACS Nano* 2:1849
38. Negreiros FR, Barcaro G, Kuntová Z, Rossi G, Ferrando R, Fortunelli A (2010) *J Chem Phys* 132:234703
39. Barcaro G, Ferrando R, Fortunelli A, Rossi G (2010) *J Phys Chem Lett* 1:111
40. Stillinger FH, Weber TA (1982) *Phys Rev A* 25:978
41. Stillinger FH, Weber TA (1984) *Science* 225:983
42. Stillinger FH (1999) *Phys Rev E* 59:48
43. Rossi G, Ferrando R (2009) *J Phys Cond Mat* 9:084208
44. Leary RH (2000) *J Global Opt* 18:367

45. Jellinek J, Krissinel EB (1999) Theory of atomic and molecular clusters. Springer, Berlin
46. Becker OM, Karplus M (1997) *J Chem Phys* 106:1495
47. Doye JPK, Miller MA, Wales DJ (1999) *J Chem Phys* 110:6896
48. Binggeli N, Martins JL, Chelikowsky JR (1992) *Phys Rev Lett* 68:2956
49. Wales DJ, Scheraga HA (1999) *Science* 285:1368
50. Hartke B (1993) *J Chem Phys* 97:9973
51. Deaven DM, Ho KM (1995) *Phys Rev Lett* 75:288
52. Johnston RL (2003) *Dalton Trans.* 4193
53. Goedecker S (2004) *J Chem Phys* 120:9911
54. Wales DJ, Doye JPK (1997) *J Phys Chem A* 101:5111
55. Sicher M, Mohr S, Goedecker S (2011) *J Chem Phys* 134:044106
56. Rossi G, Ferrando R (2006) *Chem Phys Lett* 423:17
57. Faken D, Jónsson H (1994) *Comput Mater Sci* 2:279
58. Hansmann UHE, Wille LT (2002) *Phys Rev Lett* 88:068105
59. Laio A, Parrinello M (2002) *Proc Natl Acad Sci USA* 99:12562
60. Rossi G, Anghinolfi L, Ferrando R, Nita F, Barcaro G, Fortunelli A (2010) *Phys Chem Chem Phys* 12:8564
61. Harris IA, Kidwell LS, Northby JA (1984) *Phys Rev Lett* 53:2390
62. Ferrando R, Rossi G, Levi AC, Kuntová Z, Nita F, Barcaro G, Fortunelli A, Jelea A, Mottet C, Goniakowski J (2009) *J Chem Phys* 130:174702
63. Ferrando R, Barcaro G, Fortunelli A (2009) *Phys Rev Lett* 102:216102
64. Goniakowski J, Mottet C, Noguera C (2006) *Phys Stat Sol B* 243:2516
65. Vervisch W, Mottet C, Goniakowski J (2002) *Phys Rev B* 65:245411
66. Tian W, Sun HP, Pan XQ, Yu JH, Yeadon M, Boothroyd CB, Feng YP, Lukaszew RA, Clarke R (2005) *Appl Phys Lett* 86:131915
67. Baletto F, Ferrando R, Fortunelli A, Montalenti F, Mottet C (2002) *J Chem Phys* 116:3856
68. Wulff G (1901) *Z Kristallogr* 34:449
69. Henry CR (2005) *Prog Surf Sci* 80:92
70. Robach O, Renaud G, Barbier A (1998) *Phys Rev B* 60:5858
71. Revenant C, Renaud G, Lazzari R, Jupille J (2006) *Nucl Instr Meth B* 246:112
72. Ferrando R, Barcaro G, Fortunelli A (2011) *Phys Rev B* 83:045418
73. Pauwels B, Tendeloo GV, Bouwen W, Kuhn LT, Lievens P, Lei H, Hou M (2000) *Phys Rev B* 62:10383

Chapter 7

Structure and Chemical Ordering in Nanoalloys: Toward Nanoalloy Phase Diagrams

Christine Mottet

7.1 Introduction

Bulk alloys have received a large interest in the second part of the twentieth century with the industrial development in the transports, the nuclear energy, or catalysis. Indeed, the mixing of two or more metals has become a way to improve and design new properties either mechanical or electronic but also in the heterogeneous-catalysis for the activity/selectivity of the reactions. A fundamental study of the order and structure of bulk alloys has been given by F. Ducastelle [1] where the modern tools of solid state physics (electronic structure and statistical dynamics) are described to understand ordering effects in alloys and to determine phase diagrams. The phase diagrams represent the different phases of a system as a function of its concentration and the temperature (zero pressure). It is an essential tool in order to address a system, at least for what concerns its equilibrium properties [2]. These phases (order or phase separate) are the results, at low temperature, of the interatomic interactions. In a simple pair interaction model, the way to characterize the tendency of a system made of element *A* and element *B* to order or phase separate is given by the sign of the so-called *V* interactions defined as:

$$V = \frac{1}{2}(V_{AA} + V_{BB} - 2V_{AB}), \quad (7.1)$$

where V_{AA} , V_{BB} , and V_{AB} are the homo-atomic and heteroatomic pair interactions. These interactions being negative, $V > 0$ means the system has the tendency to order and $V < 0$ means the system prefers to phase separate. In the first case, the system makes ordered phase (ordered compounds) at low temperature which can chemically disorder above a critical temperature, while remaining on a crystalline

C. Mottet (✉)

CINaM-CNRS, Campus de Luminy, case 913, 13288 Marseille Cedex 9, France

e-mail: mottet@cinam.univ-mrs.fr

solid (solid solution) before melting at higher temperature. In the second case, the solubility limit increases with the temperature until it leads to a solid solution at high temperature eventually or not before melting. More recently, the alloys have been studied in presence of a surface (alloys surfaces) giving rise to possible “surface alloys” which were new compounds developed near the surface [3].

Following the size reduction, the new systems of interest are the alloy nanoparticles or “nanoalloys”. These systems have been used a long time ago, for example, in antic art or medieval stained glass, because of their optical properties (various color) but of course in a fully empirical way. The first to identify devised metal (gold) particles in colloidal solutions was Michael Faraday at the Royal Institution in 1857 [4]. Today, these metallic nanoparticles are widely used in many different industrial domains such as the chemical industry but still in a rather empirical way. The fundamental research on these systems aims at rationalizing the link between the structure and the chemical activity of nanoparticles and nanoalloys [5, 6]. Experimental and theoretical studies of bimetallic clusters showed that the size effect associated with the alloying effect provides interesting catalytic properties notably in the optimization of the reactivity/selectivity [7, 8]. With the recent development of nanotechnology and nanosciences, bimetallic clusters found also some applications in various domain going from the ultra-high density data storage [9] to plasmonic [10, 11] and biomedical applications [12–14]. The first review on nanoalloys has been realized by Ferrando et al. [15] in 2008, following a Faraday discussion [16]. The goal of this contribution is to make a short review on the recent theoretical developments in the description of phase diagrams in nanoalloys. This means how to include the finite size effects and the size variation in the structure and chemical ordering of nanoalloys going from some hundreds to some thousands of atoms in a particle. Some experimental studies will be reported in order to compare the theory with the experiences. Theoretical tools are essentially the numerical simulations using molecular dynamics or Monte Carlo simulations with semiempirical potentials. Density functional theory (DFT) is only used when it is possible, which means at small size (less than about 200 atoms) and zero temperature in the ground state.

The theoretical model will be described in the second part. The third and fourth part will be devoted to, respectively, the phase order tendency systems (with example on Co-Pt, Pd-Au, ...) and to the phase separation systems (Cu-Ag). The discussion and conclusions will be given in Sect. V.

7.2 Theoretical Model

We use numerical simulations to describe the theoretical phase diagrams of nanoalloys. The statistical methods are in general the Monte Carlo simulations performed either in the canonical ensemble or, the semi-grand canonical ensemble, and eventually, the parallel tempering method in order to better characterize the transition in some cases. Molecular dynamics methods can be used to describe

the melting transition but are much less efficient than Monte Carlo methods in concentrated alloys. Finally, global optimization methods or quenched molecular dynamics are used to determine the ground state structures at 0 K. These statistical approaches require a quite simple energetic model (semiempirical potential) in order to be able to perform a great number of total energy calculations to explore the energy landscape. The one we chose here is a many-body potential [second moment approximation (SMA)] derived from the electronic structure in the framework of the tight-binding approximation. This model combines the lessons of the tight-binding Ising model (TBIM) on a rigid lattice and the SMA, taking into account essentially the difference in the bandwidth of the two constituents but authorizing lattice relaxations. Whereas the first method has proven to give a rigorous description of order/disorder effects in bulk and surface alloys, on rigid lattice, the second one takes into account the interatomic distance variation such as the complex atomic relaxations in a fivefold symmetry cluster, but with an oversimplification of the order/disorder phenomena. We will see at the end that a new method with an approximation to the fourth moment could be able to better integrate the coupling between chemical ordering and atomic relaxation but with the loss of the analytical form of the potential. However, the recursion method used to calculate the energy up to the fourth moment is still much faster than *ab initio* methods, enabling to perform Monte Carlo simulations on quite large time scale and size scale systems. Finally, DFT methods are used either in fitting the semiempirical potentials or to determine more accurately the lower energy structure of different isomers.

7.2.1 Energetic Model

Many aspects of ordering phenomena in alloys have been described using an effective tight-binding Ising model obtained by developing the energy in a perturbation form with respect to the energy of the disordered state on a rigid lattice [17, 18]. Such a model has been extended to the surfaces of alloys, referred to as the TBIM [19]. It describes in a realistic way surface segregation and ordering phenomena at bimetallic surfaces [20, 21] and in nanoalloys [22–25]. Similar approaches using the Cluster Expansion Method (CEM) [26] have been performed with effective interactions fitted to *ab initio* total energy calculations [27, 28].

However, to study the coupling between structural and chemical arrangements in the peculiar case of clusters, one has to be able to go beyond the rigid lattice assumption of the TBIM in order to perform atomic relaxations in the same time as the optimization of the chemical configuration. This has been done partially in the “hybrid cluster expansion” method [29] where the structural relaxations effects have been introduced through the effective cluster interactions to model the lattice distortion energy. However, to my knowledge, this method has not been applied up to now on nanoalloys. The other alternative to model nanoalloys is then to define an interatomic potential depending on the distances between the atoms which allows both to displace and to exchange atoms of different species. This is

the case of the many-body potential derived within the SMA of the tight-binding model [30, 31], which is equivalent to other semiempirical potentials such as the embedded atom method (EAM) [32], the effective medium theory (EMT) [33], the Finnis–Sinclair potential [34, 35], and more recently, the bond-order potential applied to nanoalloys [36, 37]. Such potentials have been widely used for pure metal clusters [38–41] and nanoalloys [42–51]. But it is necessary to emphasize that such models are, in principle, not sufficient to account properly for ordering effects. In particular in the SMA model, the hopping integrals introduce only nondiagonal disorder, whereas most ordering effects in transition alloys have been explained by including essentially diagonal disorder effects in the TBIM scheme [1], assuming the hopping integrals to be independent of the nature of the atoms. A consistent treatment of both chemical and structural effects requires to go beyond the second moment model. Nevertheless, it is possible to use the SMA potential but with a parametrization which takes into account the main results of the TBIM, as discussed in the following [52].

7.2.1.1 The Tight-Binding Ising Model

When only chemical order in an A_cB_{1-c} alloy is studied on a rigid lattice, the tight-binding formalism allows us to derive some effective pair interactions describing chemical ordering and segregation effects near a surface. In this model, the (small) part of the total energy of the system, which involves the chemical configuration dependence, obeys the following Hamiltonian:

$$H^{\text{eff}} = \sum_n p_n \left(\Delta h_n^{\text{eff}} - \sum_{m \neq n} V_{nm} \right) + \sum_{n, m \neq n} p_n p_m V_{nm}, \quad (7.2)$$

where:

- p_n is the occupation number equal to 1 or 0 depending on whether the site n is occupied or not by an atom of type A (for a binary alloy A_cB_{1-c} , $p_n = 0$ means that the site n is occupied by an atom of type B).
- The local surface field Δh_0^{eff} is identical to the difference in surface energies between the pure constituents A and B ($\Delta h_0^{\text{eff}} = \gamma^A - \gamma^B$) and $\Delta h_p^{\text{eff}} = 0$ if $p \neq 0$.
- The (alloy) effective pair interaction:

$$V_{nm} = \frac{1}{2} (V_{nm}^{AA} + V_{nm}^{BB} - 2V_{nm}^{AB}) \quad (7.3)$$

between atoms at sites n and m characterizes the tendency to bulk ordering ($V > 0$) or to phase separation ($V < 0$). It is negligible in general for fcc alloys beyond first neighbors; this is why we will use $V = V_{nm}$ in the following, considering only the first neighbors.

Because of the rigid lattice assumption made in the TBIM, such model does not treat the possible atomic relaxations induced by the size mismatch between the two components. Moreover, in the particular case of clusters which present some bulk symmetry deviations together with important atomic structure relaxations, we need to go beyond the TBIM assumption in order to treat reasonably the geometrical effects.

7.2.1.2 The SMA Model

Within SMA [30], the band energy of an atom of type i located at site n is proportional to the square root of the second moment of the local density of states, leading to the many-body character of the potential. This band energy term writes

$$E_{n,i}^b(\{p_m^j\}) = -\sqrt{\sum_{\substack{m \\ r_{nm} < r_c}} \sum_{j=A,B} p_m^j \xi_{ij}^2 e^{-2q_{ij}\left(\frac{r_{nm}}{r_{ij}^o} - 1\right)}} \quad (7.4)$$

and is counterbalanced by a repulsive term of the Born–Mayer type

$$E_{n,i}^r(\{p_m^j\}) = \sum_{\substack{m \\ r_{nm} < r_c}} \sum_{j=A,B} p_m^j A_{ij} e^{-p_{ij}\left(\frac{r_{nm}}{r_{ij}^o} - 1\right)}, \quad (7.5)$$

where r_{nm} is the distance between the atoms at sites n and m , r_{ii}^o , $i = A, B$ is the first-neighbor distance in the pure metal i , $r_{ij}^o = (r_{ii}^o + r_{jj}^o)/2$ if $i \neq j$, and r_c is the cut-off distance for the interactions. $\{p_m^j\}$ represents the chemical configuration of the system, in which p_m^j is the occupation number (as mentioned before) equal to 1 or 0 depending on that the site m is occupied or not by an atom of chemical type j , ($j = A, B$) (for a binary alloy AB , $p_m^A = 1 - p_m^B = p_m$). The parameters (A_{ij} , p_{ij} , q_{ij} , ξ_{ij}) are fitted to different experimental values: the cohesive energies, atomic radii, and elastic constants of the pure elements and solution energies for the alloys.

The total energy of the system is then written as follows

$$E_{\text{tot}}(\{p_n^i\}) = \sum_n \sum_{i=A,B} p_n^i \left(E_n^{i,b}(\{p_m^j\}) + E_n^{i,r}(\{p_m^j\}) \right). \quad (7.6)$$

The parametrization of the SMA potential should take into account the segregation driving forces of the TBIM which are:

- The difference in surface energies: the element with the lower surface energy is the one with the tendency to segregate.
- The alloying effect with the tendency to make ordered phases ($V > 0$) with an oscillating profile near the surface and the segregation of the majority species or to phase separation ($V < 0$) with one element at the surface and the other in the core.

Plus the size mismatch: the element with the larger atomic size will segregate because of the anisotropy of the potential in tension/compression.

As the semiempirical potentials usually underestimate the surface energy, it is important to fit at least the difference of the surface energies in order to get the right segregating metal. Concerning the mixed parameters, they have to be fitted in order to reproduce the main properties of the bulk phase diagram [2]. A very detailed study has been performed on the description of the surface segregation driving forces into these three elementary contributions (surface energy, alloy effect, and size mismatch) in order to get a universal description for any type of transition metal alloys and at least concerning systems sufficiently different as Cu-Ag and Co-Pt [53]. As a conclusion, even if these contributions are more or less coupled, it has been found that the difference of atomic radii of the components leads to a variation of the effective pair interactions as used in the TBIM between the surface and the bulk (or the core).

To go beyond these models, we developed recently a fourth moment approximation (FMA) still in the tight-binding framework but with the advantage to combine in the same approach the diagonal disorder (which was neglected in the SMA) and the nondiagonal disorder. Thanks to this extension in moments of the description of the electronic density of states, it has been possible to describe general maps ranging any metallic alloys according to its tendency to make ordered or separated phases [54] as a function of the difference in the d orbital levels of each elements of the system (diagonal disorder), the difference of its d bandwidth (nondiagonal disorder), and the average d band filling in the alloys. As compared to before where this tendency to order or phase separate was only considered through the diagonal disorder [1], this new approach allowed to include very important systems such as Cu-Au or Co-Pt where the weak diagonal disorder (≤ 1) prevented to class them in the right place. We expect to use such nonanalytical potential in Monte Carlo simulations to describe nanoalloys as it has proven to be very efficient in the description of carbon nanotube on Ni clusters [55] or Ni clusters [56].

7.2.2 *Statistical Models*

Different statistical methods are used depending on the problem addressed. There are two traditional classes of methods: molecular dynamics [57] and Monte Carlo [58] simulations. Both these methods are able, theoretically, to reach ergodic sample in order to define the equilibrium configuration in complex energy landscape. However, molecular dynamics is more suited to describe in a first approximation some dynamics (kinetics) phenomena, whereas Monte Carlo simulations are essentially devoted to characterize equilibrium states. Molecular dynamics needs to use an analytical potential in order to derive atomic forces, whereas Monte Carlo simulations can be used with more complicated expressions (nonanalytical) of the energy. These methods can be used at finite temperature but also near 0 K, in order to find the ground state. This is the case, for example, of the quenched molecular dynamics where the system is directed toward the nearest energy minimum (local minimum energy). Such method is not able to find the global-minimum energy,

i.e., the structure with the optimal chemical order with the more stable state. The best methods to use in such case are the global optimization methods which are explicated in this book in the chapter of Riccardo Ferrando.

In this chapter, we will use the canonical molecular dynamic method, at constant temperature, with the Andersen thermostat [59] to simulate the melting properties of some magic core-shell nanoalloys and some diluted nanoalloys. Such transition implying mainly a structural transition rather a chemical order transition, the molecular dynamic simulation is well suited. Indeed, molecular dynamic on solid phases is not realistic because of its too long time scale. One step of the simulation is being scaled on the vibration frequency of one atom in the solid, i.e., about one femtosecond; a current simulation represents not much than one millisecond in real time, which corresponds to 1,000 mega steps of calculations. It is worth noticing that such time scale is nevertheless relevant in what concerns some growth processes in nanoalloys since the atomic diffusion mechanisms are probably accelerated in clusters as compared to the bulk, thanks to the large proportion of surface atoms [44]. The quenched molecular dynamic is also used in order to optimize the atomic structure at 0 K, after Monte Carlo simulations which are more efficient to optimize the chemical configuration.

Concerning properly the chemical order transition in solid states, Monte Carlo simulations are much more suited because they allow to perform “unphysical” atoms exchanges between atoms of different species without taking into account the diffusion processes as in molecular dynamic simulations. Monte Carlo steps, including random atomic displacements and random exchanges of atoms of different nature, allow a good exploration of the energy landscape. Each Monte Carlo step is accepted with a Boltzmann probability according to the Metropolis criterion [60]:

$$acc(C \rightarrow C') = \min \left\{ 1, \exp \left(- \frac{E(C') - E(C)}{kT} \right) \right\}. \quad (7.7)$$

There are several thermodynamical ensembles to perform Monte Carlo simulations among which we will consider in particular the canonical and semi-grand canonical ones. Both keep the temperature constant, and we choose to keep the pressure constant (varying the volume). The canonical ensemble keeps the number of atoms of each species constant, whereas the semi-grand canonical ensemble keeps the chemical potential difference between the two species constant which means that the total number of atoms is constant but the concentration varies. Such ensemble enables to describe all the compositions of alloys at a given temperature giving access to segregation isotherms in alloys surfaces [3].

Finally, the parallel tempering method [61] is a very powerful tool for achieving ergodic sampling in complex energy landscapes. Indeed, apart from the fact that it can eliminate the hysteretic behavior during heating/cooling cycles, it also provides much more accurate and statistically converged equilibrium quantities in order to explore possible phases coexistence (bistability) during the transition in order to characterize the nature of the transition (first order or second order). The method consists in running simultaneously different classical Monte Carlo

simulations (trajectories) at a specific temperature and the different trajectories can be exchanged (swap of the configurations) from one temperature to another according to the Metropolis-like probability:

$$acc(C \rightarrow C') = \min \left\{ 1, \exp \left[\left(\frac{1}{kT'} - \frac{1}{kT} \right) (E(C') - E(C)) \right] \right\} \quad (7.8)$$

The exchange between two configurations (or replicas) will occur only if the potential energy distributions of adjacent replicates overlap with each other, as the swap will precisely take place in the overlapping region.

7.3 Melting Transition in Nanoalloys

The melting properties have a high impact on many applications of nanoclusters since knowing the variation of the melting temperature as a function of the cluster size, it is expected to decrease sensibly with cluster size below a diameter of 5 nm [62, 63], following the Pawlow theory. As a consequence, it is necessary to control the temperature if we want to keep their solid structure. Inversely, some applications of the nanoparticles seem to require the liquid nanodroplets as the catalytic growth of carbon nanotubes [64].

We consider here the alloying effect on the melting transition in some particular cases where the composition influences the melting temperature. We would like to emphasize that the cluster structure plays an important role in the variation of the melting temperature. By considering magic polyicosahedral core-shell nanoalloys [45], we have shown that their particular stability leads to a significant increase of their melting temperature as compared to the pure systems of same size. This specific stability is induced by the size mismatch between the two components which increases the stability of complex fivefold symmetry structures which are not stabilized in pure clusters. To push this effect to its limit, we considered only one impurity and obtained a significant increase of the melting temperature well correlated with the size mismatch between the impurity and the constituent metal of the cluster [65].

7.3.1 Melting of Magic Polyicosahedral Core-Shell Nanoalloys

A new family of core-shell nanoalloys, predicted by global optimization with SMA potentials and confirmed by density functional calculations, presents very interesting melting properties as they melt at higher temperature than the pure equivalent size clusters. This new family of nanoalloys of sizes between 34 and 55 atoms are formed by a core of Cu or Ni atoms and a shell of Ag atoms. The bulk Cu-Ag and Ni-Ag alloys form a large miscibility gap in their bulk phase diagram [2] which induces also a strong phase separation in the cluster under the shape of a

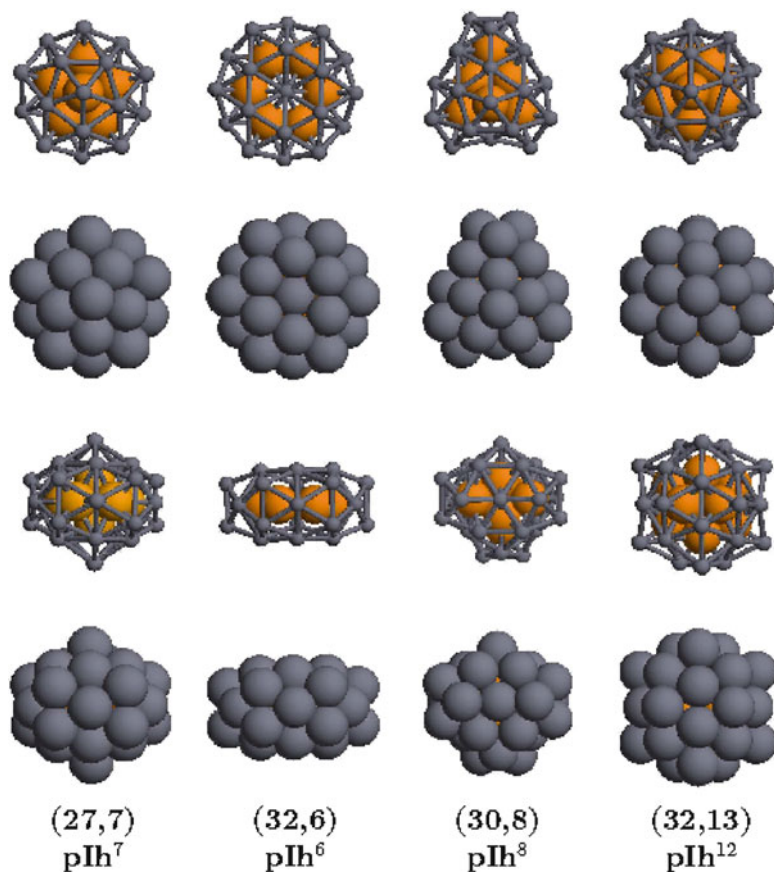
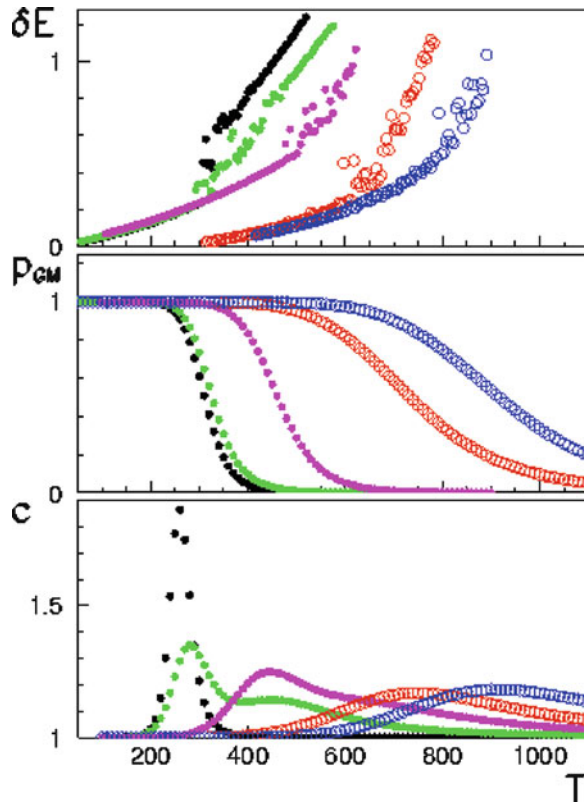


Fig. 7.1 Polyicosahedral clusters with Ni or Cu atoms in yellow and Ag atoms in gray. From the left to the right, the $(27,7)\text{pIh}^7$ has a decahedral core of 7 atoms and an anti-Mackay overlayer of 27 Ag atoms. The $(32,6)\text{pIh}^6$ has been called a *pancake* structure with the six inner atoms placed on a regular hexagonal ring. The $(30,8)\text{pIh}^8$ is the perfect core-shell structure including the maximum number of core atoms at size 38 (in competition with an FCC truncated octahedron (TOh)). Finally, the $(32,13)\text{pIh}^{12}$ corresponds to the complete anti-Mackay icosahedron of 45 atoms, with a perfect Ih_{13} core (adapted from [45])

core-shell structure with the silver whose surface energy is the lower in the shell. However, this is not the main driving force to get such polyicosahedral structure. The specific structures as illustrated in Fig. 7.1 result also from the high lattice misfit between the two elements (12–14%). They are called polyicosahedral (pIh) as they are built by packing elementary Ih_{13} clusters. Four pIh are displayed in Fig. 7.1 with 6, 7, 8, to 13 Cu or Ni atoms in the core and the others of Ag at the surface.

DFT calculations [66] showed that these structures present not only a minimum of energy as compared to other isomers but also some electronic characteristics as a large HOMO-LUMO gap and a magnetic moment in the case of Ni-Ag systems [45].

Fig. 7.2 Melting of the $(27,7)\text{pIh}^7$ with Cu or Ni in the core (respectively *circles and squares*) and pure Ag, Cu, and Ni clusters of 38 atoms (respectively *stars, diamonds, and triangles*). The *top panel* shows the molecular dynamics caloric curves δE (in eV) versus T (in K), where $\delta E = E - E_{\text{GM}} - 3(N-1)k_{\text{B}}T$, E_{GM} being the ground state (global minimum) and the other part, the harmonic contribution. The *middle panel* reports the probability of finding the cluster in its global-minimum structure as a function of T . The *bottom panel* reports the vibrational specific heat per degree of freedom (in units of the Boltzmann constant k_{B}) (adapted from [45])



As a result of such properties at 0 K, in the steady state, we also investigated the thermodynamic properties of such structure, in particular the $(27,7)\text{pIh}^7$. Using molecular dynamics and the SMA potentials, the caloric curve of the $\text{Cu}_7\text{Ag}_{27}$ and $\text{Ni}_7\text{Ag}_{27}$ has been calculated together with the probability of finding the cluster in its global minimum as a function of the temperature (structural order parameter) and the vibrational specific heat in the harmonic superposition approximation (Fig. 7.2). As compared to the same quantities for pure clusters of 38 atoms (i.e., the nearest magic size for pure systems), we can see that the nanoalloys of 34 atoms melt at much higher temperature than the pure clusters of the constitutive metals with 38 atoms. According to the Pawlow theory, the slight size difference between the pure clusters and the nanoalloys would be in favor of a decreasing melting temperature with decreasing size. However, such theory is rather adapted to larger sizes. From the point of view of bulk alloys phases diagram, and in particular concerning the Cu-Ag and Ni-Ag systems, they both present an eutectic corresponding to a lowering of the melting temperature of the alloy compared to the pure metals, which is in the opposite from what happens in nanoalloys.

The melting behavior of the nanoalloys is clearly in opposition with the bulk alloys' behavior. The reason comes from the very high stability of the structure of

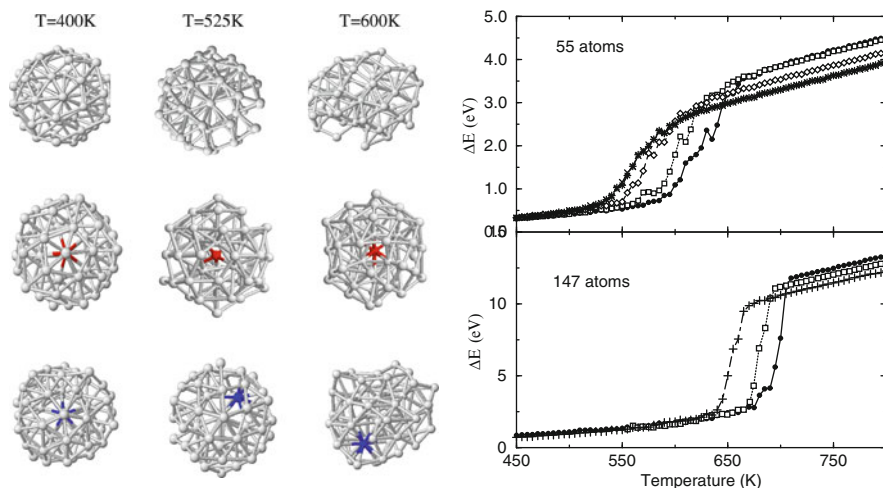


Fig. 7.3 *Left panel:* snapshots from the melting dynamic molecular simulations: pure Ag_{55} (top row), Ag_{54}Ni (middle row) and Ag_{54}Pd (bottom row) at different temperature. The impurity is colored. *Right panel:* caloric curves using the same energy definition as in Fig. 7.2 for Ag clusters of 55 and 147 atoms. Pure Ag clusters (crosses) and Ag clusters with Cu (squares), Pd (diamonds), and Au (asterisk) impurity (adapted from [65])

the nanoalloys which, thanks to the difference in atomic size, accommodates these pIh structures by removing the strain in compression in the core. Indeed, usually, the fivefold symmetry structures optimize the surface at the expense of the core which undergoes a strong compression. It has been shown that removing the central atoms of icosahedra improved their stability [67]. Here, it is shown that replacing the core atoms by smaller ones allows to form new pIh structures which are more stable than pure systems. This result has been generalized on a large family of systems [68].

7.3.2 Single Impurity Effect on the Melting of Nanoclusters

As mentioned just before, the size mismatch between the two elements of the nanoalloys seems to be the most important driving force to stabilize magic core-shell nanoalloys. Pushing this argument to its limit, we have investigated the extreme case with only one impurity in the cluster [65]. Figure 7.3 displays the snapshots of pure Ag cluster of 55 atoms with the Ih structure and with one Ni or Pd impurity. We see clearly that the pure cluster and the cluster with one Pd impurity are melted at 600 K, whereas the cluster with one Ni impurity is still icosahedric at this temperature.

The caloric curves (Fig. 7.3) performed on these clusters including also Cu and Au impurities show that the melting transition is shifted toward higher temperature according to the atomic size of the impurity. The smaller the impurity the higher the melting temperature. We check on these curves for the 55 atoms size and the 147

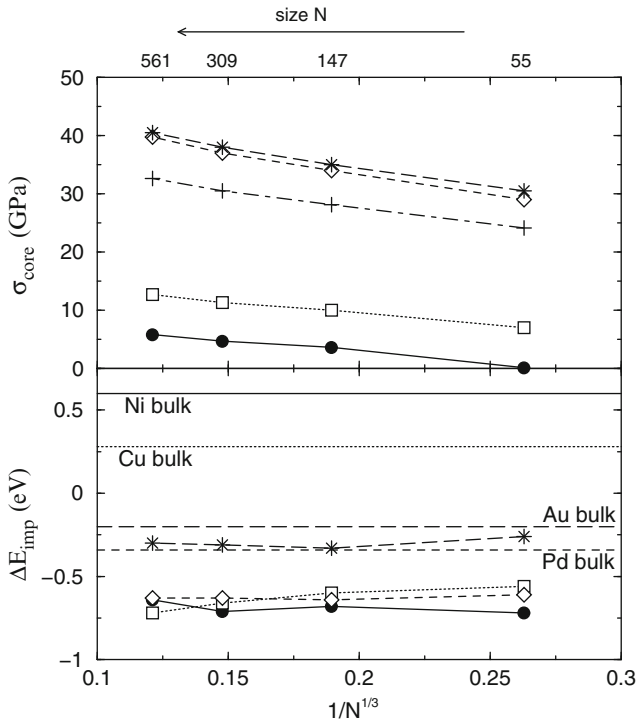


Fig. 7.4 Atomic stress on the central site σ_{core} and impurity solution energy ΔE_{imp} for icosahedral clusters of different magic sizes together with the one in the bulk phase [2] for comparison. The symbols are the same as in Fig. 7.3 (adapted from [65])

atoms size that the Ni impurity with the smaller atomic radius (14% misfit) leads to the more shifted melting transition, followed by Cu then Pd, and finally Au (with no misfit) which does not influence the transition.

The correlation between the size of the impurity and the strain and the chemical nature of the impurity in terms of solution energy has been performed and is illustrated in Fig. 7.4. The calculations are performed at 0 K. They confirm the correlation between the stability of the clusters (higher melting point) and the size mismatch of the impurity compared to Ag. The higher stress is obtained in the pure cluster or with the impurity of gold which makes almost no difference, whereas the stress decreases when the atomic size of the impurity decreases. Also we observe the stress increases for all the systems as a function of the cluster size. Concerning the dissolution energies, we notice that for the gold impurity, it is almost the same in the cluster than in the bulk there is a slight difference for the palladium impurity, and it is almost opposite in the case of the Cu and Ni impurity. Allowing the

atomic relaxations around the impurities, we can conclude that the chemical effect is strongly counteracted by the stress effect which is much more important in the clusters than in the bulk.

7.4 Segregation Transition in Cu-Ag Nanoalloys

The core-shell structures mentioned in the precedent section were a result of a strong size mismatch and a difference in surface energy leading the element with the lower surface energy at the surface. The other important driving force for such core-shell structure is the tendency to phase separation, preventing the alloy to mix. I will now discuss in more details and in a larger size range the segregation transition in nanoalloys. We consider the Cu-Ag system as it presents a strong tendency to phase demixion and all the driving forces lead to the surface segregation of silver. We will report here the work performed by the group of B. Legrand, J. Creuze, F. Berthier, and coworkers [69]. This system has attracted much interest in the past to describe theoretically and experimentally the surface segregation phenomena on alloy surfaces (see [3]). Surface segregation is a very important phenomena in practical for alloy surfaces and interfaces applications, mainly in the cases of thin films as used in microelectronics and magnetic multilayers. The same phenomena occurs in the bimetallic nanoparticles where we observe the formation of core-shell nanoalloys or Janus nanoparticles (see the contribution by F. Baletto in this book). A nice experimental observation of these structures has been performed by C. Langlois et al. [70], where the image by transmission electron microscopy (TEM) shows clearly the bimetallic nanoparticles and the demixion of the Cu and Ag phases inside one particles. The experimental sizes of the nanoclusters are still much larger than the one usually considered in the theoretical investigations. Also, the experimental precision does not allow to distinguish the composition at the surface layer, as we will discuss in the following using numerical simulations. This is why the theoretical approach is still very important and complementary to the experimental study (Fig. 7.5).

The superficial segregation in bimetallic Cu-Ag nanoparticles has been addressed using different approximations: the TBIM energetic model on rigid lattice with Monte Carlo and mean-field approximation analysis [24, 25, 71], and the SMA energetic model allowing atomic relaxations with Monte Carlo simulations [72] in canonical and semi-grand canonical ensembles.

Taking a model cuboctahedron system on a rigid lattice, it presents four types of inhomogeneous sites at the surface (the (111) and (100) facets, the edges, and the vertices) and the core sites which differ essentially by their coordination numbers (see Fig. 7.6). Hence, in the mean-field approximation where the short-range order is neglected, the system is described as an ensemble of p classes with homogeneous concentrations c_p according to the well-known segregation equation:

$$\frac{c_p}{1 - c_p} = \frac{c}{1 - c} \exp\left(-\frac{\Delta H_p^{\text{seg}}}{k_B T}\right), \quad (7.9)$$

Fig. 7.5 Energy filtered imaging by transmission electron microscopy (EFTEM) of Cu-Ag nanoparticles with color-coded chemical map (Ag in blue/dark and Cu in yellow/bright). Note the presence of pure Ag nanoparticles that have nucleated separately on the substrate (adapted from [70])

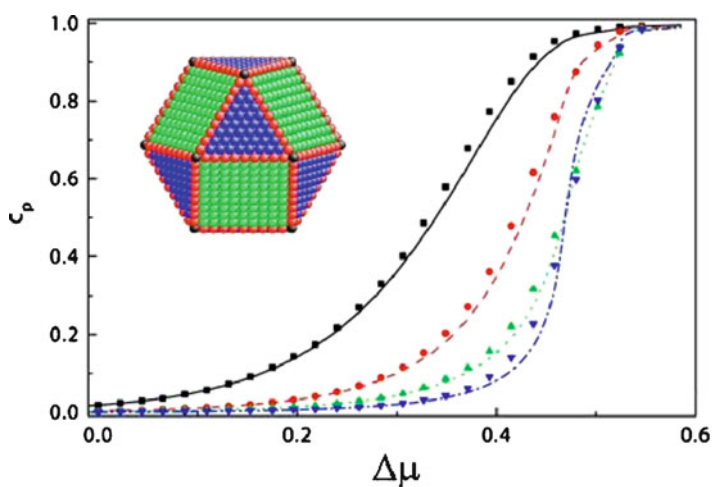
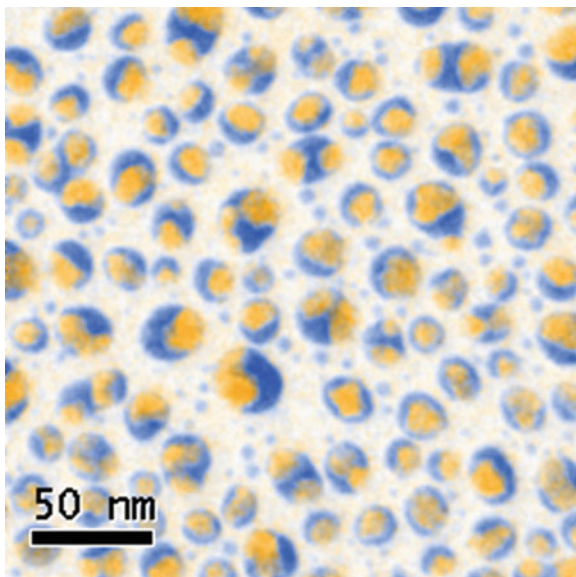


Fig. 7.6 Segregation isotherms ($T = 1,100$ K) of a cuboctahedral cluster of 3,871 atoms for the different classes of sites of the external shell (vertices with *solid line and squares*, edges with *dashed line and circles*, (100) facets with *dotted line and up triangles*, (111) facets with *dashed-dotted line, and down triangles* and core with *dashed-dotted line and diamonds*). The lines represent the mean-field calculations and the symbols the Monte Carlo simulations (adapted from [25])

where c is the bulk concentration in the $Cu_{1-c}Ag_c$ alloy and ΔH_p^{seg} is the segregation energy to put an impurity atom from the bulk to the surface. This expression is commonly used in semi-infinite systems where the bulk concentration reference is

well defined. This is no more the case in clusters where the finite size induces a coupling between the surface and core concentration, and the core concentration is not equal to the nominal concentration c . This is why it is more convenient in nanoparticles to use the semi-grand canonical ensemble which keeps constant the difference in chemical potentials: $\Delta\mu = \mu_{\text{Ag}} - \mu_{\text{Cu}}$ and let evolve the average concentration c in the cluster. The last equation can be expressed in the following way (see [25] for more details):

$$\frac{c_p}{1 - c_p} = \exp\left(-\frac{\Delta H_p^{\text{perm}} - \Delta\mu}{k_B T}\right) \exp\left(4\frac{T_c^p}{T} c_p\right), \quad (7.10)$$

where ΔH_p^{perm} is the permutation energy corresponding to the energy balance due to the transformation of an impurity atom of type B in an atom of type A on a p -class site and T_c^p is the critical temperature of phase transition $T_c^p = -\frac{Z_p V}{2k_B}$, where Z_p is the coordination number in the p -class. The segregation isotherms (in silver concentration) are shown in Fig. 7.6 for each type of surface sites and in the core as a function of $\Delta\mu$.

At temperature higher than the critical temperature of the miscibility gap, first-order phase transitions (van Der Waals loop) are not expected. The segregation isotherms are continuous, and the mean-field approximation is quite equivalent to the Monte Carlo simulations. As a function of $\Delta\mu$ or N_A , the surface segregation begins at the corners, then on the edges and on the different facets following the increasing order of coordination numbers, as expected from the linear dependence of ΔH_p^{perm} with the coordination number. As a function of the Ag atoms number, we notice that once the surface is pure in Ag, the core begins only very slowly to be enriched in silver, leading to a core/shell structure even at high temperature. The facets segregation is very similar to the corresponding semi-infinite alloy surfaces modeled in the same way. The equivalent of Fig. 7.6 is shown in Fig. 7.7 at lower temperature ($T = 300$ K) where only the stable states have been represented (the metastable and unstable states of the van der Waals loop have been suppressed) [24]. We observe an inversion of the order of segregation between the facets sites, the (111) facets being enriched before the (100) ones, these transitions being much more abrupt for the facets (first order) and the mean-field calculation differs from the Monte Carlo simulations. In fact, there is a coupling between the facets and the edges which is stronger for the (111) facets. As this coupling depends on the cluster size and also its morphology, this reversal should disappear for larger sizes and other truncated octahedra. If Monte Carlo simulations and mean-field approach are in good agreement about the relative position of the isotherms, they differ on their nature: the transitions in the mean-field approximation are of first order for the edges and facets, whereas they are continuous in Monte Carlo for any kind of site, even if they present a very stiff variation in a narrow $\Delta\mu$ range for the facets. By a more detailed study of the facets segregation, we notice that the facet is inhomogeneously enriched: it begins to be colored by silver atoms from the border (near the edges) to the center.

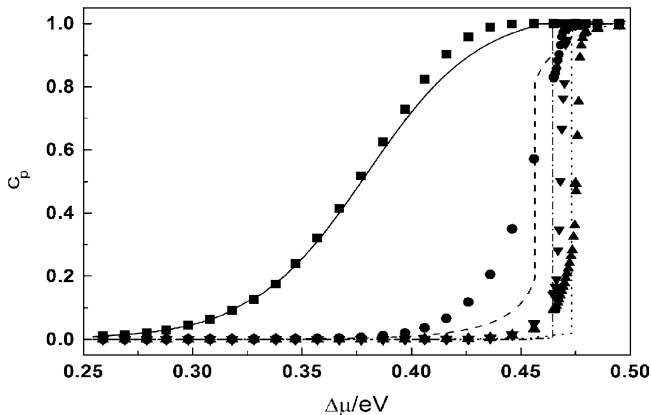


Fig. 7.7 Segregation isotherms ($T=300$ K) of a cuboctahedral cluster of 3,871 atoms for the different classes of sites of the external shell (same symbols as in Fig. 7.6) (adapted from [24])

Moreover, at the neighborhood of the transition, looking at two instantaneous configurations of the clusters (Fig. 7.8), we observe that some of the (100) facets are pure in silver, whereas some other are pure in Cu and the same facet, at two different instants, change from pure Ag to pure Cu. This is why it has been interesting to plot the instantaneous facet concentration as a function of the number of Monte Carlo steps (Fig. 7.8). When considering one single facet, the transition is sharp between a pure Ag facet and a pure Cu facet, whereas when considering all the (100) facets (there are 6), the average concentration is intermediate because there is no collective transition of all the facets. Some of the facets play the role of a reservoir for the transition of other ones.

This study on rigid lattice using the TBIM model puts in evidence interesting results on the type of transition concerning the surface segregation but also on the wetting phenomenon [24] which is not detailed here. However, concerning the nanoclusters, such hypothesis does not take into account all the strain effects which are very important in the clusters. In the following, we will consider the atomic relaxations performing atomic displacements in Monte Carlo simulations using the many-body SMA potential on a 405-atom TOh at 300 K [72]. The segregation isotherms are illustrated in Fig. 7.9 for the four different types of surface sites at 300K. The range of $\Delta\mu$ is chosen in order to consider only the outer shell enrichment in Ag, the underlying shells remaining Cu pure. These isotherms are continuous and reversible but display quite stiff variations, especially the one of the (100) facets.

To detail this variation, Fig. 7.10 plots the evolution of the concentration of the six (100) facets as a function of the number of Monte Carlo steps for $\Delta\mu = 0.39$ eV. We observe also a dynamical equilibrium between two configurations, as in the TBIM approximation, but now, the chemical transition is accompanied by a structural change of the shape of the facets from square to diamond shape, as illustrated in Fig. 7.10. Moreover, the transition of one facet is no more independent of the others,

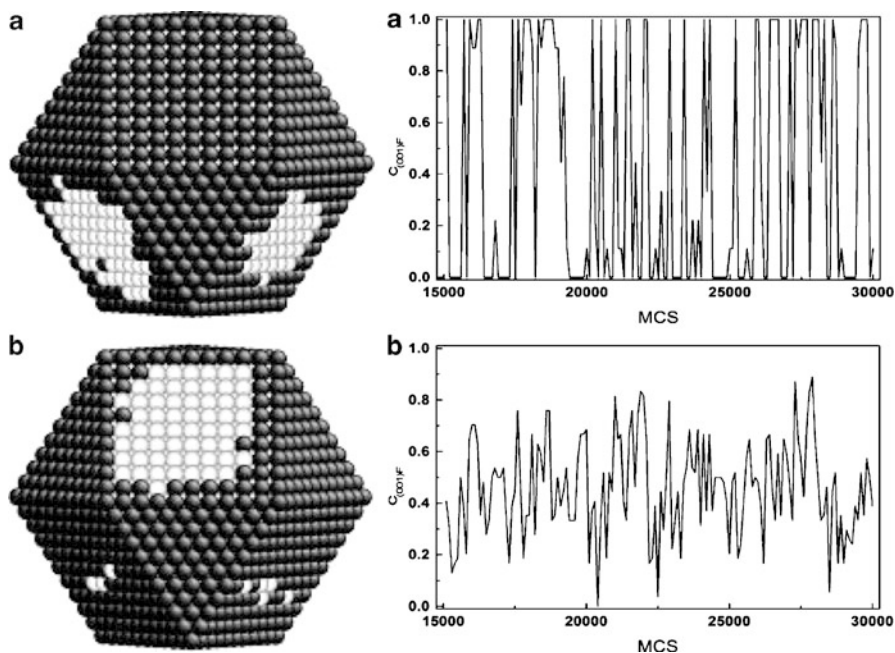


Fig. 7.8 Two snapshots obtained by Monte Carlo simulations at $T=300$ K for $\Delta\mu = 0.476$ eV. Cu atoms are in *white* and Ag atoms in *black*. On the right side, the instantaneous concentrations for one individual (100) facet (a) in the same conditions as the snapshots and for the average concentration on all the (100) facets (b) as a function of the number of Monte Carlo steps (from [24])

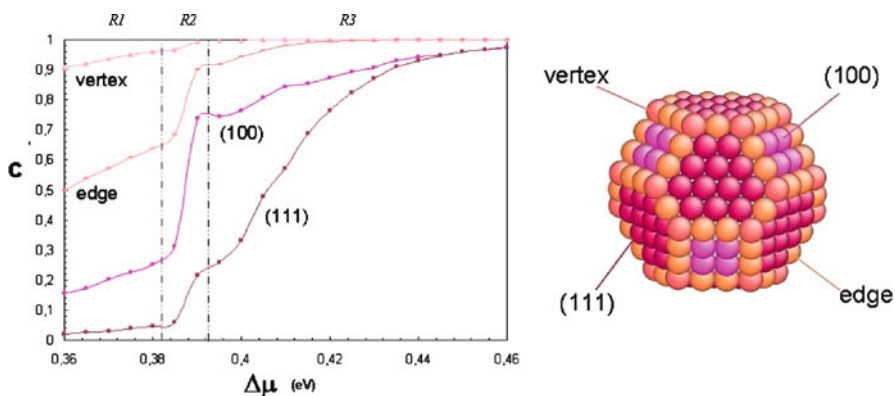


Fig. 7.9 Segregation isotherms at $T=300$ K on the 405-atom TOh with the different site concentrations "c" of the outer shell: vertices, edges, (001) and (111) facets (adapted from [72])

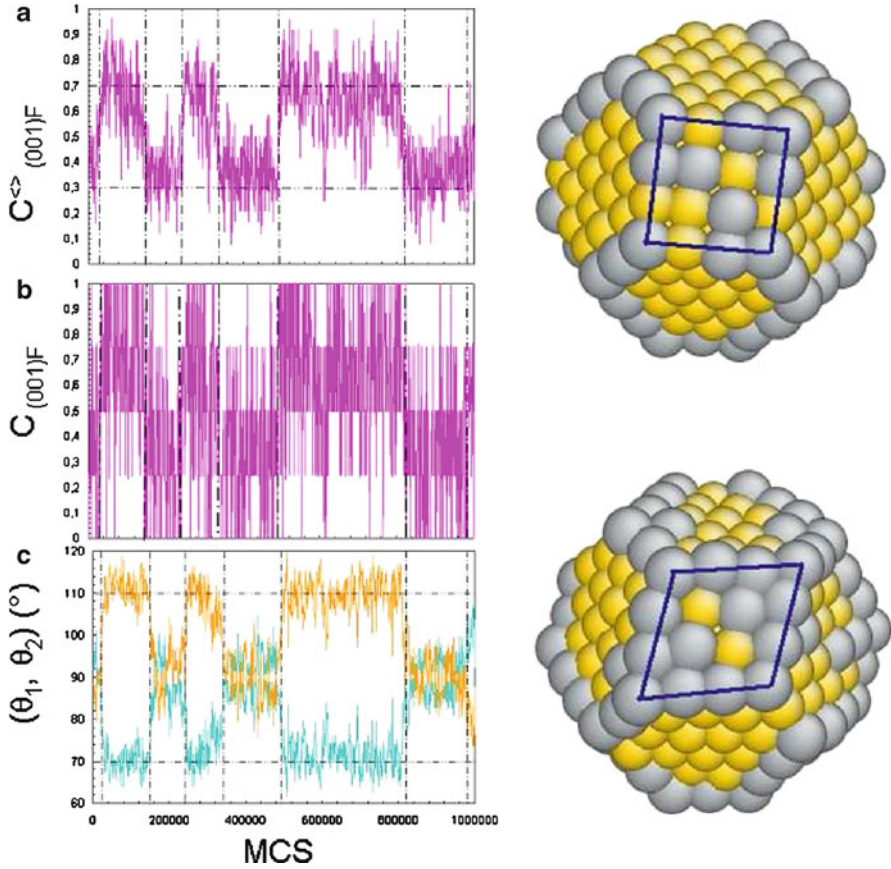


Fig. 7.10 Evolution of the concentration “c” of the 6 (001) facets (a), of a unique (001) facet (b), and of the angles (θ_1, θ_2) of one (001) facet (c) as a function of the Monte Carlo steps (MCS) at 300 K and $\Delta\mu = 0.39$ eV. On the right, the representation of the cluster with the *square* (90,90) and the *diamond* (70,110) shape. Ag atoms in gray and Cu atoms in yellow (adapted from [72])

and all the six facets are changing collectively in order to allow the morphological transformation. Plotting the angles of these facets, we can follow the structural variation of the facets which is exactly correlated to the chemical variation of composition of the facets from Cu pure (square shape) to Ag pure (diamond shape). This diamond shape corresponds to a pseudo (111) facet orientation of the Ag atoms on top of the (001) underlying Cu facet, which recalls the heteroepitaxial structure obtained in the deposition of one monolayer of Ag on a Cu(001) infinite substrate [73, 74] where the Ag surface adopts an hexagonal structure on the square substrate. However, the size of the cluster facet is much smaller than the optimal $c(10 \times 2)$ Ag/Cu(001) obtained in the semi-infinite system.

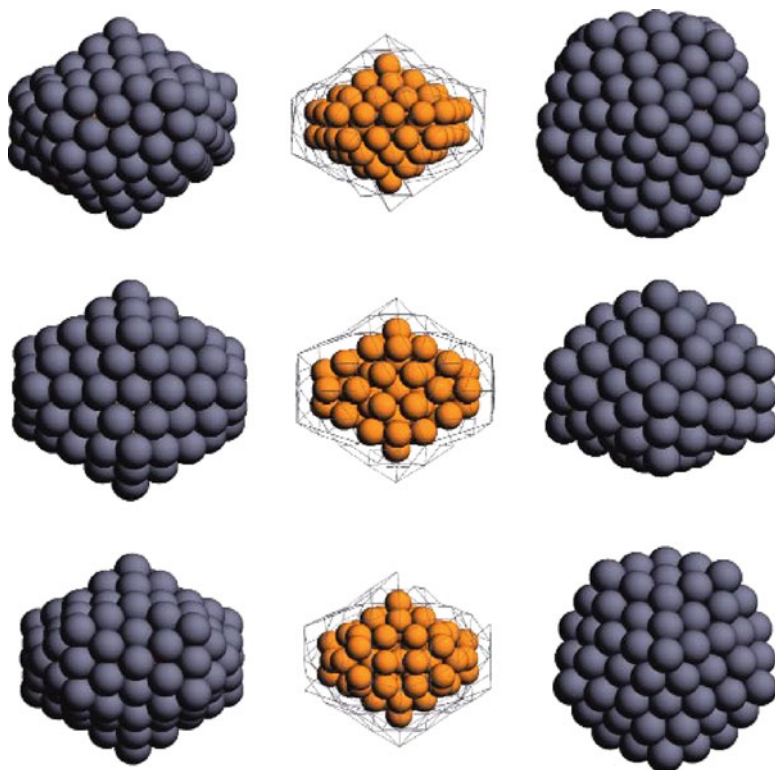


Fig. 7.11 (*top row*) Chiral structure of $\text{Ag}_{107}\text{Cu}_{85}$. (*middle row*), Achiral pental structure of $\text{Ag}_{90}\text{Cu}_{56}$. (*bottom row*) Achiral eptal structure of $\text{Ag}_{102}\text{Cu}_{75}$ (adapted from [75])

In nanoclusters, the structure being so flexible, we can expect also a lot of possible coupling between the chemical and the atomic structure. As an example, and to remain with the same Ag-Cu alloys, global optimization calculations at 0 K (see the contribution by R. Ferrando in this book) has shown the stability of high-symmetry core-shell chiral structures in many nanoalloys (AgCu, AgCo, AgNi, and AuNi), all of them presenting a strong size mismatch between the core atoms and the surface shell atoms [75]. The chiral shell (see Fig. 7.11) is obtained by a transformation of an anti-Mackay icosahedral shell by a concerted rotation of triangular atomic islands which breaks all mirror symmetries. This transformation becomes energetically favorable as the cluster size increases, for example, at the size of $\text{Ag}_{132}\text{Cu}_{147}$ with the same SMA potential as used before, but at a larger size ($\text{Ag}_{212}\text{Cu}_{309}$) if we consider another parametrization of the SMA potential in order to better fit the small nanoalloys on DFT calculations. Indeed, *ab initio* calculations do not stabilize the chiral structure of the $\text{Ag}_{132}\text{Cu}_{147}$ system, but there are no DFT calculations at larger size to confirm the prediction of the other potential.

7.5 Order/Disorder Transition in Co-Pt Nanoalloys

Other categories of alloys concern the one with the ordering tendency (Cu-Au, Fe-Pt, Co-Pt). For ultra-high density magnetic recording [76], the systems composed of one 3d ferromagnetic metal and one 5d metal present a strong spin-orbit coupling in order to increase the magneto-crystalline anisotropy. This is particularly interesting to increase the blockage temperature of the nanoparticles preventing their superparamagnetism at room temperature [77]. The question arises whether the nanoparticles can be ordered at any size as in the bulk where the $L1_0$ ordered phase displays an important magneto-crystalline anisotropy with the alternance of pure atomic layers of the two metals. For example, an article by Miyazaki et al. [78] in 2005 stipulated that the ordering of $L1_0$ Fe-Pt nanoparticles was entirely inhibited for sizes less than 2 nm. However, the order/disorder transition as a function of cluster size has been further investigated demonstrating experimentally the ordering of nanoparticles as small as 2 nm in size [77, 79, 80]. In the following, we will consider the Co-Pt nanoparticles in a range of size of 1–3 nm and compare the theoretical results to experimental ones performed in TEM and grazing incidence X-ray diffraction (GIXD).

The structure and chemical ordering of Co-Pt nanoalloys at 0 K, in the ground state, has been investigated depending on the cluster size by global optimization (for sizes smaller than 150 atoms) and by Monte Carlo and quenched molecular dynamics for larger sizes up to 2,500 atoms. Below one hundred of atoms, the Co-Pt nanoclusters present polyicosahedral structures (see Fig. 7.12) with on the surface both pentagonal and hexagonal Pt rings containing, respectively, one and two Co atoms in their center [81]. Going to the core and the center of the cluster, the radial distribution illustrated in Fig. 7.12 shows an alternance of Pt and Co shells, starting with a Pt atoms at the center and with Co atoms in the more external surface shell. This is a clear signature of the tendency to order at the difference of the typical core-shell structures illustrated before. Between 100 and 600–700 atoms, the structure is decahedral with a chemical order resembling the $L1_0$ phase but along an alternance of hexagonal atomic planes (see Fig. 7.13). This structure is obtained either by global optimization for size up to 150 atoms and by Monte Carlo and quenched molecular dynamics, starting with a decahedron structure. At larger sizes, the FCC TOh ordered according to the $L1_0$ phase is the equilibrium structure. In Fig. 7.13, the energy optimization is performed by Monte Carlo simulations at finite temperature for the chemical ordering including atomic displacements and completed by quenched molecular dynamics simulations for the final atomic relaxation. The structural transition between Dh at small sizes and TOh at large sizes is predicted at about 2–2.5 nm within the tight-binding semiempirical potential used in this study [80].

We will then consider the order/disorder transition in the FCC TOh structure at finite temperature to study in which condition it is possible to obtain the $L1_0$ ordered phase. The order/disorder transition is characterized by an order parameter

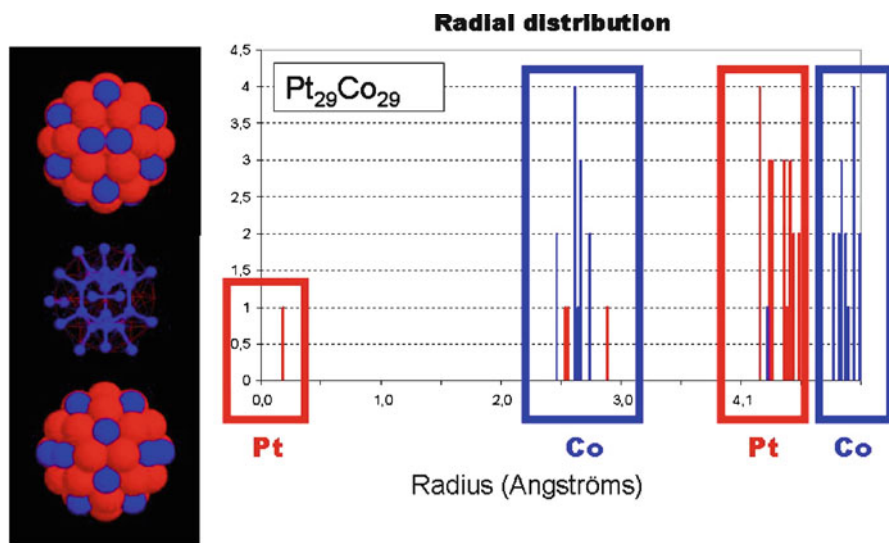
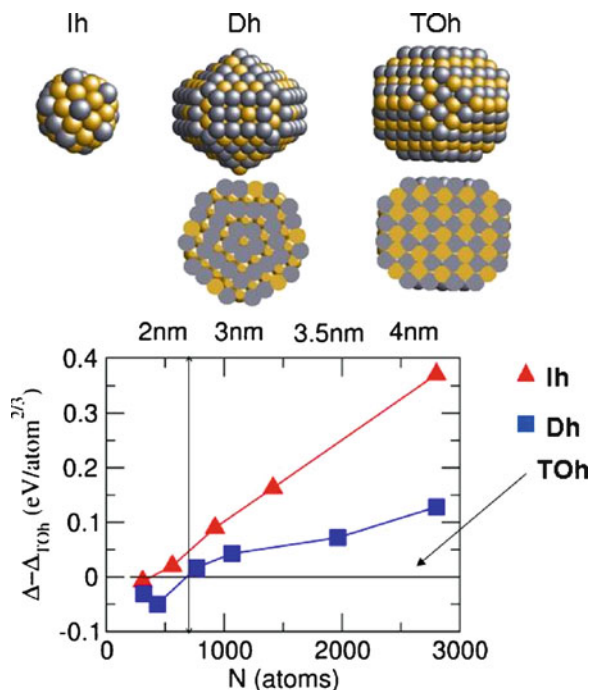


Fig. 7.12 Global-minimum structure of the $\text{Pt}_{29}\text{Co}_{29}$ system (Co atoms in *white spheres* and Pt atoms in *dark spheres*) with its radial distribution. Distances are calculated with respect to the geometrical center of the cluster. The cluster exhibits an alternance between Pt and Co shells, with the outer shell made up of Co atoms (adapted from [81])

Fig. 7.13 Phase diagram at 0 K (ground state) of Co-Pt clusters representing the energy difference as referred to the FCC truncated octahedron (TOh) for nonperiodic structures as the icosahedron (Ih) and the decahedron (Dh) of different magic sizes (TOh: 201, 314, 405, 807, 1,289, 2,075, 2,951 atoms; Ih: 309, 561, 923, 1,415, ... and Dh: 318, 434, 766, 1,067, 2,802, ...) at equi-concentration (adapted from [80])



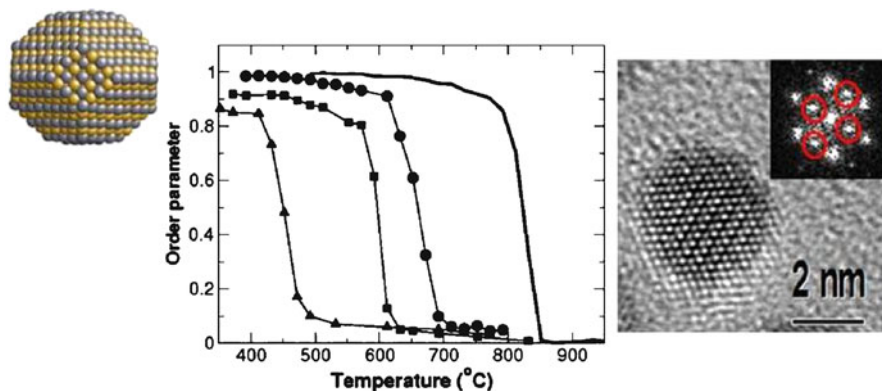


Fig. 7.14 Long-range order parameter of Co-Pt systems from Monte Carlo simulations: bulk (*full line*) and clusters of 1,289 atoms (*circle*), 807 atoms (*square*), and 405 atoms (*triangle*). TEM illustration of an ordered Co-Pt cluster (adapted from [79])

which is equal to one in the $L1_0$ ordered phase and to zero in the disordered phase. Monte Carlo simulations in canonical ensemble are used to find the equilibrium configuration at finite temperature, starting from the ordered structures, and increasing progressively the temperature. The long-range order parameter of the bulk and clusters from 2 to 3 nm are displayed in Fig. 7.14. The bulk critical temperature has been shifted in order to scale with the experimental one. In fact, our model finds a temperature about 200 K lower than the experimental one. We can notice on this figure that the critical temperature of disordering of the nanoclusters decreases as the cluster size decreases. This result is in nice agreement with the experimental study by TEM [77, 79] or by X-ray diffraction [80] and by other theoretical studies [22, 27, 36, 82]. We notice also that the transition becomes less and less sharp as the cluster size decreases, and in the same time, the hysteresis which is not shown here is more and more narrow. These arguments favor a progressive transition in case of finite size systems as compared to bulk one.

The nature of the order/disorder transition in nanoalloys has been questioned notably by theoreticians [23]. But also experimentally [80]. Using Monte Carlo simulations based on a lattice-model framework, calculating the canonical distribution functions, it has been shown that the size dependence of the order/disorder temperature and the continuous nature of the ordering transition can be understood as being natural manifestations of a disordering mechanism that is surface induced [23]. Using the SMA potential which allows atomic relaxations, we performed parallel tempering Monte Carlo simulations to alleviate slow convergence and circumvent hysteretic behavior. By this method, we have shown the coexistence between ordered and disordered phases, as evidenced by the bimodal distributions for the bulk sample and 807-atom TOh Co-Pt cluster (Fig. 7.15).

While the disordered phase nucleates from local surface defects as illustrated in Fig. 7.16, it requires significant lattice deformations to proceed completely. Indeed,

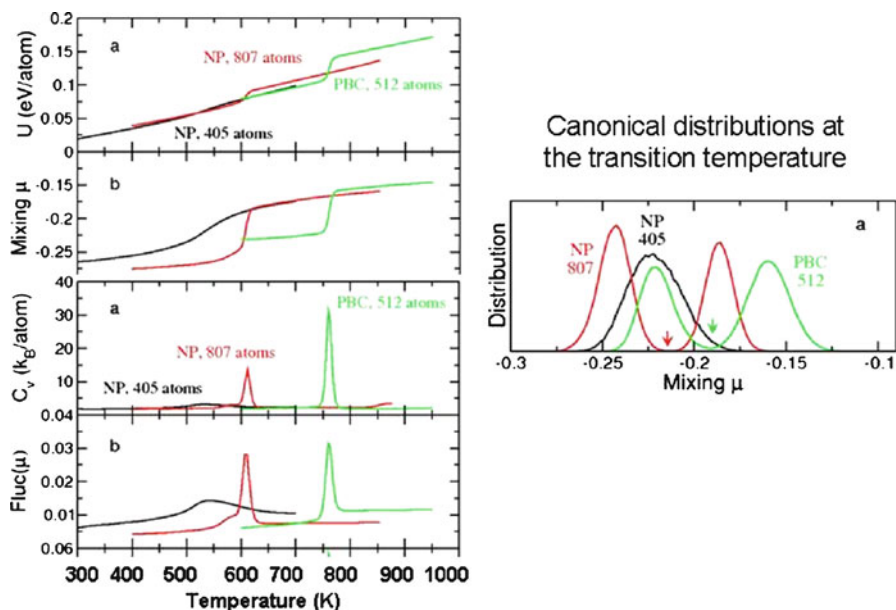


Fig. 7.15 Energy and order parameter $\mu = \frac{n_{\text{CoCo}} + n_{\text{PtPt}} - n_{\text{CoPt}}}{n_{\text{CoCo}} + n_{\text{PtPt}} + n_{\text{CoPt}}}$ where n_{AB} is the number of pairs of first neighbors of type A and B as a function of the temperature averages obtained from parallel tempering Monte Carlo simulations. Co-Pt nanoparticles of 807 and 405 atoms in the TOh structure are compared to a bulk sample with 512 atoms in the simulation box. The same colors are kept to represent the heat capacity C_v and the fluctuations of the order parameter μ . Finally, the canonical distributions of the order parameter μ is represented on the right side for the three systems (adapted from [83])

we found that the tetragonalization of the $L1_0$ phase, associated to the order/disorder transition as compared to the FCC disordered phase, is a clear signature of the transition in the Monte Carlo simulations, as in the experiments where either by TEM but also by GIXD, we can follow the ordering through the appearance of superlattice peaks at high annealing temperatures. In Fig. 7.17, the GIXD spectra of Co-Pt nanoparticles [80] grown in situ and observed during the annealing are represented at different temperatures during the growth (right panel of Fig. 7.17). The experimental spectra are fitted with simulated ones obtained from the modeled clusters as presented in Fig. 7.13 but in the disordered chemical state. Until 900 K, the nanoparticles are disordered and then, at 900 K, we observe the two peaks of superstructure corresponding to the tetragonalization of the ordered $L1_0$ phase. On the left panel of Fig. 7.17, the GIXD calculated spectra are displayed for different values of the order parameter (LRO) in order to fit the experimental one. The best fit is obtained for a coexistence of an ordered and a disordered state in the same particle, as illustrated in Fig. 7.16, which can be understood also in the experimental sample as a coexistence of fully ordered nanoparticles and fully disordered ones at the same time. This is the first experimental signature of a bistability in phase

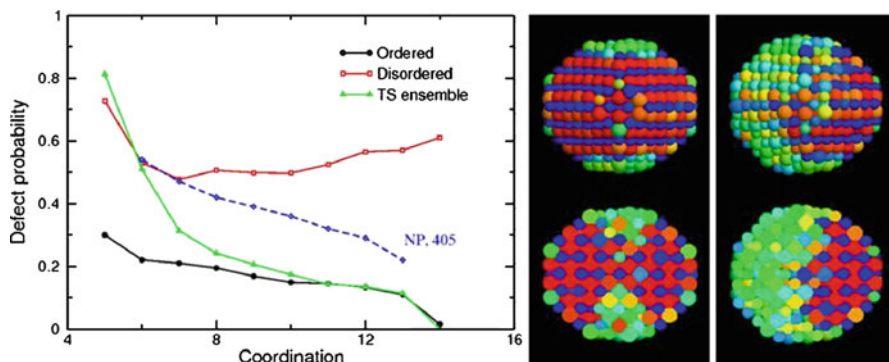


Fig. 7.16 Probability that an element differs from its reference in the perfect-ordered 807-atom nanoparticle as a function of its coordination, at the transition temperature. The results are shown for three samples of configurations in the ordered and disordered phases of the coexistence regime and for the transition state ensemble using the parallel tempering Monte Carlo simulations. Adapted from [83]. On the right, the 807-atom TOh cluster is represented with color code corresponding to average probabilities obtained by canonical Monte Carlo: in *red/blue*, a probability of one to have a Co/Pt atoms on the site, and in *green*, a probability of one-half

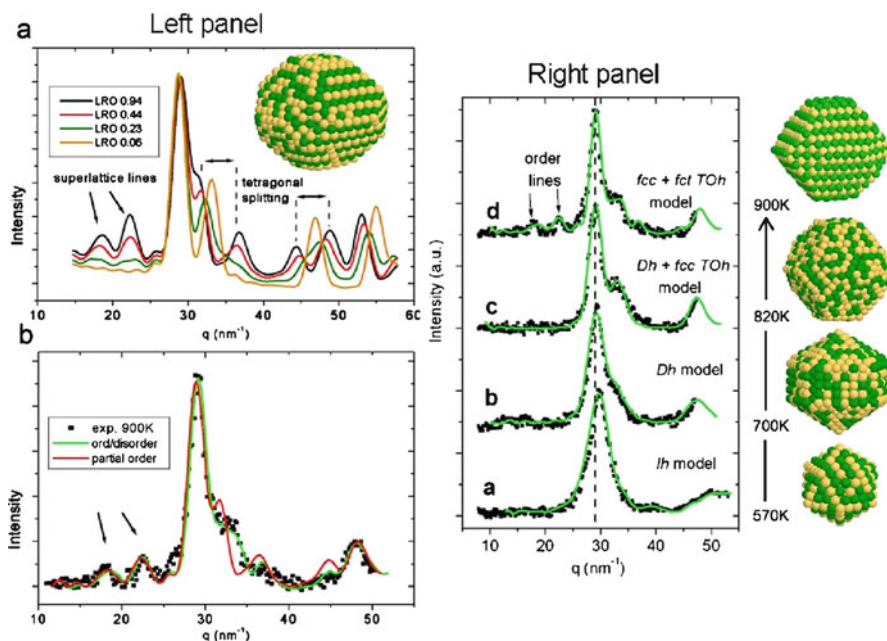


Fig. 7.17 On the *right panel*, experimental and calculated GIXD spectra of Co-Pt clusters at increasing temperature during the growth in situ. As the temperature increases, the structure evolves from Ih to Dh and FCC TOh. The insets show the snapshots of the simulated clusters. A vertical dashed line corresponding to the FCC(100) line is given for comparison. On the *left panel*, calculated GIXD spectra for different long-range order (LRO) parameters of the FCC TOh Co-Pt clusters and their comparison with the experimental one obtained at 900 K (adapted from [80])

transition of nanoparticles. This result is comparable to the theoretical one obtained in the precedent section concerning the bistability in the segregation transition of the Cu-Ag nanoalloys.

7.6 Conclusions

The study of the atomic structure and chemical ordering of nanoalloys is a fundamental task with a lot of industrial applications needing to build a strong link between the theoretical and experimental characterization of these systems in order to elaborate nanoalloy phase diagrams and the technical applications in various domains such as the heterogeneous catalysis, the ultra-high density magnetic storage, some optical properties in plasmonic, and some biomedical applications. The physical and chemical properties of these objects are very sensitive to their size, structure, and morphology, all depending on their elaboration condition. The recent numerical simulations in relation with very controlled experiments allow to draw a first picture toward nanoalloy phase diagrams as it has been shown here in two typical systems with the phase separation tendency (Cu-Ag) and with the ordering tendency (Co-Pt).

Acknowledgements It is a great pleasure to thank G. Tréglia, B. Legrand, R. Ferrando, C. Ricolleau, P. Andreazza, and F. Calvo for very fruitful discussions; some of them being the authors of many results presented in this chapter.

References

1. Ducastelle F (1991) In: de Boer FR, Pettifor DG (eds) Order and phase stability of alloys, Cohesion and Structure series, vol. 3. North-Holland, Amsterdam
2. Hultgren R, Desai PD, Hawkins DT, Gleiser M, Kelley KK (1981) In: Selected values of the thermodynamic properties of binary alloys. American Society for Metals, Berkeley, Jossey-Bass
3. Tréglia G, Legrand B, Ducastelle F, Saúl A, Gallis C, Meunier I, Mottet C, Senhaji A (1999) *Comp Mater Sci* 15:196
4. Faraday M (1857) *Philos Trans* 147:145
5. Sinfelt JH (1979) *Rev Mod Phys* 51:569
6. Sinfelt JH (1983) *Bimetallic catalysts: discoveries, concepts and applications*. Wiley, New York
7. Campbell CT (2004) *Nature* 432:282
8. Norskov JK, Bligaard T, Rossmeisl J, Christensen CH (2009) *Nature Chem* 1:37
9. Sun S, Murray CB, Weller D, Folks L, Moser A (2000) *Science* 287:1989
10. Benten W, Nilius N, Ernst N, Freund H-J (2005) *Phys Rev B* 72:045403
11. Gaudry M, Cottancin E, Pellarin M, Lerm J, Arnaud L, Huntzinger JR, Vialle JL, Broyer M, Rousset JL, Treilleux M, Mlinon P (2003) *Phys Rev B* 67:155409
12. Huang X, Jain PK, El-Sayed IH, El-Sayed MA (2007) *Nanomedicine* 2:681
13. Lacroix L-M, Bel Malaki R, Carrey J, Lachaize S, Goya GF, Chaudret B, Respaud M (2009) *J Appl Phys* 105:023911

14. Purushotham S, Ramanujan RV (2010) *J Appl Phys* 107:114701
15. Ferrando R, Jellinek J, Johnston RL (2008) *Chem Rev* 108:845
16. Johnston RL, Ferrando R, Henry CR, Horswell SL, Johnson BFG, Lievens P (2008) *Faraday Discussion Nanoalloys: From Theory to Applications* 138
17. Ducastelle F, Gauthier F (1976) *J Phys F6*:2039
18. Turchi P, Sluiter M, de Fontaine D (1987) *Phys Rev B* 36:3161
19. Tréglia G, Legrand B, Ducastelle F (1988) *Europhys Lett* 7:575
20. Legrand B, Tréglia G (1990) *Surf Sci* 236:398
21. Tréglia G, Legrand B, Eugène J, Aufray B, Cabané F (1991) *Phys Rev B* 44:5842
22. Müller M, Albe K (2005) *Phys Rev B* 72:094203
23. Yang B, Asta M, Mryasov ON, Klemmer TJ, Chantrell RW (2006) *Acta Materialia* 54:4201
24. Lequien F, Creuze J, Berthier F, Legrand B (2008) *Faraday Discuss* 138:105
25. Lequien F, Creuze J, Berthier F, Braems I, Legrand B (2008) *Phys Rev B* 78:075414
26. Connolly JWD, Williams AR (1983) *Phys Rev B* 27:R5169
27. Chepulsii RV, Butler WH (2005) *Phys Rev B* 72:134205
28. Chepulsii RV, Butler WH, van de Walle A, Curtarolo S (2010) *Scripta Materialia* 62:179
29. Geng HY, Sluiter MHF, Chen NX (2006) *Phys Rev B* 73:012202
30. Rosato V, Guillopé M, Legrand B (1989) *Phil Mag A* 59:321
31. Cleri F, Rosato V (1993) *Phys Rev B* 48:22
32. Foiles SM, Baskes MI, Daw MS (1986) *Phys Rev B* 33:7983
33. Jacobsen KW, Stoltze P, JK Norskov (1996) *Surf Sci* 336:394
34. Finnis NW, Sinclair JE (1984) *Phil Mag A* 50:45
35. Rafii-Tabar H, Sutton AP (1991) *Phil Mag Lett* 63:217
36. Müller M, Erhart P, Albe K (2007) *Phys Rev B* 76:155412
37. Müller M, Albe K (2007) *Acta Materialia* 55:6617
38. Mottet C, Tréglia G, Legrand B (1997) *Surf Sci Lett* **383** L719
39. Baletto F, Ferrando R, Fortunelli A, Montalenti F, Mottet C (2002) *J Chem Phys* 116:3856
40. Soler JM, Beltrán MR, Michaelian K, Garzón IL, Ordejón P, Sánchez-Portal D, Artacho E (2000) *Phys Rev B* 61:5771
41. Baletto F, Ferrando R (2005) *Rev Modern Phys* 77:371
42. Mottet C, Tréglia G, Legrand B (2002) *Phys Rev B* 66:045413
43. Baletto F, Mottet C, Ferrando R (2002) *Phys Rev* 66:155420
44. Baletto F, Mottet C, Ferrando R (2003) *Phys Rev Lett* 90:135504
45. Rossi G, Rapallo A, Mottet C, Fortunelli A, Baletto F, Ferrando R (2004) *Phys Rev Lett* 93:105503
46. Wang G, Van Hove MA, Ross PN, Baskes MI (2005) *J Chem Phys* 122:024706
47. Liu HB, Pal U, Perez R, Ascencio JA (2006) *J Phys Chem B* 110:5191
48. Van Hoof T, Hou M (2005) *Phys Rev B* 72:115434
49. Mariscal MM, Oldani NA, Dassie SA, Leiva EPM (2008) *Faraday Discuss* 138:89
50. Atanasov I, Hou M (2009) *Surf Sci* 603:2639
51. Parsina I, Baletto F (2010) *J Phys Chem C* 114:1504
52. Tréglia G, Goyhenex C, Mottet C, Legrand B, Ducastelle F. In: Alloyeau D, Mottet C, Ricolleau C (eds) (2012) *Nanoalloys: synthesis, structure and properties*. Springer London Heidelberg New York Dordrecht
53. Creuze J, Braems I, Berthier F, Mottet C, Tréglia G, Legrand B (2008) *Phys Rev B* 78:075413
54. Los JH, Mottet C, Tréglia G, Goyhenex C (2011) *Phys Rev B* 84:180202(R)
55. Amara H, Bichara C, Ducastelle F (2008) *Phys Rev Lett* 100:056105
56. Los JH, Pellenq JM (2010) *Phys Rev B* 81:064112
57. Frenkel D, Smit B (1996) *Understanding molecular simulation: from algorithms to applications*. Academic, San Diego
58. Binder K, Heermann DW (1988) *Monte Carlo simulation in statistical physics: an introduction*, Springer series in solid states sciences. Springer, Berlin
59. Andersen HC (1980) *J Chem Phys* 72:2384

60. Metropolis N, Metropolis AW, Rosenbluth MN, Teller AH, Teller E (1953) *J Chem Phys* 21:1087
61. Swendsen RH, Wang JS (1986) *Phys Rev Lett* 57:2607
62. Buffat Ph, Borel J-P (1976) *Phys Rev A* 13:2287
63. Borel J-P (1981) *Surf Sci* 106:1
64. Journet C, Maser WK, Bernier P, Loiseau A, Lamy de la Chapelle M, Lefrant S, Deniard P, Lee R, Fisher JE (1997) *Nature (London)* 388:756
65. Mottet C, Rossi G, Baletto F, Ferrando R (2005) *Phys Rev Lett* 95:035501
66. Aprá E, Fortunelli A (2003) *J Chem Phys* 107:2394
67. Mottet C, Tréglia G, Legrand B (1997) *Surf Sci* 383:L719
68. Ferrando R, Fortunelli A, Rossi G (2005) *Phys Rev B* 72:085449
69. Legrand B. In: Alloyeau D, Mottet C, Ricolleau C (eds) (2012) Segregation and phases transitions in reduced dimensions. Springer London Heidelberg New York Dordrecht
70. Langlois C, Alloyeau D, Le Bouar Y, Loiseau A, Oikawa T, Mottet C, Ricolleau C (2008) *Faraday Discuss* 138:375
71. Lequien F, Creuze J, Berthier F, Legrand B (2006) *J Chem Phys* 125:094707
72. Delfour L, Creuze J, Legrand B (2009) *Phys Rev Lett* 103:205701
73. Braems I, Berthier F, Creuze J, Ttot R, Legrand B (2006) *Phys Rev B* 74:113406
74. Mottet C, Tréglia G, Legrand B (1992) *Phys Rev B* 46:16018
75. Bochicchio D, Ferrando R (2010) *Nano Lett* 10:4211
76. Plumer ML, von Ek J, Weller D (2001) *The physics of ultra-high-density magnetic recording*. Springer, Berlin
77. Tournus F, Tamion A, Blanc N, Hannour A, Bardotti L, Prével B, Ohresser P, Bonet E, Epicier T, Dupuis V (2008) *Phys Rev B* 77:144411
78. Miyazaki T, Kitakami O, Okamoto S, Shimada Y, Akase Z, Murakami Y, Shindo D, Takahashi YK, Hono K (2005) *Phys Rev B* 72:144419
79. Alloyeau D, Ricolleau C, Mottet C, Oikawa T, Langlois C, Le Bouar Y, Braidly N, Loiseau A (2009) *Nature Mat* 8:940
80. Andrezza P, Mottet C, Andrezza-Vignolle C, Penuelas J, Tolentino JCN, De Santis M, Felici R, Bouet N (2010) *Phys Rev B* 82:155453
81. Rossi G, Ferrando R, Mottet C (2008) *Faraday Disc* 138:193
82. Yang B, Asta M, Mryasov ON, Klemmer TJ, Chantrell RW (2005) *Scripta Materialia* 53:417
83. Calvo F, Mottet C (2011) *Phys Rev B* 84:035409

Chapter 8

Modelling Janus Nanoparticles

Francesca Baletto

8.1 The Janus World: An Introduction

In 1992, during his Nobel speech, P.-G. de Gennes raised the concept of “Janus particles,” referring to them as “new animals” [1, 2]. These new animals were Janus grains, first made by Casagrande and Veyssié [3, 4]. They are named after the ancient Roman god Janus, who has two faces simultaneously looking to the future and to the past. The Casagrande’s grains have similarly two sides: one apolar while the other polar, with obviously two opposite behaviours, as schematically reported in Fig. 8.1.

Somehow, as discussed in the following, this concept has been extended and a “Janus principle” has been proposed whenever a small particle is formed by the combination of two incompatible elements and it presents two opposite regions [6]. An additional requirement is that its size has to be small enough to ensure that its motion is Brownian when it is on suspension. Usually, this requirement is satisfied when the considered particle has a diameter less than a few micrometers [7].

The Janus principle has been widely applied in colloidal physics, where these objects have a special architectural feature of two different chemical make-ups; the most common one is to have opposite polarity, for example, being hydrophilic on one side and hydrophobic on the other. In the last few years, the term Janus has been extended to describe not only the half–half geometry, but different particles such as dendritic macromolecules, block copolymer micelles, or inorganic materials [5]. All these systems respect the Janus balance, which has been defined as the ratio between the energy required to move the Janus particle itself from the water–oil interface into the oil phase divided by the energy required to move it in the water phase [8]. This is a critical parameter for the description of Janus particles and for the control of

F. Baletto (✉)

Physics Department, King’s College London, London WC2R 2LS, UK

e-mail: Francesca.baletto@kcl.ac.uk

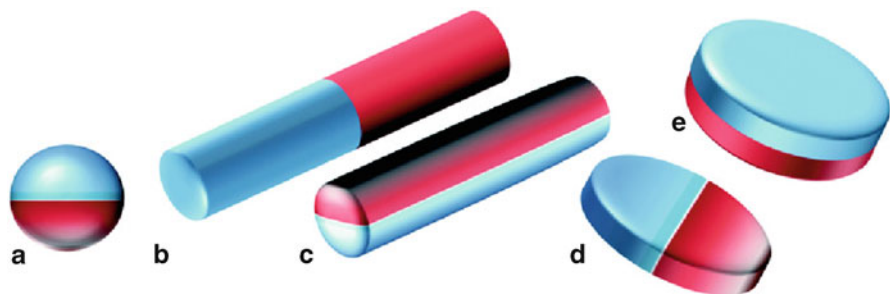


Fig. 8.1 Schematic representation of compartmentalised colloidal particles with various architectures. The *blue* and *red* sides are characterised by opposite polarity. Reproduced from Walther and Müller [5], by permission of The Royal Society of Chemistry

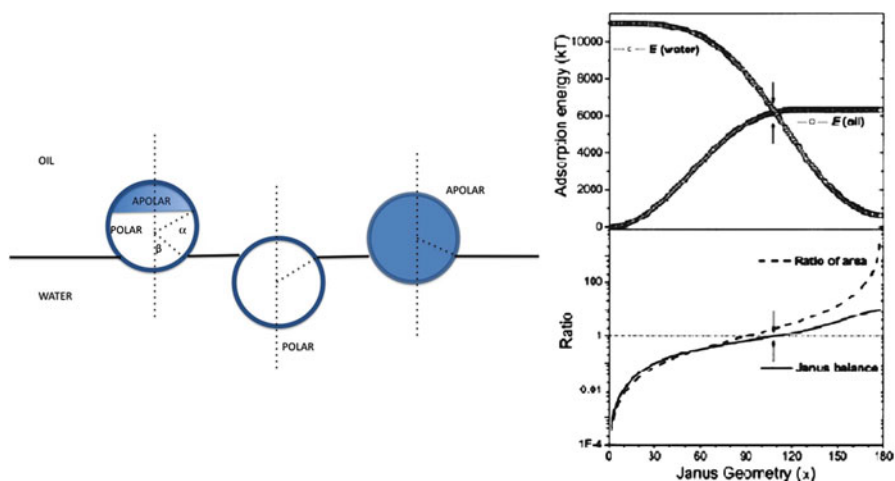


Fig. 8.2 *Left panel*: geometrical, α , and contact, β , angles in a Janus particle at the oil–water interface. α is a measure of how large the polar and apolar hemispheres are. *Right panel*: behaviour of the adsorption energy (*top*) and Janus balance (*bottom*) as a function of α . Adapted with permission from Jiang and Granick [8]. Copyright AIP Journal

their geometry and coverage during the fabrication of the particle itself. The Janus balance has been shown to depend strongly on the angle between the oil–water interface and the level of the hydrophobic hemisphere, as shown in the left panel of Fig. 8.2, where the main consequence is that the half–half composition may not be the best geometry for certain applications. In these cases, it has been preferred to use the terminology “patchy particle”, meaning a particle with at least one well-defined patch through which it can experience a strongly anisotropic, highly directional, interaction with other similar particles [9, 10]. The Janus particles can be considered as a special case among the patchy world.

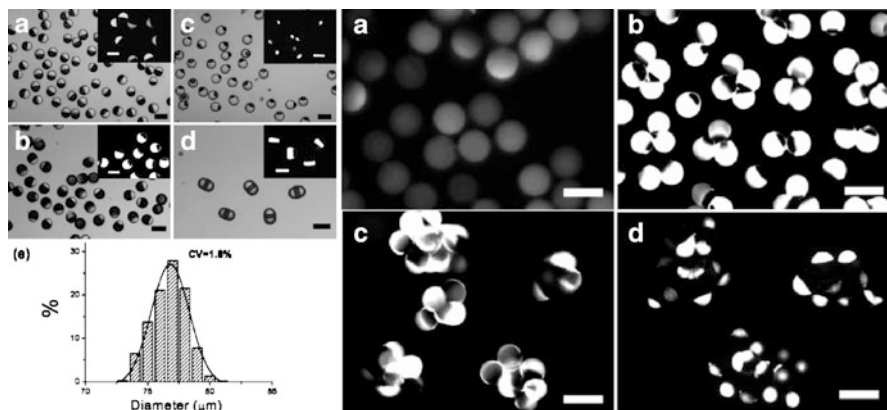


Fig. 8.3 *Left panel:* optical microscopy images of single Janus droplets produced in a microfluidic synthesis using two (a–c) or three (d) immiscible monomers, and average size. *Right panel:* fluorescence images of cluster of Janus spheres made with two immiscible polymers at water–oil interface. Scale bar is 100 μm. Adopted with the permission from Nie et al. [11]. Copyright 2006 American Chemical Society

Although not strictly unique to Janus systems, one of their most fascinating properties is the ability to form a porous layer at the boundary of two regions (i.e. water–air or water–oil) through which molecules can still diffuse. What de Gennes has described as a “skin that can breathe”, identifies small amphiphilic Janus particles which behave as surfactants at the water–air interface without forming a dense and impermeable layer, but allowing a chemical exchange between the two “worlds” thanks to the interstices among the Janus spheres themselves [2]. These nanoparticles can also be used in other important fields like drug or gene delivery, as building blocks for assembly of supra-structures. They can be employed as electronic displays and nano-motors, where the signal transduction generated by the fact that hydrophobic sides must face one another is exploited: when a nearest neighbour rotates, the next-nearest neighbour must follow and so on down the line.

Colloidal bi-compartmentalised particles, and their naturally formed clusters can provide different fluorescence images depending on the relative fraction of the aggregating part, as reported in early experiments by the Kumacheva’s group [11], and reported in Fig. 8.3.

Very recently, it has been thought to associate the flexibility and complexity of soft matter to other branches of physics, where a concept like the Janus principle can be applied to a novel class of metamaterials which simultaneously present two distinct regions. Examples are provided by a single optical device acting as a lens and as a beam shifter [12], a self-assembly of bimetallic atoms with a non-magnetic and a magnetic face [13], or a optical and a magnetic part [14]. In the following, the “Janus nomenclature” is going to be used for the description of bimetallic nanoalloys presenting an asymmetry in their chemical pattern, even in the core region, for which two distinct parts can be recognised, as in colloidal soft matter.

In this chapter, the attention is focused on the metallic alloying which represents one of the most important and fundamental mechanisms to modify the behaviour and properties of a material. With the manipulation of their size and shape, nanoscale systems offer a huge variety of ways to explore the interdependence between finite size and surface effects in order to obtain nanomaterials with desired physical and chemical properties [15, 16]. Playing with size and chemical ordering, bimetallic clusters with new and interesting magnetic, optical and catalytic features can be produced. First of all, let us explain why a bimetallic nanoparticle can be associated to a Janus bead.

Generally speaking, a bimetallic nanoparticle, made of metals A and B , can present various chemical orderings ranging from mixed to completely segregated morphologies [15, 17], as depicted schematically in Fig. 8.4. Mixed alloys can be either random or ordered, as the case for the $L1_0$ geometry of AuCu and AuAg alloys [18–20], while segregated motifs often manifest themselves as a core/shell order where a core of metal A is surrounded by a B -shell [21, 22], or multishell alloys, where the A and B metallic layers are alternating as $A-B-A$ [23] or $A-B-A-B$ [24]. When two metallic elements are mixed at the nanoscale, one possible chemical pattern is having a layered structural motif reminiscent of the Janus architecture, as cartooned in the middle row of Fig. 8.4.

Although in the last decade, a huge effort has been done to produce and to model core–shell bimetallic motifs, for their possible use as nano-catalysts, the preparation of bi-compartmentalised particles is still in its infancy. With a successful preparation of these clusters, a new chemistry, based on nanoparticles instead of atoms, could be envisioned, in which combining specific physical properties (e.g. optical, magnetic, electrical) results in revolutionary material combinations. Bimetallic Janus clusters can, for example, be applied as magnetic switchers and to create structural colouration, via plasmonic effects, on fibres and textiles. This can potentially transform the textile industry in anti-counterfeiting, positive identification of paper or clothing, and/or the development of fibres and woven materials with cloaking properties within certain wavelength ranges. Since the physical and chemical properties of a nanoparticle are a direct consequence of its electronic structure, which depends on its geometrical configuration, our main aim is to be able to design clusters with the optimal geometry for a given application simply by tuning their size and chemical composition [16].

After a brief summary of the state-of-the-art in the modelling of colloidal Janus particles, a discussion on how the growth of metallic nanoalloys can be modelled by means of molecular dynamics simulations follows, with a focus under which conditions chemical asymmetries can be observed and tailored. Different methodologies are reported, although for a complete review of the use of atomistic numerical simulations for the description of physical and chemical properties of nanoparticles, we refer to other specific texts; see, for example, Barnard [25], Johnston [26], Ferrando et al. [27] and references therein.

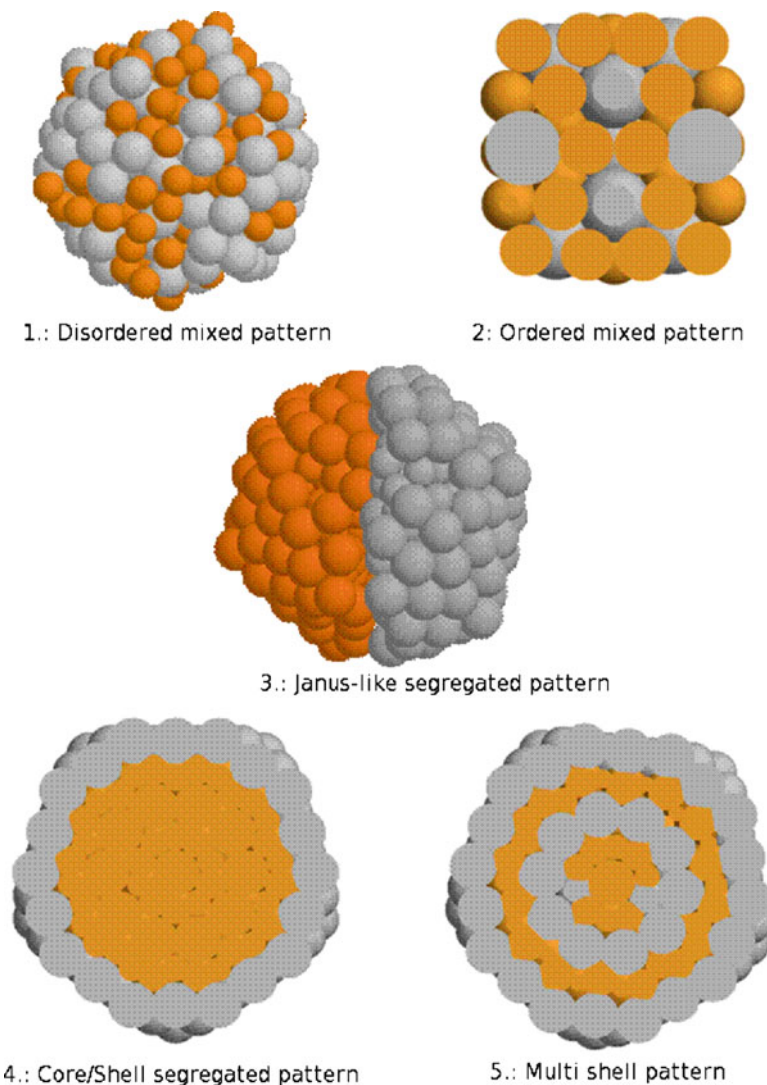


Fig. 8.4 Chemical patterns in bimetallic nanoalloys: (1 and 2), completely alloyed (1) random, and (2) ordered. Different segregation motifs: (3) Janus; (4) Core/shell and (5) multi-shell

8.2 Colloidal Janus Particles

After the work of Casagrande et al. [3,4], a huge effort has been put into fabricating Janus grains whose intrinsic surface chemical anisotropy leads to asymmetric interaction offering the possibility of spontaneous clusterisation, as is the case for phospholipids [28]. Under microscope, some interesting structures were observed—e.g. micelles and the elongated string shapes have formed when individual Janus

beads polymerise into superstructures. The engineering of colloidal surfaces, specifically the controlled design of their anisotropy, and the patchy formation have attracted the attention of many researchers dedicated to the improvement of the synthesis techniques as well as to the exploration of novel technological applications [29–31].

To this end, over the last two decades many preparation methods have been proposed, developed, and implemented including Pickering emulsions, controlled surface nucleation, partial masking, tunable liquid optics, sensors, micro-rheological probes and microfluidic techniques. The interested reader is directed to recent reviews, like, for example, Walther and Müller [32], Perro et al. [5] and Pawar and Kretzschmar [33], and to references therein for more detailed information. In particular, microfluidic-based assembly offers a quite straightforward procedure to form clusters of colloidal granules with well-controlled size, morphology, and composition [28, 34]. The self-aggregation of Janus particles, being the most simple example of surfactant molecules characterised by a solvophilic and a solvophobic side, is one of the most promising bottom-up process to tailor and design materials with target properties. Being inspired by the large variety of structures present in the phase diagram of colloids, ranging from micelles to lamellae to unimers, the study on how Janus spheres cluster and on their phase separation has attracted recently a lot of attention. Janus particles, contrary to micelles, show a clear phase separation and even a gas–liquid critical point, although a micellar phase is still present at low temperatures [35–38].

Theoretical models, usually based on Monte Carlo (MC) numerical simulation technique, have been put forward in order to take into account the effect of directionality of the short-range attractive forces on the fluid–solid phase boundaries. One of the first attempts to model Janus colloids was performed by Hong and co-workers [34], where the authors considered spherical shells made of more than 12,000 particles, packed following the Hardin’s icosahedral algorithm [39], and the interaction between two particles is modelled as an attractive or repulsive square well potential, depending on the relative sign of their facing hemispheres. Using a potential width equal to 10% of the diameter of the Janus sphere, a pair potential has been fitted, taking into account all the possible orientations of a pair. The so-fitted colloidal pair potential has been subsequently used to describe the interaction of Janus particles, modelled as hard spheres, in MC numerical simulations where periodic boundary conditions have been applied. After a quite long thermalisation annealing time, the cluster shapes obtained from MC simulations were compared to experimental data obtained by epifluorescence microscopy measurements. The agreement has been found to be excellent as reported in Fig. 8.5. Additionally, it has been demonstrated that the charge asymmetry of individual Janus particles is preserved even when they cluster together.

Recently [36], grand-canonical Monte Carlo simulations have been used to investigate the phase diagram of the assembly of Janus beads; see Fig. 8.6. Each Janus sphere has been modelled as hard-core particle of diameter, σ , and the one-patch Frenkel’s model [40], inspired by the electrostatic repulsion of hydrophilic regions and the attraction of hydrophobic ones, has been applied.

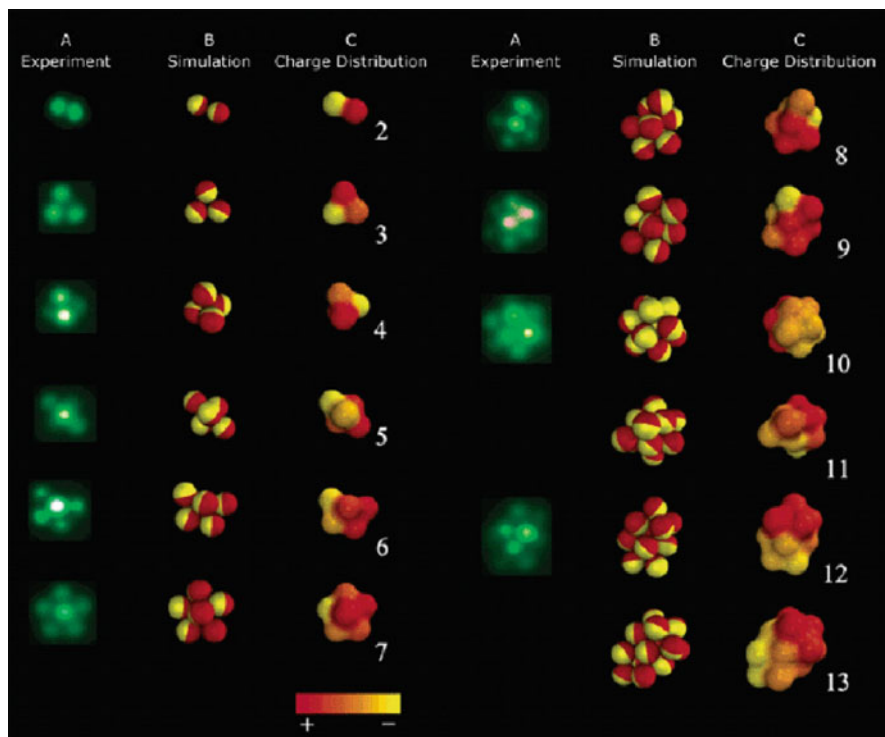


Fig. 8.5 Comparison between epifluorescence images (in *green*) and Monte Carlo simulations as a function of the cluster size. Each Janus particle of the cluster has the two hemispheres near-equally positive and negative charged (*yellow-* and *red-coloured regions*). Reproduced with the permission from Hong et al. [34]. Copyright 2006 American Chemical Society

A large number of particles have been considered to avoid size effects, and a simulation box size between 7- and 24-fold the diameter of the Janus sphere has been chosen. The total energy per particle is monitored as a function of density and temperature. First of all, it should be noted that the phase diagram depends strongly on the relative coverage of the patchy sphere itself, as reported in panel (a) of Fig. 8.6. The interaction between Janus objects is hard core, except when the segment joining their centre passes through their two attractive hemispheres. In this case, they interact via a square well potential of depth u_0 and a range half the diameter of the Janus particle itself. As main result, and quite surprisingly, it has been found that the coexisting curve in the P–T plane is characterised by a negative slope, meaning that the gas phase is more stable thanks to the formation of orientation ordered agglomerates, as micelles and/or vesicles, while the liquid phase is stabilised by a directional entropic contribution, as depicted in the panel (b) of Fig. 8.6.

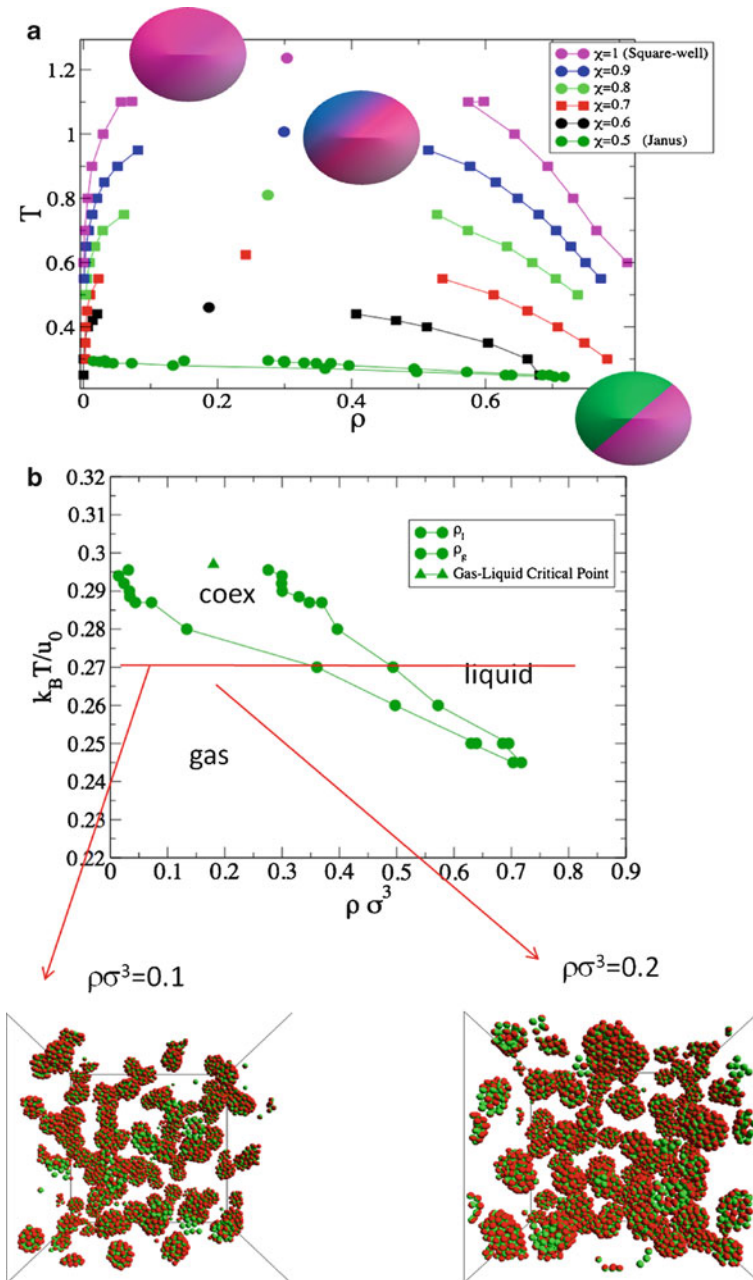


Fig. 8.6 Panel (a): phase diagram of the one-patch Kern–Frenkel model as a function of the coverage of the sphere ranging between 0.5 (Janus case, *green–purple*) and 1 (hard sphere case, *purple*). Panel (b): zoom in of the phase-diagram of the Janus particles showing the gas–liquid coexistence lines. A schematic representation of simulation snapshots at different densities, taken at $\frac{k_B T}{u_0} = 0.27$. Adapted from Sciortino et al. [37]. Reproduced by permission of PCCP Owner Societies

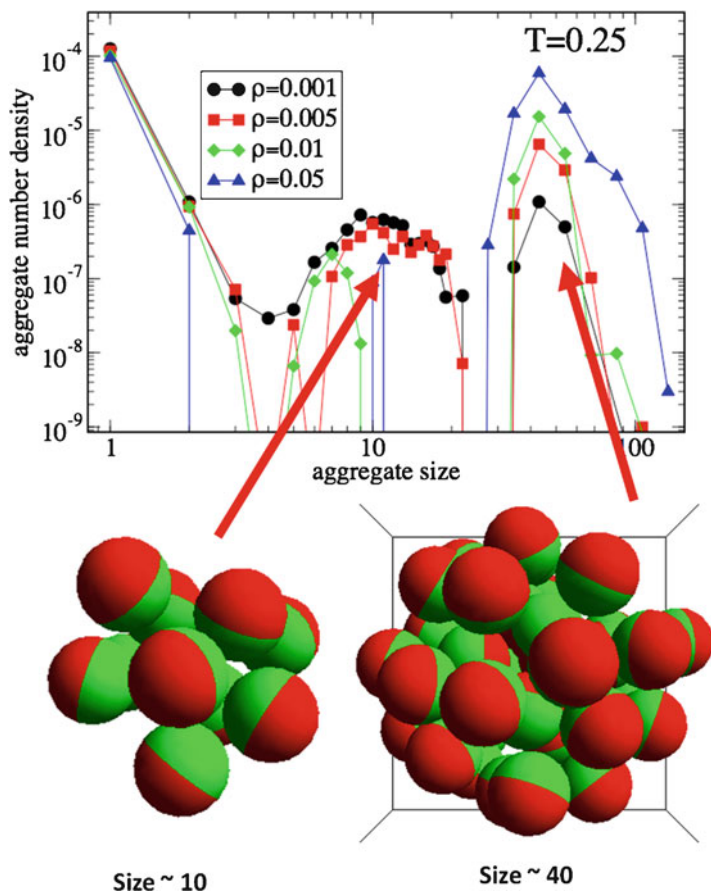


Fig. 8.7 Clustering of Janus spheres: micelles and vesicles, depending on the number of particles in the cluster. Taken from Sciortino et al. [37]. Reproduced by permission of PCCP Owner Societies

If their number is less than 20, Janus spheres agglomerate as micelles, where the attractive hemispheres all point towards the centre. Vesicles appear at larger sizes, where a double-layer motif with a repulsive outer shell is formed, as shown in Fig. 8.7. It should be added that the stability of these clusters depends strongly on their entropy, due to the internal flexibility of the spheres within the aggregate, and on the cluster morphology, both of which are controlled by the range width of the potential [37, 41].

The kinetics and chemical anisotropy during the assembly of colloidal Janus particles have been studied combining molecular dynamics (MD) simulations and experimental data [42]. Here, NVT ensemble MD simulations, using a velocity-Verlet algorithm and a Langevin thermostat, have been carried out in a simulation box 15-fold the Janus diameter σ , and periodically repeated along x and y axis while

the top and bottom walls are represented by truncated Lennard–Jones potentials. The attractive potential between Janus particles depends on their distance and angles between the director and the separation lines, with a sufficiently small interaction range to ensure contact interactions. A gravitational force of $0.54 \frac{k_{\text{B}}T}{\sigma}$ has been added along the z -axes in order to allow sedimentation during the aggregation process. The agreement between numerical and experimental data is excellent, where at both levels the formation of small and stable clusters has been shown to happen before their equilibration into helices for an average cluster size of 4–6 Janus beads. Additionally, since the helix formation is a direct consequence of the directionality of the pairwise interaction, it can be tuned by salt concentration: at high salt levels, an irreversible aggregation is caused by van der Waals forces, while at low to middle salt concentrations, the assembly of Janus particles can experience a hydrophobic attraction and the number of nearest neighbour is limited to six.

8.3 Bimetallic Janus Nanoparticles

At the nanoscale, when referring to metallic objects with a diameter below 100 nm which are neither in their solid nor molecular state, two important facts have to be borne in mind: the ratio of the number of surface to the volume atoms is large and the translation invariance has not to be imposed. The first consideration implies that the surface effects on the cohesive properties of the particle are not negligible; while the second means that even non-crystallographic geometries, e.g. fivefold axis, are allowed. Because of that, clusters do not react as bulk metals do, due to the different facets they expose and their localised or extended defects. The major consequence is that the electronic structure of metallic nano-aggregates and their mechanical and thermal stability depend strongly on their morphology. Thus, the identification of the geometrical motif of a nanoparticle as a function of its size is of crucial importance. In the case of nanoalloys, thanks to our growing ability in controlling their size and stoichiometry, there is a quite strong need of mapping the chemical ordering of multi-metallic nano-objects towards their size and chemical composition in order to create “new” materials matching specific requirements [15]. The outlook of possible chemical orderings for a bimetallic object has been schematically cartooned in Fig. 8.4. Only recently amid the numerical computational modelling community the interest in tailoring asymmetries in metallic nanoalloys has been growing, thanks to their various technological applications. The phase diagram of bimetallic clusters could be dramatically different from bulk. For example, the melting transition can be depressed or increased depending on the particle shape and number of impurities [43–48]; immiscible metals in the bulk could become miscible at the nanoscale, as AgFe; surface segregation effect can be dramatic (as for the case of bi-compartmentalised, or Janus, cluster reported in panel (c) of Fig. 8.4). A rather complete thermodynamic analysis of the segregation/mixing, based on the calculation of the Gibbs energy, has been reported in Shirinyan and Wautelet [49]

and Vallée et al. [50]. However, this analysis is limited to the case of spherical objects, and the effect of the shape has been introduced only through an effective geometrical factor.

Generally speaking, segregation effects, present in both core/shell and Janus like chemical patterns, are due essentially to the interplay between size mismatch of atomic species (since bigger atoms try to be at the surface) and surface energies (the outer shell is likely formed by the chemical species with the lowest surface energy). The immiscibility/miscibility gap are driven, therefore, by the high surface-to-volume ratio and the surface free energies together with the tendency of clusters to coalesce at temperatures smaller than their melting ones. Hence, it is extremely intriguing to calculate and to measure the phase diagram of nanoalloys, addressing, in particular, when they are completely mixed or when a segregation happens, leading to a core/shell or a bi-compartmentalised morphology. The reader interested in the modelling of phase diagram is redirected to the chapter in this book by Mottet. Chemical asymmetries are usually driven by out-of-equilibrium reactions during the growth process, resulting in an average shape which corresponds neither to the lowest energy minimum nor to the free-energy minimum structure. Although all the efforts in developing efficient techniques, such as genetic algorithms and basin hopping methods [51–53], to find the best structure at a given size and chemical composition, these tools are unable to give any information about the mechanical and thermal stability of the cluster itself. Nonetheless, even the knowledge of the minimum free-energy surface, when the entropic effects are directly considered, both in the quasi-harmonic approximation [54] or throughout the Metadynamics methods [55, 56], as recently applied to the study of gold [57] and salt clusters [58], is sometimes not sufficient for the prediction of the average cluster shape and its chemical pattern. Thus, the kinetic of the formation process is crucial to the full design and characterisation of bimetallic objects. It has been widely shown already for monometallic systems [59–61] that the final geometry of a nanoparticle is strongly influenced by the growth process because the short experimental time, of the order of milliseconds, allows the observation of kinetic trappings. These trappings can be due to the higher temperatures history, or to the memory of the geometrical shape at smaller sizes or to a partial coalescence, as observed in Yacaman's experiments of gold–palladium and gold–cobalt clusters; see Fig. 8.8.

As a result, it is important to model the growth of nanoalloys in order to understand their chemical ordering as a function of size and composition and to complete the outlook arising from the sampling of their lowest energy sequences and free-energy landscape.

Atom clusters can be produced in different ways by means of either chemical or physical processes and assembled into materials that can be studied by a variety of conventional surface science techniques. In the following the discussion is limited to the modelling of the growth as happens in a gas-condensation apparatus, with a particular focus to inert gas aggregation (IGA) sources. As other physical preparation techniques, including thermal ablation and ionic erosion, these sources

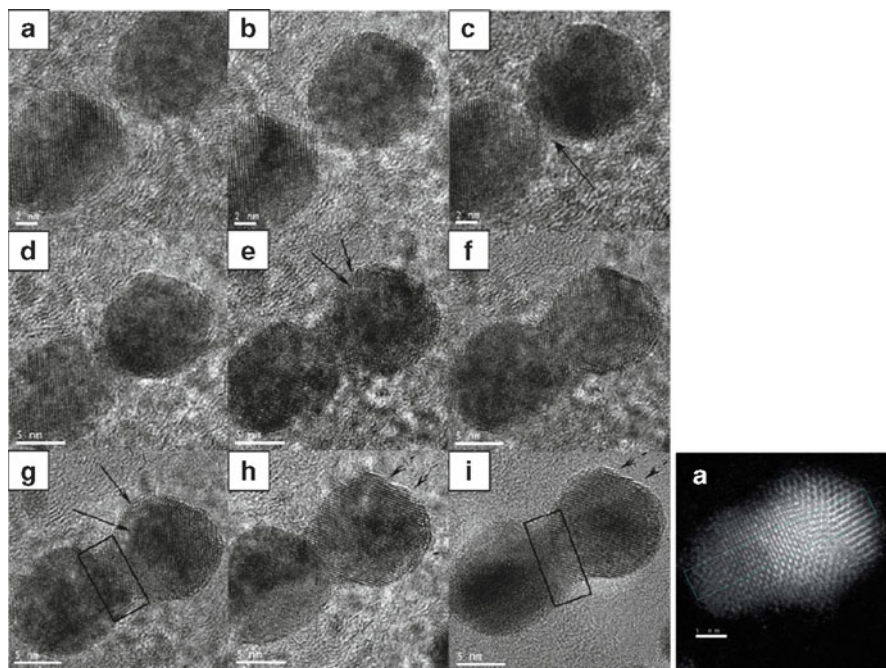


Fig. 8.8 *Left panel:* temporal evolution of AuPd clusters of 11 nm obtained via coalescence: (a) approaching; (b) first contact and reorientation of the planes; (c, d) neck formation and melting of surface atoms with planes that tend to align; (e) surface and core have a different contrast; (f, g) surface layer is still visible, and the neck of coalescence continues to align; (h) surface reconstruction appears, as indicated by *arrows*; and (i) the boundary between the particles is visible; the coalescence is still partial. Reproduced with the permission from Yacamán et al. [62]. Copyright 2005 American Chemical Society. *Right panel:* Cs corrected STEM-HAADF images of AuCo clusters with a brighter gold rich zone. Adapted by Mayoral et al. [63] by permission of The Royal Society of Chemistry

allow for a better control of the size of the cluster with respect to chemical routes which usually present a broader size and shape distribution. Anyway, for a detailed review of different vapour-phase synthesis of nanoparticles, the reader is directed to a recent review [64].

In IGA sources, schematically reported in Fig. 8.9, metal clusters are produced by evaporation and then condensation from a vapour in an inert gas atmosphere with a typical growth timescale of the order of a few milliseconds, for objects of several nanometers in diameter. The final nanoparticle geometry depends on the growth rate, usually tunable through the pressure and the mixture of the inert gases used, i.e., neon or argon/neon mixture [65–68]. Cluster morphology, as well as their chemical ordering in the case of bimetallic systems, can be systematically measured by microscopy measurements, like atomic force, scanning tunnelling and higher-resolution transmission electron microscopy. The scanning transmission electron microscopy (STEM) has been demonstrated possessing capability of exploring the

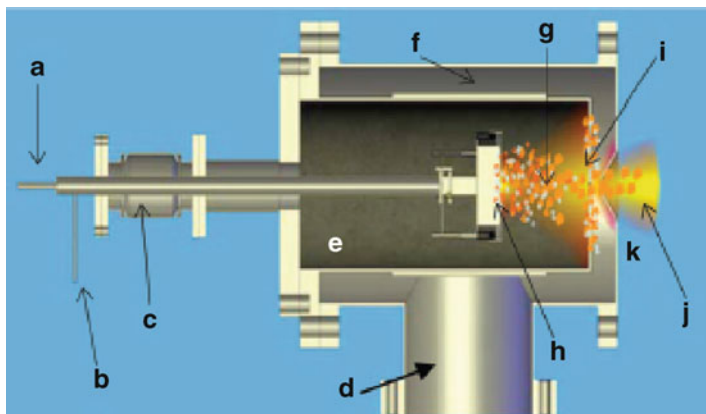


Fig. 8.9 Inert gas aggregation source: (a and b) gas and cooling water lines, (c) linear drive actuator, (d) vacuum pump, (e) partial pressure inside the aggregation chamber (~ 0.01 Torr), (f) cooling lines, (g) cluster zone formation, (h) metallic vapour (crucible), (i) skimmers, (j) nanoparticle beam and (k) partial pressure outside the aggregation chamber (typical values around 10^{-4} Torr). Reprinted with permission from Gracia-Pinilla et al. [65]. Copyright 2008 American Chemical Society

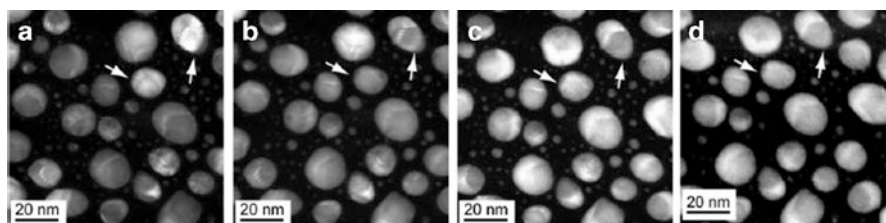


Fig. 8.10 Effect of the camera length (reciprocal of the collection angle) on HAADF images for AgCu nanoparticles: 520 mm (a), 285 mm (b), 100 mm (c) and 52 mm (d). The particles labelled by arrows underwent a contrast inversion. In panel (d), this is large enough to cancel partly the Bragg diffraction. Thus, the contrast can be attributed to the different chemical species in the sample. Taken from Langlois et al. [70], reproduced with the permission of corresponding authors

three-dimensional shape and structure of nanoparticles, especially, when used in association with the high-angle annular dark field (HAADF) imaging technique [69]. The STEM–HAADF method has been used to detect variation in chemical composition down to single-atom level in suitable samples; it can be successfully used to distinguish between chemical species characterised by a high Z-contrast [70–74], as reported in the right panel of Fig. 8.10.

Thanks to these techniques, we have got a strong experimental evidence of bimetallic clusters with asymmetries that can be identified as Janus-like, as reported in Fig. 8.8, for the gold–palladium case, and Fig. 8.11, after the co-deposition of copper–silver clusters.

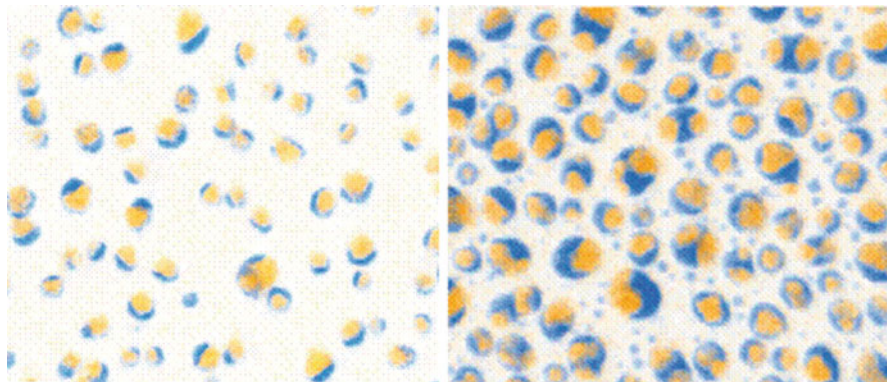


Fig. 8.11 HAADF-STEM measurements showing both core/shell and Janus chemical ordering for AgCu clusters. Adopted from Langlois et al. [72]. Reproduced by permission of Springer Publisher

From a computational point of view, there are few alternative ways to model the formation of metallic cluster, in contact with a thermal bath, based on classical molecular dynamics (cMD) numerical simulations:

- The coalescence of two pre-existing (parent) nanoparticles, where the daughter object is obtained from their collision. Critical parameters are the relative kinetic energy of the parent cluster and their impact factor.
- The one-by-one growth, where the cluster grows by the addition of atoms one-by-one starting from a small seed. Critical parameters are the deposition rate and the temperature T , kept constant.
- The cooling of liquid droplets, when the cluster is formed in a liquid state and then solidifies. The cluster size is kept fixed during the overall simulation and the temperature is reduced at a given rate, which is the main parameter to be set.
- Clusters are in contact with a liquid environment, where their shape and chemical ordering can vary due to the presence of chemicals around it, but their size remains the same.

It is worthy noting that, despite the importance of coated metallic nanoalloys, especially in biomedical applications, the modelling of the growth of mono- and bimetallic nano-objects in a wet environment is poorly documented and today this is limited to the case of gold cluster coated with thiols [75]. Before dealing with their details, the reason why a classical approach is adopted needs to be explained.

In the case of small systems, with a size less than several hundreds of atoms, with the today computational resources is possible to simulate times of the order of several tens of microseconds, which is comparable with experimental timescales.

On the other hand, the use of cMD is justified whenever the interatomic interaction can realistically be described in terms of empirical potentials, such as Gupta [76], Rosato–Guillope–Legrand [77], Sutton–Chen [78] and embedded atom [79]. In all these cases, the cMD approach offers an accurate and detailed description of the growth process, allowing for the description of the microscopic details leading to structural transformations, since it does not imply restrictive choices about the possible processes or the assumption of some rate theory to hold, as done, for example, in canonical Monte Carlo simulations. It has to be said, however, that growth of supported clusters or very large clusters require longer CPU time, for which the molecular dynamics tool is unfortunately too expensive. In these cases, kinetic Monte Carlo (KMC) is still to be preferred for the study of their chemical ordering and to detect their structural changes [80].

A final comment regards that, due to the intrinsic size limit, very few computational works have lead to bi-compartmentalised nanoparticles, which realistically could appear at large sizes. Moreover, the study of magneto-optical properties of bimetallic nanoparticles will require more accurate computational tools, such as spin density-functional-theory (DFT) and even all-electron-density-functional-theory, which are available only for small sizes, in most cases less than 200 atoms. To overcome this limit, the idea resides in coupling an efficient semi-empirical approach in order to get the most favourable structures from an energetic and thermodynamically point of view, with a spin-DFT approach, for the description of the magneto-optical properties, restricted to these sets of particles, or to smaller ones but with the same chemical motif. This should lead to the explanation of how magneto-optical properties depends on particle size and stoichiometry. However, this lies beyond the scope of this chapter which is focus on the modelling of asymmetries in nanoalloys, and we refer to other works for an explicit treatment of computational simulations and for the parametrisation of analytical theories [25, 81–83].

In the next sections, a detailed summary of the computational techniques based on cMD is discussed. The attention is put on case studies where Janus segregation has been observed: the coalescence of gold and platinum clusters of same size and same geometry, which leads easily to the formation of quite well-defined Janus objects with a prolate ellipsoidal shape 40 ps after the collision of the two parents clusters; the one-by-one and cooling of silver and cobalt nanoalloys which can lead to core–shell or quasi-like Janus patterns depending on the cobalt concentration.

8.4 Coalescence of Janus Nanoalloys

Coalescence refers to the physical process where two colliding objects merge to form a single new aggregate. In nanocluster physics, the formation of metal particles by condensation in an inert gas atmosphere has supposed to happen via coalescence of small and medium clusters inside the chamber. This hypothesis has been supported by the observation of “necklace-like” aggregates in first experiments where

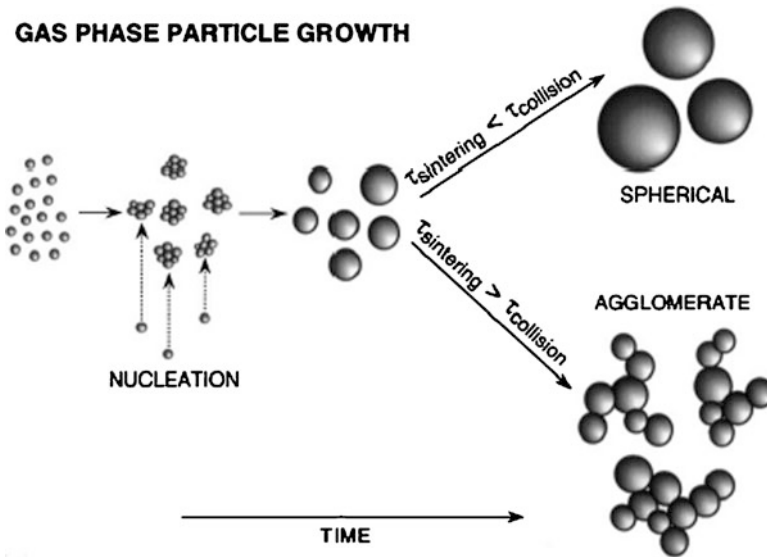


Fig. 8.12 Time evolution in a vapour-gas source: the final shape can be almost spherical or necklace agglomerate, depending if the collision time is faster than the sintering process. Taken from Zachariah and Carrier [87] with the permission of Pergamon publisher granted by CCC

metallic particles were grown in evaporation gas sources [84–86]. A schematic representation of the temporal evolution of the process is depicted in Fig. 8.12.

Within the classical nucleation theory, the activation barrier of the formation process is a balance between the bulk and the surface contributions to the free enthalpy of newly formed aggregates. A coalescence procedure has been applied for a variety of substances. For pure chemical species, the parameter describing the nucleation can be identified as the ratio of the vapour pressure of the system and the vapour pressure of the nucleating substance at the same temperature. For binary mixtures, instead, the partial pressure of one species divided by the pure substance vapour pressure at the same temperature should be used as order parameter to describe nucleation [88]. In addition, when the formation happens through coalescence, during the “collision” the total surface area of the cluster decreases, leading to the heating of the particle itself. This competes with the heat transfer by conduction to the colder carrier gas and radiation. This heating has to be taken into account when modelling the collision process [89].

The coalescence mechanism has been applied for the study of the nucleation of both monometallic [66, 90, 91] and bimetallic systems [92–95], in particular to detect the thermal evolution, stability versus melting. One of the first computational applications has been performed for the analysis of how the rate of coalescence influences the final morphology in the case of silicon particles, where the Si–Si interaction has been modelled by Stilling–Weber potential [96]. An average temperature behaviour is reported in Fig. 8.13 where two silicon nanoparticles of 240

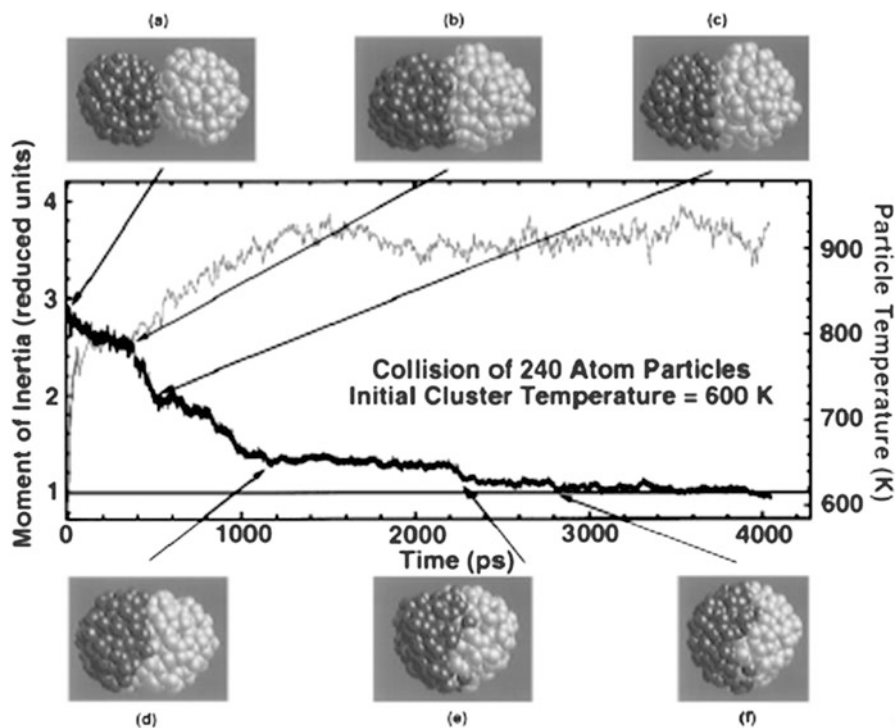


Fig. 8.13 Time evolution of the inertia momentum (*dark*) and of temperature (*grey*) of daughter aggregate after the collision of 240 Si atoms particles. Typical snapshots during the simulation are reported as well. Taken from Zachariah and Carrier [87] with the permission of Pergamon publisher granted by CCC

atoms are colliding after being equilibrated at 600 K. Rather independently of the chemical species considered, three main stages can be envisioned in the coalescence process, modelled through constant-energy molecular dynamics simulations:

- Equilibration: the parent clusters have been equilibrated at the desired temperature, and the averaged properties of each cluster have been collected.
- Collision: the two clusters are displaced at a distance between 0.4 and 0.6 nm where the atom–atom interaction is still weak. The same velocity with opposite sign is assigned to each particle in order to generate collision. The centre of mass (COM) of the total system has conveniently been chosen as reference, in order to avoid a non-zero linear momentum due to momentum conservation. The choice of the impact parameter, meaning the distance between the direction lines of the parent clusters, and their momentum are the critical parameters of the simulation [14].
- Nucleation and relaxation: the structural evolution of the daughter aggregate is analysed towards the time and the temperature.

It has been generally found that a neck rapidly forms between the colliding particles, which transforms into a spherule, and slowly approaches a sphere, as depicted in (8.8). The sintering is essentially driven by surface diffusion and, therefore, by the energy barriers which characterise the jump and exchange of adatoms. The exponential behaviour of the diffusion coefficient by the temperature, justifies the sensitivity to temperature. If the gas temperature around the cluster is high enough, the particle temperature increases due to heat release from coalescence (surface energy contributions) will be faster than the heat transferred to the surroundings. This will effectively increase the temperature of the cluster. If the gas is quite cold, conduction and radiation will dominate, and thus the particle will roughly remain at the gas temperature [97]. Therefore, when T is low enough to allow for allowing a solid–solid coalescence, the final structure will result to be highly defected with a considerable number of stacking faults, due to the finite timescale. Nonetheless, a complete melting can occur after the collision, and the formed cluster can solidify inside or outside the aggregation chamber. In the specific case of lead clusters [66], the authors have introduced a collision time of 1 ns, comparable with typical times of an IGA source. The collision of two icosahedral objects of 565 atoms, put at an initial distance of 0.5 nm, was followed by constant-energy MD simulations. After the collision, a neck is formed between the particles and its growth releases surface energy, causing the heating of the cluster. An almost spherical shape was reached just after 0.5 ns. In this way, the authors were able to detect how the final shape depends on the heating and whether—or not—the cluster undergoes to a melting transition.

Quite recently, the coalescence procedure has been applied for the study of bimetallic clusters, as reported by Paz et al. [14], Li et al. [92] and Mariscal et al. [95]. A cartoon of different snapshots at different stages and temperatures after the collision with a zero impact parameter of Cu_{682} and Ni_{682} clusters is reported in Fig. 8.14.

Many of the studies available in literature consider a zero impact factor, meaning that the two colliding particles have been aligned along a specific axis. On the other hand, in the case of bimetallic nucleation, the impact parameter should influence the final shape of the particle, as recently demonstrated by Mariscal and co-workers [14]. They have analysed the effect of introducing a non-zero impact parameter ξ , defined as the distance between the two COM with respect to the direction of the initial momenta, divided by the radius of the two clusters, as depicted in Fig. 8.15.

The main consequence of applying a small but non-zero impact parameter, $0 < \xi < 1$, is that the formed aggregate will acquire a vibrational–rotational dynamics coupled with the translation one, which could affect its final geometry and chemical order. If the collision momenta are large and for cluster configurations close to a spherical shape, the effect of ξ can be averaged over different initial orientations of the two nanoparticles, without loosing in the qualitative picture, as schematically summarised in Fig. 8.16, where the temporal evolution of gold–platinum clusters (Au_{586} and Pt_{586} initially presenting a crystalline geometry) is shown for different impact factors (y -axis) and for two different initial momenta (upper and lower panel).

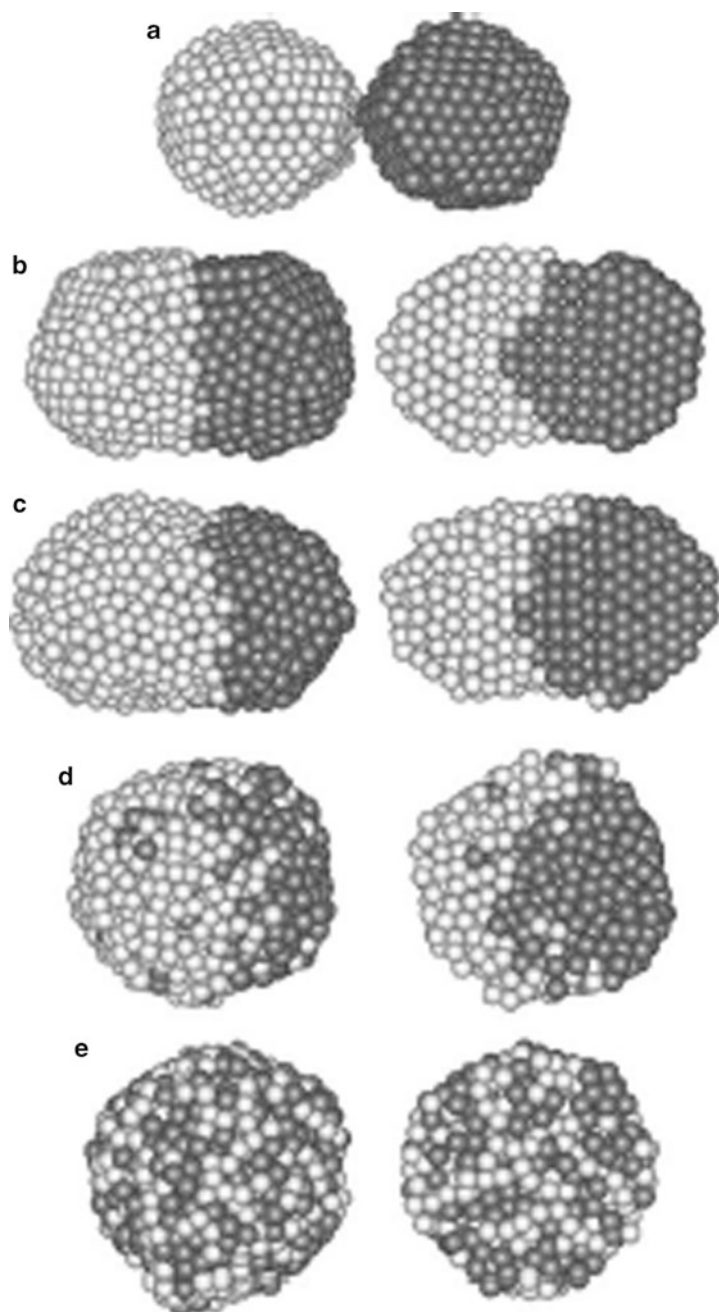
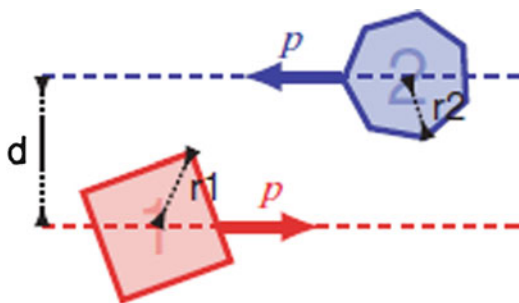


Fig. 8.14 Panel (a): initial Cu and Ni cluster after being thermalised at 640 K. For (b–e) panel, the *left column* refers to the whole structure, while the *right one* is a cross-section. Temperature is changing from 640 K (a and b) to 920 K in panel (c), to 1,080 K (d) and 1,400 K (e). Taken from Li et al. [92] with the permission of Springer publisher

Fig. 8.15 Definition of the impact parameter ξ in reduced units. Reproduced from Paz et al. [14] with the permission of AIP



It is important to point out that when high momenta are considered, $Pt_{shell}-Au_{core}$ and Janus-like motifs are formed for impact factor lower or bigger than 0.49, respectively. While the Janus-like formation takes place when ξ is bigger than 0.49, showing that the shell formation is slowed down as the impact factor increases. This can be due to a decreasing of the potential energy just after the collision (increment of the total average coordination), to an increasing of the internal energy of the cluster, to the elongation of the neck between the two colliding particles. An analysis is provided by the same authors and summarised in Fig. 8.17, where the shape is roughly divided in spheres, oblates and prolates, or equivalently in terms of their axes a , b and c . These geometries can be identified by the triaxial parameter $k = \ln(ca/b^2)$: the prolate has a positive k , an oblate motif a negative one, while a sphere is characterised $a = b = c$ and $k = 0$.

For $0.49 < \xi < 0.98$, the shape of the daughter aggregate is a prolate one and a Janus chemical pattern can be observed. A spherical and probably core/shell particle result at lower ξ and when the collision of the parent cluster is quite kinetic.

8.5 The One-by-One Growth of Janus Nanoalloys

The one-by-one growth technique [98, 99] has been used to successfully study the growth of bimetallic nanoparticles [100]. Its importance resides in the ability of this simple model to detect kinetic effects during the formation of particles, and to show segregation effect in silver alloys, as the core/shell, the three onion-core shells and Janus-like motifs [13, 23].

This model follows the deposition–diffusion–aggregation method used to mimic the formation of island on flat surfaces. The building up of a cluster is due to the deposition of adatoms onto a small seed which is in contact with an inert gas, which acts as a thermal bath and keeps the temperature constant, as depicted in Fig. 8.18. The incoming adatom adsorbs on a cluster and it is free to move on the surface, to reach and attach on islands or steps, as happens on a flat surface, or to penetrate in the core. Desorption is allowed, although it has been never observed in the case of metallic or bimetallic systems, even because the adsorption energies in metallic

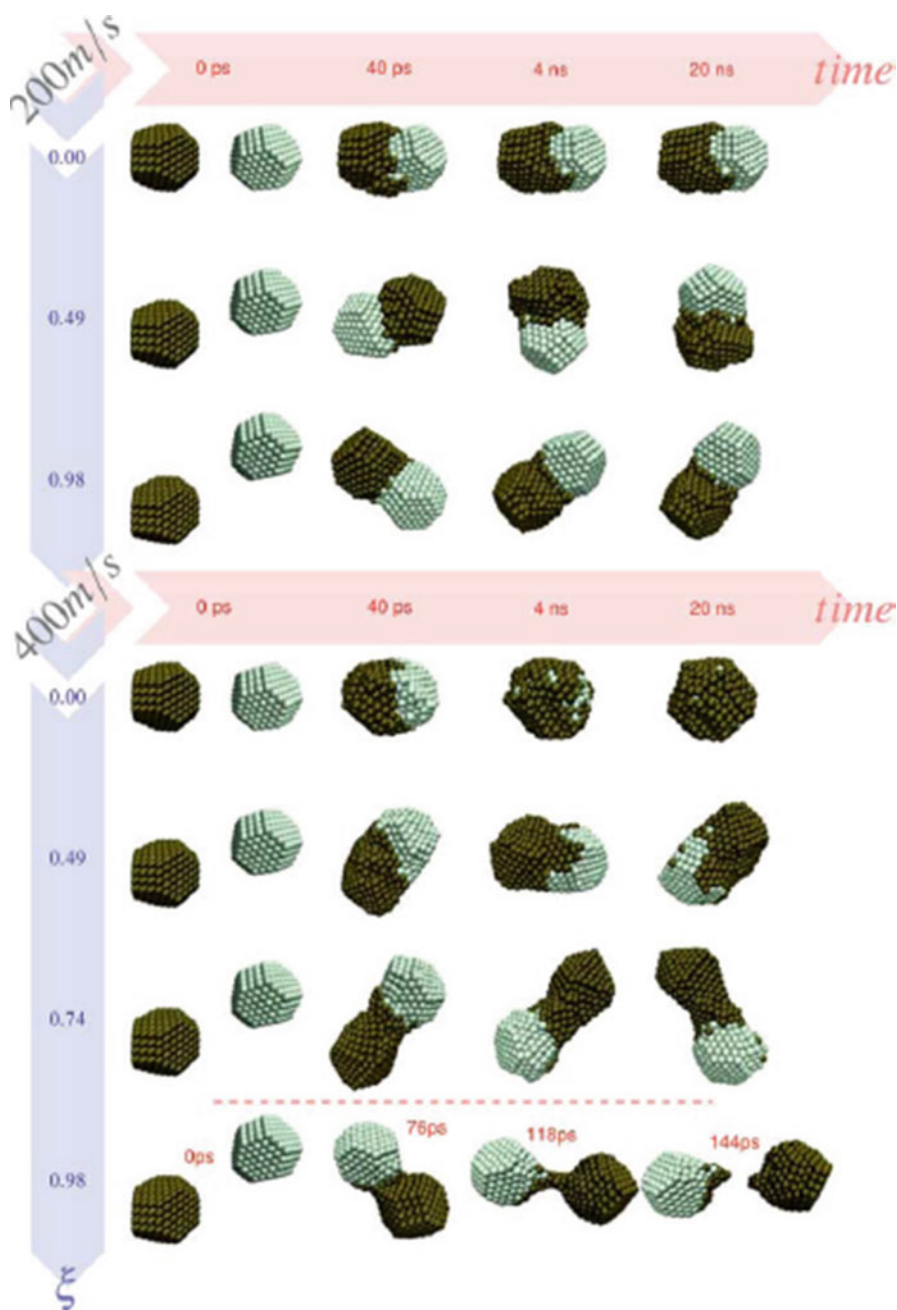


Fig. 8.16 Different snapshots arisen after collision of Au₅₈₆ (golden sphere) and Pt₅₈₆ (dark) as a function of their impact parameter ξ , as defined in the text. Two different momenta, 200 and 400 m/s, *top* and *bottom* panels, respectively, have been considered. Time is reported on the horizontal axes, where $t = 0$ ps is the beginning of the simulation itself. Reproduced from Paz et al. [14] with the permission of AIP

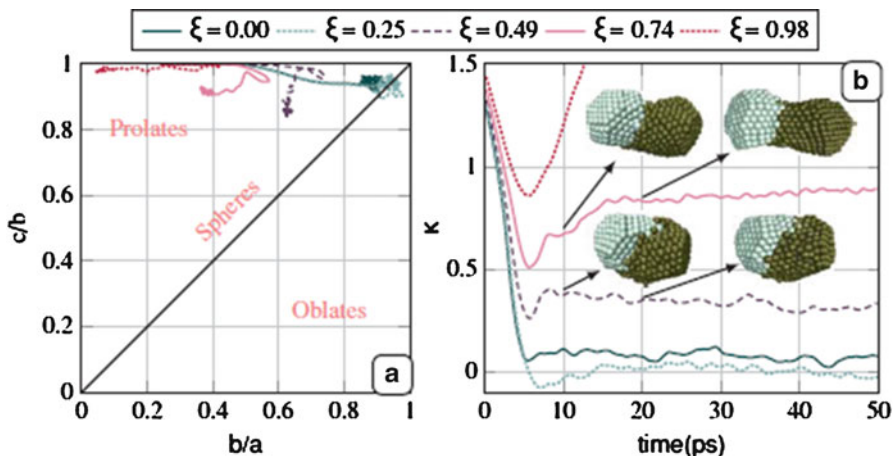


Fig. 8.17 Time evolution of the triaxial parameter k , as defined in the text, for different impact parameters. The final shape after coalescence is a prolate one, except for $\xi = 0.98$ where the steep increase is due to the detachment of the particles. Reproduced from Paz et al. [14] with the permission of AIP

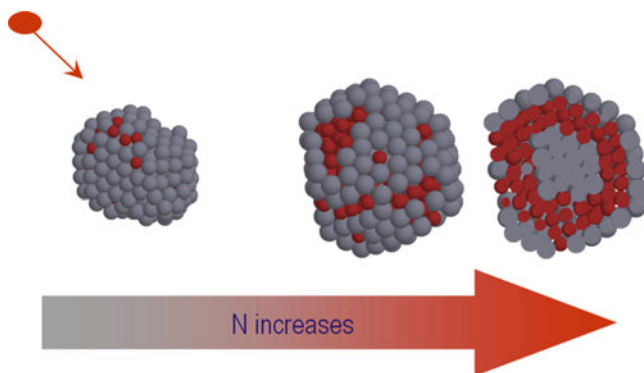


Fig. 8.18 Schematic representation of the one-by-one growth: atoms in *red* are deposited one-by-one over a free nanoclusters

system are quite high, larger than 1 eV (while at room temperature the Boltzmann factor is ~ 0.023 eV). The presence of the thermal bath leads to the introduction of an Andersen thermostat [101], where the average collision frequency of the thermostat ν , has been chosen according to two opposite needs: ν has to be large in order to have an efficient thermostat, but it must be not too large because the thermostat must not influence the diffusive properties [99].

Free nanocluster growth simulations started from a small seed, taken from one of the best minima for a given metallic system, and further atoms have been deposited one by one at time intervals τ_d . The initial position of the incoming particle is chosen on a random point on a large sphere centred around the COM of the nanoparticles

and far enough in order to neglect the interaction with the seed itself. It approaches towards the cluster with a constant velocity corresponding to a typical evaporation temperature of the material and in such a way that its kinetic energy is smaller than the adsorption energy. Between two subsequent depositions, all the atoms of the cluster are thermalised at the desired temperature T , and they are free to move following the Newton's equations, solved throughout the velocity-Verlet algorithm [102]. The deposition time τ_d is the reciprocal of the adatom flux ϕ^M given by

$$\phi^M = \frac{PA_{\text{eff}}}{\sqrt{2\pi m_M k_B T}}, \quad (8.1)$$

where T and P are the temperature and pressure of the metallic vapour, respectively, the atomic mass is m_M and the effective area of the cluster is A_{eff} . Referring again to the case of inert gas sources, the flux has been estimated to be of the order of one atom each 100 ns [103, 104], being quite close to the simulation deposition time of one atom per several nanoseconds, used for studying the formation of clusters up to a radius of 1.5–2 nm. The growth process can be analysed monitoring the excess energy, Δ , defined as

$$\Delta = \frac{E_{\text{tot}} - \left(N^{\text{Ag}} \epsilon_{\text{Ag}}^{\text{coh}} + N^{\text{Co}} \epsilon_{\text{Co}}^{\text{coh}} \right)}{N_{\text{tot}}^{3/2}}, \quad (8.2)$$

where E_{tot} is the total energy of the cluster and ϵ^{coh} is the cohesive energy of an atom in its bulk crystal. A stable structure is identified by a dip in the Δ quantity.

As a prototype application of the one-by-one model, the case of silver–cobalt is considered here. When cobalt is deposited over silver, it has been shown that silver–cobalt nanoalloys can present controlled asymmetries already at small sizes. First, cobalt atoms have been deposited over small silver seeds, such as the icosahedron Ag–Ih₅₅ and the decahedron Ag–Dh₇₅ [105]. Except, low temperatures, where the formation of asymmetric structures is very likely at an initial stage of the growth, the core/shell structures have been observed after the addition of 30 or 60–70 cobalt atoms. The latter corresponds to a rather spherical shape and with an external Ag_{shell}, equivalent to the anti-Mackay icosahedron at $N_{\text{tot}} = 127$ atoms, as found when Ag is deposited on a Co seed [100]. It is worth noting that the Dh₇₅ undergoes a complete structural transformation towards an icosahedral shape after the deposition of a few cobalt atoms. Anyway, as soon as the initial silver seed is slightly bigger, such as the decahedron, Dh₁₄₆, and the icosahedron, Ih₁₄₇, the formation of asymmetric Janus-like motifs happens when the cobalt concentration is smaller than 30%, as reported in Fig. 8.19. Low growth temperatures favour the formation of asymmetries, while, above 550 K, the growth over Ag–Dh₁₄₆ leads to a fully structural transformation towards a core/shell structure, where cobalt is forming an icosahedral core of 147 atoms and silver is displaced over an anti-Mackay stacking, reminiscent of the perfect Ag₁₃₂Co₁₄₇ [100]. The formation of a well-defined core is highlighted by deep dips in the Δ quantity around $N_{\text{dep}}^{\text{Co}} \sim 174$, as shown in the left column of Fig. 8.19.

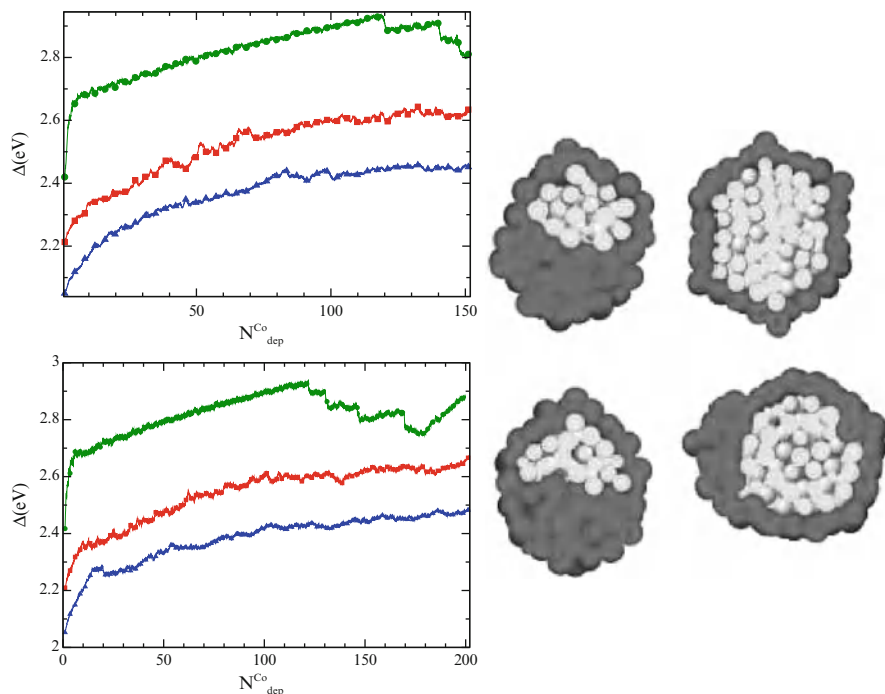


Fig. 8.19 Energy in excess Δ during the deposition of Co (light grey) over Ag (dark grey), Ih_{147} (top) and Dh_{146} (bottom) at different temperatures, from bottom to up: $T = 450$ K, up-triangle; $T = 550$ K square and $T = 650$ K, circle. For cobalt poor composition, a Janus-like asymmetry (first snapshot) is formed which evolves towards an icosahedral core/shell structure (second snapshot) for Co concentration higher than 30%

When the deposition has been performed over bigger Ag cores, like the truncated octahedron at 201 atoms, TO_{201} and the icosahedron Ih_{309} , the asymmetry formation results in a rather wide range of chemical compositions. In both the considered cases, the formation of Janus-like structures appears when a perfect Co(core)/Ag(shell) is joined to a pure silver clusters, as shown in the dips of the excess energy, Δ in Fig. 8.20, especially at high temperatures.

This is mainly due to the fact that, at these sizes, the best adsorption sites for cobalt are around subsurface positions where Co atoms bunch up, respecting an icosahedral packing, thanks to the softness of their interatomic potential [105], and as revealed by a geometrical analysis of the environment of each pair of nearest neighbour. This leads to the formation of an object delimited by (111) facets and presenting a Janus-like order, with two well-separated regions: one pure silver cluster and a well-defined cobalt icosahedral core covered by a silver layer over an hcp stacking. It is worth noting that these AgCo Janus-like structures naturally evolve towards a core/shell geometry for cobalt concentration of more than 40–45% for a medium-size nanoparticle, suggesting that chemical asymmetries can be tailored playing with the relative stoichiometry.

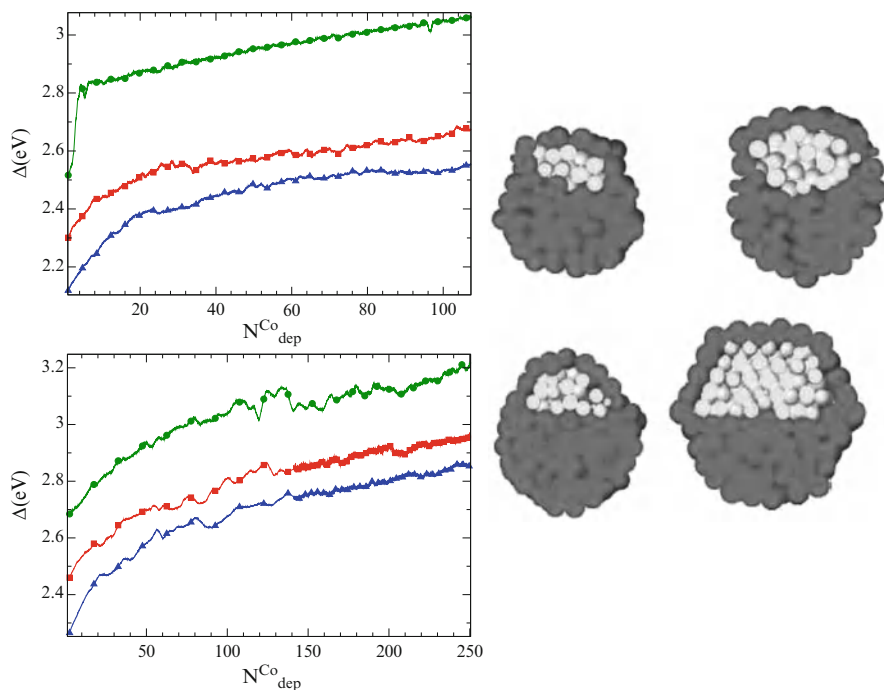


Fig. 8.20 Deposition of Co atoms over 201 and 309 Ag cores, *upper* and *lower* panel, respectively. Janus-like motifs have been obtained at different temperatures and for Co concentration up to 30–40%. Symbols as in Fig. 8.19

To fully demonstrate this idea, the deposition of silver atoms over the core/shell obtained at $\text{Ag}_{146}\text{Co}_{178}$ has been considered. One-by-one growth simulations have clearly shown that Ag preferentially agglomerates on one side of the core/shell, around one fivefold axis, allowing the formation of a well-defined Janus-like cluster as soon as the cobalt concentration drops below 47% as demonstrated by analysing the distance between the COM of the cobalt and silver regions, respectively, Δr_{COM} , as a function of the chemical composition of the cluster, as reported in Fig. 8.21. The increase of this quantity shows the formation of a Janus chemical pattern as silver is deposited.

8.6 Cooling into Janus Nanoalloys

As it has been found in experiments, such as inert gas aggregation and vapour condensation, and allowed in coalescence and one-by-one growth modelling, the formation of a nano-objects should not take place in a solid phase but they can build up as liquid droplets and then solidify [25]. Their final shape is, therefore, driven by

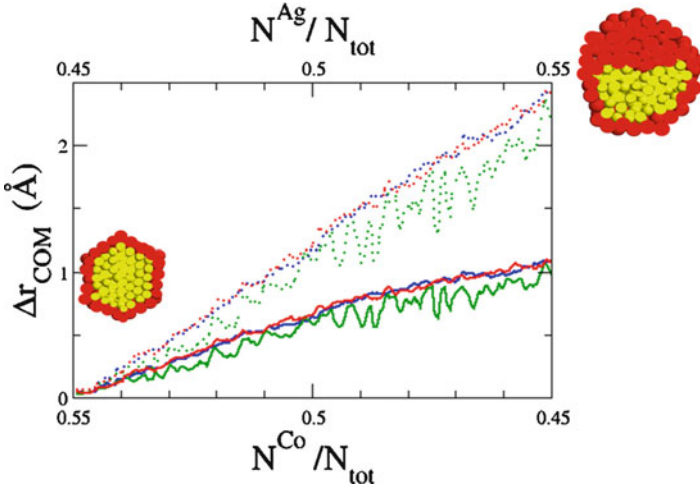


Fig. 8.21 Evolution of the distance between the centre of mass of Ag (*dark*) and Co (*light*) regions as silver is deposited showing the transition from a core/shell to a Janus-like motif. Typical initial and final snapshots are shown. *Dotted line* is the distance between the COM of the whole cluster and the one of Ag subcluster (*dotted line*), while the *broken line* is the distance between the COM and the Co subunits centre

the cooling process, that can take place inside or outside the condensation chamber. In the latter case, the cooling is dramatically fast due to the free expansion in the vacuum. Let us focus on the solidification inside the chamber, which depends on the choice of temperature and pressure of the gas. In order to mimic a thermal contact with a cold atmosphere, the cluster should be frozen at a rate $\tau_c = \frac{\partial T}{\partial t}$. The experimental rate of reference in an inert gas-aggregation source for cooling a spherical object of effective area A_{eff} , is given, similarly to (8.1),

$$\phi^C = \frac{PA_{\text{eff}}}{\sqrt{2\pi m_G k_B T_G}}, \quad (8.3)$$

where the temperature, T_G , and pressure P are referred to the inert gas. In the harmonic approximation, the energy loss per collision with an inter-gas atom is roughly $\frac{\partial T}{\partial t} \sim \phi^C \frac{\Delta E}{3Nk_B}$ leading to a reference value of 10^{-1} K/ns for a cluster of 1 nm radius, and an inert gas at room temperature at a pressure of 3 mbar.

CMD simulations have been performed keeping constant the cluster size N and rescaling the temperature accordingly with a freezing rate similar to the experimental one. An Andersen thermostat has been applied to change and to monitor the temperature of the cluster during the overall simulation. Since the process has been performed at fixed N , one can refer to this model as “growth at constant size” [106].

Between two subsequent temperatures, all the atoms are free to move accordingly with Newton’s equation of motion, and the physical quantities are averaged after

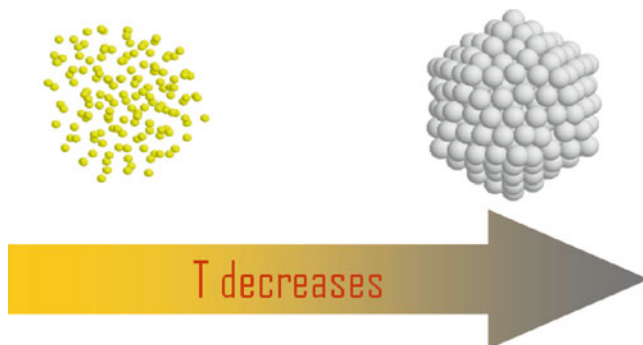


Fig. 8.22 Starting with a liquid seed with a given chemical composition and size. The temperature is lowered with a fixed rate, $\frac{\Delta T}{\delta t}$, where $\Delta T \sim 5$ K and δt is between 10^{-10} and 10^{-7} s

a short equilibration time at each new temperature. A schematic cartoon of the simulation process is reported in Fig. 8.22. It has been found to be more realistic, varying the temperature of small quantities, between 5 and 10 K, and reducing the time interval δt between 10^5 and 10^7 time step, which for a metal is in the range of few femtoseconds [106]. For a detailed description of the effect of the cooling rate, the reader is redirected to Shibuta and Suzuki [107] and VanHoang and Odagaki [108].

Freezing simulations can help us to determine the likeliest configuration at high temperatures and to check if any and which kinetic trappings appear during the solidification process. Moreover, it is an efficient tool to establish the thermal stability of a given structural motif or chemical ordering with respect another as a function of temperature [109–112].

In the previously proposed paradigmatic example of silver–cobalt, nanodroplets at $N_{\text{tot}} = 235$ and 265 with different chemical compositions have been considered. Their freezing temperatures are 570 ± 10 K and 600 ± 10 K, respectively. To detect the freezing/melting transition has been found extremely helpful to introduce the common neighbour analysis (CNA), which is more sensitive than other order parameter such as the Lindemann criterion [113]. The CNA geometrical analysis is based on the assignment to each pair of first neighbours of a triplet of integers (r, s, t) , where r is the number of common nearest neighbours of two atoms of the couple, s is the number of nearest-neighbour bonds among these r atoms, and t is the length of the longest chain which can be formed with the s bonds. The liquid/solid transition can be monitored considering the percentage (P) of $(r, s, t) = (5, 5, 5)$, $(4, 2, 1)$ and $(4, 2, 2)$, which describe the bulk and the P(3,1,1) and the P(3,2,2) for the description of (1 1 1) surfaces [88, 114]. As soon as the cluster become solid, the CNA percentages present a drastic change, rather simultaneously if core and surface melts/freezes at the same time. In particular, a jump of P(5,5,5) means the formation of solid fivefold symmetries, as reported in Fig. 8.23.

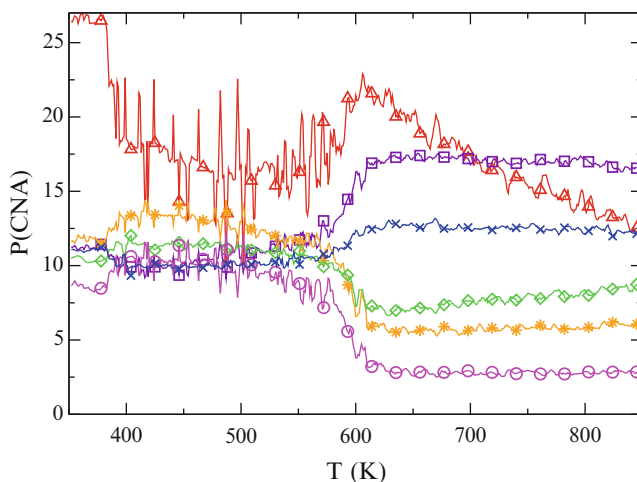


Fig. 8.23 CNA percentages as a function of T for a $(\text{AgCo})_{265}$ cluster. The solidification is identified by their fast change, happening almost simultaneously around 650 K. Colour scheme: P(5,5,5), *up-triangle*; P(4,2,2), *star*; P(4,2,1), *circle*; P(4,3,3), *square*; P(3,1,1), *diamonds*; P(3,2,2), *crosses*

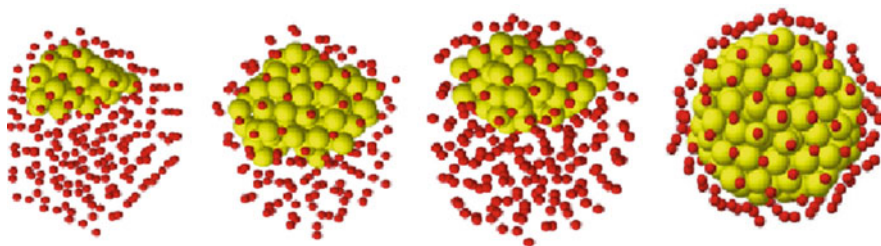


Fig. 8.24 Final snapshots after freezing of $\text{Ag}_{147}\text{Co}_{48}$, $\text{Ag}_{201}\text{Co}_{34}$, $\text{Ag}_{201}\text{Co}_{64}$ and $\text{Ag}_{147}\text{Co}_{118}$ confirming the formation of Janus-like chemical ordering when the cobalt concentration is less than 40%

The Janus-like structural motif has been easily identified in the final snapshot in all the considered cases with a cobalt concentration lower than 40%, as reported in Fig. 8.24, demonstrating the delicate role played by the chemical composition during the cluster formation.

In summary, the formation of chemical asymmetries, such as the Janus-like motif, in metallic nanoalloys has been reported. It has been shown that this type of segregation is mainly due to kinetic effects proper to the growth process and the short experimental timescale. Three different numerical simulation procedures have been identified to mimic this out-of-equilibrium process: coalescence, one-by-one growth and cooling. Notwithstanding their differences, these procedures are based on cMD, where velocity-Verlet algorithm is used for the numerical solution of the Newton's equation of motion and the atomic interactions are described by

empirical potentials. The methodology is quite well established; nonetheless, more studies should be carried out, given the variety of metallic nanoalloys for which both geometrical and chemical anisotropies can be exploited for technological applications, in particular as magnetic switchers.

References

1. Gennes PD (1992) *Angew Chem-Int Ed* 31:842
2. DeGennes P (1992) *Rev Mod Phys* 64:645
3. Casagrande C, Veyssie M (1988) *Compt Rend Ac Sci* 306:1423
4. Casagrande C, Fabre P, Raphaël E, Veyssie M (1989) *Europhys Lett* 9:251
5. Walther A, Müller A (2008) *Soft Matter* 4:663
6. Jiang S, Granick S (2008) *Langmuir* 24:2438
7. Granick S, Jiang S, Chen Q (2009) *Phys Today* 62:68
8. Jiang S, Granick S (2007) *J Chem Phys* 127:161102
9. Zhang Z, Glotzer S (2004) *Nano Lett* 4:1407
10. Glotzer SC, Solomon MJ (2007) *Nat Mater* 6:557
11. Nie Z, Li W, Seo M, Xu S, Kumacheva E (2006) *J Am Chem Soc* 128:9408
12. Zentgraf T, Valentine J, Tapia N, Li J, Zang X (2010) *Adv Mater* 22:2561
13. Parsina I, Baletto F (2010) *J Phys Chem C* 114:1504
14. Paz S, Leiva E, Jellinek J, Mariscal MM (2011) *J Chem Phys* 134:094701
15. Ferrando R, Jellinek J, Johnston R (2008) *Chem Rev* 108:845–910
16. Franceschetti A, Zunger A (1999) *Nature* 402:60
17. Jellinek J (2008) *Faraday Discussion* 138:193
18. Darby S, Mortimer-Jones TV, Johnston RL, Roberts C (2002) *J Chem Phys* 116:1536
19. Zhang M, Fournier R, Mol J (2006) *Struct-Theochem* 762:49–56
20. Chen F, Curley BC, Rossi G, Johnston RL (2007) *J Phys Chem C* 111:9157–9165
21. DeLaHoz M, Tovar J, Callejas R, Balbuena P (2009) *Mol Simul* 35:785–794
22. Rossi G, Rapallo A, Mottet C, Fortunelli A, Baletto F, Ferrando R (2004) *Phys Rev Lett* 93:105503
23. Baletto F, Mottet C, Ferrando R (2003) *Phys Rev Lett* 90:135504
24. Chen D, Wang W, Huang S (2006) *J Phys Chem B* 110:16193
25. Barnard A (2010) *Rep Prog Phys* 73:086502
26. Johnston RL (2002) *Atomic and molecular clusters*. Taylor and Francis, London
27. Ferrando R, Fortunelli A, Johnston R (2008) *Phys Chem Chem Phys* 10:640–649
28. Hong L, Jiang S, Granick S (2006) *Langmuir* 22:9495
29. Liddell CM, Summers CJ, Gokhale AM (2003) *Mater Charact* 50:69
30. Langer R, Tirrell DA (2004) *Nature* 428:487
31. Grätzel M (2001) *Nature* 414:338
32. Perro A, Reculosa S, Ravaine S, Bourgeat-Lami E, Duguet E (2005) *J Mater Chem* 15:3745
33. Pawar A, Kretzschmar I (2010) *Macromol Rapid Commun* 31:150
34. Hong L, Cacciuto A, Luijten E, Granick S (2006) *Nano Lett* 6:2510
35. Bianchi E, Blaak R, Likos C (2011) *Phys Chem Chem Phys* 13:6397
36. Sciortino F, Giacometti A, Pastore G (2009) *Phys Rev Lett* 103:237801
37. Sciortino F, Giacometti A, Pastore G (2010) *Phys Chem Chem Phys* 12:11869
38. Fantoni R, Giacometti A, Sciortino F, Pastore G (2011) *Soft Matter* 7:2419
39. Hardin RH, Sloane NJA, Smith WD (1994) <http://www2.research.att.com/njas/icosahedral.codes/>
40. Kern N, Frenkel D (2003) *J Chem Phys* 118:9882
41. Giacometti A, Lado F, Largo J, Pastore G, Sciortino F (2010) *J Chem Phys* 132:174110

42. Chen Q, Whitmer J, Jiang S, Bae S, Luijten E, Granick S (2011) *Science* 331:199
43. Delogu F (2010) *Mater Sci Forum* 653:31
44. Haberland H, Hippler T, Donges J, Kostko O, Schmidt M, von Issendorff B (2005) *Phys Rev Lett* 94:035701
45. Hock C, Strassburg S, Haberland H, von Issendorff B, Aguado A, Schmidt M (2008) *Phys Rev Lett* 101:023401
46. Mottet C, Rossi G, Baletto F, Ferrando R (2005) *Phys Rev Lett* 95:035501
47. Cheng D, Wang W, Huang S (2008) *Phys Chem Chem Phys* 10:2513–2518
48. Cheng D, Huang S, Wang W (2006) *Eur Phys J D* 39:41–48
49. Shirinyan A, Wautelet M (2004) *Nanotechnology* 15:1720
50. Vallée R, Wautelet M, Dauchot J P, Hecq M (2001) *Nanotechnology* 12:68
51. Wales D (1994) *J Chem Phys* 101:3750
52. Paz-Borbon L, Johnston R, Barcaro G et al (2007) *J Phys Chem C* 111:2936
53. Rossi G, Ferrando R (2006) *Chem Phys Lett* 423:17–22
54. Doye JPK, Wales DJ (1998) *Phys Rev Lett* 80:1357
55. Laio A, Parrinello M (2002) *Proc Natl Acad Sci USA* 99:12562
56. Laio A, Gervasio FL (2008) *Rep Prog Phys* 71:126601
57. Santarossa G, Vargas A, Iannuzzi M, Baiker A (2010) *Phys Rev B* 81:174205
58. Bealing C, Fugallo G, Martonak R, Molteni C (2010) *Phys Chem Chem Phys* 12:8542
59. Haberland, H (ed) (1994) *Clusters of Atoms and Molecules: Theory, Experiment, and Clusters of Atoms*. Berlin/Heidelberg, Germany: Springer-Verlag.
60. Baletto F, Levi A, Ferrando R (2003) Growth simulations of nanoclusters. In: *Encyclopedia of nanoscience and nanotechnology*. American Scientific Publishers, New York
61. Baletto F, Ferrando R (2005) *Rev Mod Phys* 371:77
62. Yacamán M, Gutierrez-Wing C, Miki M, Yang D-Q, Piyakis K, Sacher E (2005) *J Phys Chem B* 109:9703
63. Mayoral A, Mejía-Rosales S, Mariscal MM, Pórrüez-Tijerina E, Yacamán M-J (2010) *Nanoscale* 2:2647
64. Swihart M (2003) *Curr Opin Colloid Interface Sci* 8:127
65. Gracia-Pinilla M, Perez-Tijerina E, Garcia J, Fernandez-Navarro C, Tlahuice-Flores A, Mejía-Rosales S, Montejano-Carrizales J, Yacamán M (2008) *J Phys Chem C* 112:13492
66. Doye JPK, Hendy SC (2003) *Eur Phys J D* 22:99
67. DeHeer WA (1993) *Rev Mod Phys* 65:611
68. Knight WD, Clemenger K, Heer WAD, Saunders WA, Chou MY, Cohen ML (1984) *Phys Rev Lett* 52:2141
69. Li Z, Juan J, Chen Y, Palmer RE, Wilcoxon JP (2005) *Appl Phys Lett* 87:243103
70. Langlois C, Wang Z, Ricolleau PDC, Li Z (2010) *J Phys-Conf Ser* 241:012043
71. Li Z, Young N, Vece MD, Palomba S, Palmer R, Bleloch A, Curley B, Johnston R, Jiang J, Yuan J (2008) *Nature* 451:46
72. Langlois C, Oikawa T, Bayle-Guillemaud P, Ricolleau C (2008) *J Nanopart Res* 10:997
73. Langlois C, Alloeyau D, Bouar YL, Loiseau A, Oikawa T, Mottet C, Ricolleau C (2008) *Faraday Discussion* 138:375
74. Mejía-Rosales S, Fernandez-Navarro C, Perez-Tijerina E, Blom D, Allard L, Yacamán M (2007) *J Phys Chem C* 111:1256
75. Olmos-Asar J, Rapallo A, Mariscal M (2011) *Phys Chem Chem Phys* 13:6500
76. Gupta RP (1981) *Phys Rev B* 23:6265
77. Rosato V, Guillopé M, Legrand B (1989) *Philos Mag A* 59:321
78. Sutton A, Chen J (1990) *Philos Mag Lett* 61:139
79. Foiles S, Baskes M, Daw M (1986) *Phys Rev B* 33:12
80. Alloeyau D, Ricolleau C, Mottet C, Oikawa T, Langlois C, Bouar YL, Braidly N, Loiseau A (2009) *Nat Mater* 8:940
81. Gaston N, Paulus B (2007) *Phys Rev B* 76:214116
82. Durante N, Fortunelli A, Broyer M, Stener M (2011) *J Phys Chem C* 115:6277
83. Barcaro G, Fortunelli A, Polak M, Rubinchikov L (2011) *Nano Lett* 11:1766

84. Granqvist C, Buhrman R (1976) *J Appl Phys* 47:2200
85. Yatsuya S, Kasukabe S, Uyeda R (1973) *Jpn J Appl Phys* 12:1675
86. Kimoto K, Kamiya Y, Nonoyama M, Uyeda R (1963) *Jpn J Appl Phys* 2:702
87. Zachariah M, Carrier M, Aeresol J (1999) *Science* 30:1139
88. Lummen N, Krasha T (2007) *Model Simul Mater Sci Eng* 15:319
89. Lehtinen K, Zachariah M, Aerosol J (2002) *Science* 33:357
90. Ding F, Rosen A, Bolton K (2004) *Phys Rev B* 70:075416
91. Lummen N, Kraska T (2005) *Phys Rev B* 71:205403
92. Li G, Wang Q, Liu T, Wang K, He J, Cluster J (2010) *Science* 21:45
93. Lummen N, Kraska T (2007) *Eur Phys J D* 41:247
94. Mariscal M, Dassie S, Leiva E (2005) *J Chem Phys* 123:184505
95. Mariscal M, Oldani N, Dassie S, Leiva E (2008) *Faraday Discussion* 136:6
96. Stillinger F, Weber T (1985) *Phys Rev B* 31:5262
97. Zacarias AG, Castro M, Tour JM, Seminario JM (1999) *J Phys Chem A* 103:7692
98. Baletto F, Mottet C, Ferrando R (2000) *Phys Rev Lett* 84:5544
99. Baletto F, Mottet C, Ferrando R (2000) *Surf Sci* 446:31
100. Rossi G, Schiappelli G, Ferrando R (2009) *J Comput Theor Nanosci* 6:841
101. Anderson JB, Fenn JB (1985) *Phys Fluids* 8:780
102. Frenkel D, Smit B (1996) *Understanding molecular simulations*. Academic, London
103. Reinhard D, Hall BD, Ugarte D, Monot R (1997) *Phys Rev B* 55:7868
104. Reinhard D, Hall BD, Berthoud P, Valkealahti S, Monot R (1998) *Phys Rev B* 58:4917
105. Baletto F, Ferrando R, Fortunelli A, Montalenti F, Mottet C (2002) *J Chem Phys* 116:3856
106. Baletto F, Mottet C, and Ferrando R (2002) *Chem Phys Lett* 354:82–87
107. Shibuta Y, Suzuki T (2011) *Chem Phys Lett* 502:82
108. VanHoang V, Odagaki T (2008) *Philos Mag* 88:1461
109. Barnard A, Lin X, Curtis L (2005) *J Phys Chem B* 109:24465
110. Chen F, Johnston R (2008) *ACS Nano* 2:165
111. Lobato I, Rojas J, Landauro C, Torres J (2009) *J Phys-Cond Matter* 21:055301
112. Mayoral A, Estrada-Salas HBR, Vazquez-Duran A, Jose-Yacamán M (2010) *Nanoscale* 2:335
113. Lindemann F (1910) *Z Phys* 11:609
114. Faken D, Jonsson H (1994) *Comput Mater Sci* 2:279

Chapter 9

Modeling of Protected Nanoparticles

Jimena A. Olmos-Asar and Marcelo M. Mariscal

9.1 Why Study Nanoparticles?

Systems in the range between 1 and 50 nm have an intermediate size between single molecules and bulk materials. This is why they exhibit unique electronic properties which obey quantum-mechanical rules [1] that strongly depend on particle size and shape, as well as on interparticle interactions and protecting agents, if there were some. In these small systems, the outer electrons can tunnel between close particles. Mobile electrons are trapped and oscillate collectively, resulting in a plasmon resonance band. All quantum effects occur when the de Broglie wavelength of the valence electrons is of the order of the size of the particle itself.

On the other hand, unlike bulk metals, nanoparticles (NPs) can show some insulator character due to the fact that sometimes there is a gap between valence and conduction band. As a result, conduction—as well as other properties—can be tuned by varying the temperature, which confers NPs many applications in nanoelectronics, biosensing and catalysis [2, 3].

Perhaps the most important characteristic of materials at the nanoscale is the fact that they have a large fraction of their atoms on the surface. Since the volume of a nanoparticle decreases faster than the surface, when the nanoparticle size decreases, there is a limit where almost all atoms belong to the surface. This high ratio surface-to-volume gives to these materials unique properties, due to the fact that those atoms on the surface have a different surrounding from that in the bulk, and thus have a direct interaction with the close environment.

J.A. Olmos-Asar • M.M. Mariscal (✉)
INFIQC/CONICET, Departamento de Matemática y Física, Facultad de Ciencias Química,
Universidad Nacional de Córdoba, Córdoba, Argentina
e-mail: jimenaolmos@gmail.com; marmariscal@fcq.unc.edu.ar

9.2 Why Passivate Nanoparticles?

There are several methods for synthesizing metal nanoparticles. As the properties of these materials strongly depend on their size and shape, it is desirable to have a method of synthesis that allows scientist to have a well-distributed sample, with a narrow dispersion of sizes. Small particles tend to aggregate in order to reduce surface energy. For avoiding coalescence, agglutination or agglomeration and keeping them in a disperse state, these metal systems are usually passivated, in most cases by means of adsorption of some selected organic molecules. This passivation also allows controlling particle shapes and sizes in chemical synthesis.

In addition, adsorption of some specific organic compound serves as protection agent, for avoiding reaction of the metal with the media. Moreover, the protecting agent is the one exposed to the environment. So, many properties of the nanoparticle depend on the protecting ligands, for instance, solubility and chemical reactivity.

Recently, the functionalization of NPs by the adsorption of some specific receptors to the surface has had big implications in biomedicine. These agents react specifically with another agent in the human body, acting as a target. This is having applications in tumor targeting [4], cancer therapy, drug delivery [5], biosensors, etc.

One of the most widely investigated systems is perhaps gold NPs covered by alkanethiols molecules. One of the reasons for this is that gold NPs are among the most stable metal NPs [6]. Gold is easy to obtain and it is quite inert: it does not react with atmospheric oxygen or with many chemicals, and it does not oxidize under its melting point [7]. On the other hand, it is well known that the S–Au bond has a strong covalent character, with high adsorption energy. So, there are relatively simple routes of synthesis, where self-assembly plays an important role. Also, these systems are chemically stable. Some of the methods produce a narrow size distribution sample, while in others, it is necessary to fraction the product with some technique based on the mass.

9.3 Chemical Synthesis and Passivation

We will mostly refer now to one of the most common systems: gold NPs.

The molecules that attach to the metal surface can be described as composed of three different parts: a head group that bounds to the surface through covalent, non-covalent, or ionic interactions; a spacer part that makes up the interphase between the metal core and the medium; and a terminal group that is in direct contact with the environment.

The head group or linker determines how strong the interaction between the molecule and the metal is, and this bonding energy is usually independent of the rest of the molecule. The stronger the attachment of the surfactant, the more stable the passivated system is. If covalent bond is formed between the linker and the substrate, chemical adsorption is said to occur.

The spacer chains of adjacent molecules interact via van der Waals and/or ionic interactions, and confer stability to the adsorbed monolayer. If molecules interact strongly, the monolayer will be well packed, and the nanoparticle will be more protected. Steric effects can play an important role in the self-assembly process when voluminous molecules are used, and these, in turn, can partially control the interaction between passivated systems.

The tail or terminal group can be chosen for functionalizing the nanoparticle, and it determines the properties of the outer layer, which is, in fact, the one that interacts with the environment. For example, if charged polymers are employed as passivants, multilayers of opposite charged molecules can be obtained onto the surface; on the other hand, affinity with the media can be managed through some groups, such as $-\text{NH}_2$, $-\text{COOH}$ or $-\text{OH}$ that make the system hydrophilic and $-\text{CH}_3$ or $-\text{CF}_3$ that turn the system hydrophobic. The possibility of choosing the terminal group of molecules in such a way that they can selectively bond to specific targets represents an important challenge to medical and technological applications.

In the 1950s, Turkevitch [8] presented one of the most popular methods of synthesis of gold NPs by reduction of chloroauric acid (HAuCl_4), using sodium citrate as both reducing and capping agent in water. With this method it is possible to obtain nearly spherical NPs of approximately 20 nm, but the size is not controlled in the synthesis procedure, although if the sample is sufficiently stirred, the particles could be uniformly distributed. In the 1970s, Frens [9] proposed a procedure for preselecting the diameter of the NPs (between 16 and 147 nm) obtained just by controlling the ratio between reducing/stabilizing agents and gold amount.

In the 1990s, it was found that NPs could be stabilized by the addition of alkanethiols of different chain lengths [10].

The appearance of the Brust–Schiffrin method [11] for synthesizing gold NPs had a great impact in this area, because it allows to obtain in an easy way thermally and air-stable gold NPs [6] of controlled size (between 1.5 and 5.2 nm in diameter) and low dispersity. Moreover, the synthesized NPs can be redissolved in an organic media and then functionalized. The reaction is held in a two-phase system. In this technique, AuCl_4^- is transferred to toluene (anticoagulant) using the tetraoctylammonium bromide (TOAB) as phase-transfer and stabilizing agent, and sodium borohydride (NaBH_4) as reducing agent. It is known that TOAB is a weak stabilizing agent for gold nanocrystals; so NPs can grow with the addition of more reducing agents, and this growth will depend on the TOAB/Au ratio and the speed of addition of the NaBH_4 [12]. To prevent aggregation, another stabilizing agent is added to the media: alkanethiols, which strongly bind to the surface and keep passivated NPs in a colloidal dispersion with a defined size for a long time. This procedure is schematized in Fig. 9.1.

With this method, mostly icosahedral and cuboctahedral structures of 1–3 nm are obtained. Size is controlled by tuning the thiol/gold ratio. The larger the ratio, the smaller the average sizes. On the other hand, monodispersity can also be improved by fast reductant addition and cooling. Moreover, small sizes are produced when reaction is stopped immediately after reduction or adding voluminous ligands [6].

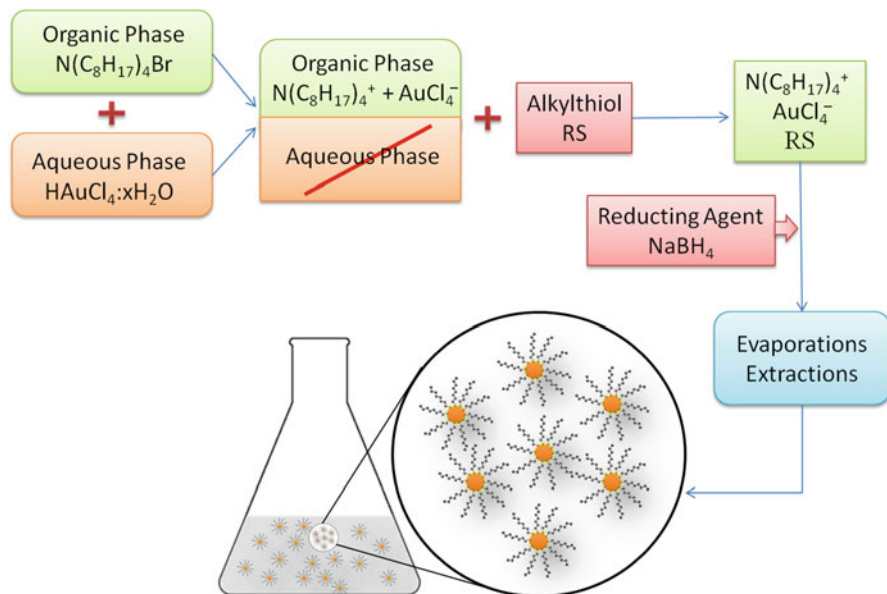


Fig. 9.1 Scheme of the two-phase Brust-Schiffrin method for synthesis of gold nanoparticles

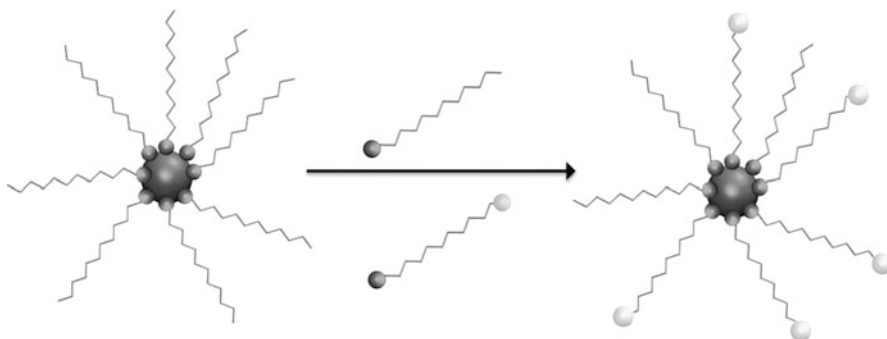


Fig. 9.2 Scheme for ligand exchange in passivated nanoparticles

The Brust-Schiffrin method was extended to other thiol ligands rather than alkanethiols, like xanathes, di- and tri-thiols, and disulfides [13–15]. Anyway, the latter are not as good stabilizers as thiols. This opened the way for synthesizing gold NPs with different functional ligands [16–19]. The method was also modified to be performed in only one phase, where the thiol/ Au^{3+} ratio controls the sizes of the NPs. Moreover, interchange of ligands has been studied [20], as shown schematically in Fig. 9.2. The exchange makes it possible to modify synthesized

NPs, replacing the adsorbed molecules by others that cannot be used in the synthesis procedure (because of, for example, incompatibilities with the medium conditions).

Concerning the mechanisms involved in the Brust–Schiffrin methods, there still exists a controversy about the intermediate steps. It was previously believed that the intermediate step in two-phase Brust–Schiffrin reactions involves the generation of soluble Au(I) alkanethiolate species. However, very recently it has been shown that tetra-alkylammonium metal complexes appear as precursors of two-phase reactions, while Au(I) thiolates are shown to be precursors of one-phase reactions conducted in polar solvents. These mechanisms were proposed after using [1]H NMR spectroscopy [21] to quantify the existence of the species mentioned.

In 2009, Perrault and Chain proposed a synthesis method that uses hydroquinone as a reducing agent in aqueous solution with gold seeds [22]. These seeds start to grow and can also catalyze the reduction of more Au(III) onto their surfaces. To control all process, citrate can be used as stabilizer. Seeds can be produced by the method proposed by Frens [9], complemented with the Perrault method. In this way, larger NPs can be produced (30–250 nm).

Recently, another method of synthesis has been proposed [23], in which it is possible to obtain naked gold NPs in an aqueous solution, with a nearly monodisperse size distribution, around 3 and 5 nm. HAuCl_4 is reduced with NaBH_4 , just stabilizing HAuCl_4 and NaBH_4 with HCl and NaOH. Gold NPs obtained are then covered with dodecanethiol and transferred to hexane just by stirring of a mix of water, hexane, and acetone. All subproducts remain in the water–acetone phase, while passivated NPs are in the organic phase, so, there is no need of washing after synthesis. These coated NPs stay in the air–toluene interface of a toluene droplet and form a 2D monolayer film, which remains as such after toluene evaporation, forming a monolayer of auto-assembled coated NPs, spatially uniform, which can be then deposited onto any substrate.

The two-phase Brust–Schiffrin method has been extended to triphenylphosphine (PPh_3) in order to improve the synthesis of Schmid's cluster [24]. PPh_3 and NaBH_4 are added to a mixture of water and toluene, using $\text{HAuCl}_4 \cdot 3\text{H}_2\text{O}$ and $\text{N}(\text{C}_8\text{H}_{15})_4\text{Br}$ [25]. With this method, bigger particles are obtained, and the NP diameter increases with reaction time and temperature [26].

Other wet techniques for synthesizing NPs are based on the generation of the metal particle inside some microemulsion, micelle, membrane, and other amphiphilic systems in the presence or absence of thiols [27,28]. The surfactant acts maintaining the required environment for the formation of the NP and stabilizing it, as well as transferring the metal ions to the organic phase. Obtained NPs have narrow size dispersion, and they can pack in a 2D array. In addition, polyelectrolytes can serve as stabilizers of NPs, functionalizing them at the same time [29,30].

9.4 Chemical Functionalization of Clusters and Nanoparticles

Functionalization of capped NPs can be achieved by some of the following methods: by exchange of some of the ligands attached to their surface, by reactions on the existing protecting agent, or by the combination of these two methods.

The exchange of ligands has been applied in the Brust method [11], for example, replacing the citrate by thiol molecules, which strongly bind to the surface of gold NPs, or simply by replacement of some thiol for another molecule. If the exchange is randomly located, then the number of exchanged ligands follows a Poisson distribution [31].

Another example is the replacement of some capping agent by single-stranded (ss) DNA with defined sequence. This modified NP can bind specifically to another ssDNA by base-pairing interactions [32] and self-assemble. Murray et al. [33] proposed another method for functionalizing NPs, in which they adsorb two noncomplementary oligonucleotides to gold NPs, and then add to the solution an oligonucleotide duplex with ends complementary to the two sequences attached to the NPs. Self-assembly of nanocrystals then occurs, thermally reversible by denaturation.

9.5 Simulating Nanoparticles

The aim of computer simulations is to offer some explanation to experimental results, to predict some expected results, or even more, to give some answers about systems that, a priori, cannot be managed experimentally.

Nanomaterials can be simulated under two levels of theory. The first one involves *ab initio* or quantum mechanics methods, which are based on solving Schrödinger equation, and calculating the electronic structure of all atoms in the system, or estimating the electronic density of the system. The second group involves classical methods, where electronic information is included in semiempirical potentials that describe interactions between particles. These potentials are adjusted to reproduce some properties of the systems, and it is preferable that they are transferable. This means that they can be used in the simulation of other systems or under different conditions.

Ab initio calculations are the most reliable method, as a complete electronic description can be obtained. However, these methods have a high computational cost. It is necessary to have powerful computer hardware and still having it, only small systems can be achieved, and results are obtained in a relatively long time.

Moreover, classical simulations allow handling bigger systems and, because of the possibility of simulating a large amount of particles, more experimental conditions can be reproduced. Besides, classical simulations reproduce van der Waals interactions better than some quantum methods, through the introduction of

experimental results in the parameterization of the force field. It is well known that density functional theory (DFT) calculations underestimate the weak van der Waals interactions, which are a direct result of long-range electron correlation. However, reliable, robust, and transferable semiempirical potentials are the key for performing classical simulations.

Calculations show that computational effort for the quantum mechanical formulations of the electronic structure of atomic systems scale as the cube of the number of atoms of the system. This makes it very difficult to reach system sizes larger than a few hundreds of atoms. However, with the introduction of linear-scaling algorithms in the last decade, the so-called $O(N)$ methods can achieve systems of nearly 10^3 atoms and, in the case of quantum molecular dynamics, a few picoseconds can be run. With classical simulations, systems of more than one million atoms can be handled, and molecular dynamics can be performed simulating over the microsecond scale.

For the sake of clarity, from here on we are going to differentiate systems as a function of their sizes. We are going to define “nanoclusters” as those systems where the metal core contains up to 100–150 atoms, and NPs as all other larger system within the nanoscale.

Using *ab initio* methods, only nanoclusters and a few NPs, mostly in vacuum, can be simulated.

9.6 What Is It Interesting to Study When Simulating Nanoparticles?

Passivated NPs consist of a core (usually metallic) and a capping agent (usually some organic molecule). When the molecule that can attach to a given substrate is identified, it can be interesting to know, for example, how many of these molecules can adsorb onto the surface, and then calculate a coverage degree. Another important quantity to obtain is adsorption energy and preferred adsorption site of a molecule on a crystalline surface. Structural analysis can also be interesting as morphology of passivated NPs and molecular rearrangement after adsorption.

Simulations can give us some results that cannot be obtained or are difficult to get from experiments, and can help understand what is happening in the systems when reactions take place. Simulations and real experiments must work in parallel to answer to different problems and generate more questions.

Gold NPs covered with thiols have been intensively studied, both experimentally and theoretically. One topic that caused discussions and lots of studies for many years is the binding site of alkanethiolates on the gold surfaces.

In the 1980s, the first experimental results showed that alkanethiols and disulfurs self-assemble on gold perfect surfaces to form self-assembled monolayers (SAMs) [34–36]. This self-assembly implies spontaneous formation of nanometric units that form a secondary structure from simple building blocks [34]. SAMs of alkanethiols

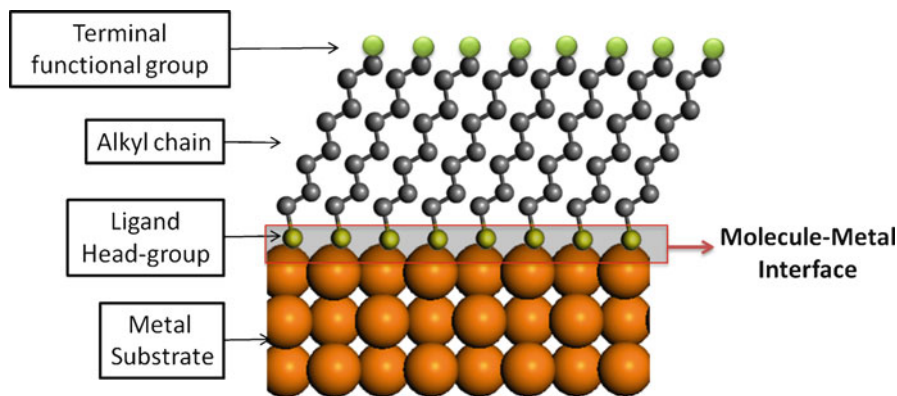


Fig. 9.3 Scheme of an organized monolayer on a crystalline substrate

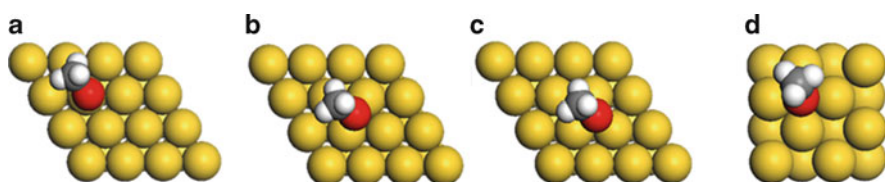


Fig. 9.4 Adsorption sites on perfect crystalline surfaces. (a) on-top site on a (111) surface; (b) bridge site on a (111) surface; (c) hollow site on a (111) surface; (d) hollow site on a (100) surface

on gold are easy to prepare, thermally stable, and allow the functionalization of the surface by selecting the terminal group. The great stability of these SAMs is mostly due to the non-covalent van der Waals interactions between the alkyl chains, which adopt a uniform molecular tilt [35].

The head group is the functional part of the molecule that directly attaches to the substrate, see a schematic representation of a SAM supported on a metal substrate in Fig. 9.3. On perfect crystalline surfaces, adsorption sites are well defined and differentiated by the coordination of the head group: in (111) surfaces, there are one mono-coordinated site (*on-top*), one bi-coordinated site (*bridge*), and two tri-coordinated sites (*hollow-fcc* and *hollow-hcp*); in (100) surfaces, there is no tri-coordinated site, but a tetra-coordinated one (*hollow*). All these sites are shown in Fig. 9.4.

Electron diffraction [36] and STM images [37] showed a hexagonal arrangement of the molecules onto the substrate, and the proposed adsorption site was a hollow tri-coordinated one.

Immediately, simulations of these systems started to play an important role. The first semiempirical pair-wise potentials were devised to handle the strong covalent interaction S–Au. Kautman and Klein simulated a SAM of alkanethiols onto a Au planar surface [38]. The functional form of the employed potential was a

12-3 one, fitted to reproduce adsorption energy, estimated from thermal desorption measurements of dimethyl disulfide on a (111) Au surface. Adsorption energy of a molecule on a surface is calculated as

$$E_{\text{adsorption}} = E_{\text{molecule-substrate}} - E_{\text{molecule}} - E_{\text{substrate}}$$

where $E_{\text{molecule-substrate}}$ is the energy of the total system after adsorption, E_{molecule} is the energy of the molecule in vacuum in gas phase, and $E_{\text{substrate}}$ is the energy of the clean metal surface.

In the 1990s, after the publication of the first ab initio calculations of gold surfaces coated with alkanethiols [39], a pair-wise additive Morse potential for simulating alkanethiol adsorption onto smooth, immobile perfect (111) surfaces (atomically described) was used. Within this approximation, SAMs onto gold were simulated in planar substrates [40] and NPs [41, 42]. In the first case, a coverage degree of 0.33 ML was found and mostly a $(\sqrt{3} \times \sqrt{3})R30^\circ$ superlattice. In the case of NPs, it must be noted that the use of this potential is not accurate, because it would work only with perfect planar (111) surfaces (edges, corners, and more open facets are not taken into account during the parameterization).

Using these additive potentials, highly coordinated sites are preferred for the adsorption of a molecule on the surface, because total potential energy is lowered as more bonds are formed. However, they were useful, because the predicted site was the most coordinated one.

Some years later, a controversy appeared on ab initio calculations for the adsorption site of methanethiol onto Au (111) surfaces. On the one hand, some results still predicted a three-coordinated *hollow* site [43, 44]. On the other, a new site was proposed, which is a hybrid between the *bridge* and the *hollow-fcc* site, and it was denominated *fcc-bridge* [45–48].

The controversy got worse when, in 2003, the result of an experiment of scanned-energy and scanned-angle photoelectron diffraction (PD) was that CH_3S adsorbs on a mono-coordinated *on-top* site on the surface at room temperature [49], the site that had been found in theoretical results to have the lower adsorption energy. This result was supported by normal-incidence X-ray standing waves (NIXSW), which also found molecules exclusively adsorbed on the *on-top* site [50]. Deficiencies in theoretical methods, coverage effects, and surface reconstruction at elevated temperature were proposed as possible explanations to this discrepancy.

This issue promoted new ab initio calculations. Already in 2002, a work by Molina and Hammer [51] warned that defects on planar gold surfaces cannot be neglected. They proposed that the formation of the $(\sqrt{3} \times \sqrt{3})R30^\circ$ superlattice is stabilized by the presence of vacancies on the surface. The energetic cost of generating these holes and adatoms is compensated by the gain of the adsorption of the molecule in these sites. The energy needed to create each vacancy was estimated as

$$E_{\text{defect}} = E_{\text{Au(reconstructed)}} + nE_{\text{Au(bulk)}} - E_{\text{Au(perfect)}}$$

where $E_{\text{Au(perfect)}}$ is the energy of the unconstructed Au (111) surface, $E_{\text{Au(reconstructed)}}$ is the energy of the reconstructed surface, $E_{\text{Au(bulk)}}$ is the energy per atom in the

bulk phase, and n is the number of vacancies created in the unit cell. Calculations revealed that adsorption of thiol molecules (at least of short-chain) *on-top* gold adatoms, which are placed on a *hollow* site on the surface, is the most favorable adsorption site. These results were later supported by another ab initio calculations [52], where it was predicted that the S group adsorbs not only on an isolated Au adatom but also on a $(\sqrt{3} \times \sqrt{3})R30^\circ$ structure. The calculated S–Au distance was shorter than that on a perfect surface, indicating a stronger binding.

In 2006, new NIXSW measurements [53] led to the conclusion that it is not the alkanethiolate bound to the adatom on the surface, but a complex Au–SR (where R is the alkyl chain), the one which may be occupying either of the two hollow sites on the Au (111) substrate. The facile movement of these complexes on the surface [52] provides an explanation to the interchange between the different observed superlattices.

A new model for the adsorption of methanethiolate on Au (111) surfaces was proposed based on a scanning tunneling microscopy (STM) study [54]. In this model, an Au adatom mediates de-adsorption of a pair of RS species, forming structures of the type RS–Au–SR, where both molecules are asymmetrically antiparallel to each other, separated by the adatom. It is known that metal adatoms are formed spontaneously at elevated temperatures.

DFT calculations show that in these RS–Au–SR complexes, the thiol group of each molecule attaches an *on-top* site to the surface, whereas the Au adatom is placed on a twofold *bridge* site. Therefore, each S atom forms two bonds with Au: one bond to the gold adatom, and another bond to the underlying gold atom in the lattice. As expected, the presence of the adatom increases the adsorption energy of both attached molecules.

Each of the formed units is highly stable, and can be imaged by STM at voltages up to 4.5 V without any evidence of diffusion or decomposition, and can sustain currents up to 20 nA, whereas simple SR molecule shows diffusion with pulses of less than 1 V and currents of only 1 nA [54].

Further support for this model is the observation of lifting of the Au (111) $22 \times \sqrt{3}$ -herringbone reconstruction, which always occurs in thiolate self-assembly. It suggests that the reconstruction can provide Au adatoms by ejecting them for relaxing the surface structure.

Quantum molecular dynamics of methylthiolate (MT) on gold (111) were performed starting from molecules at an *on-top* position in the metal [55]. Quickly, the adsorbates migrate to *bridge* sites, or the novel motif MT–Au–MT, which have lower potential energies. These simulations are short (10 ps of trajectory after 4 ps of equilibration) because of the complexity of the calculation, and in 4 ps the molecule migrates, and the new structures keep on stables for the remaining 10 ps of run. It was also noted that, starting from molecules onto *bridge* positions, migration to the motif structure is possible just by raising temperature, which indicates that the process has some activation energy barrier, but reachable at lower temperatures in longer times of simulations. The conclusion was that both, *bridge* and motif configurations, coexist in equilibrium.

It was also stated that the motif configuration is not consistent with the $(\sqrt{3} \times \sqrt{3})R30^\circ$ superlattice, but the mix of bridge and motif configurations can form this superstructure.

Nagoya and Morikawa [56] made a study of adsorption energy of methylthiolate on many sites onto Au (111), and compared them. The MT–Au–MT configuration was found to be the most stable among all, and they pointed out that, although it is energetically expensive to generate adatoms pulling them out from the perfect surface, the bonding of the molecules to this new adatom is very strong, which significantly stabilizes the motif creation. In the case of adsorption of a single MT on the adatom, this bond is also strong, but it is only one, and it is not enough to compensate for the energy expenditure in generating the adatom. Supporting the existence of the motifs, they found a strong correlation between their theoretical results for the adsorption energy in this configuration and available experimental data.

In 2007, the full structure of a Au_{102} cluster protected by *p*-mercaptobenzoic acid (*p*-MBA) was experimentally determined through crystallization and X-ray analysis [57]. It was found that the metallic core is protected with 44 *p*-MBA molecules. In fact, there exist an internal core, with Marks decahedra structure, of 79 gold atoms, and it is protected by complexes RS–Au–SR (SR in this case is *p*-MBA). Hence, $\text{Au}_{102}(\textit{p}\text{-MBA})_{44}$ compound is more precisely described as $\text{Au}_{79}[\text{Au}_{23}(\textit{p}\text{-MBA})_{44}]$. The stability of this structure can be explained because it implies a geometrical and electronic closed shell [58] (each gold atom contributes with one valence electron, and 44 are bonding *p*-MBA).

The electronic structure of this passivated system was determined later [59], and it was found that the internal 79 atoms core is neutral in charge (metallic state), whereas the gold forming the complexes RS–Au–SR are oxidized. The external $\text{Au}_{23}(\textit{p}\text{-MBA})_{44}$ shell is composed by 19 RS–Au–SR units, and $2\text{RS}-(\text{Au}\text{-SR})_2$ units, attached to the surface in on-top positions. So, since there are 21 units, 42 available *on-top* positions are necessary. Au_{79} has only 40 atoms on the surface. This is solved by double anchoring onto two gold atoms.

A relatively large gap between highest occupied molecular orbital (HOMO) and lowest occupied molecular orbital (LUMO) in this structure suggests electronic stability. In fact, in this system, there exists a 58 closed electronic shell, with all Au core atoms passivated, which means that all atoms have at least one covalent bond.

So far, it was clear that, for short-chain alkanethiols, the presence of adatoms and vacancies and the formation of complexes RS–Au–SR were of vital importance in the adsorption process. Moreover, these complexes were observed experimentally for low and high coverage, and the results were supported by DFT calculations.

As adsorption energies for alkanethiols of longer chains are similar to those of methanethiol on different surface sites, it is natural to assume that the structural motif RS–Au–SR can be formed within longer chain SAMs. It was shown [60] that for hexanethiol (HT), the RS–Au–SR configuration is the most stable one, in competition with the bridge position when vacancies exist on the surface.

Because of the possibility of interconversion between these adsorption sites, it is suggested that both static and dynamic disorders are expected to exist in the Au (111) interface.

Quantum molecular dynamic simulations were performed to compare short and long chain molecules, and they showed that in the case of HT, intermolecular interactions hampered the dynamics; consequently, the interconversion between sites is reduced with respect to the MT case. For example, the initial *on-top* configuration evolves to a more stable one for both molecules, but the process takes 4 ps in the case of HT at 500 K, whereas the conversion is seen in less than 1 ps for the MT at similar temperatures. At 300 K, formation of RS–Au–SR structure was observed for MT after 4 ps, but not observed for HT in the 10 ps of the simulation duration.

Because of molecule–molecule interactions, HT chains retain an ordered hexagonal structure, with a defined tilted angle of about 30° with respect to the normal to the surface in high coverage SAMs, in contrast with MT SAMs, where the surface is more dynamic. These observations suggested that, for the formation of hexagonal superstructures, some key aspects are needed: similar concentrations of adatoms and vacancies on the surface (in the case of long chains alkanethiols, more localization of these defects is needed, because of the reduced mobility due to longer alkyl chains); SR groups should be located onto *bridge* or RS–Au–SR (with molecules onto *on-top* sites) configuration in similar proportions; and alkyl chains must retain an hexagonal array. Although the SAM is ordered, the Au–S interface is affected by a dynamical disorder because of the delocalization of adatoms and vacancies on the surface. Packing is given by the alkyl chains, which leads to an ordered interface.

Grönbeck and collaborators [61] have performed DFT calculations of different adsorption models proposed in the literature on perfect and defective Au surfaces. All configurations resemble the $c(4 \times 2)$ superlattice.

The studied structures are shown in Fig. 9.5 together with the S–Au bond distance and the total energy difference, ΔE , defined as:

$$\Delta E = E[\alpha] - E[4\text{RS}/\text{Au}(111)] - xE[\text{Au}(\text{bulk})]$$

where $E[\alpha]$ is the energy of each structure and $E[4\text{RS}/\text{Au}(111)]$ is the energy of a unit cell with four RS molecules attached to *bridge-fcc* positions. In Fig. 9.5, structure 1 corresponds to the *bridge* adsorption onto an unreconstructed Au (111) surface. Starting from CH_3SSCH_3 molecules, the dissociative adsorption energy is about 0.39 eV, which is very low compared to the experimental value estimated from temperature-programmed desorption (about 1.3 eV) [62]. In structure 2, the energy required to generate adatoms leads to positive adsorption energy, the adsorption process being endothermic. If the MT is allowed to bridge between gold adatoms, as in structure 3, polymers of the form $(\text{Au} - \text{SR})_x$ can be formed, and the adsorption now is exothermic. More stabilization is gained in the formation of tetramers, as in structure 4, because strain is reduced when angles Au–S–Au are close to 90°. Structure 5 contains molecules attached to near gold vacancies, and this configuration is preferred over those previously mentioned, even over structure

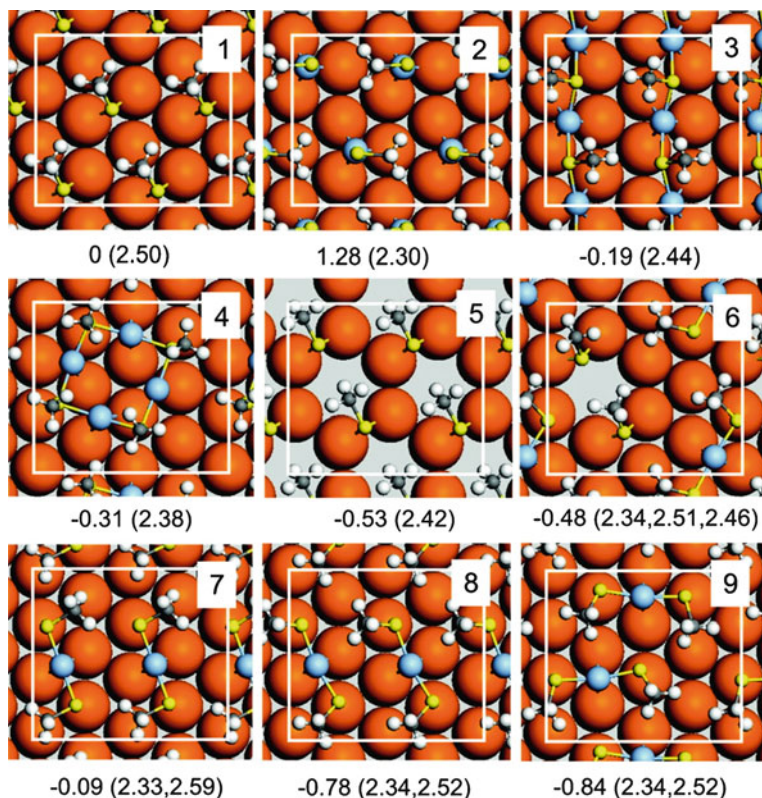


Fig. 9.5 Gronbeck's atomic models of optimized structures. The total energy difference with respect to 1 is reported in eV per unit cell. The average Au-S distances (Å) are shown in parenthesis. Atomic color codes: orange (Au), yellow (S), gray (C), and white (H). Au adatoms are shown in blue. Reprinted with permission from [61]. (Copyright 2008 by the American Chemical Society)

6, which contains a mix of two RS groups adsorbed onto a *bridge* position close to a Au vacancy and two forming a RS–Au–SR complex. Structure 7 contains all RS–Au–SR motifs with chains in a *trans* configuration, and is similar in energy to structure 1. However, if the molecules are positioned in a *cis* configuration, as in structures 8 and 9, the adsorption process becomes highly exothermic. It suggests that adsorption energy is strongly dependent on molecular orientation. Although structure 6 also has molecules in a *cis* configuration, more energy stabilization is gained in the formation of more RS–Au–SR motifs.

The adsorption of molecules forming RS–Au–SR complexes on the surface enables sulfur sp^3 hybridization and the existence of Au–S–Au angles close to 90° . The energy required to form the adatoms is strongly compensated by the gain in adsorption energy of the complex. The bond between complexes and the surface is polar-covalent. Although RS–Au–SR is anionic, calculated charge transference is negligible.

Table 9.1 Calculated adsorption energy for RS onto perfect and defected Au (111) surfaces

Adsorption site	Adsorption energy (eV)	Basis	Functional	Reference
On-top	-1.43, -1.00	Pw	GGA	[47]
	-1.42	Pw	GGA-PBE	[55]
	-1.34	Pw	GGA-PBE	[56]
	-1.40	Pw	GGA-PBE	[60]
Bridge	-1.67, -1.19	Pw	GGA	[47]
	-1.72	Pw	GGA-PBE	[55]
	-1.71	yPw	GGA-PBE	[56]
	-1.70	Pw	GGA-PBE	[60]
Bridge-fcc	-1.72, -1.25	Pw	GGA	[47]
	-1.73	Pw	GGA-PBE	[48]
	-2.30 (lc)	triple- ζ STOs	BP86	[52]
	-1.92 (hc)	triple- ζ STOs	BP86	[52]
	-1.46	Pw	GGA-PBE	[56]
	-0.39 ^a	Pw	GGA-PBE	[61]
Hollow	-1.49, -1.03	Pw	GGA	[47]
	-1.49	Pw	GGA-PBE	[48]
Adatom	-2.94 (lc)	triple- ζ STOs	BP86	[52]
	-2.43 (hc)	triple- ζ STOs	BP86	[52]
	-1.35	Pw	GGA-PBE	[56]
RS-Au-SR	-2.40	Pw	PW91	[54]
	-1.83	Pw	GGA-PBE	[55]
	-1.95	Pw	GGA-PBE	[56]
	-1.90	Pw	GGA-PBE	[60]
	-1.23 ^b	Pw	GGA-PBE	[61]

lc low coverage, *hc* high coverage, *pw* plane waves, *STOs*, Slater type orbitals

^aThis result takes into account the dissociation energy of RSSR

^bThis result takes into account the energy for the formation of the adatom

As a summary, we collect in Table 9.1 some of the calculated values of adsorption energy of alkanethiols on Au surfaces from different authors.

Summing up, results shown above are a typical example of how simulations can be helpful to elucidate some problems. Simulations always go in parallel with experiments, answering questions, and generating new challenges to be measured.

9.7 First Principles Calculations: Simulating Nanoclusters

As we stated before, first principles calculations are very expensive, in a computational jargon. Even if we had large supercomputers, only small systems could be handled.

In most of these calculations, energy optimizations are performed, neglecting entropy effects, which in the case of molecular adsorption at a finite temperature cannot be neglected a priori. For doing this, Schrödinger equation is solved

(or Kohn–Sham equations in the case of DFT) only with the input of atomic identities and coordinates, and energy is calculated as a function of the atomic positions. Taking derivatives of the energy landscape, forces are obtained, and the system evolves to the energy minimum, which means, zero forces. This is the reason why, in this type of simulations, local wells and minima are explored from the initial configuration, and the initial guest structures are of crucial importance.

The initial configuration can be chosen in several ways. Semiempirical calculations results (e.g., from global minimization algorithms or classical molecular dynamics) can be used as the starting point for the geometry optimization. If experimental evidence is available, such as X-ray diffraction or microscopy images, coordinates can be taken from that information.

If forces are used to solve Lagrangian equations, quantum molecular dynamics can be performed, and the time evolution of the system is obtained. Nevertheless, only short times can be simulated (c.a. few nanosecond in best cases), because these operations are extremely expensive. If the second derivative of the energy is taken, the Hessian matrix is obtained, and vibrational modes can be calculated by diagonalizing it.

- A Paradigmatic Example: $\text{Au}_{38}(\text{SCH}_3)_{24}$

Passivated nanoclusters have been synthesized and isolated in the last years. One of the first and smallest passivated nanosystems successfully isolated in large quantities in solution was $\text{Au}_{38}(\text{SCH}_3)_{24}$ [63, 64]. The first ab initio calculation of passivated clusters deals with this system, determining its electronic structure, geometry, and other relevant properties [65]. It is known that bare gold nanoclusters of 38 atoms adopt truncated octahedral morphology [66]. In that study [65], they started from a classical molecular dynamics result of the structure of the bare cluster using the embedded atom (EAM) potential, and relaxed it with ab initio calculations, obtaining essentially the same structure. After this relaxation, the metal core was passivated by 24 methylthiolate (SCH_3) molecules symmetrically placed onto the (111) facets. The system was optimized, and relaxation of the inner and outer corner gold atoms was observed, through expansion of some interatomic distances.

Density of states (DOS) were obtained for both bare and passivated clusters. In general, they noted in the passivated system addition of two narrow bands corresponding to molecular orbitals, shift of gold states, filling of the gap, and reduction of holes around the Fermi level.

Regarding charge transfer, results showed a deficit of about two electrons in the gold core, transferred to the molecular layer. This charge movement could explain the expansion of the Au–Au distance in the core, due to the Coulombic increased repulsion between nuclei. It was also found that extra addition or removal of charge takes place only in the molecular environment.

Garzón et al. [67] found that, after molecular adsorption, structural deformation is observed in the metal core due to the strong interaction between sulfur and gold atoms, and some sulfur atoms are incorporated into the cluster surface. This deformed structure has a lower energy minimum than the ordered structure proposed by Häkkinen et al. [65]. The results were obtained using scalar-relativistic

norm-conserving pseudopotentials, as well as plane wave as basis set. They also calculated chirality of this bare and passivated nanocluster [68] and showed that achiral clusters can become chiral, as in the case of $\text{Au}_{38}(\text{SCH}_3)_{24}$, or clusters that are already chiral can increase their index of chirality, as in the case of Au_{28} , when passivated. On the other hand, charge transference is found to occur with different patterns [67], in contrast to the results of the previous model [65]. It is interesting to mention that in a previous work [69], they had demonstrated that amorphous bare gold clusters coexist with crystalline ones.

At the time in which both works were performed, the polymeric passivant structures $(\text{Au} - \text{SR})_x$ were still unknown, and because of this all 38 gold atoms were considered as an entire core, and only molecules were taken as the protective agents. However, in Garzón's model, some structures of the form RS-Au-SR and RS-Au-SR-Au-SR are present in the nanocluster surface. Nevertheless, the importance of these motifs was still unrecognized.

A few years later, the structure of the $\text{Au}_{38}(\text{SCH}_3)_{24}$ was relaxed using a different correlation-exchange functional [70], and an ordered and symmetric structure was found, with six planar cyclic tetramers of the form $(\text{AuSCH}_3)_4$ as protecting agents. They stated that bonding in thiol-protected gold nanoclusters can be viewed as a competition between maximizing cohesion energy and forming ring-like complexes on the surface, which reduces the number of gold-gold bonds in the core. Calculated charge transfer was about 4.5 electrons from the metal atoms to the thiolates. These authors also stated that all calculations performed to elucidate the structure of passivated clusters use SCH_3 as passivating agents. If longer molecules were used, chain-chain and steric effects would not be negligible in the prediction of the most stable configuration. Ordering promoted by these intermolecular interactions should make disordered cores energetically unfavorable.

These results clearly show that the predictions made by DFT depend on the exchange-correlation functional chosen. However, the last work mentioned above introduced a key concept: part of the gold atoms—all of which had been thought of as an entire core before—can be forming part of the protective layer, and the remaining atoms constitute the internal core, and both kinds of atoms are different.

After the experimental elucidation of the total structure of the $\text{Au}_{102}(\text{p} - \text{MBA})_{44}$ [57], which reveal the existence of motifs of the form RS-Au-SR and RS-Au-SR-Au-SR onto the surface, it was proposed that instead of the cyclic tetramers [71], this kind of passivant should be present in $\text{Au}_{38}(\text{SCH}_3)_{24}$. In that work, the authors created polymeric structures by hand, passivating the initial truncated octahedron and relaxing the system with DFT calculations, and they found a disordered core of 24 gold atoms, covered with four linear RS-Au-SR-Au-SR and six RS-Au-SR motifs.

That structure was later reconsidered by the same authors [72] who proposed another configuration in which a disordered core of 23 gold atoms are protected with six RS-Au-SR-Au-SR and three RS-Au-SR motifs. This structure appears to be more stable, but still has a disordered core.

At the same time, Zeng et al. [73] proposed a face-sharing bi-icosahedral Au_{23} core protected by six RS-Au-SR-Au-SR and three RS-Au-SR motifs. The main

difference with the previous model is the ordering in the internal core, which makes the structure more stable. This model also presents good agreement with optical spectrum and X-ray diffraction experiments [74].

- $\text{Au}_{102}(\text{p-MBA})_{44}$

In 2007, the synthesis, crystallization, and atomic description of the $\text{Au}_{102}(\text{p-MBA})_{44}$ cluster made by Kornberg and collaborators [57] provoked a breakthrough in total structural determination of protected gold nanoclusters. The structure was described as an internal 49-atom core with Mark's decahedra geometry and two 20-atom caps in the poles of the core. It gives as a result an 89-atom structure with fivefold symmetry. The remaining 13 atoms lie in the equator of the cluster without any symmetry due to the interaction between these atoms and protecting molecules, which confers chirality to the system.

Another description was made for this cluster [75]. It was described as a 79-atom internal core with truncated decahedral geometry, where two 15-atom caps are placed at the poles, rotated with respect to the ideal decahedral shells, placing all the 40 surface atoms in a common sphere. The remaining 23 atoms form the external shell and connect molecules with the internal core. So, the structure can be better named as $\text{Au}_{79}[\text{Au}_{23}(\text{p-MBA})_{44}]$.

The great stability of the system was attributed to the fact that each of the gold atoms donates a valence electron and 44 of these electrons are taken by the molecules into localized orbitals. Then, 58 electrons remain in the metallic cluster, corresponding to an electronic closed shell. Noble metal clusters with a closed shell have a large HOMO-LUMO gap, which confers stability to these systems.

Geometric analysis was performed for $\text{Au}_{102}(\text{SCH}_3)_{44}$ cluster. Starting from coordinates obtained from the crystallographic experiment but replacing p-MBA by SCH_3 molecules, local minima was found by DFT calculations [76]. The authors state that since the structural configuration is almost the same as with p-MBA, electronic structures can be compared.

In this analysis, it is considered that if five extra vertex atoms are also considered with the 49 Mark's decahedra internal core, a perfect 54-atom decahedral structure can be seen. This can be viewed as five 20-atom tetrahedral subunits forming a non-perfect "penta-star" with fivefold symmetry. This structure is intrinsically strained, because of solid-angle deficiency, and it is not energetically stable. This fact indicates that the presence of the passivant is what makes this decahedral structure favorable. At each side of the penta-star, five wings (eight rhombuses and two triangles) are seen. The 13 equatorial atoms described by Jadzinsky et al. [57] consist of five atoms from the corner of the penta-star and eight from the corner of the wings. On the top of the wings, an additional pentagonal cap is formed at each side of the structure.

Hence, the need of formation of 88 total Au-RS bonds leads to a configuration that can be viewed as a multilayer structure: $\text{Au}_{54}(\text{penta-star})@\text{Au}_{38}(\text{ten wings})@\text{Au}_{10}(\text{two pentagon caps})$, see Fig. 9.6.

Electronic calculations were performed under DFT formalism for bare and passivated Au_{102} nanocluster. A big difference in values of HOMO-LUMO gaps

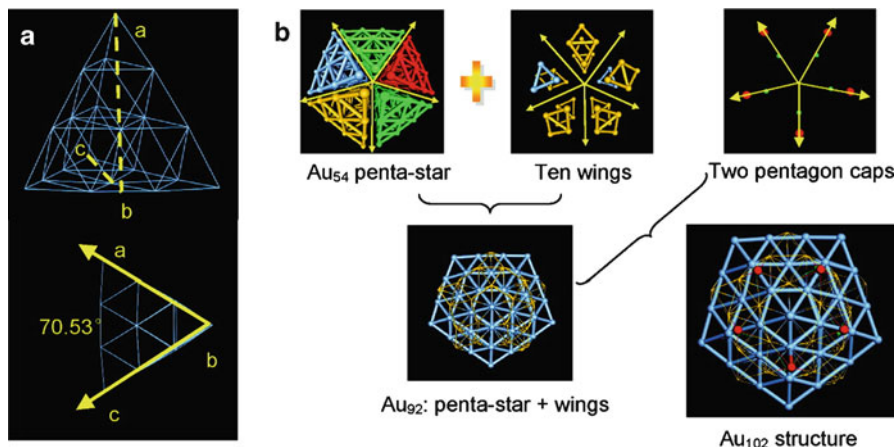


Fig. 9.6 (a) Perfect tetrahedral $T_d - Au_{20}$; $\angle abc = 70.53^\circ$. (b) Graphitic anatomy of embedded Au_{102} structure. An Au_{54} penta-star consists of five twinned Au_{20} tetrahedral subunits (in five colors). Ten wings (taking 38 Au atoms) include eight rhombuses and two triangles (in blue), five on each side of the penta-star. The Au_{54} penta-star (in blue) plus the wings (in yellow) form a Au_{92} structure. Adding a five-atom pentagonal cap (in red and green) on each side of the Au_{92} gives rise to the Au_{102} structure. Reprinted with permission from [76] (Copyright 2008 by the American Chemical Society)

of these structures was found. In the case of bare metal cluster, the gap is notably smaller than in the protected one, what indicates that the last is chemically more stable, and gives a support to the application of a spherical Jellium model to passivated metal nanoclusters. To have another evidence of this fact, extra calculations were performed on other systems, showing that configurations with closed electronic shells are largely more stable than others [76]. Charge analysis shows that slight electronic transfer occurs between metal and thiolate groups. In general, for a $Au_m(SCH_3)_n$ cluster, each gold atom donates an electron, and each molecule accepts one into a localized state, and total effective number of valence electrons can be estimated as $m-n$. Higher stabilities are found when this number corresponds to a closed electronic shell.

Walter and collaborators [59] have performed a DFT study of several gold clusters covered by different passivants. They suggest that in the passivation processes, electronic shell closure, sterically complete protective layer and compact and symmetric metal core play an important role. In that work, a large HOMO-LUMO gap was also found for $Au_{102}(RS)_{44}$, and it was also stated that small charge transfer between internal Au_{79} core and $Au_{23}(RS)_{44}$ protective shell occurs, and bonds are weakly polarized. The positive charging of the surface atoms induces formation of holes in the $5d^{10}$ shell of Au, which indicates magnetic behavior.

It was also found that the energy gap present in passivated nanoclusters is almost not sensitive to the adsorbed thiolate, although molecules in the gas phase exhibit

very different energy gaps [77]. However, the presence of an aromatic ring in aryl thiolates modifies the charge distribution, and it may change surface dipoles and position of energy levels, and with it, electron affinities and ionization potentials.

The adsorption energy of each *p*-MBA radical in a staple motif onto a Au₁₀₂ cluster fully passivated was estimated to be -1.96 eV . When calculations are performed for a *p*-MBA radical in a unique adsorbed staple motif, the estimated value is slightly higher: c.a. -2.16 eV . The decrease in adsorption energy when increasing the coverage degree can be attributed to the steric repulsion between adsorbed molecules, and the limitation of gold atoms to relax [76].

In all ab initio calculations of this system, local minimizations of the previous known structure are performed, and the results show that this configuration is energetically stable. It was found that adding or removing some molecule or group, these ordered structures are not stable anymore due to the lack of a closed electronic shell [59, 75].

9.8 Modeling Passivated Nanoparticles

In order to avoid any confusion with the terminology, we recall the differences on systems according to their sizes. Before, we have defined “nanoclusters” as all systems where the metal core contains up to 100–150 atoms and NPs as all larger systems within the nanoscale. In what follows, we will refer to modeling of protected nanoparticles, mainly tackled with semiempirical interatomic potentials and mean-field approximations. First-principle calculations are practically absent in the present scale (nanoparticles diameter: 2–20 nm) due to the high computational cost needed to treat such large amount of particles. For instance, a nanoparticle of approximately 2 nm contains 147 core atoms and 70 surfactant molecules, leading to a total number of atoms of 1,057 (for dodecanethiol within the united atom approximation).

As stated in previous sections, one of the most studied surfactant-protected metal nanoparticles is thiol-passivated Au NPs, due to the fact that they have many potential applications in several areas. For instance, it is worth noting the imminent application of these systems in novel methods to diagnose and treat cancer, drug delivery, etc.

With regard to semiempirical approaches, it is worth mentioning the pioneer work performed by Luedtke and Landman [41, 42, 78] where the structure, dynamics, and thermodynamic aspects of gold nanocrystallites passivated by alkylthiolates and the energetics of formation of superlattices made through the assembly of passivated nanoclusters were investigated by means of molecular dynamics simulations.

In those early works, Luedtke and Landman focused on two prototype systems: Au₁₄₀ and Au₁₂₈₉ and they found that in the passivated forms of Au₁₄₀(C₁₂H₂₅S)₆₂ and Au₁₂₈₉(C₁₂H₂₅S)₂₅₈, the thiol molecules adsorb on the (111) and (100) crystalline facets of the nanocluster/nanoparticles to form compact monolayers. The SAMs on the nanocrystallites were found to form larger packing densities compared

to dodecanethiol SAM on flat Au(111). Despite the impressive work presented by Landman, in such studies the gold atoms of the nanocrystallites were kept fixed during the entire dynamics simulation. Therefore, the structural information of the gold nanoparticles—a very important aspect to understand the properties and structures of capped nanoparticles, particularly considering the strong interaction between S and Au—was unavailable. In all the works by Landman, the bonding interaction between S and Au was modeled via a pair-wise additive Morse potential with the following functional form:

$$U_{S-Au}(r) = D_e \exp(-\beta(r - r_e)) [\exp(\beta(r - r_e)) - 2]$$

where $D_e = 0.4 \text{ eV}$, $\beta = 1.3 \text{ \AA}^{-1}$, and $r_e = 2.9 \text{ \AA}$. These parameters are known to correctly reproduce binding energies, equilibrium distances, and vibrational force constants of alkyl thiolates adsorbed on planar gold surfaces.

Zachariah and coworkers [79] have reported a molecular dynamics study of an all-mobile-atom approach to study the mechanochemical stability of thiol-protected Au NPs. In their work, they reported that the surface of gold nanoparticles becomes highly corrugated by the adsorption of thiol molecules. In addition, it was shown that as temperature increases, alkanethiol molecules go through the gold nanoparticles even at temperatures much lower than the melting temperature of gold nanocrystallites.

However, the interatomic potential used to describe the S–Au interface fails to represent the bond-order dependence of the S–Au bond, due to the fact that they used a pair-wise Morse potential (similar to the Landman's approach), parameterized to reproduce the adsorption energy of thiols on Au(111) perfect flat surfaces. Therefore, it is trivial to understand that the S– head group of the thiolate molecules will try to over-coordinate with Au atoms in order to minimize the overall internal energy of the system. As a consequence, the use of additive pair-wise potentials with non-fixed metal atoms will produce unrealistic results.

Vlugt and coworkers [80] have reported a Monte Carlo study of gold nanocrystals protected with alkyl thiols, with and without explicit solvent (*n*-hexane). They found that the geometry of the gold surface strongly influences the formation and structure of the capping monolayer. Even more, they showed that the solvent plays an important role in the thermodynamic properties of thiol monolayers on both flat Au(111) surfaces and nanoparticles. Therefore, they stated that phenomena observed in vacuum may be different from those observed in solution. To perform the MC simulations they used the Hautman and Klein [38] potential, where an unidirectional effective potential is used indistinctly for planar Au(111) and curved surfaces (nanoparticles). The effective potential between S and Au is taken according to the following function:

$$V_{\text{eff}}(z) = \frac{C_{12}}{(z - z_0)^{12}} - \frac{C_3}{(z - z_0)^3}$$

where z represents the distance of a united atom to the Au surface, and C_{12} , C_3 , and z_0 are fitted parameters to reproduce adsorption energy on a hollow site of a planar Au(111) surface. Therefore, as in the case of Landman's approach, any local environment effects are neglected.

Very recently, Jiménez et al. [81] reported a molecular dynamics simulations of SAMs of alkanethiol molecules on gold nanoparticles to determine the surface per ligand molecule as a function of the NPs size. For their molecular dynamics calculations they employed a classical Morse potential to describe the S–Au bond with parameters taken from a study of self-assembly of 1,4-benzenedithiolate (BDT) on a Au (111) surface [82] and all gold atoms were held fixed during the simulation. A very good agreement with experimental estimations was found in the coverage degree as a function of the nanoparticles diameter. They also conclude that the nearest CH_2 group to the surface plays the most important role in the value of the surface tension.

As shown in previous sections, ab initio theoretical calculations using DFT show that the energy and the adsorption site of alkanethiols on metallic substrates depend very strongly on the coordination number of the thiolate groups, as well as on the coordination of Au atoms.

In view of the large amount of DFT results, and considering the evolution of different S–Au adsorption models, Olmos-Asar and Mariscal [83, 84] have developed a new semiempirical potential to accurately describe molecular adsorption on metal surfaces, by introducing local environment effects in the functional form.

The main characteristic of the potential is the existence of variable parameters of the Morse potential function that depend on the bond order of both the head group of the molecule (i.e. sulfur, nitrogen, etc.) and the closest metal atoms. This is carried out by introducing a bond-order $n_{j(\text{Mol},\text{Metal})}$, dependence on the D_e and r_e parameters of the Morse function. The first one takes into account the binding energy and the second one the equilibrium bond distance. The modified Morse potential function can be described by the following functional form:

$$V_{\text{Mol-Metal}} = D_e (n_{j(\text{Mol},\text{Metal})}) \exp \left[-\alpha (r - r_e (n_{j(\text{Mol},\text{Metal})})) \right] \left\{ \exp \left[-\alpha (r - r_e (n_{j(\text{Mol},\text{Metal})})) \right] - 2 \right\}$$

where $D_e(n_{j(\text{Mol},\text{Metal})})$, α , and $r_e(n_{j(\text{Mol},\text{Metal})})$ are fitted parameters and the bond order is calculated as follows:

$$n_j = \sum_{i \neq j} f(r_{ij})$$

$$f(r) = \left\{ \begin{array}{ll} 1 & r \leq C_1 \\ 0 & r \geq C_2 \\ \frac{1}{2} - \frac{15}{16} \left[Y(r) - \frac{2}{3}Y(r)^3 + \frac{1}{5}Y(r)^5 \right] & C_1 < r < C_2 \end{array} \right.$$

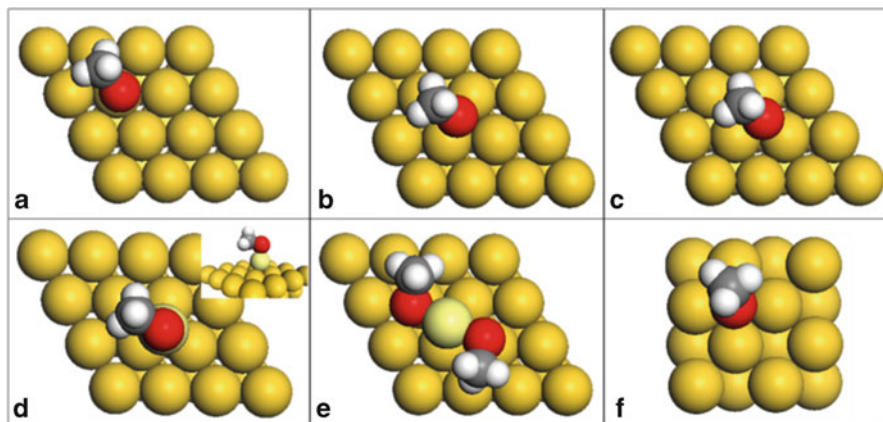


Fig. 9.7 Adsorption sites considered for the fitting procedure: (a) on-top (b) bridge (c) hollow (111) (d) on-top adatom—inset: lateral view—(e) staple motif “RS–Au–SR” and (f) hollow (100). Reprinted with permission from [84]—(Copyright 2011 by the PCCP Owner Societies)

where:

$$Y(r) = \frac{2r - C_2 - C_1}{C_2 - C_1}$$

For thiolate molecules adsorbed on gold, the values of $C_1 = 2.75 \text{ \AA}$ and $C_2 = 3.45 \text{ \AA}$ are chosen in order to obtain a smooth slope in the $f(r)$ function, but maintaining all configurations used for the fitting procedure with well-defined bond-order values. When using amines on gold surfaces, the values considered are: $C_1 = 3.55 \text{ \AA}$ and $C_2 = 3.80 \text{ \AA}$. For calculating gold bond orders, the same functions are used, but taking $C_1 = 2.90 \text{ \AA}$ and $C_2 = 4.06 \text{ \AA}$.

For thiol-gold system, to obtain the set of parameters mentioned above, six adsorption sites on different surfaces are considered during the fitting procedure: i.e., two mono-coordinated sites (on-top in a perfect (111) flat surface and on a Au adatom), one bi-coordinated site (the bridge position on a perfect (111) surface), one tri-coordinated site (the hollow position in a (111) surface), a tetra-coordinated site (the hollow position in a perfect (100) surface), and the staple motif (RS–Au–SR) mentioned in the previous section (see Fig. 9.7).

In each of the configurations selected, with the molecule adsorbed on the equilibrium position (it implies head group-metal distance at the r_e value), D_e parameter was changed self-consistently, keeping α as a constant, until the adsorption energy value predicted by DFT calculations was reproduced. The optimized values are shown in Table 9.2.

Table 9.2 Optimized values of the parameter D_e and r_e in the six selected configurations for both alkylthiolates and alkylamines on gold surfaces. D_e in eV units and r_e in Å

Adsorption site	Thiol/Au D_e	Thiol/Au r_e	Amine/Au D_e	Amine/Au r_e
On-top (111)	0.404764	2.43	0.189	2.45
On-top (100)	–	–	0.231	2.38
Bridge (111)	0.271479	2.64	0.058	3.23
Hollow (111)	0.286784	2.68	0.051	3.41
Hollow (100)	0.293681	2.81	0.049	3.58
Top/adatom Au (111)	1.759618	2.30	1.039	2.23
Motif (RX-Au-XR)/XR	0.782176	2.55	–	–

Figure 9.8 shows the resulting potential energy surfaces (PES), which were constructed using the six configurations mentioned above (without low-coordination sites on non-perfect surfaces) through cubic splines interpolations of the form:

$$D_e = D_e^a \left[2 \left(\frac{n - n_a}{n_b - n_a} \right)^3 - 3 \left(\frac{n - n_a}{n_b - n_a} \right)^2 + 1 \right] \\ + D_e^b \left[3 \left(\frac{n - n_a}{n_b - n_a} \right)^2 - 2 \left(\frac{n - n_a}{n_b - n_a} \right)^3 \right]$$

in order to obtain values at intermediate positions, while satisfying the continuity of the potential energy landscape (D_e^a, D_e^b are the values of the potential depth at the limits a and b of each interval and n_a, n_b the bond orders at those points).

In the case of thiols, the adsorption on the staple motif is the most favorable adsorption site, followed by the adsorption on the on-top Au adatom, which fully agrees with previous DFT calculations [85].

In the case of amines, the top position was found to be the most favorable site, but in general there are no considerable effects on the bond order, and in principle the use of classical Morse functions will describe accurately the main features of the system, particularly on the capping effect. However, it is interesting to mention that the modified Morse potential can reproduce the top position by means of simple MD calculations or local relaxations, indicating the power of the method, since any pair-wise potential without local environment effects (like conventional Morse) will predict adsorption on high coordinated sites in order to minimize overall internal energy of the system.

In Fig. 9.8, PES obtained are shown for two paradigmatic cases: alkylthiol and alkylamines on gold surfaces.

The new semiempirical potential has been used to explore some key properties of dodecanethiolate and dodecaneamine protected gold clusters and nanoparticles of various sizes and core geometries. For a direct comparison, in Fig. 9.9, two Au nanoparticles of similar size are shown. As can be seen, the structure of the particles presents the same behavior, i.e. a strong surface disorder with nonexistence of crystalline structure.

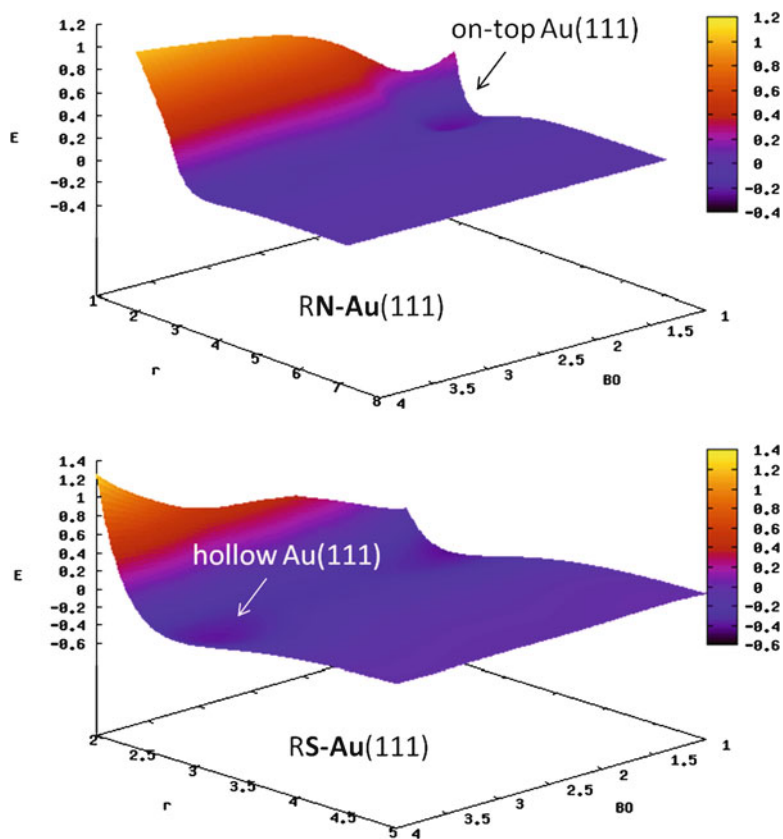


Fig. 9.8 Potential energy surfaces (PES) for amines (*top panel*) and thiols (*lower panel*) adsorbed on gold surfaces

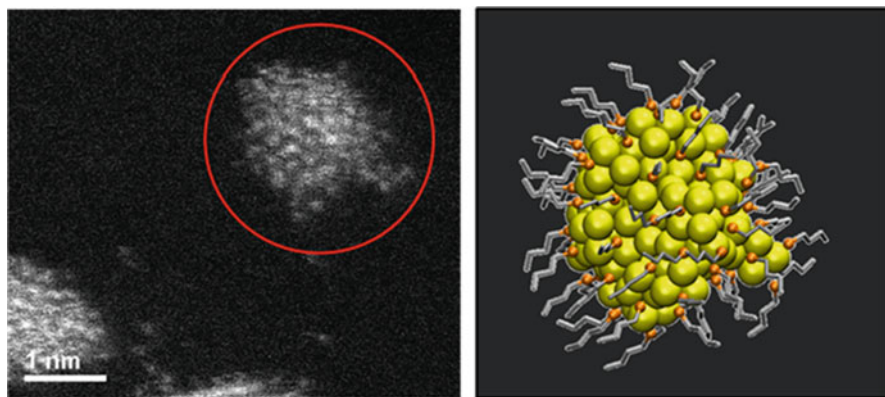


Fig. 9.9 A comparison between two gold nanoparticles capped by alkanethiol molecules of very similar size. (*Left*) HRTEM image; (*right*) simulated

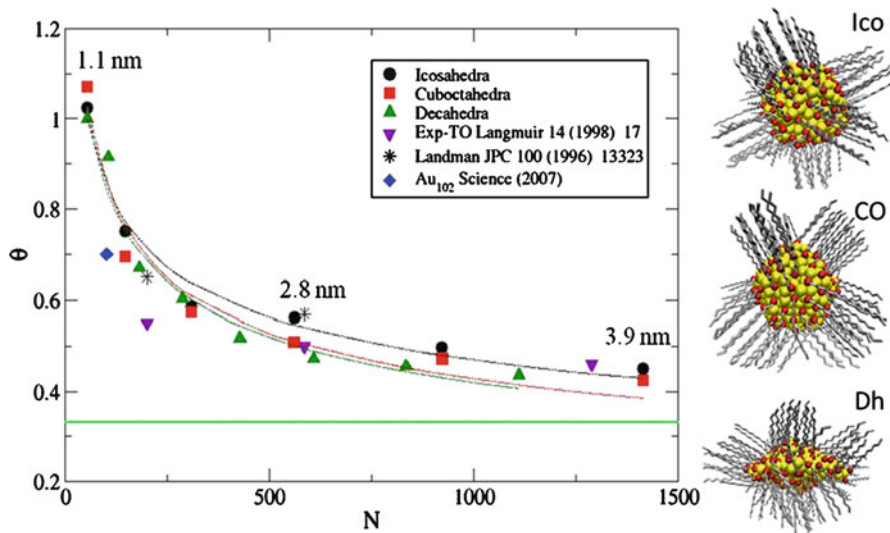


Fig. 9.10 Dodecanethiol-protected Au nanoparticles. Coverage degree as a function of the nanoparticles size for different core geometries. Reprinted with permission from [84]—(Copyright 2011 by the PCCP Owner Societies)

In Fig. 9.10 the maximum coverage degree for nanoparticles of different geometry, i.e., cuboctahedra (CO), icosahedra (Ico), and regular decahedra (Dh) for several sizes, are shown. We define the coverage degree (θ) as the ratio between the number of adsorbed molecules and the initial number of surface gold atoms in the NP. As can be noted in the figure, the coverage degree increases markedly as the nanoparticle diameter decreases, reaching a limit value close to one when the NP diameter is near 1 nm. It is important to note that when the nanoparticles diameter reaches a value of approximately 4 nm, the coverage degree tends toward the value of the planar surface, i.e. 0.33 ML (marked in Fig. 9.10 with a solid green line). Note that an experimental estimation [86] of the coverage degree is also plotted, as well the results taken from the early work by Landman [42] and the novel discoveries by Kornberg [57] and coworkers.

As we mentioned at the beginning of the section, most of the previous potentials fail to study the structure of the gold atoms due to the fact that they were held fixed during the fitting procedure. Langevin dynamics have been performed for both thiol- and amine-protected Au nanoparticles, to explore the internal structure of passivated gold nanoparticles and to compare the effect of hard and soft surfactant molecules, respectively. Simulations were performed at a constant temperature of 300 K by coupling the system to an external bath.

Simulations were carried out starting from relaxed Au cores and adding later on an excess of randomly distributed dodecanethiolate or dodecaneamine molecules around the relaxed Au NP. Within this approach, the adsorption sites are not assumed a priori and molecules are, in principle, able to diffuse on the gold surface.

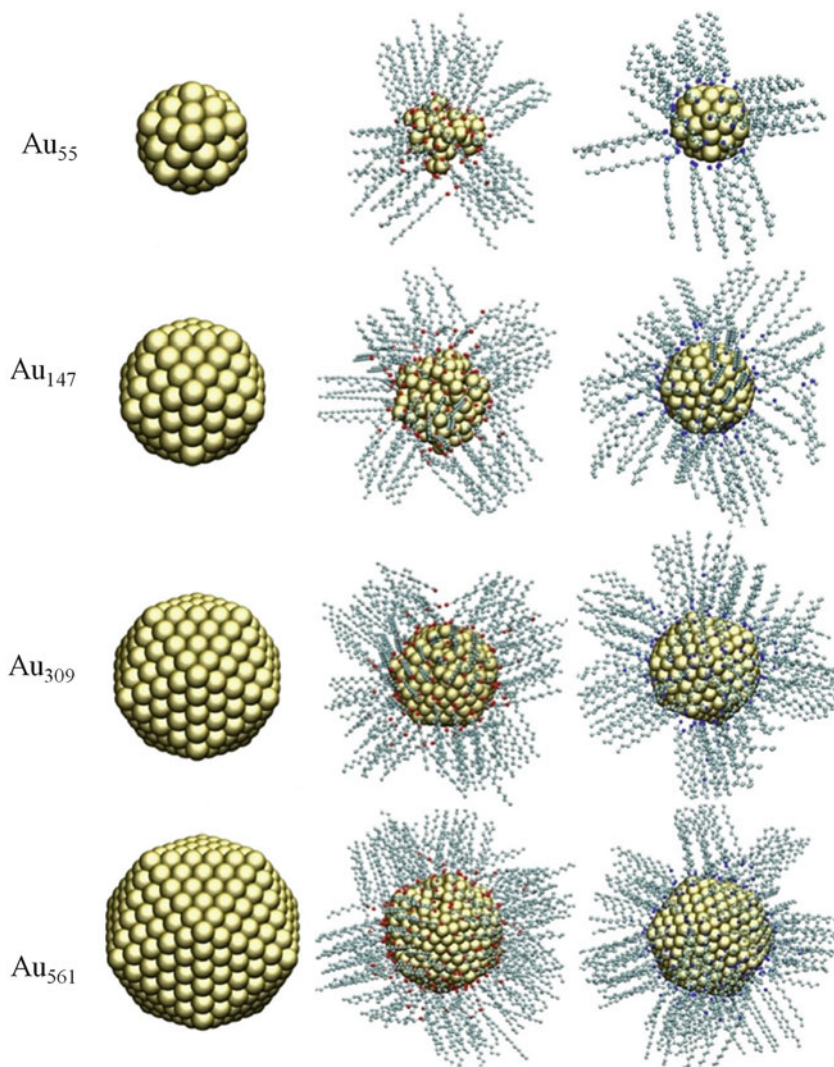


Fig. 9.11 *Left: bare; middle: dodecanethiol; right: dodecaneamine protected Au nanoparticles of difference sizes with icosahedral core*

Moreover, concerted diffusion processes are allowed during the dynamics evolution. In Fig. 9.11, the atomic structures of bare and passivated Au nanoparticles are shown for different core sizes. In the case of dodecanethiolate surfactant, for clusters and small NPs, the icosahedra structure is completely lost due to the strong S–Au interaction, comparable in magnitude to the Au–Au interaction on the outer layers of the gold clusters. At 300 K, there is a competition between perpendicular bonding (S–Au) and lateral ones (Au–Au). As the nanoparticles diameter increases,

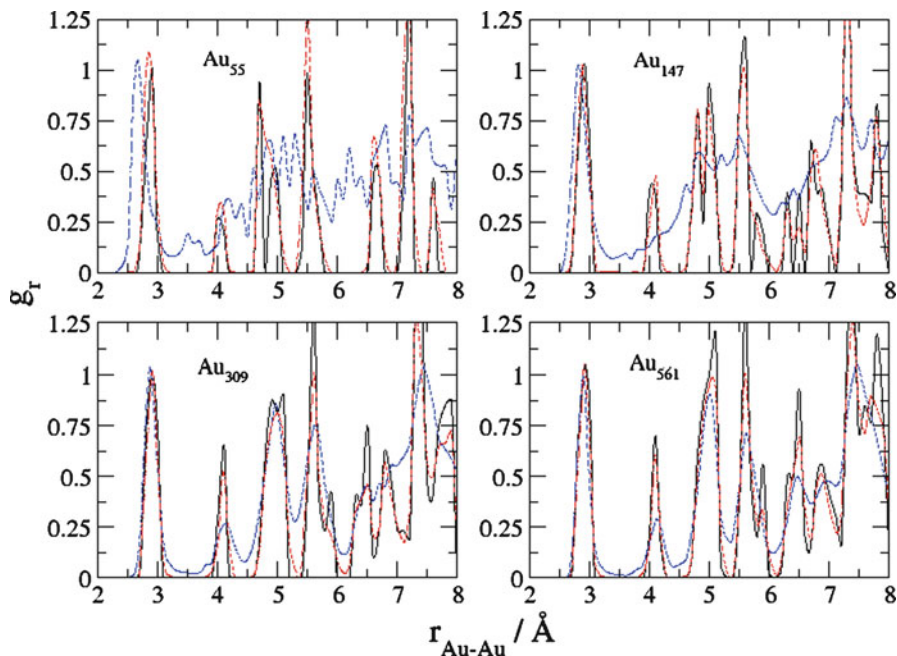


Fig. 9.12 Pair distribution functions for bare (black lines), dodecanethiol (blue), and dodecaneamine (red) protected Au clusters and nanoparticles of difference sizes with icosahedral core

the surface of the NPs appears slightly disordered, but the internal core keeps the icosahedra structure. In the case of softer surfactants such as amines, the gold core remains intact as expected, on account of the low bonding energy between N–Au -0.28 – 0.59 eV, compared to -1.34 – 2.21 eV for S–Au.

Inspection of the atomic configurations, by means of computing the pair distribution function

$$g_r = \frac{V}{N^2} \left\langle \sum_i^N \sum_{j \neq i}^N \delta(r - r_{ij}) \right\rangle$$

reveals the structural disorder in the case of thiol molecules (see Fig. 9.12). However, in the case of amine-protected particles the Au core preserves the characteristic peaks of bare icosahedral gold NPs.

At this point it is interesting to compare the structures predicted with experimental evidence. One of the most sensitive techniques to monitor the atomic structure of nanoparticles is aberration-corrected STEM coupled with a HAADF detector. Very recently [83], it has been revealed that when the nanoparticles size is lower than 2–3 nm, the surface of dodecanethiolate-protected gold nanoparticles is highly disordered. In addition, when the gold clusters are smaller than 2 nm, a crystalline structure cannot be resolved by aberration-corrected STEM. Evidence of small Au nucleus and isolated adatoms and chain of gold with unusual Au–Au distances are also observed.

A different approach to study surfactant-protected nanoparticles is the work reported by Schapotschnikow [87], where the potential of mean force (PMF) between alkylthiol capped Au nanoparticles, using atomistic simulations, was computed. The potential well depth reported ranges from $30k_bT$ for nanoclusters (Au_{147}) to $180k_bT$ for nanoparticles of Au_{561} . The minimum of the PMF lies at a distance of approximately 1.25 times the distance of the core diameter (defined as twice the radius of gyration). Results suggested a strong thermodynamic stability of the nanoparticles structures. To obtain the PMF between two nanoparticles Steered MD was needed, using classical force fields and fixed gold atoms.

Chakrabarti and collaborators [88] have reported a study of the assembly of surfactant-protected gold nanoparticles by both phenomenological modeling and computer simulations. They have developed an effective NP–NP pair potential by treating the ligands molecules as flexible polymer chains and considering a free energy of mixing approaches. Even more, they included elastic contributions from compression of the ligands to the effective NP–NP potential. The pair potential was later on used to perform Brownian Dynamics simulations to obtain a broad perspective in the dispersed-phase to solid-phase transition.

9.9 Summary

In this chapter, we have discussed the most outstanding experiments concerning surfactant-protected nanoparticles. In particular we have focused on thiol-capped metal nanosystems, due to their potential applications in a wide range of areas. The exciting future of thiol–Au clusters and nanoparticles lies in their biological applications as hybrid biological-inorganic systems.

We have considered the most significant efforts to understand the complexity of these systems from theoretical considerations. In this sense, we have shown a wide diversity of models, high-accuracy calculations, and computer simulation techniques applied to the modeling of protected metallic clusters and nanoparticles.

The development of new semiempirical approaches give thermodynamics and kinetics a new and significant role, since with the introduction of new methodologies along with the enormous growth in computer power, the future seems very promising for this field of research.

Acknowledgments The authors wish to acknowledge CONICET PIP: 112–200801–000983, Secyt UNC, Program BID (PICT 2007 N1 00340), and PME: 2006–01581 for financial support, and Gabriela Diaz Cortez for her language assistance.

References

1. Alivisatos AP (1996) *Science* 271:933
2. Andres RP, Bein T, Dorogi M, Feng S, Jenderson JI, Kubiak CP, Mahoney W, Osifchin RG, Reifenvenger R (1996) *Science* 272:1323

3. Toshima N, Yonezawa T (1998) *New J Chem.* 22:1179
4. Qian X, Peng X-H, Ansari DO, Yin-Goen Q, Chen GZ, Shin DM, Yang L, Young AN, Wang MD, Nie S (2008) *Nature Biotechnol* 26:83
5. Gibson JD, Khanal BP, Zubarev ER (2007) *J Am Chem Soc* 129
6. Daniel MC, Astruc D (2004) *Chem Rev* 104:293
7. Love JC, Estroff LA, Kriebel JK, Nuzzo RG, Whitesides GM (2005) *Chem. Rev.* 105:1103
8. Turkevitch J, Stevenson PC, Hiller J (1951) *Discuss Faraday Soc* 11:55
9. Frens G (1973) *Nature Phys Sci* 241:20
10. Giersig M, Mulvaney P (1993) *Langmuir* 9:3408
11. Brust M, Walker M, Bethell D, Schiffrin DJ, Whyman RJ (1994) *J Chem Soc Chem Commun* 801
12. Saunders AE, Sigman MB Jr., Korgel BA (2004) *J Phys Chem B* 108:193
13. Tzhayik O, Sawant P, Efrima S, Kovalev E, Klug JT (2002) *Langmuir* 18:3364
14. Porter LA Jr., Ji D, Wescott SL, Graupe M, Czernuszewicz RS, Halas NJ, Lee TR (1998) *Langmuir* 14:7378
15. Tan Y, Li Y, Zhu D (2002) *Langmuir* 18:3392
16. Brust M, Fink J, Bethell D, Schiffrin DJ, Kiely CJ (1995) *J Chem Soc Chem Commun* 1655
17. Chen S (1999) *Langmuir* 15:7551
18. Chen S, Murray RW (1999) *Langmuir* 15:682
19. Templeton AC, Hostetler MJ, Kraft CT, Murray RW (1998) *J Am Chem Soc* 120:1906
20. Hostetler MJ, Templeton AC, Murray RW (1999) *Langmuir* 15:3782
21. Goulet PJG, Lennox RB (2010) *J Am Chem Soc* 132:9582
22. Perrault SD, Chan WCW (2009) *J Am Chem Soc* 131:17042
23. Martin MN, Basham JI, Chando P, Eah SK (2010) *Langmuir* 26:7410
24. Schmid G, Pfeil R, Boese R, Bandermann F, Meyer S, Calis GHM, van der Velden JWA (1981) *Chem Ber* 114:3634
25. Weare WW, Reed SM, Warner MG, Hutchison JE (2000) *J Am Chem Soc* 122:12890
26. Yamamoto M, Nakamoto M (2003) *Chem Lett* 32:452
27. Taleb A, Petit C, Pileni MPJ (1998) *Phys Chem B* 102:2214
28. Chen F, Xu G-Q, Hor TSA (2003) *Mater Lett* 57:3282
29. Gittins DI, Carusso F (2001) *J Phys Chem B* 105:6846
30. Mayya KS, Schoeler B, Carusso F (2003) *Adv Funct Mater* 13:183
31. Dass A, Holt K, Parker JF, Feldberg SW, Murray RW (2008) *J Phys Chem C* 112:20276
32. Alivisatos AP, Johnsson KP, Peng X, Wilson TE, Loweth CJ, Bruchez MP Jr., Schultz PG (1996) *Nature* 382:609
33. Mirkin CA, Letsinger RL, Mucic RC, Storhoff JJ (1996) *Nature* 382:607
34. Nuzzo RG, Allara DL (1983) *J Am Chem Soc* 105:4481
35. Porter MD, Bright TB, Allara DL, Chidsey CED (1987) *J Am Chem Soc* 109:3559
36. Strong L, Whitesides GM (1988) *Langmuir* 4:547
37. Poirier GE, Pylant ED (1996) *Science* 272:1145
38. Hautman J, Klein ML (1989) *J Chem Phys* 91:4994
39. Sellers H, Ulman A, Shnidman Y, Eilers JE (1993) *J Am Chem Soc* 115:9389
40. Mahaffy R, Bhatia R, Garrison B (1997) *J Phys Chem B* 101:771
41. Luedtke WD; Landman U (1996) *J Phys Chem* 100:13323
42. Luedtke WD; Landman U (1998) *J Phys Chem B* 102:6566
43. Grönbeck H, Curioni A, Anderoni W (2000) *J Am Chem Soc* 122:3839
44. Yourdshahyan Y, Zhang HK, Rappe AM (2001) *Phys Rev B* 63:081405
45. Hayashi T, Morikawa Y, Nozoye H (2001) *J Chem Phys* 114:7615
46. Akinaga Y, Nakajima T, Hirao K (2001) *J Chem Phys* 114:8555
47. Gottschalck J, Hammer B (2002) *J Chem Phys* 116:784
48. Yourdshahyan Y, Rappe AM (2002) *J Chem Phys* 117:825
49. Kondoh H, Iwasaki M, Shimada T, Amemiya K, Tokoyama T, Ohta T (2003) *Phys Rev Lett* 90:066102

50. Roper MG, Skegg MP, Fisher CJ, Lee JJ, Dhanak VR, Woodruff DP, Jones RG (2004) *Chem Phys Lett* 389:87
51. Molina LM, Hammer B (2002) *Chem Phys Lett* 360:264
52. Cometto FP, Paredes-Olivera P, Macagno VA, Patrio EM (2005) *J Phys Chem B* 109:21737
53. Yu M, Bovet N, Satterley CJ, Bengió S, Lovelock KRJ, Milligan PK, Jones RG, Woodruff DP, Dhanak V (2006) *Phys Rev Lett* 97:166102
54. Maksymovych P, Sorescu DC, Yates JT Jr. (2006) *Phys Rev Lett* 97:146103
55. Mazzarello R, Cossaro A, Verdini A, Rousseau R, Casalis L, Danisman MF, Floreano L, Scandolo S, Morgante A, Scoles G (2007) *Phys Rev Lett* 98:016012
56. Nagoya A, Morikawa Y (2007) *J Phys Cond Matt* 19:365245
57. Jadzinsky P, Calero G, Ackerson CJ, Bushnell DA, Kornberg RD (2007) *Science* 318:430
58. Martin TP (1996) *Phys Rep* 273:200
59. Walter M, Akola J, Lopez-Acevedo O, Jadzinsky PD, Calero G, Ackerson CL, Whetten RL, Grönbeck H, Häkkinen H (2008) *Proc Natl Ac Sci* 105:9157
60. Cossaro A, Mazzarello R, Rousseau R, Casalis L, Verdini A, Kohlmeyer A, Floreano L, Scandolo S, Morgante A, Klein ML, Scoles G (2008) *Science* 321:943
61. Grönbeck H, Häkkinen H, Whetten RL (2008) *J Phys Chem C* 112:15940
62. Lavrich DJ, Wetterer SM, Bernasek SL, Scoles G (1998) *J Phys Chem B* 102:3456
63. Schaaff TG, Shafiqullin MN, Khoury JT, Vezmar I, Whetten RL, Cullen WG, First PN, Gutiérrez-Wing C, Ascencio J, Yacamán MJ (1997) *J Phys Chem B* 101:7885
64. Chen S, Ingram RS, Hostetler MJ, Pietron JJ, Murray RW, Schaaff TG, Khoury JT, Alvarez MM, Whetten RL (1998) *Science* 280:2098
65. Häkkinen H, Barnett RN, Landman U (1999) *Phys Rev Lett* 82:3264
66. Rossi G, Ferrando R, Rapallo A, Fortunelli A, Curley BC, Lloyd LD, Johnston RL (2005) *J Chem Phys* 122:194309
67. Garzón IL, Rovira C, Michaelian K, Beltrán MR, Ordejón P, Junquera J, Sánchez-Portal D, Artacho E, Soler JM (2000) *Phys Rev Lett* 85:5250
68. Garzón IL, Reyes-Nava JA, Rodríguez-Hernández JI, Sigal I, Beltrán MR, Michaelian K (2002) *Phys Rev B* 66:073403
69. Garzón IL, Michaelian K, Beltrán MR, Posada-Amarillas A, Ordejón P, Artacho E, Sánchez-Portal D, Soler JM (1998) *Phys Rev Lett* 81:1600
70. Häkkinen H, Walter M, Grönbeck H (2006) *J Phys Chem B* 110:9927
71. Jiang DE, Tiago ML, Luo WD, Dai S (2008) *J Am Chem Soc* 130:2777
72. Jiang DE, Tiago ML, Luo WD, Dai S (2008) *J Phys Chem C* 112:13905
73. Pei Y, Gao Y, Zeng XC (2008) *J Am Chem Soc* 130:7830
74. Tsunoyama H, Nickut P, Negishi Y, Al-Shamery K, Matsumoto Y, Tsukuda T (2007) *J Phys Chem C* 111:4153
75. Whetten RL, Price RC (2007) *Science* 318:407
76. Gao Y, Shao N, Zeng XC (2008) *ACS Nano* 2:1497
77. Li Y, Galli G, Gygi F (2008) *ACS Nano* 2:1896
78. Landman U, Luedtke WD (2004) *Faraday Discuss* 125:1
79. Henz BJ, Hawa T, Zachariah MR (2008) *Langmuir* 24:773
80. Pool R, Schapotschnikow P, Vlught TJH (2007) *J Phys Chem C* 111:10201
81. Jimenez A, Sarsa A, Blazquez M, Pineda T (2010) *J Phys Chem C* 114:21309
82. Zhao XC, Leng YS, Cummings PT (2006) *Langmuir* 22:4116
83. Mariscal MM, Olmos-Asar JA, Gutierrez-Wing C, Mayoral A, Yacamán MJ (2010) *Phys Chem Chem Phys* 12:11785
84. Olmos-Asar JA, Rapallo A, Mariscal MM (2011) *Phys Chem Chem Phys* 13:6500
85. Jiang DE (2010) *Acta Phys Chim Sin* 26:999
86. Hostetler MJ, Wingate JE, Jian Zhong C, Harris JE, Vachet RW, Clark MR, Londono JD, Green SJ, Stokes JJ, Wignall GD, Glish GL, Porter MD, Evans ND, Murray RW (1998) *Langmuir* 14:17
87. Schapotschnikow P, Pool R, Vlught TJH (2008) *Nano Lett* 8:2930
88. Khan SJ, Pierce F, Sorensen CM, Chakrabarti A (2009) *Langmuir* 25:13861

Chapter 10

Thermodynamic Modeling of Metallic Nanoclusters

Oscar A. Oviedo and Ezequiel P.M. Leiva

10.1 Historical Development

Gas–liquid, gas–solid, and liquid–solid phase transitions, among others, have drawn the attention of numerous scientists for more than a century [1, 2]. In 1878, Gibbs presented his celebrated manuscript “On the equilibrium of heterogeneous substances” [1], where a thermodynamic theory devoted to the understanding of the behavior of interfaces between fluids and solids was formulated for the first time. In that formulation, Gibbs introduced the concept of “dividing surface” as a mental construction for the structure of the interface, according to which, all the excess thermodynamic quantities depend on the location of this dividing surface that is defined according to each case. It is remarkable that although Gibbs presented his theory for both fluids and solids at the same time, most advances have been made in liquid condensation from the vapor phase [3]. According to Finney and Finke [4], the first review and compilation concerning work on nucleation and growth of metallic nanoparticles (NPs) was undertaken only in 2008.

The theoretical treatment for the formation of a nucleus depends on its nature, that is, fluid or solid. In Gibbs’ model [1, 2] this is a natural consequence of the definition of surface tension. While the thermodynamic definition implies accounting for the work of surface formation per unit area, the mechanical definition involves an excess of surface stress. Both definitions have different values for a solid, but the same for a fluid. Shuttleworth [5] and later Herring [6] related both definitions on the basis of mechanical considerations and settled the theoretical basis for the experimental determination of both. A recent compilation on these topics applied to chemical equilibrium may be found in the review work by Rusanov [7].

O.A. Oviedo • E.P.M. Leiva (✉)

Instituto de Investigaciones en Físico-Química de Córdoba, CONICET, Departamento de Matemática y Física, Facultad de Ciencias Químicas, Universidad Nacional de Córdoba, Córdoba, Argentina.

e-mail: ooviedo@fcq.unc.edu.ar; eleiva@fcq.unc.edu.ar

The most important concept to understand the properties of nucleation and growth of heterogeneous systems is surface tension, and probably the most widespread model used to compute such properties is that developed within the classical nucleation theory (CNT) [3]. This was originally developed by Volmer and Weber [8], Becker and Döring [9], Frenkel [10], and Zeldovich [11]. The CNT model was settled on the basis of the fluctuation theory and has as a final goal the computation of the rates at which these fluctuations occur. The latter drive the particles of the systems to become a fragment of the new nanophase [12]. Within this approach, a cluster of the new phase is represented as a nucleus with spherical symmetry and the same density as the stable bulk phase. This nucleus is immersed in a metastable phase with ideal properties. A particularly relevant concept that emerged from this formulation is that of *critical cluster size (or critical nucleus size)*, which refers to a cluster where the rate of growth and dissolution are exactly the same. Thus, clusters smaller than this will tend to disintegrate rather than to grow, and the opposite will occur with clusters larger than the critical one. The notable aspect of this model is the presence of an uncharged interface. The latter is characterized by its surface tension, which is assumed to be equal to that of a piece of macroscopically sized material. The cluster is considered to be in a diluted medium to such an extent that London–van der Waals interactions between the clusters may be considered negligible [13–16].

Many schemes and improvements to the CNT have been developed. For example, Buff [17, 18] extended the classical concepts to consider curved surfaces, using the mechanical and thermodynamic definition of surface tension developed by Shuttleworth [5]. A remarkable prediction using this model was made in the 1960s by Walton, who showed numerically that the critical nuclei size obtained in many experiments should contain less than seven atoms [19].

In 1961, Lothe and Pound (L&P) [20] discussed on the need to incorporate new contributions to the free energy of cluster formation that Volmer and Weber had not originally considered [8]. While the classical theory of nucleation was related to the formalism developed by Gibbs for infinite interfaces, the new contributions suggested by L&P resulted from considering the finite nature of the phenomenon. L&P argued that a statistical mechanical description should include the translational, rotational, and vibrational terms of the cluster being formed, since these terms correspond to the treatment of finite systems. This consideration was denominated “translational-rotational paradox in nucleation theory” and sparked a heated discussion that is still going on today [21–24]. Reiss et al. [25, 26] considered this problem and proposed modifications to the CNT, based on a suitable representation of the statistical mechanical model. These authors noted that it is actually necessary to consider only the contribution due to translation of the center of mass of the cluster.

For their part, Langer et al. [27–29] and Katz et al. [30] showed that the nucleation rate may be formally estimated, using some considerations based on kinetics equation. Choosing the equilibrium state under saturation conditions as the reference state, these authors arrived at the same conclusions as those drawn from the CNT. However, some inconsistencies emerged between both approaches

(thermodynamic and kinetic). Katz et al. [31] and then Girshick et al. [32] showed that the wrong choice of the excess of free energy in the CNT introduced an error in the determination of the nucleation rate, thus originating inconsistencies between both formulations. An empirical modification was proposed that allowed the interpretation of several experiments [31–33], but the physical/mathematical explanation was far from being understood.

In the 1990s, the increasing computational power allowed a new way to compare the predictions of theoretical models with experiment, which resulted in the so-called “computer simulations” [34–38]. For example, Duijneveldt et al. [39] estimated the free energy barriers that separate crystalline phases from their liquid counterparts. These early computer experiments generally used hard spheres or Lennard–Jones potentials, which limited the extrapolation of their behavior to that of metallic systems. However, they were already able to predict changes in structure of NP with increasing size, like the *bcc* to *fcc* transition. At the same time, density functional calculations started to be applied to the calculation of properties of very small clusters [40]. Most of these computer simulations have been devoted to study the nucleation of liquid drops from a gas phase, or to consider the formation of solid phases from a supersaturated gas. The application of computational studies to the nucleation of solid phases from a solution has been rather scarce, and most approximations to these problems are rooted in extrapolations from the liquid–gas and solid–gas studies mentioned above. The first attempt to such an approach was undertaken in the early 2000s by Ciacchi et al. [41–43], who analyzed the nucleation of Pt in aqueous solution on the basis of density functional theory (DFT) calculations.

Going back to the developments in the theoretical field, in 1996 Ford [44] extended the concepts of nucleation and growth adding the so-called second theorem of nucleation and growth to the standard formulation (first theorem). While the first theorem refers to the changes of nucleation rate with supersaturation, the second theorem refers to the changes of nucleation rate with temperature. As noted by Ford [44], the basic assumptions of CNT are a good approximation to relatively large NPs, where the deviations of the thermodynamic properties from bulk properties are only attributed to the existence of an interface. In this approach, a large NP is envisaged as consisting of two parts, a bulk and a surface. While the former is assumed to keep the properties of the bulk phase, the surface tension of the latter is assumed to have the value for an infinitely large flat surface. An improvement to this assumption is to consider the change of the surface tension with NP size. This approach was introduced for example in the equations derived by Tolman [45] and Plieth [46], which appears to be suited to describe NPs of intermediate sizes. However, in the case of small NPs, like for example one made of 100 atoms or less, the deviations of thermodynamic properties from bulk properties are related not only to the existence of the interfacial region but also to the specific assumptions of the model. For example, the mass density of a 100 atoms NP may be remarkably different from that of the bulk state, and even the meaning of surface tension becomes questionable. In this small-size limit, the proper tools to describe the thermodynamic behavior of the system is nanothermodynamics,

statistical mechanics, and of course quantum mechanics. In the late 1950s, Hill [47] developed an extension of thermodynamics to small systems, which is now addressed as nanothermodynamics [48]. This is a generalization of macroscopic thermodynamics, where the latter is included.

A further improvement undertaken by Ford [49] was the derivation of exact expressions for the two nucleation theorems. Many problems, such as the law of mass action [50], the positional entropy [51], and the discrepancy between the kinetic and thermodynamic approaches discussed above, were enlightened and solved. However, the practical application of this theoretical framework to simulations and/or experiments requires the choice of a model for a NP (e.g., the definition of its physical limits), and depending on this, the nucleation rate becomes different [52–54]. Since the previous concepts were not developed for the nucleation of solids in solution, such effects as electrochemical equilibrium, ligands, solvent, etc. were not originally included in them.

The increasing computational power mentioned above has acted in two ways on the evolution of nucleation and growth modeling. On one hand, it acted on evaluating and testing efficiently the theory of nucleation [55–57]. On the other hand, the availability of interaction potentials with improved accuracy [58] has shortened the gap between theory and experiment. Nowadays, it is common to find TEM-imaging of NPs with sizes that make it possible to simulate their behavior in a computer (see for examples Chap. 1 by Mejia-Rosales and Yacamán in the present book). However, much care must be taken when extrapolating the results from simulations to experiment. As noted by Reguera et al. [22], the kind of fluctuations that the system is allowed to perform is determined by the constraints applied to the system, and these are different for the different simulation ensembles. For example, one cannot simply straightforwardly extrapolate the results obtained in the canonical ensemble to the analysis of nucleation, which takes place mostly under different conditions.

Regarding its application to electrochemical systems, recently Oviedo et al. [59] have presented an extension of the classical nucleation and growth model to the so-called core–shell NPs. Motivated by the control of electrodeposition in the synthesis of bimetallic NPs in liquid phase [60], these authors formulated a model that describes the electrodeposition of a metal on a nanostructure made (or not) of a different material. In this approach, the structure of bimetallic NPs may be obtained as a function of the deposition potential, the concentration of depositing species, and temperature.

The methods for the synthesis of NPs are generally based on a kinetic control of the reaction conditions [61]. These concepts were originally introduced by LaMer in the 1950s [62], applying the theory of nucleation and growth, which considers the system out of equilibrium. However, recent advances in the theoretical–computational field have shown that under electrochemical control it should be possible to control the decoration of NP core seeds on purely thermodynamic grounds [63, 64]. It is worth mentioning that the latter assessment is still waiting for experimental confirmation.

10.2 Theoretical Background

10.2.1 Nanothermodynamics

For systems containing a large (massive) number of particles, that is, of the order of Avogadro's number, $N_{\text{Av}} \sim 10^{23}$, nowadays there is a very well developed framework that allows the determination of their thermodynamic properties [65]. Phenomena like conversion of heat into work, phase transitions, and critical points are clear examples of the predictive power of thermodynamics. There are even slight modifications to this machinery that allow computation of thermodynamic properties for systems sized down to a few nanometers [5, 6, 45, 46]. This is possible since macroscopic thermodynamics describes the most probable behavior of macroscopic systems where fluctuations are negligible. As an example, let us consider the energy fluctuations in a system made of water molecules. In the canonical ensemble, the relative energy fluctuations, σ_U , will be given by $\sigma_U = (kT^2 C_V)^{1/2} / \bar{U}$, where \bar{U} and C_V are the average internal energy and heat capacity at constant volume, respectively. The substitution of numerical values at room temperature shows that these fluctuations are of the order of $10^{-10}\%$ for $N = 10^{20}$ and 1% for $N = 20$, showing that these fluctuations may be small but meaningful for very small water clusters. On the other hand, similar calculations for Au yield $10^{-10}\%$ and $10^{-1}\%$ for the same number of particles, showing that in the case of a metal energy, fluctuations are one order of magnitude smaller. However, this is an approximation and exact heat capacities should be employed. As another example, let us consider an icosahedral arrangement of size N , and analyze for which size the number of surface atoms, N^{surf} , is lower than 10% . The total number of atoms N can be written as $N = (10m^3 + 15m^2 + 11m + 1)/3$, where m is an integer and represents an element of the icosahedra family. Using this formula we can state that $N^{\text{surf}} \sim 10\%$ if $N \sim 6 \times 10^4$, which translated into a size would yield an icosahedron of ca. 6 nm radius in the case of Au. Thus, we see that for systems smaller than 6×10^4 atoms (or 6 nm), the number of surface atoms will be relatively important, so their contribution to the properties of the system (like melting point, for example) cannot be ignored.

From the previous discussion we see that the predictive power of macroscopic thermodynamics starts to fade when the size of the piece of matter considered is below a few nanometers. Thus, many objects considered in nanoscience and nanotechnology put into question the knowledge of conventional thermodynamics and show that their behavior is far from being explained by this discipline. The decrease in the melting temperature of NPs [66, 67], and the reversion of phase stability between diamond and graphite [68] are classical and representative—but by no means unique—examples. Along the lines of the previous examples, we can include nucleation processes which only involve a few atoms. Classical definitions of clusters may no longer be valid at the nanoscale, and theoretical predictions may deviate strongly from experimental behavior if these features are not properly

accounted for [69]. This point is particularly important in the case of metals, where binding energies are of the order of the electron-volt (eV), i.e., considerably larger than thermal energy at room temperature (0.023 eV) [70].

Statistical mechanics and quantum mechanics are undoubtedly key tools to understand materials at the nanoscale, but the computational (and theoretical) effort to get a proper description of their properties is too large, even for the fastest computers existing nowadays. This is so because even setting aside the quantum nature of matter, the number of variables required to characterize the system at a molecular level is extremely large: $6N$ for a piece of matter made of N atoms. In contrast, in macroscopic thermodynamics we only need a few variables (typically three, four, etc.) to characterize its behavior [65]. It is for this reason that it is necessary to develop extensions of thermodynamics that would be able to predict correctly the properties of matter at this scale, using only a reduced number of variables.

Almost 50 years ago, in a visionary approach, Terrell L. Hill settled the theoretical basis to understand matter at the nanoscopic scale in his book “Thermodynamics of Small Systems” [47]. Keeping the pace of “nano times,” this theoretician extraordinarius [71] gave this area of study a new name: he called it nanothermodynamics [48], so we keep this terminology.

Before starting with the consideration of the main features of nanothermodynamics, we want to emphasize that in the present chapter we will only refer to the equilibrium state or its close neighborhood. We refer the reader interested in the consideration of small systems out of equilibrium and the consequences of their size for the three laws of thermodynamics, to the discussions of Esfarjani et al. [72] and Gross et al. [73].

In the following discussion, we will focus on the open system formulation applied to the formation of metallic NPs. The reader may find in Hill’s book other related systems and ensembles [47].

As analyzed by Hill [47], let us consider an ensemble made of ξ one-component systems, all equivalent, distinguishable, and independent. Each of them has a fixed center of mass and is characterized by the variables N , P , and T . Some of the previous considerations are not strictly necessary, but allow eliminating the translational degrees of freedom. Rotational degrees of freedom are not included at this stage, but will be considered in the next section. The fundamental differential equation for the macroscopic system constituted by the whole ensemble is:

$$dU_T = TdS_T - PdV_T + \mu dN_T \quad (10.1)$$

where subindex T means total, and we have defined $U_T = \xi \bar{U}$, $S_T = \xi \bar{S}$, $V_T = \xi \bar{V}$, and $N_T = \xi \bar{N}$, which correspond to the internal energy, entropy, volume, and total number of particles of the ensemble, respectively. To extend this formalism to nanothermodynamics, it is necessary to add a new term to (10.1), corresponding to the change of the number of systems in the ensemble, so we get:

$$dU_T = TdS_T - PdV_T + \mu dN_T + \varepsilon d\xi \quad (10.2)$$

where ε is denominated subdivision potential and is defined as $\varepsilon = (\partial U_T / \partial \xi)_{S_T, V_T, N_T}$. The meaning of ε will be clarified later on. We note that the present formalism implies that the functional form of the energy is $U_T = U_T(S_T, V_T, N_T, \xi)$, instead of the usual one $U_T = U_T(S_T, V_T, N_T)$ in macroscopic thermodynamics; U_T is a first-order homogeneous function with respect to S_T, V_T, N_T , and ξ . Integration of (10.2) leads to:

$$U_T = TS_T - PV_T + \mu N_T + \varepsilon \xi \quad (10.3)$$

and its subsequent division by ξ leads to the generalization of Euler's equation to nanothermodynamics:

$$\bar{U} = TS - P\bar{V} + \mu N + \varepsilon \quad (10.4)$$

where we can see the occurrence of the new term ε , not included in macroscopic thermodynamics. Differentiation of (10.4) and use of (10.2) lead to:

$$d\varepsilon = -SdT + \bar{V}dP - Nd\mu \quad (10.5)$$

which is the generalization of Gibbs–Duhem equation to small systems ($d\varepsilon = 0$ in macroscopic thermodynamics). This shows that the subdivision potential is a function of the form: $\varepsilon = \varepsilon(T, P, \mu)$. Thus, (10.2), (10.4), and (10.5) are the nanothermodynamic counterparts of well-known macroscopic thermodynamic equations.

Since relative fluctuations are small in macroscopic systems, in a given problem one can choose between different ensembles on the basis of mathematical convenience. However, we have seen that this may not be the case of nanoscopic system, so that it is necessary to derive the equations for each of the ensembles. Thus, if a global approach to a given problem involving theory, simulations, and experiments is attempted, it is necessary that both the theoretical modeling and the simulations reflect the experimental conditions. Another remarkable feature of nanosystems is that we have to abandon the macroscopic concept of intensive and extensive variables. In nanothermodynamics, some of the properties that in the macroscopic limit did not depend on the system size now will. However, following Hill's didactic approach, we will refer to the behavior of extensive and intensive properties in the macroscopic limit.

Surface effects play a fundamental role in nanothermodynamics. This bears direct consequences for the interactions between systems and their reservoirs, since—in contrast with the macroscopic treatment—these interactions cannot be neglected. In the N, P , and T ensemble, the nexus between nanothermodynamics and statistical mechanics is given by the equation:

$$kT \ln [\Delta_T(N, P, T)] = TS_T - U_T - P\bar{V} \quad (10.6)$$

where Δ_T corresponds to the open partition function of the whole ensemble, made of ξ one-component systems. Due to the equivalence, independence, and distinguishability of the systems, we have $\Delta_T(N, P, T) = [\Delta(N, P, T)]^\xi$, where $\Delta(N, P, T)$ is the open partition function of a single system. Taking into account (10.3), (10.6) may

be rewritten as:

$$-kT \ln[\Delta(N, P, T)] = \mu N + \varepsilon \quad (10.7)$$

in macroscopic thermodynamics the *rhs* of (10.7) is just (μN) . However, in nanothermodynamics we find the term $(\mu N + \varepsilon)$, which serves as a nexus with statistical mechanics.

It must be pointed out that the small systems that we will study in the present chapter are too small to be modeled by macroscopic thermodynamics, but still large enough to be able to model “extensive” properties as continuous variables. The nanothermodynamics formalism may characterize systems, even when they are very small [47].

We illustrate now the origin of the subdivision potential ε . Let us think of a macroscopic system defined by a metal piece (one component) at temperature T . The Gibbs free energy is $G(N, P, T) = Ng(P, T)$ where N is the number of atoms in the system and $g(P, T)$ is the free energy per particle. In this (macroscopic) limit, $g(P, T) = \mu = (\partial G / \partial N)_{P, T}$. If we divide the system into two macroscopic pieces, say 1 and 2, then the free energy of system 1 can be computed from $G_1(N_1, P, T) = N_1 g(P, T)$, and that of system 2 from $G_2(N_2, P, T) = N_2 g(P, T)$. We can note that the free energy per particle is the same in both systems; this is the principle of thermodynamic extensivity. If we divide the system successively, say 10^{20} times, then each system will contain a few thousand atoms. If we assume that each system has a compact (3D) structure, about half of the atoms may be on its surface, therefore the number of atoms in the surface and inside the nanostructure will be comparable. In this (nanoscopic) limit, we can no longer calculate the free energy for the i -system as $G_i(N_i, P, T) = N_i \mu$, but we can still write $G_i(N_i, P, T) = N_i \hat{\mu}$ where $\hat{\mu} = \hat{\mu}(N_i, P, T)$ is now not only a function of P and T but also of the number of particles N_i . $\hat{\mu}$ contains correction terms that must be added for the proper calculation of the Gibbs free energy. This correction will contain terms of the type $N_i^{2/3}$, $N_i^{1/3}$, $\ln N_i$, etc., due to surface, curvature, and rotational contributions (among others), which must be taken into account. It can be shown that [47]:

$$G_i(N_i, P, T) = g(P, T)N_i + \alpha(P, T)N_i^{2/3} + \beta(P, T)N_i^{1/3} + \dots \quad (10.8)$$

where we can see that only in the macroscopic limit ($N_i \rightarrow \infty$) these quantities are negligible with respect to the first term on the *rhs*. Thus, we find that in the nanoscale it is necessary to specify the size of the system for a proper (and correct) thermodynamic characterization so that small systems have one more degree of freedom than large ones.

We can now take the derivative of (10.8) with respect to N , for constant P and T to get:

$$\left(\frac{\partial G_i(N_i, P, T)}{\partial N_i} \right)_{P, T} = g(P, T) + \frac{2}{3} \alpha(P, T) N_i^{-1/3} + \frac{1}{3} \beta(P, T) N_i^{-2/3} + \dots \quad (10.9)$$

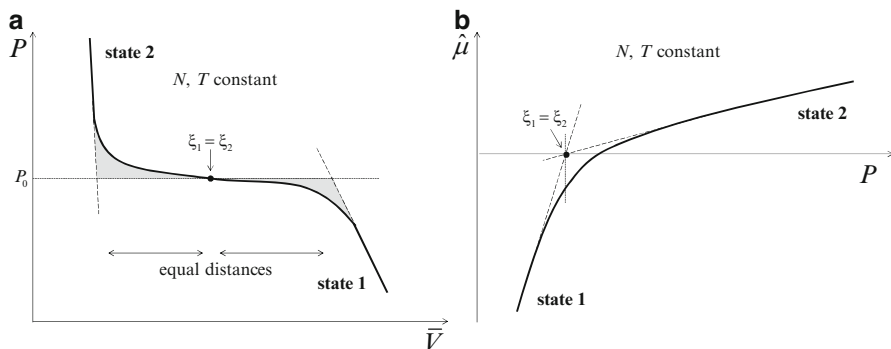


Fig. 10.1 Schematic representation of (a) P vs. \bar{V} and (b) $\hat{\mu}$ vs. P isotherms for a small system containing N atoms at a temperature at which the related macroscopic system presents a first-order phase transition between two states

Further multiplication by N results in:

$$\mu N = g(P, T)N + \frac{2}{3}\alpha(P, T)N_i^{2/3} + \frac{1}{3}\beta(P, T)N_i^{1/3} + \dots \quad (10.10)$$

and taking into account (10.7), we find that the subdivision potential is given by:

$$\varepsilon = \frac{2}{3}\alpha(P, T)N_i^{2/3} + \frac{1}{3}\beta(P, T)N_i^{1/3} + \dots \quad (10.11)$$

Summarizing, the subdivision potential is related to all nanoscale contributions.

10.2.2 Phase Transitions in Nanothermodynamics

A macroscopic system may present discontinuities in the variation of some of its thermodynamic functions below its critical point. The latter corresponds to the definition of a first-order phase transition. In principle, these discontinuities are very sharply defined only in the limit of infinitely large systems. In contrast, small systems may exhibit a gradual change in their thermodynamic functions. The occurrence of a first-order phase transition in the macroscopic material does not necessarily imply that this will also be the case in the nanoscopic scale. Even if this is the case, the transition will not necessarily occur in the same interval of order parameter. The decrease in the melting point with NP size is a good example of the latter.

Isothermal P vs. \bar{V} and $\hat{\mu}$ vs. P state curves for a nanosystem are shown schematically in Fig. 10.1. The smooth change in P and/or $\hat{\mu}$ indicates that the phase transition occurs gradually and not in an abrupt fashion, as it is the case in a macroscopic system.

It is clear that we cannot formally study the phase transition because there is no discontinuity. However, if we accept the two-states approximation, which consists in the assumption that there are only two states available for each system [74], we can state two important theorems on the basis of the simple geometric constructions shown in Fig. 10.1. There, we show the pressure and chemical potential as a function of volume and pressure, respectively, for a nanosystem that presents two different states, as could be the case of the gas–liquid transition to yield a nanodrop. We find a gradual change of P and $\hat{\mu}$, shown in the full lines of Fig. 10.1. On the other hand, the discontinuous lines on the left and on the right of each curve show the evolution of the pressure or chemical potential for a very large system. These could represent the evolution of a gas (state 1) and of a liquid (state 2) at constant N and T .

In the first place, we have the so-called equal-distances theorem. If the experimental curve P vs. \bar{V} and their extrapolations P_1 and P_2 are available (see Fig. 10.1a), it is possible to draw a segment parallel to the \bar{V} axis, such that it connects the two extrapolated curves so that the segment is divided by $P(\bar{V})$ curve into two equal parts. We will denote the P value where the parallel segment is located with P_0 . This value corresponds to the pressure at which the population in the ensemble is $\xi_1 = \xi_2$. The segment and the point are marked in Fig. 10.1a. The same geometrical construction may be made for $\hat{\mu}$ vs. P isotherms (see Fig. 10.1b).

The second theorem corresponds to that of equal-areas. This theorem establishes the equality of areas in curves P vs. \bar{V} , shaded in gray in Fig. 10.1a. It can be shown that the following equation is valid:

$$\int_{P_1}^{P_0} (\bar{V}_1 - \bar{V}) dP = \int_{P_0}^{P_2} (\bar{V} - \bar{V}_2) dP \quad (10.12)$$

where the meaning of the different limits are denoted in the figure. The simultaneous application of the two theorems allows the analysis of phase transitions in a nanosystem and the identification of P_0 .

10.2.3 The Hill and Chamberlin Metastability Model

In the present section we will focus on the problem of metastability and stability of nanosystems. With this purpose, we will use the model of Hill y Chamberlin (HC) [75] originally developed to study the conversion of metastable (nanometric) drops of a liquid into its bulk phase. Before starting the discussion of the HC model, it must be noted that the grand canonical partition function $\Xi(\mu, V, T)$ or the partition function of a completely open system $\Upsilon(\mu, P, T)$ may be reduced to a function of (μ, T) if we consider that the system is incompressible. Following Hill, we will denote the partition function of such a system with $\Upsilon(\mu, T)$. A demonstration for a similar case may be found in Hill's book, page 59 (Vol I) [47].

The partition function of an incompressible, completely open system may be written as follows:

$$Y(\mu, T) = \sum_{N=1}^{\infty} Q(N, T) \exp[\mu N/kT] \quad (10.13)$$

If we further consider that the system is made of a spherical cluster, $Q(N, T)$ takes the form:

$$Q(N, T) = c(T)N^4 \exp\left[-\alpha(T)N^{2/3} + \mu_0 N/kT\right] \quad (10.14)$$

The term $c(T)N^4$ corresponds to rotational and translational contributions, $\alpha(T)$ is proportional to the surface tension, and the term $\mu_0 N/kT$ is related to the partition function of N molecules in the bulk liquid phase (assuming Einstein model for a system of harmonic oscillators). Replacing (10.14) into (10.13) we get:

$$Y(\mu, T) = c(T) \sum_{N=1}^{\infty} N^4 \exp\left[-\left(\varphi N + \alpha(T)N^{2/3}\right)\right] \quad (10.15)$$

where the coefficient of saturation has been defined as $\varphi = (\mu_0 - \mu)/kT$. If $\varphi > 0$, the system is in a subsaturation region; if $\varphi < 0$, the ensemble is in supersaturation conditions. If $\varphi = 0$, the ensemble is right at the saturation limit. We note that temperature cannot change the sign of φ , but it can change its intensity. Thus, the effects driven by μ may become more or less evident, depending on T .

Going back to the previous discussion, the probability of observing a cluster made of N atoms may be written as follows:

$$P_N(\mu, T) = \frac{c(T)N^4 \exp\left[-\left(\varphi N + \alpha(T)N^{2/3}\right)\right]}{Y(\mu, T)} \quad (10.16)$$

The main idea in the HC model is to analyze nanodrop stability in terms of the numerator of $P_N(\mu, T)$, since $Y(\mu, T)$ is fixed for given μ and T . Then, a plot of $f(N, \mu, T)$ defined as $f(N, \mu, T) = P_N(\mu, T)Y(\mu, T)$ will present the same behavior as $P_N(\mu, T)$ out of a constant factor. A more suitable form to represent f is to make the changes of variables $n = \alpha^{3/2}N$ and $\delta = \alpha^{-3/2}\varphi$ to get:

$$f(N, \mu, T) = f(n) = n^4 \exp[-\delta n] \exp\left[-n^{2/3}\right] \quad (10.17)$$

Figure 10.2a shows a contour plot of $f(n)$ as a function of δ and $\log(n)$ at 300 K. We have selected to this purpose four representative iso-saturation lines, $\delta = 0, -0.04, -0.07$, and -0.09 , which are plotted in Fig. 10.2b–e. Each of the factors in (10.17) has been marked in Fig. 10.2b–e to illustrate the different contributions to $f(n)$. Generally speaking, we can mention that the surface component is always a decreasing quantity (green curve), and that its value depends on the surface energy

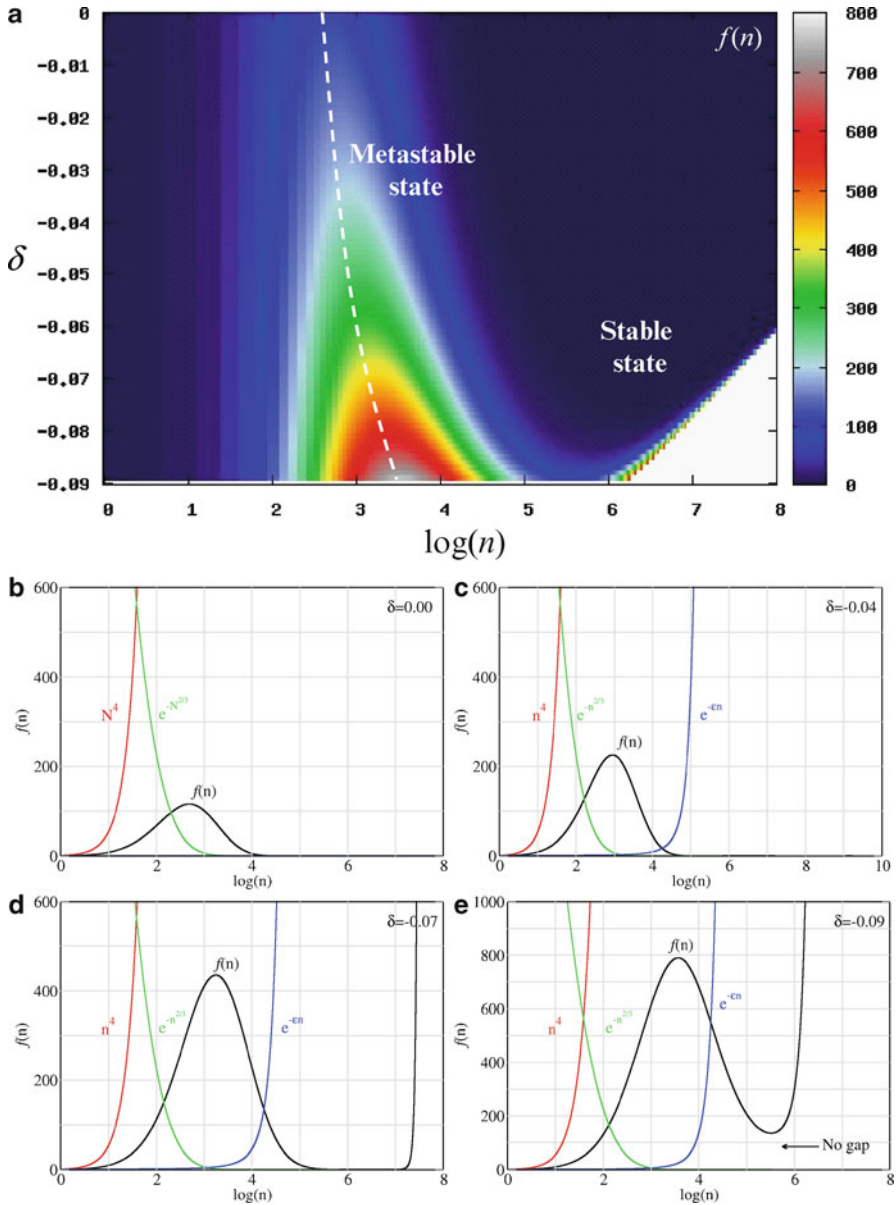


Fig. 10.2 (a) Contour plot of the function $f(n)$ defined in (10.17) at a constant temperature. Contributions of the different factors in (10.17) at diverse values of the supersaturation δ . (b) $\delta = 0$, (c) $\delta = -0.04$, (d) $\delta = -0.07$, and (e) $\delta = -0.09$. In (b)–(e) the *green curve* has been multiplied by a factor 10^4 to fit into scale. See discussion in the text

of the NP being formed. The rotational–translational contribution (red curves) is always a monotonically increasing function. The product of the two former components (the case of $\delta = 0$, black curve) determines a maximum of $f(n)$ around $\log(n) \approx 2.6$ (Fig. 10.2b). This maximum indicates a finite probability of finding nanodrops of a given size at $\delta = 0$ and is a consequence of the rotational–translational contribution. At moderate supersaturation conditions, for example $\delta = -0.04$, the term containing the chemical potential (blue curve) starts to be noticeable, and the maximum of $f(n)$ is shifted toward larger n values, while its value increases (see Fig. 10.2c). At larger supersaturations, for example $\delta = -0.07$, Fig. 10.2d, the behavior remains the same, and a steep increase is found in $f(n)$ above $\log(n) \approx 7$. This sudden increase in $f(n)$ after the maximum denotes the mathematical divergence of the probability density for $n \rightarrow \infty$, as a consequence of the fact that the supersaturation term is dominating the probability density for large nanodrop sizes. In the HC model, this divergence is associated with the occurrence of the bulk liquid phase.

In Fig. 10.2d, it can be noted that in the region $5.7 < \log(n) < 7$ the probability density of finding a liquid nanodrop is practically negligible. The two-state approximation mentioned in Sect. 10.2.2 [74] suggests that this zone of low probability acts as a bottleneck for the transition of a n -sized liquid nanodrop toward the bulk liquid phase. However, this situation reaches a limit at larger supersaturations. For example, Fig. 10.2e shows that at $\delta = -0.09$ the region where $f(n) \sim 0$ has disappeared, and it can be expected that small fluctuations, even of one particle, may lead to the transition to the bulk liquid. At very large supersaturations (not shown here) the metastable nanodrop should no longer be observed, remaining only a monotonic growth toward the bulk phase. In Fig. 10.2a it can be observed how the region corresponding to the bottleneck progressively becomes thinner with increasing supersaturation. The rate at which the steep increase in $f(n)$ moves toward small n for decreasing δ is larger than the rate at which the metastable state moves toward large n . This is represented by white broken lines in Fig. 10.2a. The broken line on the left shows the position of $f(n)$ maximum, while the broken line on the right shows the evolution of a point at which $f(n) = 10^3$. Although the two lines have not converged to a representative point in the region analyzed in Fig. 10.2a, it can be seen that the dark blue region (bottleneck), i.e., the one with a negligible probability, has disappeared for $\delta = -0.09$, so that the system will no longer be confined to a metastable state at this supersaturation value.

The bottleneck in Fig. 10.2 represents a kinetic hindrance for the phase transition under consideration. The size of the gap may be related to an activation energy [76], in the sense that if this activation energy is large enough (wide probability gap), the transition will not take place in the timescale of experiment. This “confination” allows the computation of the thermodynamic properties of the nanodrops, even when their structures do not correspond to a global minimum of the free energy of the system.

From the previous analysis it emerged the idea of what Hill and Chamberlin called physical convergence of the probability density [75]. When the mathematical divergence is shifted to large drop sizes ($\delta \rightarrow 0^-$, to denote that we are approaching

the zero from small negative values), and we are interested in the calculation of properties of the metastable liquid drop, the sum in (10.15) may be truncated to give:

$$\Upsilon(\mu, T) = c(T) \sum_{N=1}^{N_0} N^4 \exp \left[- \left(\varphi N + \alpha(T) N^{2/3} \right) \right] \quad (10.18)$$

where N_0 corresponds to a value of N at the minimum of the argument of the sum. Note that $N_0 = N_0(\mu, T)$ is a function of chemical potential and temperature. As it is always the case, knowledge of the partition function allows calculation of all properties related to the metastable nanodrop.

When the system is in undersaturation conditions ($\delta > 0$), no divergence is found in the probability density, since under these conditions the sum (10.15) always converges. At moderate undersaturations ($\delta \rightarrow 0^+$, to denote that we are approaching the zero from small positive values), $f(n)$ presents a maximum and the nanodrop properties may be evaluated straightforwardly, since the local maximum in $f(n)$ is also a global one.

All the previous concepts will be very useful to analyze the behavior of core/shell NPs as described in Sect. 10.4.

10.2.4 Nucleation Theorems

As pointed out in Sect. 10.1, currently there is a nucleation and growth theory, deduced from statistical mechanics that allows contrasting models, simulations, and experiments. Many improvements were achieved along the evolution of the theoretical framework. One of the most widely accepted alternatives is that developed by Ford [49, 55]. This derivation of the nucleation theorems was developed on the basis of statistical–mechanical and kinetic considerations that we will not discuss here, since there are very clearly discussions of them in the reference material [44, 49, 55, 77]. In these publications, Ford defined the saturation coefficient as $s = N_1^e / N_1^{es}$, where N_1^e and N_1^{es} are the number of monomers in the supersaturated and saturated phases, respectively. With this definition, the first nucleation theorem can be summarized in the following equation:

$$\left(\frac{\partial \ln J}{\partial \ln s} \right)_T = 1 + N^* \quad (10.19)$$

where J is the nucleation rate and N^* is the number of particles of the critical cluster size, measured at a constant temperature.

The second nucleation theorem relates the changes in J with temperature at a constant supersaturation, and can be written as:

$$\left(\frac{\partial \ln J}{\partial T} \right)_{\ln s} = \frac{1}{kT} [L - kT + \Delta U(N^*)] \quad (10.20)$$

where L is the latent heat per particle at the vapor-condensed phase transition, and $\Delta U(N^*)$ is the excess of internal energy of the liquid drop, defined as: $\Delta U(N^*) = U(N^*) - N^*U_L$, where U_L is the internal energy in the bulk liquid state. Defined in this way, $\Delta U(N^*)$ contains the surface energy as a major contribution. In Sect. 10.2.8, we will extend these concepts to the nucleation of a crystalline phase via an electrochemical process.

10.2.5 Size Distribution of Nanoparticles

In this section we analyze a model for the estimation of the size distribution of NPs. This quantity is very important because it is directly related to the experimental histograms.

We start with the classical statistical mechanical representation of the partition function in the grand canonical ensemble:

$$\Xi(\mu, V, T) = \sum_{N=0}^{\infty} \frac{1}{N!h^{3N}} \int d\Gamma \exp\{-[H(N) - \mu N]/kT\} \quad (10.21)$$

where $H(N)$ is the Hamiltonian of a system containing N atoms, Γ is a $6N$ dimensional vector, defined in the phase space of N particles, and h is Planck's constant. The integral in (10.21) is subtended to all the region of the phase space available for the system. The term $N!$ takes into account the indistinguishability of the atoms that make up the NPs.

In the following section we discuss some implications of (10.21) for metallic NPs. Let us analyze a given cluster, for example that corresponding to $N = 3$. The integral will be $\int \exp\{-[H(3) - 3\mu]/kT\}d\Gamma$. This integral computes all possible configurations containing three atoms in a volume V at temperature T and chemical potential μ . This evaluation involves infinite possibilities, since the three atoms may assume diverse configurations that range from a compact triangular arrangement up to a gas-like structure, where they are widely separated from each other. Due to the nature of metal bond, many of these configurations will have relatively large configurational energies, and just a few structures need to be taken into account at the time of modeling the growth of the new phase. To fix ideas, let us consider the case of three Au atoms in three representative configurations, as shown in Fig. 10.3.

Figure 10.3 represents three possible configurations compatible with the same μ , V and T . Considering nearest-neighbor interactions only, we find 3, 2, and 1 bonds in Fig. 10.3a, b, and c, respectively. As an example, let us assume that the average binding energy per Au–Au bond is approximately -0.64 eV and that the interactions are additive. Let us also consider room temperature conditions, where kT amounts to ca. 0.023 eV. The relative probability of observing any of these configurations $p_{i,j}^{\text{rel}}$ will be given by $p_{i,j}^{\text{rel}} = \exp[-(U_i - U_j)/kT]$, where U_i and U_j are the energies of the corresponding configurations. Using the binding energies

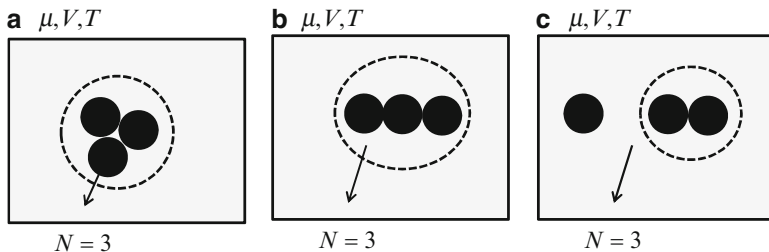


Fig. 10.3 Three possible configurations of a three-atom arrangement. These correspond to (a) 3, (b) 2, and (c) 1 nearest-neighbor interactions. See text for discussion

mentioned above, we get $p_{2,3}^{\text{rel}} = 10^{13}$ and $p_{1,3}^{\text{rel}} = 10^{25}$, showing that on purely energetic grounds those structures that differ in more than a bond show extremely different probabilities of existence, being the more compact structures strongly favored. However, the less compact structures often present a larger number of isoenergetic configurations that must be taken into account when estimating the relative probability of the different structures. Thus, from an entropic viewpoint and at finite temperatures, those systems with a larger number of configurations will be favored. How many configurations, let say Ω , compatible with given energy, are necessary to counterbalance the previous energetic effects? To estimate this point, let us make the following computations. To have comparable energetic and entropic contributions, we must have $\Delta U \approx T\Delta S$. Assuming that all configurations with the same number of bonds have identical weights, we can estimate the entropic contribution from $S = k \ln \Omega$. This yields a number of configurations of the order of $\Omega \sim 10^{13}$ and $\Omega \sim 10^{25}$ for those systems differing in one and two bonds, respectively. There is certainly no such number of possibilities in the way of arranging, clusters with, say 3 or 2 bonds. In the case of the configuration in Fig. 10.3c, rather than being considered a three atomic one, it will be computed as consisting of two different clusters: one containing 1 atom and the other 2. According to this discussion, in the case of metallic NPs, a good approximation is to consider the lowest energy configurations or their equivalent, those presenting the closest packed configurations. For a more detailed discussion, the reader may consult the reference [63].

The next step consists in writing the Hamiltonian of a N -atoms system as the sum of small contributions, $H(N) \approx \sum_{i=1}^{i_{\text{max}}} n_i h(i)$ where n_i and $h(i)$ refer to the number of clusters of size i and their corresponding Hamiltonian, respectively. The upper value of the sum index, i_{max} , is assumed to be larger than the critical size [77]. Thus, for example, for the configuration in Fig. 10.3c, the number of clusters with 1 and 2 atoms are $n_1 = 1$, and $n_2 = 1$; $h(1)$ and $h(2)$ are the one- and two-particle Hamiltonians, respectively.

The mass balance involves the condition $N = \sum_{i=1}^{i_{\text{max}}} i n_i$, which in the last example is $N = (1 \times 1) + (2 \times 1) = 3$. This approximation has the implicit assumption that

we are dealing with noninteracting clusters. If the clusters are suitably separated in space (diluted solutions), the previous approximation will be valid.

Assuming that the clusters behave as ideal gas mixtures [77], (10.21) can be rewritten as:

$$\Xi(\mu, V, T) \approx \sum_{\{n_i\}} \left(\prod_{i=1}^{\infty} \frac{Z_i^{n_i}}{n_i!} \right) \quad (10.22)$$

where the sum now corresponds to the different population distributions. $Z_i = \frac{1}{i!h^{3i}} \int' \prod_{j=1}^i d\Gamma \exp\{-[F(i) - \mu i]/kT\}$ corresponds to a modified canonical partition function. The next usual step consists in calculating the most probable distribution, that is, the most often observed at equilibrium. The mathematical problem is solved by differentiation of the logarithm of equation (10.22) with respect to the distribution n_i :

$$\frac{\partial}{\partial n_i} \sum_{i=1}^{\infty} \ln \left(\frac{Z_i^{n_i}}{n_i!} \right) = 0 \quad (10.23)$$

along with the mass balance condition given above. This procedure leads to the equilibrium distribution n_i^e :

$$n_i^e = \exp\{-[F(i) - i\mu]/kT\} \quad (10.24)$$

where it is now clear that the most probable distribution is closely related to the excess of free energy with respect to the gas phase.

The chemical potential μ may be referred to the chemical potential of the saturated phase μ_s , according to $\mu = \mu_s + kT \ln s$, where s is a saturation coefficient. The preceding equations are strictly valid to study cluster formation in undersaturation regions and at the saturation limit, since in this region the population n_i^e does not diverge for $i \rightarrow \infty$. However, the preparation methods of metal NP are generally carried out in the supersaturation region [61]. To study properties of NP in these conditions, it is usually assumed that the system may be kept in a ‘‘constrained equilibrium,’’ so that the preceding equations remain valid. Multiplying and dividing (10.24) by n_1 yields:

$$n_i^e = n_1 \exp\{-[F(i) + kT \ln n_1 - i(\mu_s + kT \ln s)]/kT\} \quad (10.25a)$$

$$n_i^e = n_1 \exp\{-[W(i) + ikT \ln s]/kT\} \quad (10.25b)$$

where $W(i)$ is the work of formation. Equation (10.25b) is the most widely used expression to estimate the nucleation rate along with (10.19). This is made for example by inserting $W(i)$ evaluated at $i = N^*$ in (10.19).

10.2.6 Contributions to the Free Energy of Metal Nanoparticles

In this section, we analyze models for the statistical mechanical treatment of the different contributions to the free energy of metal NPs.

$F(i)$ in (10.25a) contains different contributions: static, vibrational, rotational, and translational. If the partition function is assumed to be separable in the form:

$$Q(i, V, T) = \exp \left[-\frac{U^{\text{static}}(i)}{kT} \right] q^{\text{vibra}} q^{\text{rota}} q^{\text{trasla}} \quad (10.26a)$$

then the free energy may be written as:

$$F(i) = U^{\text{static}}(i) + F^{\text{vibra}}(i) + F^{\text{rota}}(i) + F^{\text{trasla}}(i) \quad (10.26b)$$

where the upper index denotes the type of the contributions. To estimate the order of magnitude of the different terms in (10.26b) we can use some simple models of statistical mechanics. The static energy, $U^{\text{static}}(i)$, corresponds to the potential energy calculated at the average positions of the atoms constituting the NP. Its values depend on the choice of the model and the interaction potentials employed. In the many-particles metal systems, the usual choice are semiempirical potentials like EAM [78], Tight Binding [79], and MEAM [80]. For small systems, DFT calculations [81] are becoming an option due to the increasing computational power available. Good compilations for metallic systems can be found in the reviews of Li [82] and Xiao [83].

The vibrational contribution may be estimated from the fluctuations of the atomic positions from their average value. An often used approximation consists in approximating the potential energy as a quadratic function of the atomic displacements. In the classical limit, each vibrational mode contributes in the amount $kT/(\hbar\omega)$, where \hbar and ω are $h/2\pi$ and the angular frequency of the mode respectively. The vibrational contribution of a cluster containing i atoms may be written as:

$$q^{\text{vibra}} = \prod_{j=1}^{3i-6} \frac{kT}{\hbar\omega_j} \quad (10.27)$$

The rotational and translational contributions correspond to the 6 degrees of freedom not included in (10.27). The rotational contribution, involving 3 degrees of freedom, may be calculated according to the classical approximation as:

$$q^{\text{rota}} = \pi^{1/2} \left(\frac{8\pi^2 I kT}{h^2} \right)^{3/2} \quad (10.28)$$

where I represents the momentum of inertia of the NP with respect to its center of mass in the case of an spherical particle.

Finally, the translational contribution due to the 3 remaining degrees of freedom may be calculated from:

$$q^{\text{trasla}} = V \left(\frac{2\pi M k T}{h^2} \right)^{3/2} \quad (10.29)$$

where M is the reduced mass of the NP. Since the connection between statistical mechanics and the free energy in the canonical ensemble is: $F(i) = -kT \ln Q(i, V, T)$, the total free energy, as given by (10.26b), may be obtained from:

$$F(i) = U^{\text{static}}(i) - kT \ln \left[\prod_{j=1}^{3i-6} \frac{kT}{\hbar \omega_j} \right] - kT \ln \left[\pi^{1/2} \left(\frac{8\pi^2 I k T}{h^2} \right)^{3/2} \right] - kT \ln \left[V \left(\frac{2\pi M k T}{h^2} \right)^{3/2} \right] \quad (10.30)$$

Similar arguments may be used to calculate the chemical potential of a neutral atom of mass m in the gas saturated phase:

$$\mu_s = U^{\text{static}} - kT \ln \left[V \left(\frac{2\pi m k T}{h^2} \right)^{3/2} \right] \quad (10.31)$$

The quantity $F(i)$ in (10.30) minus i times (10.31), defines an excess of free energy, which takes into account the stabilization/destabilization of i atoms in the gas phase upon formation of the NP, see (10.24). Estimation of the most important contribution to $F(i)$ indicates that it is of the order of $\sim i^{2/3}$, thus supporting the application of (10.15). However, (10.30) and (10.31) deliver extra terms which are also important in the case of small NPs.

10.2.7 Electrochemical Nucleation

The theoretical methodology by which this phenomenon has been theoretically analyzed was developed initially by Gibbs [1, 2] in 1878. For an infinite planar interface in equilibrium, the results obtained by Gibbs' model are identical to those obtained using a model that consists of an interfacial region of finite width. This is a good reason to assume that the formulation is essentially correct [84]. Going beyond the traditional experiments with planar interfaces [85, 86], Fonticelli et al. [60] have shown the possibility of modifying the deposition potential in NPs by a suitable redox couple. Figure 10.4 summarizes both approaches.

If an electron transfer occurs at the metal/solution interface between species that may or may not be in both phases, we are dealing with an electrochemical system and the prediction of their equilibrium properties is a matter of electrochemical thermodynamics.

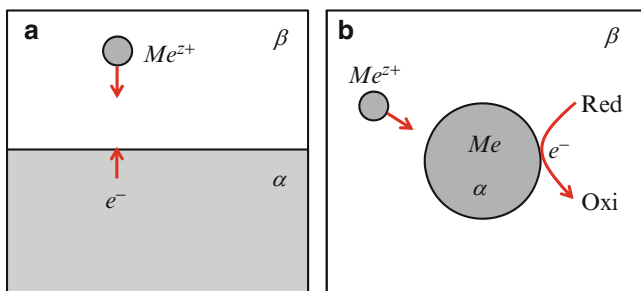


Fig. 10.4 Schematic representation of an electrochemical system for metal deposition on (a) a bulk electrode and (b) a nanoparticle in solution. In both cases β is the solution phase and α is the metal phase

The thermodynamic treatment of an electrochemical interface involving an NP—like the one shown in Fig. 10.4b—may be tackled in a very similar way to that of the infinitely flat phase shown in Fig. 10.4a. If the NP radius is large enough, the interface may be considered to be a planar one, and its energy will differ from the bulk phase by a term of the type γA , where γ is the surface tension and A the area. To introduce the influence of the cell electrode potential, the usual strategy is the introduction of the charge transfer equilibrium explicitly and the replacement of the electrochemical potential of one of the species in solution by the electrostatic potential of the electrode. The reader may consult the book by Bockris et al. [84] for a more detailed discussion.

In the following approach, we want to develop a valid formulation even for the case of small NPs, where the concept of surface energy becomes ambiguous due to the absence of properly defined bulk and surface regions. For this reason, we will avoid any reference to this quantity and its influence should come out in the limit of large NPs.

Metal deposition on an NP in solution, see Fig. 10.4b, is usually accomplished by adding a reducing agent R^u that oxidizes itself to yield O^{u+n} species, to a solution containing the metal ions to be deposited, according to the following half-reaction:



where u represents the charge of the reduced species and n denotes the number of electrons transferred in the half-reaction. This reaction allows further formation of nuclei and their subsequent growth via a redox mechanism. When clusters of a single metal Me are generated, we have to consider:



where z denotes the charge of the ion being reduced and p is the number of atoms constituting the NP. Some other chemicals (i.e., ligands) may occur in the

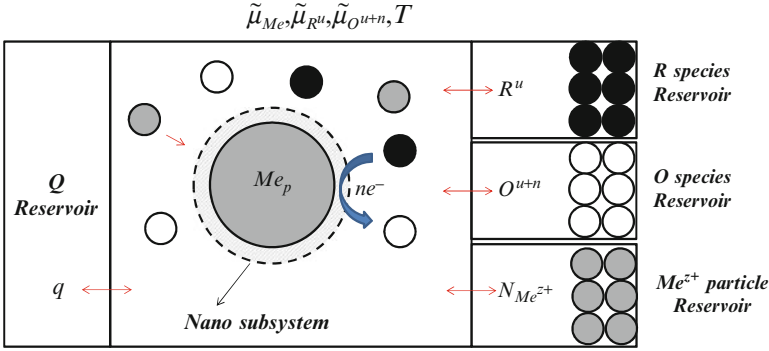


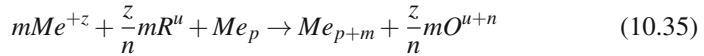
Fig. 10.5 Thermodynamic view of an electrochemical system made of a nanoparticle, a redox couple, and metal ions, which is connected with heat, Me^{z+} , R^u , and O^{u+n} reservoirs. The system is composed of two subsystems: the so-called “nano” part, which contains the nanoparticle, and the solution, called “macro” part. Both subsystems are in thermal, mechanical, and electrochemical equilibrium

stoichiometry of half-reaction (10.33), but we will ignore them at this point for the sake of simplicity. We will incorporate the ligands in Sect. 10.4.

When *seed growth* takes place on the same preexisting NP, we will rewrite (10.33) as:



Adding half-reactions (10.32) and (10.34), we get:



This reaction describes the formation of an NP made of $p + m$ atoms through a chemical redox reaction. In order to consider the relative stability of different structures, we need to define a suitable thermodynamic function for this system. Since the usual electrochemical conditions are constant pressure and temperature, the proper quantity is the Gibbs free energy. Furthermore, we assume that NP formation takes places in an environment where the electrochemical potentials of the reducing species $\tilde{\mu}_R$, the oxidized species $\tilde{\mu}_O$, and the metal ions being reduced $\tilde{\mu}_{Me^{z+}}$ are fixed. For the sake of simplicity, we use the nomenclature $\tilde{G} = \tilde{G}(\tilde{\mu}, P, T)$. We now recall the discussion made in Sect. 10.2.3 to note that the metallic NP are incompressible, so $\tilde{G}(\tilde{\mu}, P, T) \rightarrow \tilde{G}(\tilde{\mu}, T)$.

We consider the system to be made of two parts. One, denoted as “nano” part, corresponds to the NP, and the other, denominated as “macro” part, corresponds to the rest of the system, containing the solution with the Me^{z+} , R^u and O^{u+n} participating in the reaction. Figure 10.5 shows a schematic picture of the system.

The free energy change associated with reaction (10.35) can be written as [59]:

$$\Delta\tilde{G} = \Delta G_{\text{nano}} + \Delta N_O \tilde{\mu}_O - \Delta N_R \tilde{\mu}_R - \Delta N_{Me^{z+}} \tilde{\mu}_{Me^{z+}} \quad (10.36)$$

where ΔN_O , ΔN_R , and $\Delta N_{Me^{z+}}$ are the changes in the number of O^{u+n} , R^u , and Me^{z+} species. Then, according to (10.36) and taking into account the stoichiometry:

$$\Delta \tilde{G} = \Delta G_{\text{nano}} + \frac{z}{n} m \tilde{\mu}_O - \frac{z}{n} m \tilde{\mu}_R - m \tilde{\mu}_{Me^{z+}} \quad (10.37)$$

The electrochemical potentials for type A species (which $A = O^{u+n}$, R^u , and Me^{z+}) can be written as:

$$\tilde{\mu}_A = \mu_A - z_A \phi \quad (10.38)$$

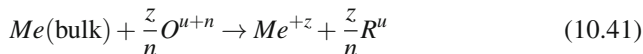
where μ_A is the chemical potential of A species and ϕ is the electrostatic potential. The value of the electrochemical potentials $\tilde{\mu}_A$ is constant in all the system (thermodynamic equilibrium). If we chose a point in the bulk of the solution, μ_A will take the bulk value μ_A^{bulk} and ϕ will be equal to the average electrostatic potential in the solution ϕ^{bulk} . Thus, taking into account (10.37) and (10.38), we have:

$$\Delta \tilde{G} = \Delta G_{\text{nano}} + \frac{z}{n} m \mu_O^{\text{bulk}} - \frac{z}{n} m \mu_R^{\text{bulk}} - m \mu_{Me^{z+}}^{\text{bulk}} \quad (10.39)$$

Adding and subtracting $m \mu_{Me(\text{bulk})}$, where $\mu_{Me(\text{bulk})}$ is a chemical potential of the bulk metal, we get:

$$\Delta \tilde{G} = \Delta G_{\text{nano}} + \frac{z}{n} m \mu_O^{\text{bulk}} - \frac{z}{n} m \mu_R^{\text{bulk}} - m \mu_{Me^{z+}}^{\text{bulk}} + m \mu_{Me(\text{bulk})} - m \mu_{Me(\text{bulk})} \quad (10.40)$$

To identify the different contributions in the last equation, we consider the formation of Me^{+z} ions from the bulk metal phase, according to the following redox reaction:



The thermodynamic potential difference for this reaction can be obtained using standard thermodynamics [87], and it is related to the electrical potential difference of the electrochemical cell:

$$-zF\Delta E = \frac{z}{n} \mu_R^{\text{bulk}} + \mu_{Me^{z+}}^{\text{bulk}} - \frac{z}{n} \mu_O^{\text{bulk}} - \mu_{Me(\text{bulk})} = -zF\eta \quad (10.42)$$

Since this potential difference defines an overpotential η with respect to the bulk deposition of the metal Me at the metal activity $a_{Me^{z+}}$, we will replace ΔE by η in the subsequent equations. With this provision, and substituting (10.42) into (10.40), we get:

$$\Delta \tilde{G} = (G_{Me_{m+p}} - G_{Me_p}) - m \mu_{Me(\text{bulk})} + mzF\eta \quad (10.43)$$

where we have replaced $\Delta G_{\text{nano}} = (G_{Me_{m+p}} - G_{Me_p})$, which corresponds to the free energy change resulting from the addition of m atoms to the p -atoms NP. The term:

$$\Phi(m, p) = (G_{Me_{m+p}} - G_{Me_p}) - m \mu_{Me(\text{bulk})} \quad (10.44)$$

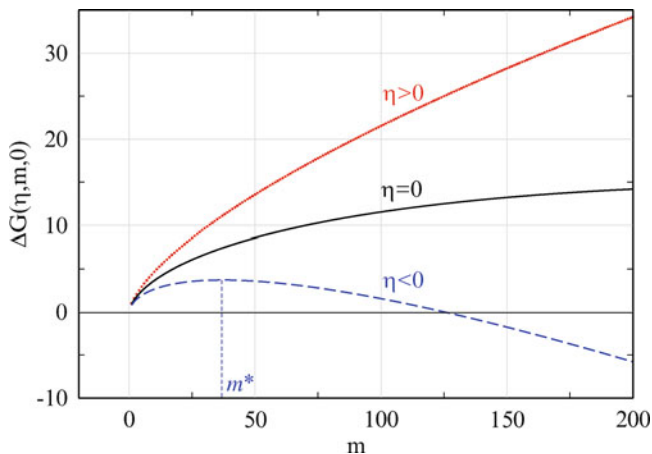


Fig. 10.6 Qualitative scheme of the excess of Gibbs energy, $\Delta\tilde{G}(\eta, m, 0)$, as a function of the number of atoms of the conglomerate m without initial seed ($p = 0$). Note the monotonically growing behavior for $\eta \geq 0$ and the occurrence of a maximum for $\eta < 0$

clearly defines an excess of free energy with respect to the bulk metal Me , so we finally end up with:

$$\Delta\tilde{G}(\eta, m, p) = \Phi(m, p) + mzF\eta \quad (10.45)$$

This is an equation formally identical to that employed to analyze nucleation and growth phenomena [85,86], where usually η is a negative quantity currently written as $\Delta G = \Phi(m) - mzF|\eta|$. However, we will use it in the form (10.45), since it also makes sense for $\eta > 0$, and it will be found to be applicable to NP seed growth too.

We will discuss now qualitatively the behavior of $\Delta\tilde{G}(\eta, m, p)$ for $p = 0$, that is, the generation of a NP without the existence of any previous seed. According to Sect. 10.2, the first term of the right side of (10.45) is proportional to $m^{2/3}$ and the second one (electrochemical term) is proportional to m . Thus, the electrochemical factor has a larger power dependence on m than the surface term and the former will predominate in the limit $m \rightarrow \infty$. Thus, the behavior of $\Delta\tilde{G}(\eta, m, 0)$ will be of two different types, depending on whether $\eta \geq 0$ or $\eta < 0$. This situation is shown in Fig. 10.6.

In the first case, $\eta \geq 0$, the electrochemical factor will add the monotonic growing function $mzF\eta$ to the surface energy term $\Phi(m, 0)$, so that $\partial\Delta\tilde{G}(\eta, m, p)/\partial m|_{\eta \geq 0} > 0$ for all m . This behavior is the natural consequence of the increasing area of the growing NP.

In the second case, where $\eta < 0$, the electrochemical contribution will add a monotonic decreasing term to the monotonic increasing surface term, so that a maximum will come up at $m = m^*$, corresponding to the critical cluster size discussed in the introduction and used in (10.19). This situation is illustrated qualitatively in the broken line of Fig. 10.6, and corresponds to systems where the

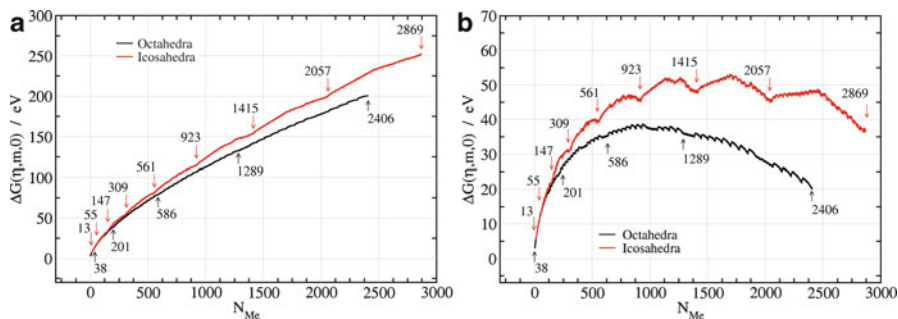


Fig. 10.7 Energy excess, $\Delta\tilde{U}(\eta, m, 0)$, as a function of the number of atoms m in a metal NP for octahedra (black lines) and icosahedra (red lines) (a) $\eta = 0$ and (b) $z\eta = -75$ mV. Some selected numbers of atoms were marked with arrows in the figure

thermodynamic stable state is the bulk material. The application of a more negative over-potential shifts m^* to lower values, but the maximum still persists.

Figure 10.7 shows the energetic contribution $\Delta\tilde{U}(\eta, m, 0)$ to $\Delta\tilde{G}(\eta, m, 0)$ for the growth of a Au-NP with two different crystalline structures. It can be observed that the overall behavior is that described in Fig. 10.6. However, the presence of a crystalline structure generates growth on different facets, evident in the saw tooth behavior of the curve, something that is characteristic of this type of systems [63, 64]. The layer-by-layer growth characteristic for these metastable systems [61, 88] may be understood in terms of the presence of local minima, separated by barriers of the order of the eV.

The beginning of crystal growth (nucleation) takes place under supersaturation conditions. That is, the electrochemical potential of the metal ions must be larger than that corresponding to the bulk phase ($\eta < 0$). This difference determines electrochemical supersaturation.

Undersaturation and supersaturation conditions in electrochemical systems at equilibrium for a bulk system and for a NP are illustrated in Fig. 10.8. In the case of bulk materials, the set of equilibrium points is defined by Nernst equation, shown in Fig. 10.8 by a continuous line:

$$E_{\text{eq}} = E_{\text{Me}/\text{Me}^{z+}}^0 + \frac{RT}{zF} \ln \left(\frac{a_{\text{Me}^{z+}}}{a_{\text{Me}}} \right) \quad (10.46)$$

where $E_{\text{Me}/\text{Me}^{z+}}^0$ is the standard potential, $a_{\text{Me}^{z+}}$ is the ion activity, and a_{Me} is the activity of the bulk metal atoms, usually assumed as equal to 1 for convenience.

The region located below the equilibrium curve corresponds to supersaturation conditions $E - E_{\text{eq}} = \eta < 0$, i.e., potential/activity pairs where metal ions would get deposited.

The opposite case, points located above the equilibrium line, corresponds to electrochemical undersaturation $\eta > 0$. In this region, electrochemical dissolution of the metal deposit should occur. When $\eta = 0$, both phases are in thermodynamic

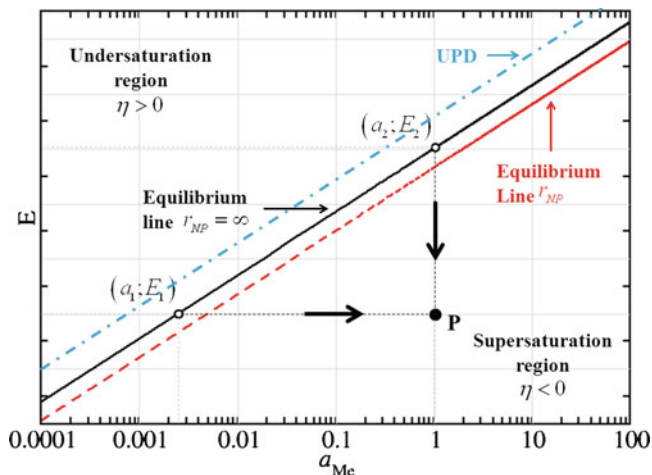


Fig. 10.8 Qualitative scheme of the variation of the deposition potential as a function of the ion activity. The *continuous black curve* shows the infinitely flat surface at equilibrium conditions, the *broken red curve* shows the “equilibrium” line for a given size of NP, and the *dotted-line blue curve* shows a line corresponding to underpotential deposition conditions

equilibrium and the solid curve in Fig. 10.8 indicates stability limits for very large metal crystals.

As stated above, usually a_{Me} is a constant equal to 1 for pure and bulk condensed metal phases. However, in the case of a NP, the “equilibrium” potential for a given $a_{Me^{z+}}$ should occur at points below that corresponding to the bulk metal (dotted line in Fig. 10.8), yielding formal values of $a_{Me} > 1$. We wrote “equilibrium” because the states represented in the dotted line are actually unstable points of the free energy of the system. For a given NP size, a potential can be found where this NP is the critical one. A small (finite) change in the number of particles would turn it unstable, leading alternatively to its dissolution or to its growth toward the bulk state. On the other hand, stable states may be obtained in the case of cavity decoration [89], as long as the interaction of the metal being deposited is stronger with the substrate than with itself. For a detailed discussion on the stability of electrochemical nanostructures, the reader should consult the reference [89].

As in the case of the bulk material, the driving force for NP formation is the overpotential η , which is related to the electrode potential via (10.42). Figure 10.8 shows two different ways to force nucleation and growth in electrochemical systems. On one hand, by decreasing the deposition potential (generating overpotential) at a constant metal activity, corresponding to the motion along a vertical line, say from point (2) to P . On the other hand, by increasing the activity of the ion being deposited, corresponding to the motion along the horizontal line, say from point (1) to P . Both possibilities are valid and show the potentiality of electrochemistry for inducing nucleation and growth processes. The first mechanism is the one usually employed to generate nanostructures via potentiostatic or galvanostatic control

[85, 86]. The second one has been used to induce localized electrodeposition of a metal. In this method, a metal from the electrolyte solution is deposited onto the uncovered part of a STM tip, and a potential pulse is applied to it, producing local supersaturation that leads to a nucleation and growth process [90–97]. This method appears particularly appealing as compared to other top-down nanostructuring methods, since mechanical contact is not established between the tip and the surface and in principle any mechanical damage should be prevented.

10.3 Size Control Based on Kinetic Effects

In the discussions of the previous section, it was shown that most of the methods employed in the formation of NPs require a supersaturation to proceed. Different alternatives exist to control the size of NPs in this regime. Since the system is not in equilibrium, we will denote these methods as kinetic-based ones.

10.3.1 Burst Nucleation

Research on the preparation of monodisperse NPs dates back to the 1950s. LaMer and his colleagues proposed the concept of “burst nucleation” [62]. In this process, many nuclei are generated at the same time, and then these nuclei start to grow. Because all of the particles nucleate almost simultaneously, their growth histories are nearly the same. This is the essence of the “burst nucleation” process which makes it possible to control the size distribution of the ensemble of particles as a whole during growth. “Burst nucleation” has been adopted as an important concept in the synthesis of monodisperse NPs. As a synthetic strategy, this method is often referred to as “the separation of nucleation and growth.” In this homogeneous nucleation process, there exists a high free energy barrier, mainly due to the appearance of a new interface between the new (growing) phase and the original one (precursor).

How does burst nucleation work? Let us make the following *gedanken experiment*, where we will take some snapshots of our system. At a given moment, the precursor agent is injected. Let us further assume that diffusion is infinitely fast, so that matter is uniformly dispersed all over the volume of the system, and that its temperature remains unchanged. As matter is added to the system, the saturation coefficient s goes from a small value to a value close to the unity. A typical point in this region would be for example point P_1 in Fig. 10.9b. The work of nucleation should be similar to that described in curve P_1 in Fig. 10.9a. If we were able to take an infinitely large snapshot of the system to observe many NPs, we would find that their size distribution would be given by (10.25b). When $s = 1$, the equilibrium concentration has been reached. Upon further addition of matter, the saturation coefficient grows above unity, locating the system in the supersaturation

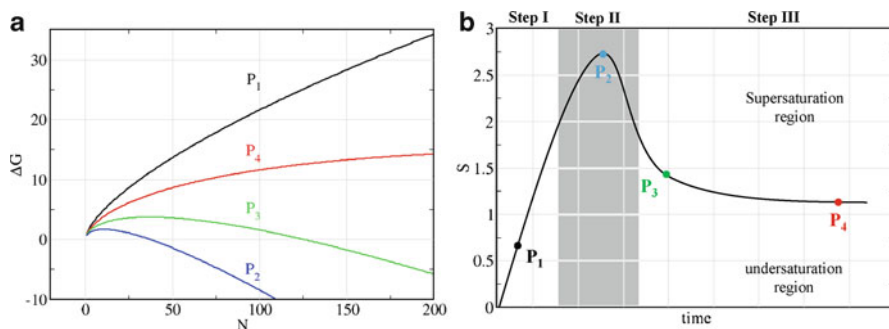


Fig. 10.9 (a) Typical free energy profile for the growth of a NP according to the classical nucleation model. (b) LaMer plot, change of saturation as a function of time

region. Supersaturation increases continuously until the injection of matter stops. This point corresponds to step II, called “the nucleation stage.” At this moment, the amount of metallic precursor is maximal, so that the metal activity and s take their largest value. This corresponds to the point marked as P_2 in Fig. 10.9b. The work of nucleation under these conditions will look like the curve P_2 in Fig. 10.9a. At this time, the critical nucleus N^* reaches its lowest value. As the system is in supersaturation conditions, very frequently growth nuclei are formed, many of them being unstable, but occasionally large fluctuations are produced such that these fluctuations overcome N^* . These NPs are stable and begin their growth toward the bulk state. At the same time as these nuclei grow, other new nuclei are formed, and the precursor concentration decreases drastically. The situation at this intermediate time is for example that of point P_3 in Fig. 10.9b, and its work of nucleation is described by curve P_3 in Fig. 10.9a. In LaMer’s curves this corresponds to the third stage of the process, and the latter is generally called the “growth stage.” When the precursor concentration decreases, s decreases and N^* displaces toward larger values. At this stage the probability of nucleation is relatively low. This prevents the formation of new nuclei and favors the growth of those already existing. Growth continues and s decreases asymptotically. At that moment, the critical nucleus has reached a very large value, a typical point for this situation has been marked as P_4 in Fig. 10.9a, b. At this stage, the nucleation process is practically suppressed and only the growth of nucleus previously formed is observed.

The experiment described above is the essence of the separation between the nucleation and growth processes. As the transition time between stages I and II becomes faster, the monodispersity of the NPs formed increases.

Modification of the initial conditions such as temperature (see (10.20) of second nucleation theorem) and/or injection rate of precursor [98] may improve or worsen the monodispersity of the NPs formed.

Two different techniques that apply the concept of homogeneous nucleation to synthesize monodisperse NPs in organic solutions are available: “hot-injection” [99–102] and “heating-up” methods [103]. The first produces a high degree of

supersaturation by the rapid injection of excess precursor into a hot surfactant solution, resulting in burst nucleation by relieving the excess free energy due to supersaturation. Note that according to (10.19) and (10.20), temperature and supersaturation conditions modified nucleation rate. The heating-up method is a batch process in which the precursors, reagents, and solvent are mixed at a low temperature and heated up to a certain temperature to initiate the crystallization reaction. Because of its simplicity, this method is particularly favorable for large-scale production.

The LaMer picture discussed so far has some limitations concerning the prediction of NP sizes, since it is assumed that the surface tension γ is a constant. However, this value is strongly size dependent for nanometer-sized NPs. As NP size decreases, the ratio of surface atoms to bulk atoms dramatically increases. As a result, there is a strong driving force, especially for NPs with a size of a few nanometers, leading to the minimization of the surface free energy by reconstructing the surface structure or by changing the crystal structure (e.g., through phase transitions or lattice contraction). This driving force also plays an important role in the formation of “magic number” metal clusters, which are composed of some particular numbers of metal atoms [104]. The occurrence of this “configurational magic numbers” is attributed to the extra stability of closed-shell structures.

10.3.2 *Focusing and Defocusing Effects*

The first theoretical studies on the narrowing of size distribution during the cluster growth process were performed by Reiss in the 1950s [105]. In this model, known as the “growth by diffusion” model, the growth rate of spherical NPs depends solely on the flux of the monomers supplied to the particles (J). In this case, the relationship between the monomer flux and the growth rate is given by:

$$J = \frac{4\pi r^2}{V_m} \frac{dr}{dt} \quad (10.47)$$

where V_m is the molar volume of the bulk crystal. If the average distance between the NPs is large enough, then the diffusion layer formed at the periphery of each of them is undisturbed. Consequently, it is possible to treat each growing NP independently. For each spherical NP in a homogeneous medium, there is a concentration gradient around it with spherical symmetry. Fick’s law gives the flux J of monomers, diffusing through the surface of a sphere enclosing the NP:

$$J = 4\pi x^2 D \frac{da_{Me}}{dx} \quad (10.48)$$

where D is the diffusion coefficient, a_{Me} is the activity Me , and $x_{(\geq r)}$ is the distance from the center of the NP. If J is assumed to be a constant, using (10.47) and (10.48), we obtain:

$$\frac{dr}{dt} = \frac{V_m D}{r} (a_{Me(\text{bulk})} - a_{Me(\text{surf})}) \quad (10.49)$$

where $a_{Me(\text{bulk})}$ and $a_{Me(\text{surf})}$ are the metal activity of the bulk solution and the activity at the surface of the NP. In this simple model, the growth rate of a particle is inversely proportional to its radius. The time variation of the radius distribution σ^2 can be written as:

$$\frac{d(\sigma^2)}{dt} = 2V_m D (a_{Me(\text{bulk})} - a_{Me(\text{surf})}) \left[1 - \bar{r} \left(\frac{1}{\bar{r}} \right) \right] \quad (10.50)$$

where \bar{r} and $1/\bar{r}$ are the mean values of r and $1/r$, respectively. It can be shown that for an ensemble of spherical NPs, the variation of the radius distribution σ^2 decreases during growth. Thus, for $a_{Me(\text{bulk})} > a_{Me(\text{surf})}$, the right-hand side of (10.50) is always negative. In other words, the variance of the size distribution of an ensemble of NPs always decreases regardless of the initial size distribution, as long as all of the NPs are growing and no additional nucleation occurs. This is a self-regulating mechanism of the size distribution during the growth process and is often referred to as the “focusing” effect. However, the previous model [106] is an oversimplification because it does not consider the reaction kinetics of crystal growth and its dependence on NP size.

In order to introduce the kinetics of NP growth, it is necessary to take into account the change in chemical potential $\mu_{Me}(r)$ that a spherical crystal with radius r undergoes with respect to the bulk crystal $\mu_{Me(\text{bulk})}$. This may be expressed by the following equation:

$$\Delta\mu = \mu_{Me}(r) - \mu_{Me(\text{bulk})} = \gamma \frac{\partial A}{\partial N_{Me}} \quad (10.51)$$

where A is the surface area. Assuming a spherical geometry for the NP leads to:

$$\Delta\mu = \frac{2\gamma V_m}{r} \quad (10.52)$$

which is known as Gibbs–Thomson relation. The activated complex theory (ACT) can be adopted to assess the effect of the chemical potential change of a crystal on the precipitation and dissolution reactions. According to ACT, the variation of the precipitation k_p and the dissolution k_d constant with $\Delta\mu$ is given by:

$$k_p = k_p^0 \exp[-\alpha \Delta\mu / kT] = k_p^0 \exp \left[-\alpha \frac{2\gamma V_m}{rkT} \right] \quad (10.53a)$$

$$k_d = k_d^0 \exp[(1 - \alpha) \Delta\mu / kT] = k_d^0 \exp \left[(1 - \alpha) \frac{2\gamma V_m}{rkT} \right] \quad (10.53b)$$

In these equations, α is the transfer coefficient and k^0 is the rate constant for the bulk crystal ($r \rightarrow \infty$) [107]. Qualitatively, (10.53a) and (10.53b) reveal that small NPs will tend to dissolve rather than to grow, as compared with larger ones, due to their higher chemical potential. This effect contradicts the “focusing” mechanism, leading to a larger size dispersion in the NP ensemble. To combine this effect with Reiss’ model, the assumption that $a_{Me(\text{bulk})}$ is constant for all NPs should be modified. The atomic fluxes toward/from the surface of a NP due to precipitation/dissolution (J_p and J_d , respectively) are given by:

$$J_p = 4\pi r^2 k_p^0 a_{Me(\text{bulk})} \exp\left[-\alpha \frac{2\gamma V_m}{rkT}\right] \quad (10.54a)$$

$$J_d = 4\pi r^2 k_d^0 \exp\left[(1 - \alpha) \frac{2\gamma V_m}{rkT}\right] \quad (10.54b)$$

The net flux J corresponding to the sum of J_p and J_d can be rewritten in a dimensionless form [107]:

$$\frac{dr'}{d\tau'} = \frac{s - \exp[1/r']}{r' + K \exp[\alpha/r']} \quad (10.55)$$

where r' and τ' are related to r and t by constant factors, and K is also a system-dependent positive constant [107]. Since $s > 1$ in the supersaturation region, (10.55) shows that $dr'/d\tau'$ has always a positive value. This is clearly a “defocusing” effect, showing that monodispersity cannot be improved by this way. The value of the $dr'/d\tau' = 0$, where precipitation and dissolution velocity are equal is r^* , which is related to N^* .

According to Park et al. [107], for an ensemble of particles, it is very difficult to trace the time evolution of the size distribution, mainly because $a_{Me(\text{bulk})}$ is not a constant but rather a function of the size of all the particles in the ensemble. Furthermore, the growth rates also depend on $a_{Me(\text{bulk})}$. This mutual dependence makes it very difficult, if not impossible, to derive the time evolution of the particle size distribution analytically. Simulations may be helpful to understand this phenomenon [108, 109].

10.3.3 Critical Cluster Size in Electrochemical Nucleation and Growth

As mentioned above, in many of the experimental situations, critical nuclei contain less than seven atoms in the case of the gas–liquid phase transition [19]. In the particular case of metal NPs, and assuming that the critical cluster is only produced by particle collision, it is not probable that this is made of more than three particles. The energy values reported by Lee [110] show that the deposition potential that should be applied to make the three-atoms clusters the critical one, is extremely

large. This value, of the order of -3 eV for Au, is far too large as compared with any known value of a redox couple able to reduce the metal ions. However, experiments show that reactions take place and NPs are formed! What is missing in the theoretical considerations?

There are actually no fundamental flaws in the theory, but rather omissions and oversimplifications. Critical clusters are generally made of a few particles. In this scale size they may be charged or not, may present several oxidation states, may be complexed with water, with protecting molecules, etc. Thus, the experimental reality is much more complex than we have simulated or modeled. For example, Wang et al. [111] found that the reduction of HAuCl_4 occurs before the formation of the Au^0 cluster, involving Au(I) intermediate species, but this behavior cannot be extrapolated to other systems. Henglein et al. [112–114] have proposed the formation of $\text{Pd}^{\text{II}}(\text{NH}_3)_4\text{Cl}_2$ and $\text{Pt}^{\text{II}}\text{Cl}_2(\text{H}_2\text{O})_2$ intermediates for the formation of Pd and Pt NPs, respectively. The presence of ammonia, water molecules, and chloride ions may bond Pd or Pt ions, stabilizing them and producing a decrease in the free energy of reaction for the formation of the critical nucleus. The effect produced by ligands is even more controversial. While the increase in ligand concentration produces smaller NPs in the case of Au or Ag [115], the opposite effect is observed in the case of CoPt NPs [116]. As we see, the effect of the synthesis medium plays a decisive role in the determination of the critical cluster size.

10.4 Size Control Based on Thermodynamic Effects

From the preceding section, we note that the free energy cost for NP growth must be compensated by supersaturation and/or the application of an overpotential. Thus, it is not possible, on thermodynamic grounds, to control the size of NPs since it is necessary to bring the system out of equilibrium to produce the nucleation process. However, we will see that when a second metal component is introduced in the system, the situation may be different, in the sense that the status of the NP may be controlled thermodynamically. In this section we discuss two models that may help to visualize these ideas.

10.4.1 Bimetallic Nanoparticles

In the present section we make considerations similar to those elaborated in Sect. 10.2.7. Figure 10.10 shows a scheme of the model; note the similarities and differences with Fig. 10.5. We will not consider here ligand effects; these will be introduced in the next section. The conclusions of the present discussion will be valid when the interaction of ligands with the metal is not too important or when it remains about the same all along the reaction. The same approach could be used

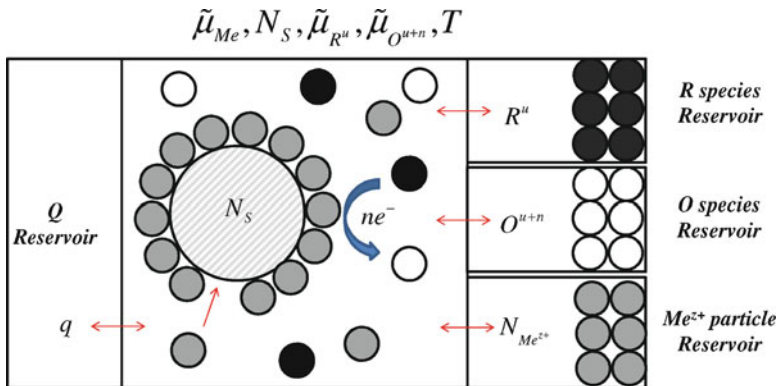


Fig. 10.10 Schematic representation of the model employed to study metal deposition to yield a bimetallic nanoparticle

to study the formation of alloyed NPs, within a double grand canonical system [117]. We assume that these bimetallic clusters are made of two components, Me and S , arranged in such a way that the system is made of small core(S)/shell(Me) aggregates where the core atoms are not ionic species. This model corresponds to an experimental design where a metal core is modified by another material; this core is built in a previous synthesis routine. The reader can find experiments using this approach in reference [60].

For the present purpose, we consider a small incompressible bimetallic NP immersed in a liquid solution containing ions of the species being deposited (Me).

We begin by considering the completely open partition function in the component Me of a single NP $\Upsilon(\mu_{Me}, N_S, T)$. This is related to the corresponding canonical partition function $Q(N_{Me}, N_S, T)$ through:

$$\Upsilon(\mu_{Me}, N_S, T) = \sum_{N_{Me}=0}^{\infty} Q(N_{Me}, N_S, T) \exp\left[\frac{N_{Me}\mu_{Me}}{kT}\right] \quad (10.56)$$

where N_{Me} is the number of Me atoms deposited on a core made of N_S atoms of metal S . In principle, the sum runs over all positive integers but we will find that it can be drastically reduced on physical grounds, as proposed in the HC model, see discussion on Sect. 10.2.3.

In order to write (10.56) in a more suitable form, we will consider that the Helmholtz free energy of the bulk metal Me , say $F_{Me(\text{bulk})}(N_{Me}, T)$, can be written in terms of its partition function $Q_{Me(\text{bulk})}(N_{Me}, T)$ according to:

$$F_{Me(\text{bulk})}(N_{Me}, T) = -kT \ln Q_{Me(\text{bulk})}(N_{Me}, T) \quad (10.57)$$

In the case of a bulk piece of Me made of N_{Me} atoms, the chemical potential of Me , say $\mu_{Me(\text{bulk})}$, is given by:

$$\mu_{Me(\text{bulk})} = \frac{F_{Me(\text{bulk})}(N_{Me}, T)}{N_{Me}} \quad (10.58)$$

Then, the free energy of a piece of bulk metal Me made of N_{Me} atoms will be given by:

$$F_{Me(\text{bulk})}(N_{Me}, T) = N_{Me}\mu_{Me(\text{bulk})} \quad (10.59)$$

With this in sight, we can rewrite (10.56) as:

$$\begin{aligned} \Upsilon(\mu_{Me}, N_S, T) &= \frac{Q_{Me(\text{bulk})}(N_{Me}, T)}{Q_{Me(\text{bulk})}(N_{Me}, T)} \Upsilon(\mu_{Me}, N_S, T) \\ &= \sum_{N_{Me}=0}^{\infty} \exp\left\{-\left[F(N_{Me}, N_S, T) - F_{Me(\text{bulk})}(N_{Me}, T) \right. \right. \\ &\quad \left. \left. - N_{Me}\mu_{Me} + N_{Me}\mu_{Me(\text{bulk})}\right]/kT\right\} \end{aligned} \quad (10.60)$$

That can be rearranged to yield:

$$\Upsilon(\mu_{Me}, N_S, T) = \sum_{N_{Me}=0}^{\infty} \exp\left\{\left[F(N_{Me}, N_S, T) - F_{Me(\text{bulk})}(N_{Me}, T) - N_{Me}\Delta\mu_{Me}\right]/kT\right\} \quad (10.61)$$

where we have defined the quantities: $\Delta\mu_{Me} = \mu_{Me} - \mu_{Me(\text{bulk})}$ and $F(N_{Me}, N_S, T) = -kT \ln Q(N_{Me}, N_S, T)$. Thus, $\Delta\mu_{Me}$ represents an excess of chemical potential with respect to the chemical potential of the bulk Me material.

On the other hand, we can multiply and divide by the canonical partition function of the core (made only of metal S):

$$\begin{aligned} \Upsilon(\mu_{Me}, N_S, T) &\frac{Q(N_S, T)}{Q(N_S, T)} \\ &= \exp[F(N_S, T)/kT] \sum_{N_{Me}=0}^{\infty} \exp\left\{-\left[\Delta F(N_{Me}, N_S, T) + N_{Me}\Delta\mu_{Me}\right]/kT\right\} \end{aligned} \quad (10.62)$$

where we have defined $\Delta F(N_{Me}, N_S, T) = F(N_{Me}, N_S, T) - F(N_S, T) - F_{Me(\text{bulk})}(N_{Me}, T)$ and $F(N_S, T) = -kT \ln Q(N_S, T)$. Note that $\Delta F(N_{Me}, N_S, T)$ corresponds to the excess of free energy of the Me type atoms in the cluster referred to the bulk metal Me .

In the case of electrochemistry, we can replace $\Delta\mu_{Me}$ by $-zF\eta$. However, it must be kept in mind that in the electrochemical environment, we can under-saturate or super-saturate the solution via concentration or potential changes, see Fig. 10.8. In the electrochemical jargon, $\eta > 0$ corresponds to underpotential deposition (upd) conditions, while $\eta < 0$ correspond to overpotential (opd) deposition. In short, while opd corresponds to the usual case of metal deposition on a surface of the same metal, upd may occur when a metal is deposited on a surface of a different metal, as long as it shows a stronger affinity for this foreign surface than for itself. This phenomenon leads to an apparent violation from Nernst equation, since metal adatoms may subsist on a surface at a potential at which they should dissolve [118]. A hypothetical E vs. $\ln a$ upd line is shown in Fig. 10.8, see dotted-line (blue) curve.

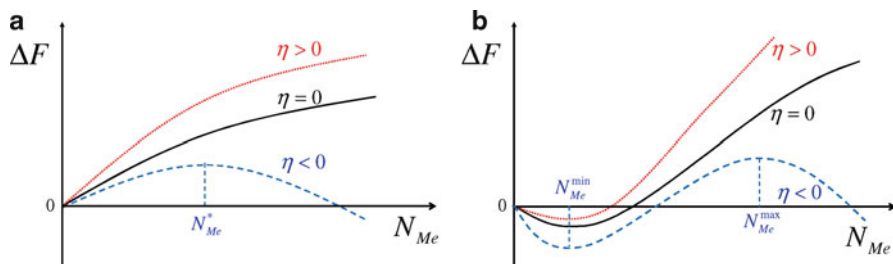


Fig. 10.11 Qualitative scheme of the excess Helmholtz free energy as a function of the number of atoms for the formation of a shell on a core of a different metal. **(a)** When the interaction among shell atoms is stronger than the interaction between shell and core atoms; **(b)** when the interaction among shell atoms is weaker than the interaction between shell and core atoms

It will be shown that the behavior of ΔF may be of two different types at $\eta = 0$, depending on the interactions between system components. The situation is illustrated qualitatively in Fig. 10.11a, b [59, 89].

The curves shown in Fig. 10.11a correspond to the case where the interaction between shell atoms is comparable with (or larger than) the interaction between shell and core atoms. In this case, the behavior of the curve of excess of free energy is monotonically increasing with N_{Me} at zero overpotential. This behavior is similar to that of the energy curves found for the formation of pure metal NPs, as illustrated in Sect. 10.2.7 (Fig. 10.6). The curves shown in Fig. 10.11b correspond to the case where the interaction between shell atoms is weaker than the interaction between shell and core atoms. In this case, ΔF shows a negative slope for a small N_{Me} , with the slope becoming positive beyond a certain N_{Me} value, say N_{Me}^{\min} . This type of systems yields a thermodynamic stable core–shell structure, which may be stable even at positive η s. In fact, according to (10.62), the application of a positive η will add a linear function, shifting N_{Me}^{\min} to lower values, but the minimum may still persist and will be a global one, see Fig. 10.11b. On the other hand, if a negative overpotential is applied to the system, the minimum will still remain, but will define a metastable state, since the global minimum will correspond to the bulk Me deposit ($N_{Me} \rightarrow \infty$).

Taking into account that ΔF presents static, vibrational, rotational, and translational contributions, as discussed for a small particle in Sect. 10.2.6, we can write:

$$\Delta F(N_{Me}, N_S, T) = \Delta U_i^{\text{static}} + \Delta F_i^{\text{vibra}} + \Delta F_i^{\text{rota}} + \Delta F_i^{\text{trasla}} \quad (10.63)$$

where $\Delta U_i^{\text{static}}$ corresponds to the excess of binding energy of the Me adatoms in the NP with respect to the cohesive energy of bulk metal Me . It can be shown that only $\Delta U_i^{\text{static}}$ makes a meaningful contribution to $\Delta F(N_{Me}, N_S, T)$ [119–121], so that a reasonable approximation to (10.62) is:

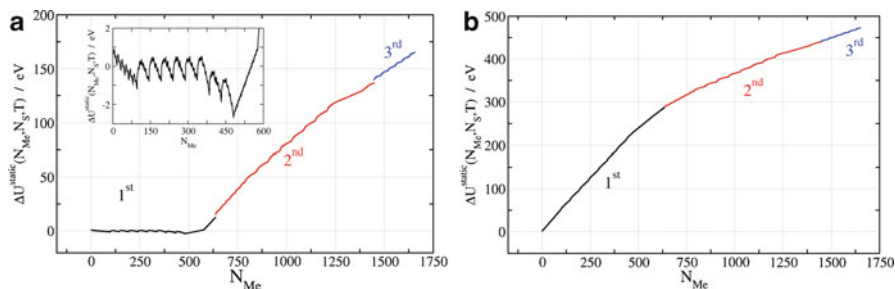


Fig. 10.12 Energy excess as discussed below (10.63) for the deposition of (a) Ag atoms and (b) Pd atoms on a Au NP made of 1,289 atoms with octahedral structure. The *different color lines* denote in both cases the completion of a monolayer

$$\Upsilon(\eta, N_S, T) = A(N_S, T) \sum_{N_{Me}=0}^{\infty} \exp \left\{ - \left[\Delta U^{\text{static}}(N_{Me}, N_S, T) - zFN_{Me}\eta \right] / kT \right\} \quad (10.64)$$

where $A(N_S, T)$ is a function of the structure of the core and the temperature. Figure 10.12 shows the behavior of $\Delta U^{\text{static}}(N_{Me}, N_S, T)$ as a function of the number of metal atoms constituting the shell, N_{Me} , for the deposition of Ag atoms on a Au(1289) truncated octahedral NP and for the deposition of Pd atoms on a Au(1289) NP. We note that the general behavior is similar to Fig. 10.11. However, the discrete atomic nature and the packing of atoms in the NP produce deviations from the simplified behavior shown there. A magnification of Fig. 10.12a (see inset) shows a more complex saw tooth behavior, with 14 maxima, grouped in two families (6+8). These maxima correspond to a 2D nucleation and growth phenomenon located on each of the facets of the truncated octahedron. However, this saw motif should be wiped out by thermal effects at 300 K. While decoration of the NP is expected at different overpotentials for the system Ag/Au(1289) (Fig. 10.12a), no decoration is predicted for the system Pd/Au(1289) in a wide potential range (Fig. 10.12b). This variety of behavior is similar to the occurrence of upd and opd depositions on planar surfaces. So, we can correlate these observations with the strength of the interaction of Me atoms with S on perfect plane infinite surfaces. In the first, Ag/Au, the interaction of Ag adatoms with Au atoms on flat surfaces is stronger than the interaction between Ag atoms in the bulk state. This is an upd system and the consequence of this is the formation of a monolayer of Ag on Au at underpotentials. In the other system, the interactions of Pd with Au is smaller than the bulk Pd cohesive energy and overpotential deposition is expected. Thus, in a first approach we could conclude that decoration of a metal core by a different one may be predicted on the previous knowledge of the similar process for planar surfaces.

To analyze the thermodynamic stability of the system in the underpotential region (undersaturation), it is not necessary to appeal to extra-thermodynamic assumptions, since in these region the partition function mathematically converges to finite values

(see Sect. 10.2.3). We will focus our discussion on the system Ag/Au(OT1289), which is the one presenting a behavior different from that predicted by CNT.

The assumption made in the HC model is analogous to (10.17) in that we can define a modified probability $g(N_{Me})$ by:

$$g(N_{Me}) = \frac{f(N_{Me})}{f(N_{Me}^{\max})} \quad (10.65)$$

with $f(N_{Me})$ given by:

$$\begin{aligned} f(N_{Me}) &= P(N_{Me}, \eta, N_S, T) Y(\eta, N_S, T) \\ &= \exp \left\{ - \left[\Delta U^{\text{static}}(N_{Me}, N_S, T) - zFN_{Me}\eta \right] / kT \right\} \end{aligned} \quad (10.66)$$

and $f(N_{Me}^{\max})$ is the maximum probability found in the region between $N_{Me} = 0$ and the bottleneck, see Fig. 10.11b.

Figure 10.13a depicts contour plots describing the behavior of $g(N_{Me})$ at different under/overpotentials for the prototypical Ag/Au(1289) system (compare similitudes and differences with HC model in Fig. 10.2a). It is possible to force the global minima to occur in the underpotential deposition zone, since $Y(\eta, N_S, T)$ is convergent in this region, see Fig. 10.13b. For this cluster size, decoration may be selected to occur alternatively at [111] plus [100] facets or only at [100] facets, both in the upd range.

As it is the case of the HC model for supersaturation conditions, the partition function diverges in the overpotential deposition region, so that it is necessary to consider its physical convergence, see Fig. 10.13c. From this figure we can see that the overpotential required to cause shell massive growth is between -100 and -220 mV. These overpotential values could be suitably controlled experimentally by using alternatively a potentiostat or a redox couple in solution.

Besides the metal pair involved, metal deposition in the present systems has an interesting new condiment with respect to the bulk material that is provided by NP size. Figure 10.14 shows simulations of the behavior of $g(N_{Me})$ for the case of deposition of Ag atoms at $\eta = 0$ on Au-NP of different sizes used as growth seeds. It must be noted that for small NPs the highest normalized probability density is found at $N_{Me} = 0$. This clearly indicates the nonoccurrence of spontaneous core-shell formation at $\eta = 0$. Something very different is found for large NPs, where two important phenomena are observed comparing the results for Au(1289) and Au(2406) NPs. First, the weight of $g(N_{Me}^{\max})$ in the distribution becomes relatively more important as N_S increases. Second, the coverage of the NP increases with increasing core size, N_S . In fact, at $\eta = 0$ the most probable coverage for Ag on Au(1289) is 75% while for Au(2406) it is 80%. From these results, it can be inferred that in the limit $N_S \rightarrow \infty$ the NP should reach 100% coverage, with a sharply peaked distribution function. The former is a natural consequence of the decrease of the fraction of border atoms for increasing NP size. We can summarize the previous discussion by stating that depending on core size we may have upd or opd on NPs.

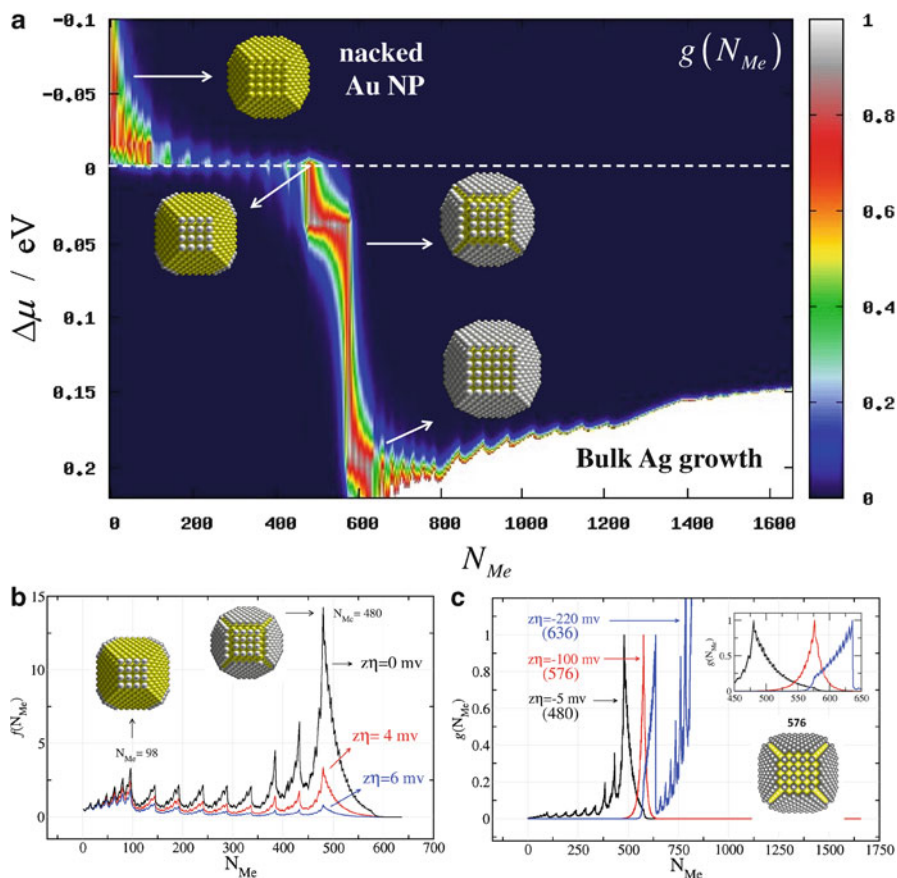


Fig. 10.13 Computer simulations corresponding to Ag deposition on a Au(OT_1289) nanoparticle at different deposition potentials (a) contour plots of the distribution function in (10.65). The white region does not fit into scale, since the partition function is normalized according to (10.65); see discussion below. Cross sections along constant η are shown for (b) underpotential conditions with $\eta = 0, 4$, and 6 mV distribution function defined in (10.66) and (c) overpotential deposition, distribution function defined in (10.65). Representative structures are shown in the figure. Similar calculations were performed in [63]

10.4.2 Ligand-Assisted Growth of Metallic Nanoparticles

Gold Nanoparticles (Au-NPs) is by far the most commonly analyzed system in the literature, being the subject of reviews specifically devoted to them [122]. A large number of synthesis methods of Au-NPs are based on the reduction of Au(III) to metallic Au. In this and many other reactions, ligand effects may be important and should be included in the theoretical considerations. The present section is devoted to these effects. The reader is advised to refresh the concepts developed in Sect. 10.3.3.

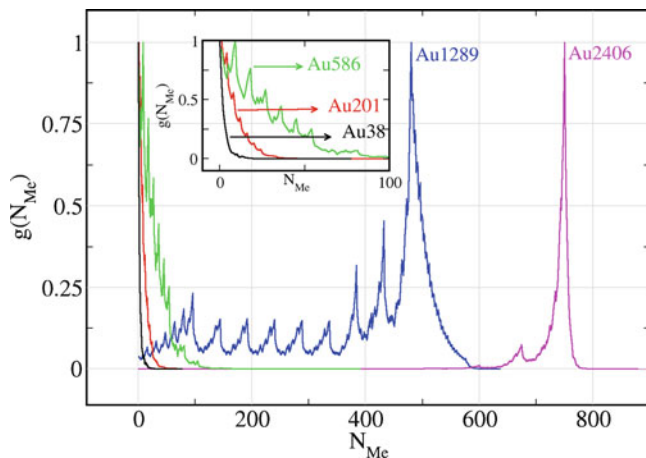


Fig. 10.14 Probability density according to (10.66) of having a certain number of Ag atoms deposited on different Au cores as a function of the number of atoms conforming the shell at zero overpotential. The core sizes are $N_C = 38, 201, 586, 1289, \text{ and } 2,406$

The method developed by Turkevitch et al. [123, 124] in 1951 consisting in the reduction HAuCl_4 by citrate in aqueous solution is probably the most widespread method to synthesize Au-NPs. Two decades later, Frens [125, 126] showed the possibility of Au-NPs size control via modification of the mole ratio of the precursors in the electrolyte solution, in this case citrate/Au. Another method of widespread use is addressed in the literature as the Brust NPs synthesis [127]. Unlike Turkevitch's reaction, the original Brust's scheme consists in a two-phase reaction (organic/aqueous) using NaBH_4 as reducing agent. The strong reducing power of the latter allows obtaining relatively small Au-NPs. In subsequent works, Brust et al. [128] extended the synthesis method to routines involving a single phase. In this type of synthesis, it is also possible to control NP size by modifying the ratio of precursors, in this case thiol/Au [129, 130]. Leff et al. [131] have further extended Brust's synthesis to the use of primary amines as passivating agents. As in the previous case, size control was achieved through variation of the capping agent/Au ratio, though particle sizes were larger in the case of amines than for thiols. These authors suggested that the stability of the particles appears to be largely kinetic, rather than thermodynamic, in nature. This contradicts the observation made by Leff et al. [132] in the case thiol-capped Au-NPs, according to whom size control was based on thermodynamic grounds. Most of the other methods used to make small Au-NPs (1–5 nm) also take advantage of the strong capping action of thiols. Capping agents include disulfides [133], polymers with mercapto and cyano functional groups [134], and dendrimers [135]. In general, varying the capping agent concentration allows size control between 1 and 4 nm with reasonable monodispersity.

Other size control parameters (fine tuning) are the lateral interaction of the capping agent. For example, in the case of nonionic alkanethiol-stabilized Au-NPs, changes in molecular lengths produced small differences in particle size [136]. In the quaternary ammonium alkylisocyanides [137] and alkylamine [138] cases, longer alkyl chains promote a decrease in the average size of NPs. Other less common alternative routines have been developed for Au-NPs synthesis; the reader is referred to the reviews done by Daniel [122], Tao [139], and Templeton [140] for further details.

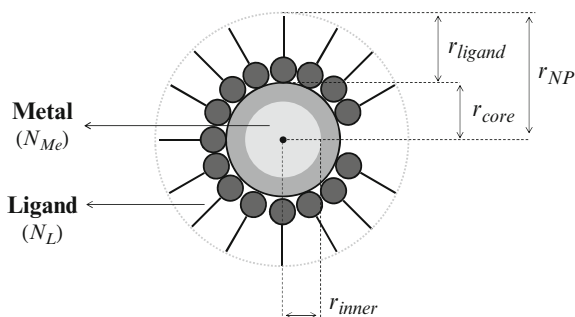
Recently, it has been experimentally demonstrated that ligand molecules may control particle formation by thermodynamic rather than kinetic means. In this respect, Klabunde and coworkers discovered a process that they denominated “digestive ripening.” Upon heating a highly polydisperse gold colloid with ligand excess, it was found that it evolved into a nearly monodispersed system [141–145]. The explanation proposed is that larger particles break down in solution, while at the same time small particles grow until they reach a stable size. This process is the reverse of “Ostwald ripening” which, driven by the tendency to lower the surface energy, always favors particle growth. Although this method of generating colloidal NPs is not generally applicable, it has been extended successfully to the production of various types of metal NPs.

As can be inferred from the previous bird-eye view of the synthesis methods of NPs, there is a huge amount of work and experience in this area, for which a theoretical counterpart is missing or has only been scarcely developed. A first important step in this direction was taken by Leff et al. [132]. These authors developed a model based on thermodynamic considerations to explain the variation in the size of Au-NPs with the gold/thiol reactant molar ratios, obtaining a good agreement between experimental and theoretical predictions. This fact seems to be an indication that in the case of their synthesis method the size control of the NPs is driven by thermodynamics. On the other hand, Kuo et al. [146] have reported on the functionalization of monolayer-protected Au-NPs, considering ligand place-exchange reaction for different systems. In this work, a thermodynamic model was proposed, based on the Gibbs–Thomson equation. According to the latter modeling, a weaker headgroup-gold adsorption should develop larger NPs. In spite of their apparent achievements, some of the theoretical models present gaps in their formulations. In some cases, their predictions are not completely in rule with the experimental observation, requiring further corrections to deliver proper results.

10.4.3 Modeling of the Stability of Capped Nanoparticles

To introduce a model for the present problem, let us consider an experimental setup where a monodisperse set of NPs is put in contact with ligands present in solution at a certain temperature and concentration. Thus, the total number of atoms and the number of ligand molecules is a constant, so that the proper ensemble to use is the N , P , and T one.

Fig. 10.15 Model employed to analyze the stability of capped nanoparticles. The nanoparticle radius is given by $r_{\text{NP}} = r_{\text{core}} + r_{\text{ligand}}$, where r_{core} and r_{ligand} correspond to the core metal radius and the effective thickness of the ligand layer



In the next discussion we follow the derivation given by Kuo et al. [147], deviating from it in the points concerning the use of the chemical potential for the reasons we explain in detail below.

Let us consider an ensemble made of ξ spherical, *all identical* NPs, specified by the variables N_{Me} , P , and T . Let r_{NP} be the NP radius, given by $r_{\text{NP}} = r_{\text{core}} + r_{\text{ligand}}$, where r_{core} and r_{ligand} correspond to the core metal radius and the effective thickness of the ligand layer, respectively. Figure 10.15 shows a scheme of the geometrical arrangement of the model. Similar to the CNT discussed in the previous sections, we will assume that the system is diluted enough to neglect the interactions between neighboring NPs.

The free energy of this ensemble may be written as:

$$G^{\text{total}} = \xi G_{\text{NP}} = \xi (G_{\text{NP}(\text{bulk})} + G_{\text{NP}(\text{surf})} + G_{\text{NP}(\text{ads})}) \quad (10.67)$$

where G_{NP} corresponds to the Gibbs free energy of the stabilized NP, composed by the free energy of the bulk part of the NP, $G_{\text{NP}(\text{bulk})}$ (internal atoms), the free energy of the surface of the NPs, $G_{\text{NP}(\text{surf})}$ (surface atoms), and the free energy of the ligand molecules, $G_{\text{NP}(\text{ads})}$. Written in the present way, G^{total} is an extensive quantity (see discussion in Sect. 10.2.1). At difference with the assumption in the model proposed by Kuo et al. [147], two different chemical potentials arise in nanothermodynamics [47], namely μ and $\hat{\mu}$.¹ While the former is given by $\mu = (\partial G / \partial N_{Me})_{P,T}$, the latter is related to the Gibbs free energy of the system according to:

$$\hat{\mu} = \frac{G_{\text{NP}}}{N_{Me}} \quad (10.68)$$

In the case of infinitely large (macroscopic) systems $\hat{\mu} = \mu$ and $G_{\text{NP}} = \mu N_{Me}$, but this assumption may not be valid for a NP. Equation (10.68) may be written as a function of μ according to:

$$\mu = \hat{\mu} + N_{Me} \left(\frac{\partial \hat{\mu}}{\partial N_{Me}} \right)_{P,T} \quad (10.69)$$

¹Do not confuse this quantity with the electrochemical potential, denoted here with $\hat{\mu}$.

In the case of macroscopic systems, $(\partial\hat{\mu}/\partial N_{Me})_{P,T} = 0$, so we recover the equivalence valid in extensive systems. However, in the present case the correct approach is to write the free energy of the naked NP, $G_{\text{NP(core)}}$, as a bulk term, plus a surface correction like (10.69):

$$G_{\text{NP(core)}} = G_{\text{NP(bulk)}} + G_{\text{NP(surf)}} = \mu_{Me(\text{bulk})}N_{Me} + \alpha N_{Me}^{2/3} \quad (10.70)$$

where α is positive and proportional to the surface tension γ . Note that according to (10.70) the chemical potential of the naked NP is given by:

$$\mu = \mu_{Me(\text{bulk})} + \alpha \frac{2}{3} N_{Me}^{-1/3} = \mu_{Me(\text{bulk})} + \frac{3\alpha r_{Me}}{2r_{\text{NP}}} \quad (10.71)$$

Equation (10.71) yields the correct dependence of the chemical potential with the radius of the naked NP [Gibbs and Thomson equation, (10.52)]. When the adsorbate contribution (10.67) is now used to calculate the free energy of the nanosystem, we get:

$$G^{\text{total}} = \xi \left[\frac{\mu_{Me(\text{bulk})}}{r_{Me}^3} r_{\text{NP}}^3 + 4\pi \left(\gamma + \rho_L G_{\text{per ligand}}^{\text{ads}} \right) r_{\text{NP}}^2 \right] \quad (10.72)$$

where r_{Me} is the radius of a Me metallic atom and ρ_L is the ligand surface density. Writing now the (10.72) in terms of the total number of Me atoms, and considering mass conservation ($N_T = \xi N_{Me}$) we get:

$$G^{\text{total}} = N_T \left[\mu_{Me(\text{bulk})} + 3\nu_{Me} \left(\gamma + \rho_L G_{\text{per ligand}}^{\text{ads}} \right) \frac{1}{r_{\text{NP}}} \right] \quad (10.73)$$

G^{total} contains a bulk and a surface term, in agreement with the physical expectation. If the interaction of the ligand with the NP overcompensates the free energy required for the formation of the surface of the NP, the parenthesis in (10.73) is negative. In this case, the free energy of the systems reaches a maximum for $r_{\text{NP}} \rightarrow 0$. On the other hand, if the parenthesis is positive, the minimum free energy is reached for large r_{NP} values, corresponding to the Ostwald ripening situation. Besides the mathematics, the physical interpretation of (10.73) is straightforward. If the surface energy of the NP is dominant, the free energy of the system will be minimized decreasing the number of NP (ξ), leading to the ripening phenomenon referred to above. On the other hand, if the ligand adsorption energy overcompensates the surface energy effect, the number of NP increases and each NP will reduce their size, collapsing to the atomic state. In summary, no local minima are predicted and no thermodynamic control of NP size may be expected from the previous model.

The original derivation of Kuo et al. [147] contains an additional (linear) term in the parenthesis of (10.73), leading to the prediction of stable NPs. However, we see that this term is not obtained when considering the proper dependence of the chemical potential with the radius. Therefore, it is worth analyzing if an extension of the model shown above can be made to include a term of this type that

has a well-defined physical basis and allows for a proper evaluation of this effect. According to the proposal of Hill [47] or the discussion given by McClurg [147], after the macroscopic and surface terms, the first leading contribution that should be taken into account, in the metal NPs, is the dependence of the free energy on the curvature, which is proportional to $N_{Me}^{1/3}$. Thus, the improved equation for the free energy is:

$$G^{\text{total}} = \xi \left[N_{Me} \mu_{\text{inner}} + \alpha N_{Me}^{2/3} + \beta N_{Me}^{1/3} + G_{\text{NP}}^{\text{ads}} \right] \quad (10.74)$$

where β is a coefficient related to the curvature energy. The translational and rotational contributions have been omitted, since their dependence on N_{Me} is weaker than $N_{Me}^{1/3}$, as discussed in Sect. 10.2.6. Taking into account that $N_{Me} = 4\pi r_{\text{NP}}^3 / 3v_{Me}$, we get:

$$G^{\text{total}} = N_T \left[\mu_{Me(\text{bulk})} + 3v_{Me} \left(\gamma + \rho_L G_{\text{per ligand}}^{\text{ads}} \right) \frac{1}{r_{\text{NP}}} + \frac{3}{2} v_{Me} \sigma \frac{1}{r_{\text{NP}}^2} \right] \quad (10.75)$$

where σ is curvature energy. The extremum condition, $\partial G^{\text{total}} / \partial r_{\text{NP}} = 0$, for (10.75) leads to:

$$r_{\text{NP}}^* = \frac{-\sigma}{\gamma + \rho_L G_{\text{per ligand}}^{\text{ads}}} \quad (10.76)$$

Equation (10.76) leads to a physically reasonable result only if $(\gamma + \rho_L G_{\text{per ligand}}^{\text{ads}}) < 0$. Thus, an extremum can be found only if the surface energy of the NP is overcompensated by the adsorption energy of the ligand. Replacement of (10.76) into the second derivative of the free energy shows that the extremum is a minimum. The curvature energy determines the critical size of the NP. If the curvature energy is large, the particles will attain its equilibrium shape at a larger radius.

It can be noted that (10.76) shows that there is a threshold in the value of the free energy of adsorption, for the ligand to be able to stabilize the NP at a finite radius. To estimate this, in the case of metallic NPs, we consider the surface energy of Au as reported in reference [148] ($\gamma = 0.787 \text{ eV nm}^{-2}$) and the ligand surface density from reference [132] ($\rho_L = 0.467 \text{ Lig nm}^{-2}$). The threshold value for $G_{\text{per ligand}}^{\text{ads}}$ is $\sim -1.60 \text{ eV}$. Ligands with a weaker binding energy could only keep NP in a metastable state. DFT calculations show that $U_{\text{per ligand}}^{\text{ads}}$ at 0 K is of the order of -0.60 eV , -2.00 eV and -2.40 eV for CH_3NH_2 , CH_3S^- , and CH_3COO^- , respectively [149]. This may give a hint of why NPs stabilized by amino and thiol groups present such different behaviors in their stability, as discussed in Sect. 10.4.2. For a further analysis on capped nanoparticles, see Chap. 9 by Olmos and Mariscal in this book.

To finish the present section, we want to note that a correct description of the behavior of molecule-stabilized NPs may include equilibrium with charged species, like for example $\text{Au}^{3+} \rightleftharpoons \text{Au}^+ \rightleftharpoons \text{Au}^0$ and /or $\text{CH}_3\text{S}^- \rightleftharpoons \text{CH}_3\text{SH}$ [150]. In these cases, potential control will aid in the selection of synthesis conditions for particle size optimization. The introduction of other effects like hydrophobicity and surface coverage is also desirable, as well as a proper statistical mechanical description in the style of that presented in Sect. 10.4.1.

10.5 Conclusions and Perspective

In the present chapter we have given an overview about different ways of modeling the thermodynamic properties of metal NPs, mainly from a statistical mechanical viewpoint. While nucleation and growth processes have been studied and modeled during many decades, the main efforts were directed to the study of liquid drops and metallic systems have been treated less extensively. The study of bimetallic systems from the perspective described in the present chapter is fairly recent, and was mainly directed to core-shell structures, since for these systems relatively inexpensive computer simulations can be performed. For these systems, interesting features appear concerning the stability/metastability of different structures, which provide stimulus for future experiments. Finally, the influence of ligands species on the stability of NPs is starting to be studied, and this appears as a particularly interesting field, where size and shape of nanoparticles may be controlled. In this respect, some of the important issues to be considered and introduced in the modeling are the electrochemical nature of the process by which the NPs are generated and the existence of equilibrium between the ligand species in solution and those adsorbed, since in many cases the species interacting with the NPs are different from those in solution. Finally, the less developed aspect is the kinetic one, and this concerns size and shape control by changing the synthesis conditions. In this respect, there is still much to do on the theoretical field, in a synchronous effort with proper experiments.

Acknowledgments The authors wish to acknowledge CONICET PIP: 112-200801-000983, Secyt UNC, Program BID (PICT 2007 N1 00340), and PME: 2006-01581 for financial support, and Gabriela Diaz Cortez for her language assistance.

References

1. Gibbs JW (1878) *Trans Conn Acad* 3:343
2. Gibbs JW (1881) *Proc Am Acad* 420
3. Kashchiev D (2000) *Nucleation: basic theory with applications*. Butterworth-Heinmann, Oxford
4. Finney EE, Finke RG (2008) *J Colloid Interface Sci* 317:351
5. Shuttleworth R (1950) *Proc Phys Soc Lond A* 63:444
6. Herring C (1953) *Structure and properties of solid surfaces*. In: Gomer R, Smith CS (eds) University of Chicago Press, Chicago
7. Rusanov AI (2005) *Surf Sci Rep* 58:111
8. Volmer M, Weber A (1925) *Z Phys Chem Leipzig* 119:277
9. Becker R, Döring W (1935) *Ann Phys* 24:719
10. Frenkel J (1939) *J Chem Phys* 7:200
11. Zeldovich J (1942) *J Exp Theor Phys* 12:525
12. Reiss H (1950) *J Chem Phys* 18:840
13. Kashchiev D (1992) *J Phys Chem* 76:5098
14. Oxtoby DW. *Phys J* (1992) *Condens Matter* 4:7627
15. Laaksonen A, Talanquer V, Oxtoby DW (1995) *Annu Rev Phys Chem* 46:489
16. Oxtoby DW (1998) *Acc Chem Res* 31:91

17. Buff FP (1951) *J Chem Phys* 19:1591
18. Buff FP (1955) *J Chem Phys* 23:419
19. Walton D (1962) *J Chem Phys* 37:2182
20. Lothe J, Pound GM (1962) *J Chem Phys* 36:2080
21. Sen S, Mukerji T (1999) *J Non-Cryst Solids* 246:229
22. Reguera D, Bowles RK, Djikaev Y, Reiss H (2003) *J Chem Phys* 118:340
23. Kusaka I (2006) *Phys Rev E* 73:031607
24. Block BJ, Das SK, Oettel M, Virnau P, Binder K (2010) *J Chem Phys* 133:154702
25. Reiss H, Katz JL (1966) *J Chem Phys* 46:2496
26. Reiss H, Katz JL, Cohen ER (1968) *J Chem Phys* 48:5553
27. Langer JS (1967) *Ann Phys* 41:108
28. Langer JS (1969) *Ann Phys* 54:258
29. Langer JS, Turski LA (1973) *Phys Rev A* 8:3230
30. Katz JL, Wiedersich H (1977) *J Colloid Interface Sci* 61:351
31. Katz JL, Donohue MD (1979) *Adv. Chem. Phys* 40:137
32. Girshick SL, Chiu C (1990) *J Chem Phys* 93:1273
33. Ford IJ (1998) *J Aerosol Sci* 29:S367
34. Allen MP, Tildesley DJ (1991) *Computer simulation of liquids*. Oxford University Press, Oxford
35. Jensen F (2007) *Introduction to computational chemistry*. Wiley, New York
36. Koonin SE, Meredith DC (1990) *Computational physics fortran version*. Addison-Wesley Publishing Company, Reading
37. Leach AR (2001) *Molecular modelling, principles and applications*. Prentice Hall, Englewood Cliffs, NJ
38. Frenkel D, Smit B (2002) *Understanding molecular simulations*. Academic Press, San Diego.
39. Duijneveldt JS, Frenkel D (1992) *J Chem Phys* 96:4655
40. Oxtoby DW (1992) *J Phys Condens Matter* 4:7627
41. Ciacchi LC, Pompe W, and De Vita A (2001) *J Am Chem Soc* 123:7371
42. Ciacchi LC, Pompe W, De Vita A (2003) *J Phys Chem B* 107:1755
43. Ciacchi LC, Mertig M, Pompe W, Meriani S, De Vita A (2003) *Platinum Met Rev* 47:98
44. Ford IJ (1996) *J Chem. Phys* 105:8324
45. Tolman RC (1949) *J Chem Phys* 17:333
46. Plieth WJ (1982) *J Chem Phys* 86:3166
47. Hill TL (1994) *Thermodynamics of small systems, Part I and II*. Dover Publication, New York
48. Hill TL (2001) *Nano Lett* 1:273
49. Ford IJ (1997) *Phys Rev E* 56:5615
50. Courtney WG (1961) *J Chem Phys* 35:2249
51. Reiss H, Kegel WK (1996) *J Phys Chem* 100:428
52. Kusaka I, Wang Z-G, Seinfeld JH (1998) *J Chem Phys* 108:3416
53. Reiss H (1999) *J Molecular Structures* 485:465
54. Senger B, Schaaf P, Corti DS, Bowles R, Voegel J-C, Reiss H (1999) *J Chem Phys* 110:6421
55. Vehkamäki H, Ford IJ (2000) *J Chem Phys* 112:4193
56. Schaaf P, Senger B, Voegel JC, Bowles RK, Reiss H (2001) *J Chem Phys* 114:18
57. Yasuoka K, Matsumoto M (1998) *Fluid Phase Equilibria* 144:369
58. Wang CX, Yang GW (2005) *Mater Sci Eng R* 49:157
59. Oviedo OA, Leiva EPM, Mariscal MM (2008) *Phys Chem Chem Phys* 10:3561
60. Fonticelli MH, Corthey G, Benitez GA, Salvarezza RC, Giovanetti LJ, Requejo FG, Shon YS (2007) *J Phys Chem C* 26:9359
61. Corain B, Schmid G, Toshima N (2008) *Metal nanocluster in catalysis and materials science*. Elsevier, The Netherlands
62. LaMer VK, Dinigar RH (1950) *J Am Chem Soc* 72:4847
63. Oviedo OA, Mariscal MM, Leiva EPM (2010) *Phys Chem Chem Phys* 12:4580
64. Oviedo OA, Mariscal MM, Leiva EPM (2010) *Electrochimica Acta* 55:8244
65. Callen HB (1985) *Thermodynamics and an introduction to thermostatics*. Wiley, New York

66. Makarov GN (2008) *Physics-Uspekhi* 51(4):319
67. Mei QS, Lu K (2007) *Prog Mater Sci* 52:1175
68. Wang CX, Yang YH, Xu NS, Yang GW (2004) *J Am Chem Soc* 126:11303
69. Strumia A, Tetradis N, Wetterich C (1999) *Phys Lett B* 467:279
70. Belloni J (2006) *Catal Today* 113:141
71. Ferguson LN (1987) *Cell Biochem Biophys* 11:11
72. Esfarjani K, Ali Mansoori G (2005) Statistical mechanical modeling and its application to nanosystems. In: Rieth M, Schommers W (eds) *Handbook of theoretical and computational nanotechnology*, Cap 16, Vol X
73. Gross DH, Kenney JF (2005) *J Chem Phys* 122:224111
74. Hill TL (1987) *Statistical mechanics*. Dover publications, New York
75. Hill TL, Chamberlin RV (1998) *Proc Natl Acad Sci* 95:12779
76. Frisch HL (1957) *J Chem Phys* 27:90
77. Ford IJ (2004) *Proc Instn Mech Engrs* 218:883 (part C)
78. Foiles SM, Baskes MI, Daw MS (1986) *Phys Rev B* 33:7983
79. Cleri F, Rosato V (1993) *Phys Rev B* 48:22
80. Baskes MI (1992) *Phys Rev B* 46:2727
81. Perdew JP, Zunger A (1981) *Phys Rev B* 23:5048
82. Li JH, Dai XD, Liang SH, Tai KP, Kong Y, Liu BX (2008) *Phys Reports* 455:1
83. Xiao L, Tollberg B, Hu X, Wang L (2006) *J Chem Phys* 124:114309
84. Bockris JO'M, Conway BE, Yeager E (eds) (1980) *Comprehensive treatise of electrochemistry* Vol 1, Plenum Press, New York, London
85. Lipkowski J, Ross PN (1999) *Imaging of surfaces and interfaces*. Wiley-Vch, New York
86. Budevski E, Staikov G, Lorenz WJ (1996) *Electrochemical phase formation and growth*. Wiley-Vch, New York
87. Schmickler W (1996) *Interfacial electrochemistry*. Oxford University Press, Oxford
88. Pérez MA (2007) Growth mechanisms of metal nanoparticles. In: *Recent advances in nanoscience*, Mariscal MM, Dassie SA (eds) *Research Signpost, Trivandrum-Kerala, India*
89. Luque NB, Reinaudi L, Serra P, Leiva EPM (2009) *Electrochimica Acta* 54:3011
90. Hofmann D, Schindler W, Kirchner J (1998) *Appl Phys Lett* 73:3279
91. Schindler W, Hofmann D, Kirchner J (2001) *J Electrochem Soc* 148:124
92. Hugelmann M, Hugelmann P, Lorenz WJ, Schindler W (2005) *Surf Sci* 597:156
93. Mariscal MM, Leiva EPM, Dassie SA (2007) *J Electroanal Chem* 607:10
94. Schindler W, Hugelmann P, Hugelmann M, Kärtner FX (2002) *J Electroanal Chem* 522:49
95. Del Pópolo MG (2002) *Computer simulation of systems related which electrochemical interface*. PhD thesis, Department of Mathematics and Physics, Faculty of Chemistry, UNC, Argentina
96. Mariscal MM (2004) *Simulation of electrochemical nanostructures*. PhD Thesis, Univerdität Ulm, Abteilung Elektrochemie
97. Mariscal MM, Dassie SA (eds) (2007) *Recent advances in nanoscience*. *Research Signpost, Trivandrum-Kerala, India*
98. Pérez MA, Moiraghi R, Coronado EA, Macagno VA (2008) *Crystal Growth Design* 8:1377
99. de Mello Doneg C, Liljeroth P, Vanmaekelbergh D (2005) *Small* 1:1152
100. Talapin DV, Rogach AL, Kornowski A, Haase M, Weller H (2001) *Nano Lett* 1:207
101. Hambrock J, Becker R, Birkner A, Weiß J, Fischer RA (2002) *Chem Commun* 68
102. Jana NR, Peng X (2003) *J Am Chem Soc* 125:14280
103. Park J, An K, Hwang Y, Park JG, Noh HJ, Kim JY, Park JH, Hwang NM, Hyeon T (2004) *Nat Mater* 3:891
104. Ferrando R, Jellinek J, Johnston RL (2008) *Chem Rev* 108:845
105. Reiss H (1951) *J Chem Phys* 19:482
106. Talapin DV, Rogach AL, Haase M, Weller H (2001) *J Phys Chem B* 105:12278
107. Park J, Joo J, Kwon SG, Jang Y, Hyeon T (2007) *Angew Chem Int Ed* 46:4630
108. Lee D, Park S, Lee JK, Hwang N (2007) *Acta Mater* 55:5281
109. Hrubý J, Labetski DG, van Dogen MEH (2007) *J Chem Phys* 127:164720

110. Lee HM, Ge M, Sahu BR, Tarakeshwar P, Kim KS (2003) *J Phys Chem B* 107:9994
111. Wang J, Boelens HFM, Thathagar MB, Rothenberg G (2004) *Phys Chem Chem Phys* 5:93
112. Michaelis M, Henglein A (1992) *J Phys Chem* 96:4719
113. Belloni J (2006) *Catal Today* 113:141
114. Henglein A, Giersig M (2000) *J Phys Chem B* 104:6767
115. Henglein A, Giersig M (1999) *J Phys Chem B* 103:9533
116. Shevchenko EV, Talapin DV, Schnablegger H, Kornowski A, Festin Ö, Svedlindh P, Haase M, Weller H (2003) *J Am Chem Soc* 125:9090
117. Vehkamäki H, Kulmala M (1995) *Aerosol Sci* 26:S213
118. Leiva EPM (1996) *Electrochimica Acta* 41:2185
119. Rojas MI, Sanchez CG, Del Pópolo MG, Leiva EPM (2000) *Surf Sci* 453:225
120. Oviedo OA, Rojas MI, Leiva EPM (2006) *Surf Sci* 51:3526
121. Chui YH, Grochola G, Snook IK, Russo SP (2007) *Phys Rev B* 75:033404
122. Daniel MC, Astruc D (2004) *Chem Rev* 104:293
123. Turkevitch J, Stevenson PC, Hillier J (1951) *Discuss Faraday Soc* 11:55
124. Kimling J, Maier M, Okenve B, Kotaidis V, Ballot H, Plech A (2006) *J Phys Chem B* 110:15700
125. Frens G (1973) *Nature Phys Sci* 241:20
126. Frens G (1972) *Colloid Polymer Sci* 250:736
127. Brust M, Walker M, Bethell D, Schiffrin DJ, Whyman R (1994) *J Chem Soc Chem Commun* 801.
128. Brust M, Fink J, Bethell D, Schiffrin DJ, Kiely C (1995) *Chem Soc Chem Commun* 1655
129. Frenkel AI, Nemzer S, Pister I, Soussan L, Harris T, Sun Y, Rafailovich MH (2005) *J Chem Phys* 123:184701
130. Zanchet D, Hall BD, Ugarte D (2000) *Chem Phys Lett* 323:167
131. Leff DV, Brandt L, Heath JR (1996) *Langmuir* 12:4723
132. Leff DV, Ohara PC, Heath JR, Gelbart WM (1995) *J Phys Chem* 99:7036
133. Yonezawa T, Yasui K, Kimizuka N (2001) *Langmuir* 17:271
134. Teranishi T, Kiyokawa I, Miyake M (1998) *Adv Mater* 10:596
135. Zhao MQ, Sun L, Crooks RM (1998) *J Am Chem Soc* 120:4877
136. Yonezawa T, Yasui K, Kimizuka N (2001) *Langmuir* 17:271
137. Yonezawa T, Imamura K, Kimizuka N (2001) *Langmuir* 17:4701
138. Wikander K, Petit C, Holmberg K, Pileni MP (2006) *Langmuir* 22:4863
139. Tao AR, Habas H, Yang P (2008) *Small* 3:310
140. Templeton AC, Wuelfing WP, Murray RW (2000) *Acc Chem Res* 33:27
141. Lin XM, Sorensen CM, Klabunde KJ (2000) *J Nanoparticle Res* 2:157
142. Soeva SI, Klabunde KJ, Sorensen CM, Dragieva I (2002) *J Am Chem Soc* 124:2305
143. Soeva SI, Prasad BLV, Uma S, Stoimenov PK, Zaikovski V, Sorensen CM, Klabunde KJ (2003) *J Phys Chem B* 107:7441
144. Prasad BLV, Stoeva SI, Sorensen CM, Klabunde KJ (2003) *Chem Mater* 15:935
145. Stoeva SI, Zaikovski V, Prasad BLV, Stoimenov PK, Sorensen CM, Klabunde KJ (2005) *Langmuir* 21:10280
146. Kuo C-T, Yu J-Y, Huang M-J, Chen C-H (2010) *Langmuir* 26:6149
147. McClurg RB, Flagan RC (1998) *J Colloid Interface Sci* 201:194
148. Perdew JP, Wang Y (1991) *Phys Rev Lett* 66:508
149. Oviedo OA, Zoloff-Michoff ME, Leiva EPM Manuscript in preparations
150. Corthey G, Giovanetti LJ, Ramallo-López JM, Zelaya E, Rubert AA, Benitez GA, Requejo FG, Fonticelli MH, Salvarezza RC (2010) *ACS Nano* 4:3413

Index

A

- Aberrations, 7–8
- Activated complex theory (ACT), 333
- Atomic shells, metal clusters, 92
 - compact structures, lithium clusters, 87
 - Lennard–Jones global minima sequence, 83–84
 - metal surface model (MSM), 86
 - models of, cluster cohesive energy, 85
 - polytetrahedral-fcc-like structural transition, 84
 - promotion energy, 86
 - quasispherical cluster geometries and cage structure, 87–88
 - surface energy, 84

B

- Basin-Hopping (BH) algorithm
 - elementary moves
 - exchange move, 201–202
 - shake, shell and Brownian move, 201
 - HISTO algorithm, 203–204
 - metal nanoclusters, 39–40
 - parallel excitable walkers (PEW) algorithm, 202–203
 - structure of, 199–200
- Bimetallic nanoparticles
 - Janus particles
 - chemical orderings, 252
 - cluster formation, 256
 - empirical potentials, 257
 - geometrical shape, 253–254
 - inert gas aggregation (IGA) source, 254–255
 - magneto-optical properties, 257

- segregation effects, 253
- STEM-HAADF method, 255–256
- optical properties, 134–135
- size control on thermodynamic effects
 - Au(1289) surface, excess energy, 339
 - computer simulations, 340–341
 - excess Helmholtz free energy, 338
 - normalized probability density, 340, 342
 - partition function, 336
 - probability, 340
 - quantities, 337
 - schematic representation, model, 335–336
- Brownian move, 201
- Burst nucleation
 - driving force, 332
 - heating-up method, 332
 - hot-injection method, 331–332
 - process, 330
 - stage I and II, 331

C

- Closed-shell metal clusters
 - atomic shells, 92
 - compact structures, lithium clusters, 87
 - Lennard–Jones global minima sequence, 83–84
 - metal surface model (MSM), 86
 - models of, cluster cohesive energy, 85
 - polytetrahedral-fcc-like structural transition, 84
 - promotion energy, 86
 - quasispherical cluster geometries and cage structure, 87–88
 - surface energy, 84

- Closed-shell metal clusters (*cont.*)
- bimetallic clusters, AB ordering
 - limit types, 90
 - onion layers, 91
 - structural principles, 91–92
 - doubly magic clusters (DMC), 83, 93
 - electronic shells, 93
 - ellipsoidal jellium model (EJM), 90
 - ionization energy, 89
 - planar and cage structures, 90
 - spherical jellium model (SJM), 89
 - golden pyramid (Au_{20}) and golden cages (Au_{16-} , Au_{17-}), 95–97
 - intermetalloids, 94
 - ligand-protected gold clusters, 97–98
 - metal-carbon compound clusters, 95
 - mixtures of atomic and electronic shells, 93
 - passivated metal clusters, 94–95
 - singly doped clusters, AB_n , 94
 - stabilizing clusters, 82
 - superatoms, 98
- Colloidal Janus particles
- helix formation, 252
 - kinetics and chemical anisotropy, 251
 - micelles and vesicles, 251
 - Monte Carlo (MC) simulation technique, 248–249
 - phase diagram, 248–250
 - self-aggregation, 248
- Contrast transfer functions (CTF), 7–8
- D**
- Defocusing effect, 334
- Density functional basin-hopping (DF-BH) method, 40–42
- Density functional empirical potentials (DF-EP) approach, 42–44
- Density-functional theory (DFT)
- bimetallic nanoparticles, 257
 - growth
 - Car–Parrinello method, 70
 - diffusion energy barriers, 72
 - Nudged Elastic Band (NEB) method, 71
 - ONIOM protocol, 70
 - Pd clusters, experiment *vs.* theory, 73–74
 - trimer and tetramer clusters, diffusion mechanisms, 73
 - vacancy diffusion, 71
 - magic clusters
 - chemical ordering phase space, 50–51
 - HOMO-LUMO gap, 46
 - magnetic ordering, PtCo, 52–53
 - mixing patterns, 49
 - nanoalloys, definition of, 49
 - optical properties, Au clusters, 51
 - PdAg_N clusters in gas phase, 46–47
 - shell structure, 48
 - structural shell closure, 45
 - supported binary particles, 1D wire approach, 50, 52
- metal nanoclusters and nanoalloys
- black-box packages, 37
 - Born–Oppenheimer approximation, 31
 - CCSD-T, 32
 - configuration interaction (CI), 33
 - definition of, Hubbard Hamiltonian, 35–36
 - delocalized basis sets, 35
 - DFT+U method, 35
 - electronic wave function, 30
 - electron-phonon coupling, 31
 - first-principles, 30
 - GW approach, 36
 - Hartree–Fock equations, 32
 - HOMO-LUMO gap, 33
 - Jacob’s ladder, 34
 - jellium, 33
 - linear scaling, 32
 - local and hybrid xc-functionals, 34
 - long range correlation effects, 33
 - range-separation, 35
 - variational/perturbative methods, 33
- palladium cluster adsorption, $\text{MgO}(100)$ surface, 66–68
- Pt metallorganic complex structures, 68–69
- silver clusters, $\text{MgO}(100)$ surface, 64–65
- structural properties
- density functional basin-hopping (DF-BH), 40–42
 - density functional empirical potentials (DF-EP), 42–44
 - energy differences and lowest-energy isomers, Ag clusters, 37–38
 - length scales and overlap regions, 45
 - Monte Carlo with minimization approach, 39–40
 - multi-scale framework, 43–44
 - particle size, computational method hierarchy, 39
 - pictorial representation, 38
- supported clusters
- adsorption, 57–58
 - Ag cluster adsorption, $\text{MgO}(100)$ surface, 61–62

- black magic, 58
 - charge transfer effects, 56, 58
 - diffusion, adsorption, and self-organization processes, 54
 - electron density, 56–57
 - extended defects, 58
 - local defects, 58
 - metal growth characteristics, 60
 - metal-on-top effect, 55
 - Ostwald ripening and sintering processes, 53
 - oxygen molecular adsorption, 62
 - particle–particle distances, 61
 - potential energy surface, Au adsorption, 58–59
 - randomly distributed defects, 61
 - regular MgO(100) surface structure, 54–55
 - shape and chemical ordering, nanoparticles, 63–64
 - work function, 57
 - surfactant coating, 68
 - Digestive ripening process, 343
 - Doubly magic clusters (DMC), 83, 93
- E**
- Electrochemical nucleation
 - critical cluster size, 334–335
 - energetic contribution, nanoparticle growth, 327–328
 - Gibbs free energy, 325
 - layer-by-layer growth characteristics, 328
 - monotonically growing behavior, 327
 - nanoparticle in solution, 324
 - overpotential, 329
 - pictorial representation, 325
 - potential difference, 326
 - schematic representation, 323–324
 - stability limits, 329
 - undersaturation and supersaturation, 328–329
 - Electronic shells, metal clusters, 93
 - ellipsoidal jellium model (EJM), 90
 - ionization energy, 89
 - planar and cage structures, 90
 - spherical jellium model (SJM), 89
 - Exchange move, 201–202
- F**
- Fe_N clusters, spin-fluctuation energies
 - bond-length contraction, 171
 - electronic structure effects, 173
 - Heisenberg-/Ising-like behavior, 169
 - local spin-fluctuation energy, 170–171
 - magnetic excitations, 168
 - structural illustration, 168, 170
 - temperature-induced structural fluctuations, 172
 - Focusing effect, 333
- G**
- Global optimization methods
 - BH algorithm (*see* Basin-Hopping (BH) algorithm)
 - crystalline and noncrystalline motifs, 195
 - electronic shell closure effect, 196
 - free nickel clusters
 - atomistic model, 204–205
 - structures of, 205, 206
 - funnels, 198
 - homotops, 197
 - oxide-supported metallic clusters
 - adsorption sites, 206
 - Ag/MgO(001), 209–212
 - atomistic model, 207–208
 - Au/MgO(001), 212
 - checkerboard arrangement, 205
 - Ni/MgO(001), 208–209
 - phase diagrams, nanoalloys, 217
 - second-moment approximation tight-binding (SMATB) potentials, 196
 - Gold-palladium nanoparticle, TEM micrograph, 4
- H**
- High angle annular dark field scanning transmission electron microscope (HAADF-STEM), 9–10
 - Hill and Chamberlin metastability model
 - chemical potential and temperature, 318
 - partition function, 314
 - phase transition, kinetic hindrance, 316–317
 - probability density, 316–317
 - surface component, 315–316
 - HRTEM simulations, 8
 - Hubbard Hamiltonian, 35–36
- I**
- Image interpretation, electron microscope
 - assumptions, 13
 - chemical composition, 16–20

Image interpretation, electron microscope
(*cont.*)
geometric phase analysis (GPA), 22–25
interatomic distances, 21–22
orientations, 16
thermal effects, 20–21

J

Janus nanoalloys
coalescence
average temperature behaviour,
258–259
impact factors and initial momenta,
260, 263
impact parameter definition, 260, 262
necklace-like aggregates, 257
schematic representation, zero impact
parameter, 260–261
stages, 259
temporal evolution, schematic
representation, 258
triaxial parameter, 262, 264
cooling
chemical composition, 270
common neighbour geometrical
analysis, 269
simulation process, 269
solidification, 268
symmetry formation, 269–270
one-by-one growth technique
asymmetry formation, 265–266
excess energy, 265
schematic representation, 262, 264
structural formation, 266–267
transition, 267, 268
Janus nanoparticle modelling
bimetallic nanoparticles
chemical orderings, 252
cluster formation, 256
empirical potentials, 257
geometrical shape, 253–254
inert gas aggregation (IGA) source,
254–255
magneto-optical properties, 257
segregation effects, 253
STEM-HAADF method, 255–256
chemical patterns, 246–247
colloidal particles
helix formation, 252
kinetics and chemical anisotropy, 251
micelles and vesicles, 251
Monte Carlo (MC) simulation
technique, 248–249

phase diagram, 248–250
self-aggregation, 248
compartmentalised colloidal particles,
243–244
fluorescence images, 245
patchy particle, 244

L

Landau damping, 107
Ligand-assisted growth, metallic nanoparticles,
341–343
Ligand-protected gold clusters, 97–98
Low-temperature spin-fluctuation energies
collective fluctuations, 174
Fe_N clusters, 168–173
Ni_N clusters, 173–175
probability, 167–168
thermal fluctuations, 175

M

Magic clusters, DFT
chemical ordering phase space, 50–51
HOMO-LUMO gap, 46
magnetic ordering, PtCo, 52–53
mixing patterns, 49
nanoalloys, definition of, 49
optical properties, Au clusters, 51
PdAg_N clusters in gas phase, 46–47
shell structure, 48
structural shell closure, 45
supported binary particles, 1D wire
approach, 50, 52
Melting transition
cluster structure, 222
magic polyicosahedral core-shell
nanoalloys, 222–225
single impurity effect, 225–227
Molecular adsorbates, spherical nanoparticle
chemical interface damping, 137
colloidal suspension, 136
dipole moment, 142, 144
exciton coupling, 143
HOMO-LUMO gap, 141–142
localized excitation, 142
model and simulation method, 137–138
peak width dependence, Hamiltonian
parameters, 138–139
plasmon resonance splitting, 142, 143
resonance energy dependence, Hamiltonian
parameters, 138, 140
scattering effect, 141

- seventy-five diatomic molecules, 138–139
 - standard deviation, atomic charges, 142, 144
 - surface impurities, 141
- Monte Carlo simulations
 - metal nanocluster structure, 39–40
 - nanoalloy structure and chemical ordering, 234–235
 - phase diagram, Janus particles, 248–250
 - transition-metal clusters
 - average magnetization, 179–181
 - bond-length relaxation effects, 186–188
 - local densities of states (DOS), 178
 - local moments and spin correlations, 181–186
- Multiconfiguration self-consistent-field (MC-SCF), 33
- Multislice method, 11–12

- N**
- Nanothermodynamics
 - energy fluctuations, 309
 - icosahedral arrangement, 309
 - intensive and extensive variables, 311
 - phase transitions, 313–314
 - statistical mechanics and quantum mechanics, 310
 - subdivision potential, 312–313
 - surface effects, 311
- Ni_N clusters, spin-fluctuation theory, 173–175
- Nucleation theorems, 318–319
- Nudged Elastic Band (NEB) method, 71

- O**
- Optical properties, metal nanoclusters
 - absorption spectra, 120–122
 - bimetallic nanoparticles, 134–135
 - collective electronic oscillations, 105
 - dipole moment, 107–108
 - dissipation mechanism, 108
 - homogeneous broadening, 107
 - inhomogeneous broadening, 108
 - kinds of aggregates, 122, 123
 - molecular adsorbates
 - chemical interface damping, 137
 - colloidal suspension, 136
 - dipole moment, 142, 144
 - exciton coupling, 143
 - HOMO-LUMO gap, 141–142
 - localized excitation, 142
 - model and simulation method, 137–138
 - peak width dependence, Hamiltonian parameters, 138–139
 - plasmon resonance splitting, 142, 143
 - resonance energy dependence, Hamiltonian parameters, 138, 140
 - scattering effect, 141
 - seventy-five diatomic molecules, 138–139
 - standard deviation, atomic charges, 142, 144
 - surface impurities, 141
- near-field properties
 - DFTB Hamiltonian, 151–154
 - electronic structure, 146
 - enhancement effects, 145
 - Raman effect, 145
 - semiempirical TB, 148–151
 - simulation method, 146–148
- perturbation, 119–120
- plasmon excitation, 105–106
- polyhedral particles
 - cuboctahedra spectra, 130–131
 - 2D scheme, 132
 - excitation lifetimes, 133
 - resonance energy, 132
 - surface defects, 133
 - surface-volume ratio, 131–132
 - types, 130
- prolates and oblate spheroids, 127–129
- quasistatic approximation, 105
- spherical particles, 125–127
- surface condition, 129–130
- surface plasmon resonance (SPR), 107
- tight-binding (TB) method
 - density functional tight-binding (DFTB), 111–114
 - Hückel method, 109
 - linear combination of atomic orbitals (LCAO), 110
 - semiempirical, noble metals, 114–115
 - transferability, 110
 - two- and three-center integrals, 110–111
- time evolution, density matrix
 - causality principle, 118
 - dipole moment and expectation values, 117
 - gold nanoparticle, 116
 - Liouville–von Neumann equation, 115
 - polarizability, 118–119
- Order-disorder transition, Co-Pt nanoalloys
 - energy optimization, chemical ordering, 234–235
 - GIXD spectra, 237–238

Order-disorder transition, Co-Pt nanoalloys
 (*cont.*)
 global-minimum structure, 234–235
 local surface defects, 236, 238
 long-range order parameter, 236
 ordered and disordered phases, 236–237
 Ostwald ripening process, 343

P

Parallel excitable walkers (PEW) algorithm, 202–203
 Passivated nanoparticles
 activation energy barrier, 284
 adsorption sites, 282
 calculation of adsorption energy, 288
 chemical functionalization, 280
 computer simulations, 280–281
 DFT calculations, 284
 electronic stability, 285
 first principles calculations
 charge distribution, 293
 charge transference, 290
 crystallization, 291
 density of states (DOS), 289
 energy optimizations, 288
 exchange-correlation functional, 290
 geometry optimization, 289
 HOMO-LUMO gap, 291
 multilayer structure, 282–292
 spherical Jellium model, 292
 Gronbeck's atomic models, 286–287
 modeling
 adsorption sites, 296
 alkylthiol *vs.* alkylamines, 297–298
 atomic structure, 301
 Brownian dynamics simulations, 302
 diffusion processes, 300
 geometry, 299
 mechanochemical stability, 294
 Morse potential function, 295
 nanocluster definition, 293
 optimized values, parameter, 296–297
 pair distribution functions, 301
 potential energy surfaces (PES), 297–298
 potential of mean force, 302
 prototype systems, 293
 randomly distributed dodecanethiolate molecules, 299
 solvent, 294
 organized monolayer, 282
 pair-wise additive Morse potential, 283
 polar-covalent, 287

quantum molecular dynamic simulations, 286
 synthesis
 ligand exchange, 278
 linker, 276
 polyelectrolytes, 279
 reducing agent, 279
 spacer chains, 277
 terminal group, 277
 two-phase Brust–Schiffrin method, 277–278
 vacancy, 283
 Phase diagrams, nanoalloys
 energetic model
 hopping integrals, 218
 parallel tempering method, 216
 second moment approximation (SMA), 219–220
 tight-binding Ising model (TBIM), 218–219
 global optimization methods, 217
 melting transition
 cluster structure, 222
 magic polyicosahedral core-shell, 222–225
 single impurity effect, 225–227
 order-disorder transition, Co-Pt
 energy optimization, chemical ordering, 234–235
 GIXD spectra, 237–238
 global-minimum structure, 234–235
 local surface defects, 236, 238
 long-range order parameter, 236
 ordered and disordered phases, 236–237
 recursion method, 217
 segregation transition, Cu-Ag
 chiral structures, 233
 dynamical equilibrium, 230, 232
 energy filtered imaging, 227–228
 facets, 230–231
 isotherms, 229–230
 surface phenomena, 227
 types of inhomogeneous sites, 227–228
 types of surface sites, 230–231
 statistical models
 configuration exchange, 222
 molecular dynamics and Monte Carlo simulations, 220
 parallel tempering method, 221
 structural transition, 221
 V interactions, 215
 Polyhedral particles, optical properties
 cuboctahedra spectra, 130–131
 2D scheme, 132

- excitation lifetimes, 133
- resonance energy, 132
- surface defects, 133
- surface-volume ratio, 131–132
- types, 130
- Protected nanoparticles. *See* Passivated nanoparticles
- S**
- Second moment approximation (SMA), 219–220
- Segregation transition, Cu-Ag nanoalloys
 - chiral structures, 233
 - dynamical equilibrium, 230, 232
 - energy filtered imaging, 227–228
 - facets, 230–231
 - isotherms, 229–230
 - surface phenomena, 227
 - types of inhomogeneous sites, 227–228
 - types of surface sites, 230–231
- Shake move, 201
- Shell move, 201
- Short-range magnetic order (SRMO), transition-metal clusters, 176–177
- Size control
 - on kinetic effects
 - critical cluster, 334–335
 - focusing and defocusing effects, 332–334
 - on thermodynamic effects
 - bimetallic nanoparticles, 335–341
 - capped nanoparticle stability, 343–346
 - ligand-assisted growth, 341–343
- Spherical particles, optical properties, 125–127
- Spin-fluctuation theory
 - d-level energies and Coulomb integrals, 163
 - Hamiltonian, 162
 - low-temperature limits
 - collective fluctuations, 174
 - Fe_N clusters, 168–173
 - Ni_N clusters, 173–175
 - probability, 167–168
 - thermal fluctuations, 175
 - Monte Carlo simulations
 - average magnetization, 179–181
 - bond-length relaxation effects, 186–188
 - local densities of states (DOS), 178
 - local moments and spin correlations, 181–186
 - partition function and properties
 - effective Hamiltonian, 164
 - exchange-field configuration, 165
 - functional-integral formalism, 163
 - local magnetizations, 166
 - temperature fluctuations, 167
 - thermodynamic properties, 164
- short-range magnetic order (SRMO), 176–177
- Statistical models, nanoalloys
 - configuration exchange, 222
 - molecular dynamics and Monte Carlo simulations, 220
 - parallel tempering method, 221
 - structural transition, 221
- Superatoms, close shell, 98
- T**
- Thermodynamic modeling
 - electrochemical nucleation
 - energetic contribution, nanoparticle growth, 327–328
 - Gibbs free energy, 325
 - layer-by-layer growth characteristics, 328
 - monotonically growing behavior, 327
 - nanoparticle in solution, 324
 - overpotential, 329
 - pictorial representation, 325
 - potential difference, 326
 - schematic representation, 323–324
 - stability limits, 329
 - undersaturation and supersaturation, 328–329
 - free energy, metal nanoparticles, 322–323
- Hill and Chamberlin metastability model
 - chemical potential and temperature, 318
 - partition function, 314
 - phase transition, kinetic hindrance, 316–317
 - probability density, 316–317
 - surface component, 315–316
- nanothermodynamics
 - energy fluctuations, 309
 - icosahedral arrangement, 309
 - intensive and extensive variables, 311
 - phase transitions, 313–314
 - statistical mechanics and quantum mechanics, 310
 - subdivision potential, 312–313
 - surface effects, 311
- nucleation theorems, 318–319
- size control (*see* Size control)
- size distribution, nanoparticles
 - chemical potential, 321
 - ideal gas mixtures, 321
 - mass balance, 320

- Thermodynamic modeling (*cont.*)
 partition function, 319
 three-atom arrangement configurations,
 319–320
- Tight-binding Ising model (TBIM), 218–219
- Tight-binding (TB) method, metal nanoclusters
 density functional tight-binding (DFTB),
 111–114
 Hückel method, 109
 linear combination of atomic orbitals
 (LCAO), 110
 semiempirical, noble metals, 114–115
 transferability, 110
 two-and three-center integrals, 110–111
- Transition-metal clusters. *See* Spin-fluctuation
 theory
- Transmission electron microscope (TEM)
 aberrations, 7–8
 Bloch wave approximation, 10
 contrast transfer functions (CTF), 7–8
 gold-palladium nanoparticle, 4
 HAADF-STEM, 9–10
 image interpretation (*see* Image
 interpretation, electron microscope)
 multislice method, 11–12
 schematic diagram, 5–6
 STEM intensity dependence, 12–14
 WPO approximation, 10
- W**
Weak phase object (WPO) approximation, 10